



NAVAL POSTGRADUATE SCHOOL

MONTEREY, CALIFORNIA

DISSERTATION

**MODELING STUDIES OF THE COASTAL/LITTORAL
CURRENT SYSTEM OFF SOUTHERN AUSTRALIA**

by

Henry A. Miller

December 2006

Dissertation Supervisor:

Mary L. Batten

Approved for public release; distribution is unlimited.

THIS PAGE INTENTIONALLY LEFT BLANK

REPORT DOCUMENTATION PAGE
Form Approved OMB No. 0704-0188

Public reporting burden for this collection of information is estimated to average 1 hour per response, including the time for reviewing instruction, searching existing data sources, gathering and maintaining the data needed, and completing and reviewing the collection of information. Send comments regarding this burden estimate or any other aspect of this collection of information, including suggestions for reducing this burden, to Washington headquarters Services, Directorate for Information Operations and Reports, 1215 Jefferson Davis Highway, Suite 1204, Arlington, VA 22202-4302, and to the Office of Management and Budget, Paperwork Reduction Project (0704-0188) Washington DC 20503.

1. AGENCY USE ONLY (Leave blank)	2. REPORT DATE December 2006	3. REPORT TYPE AND DATES COVERED Dissertation
4. TITLE AND SUBTITLE:) Modeling Studies of the Coastal/Littoral Current System off Southern Australia		5. FUNDING NUMBERS
6. AUTHOR(S) Henry A. Miller		
7. PERFORMING ORGANIZATION NAME(S) AND ADDRESS(ES) Naval Postgraduate School Monterey, CA 93943-5000		8. PERFORMING ORGANIZATION REPORT NUMBER
9. SPONSORING / MONITORING AGENCY NAME(S) AND ADDRESS(ES) N/A		10. SPONSORING / MONITORING AGENCY REPORT NUMBER
11. SUPPLEMENTARY NOTES The views expressed in this thesis are those of the author and do not reflect the official policy or position of the Department of Defense or the U.S. Government.		
12a. DISTRIBUTION / AVAILABILITY STATEMENT Approved for public release; distribution is unlimited.	12b. DISTRIBUTION CODE	

13. ABSTRACT (maximum 200 words)

Both theoretical and numerical modeling studies of the current system off western and southern Australia are conducted to characterize the features of the current system, their temporal variability, and their impact on the sound speed structure. The theoretical study examines why boundary current separation occurs off Cape Leeuwin creating an area of enhanced eddy generation. It is shown that the beta effect, vortex stretching, and streamline curvature all act to decelerate the current and to thus enhance separation. The current is then turned left under the influence of Coriolis force and subsequently forms meanders which then detach from the current as eddies.

The model results, using the Princeton Ocean Model (POM), reproduce the main features of the current system. They also provide insight into the generation of the main features. In particular, the current direction is caused by the thermohaline gradient, while topography is responsible for the location of the current along the shelf break. Current speed results from a combination of thermohaline gradient, the opposing wind, and topography, while meanders and eddies result from the opposition of the thermohaline and wind forcing. The gyre and upwelling in the Great Australian Bight are caused by the change in wind direction in summer.

Daily wind experiments are shown to capture the seasonal variability of the current system with the Leeuwin Current along the western coast stronger in winter than in summer and mesoscale activity highest in summer. Seasonal and interannual variability are highlighted with the gyre and upwelling in the bight and along Kangaroo Island appearing intermittently but always in summer. Lastly mesoscale features in the current system, advection of water by the surface current and undercurrent, eddies, and upwelling are all shown to cause significant changes in sound speed which can adversely affect sonar operations.

14. SUBJECT TERMS Leeuwin Current System, Ocean Modeling, Princeton Ocean Model, POM, eddy, mesoscale, Great Australian Bight, Australia, boundary current separation		15. NUMBER OF PAGES 430	
16. PRICE CODE			
17. SECURITY CLASSIFICATION OF REPORT Unclassified	18. SECURITY CLASSIFICATION OF THIS PAGE Unclassified	19. SECURITY CLASSIFICATION OF ABSTRACT Unclassified	20. LIMITATION OF ABSTRACT UL

THIS PAGE INTENTIONALLY LEFT BLANK

Approved for public release; distribution is unlimited.

**MODELING STUDIES OF THE COASTAL/LITTORAL CURRENT SYSTEM
OFF SOUTHERN AUSTRALIA**

Henry A. Miller
Commander, United States Navy
B.S., U. S. Naval Academy, 1990
M.S., Naval Postgraduate School, 2001

Submitted in partial fulfillment of the
requirements for the degree of

DOCTOR OF PHILOSOPHY IN PHYSICAL OCEANOGRAPHY
from the

NAVAL POSTGRADUATE SCHOOL
December 2006

Author:

Henry A. Miller

Approved by:

Mary Batten
Professor of Oceanography
Dissertation Supervisor

Terry Williams
Professor Emeritus
of Meteorology

Timour Radko
Assistant Professor
of Oceanography

Robin Tokmakian
Research Associate Professor
of Oceanography

Henry Jones
Permanent Military Professor
of Oceanography, U. S. Naval Academy

Approved by:

Mary Batten, Chair, Department of Oceanography

Approved by:

Julie Filizetti, Associate Provost for Academic Affairs

THIS PAGE INTENTIONALLY LEFT BLANK

ABSTRACT

Both theoretical and numerical modeling studies of the current system off western and southern Australia are conducted to characterize the features of the current system, their temporal variability, and their impact on the sound speed structure. The theoretical study examines why boundary current separation occurs off Cape Leeuwin creating an area of enhanced eddy generation. It is shown that the beta effect, vortex stretching, and streamline curvature all act to decelerate the current and to thus enhance separation. The current is then turned left under the influence of Coriolis force and subsequently forms meanders which then detach from the current as eddies.

The model results, using the Princeton Ocean Model (POM), reproduce the main features of the current system. They also provide insight into the generation of the main features. In particular, the current direction is caused by the thermohaline gradient, while topography is responsible for the location of the current along the shelf break. Current speed results from a combination of thermohaline gradient, the opposing wind, and topography, while meanders and eddies result from the opposition of the thermohaline and wind forcing. The gyre and upwelling in the Great Australian Bight are caused by the change in wind direction in summer.

Daily wind experiments are shown to capture the seasonal variability of the current system with the Leeuwin Current along the western coast stronger in winter than in summer and mesoscale activity highest in summer. Seasonal and interannual variability are highlighted with the gyre and upwelling in the bight and along Kangaroo Island appearing intermittently but always in summer. Lastly mesoscale features in the current system, advection of water by the surface current and undercurrent, eddies, and upwelling are all shown to cause significant changes in sound speed which can adversely affect sonar operations.

THIS PAGE INTENTIONALLY LEFT BLANK

TABLE OF CONTENTS

I.	INTRODUCTION.....	1
II.	MODEL DESCRIPTION.....	7
A.	DATA SETS	8
B.	PRE-PROCESSING	9
C.	INITIALIZATION, FORCING AND BOUNDARY CONDITIONS	11
III.	BOUNDARY CURRENT SEPARATION	15
A.	THEORETICAL DEVELOPMENT	15
1.	Theory	16
2.	Development of Scaled Approximation	18
3.	Estimations of the Critical Streamline Radius of Curvature.....	20
B.	COMPARISON OF THEORETICAL RESULTS WITH MODEL RUNS.....	21
C.	DYNAMICAL ANALYSES	22
1.	Eulerian Analysis	22
2.	Lagrangian Analysis	23
D.	SUMMARY OF BOUNDARY CURRENT SEPARATION RESULTS ..	26
IV.	PROCESS-ORIENTED EXPERIMENTS	29
A.	WIND FORCING OVER A FLAT BOTTOM	29
B.	WIND FORCING OVER TOPOGRAPHY	32
C.	THERMOHALINE FORCING OVER A FLAT BOTTOM.....	37
D.	THERMOHALINE FORCING OVER TOPOGRAPHY	40
E.	WIND AND THERMOHALINE FORCING OVER A FLAT BOTTOM.....	44
F.	WIND AND THERMOHALINE FORCING OVER TOPOGRAPHY ..	48
G.	SEASONAL WIND (JANUARY) AND THERMOHALINE FORCING OVER TOPOGRAPHY	53
H.	SEASONAL WIND (JULY) AND THERMOHALINE FORCING OVER TOPOGRAPHY	57
I.	SUMMARY OF PROCESS-ORIENTED EXPERIMENT RESULTS	60
V.	DAILY WIND EXPERIMENTS	69
A.	JANUARY DAILY ECMWF WIND FORCING	70
B.	JULY DAILY ECMWF WIND FORCING	73
C.	JANUARY DAILY NOGAPS WIND FORCING	76
D.	JULY DAILY NOGAPS WIND FORCING	83
E.	SUMMARY OF DAILY WIND RESULTS	86
VI.	EFFECTS OF THE CURRENT SYSTEM FEATURES ON SOUND SPEED STRUCTURE.....	91
A.	WARM CORE EDDY	93
B.	POLEWARD ADVECTION OF WARM WATER	93
C.	UPWELLING IN THE GREAT AUSTRALIAN BIGHT	94

D. UPWELLING SOUTH OF KANGAROO ISLAND	95
E. SUMMARY OF ACOUSTIC RESULTS	95
VII. SUMMARY AND CONCLUSIONS	97
A. SUMMARY	97
B. CONCLUSIONS	111
LIST OF REFERENCES	113
APPENDIX. TABLES AND FIGURES.....	119
INITIAL DISTRIBUTION LIST	399

LIST OF FIGURES

Figure 1.1. Geographical names for locations in the study area.....	126
Figure 1.2. System of naming the currents and undercurrents off the western and southern coasts of Australia presented by Ridgway and Condie (2004).	127
Figure 2.1a. The model domain used for Chapter III experiments extends from 24.5°S to 39°S and from 109°E to 121°E.....	128
Figure 2.1b. The model domain used for Chapter IV through VI experiments extends from 22.5°S to 40°S and from 107.5°E to 142.5°E.	129
Figure 2.2a. The topography for Chapter III experiments was first smoothed with a Gaussian filter using a weighted average of 25 by 25 points and a standard deviation of eight, then all depths greater than 2500 m were reassigned a depth of 2500m.	130
Figure 2.2b. The topography for experiments in Chapters IV through VI was first smoothed with a one-dimensional direct-iterative smoothing method, then all depths greater than 2500 m were reassigned a depth of 2500m.	131
Figure 2.3a. Annual climatological surface temperature (°C) obtained from Levitus and Boyer (1994) used in Chapter III experiments.	132
Figure 2.3b. Annual climatological surface temperature (°C) obtained from Levitus and Boyer (1994) used in Chapter IV annual forcing experiments.	133
Figure 2.3c. January climatological surface temperature (°C) obtained from Levitus and Boyer (1994) used in Experiment 7 of Chapter IV.....	134
Figure 2.3d. July climatological surface temperature (°C) obtained from Levitus and Boyer (1994) used in Experiment 8 of Chapter IV.....	135
Figure 2.4a. Annual climatological surface salinity obtained from Levitus and Boyer (1994) used in Chapter III experiments.	136
Figure 2.4b. Annual climatological surface salinity obtained from Levitus and Boyer (1994) used in Chapter IV annual forcing experiments.....	137
Figure 2.4c. January climatological surface salinity obtained from Levitus and Boyer (1994) used in Experiment 7 of Chapter IV.....	138
Figure 2.4d. July climatological surface salinity obtained from Levitus and Boyer (1994) used in Experiment 8 of Chapter IV.	139
Figure 2.5a. Annual average wind in m/s from climatological ECMWF winds obtained from Trenberth et al., 1990 used in Chapter III experiments.....	140
Figure 2.5b. Annual average wind in m/s from climatological ECMWF winds obtained from Trenberth et al., 1990 used in Experiments 1, 2, 5, and 6 of Chapter IV.	141
Figure 2.5c. January average wind in m/s from climatological ECMWF winds obtained from Trenberth et al., 1990 used in Experiment 7 of Chapter IV.	142
Figure 2.5d. July average wind in m/s from climatological ECMWF winds obtained from Trenberth et al., 1990 used in Experiment 8 of Chapter IV.....	143
Figure 3.1a. Surface velocity vectors and color-shaded sea surface temperature for day 20 for the flat-bottom model run.....	144

Figure 3.1b. Surface velocity vectors and color-shaded sea surface temperature for day 40 for the flat-bottom model run.....	145
Figure 3.1c. Surface velocity vectors and color-shaded sea surface temperature for day 60 for the flat-bottom model run.....	146
Figure 3.2a. Surface velocity vectors and color-shaded sea surface temperature for day 20 for the model run with topography. The solid line depicts the 200 m isobath, the approximate location of the shelf break.	147
Figure 3.2b. Surface velocity vectors and color-shaded sea surface temperature for day 40 for the model run with topography). The solid line depicts the 200 m isobath, the approximate location of the shelf break.	148
Figure 3.2c. Surface velocity vectors and color-shaded sea surface temperature for day 60 for the model run with topography. The solid line depicts the 200 m isobath, the approximate location of the shelf break.	149
Figure 3.3a. Surface velocity vectors depicting the Leeuwin Current approaching and rounding Cape Leeuwin at day 20 for the flat bottom model run. The red circles which are numbered in red show the locations of the analysis points used in the Lagrangian dynamical analysis.	150
Figure 3.3b. Surface velocity vectors depicting the Leeuwin Current approaching and rounding Cape Leeuwin at day 40 for the flat bottom model run. The red circles which are numbered in red show the locations of the analysis points used in the Lagrangian dynamical analysis.	151
Figure 3.3c. Surface velocity vectors depicting the Leeuwin Current approaching and rounding Cape Leeuwin at day 60 for the flat bottom model run. The red circles which are numbered in red show the locations of the analysis points used in the Lagrangian dynamical analysis.	152
Figure 3.4a. Surface velocity vectors depicting the Leeuwin Current approaching and rounding Cape Leeuwin at day 20 for the smoothed topography model run. The red circles which are numbered in red show the locations of the analysis points used in the Lagrangian dynamical analysis. The solid line depicts the 200 m isobath, the approximate location of the shelf break.....	153
Figure 3.4b. Surface velocity vectors depicting the Leeuwin Current approaching and rounding Cape Leeuwin at day 40 for the smoothed topography model run. The red circles which are numbered in red show the locations of the analysis points used in the Lagrangian dynamical analysis. The solid line depicts the 200 m isobath, the approximate location of the shelf break.....	154
Figure 3.4c. Surface velocity vectors depicting the Leeuwin Current approaching and rounding Cape Leeuwin at day 60 for the smoothed topography model run. The red circles which are numbered in red show the locations of the analysis points used in the Lagrangian dynamical analysis. The solid line depicts the 200 m isobath, the approximate location of the shelf break.....	155
Figure 4.1. Sea surface temperature (°C) and velocity vectors for Experiment 1 on day 20.....	156
Figure 4.2a. Sea surface temperature (°C) and velocity vectors for Experiment 1 on day 30.....	157

Figure 4.2b. Cross-section of meridional velocity component (m s^{-1}) at 26°S for Experiment 1 on day 30. Red is equatorward (north) and blue is poleward (south). The white contour is zero.	158
Figure 4.2c. Cross-section of meridional velocity component (m s^{-1}) near Cape Leeuwin (34°S) for Experiment 1 on day 30. Red is equatorward (north) and blue is poleward (south). The white contour is zero.	159
Figure 4.2d. Cross-section of temperature ($^\circ\text{C}$) along an east-west transect at 26°S for Experiment 1 on day 30.	160
Figure 4.2e. Cross-section of temperature ($^\circ\text{C}$) along an east-west transect near Cape Leeuwin (34°S) for Experiment 1 on day 30.	161
Figure 4.2f. Cross-section of temperature ($^\circ\text{C}$) along an north-south transect at 117°E for Experiment 1 on day 30.	162
Figure 4.3a. Sea surface temperature ($^\circ\text{C}$) and velocity vectors for Experiment 1 on day 60.	163
Figure 4.3b. Cross-section of meridional velocity component (m s^{-1}) at 26°S for Experiment 1 on day 60. Red is equatorward (north) and blue is poleward (south). The white contour is zero.	164
Figure 4.3c. Cross-section of temperature ($^\circ\text{C}$) along an east-west transect at 26°S for Experiment 1 on day 60.	165
Figure 4.3d. Cross-section of meridional velocity component (m s^{-1}) near Cape Leeuwin (34°S) for Experiment 1 on day 60. Red is equatorward (north) and blue is poleward (south). The white contour is zero.	166
Figure 4.3e. Cross-section of temperature ($^\circ\text{C}$) along an east-west transect near Cape Leeuwin (34°S) for Experiment 1 on day 60.	167
Figure 4.3f. Cross-section of zonal velocity component (m s^{-1}) at 117°E for Experiment 1 on day 60. Red is eastward and blue is westward. The white contour is zero.	168
Figure 4.3g. Cross-section of temperature ($^\circ\text{C}$) along an north-south transect at 117°E for Experiment 1 on day 60.	169
Figure 4.3h. Cross-section of zonal velocity component (m s^{-1}) in the Great Australian Bight (130°E) for Experiment 1 on day 60. Red is eastward and blue is westward. The white contour is zero.	170
Figure 4.3i. Cross-section of temperature ($^\circ\text{C}$) along an north-south transect in the Great Australian Bight (130°E) for Experiment 1 on day 60.	171
Figure 4.4. Sea surface temperature ($^\circ\text{C}$) and velocity vectors for Experiment 2 on day 20.	172
Figure 4.5a. Sea surface temperature ($^\circ\text{C}$) and velocity vectors for Experiment 2 on day 30.	173
Figure 5b. Cross-section of meridional velocity component (m s^{-1}) at 26°S for Experiment 2 on day 30. Red is equatorward (north) and blue is poleward (south). The white contour is zero.	174
Figure 4.5c. Cross-section of meridional velocity component (m s^{-1}) near Cape Leeuwin (34°S) for Experiment 2 on day 30. Red is equatorward (north) and blue is poleward (south). The white contour is zero.	175
Figure 4.5d. Cross-section of temperature ($^\circ\text{C}$) along an east-west transect at 26°S for Experiment 2 on day 30.	176

Figure 4.5e. Cross-section of temperature (°C) along an east-west transect at 29.4°S for Experiment 2 on day 30.....	177
Figure 4.5f. Cross-section of temperature (°C) near Cape Leeuwin (34°S) for Experiment 2 on day 30.....	178
Figure 4.5g. Cross-section of zonal velocity component ($m s^{-1}$) in the Great Australian Bight (130°E) for Experiment 2 on day 30. Red is eastward and blue is westward. The white contour is zero.....	179
Figure 4.5h. Cross-section of zonal velocity component ($m s^{-1}$) at 117°E for Experiment 2 on day 30. Red is eastward and blue is westward. The white contour is zero.....	180
Figure 4.6a. Sea surface temperature (°C) and velocity vectors for Experiment 2 on day 60.....	181
Figure 4.6b. Cross-section of meridional velocity component ($m s^{-1}$) at 26°S for Experiment 2 on day 60. Red is equatorward (north) and blue is poleward (south). The white contour is zero.....	182
Figure 4.6c. Cross-section of meridional velocity component ($m s^{-1}$) near Cape Leeuwin (34°S) for Experiment 2 on day 60. Red is equatorward (north) and blue is poleward (south). The white contour is zero.....	183
Figure 4.6d. Cross-section of temperature (°C) along an east-west transect at 26°S for Experiment 2 on day 60.....	184
Figure 4.6e. Cross-section of temperature (°C) along an east-west transect near Cape Leeuwin (34°S) for Experiment 2 on day 60.....	185
Figure 4.6f. Cross-section of zonal velocity component ($m s^{-1}$) in the Great Australian Bight (130°E) for Experiment 2 on day 60. Red is eastward and blue is westward. The white contour is zero.....	186
Figure 4.6g. Cross-section of zonal velocity component ($m s^{-1}$) at 117°E for Experiment 2 on day 60. Red is eastward and blue is westward. The white contour is zero.....	187
Figure 4.6h. Cross-section of temperature (°C) along an north-south transect in the western Great Australian Bight (125°E) for Experiment 2 on day 60.....	188
Figure 4.7a. Sea surface temperature (°C) and velocity vectors for Experiment 3 on day 20.....	189
Figure 4.7b. Cross-section of meridional velocity component ($m s^{-1}$) near Cape Leeuwin (34°S) for Experiment 3 on day 20. Red is equatorward (north) and blue is poleward (south). The white contour is zero.....	190
Figure 4.8a. Sea surface temperature (°C) and velocity vectors for Experiment 3 on day 30.....	191
Figure 4.8b. Cross-section of temperature (°C) along an east-west transect near Cape Leeuwin (34°S) for Experiment 3 on day 30.....	192
Figure 4.8c. Cross-section of meridional velocity component ($m s^{-1}$) near Cape Leeuwin (34°S) for Experiment 3 on day 30. Red is equatorward (north) and blue is poleward (south). The white contour is zero.....	193
Figure 4.8d. Cross-section of temperature (°C) along an north-south transect in the Great Australian Bight (130°E) for Experiment 3 on day 30.....	194

Figure 4.8e. Cross-section of zonal velocity component (m s^{-1}) at 117°E for Experiment 3 on day 30. Red is eastward and blue is westward. The white contour is zero.....	195
Figure 4.9. Sea surface temperature (°C) and velocity vectors for Experiment 3 on day 60.....	196
Figure 4.10. Sea surface temperature (°C) and velocity vectors for Experiment 3 on day 81.....	197
Figure 4.11a. Sea surface temperature (°C) and velocity vectors for Experiment 4 on day 20.....	198
Figure 4.11b. Cross-section of meridional velocity component (m s^{-1}) at 26°S for Experiment 4 on day 20. Red is equatorward (north) and blue is poleward (south). The white contour is zero.	199
Figure 4.11c. Cross-section of meridional velocity component (m s^{-1}) near Cape Leeuwin (34°S) for Experiment 4 on day 20. Red is equatorward (north) and blue is poleward (south). The white contour is zero.	200
Figure 4.11d. Cross-section of zonal velocity component (m s^{-1}) in the Great Australian Bight (130°E) for Experiment 4 on day 20. Red is eastward and blue is westward. The white contour is zero.	201
Figure 4.11e. Cross-section of temperature (°C) along an north-south transect at 117°E for Experiment 4 on day 20.	202
Figure 4.11f. Cross-section of temperature (°C) along an north-south transect in the Great Australian Bight (130°E) for Experiment 4 on day 20.....	203
Figure 4.12a. Sea surface temperature (°C) and velocity vectors for Experiment 4 on day 30.....	204
Figure 4.12b. Cross-section of meridional velocity component (m s^{-1}) at 26°S for Experiment 4 on day 30. Red is equatorward (north) and blue is poleward (south). The white contour is zero.	205
Figure 4.12c. Cross-section of meridional velocity component (m s^{-1}) near Cape Leeuwin (34°S) for Experiment 4 on day 30. Red is equatorward (north) and blue is poleward (south). The white contour is zero.	206
Figure 4.12d. Cross-section of temperature (°C) along an east-west transect at 26°S for Experiment 4 on day 30.	207
Figure 4.12e. Cross-section of zonal velocity component (m s^{-1}) at 117°E for Experiment 4 on day 30. Red is eastward and blue is westward. The white contour is zero.....	208
Figure 4.12f. Cross-section of zonal velocity component (m s^{-1}) in the Great Australian Bight (130°E) for Experiment 4 on day 30. Red is eastward and blue is westward. The white contour is zero.	209
Figure 4.12g. Cross-section of temperature (°C) along an north-south transect in the eastern Great Australian Bight (134.5°E) for Experiment 4 on day 30.	210
Figure 4.12h. Cross-section of temperature (°C) along an north-south transect at 117°E for Experiment 4 on day 30.	211
Figure 4.12i. Cross-section of temperature (°C) along an north-south transect in the Great Australian Bight (130°E) for Experiment 4 on day 30.....	212
Figure 4.15a. Sea surface temperature (°C) and velocity vectors for Experiment 5 on day 20.....	215

Figure 4.15b. Cross-section of meridional velocity component (m s^{-1}) at 26°S for Experiment 5 on day 20. Red is equatorward (north) and blue is poleward (south). The white contour is zero.	216
Figure 4.15c. Cross-section of meridional velocity component (m s^{-1}) near Cape Leeuwin (34°S) for Experiment 5 on day 20. Red is equatorward (north) and blue is poleward (south). The white contour is zero.	217
Figure 4.15d. Cross-section of temperature ($^\circ\text{C}$) along an north-south transect at 117°E for Experiment 5 on day 20.	218
Figure 4.15e. Cross-section of zonal velocity component (m s^{-1}) in the Great Australian Bight (130°E) for Experiment 5 on day 20. Red is eastward and blue is westward. The white contour is zero.	219
Figure 4.15f. Cross-section of temperature ($^\circ\text{C}$) along an north-south transect at 117°E for Experiment 5 on day 20.	220
Figure 4.15g. Cross-section of temperature ($^\circ\text{C}$) along an north-south transect in the Great Australian Bight (130°E) for Experiment 5 on day 20.	221
Figure 4.16a. Sea surface temperature ($^\circ\text{C}$) and velocity vectors for Experiment 5 on day 30.	222
Figure 4.16b. Cross-section of zonal velocity component (m s^{-1}) at 117°E for Experiment 5 on day 30. Red is eastward and blue is westward. The white contour is zero.	223
Figure 4.16c. Cross-section of zonal velocity component (m s^{-1}) in the Great Australian Bight (130°E) for Experiment 5 on day 30. Red is eastward and blue is westward. The white contour is zero.	224
Figure 4.17. Sea surface temperature ($^\circ\text{C}$) and velocity vectors for Experiment 5 on day 45.	226
Figure 4.18. Sea surface temperature ($^\circ\text{C}$) and velocity vectors for Experiment 5 on day 60.	227
Figure 4.19. Sea surface temperature ($^\circ\text{C}$) and velocity vectors for Experiment 5 on day 72.	228
Figure 4.20a. Sea surface temperature ($^\circ\text{C}$) and velocity vectors for Experiment 6 on day 20.	229
Figure 4.20b. Cross-section of meridional velocity component (m s^{-1}) at 26°S for Experiment 6 on day 20. Red is equatorward (north) and blue is poleward (south). The white contour is zero.	230
Figure 4.20c. Cross-section of meridional velocity component (m s^{-1}) near Cape Leeuwin (34°S) for Experiment 1 on day 60. Red is equatorward (north) and blue is poleward (south). The white contour is zero.	231
Figure 4.20d. Cross-section of zonal velocity component (m s^{-1}) at 117°E for Experiment 6 on day 20. Red is eastward and blue is westward. The white contour is zero.	232
Figure 4.20e. Cross-section of zonal velocity component (m s^{-1}) in the Great Australian Bight (130°E) for Experiment 6 on day 20. Red is eastward and blue is westward. The white contour is zero.	233
Figure 4.20f. Sea surface salinity for Experiment 6 on day 20.	234
Figure 4.20g. Cross-section of temperature ($^\circ\text{C}$) along an north-south transect in the eastern Great Australian Bight (134.5°E) for Experiment 6 on day 20.	235

Figure 4.21a. Sea surface temperature (°C) and velocity vectors for Experiment 6 on day 30.....	236
Figure 4.21b. Cross-section of meridional velocity component (m s ⁻¹) near Cape Leeuwin (34°S) for Experiment 6 on day 30. Red is equatorward (north) and blue is poleward (south). The white contour is zero.....	237
Figure 4.21c. Cross-section of meridional velocity component (m s ⁻¹) at 26°S for Experiment 6 on day 30. Red is equatorward (north) and blue is poleward (south). The white contour is zero.....	238
Figure 4.21d. Cross-section of temperature (°C) along an east-west transect at 26°S for Experiment 6 on day 30.....	239
Figure 4.21e. Cross-section of zonal velocity component (m s ⁻¹) at 117°E for Experiment 6 on day 30. Red is eastward and blue is westward. The white contour is zero.....	240
Figure 4.21f. Cross-section of zonal velocity component (m s ⁻¹) in the Great Australian Bight (130°E) for Experiment 6 on day 30. Red is eastward and blue is westward. The white contour is zero.....	241
Figure 4.21g. Sea surface salinity for Experiment 6 on day 30.....	242
Figure 4.21h. Cross-section of temperature (°C) along an north-south transect at 117°E for Experiment 6 on day 30.....	243
Figure 4.21i. Cross-section of temperature (°C) along an north-south transect in the Great Australian Bight (130°E) for Experiment 6 on day 30.....	244
Figure 4.21j. Cross-section of temperature (°C) along an north-south transect in the eastern Great Australian Bight (134.5°E) for Experiment 6 on day 30.....	245
Figure 4.22. Sea surface salinity for Experiment 6 on day 42.....	246
Figure 4.23. Sea surface temperature (°C) and velocity vectors for Experiment 6 on day 51.....	247
Figure 4.24a. Sea surface temperature (°C) and velocity vectors for Experiment 6 on day 60.....	248
Figure 4.24b. Cross-section of temperature (°C) along an east-west transect at 30°S for Experiment 6 on day 60.....	249
Figure 4.24c. Cross-section of meridional velocity component (m s ⁻¹) near Cape Leeuwin (34.5°S) for Experiment 6 on day 60. Red is equatorward (north) and blue is poleward (south). The white contour is zero.....	250
Figure 4.24d. Cross-section of zonal velocity component (m s ⁻¹) in the Great Australian Bight (130°E) for Experiment 6 on day 60. Red is eastward and blue is westward. The white contour is zero.....	251
Figure 4.24e. Cross-section of zonal velocity component (m s ⁻¹) at 117°E for Experiment 6 on day 60. Red is eastward and blue is westward. The white contour is zero.....	252
Figure 4.24f. Cross-section of temperature (°C) along an north-south transect in the eastern Great Australian Bight (134.5°E) for Experiment 6 on day 60.....	253
Figure 4.25. Sea surface temperature (°C) and velocity vectors for Experiment 6 on day 75.....	254
Figure 4.26a. Sea surface temperature (°C) and velocity vectors for Experiment 7 on day 20.....	255

Figure 4.26b. Cross-section of meridional velocity component (m s^{-1}) at 26°S for Experiment 7 on day 20. Red is equatorward (north) and blue is poleward (south). The white contour is zero.	256
Figure 4.26c. Cross-section of meridional velocity component (m s^{-1}) near Cape Leeuwin (34°S) for Experiment 7 on day 30. Red is equatorward (north) and blue is poleward (south). The white contour is zero.	257
Figure 4.26d. Cross-section of zonal velocity component (m s^{-1}) at 117°E for Experiment 7 on day 20. Red is eastward and blue is westward. The white contour is zero.	258
Figure 4.26e. Cross-section of zonal velocity component (m s^{-1}) in the Great Australian Bight (130°E) for Experiment 7 on day 20. Red is eastward and blue is westward. The white contour is zero.	259
Figure 4.27a. Sea surface temperature (°C) and velocity vectors for Experiment 7 on day 30.	260
Figure 4.27b. Cross-section of zonal velocity component (m s^{-1}) at 117°E for Experiment 7 on day 30. Red is eastward and blue is westward. The white contour is zero.	261
Figure 4.27c. Cross-section of zonal velocity component (m s^{-1}) in the Great Australian Bight (130°E) for Experiment 7 on day 30. Red is eastward and blue is westward. The white contour is zero.	262
Figure 27d. Sea surface temperature (°C) and velocity vectors along the southwestern coast and Great Australian Bight for Experiment 7 on day 30.	263
Figure 4.28. Sea surface temperature (°C) and velocity vectors for Experiment 7 on day 39.	264
Figure 4.29a. Sea surface temperature (°C) and velocity vectors for Experiment 7 on day 60.	265
Figure 4.29b. Sea surface temperature (°C) and velocity vectors along the southwestern coast for Experiment 7 on day 30.	266
Figure 4.29c. Cross-section of zonal velocity component (m s^{-1}) in the Great Australian Bight (130°E) for Experiment 7 on day 60. Red is eastward and blue is westward. The white contour is zero.	267
Figure 4.29d. Sea surface temperature (°C) and velocity vectors for the Great Australian Bight for Experiment 7 on day 60.	268
Figure 4.30. Sea surface temperature (°C) and velocity vectors for Experiment 7 on day 81.	269
Figure 4.31a. Sea surface temperature (°C) and velocity vectors for Experiment 8 on day 20.	270
Figure 4.31b. Cross-section of temperature (°C) along an east-west transect at 26°S for Experiment 8 on day 20.	271
Figure 4.31c. Cross-section of temperature (°C) along an east-west transect near Cape Leeuwin (34°S) for Experiment 8 on day 20.	272
Figure 4.31d. Cross-section of zonal velocity component (m s^{-1}) at 117°E for Experiment 8 on day 20. Red is eastward and blue is westward. The white contour is zero.	273

Figure 4.31e. Cross-section of zonal velocity component ($m s^{-1}$) along an north-south transect in the western Great Australian Bight ($125^{\circ}E$) for Experiment 8 on day 20. Red is eastward and blue is westward. The white contour is zero..	274
Figure 4.31f. Cross-section of zonal velocity component ($m s^{-1}$) in the Great Australian Bight ($130^{\circ}E$) for Experiment 8 on day 20. Red is eastward and blue is westward. The white contour is zero.	275
Figure 4.32a. Sea surface temperature ($^{\circ}C$) and velocity vectors for Experiment 8 on day 30.....	276
Figure 4.32b. Cross-section of meridional velocity component ($m s^{-1}$) at $26^{\circ}S$ for Experiment 8 on day 30. Red is equatorward (north) and blue is poleward (south). The white contour is zero.	277
Figure 4.32c. Cross-section of meridional velocity component ($m s^{-1}$) near Cape Leeuwin ($34^{\circ}S$) for Experiment 8 on day 30. Red is equatorward (north) and blue is poleward (south). The white contour is zero.	278
Figure 4.32d. Cross-section of zonal velocity component ($m s^{-1}$) at $117^{\circ}E$ for Experiment 8 on day 30. Red is eastward and blue is westward. The white contour is zero.....	279
Figure 4.32e. Cross-section of zonal velocity component ($m s^{-1}$) in the Great Australian Bight ($125^{\circ}E$) for Experiment 8 on day 30. Red is eastward and blue is westward. The white contour is zero.	280
Figure 4.32f. Cross-section of zonal velocity component ($m s^{-1}$) in the Great Australian Bight ($130^{\circ}E$) for Experiment 8 on day 30. Red is eastward and blue is westward. The white contour is zero.	281
Figure 4.33a. Sea surface temperature ($^{\circ}C$) and velocity vectors for Experiment 8 on day 60.....	282
Figure 4.33b. Cross-section of meridional velocity component ($m s^{-1}$) at $26^{\circ}S$ for Experiment 8 on day 60. Red is equatorward (north) and blue is poleward (south). The white contour is zero.	283
Figure 4.33c. Cross-section of meridional velocity component ($m s^{-1}$) near Cape Leeuwin ($34^{\circ}S$) for Experiment 8 on day 60. Red is equatorward (north) and blue is poleward (south). The white contour is zero.	284
Figure 4.33d. Cross-section of zonal velocity component ($m s^{-1}$) along an north-south transect in the western Great Australian Bight ($125^{\circ}E$) for Experiment 8 on day 60. Red is eastward and blue is westward. The white contour is zero..	285
Figure 4.33e. Cross-section of zonal velocity component ($m s^{-1}$) in the Great Australian Bight ($130^{\circ}E$) for Experiment 8 on day 60. Red is eastward and blue is westward. The white contour is zero.	286
Figure 4.34. Sea surface temperature ($^{\circ}C$) and velocity vectors for Experiment 8 on day 72.....	287
Figure 5.1. Sea surface temperature ($^{\circ}C$) and velocity vectors for daily wind Experiment 1 on day 20, December 21, 1980.....	288
Figure 5.2a. Sea surface temperature ($^{\circ}C$) and velocity vectors for daily wind Experiment 1 on day 30, December 31, 1980.....	289
Figure 5.2b. Cross-section of meridional velocity component ($m s^{-1}$) $33.25^{\circ}S$ for daily wind Experiment 1 on day 30, December 31, 1980. Red is equatorward (north) and blue is poleward (south). The white contour is zero.	290

Figure 5.2c. Cross-section of zonal velocity component (m s^{-1}) in the Great Australian Bight (130°E) for daily wind Experiment 1 on day 30, December 31, 1980. Red is eastward and blue is westward. The white contour is zero.....	291
Figure 5.2d. Cross-section of temperature ($^{\circ}\text{C}$) along an north-south transect in the Great Australian Bight (130°E) for daily wind Experiment 1 on day 30, December 31, 1980.....	292
Figure 5.3a. Sea surface temperature ($^{\circ}\text{C}$) and velocity vectors for daily wind Experiment 1 on day 45, January 15, 1981.....	293
Figure 5.3b. Cross-section of meridional velocity component (m s^{-1}) 33.25°S for daily wind Experiment 1 on day 45, January 15, 1981. Red is equatorward (north) and blue is poleward (south). The white contour is zero.....	294
Figure 5.3c. Cross-section of zonal velocity component (m s^{-1}) in the Great Australian Bight (130°E) for daily wind Experiment 1 on day 45, January 15, 1981. Red is eastward and blue is westward. The white contour is zero.....	295
Figure 5.3d. Cross-section of temperature ($^{\circ}\text{C}$) along an north-south transect in the Great Australian Bight (130°E) for daily wind Experiment 1 on day 45, January 15, 1981.....	296
Figure 5.4a. Sea surface temperature ($^{\circ}\text{C}$) and velocity vectors for daily wind Experiment 1 on day 60, January 30, 1981.....	297
Figure 5.4b. Cross-section of meridional velocity component (m s^{-1}) 33.25°S for daily wind Experiment 1 on day 60, January 30, 1981. Red is equatorward (north) and blue is poleward (south). The white contour is zero.....	298
Figure 5.4c. Cross-section of zonal velocity component (m s^{-1}) in the Great Australian Bight (130°E) for daily wind Experiment 1 on day 60, January 30, 1981. Red is eastward and blue is westward. The white contour is zero.....	299
Figure 5.4d. Cross-section of temperature ($^{\circ}\text{C}$) along an north-south transect in the Great Australian Bight (130°E) for daily wind Experiment 1 on day 60, January 30, 1981.....	300
Figure 5.5. Sea surface temperature ($^{\circ}\text{C}$) and velocity vectors for daily wind Experiment 2 on day 20, June 21, 1981.....	301
Figure 5.6a. Sea surface temperature ($^{\circ}\text{C}$) and velocity vectors for daily wind Experiment 2 on day 30, July 1, 1981.	302
Figure 5.6b. Cross-section of meridional velocity component (m s^{-1}) 33.25°S for daily wind Experiment 2 on day 30, July 1, 1981. Red is equatorward (north) and blue is poleward (south). The white contour is zero.	303
Figure 5.6c. Cross-section of zonal velocity component (m s^{-1}) in the Great Australian Bight (130°E) for daily wind Experiment 2 on day 30, July 1, 1981. Red is eastward and blue is westward. The white contour is zero.	304
Figure 5.6d. Cross-section of temperature ($^{\circ}\text{C}$) along an north-south transect in the Great Australian Bight (130°E) for daily wind Experiment 2 on day 30, July 1, 1981.....	305
Figure 5.7a. Sea surface temperature ($^{\circ}\text{C}$) and velocity vectors for daily wind Experiment 2 on day 45, July 16, 1981.	306
Figure 5.7b. Cross-section of meridional velocity component (m s^{-1}) 33.25°S for daily wind Experiment 2 on day 45, July 16, 1981. Red is equatorward (north) and blue is poleward (south). The white contour is zero.	307

Figure 5.7c. Cross-section of zonal velocity component (m s^{-1}) in the Great Australian Bight (130°E) for daily wind Experiment 2 on day 45, July 16, 1981. Red is eastward and blue is westward. The white contour is zero.	308
Figure 5.7d. Cross-section of temperature ($^\circ\text{C}$) along an north-south transect in the Great Australian Bight (130°E) for daily wind Experiment 2 on day 45, July 16, 1981.....	309
Figure 5.8a. Sea surface temperature ($^\circ\text{C}$) and velocity vectors for daily wind Experiment 2 on day 60, July 31, 1981.	310
Figure 5.8b. Cross-section of meridional velocity component (m s^{-1}) 33.25°S for daily wind Experiment 2 on day 60, July 31, 1981. Red is equatorward (north) and blue is poleward (south). The white contour is zero.	311
Figure 5.8c. Cross-section of zonal velocity component (m s^{-1}) in the Great Australian Bight (130°E) for daily wind Experiment 2 on day 60, July 31, 1981. Red is eastward and blue is westward. The white contour is zero.	312
Figure 5.8d. Cross-section of temperature ($^\circ\text{C}$) along an north-south transect in the Great Australian Bight (130°E) for daily wind Experiment 2 on day 60, July 31, 1981.....	313
Figure 5.9a. Sea surface temperature ($^\circ\text{C}$) and velocity vectors for daily wind Experiment 3 on day 20, December 21, 2000.....	314
Figure 5.9b. Cross-section of meridional velocity component (m s^{-1}) at 26°S for daily wind Experiment 3 on day 20, December 21, 2000. Red is equatorward (north) and blue is poleward (south). The white contour is zero.	315
Figure 5.9c. Cross-section of meridional velocity component (m s^{-1}) 33.25°S for daily wind Experiment 3 on day 20, December 21, 2000. Red is equatorward (north) and blue is poleward (south). The white contour is zero.	316
Figure 5.9d. Cross-section of zonal velocity component (m s^{-1}) at 117°E for daily wind Experiment 3 on day 30, December 31, 2000. Red is eastward and blue is westward. The white contour is zero.	317
Figure 5.10a. Sea surface temperature ($^\circ\text{C}$) and velocity vectors for daily wind Experiment 3 on day 27, December 28, 2000.....	318
Figure 5.10b. Cross-section of temperature ($^\circ\text{C}$) along an north-south transect in the Great Australian Bight (130°E) for daily wind Experiment 3 on day 27, December 28, 2000. The upper magenta contour is the 19.4°C isotherm and the lower magenta contour is the 19.2°C isotherm.....	319
Figure 5.10c. Cross-section of temperature ($^\circ\text{C}$) along an north-south transect in the eastern Great Australian Bight (134.5°E) for daily wind Experiment 3 on day 27, December 28, 2000.	320
Figure 5.11a. Sea surface temperature ($^\circ\text{C}$) and velocity vectors for daily wind Experiment 3 on day 30, December 31, 2000.....	321
Figure 5.11b. Cross-section of meridional velocity component (m s^{-1}) at 26°S for daily wind Experiment 3 on day 30, December 31, 2000. Red is equatorward (north) and blue is poleward (south). The white contour is zero.	322
Figure 5.11c. Cross-section of meridional velocity component (m s^{-1}) just north of Cape Leeuwin at 33.25°S for daily wind Experiment 3 on day 30, December 31, 2000. Red is equatorward (north) and blue is poleward (south). The white contour is zero.....	323

Figure 5.11d. Cross-section of temperature ($^{\circ}\text{C}$) along an east-west transect just north of Cape Leeuwin at 33.25°S for daily wind Experiment 3 on day 30, December 31, 2000.....	324
Figure 5.11e. Cross-section of zonal velocity component (m s^{-1}) at 117°E for daily wind Experiment 3 on day 30, December 31, 2000. Red is eastward and blue is westward. The white contour is zero.....	325
Figure 5.11f. Cross-section of zonal velocity component (m s^{-1}) in the Great Australian Bight (130°E) for daily wind Experiment 3 on day 30, December 31, 2000. Red is eastward and blue is westward. The white contour is zero.....	326
Figure 5.11g. Cross-section of temperature ($^{\circ}\text{C}$) along an north-south transect in the Great Australian Bight (130°E) for daily wind Experiment 3 on day 30, December 31, 2000.....	327
Figure 5.12a. Sea surface temperature ($^{\circ}\text{C}$) and velocity vectors for daily wind Experiment 3 on day 45, January 15, 2001.....	328
Figure 5.12b. Cross-section of meridional velocity component (m s^{-1}) at 26°S for daily wind Experiment 3 on day 45, January 15, 2001. Red is equatorward (north) and blue is poleward (south). The white contour is zero.....	329
Figure 5.12c. Cross-section of meridional velocity component (m s^{-1}) just north of Cape Leeuwin at 33.25°S for daily wind Experiment 3 on day 45, January 15, 2001. Red is equatorward (north) and blue is poleward (south). The white contour is zero.....	330
Figure 5.12d. Cross-section of temperature ($^{\circ}\text{C}$) along an east-west transect just north of Cape Leeuwin at 33.25°S for daily wind Experiment 3 on day 45, January 15, 2001.....	331
Figure 5.12e. Cross-section of zonal velocity component (m s^{-1}) at 117°E for daily wind Experiment 3 on day 45, January 15, 2001. Red is eastward and blue is westward. The white contour is zero.....	332
Figure 5.12f. Cross-section of zonal velocity component (m s^{-1}) in the Great Australian Bight (130°E) for daily wind Experiment 3 on day 45, January 15, 2001. Red is eastward and blue is westward. The white contour is zero.....	333
Figure 5.12g. Cross-section of temperature ($^{\circ}\text{C}$) along an north-south transect in the Great Australian Bight (130°E) for daily wind Experiment 3 on day 45, January 15, 2001.....	334
Figure 5.13a. Sea surface temperature ($^{\circ}\text{C}$) and velocity vectors for daily wind Experiment 3 on day 60, January 30, 2001.....	335
Figure 5.13b. Cross-section of meridional velocity component (m s^{-1}) at 26°S for daily wind Experiment 3 on day 60, January 30, 2001. Red is equatorward (north) and blue is poleward (south). The white contour is zero.....	336
Figure 5.13c. Cross-section of meridional velocity component (m s^{-1}) just north of Cape Leeuwin at 33.25°S for daily wind Experiment 3 on day 60, January 30, 2001. Red is equatorward (north) and blue is poleward (south). The white contour is zero.....	337
Figure 5.13d. Cross-section of temperature ($^{\circ}\text{C}$) along an east-west transect just north of Cape Leeuwin at 33.25°S for daily wind Experiment 3 on day 60, January 30, 2001.....	338

Figure 5.13e. Cross-section of zonal velocity component (m s^{-1}) at 117°E for daily wind Experiment 3 on day 60, January 30, 2001. Red is eastward and blue is westward. The white contour is zero.	339
Figure 5.13f. Cross-section of zonal velocity component (m s^{-1}) in the Great Australian Bight (130°E) for daily wind Experiment 3 on day 60, January 30, 2001. Red is eastward and blue is westward. The white contour is zero.	340
Figure 5.13g. Cross-section of temperature ($^\circ\text{C}$) along an north-south transect in the Great Australian Bight (130°E) for daily wind Experiment 3 on day 60, January 30, 2001.	341
Figure 5.14. Daily wind Experiment 3 close-up views of an eddy southeast of Cape Leeuwin. Black line across surface view indicates location of corresponding cross-section. a. Surface temperature ($^\circ\text{C}$) and velocity vectors, day 54 (January 24, 2001). b. Cross-section of meridional velocity component (m s^{-1}) at 36.25°S , day 54. c. Surface temperature ($^\circ\text{C}$) and velocity vectors day 57 (January 27, 2001). d. Cross-section of meridional velocity component (m s^{-1}) at 36.47°S , day 57. e. Surface temperature ($^\circ\text{C}$) and velocity vectors, day 60 (January 30, 2001). f. Cross-section of meridional velocity component (m s^{-1}) at 36.52°S , day 60. g. Surface temperature ($^\circ\text{C}$) and velocity vectors, day 63 (February 2, 2001). h. Cross-section of meridional velocity component (m s^{-1}) at 36.72°S , day 63. Note: On all cross-section figures, red is equatorward (north), blue is poleward (south), and the black contour is zero.	342
Figure 5.15a. Sea surface temperature ($^\circ\text{C}$) and velocity vectors in the Great Australian Bight for daily wind Experiment 3a on day 30, December 31, 1999.	343
Figure 5.15b. Sea surface temperature ($^\circ\text{C}$) and velocity vectors in the Great Australian Bight for daily wind Experiment 3a on day 42, January 12, 2000.	344
Figure 5.15c. Cross-section of temperature ($^\circ\text{C}$) along an north-south transect in the eastern Great Australian Bight (134.5°E) for daily wind Experiment 3a on day 42, January 12, 2000.	345
Figure 5.15d. Cross-section of temperature ($^\circ\text{C}$) along an north-south transect just east of Kangaroo Island (138.5°E) for daily wind Experiment 3a on day 42, January 12, 2000.	346
Figure 5.15e. Sea surface temperature ($^\circ\text{C}$) and velocity vectors in the Great Australian Bight for daily wind Experiment 3a on day 60, January 30, 2000.	347
Figure 5.15f. Cross-section of temperature ($^\circ\text{C}$) along an north-south transect in the eastern Great Australian Bight (134.5°E) for daily wind Experiment 3a on day 60, January 30, 2000.	348
Figure 5.15g. Cross-section of temperature ($^\circ\text{C}$) along an north-south transect just east of Kangaroo Island (138.5°E) for daily wind Experiment 3a on day 60, January 30, 2000.	349
Figure 5.16a. Multi-Channel Sea Surface Temperature (MCSST) satellite imagery for southwestern Australian coastal area for January 15, 2001. Temperatures are in $^\circ\text{C}$	350
Figure 5.16b. Multi-Channel Sea Surface Temperature (MCSST) satellite imagery for southwestern Australian coastal area for January 12, 2000. Temperatures are in $^\circ\text{C}$	351

Figure 5.17a. Sea surface temperature (°C) and velocity vectors for daily wind Experiment 4 on day 20, June 21, 2001.....	352
Figure 5.17b. Cross-section of meridional velocity component (m s ⁻¹) at 26°S for daily wind Experiment 4 on day 20, June 21, 2001. Red is equatorward (north) and blue is poleward (south). The white contour is zero.	353
Figure 5.17c. Cross-section of meridional velocity component (m s ⁻¹) 33.25°S for daily wind Experiment 4 on day 20, June 21, 2001. Red is equatorward (north) and blue is poleward (south). The white contour is zero.	354
Figure 5.17d. Cross-section of zonal velocity component (m s ⁻¹) at 117°E for daily wind Experiment 4 on day 20, June 21, 2001. Red is eastward and blue is westward. The white contour is zero.	355
Figure 5.18a. Sea surface temperature (°C) and velocity vectors for daily wind Experiment 4 on day 30, July 1, 2001.	356
Figure 5.18b. Cross-section of meridional velocity component (m s ⁻¹) at 26°S for daily wind Experiment 4 on day 30, July 1, 2001. Red is equatorward (north) and blue is poleward (south). The white contour is zero.	357
Figure 5.18c. Cross-section of meridional velocity component (m s ⁻¹) just north of Cape Leeuwin at 33.25°S for daily wind Experiment 4 on day 30, July 1, 2001. Red is equatorward (north) and blue is poleward (south). The white contour is zero.	358
Figure 5.18d. Cross-section of temperature (°C) along an east-west transect just north of Cape Leeuwin at 33.25°S for daily wind Experiment 4 on day 30, July 1, 2001.	359
Figure 5.18e. Cross-section of zonal velocity component (m s ⁻¹) at 117°E for daily wind Experiment 4 on day 30, July 1, 2001. Red is eastward and blue is westward. The white contour is zero.	360
Figure 5.18f. Cross-section of zonal velocity component (m s ⁻¹) in the Great Australian Bight (130°E) for daily wind Experiment 4 on day 30, July 1, 2001. Red is eastward and blue is westward. The white contour is zero.	361
Figure 5.18g. Cross-section of temperature (°C) along an north-south transect in the Great Australian Bight (130°E) for daily wind Experiment 4 on day 30, July 1, 2001.	362
Figure 5.19a. Sea surface temperature (°C) and velocity vectors for daily wind Experiment 4 on day 45, July 16, 2001.	363
Figure 5.19b. Cross-section of meridional velocity component (m s ⁻¹) at 26°S for daily wind Experiment 4 on day 45, July 16, 2001. Red is equatorward (north) and blue is poleward (south). The white contour is zero.	364
Figure 5.19c. Cross-section of meridional velocity component (m s ⁻¹) just north of Cape Leeuwin at 33.25°S for daily wind Experiment 4 on day 45, July 16, 2001. Red is equatorward (north) and blue is poleward (south). The white contour is zero.	365
Figure 5.19d. Cross-section of temperature (°C) along an east-west transect just north of Cape Leeuwin at 33.25°S for daily wind Experiment 4 on day 45, July 16, 2001.	366

Figure 5.19e. Cross-section of zonal velocity component (m s^{-1}) at 117°E for daily wind Experiment 4 on day 45, July 16, 2001. Red is eastward and blue is westward. The white contour is zero.	367
Figure 5.19f. Cross-section of zonal velocity component (m s^{-1}) in the Great Australian Bight (130°E) for daily wind Experiment 4 on day 45, July 16, 2001. Red is eastward and blue is westward. The white contour is zero.	368
Figure 5.19g. Cross-section of temperature (°C) along an north-south transect in the Great Australian Bight (130°E) for daily wind Experiment 4 on day 45, July 16, 2001.	369
Figure 5.20a. Sea surface temperature (°C) and velocity vectors for daily wind Experiment 4 on day 60, July 31, 2001.	370
Figure 5.20b. Cross-section of meridional velocity component (m s^{-1}) at 26°S for daily wind Experiment 4 on day 60, July 31, 2001. Red is equatorward (north) and blue is poleward (south). The white contour is zero.	371
Figure 5.20c. Cross-section of meridional velocity component (m s^{-1}) just north of Cape Leeuwin at 33.25°S for daily wind Experiment 4 on day 60, July 31, 2001. Red is equatorward (north) and blue is poleward (south). The white contour is zero.	372
Figure 5.20d. Cross-section of temperature (°C) along an east-west transect just north of Cape Leeuwin at 33.25°S for daily wind Experiment 4 on day 60, July 31, 2001.	373
Figure 5.20e. Cross-section of zonal velocity component (m s^{-1}) at 117°E for daily wind Experiment 4 on day 60, July 31, 2001. Red is eastward and blue is westward. The white contour is zero.	374
Figure 5.20f. Cross-section of zonal velocity component (m s^{-1}) in the Great Australian Bight (130°E) for daily wind Experiment 4 on day 60, July 31, 2001. Red is eastward and blue is westward. The white contour is zero.	375
Figure 5.20g. Cross-section of temperature (°C) along an north-south transect in the Great Australian Bight (130°E) for daily wind Experiment 4 on day 60, July 31, 2001.	376
Figure 5.21. Multi-Channel Sea Surface Temperature (MCSST) satellite imagery for southwestern Australian coastal area for July 31, 2001. Temperatures are in °C.	377
Figure 6.1a. Sea surface temperature (°C) and velocity vectors for daily wind Experiment 4 on day 45, July 16, 2001.	378
Figure 6.1b. Surface sound speed (m/s) and current velocity vectors for daily wind Experiment 4 on day 45, July 16, 2001.	379
Figure 6.1c. Cross-section of meridional velocity component (m s^{-1}) at 35°S for daily wind Experiment 4 on day 45, July 16, 2001. Red is equatorward (north) and blue is poleward (south). The white contour is zero.	380
Figure 6.1d. Cross-section of sound speed (m s^{-1}) at 35°S for daily wind Experiment 4 on day 45, July 16, 2001.	381
Figure 6.1e. Cross-section of sound speed (m s^{-1}) change at 35°S for daily wind Experiment 4 on day 45, July 16, 2001. Sound speed change is the difference in sound speed between Day 0 and the current day.	382

Figure 6.2a. Cross-section of zonal velocity component (m s ⁻¹) at 117°E for daily wind Experiment 4 on day 45, July 16, 2001. Red is eastward and blue is westward. The white contour is zero.	383
Figure 6.2c. Cross-section of sound speed (m s ⁻¹) at 117°E for daily wind Experiment 4 on day 45, July 16, 2001.	385
Figure 6.2d. Cross-section of sound speed (m s ⁻¹) change at 117°E for daily wind Experiment 4 on day 45, July 16, 2001. Sound speed change is the difference in sound speed between Day 0 and the current day.	386
Figure 6.3b. Cross-section of sound speed (m s ⁻¹) in the eastern Great Australian Bight (134.5°E) for daily wind Experiment 4 on day 45, July 16, 2001.	388
Figure 6.3c. Cross-section of sound speed change (m s ⁻¹) in the eastern Great Australian Bight (134.5°E) for daily wind Experiment 4 on day 45, July 16, 2001. Sound speed change is the difference in sound speed between Day 0 and the current day.	389
Figure 6.4a. Sea surface temperature (°C) and velocity vectors for daily wind Experiment 3 on day 45, January 15, 2000.	390
Figure 6.4b. Surface sound speed (m/s) and current velocity vectors for daily wind Experiment 3 on day 45, January 15, 2000.	391
Figure 6.4d. Cross-section of sound speed (m s ⁻¹) in the eastern Great Australian Bight (134.5°E) for daily wind Experiment 3 on day 45, January 15, 2000.	393
Figure 6.4e. Cross-section of sound speed change (m s ⁻¹) in the eastern Great Australian Bight (134.5°E) for daily wind Experiment 3 on day 45, January 15, 2000. Sound speed change is the difference in sound speed between Day 0 and the current day.	394
Figure 6.5b. Cross-section of sound speed (m s ⁻¹) at 138.5°E for daily wind Experiment 3 on day 45, January 15, 2000.	396
Figure 6.5c. Cross-section of sound speed change (m s ⁻¹) at 138.5°E for daily wind Experiment 3 on day 45, January 15, 2000. Sound speed change is the difference in sound speed between Day 0 and the current day.	397

LIST OF TABLES

Table 3.1. Summary of gradient and radius of curvature values for the cases of flat bottom, smoothed model topography, and the raw topography as the Leeuwin Current approaches Cape Leeuwin. Note that the curvature values for smoothed topography and raw topography are the curvature of the 100m isobath (along the path of the current).....	120
Table 3.2. Summary of separation calculations for the cases in Table 3.1.....	121
Table 3.3a. Summary of points used for Lagrangian analysis with corresponding speeds and percent change in speed in the downstream direction for flat bottom at days 20, 40, and 60.	122
Table 3.3b. Summary of points used for Lagrangian analysis with corresponding speeds and percent change in speed in the downstream direction for smoothed topography at days 20, 40, and 60.	123
Table 4.1. Summary of experimental design for process-oriented experiments showing climatology (temperature and salinity forcing), wind forcing, and bottom type for each experiment.....	124
Table 4.2. Summary of current system features and the type forcing which appears to be responsible for each feature.	125

THIS PAGE INTENTIONALLY LEFT BLANK

ACKNOWLEDGMENTS

Computing resources were provided by the Center for High Performance Computing at the Arctic Region Supercomputing Center and the Naval Oceanographic Office. I would like to thank my dissertation supervisor, Dr. Mary Batteen, for her guidance through this process. I would also like to thank the other committee members. I thank Dr. Terry Williams, who was also my master's thesis advisor, for all the guidance and encouragement over the years. Dr. Robin Tokmakian provided many insightful suggestions, all of which have improved the dissertation. Dr. Timour Radko was invaluable in helping to develop the theoretical framework for the research. CDR Henry Jones provided much valuable advise along the way, helping to ensure that the project was completed in a timely manner. In addition, Arlene Guest and Mike Cook were invaluable in helping to solve computing problems. Bob Creasey provided the winds used in the daily wind experiments and offered valuable advise. I also thank Ed Elizondo and Bruce Mackenzie for providing the Multi-Channel Sea Surface Temperature satellite products which were used in verifying the accuracy of the model results. Finally, I must thank my wife, Deena, through this entire degree program.

THIS PAGE INTENTIONALLY LEFT BLANK

I. INTRODUCTION

Along a typical subtropical eastern ocean boundary, the prevailing winds are equatorward, or at least have a large equatorward component. These equatorward winds generate an offshore Ekman transport and cause upwelling near the coast. With cold upwelled water along the coast and warmer water offshore, the sea surface slopes down toward the coast, resulting in a geostrophically balanced equatorward current moving in the same direction as the wind. Since the surface slopes downward from the equator toward the pole in the alongshore direction, this surface current flows against a pressure gradient. This pressure gradient forces a poleward undercurrent at depths of 100-300 m (McCreary et. al., 1986).

The circulation off the west coast of Australia, the eastern boundary of the Indian Ocean, is quite different from the other subtropical eastern boundary current systems even though the wind is equatorward year-round. There is no persistent upwelling. The Leeuwin Current is narrow and flows poleward in opposition to the prevailing wind, and there is an equatorward undercurrent. The sea surface slopes down toward the pole, so the current flows with the pressure gradient (Thompson, 1984; McCreary et. al., 1986; Smith et. al., 1991; Batten and Butler, 1998).

There are other examples of surface currents which flow against the wind. The Davidson Current flows poleward off the coast of California when the equatorward winds relax in late fall and winter. A poleward countercurrent also appears off the west coast of India in the winter (McCreary et. al., 1986). However, the Leeuwin Current along the west coast of Australia is unique. First, the other examples are thought to be undercurrents which surface during a short season of the year when the equatorward winds relax. In contrast, the Leeuwin Current is always a surface current and has beneath it an equatorward undercurrent (Godfrey and Ridgway, 1985; Griffiths and Pierce, 1985; Smith et. al., 1991; Morrow et. al., 2003). Additionally, these other examples are *countercurrents* which exist in addition to the normal broad, slow eastern boundary current flow. Along the western coast of Australia, however, there is no regular,

continuous equatorward surface flow within 1000 km of the coastline and there is no persistent upwelling along the coast (Smith et. al., 1991).

The Leeuwin Current flows poleward as a relatively strong and narrow jet along the outer edge of the continental shelf off western Australia. It is \sim 50 km wide, exists in the upper 250 m of the water column, and averages \sim 30 cm s $^{-1}$ with a seasonal maximum of \sim 60 cm s $^{-1}$ (Schott and McCreary, 2001). A series of eddies develop on the seaward side of the current (Griffiths and Pierce, 1985; Smith et. al., 1991; Batteen and Butler, 1998). The current carries a relatively warm and low salinity water mass formed from the tropical waters off northwestern Australia (Thompson, 1984; Ridgway and Condie, 2004). There is both a local temperature maximum and salinity minimum along the core of the current (Smith et. al., 1991). Below a depth of \sim 300 m, a more saline undercurrent flows toward the equator just offshore of the continental shelf break (Schott and McCreary, 2001; Morrow et. al., 2003). The Leeuwin Undercurrent carries an equatorward mass transport comparable to the poleward transport of the surface current (Godfrey and Ridgway, 1985). The speed of the undercurrent is about one-third that of the surface current with a mean velocity of \sim 10 cm s $^{-1}$ at 450 m depth (Smith et. al., 1991).

The sea level drops about one-third of a meter between 20°S and 32°S (Thompson, 1987), which is a far greater sea level gradient than in the Atlantic and Pacific Oceans (Schott and McCreary, 2001). There is general agreement that the pressure gradient arising from this anomalously large steric height difference is the principal forcing mechanism of the Leeuwin Current (e.g. Thompson, 1984; Godfrey and Ridgway, 1985; McCreary et. al., 1986). Even though there is a strong equatorward component to the wind stress year-round, this pressure gradient is strong enough to overwhelm the wind forcing and generate a poleward surface current (Smith et. al., 1991).

The Leeuwin Current accelerates as it flows farther south and converges to a width of \sim 20 km between Cape Naturaliste and Cape Leeuwin (see Figure 1.1 for locations of geographical names), where it reaches its maximum speed of \sim 70 cm s $^{-1}$ (Cresswell and Golding, 1980). In this area, the front separating the warm waters of the

current from the colder offshore waters becomes much stronger and sharper, with sea surface temperature in the current as high as 21°C in contrast to the offshore water of 15°C (Griffiths and Pierce, 1985). The flow hugs the shelf break around the bend of Cape Leeuwin and flows eastward along the southern coast as far east as the Great Australian Bight (Godfrey and Ridgway, 1985; Griffiths and Pierce, 1985; Godfrey et. al., 1986, Rochford, 1986; Ridgway and Condie, 2004). This flow remains a continuous flow as the Leeuwin Current and the primary forcing mechanism appears to be the pressure gradient, even though winds along the southern coast become westerly, aligned with the flow of the current.

Though the Leeuwin Current is always poleward, the strength of the flow is highly seasonal with the strongest flow in winter when the opposing winds are weakest (McCreary et. al., 1986; Batteen and Butler, 1998). The seasonal variability appears to depend almost completely upon the variability of the wind. There is little variability in the pressure gradient (Smith et. al., 1991). The location of the current appears to vary slightly with season as well. The current is relatively strong and lies along the shelf break in late summer and autumn (March-May). It is strongest and farther seaward in winter (June-August). During spring (September-December) the current is weak and again lies along the shelf break. It almost vanishes in early summer (January) (Smith et. al., 1991).

The wind stress along the coast off southern Australia is predominately eastward. Variability is caused by the passage of storms and cold fronts during the winter. This downwelling favorable wind results in an eastward coastal current which extends from Cape Leeuwin continuously to the coast of Tasmania (Cirano and Middleton, 2004). While modeling studies have shown a continuous eastward coastal current across the entire southern coast of Australia, satellite SST imagery has not been able to resolve the exact structure of the circulation due to the complexity of the SST structure (Ridgway and Condie, 2004). Drifting buoy tracks have also confirmed the existence of a narrow, shelf-edge coastal current extending from Cape Leeuwin across the entire distance of southern Australia (Godfrey et. al., 1986).

The current is narrowest and has the strongest and sharpest temperature front at Cape Leeuwin. It becomes slower and broader and the front becomes weaker with increasing distance along the southern coast (Griffiths and Pierce, 1985). The current contains a series of smaller-scale eddy-like features across the Great Australian Bight (Ridgway and Condie, 2004). Along the western Bight, the water mass in the shelf-edge current changes. A warm water mass forms in a narrow strip of shallow water between 124°E and 129°E in the western Bight (Herzfled and Tomczak, 1997; Ridgway and Condie, 2004). This water spreads eastward along the outer shelf of the Bight and is readily distinguished from the Leeuwin Current by its higher salinity. This plume is ~2-3°C warmer than the surrounding water due to heating in the shallow region. The plume can spread eastward as far as 136°E (almost to Adelaide/Kangaroo Island area) in the summer (Herzfled and Tomczak, 1997).

An anticyclonic gyre exists in the Great Australian Bight as this coastal current continues eastward along the shelf break while inshore of it, a westward current flows near the shore (Middleton and Platov, 2003). This westward current along the shore causes upwelling along the coast of the eastern Bight and advects cold water westward in the Bight (Herzfled and Tomczak, 1997). This anticyclonic circulation also causes a local high in the sea level between 120°E and 130°E (Middleton and Platov, 2003). This circulation appears to be largely unaffected by surface heat fluxes and fresh water input (Middleton and Platov, 2003).

Baroclinic instability dominates the coastal areas off southern Australia (Godfrey et. al., 1986; Batteen and Butler, 1998). The coastal current reaches its maximum speed of ~50 cm s⁻¹ in the area offshore of Kangaroo Island where the shelf is narrowest. Offshore of this region, between the Eyre Peninsula and Tasmania, lies a complex weak eddy field. There the Flinders Current surfaces and flows toward the northwest in winter (Cirano and Middleton, 2004). Anticyclonic loops in the coastal current have been observed east of 124°E (Godfrey et. al., 1986).

As the continental shelf becomes oriented more meridionally in the east, the coastal current continues to follow the shelf break poleward along the west coast of Tasmania. In this area, the current is called the Zeehan Current (Cirano and Middleton,

2004; Ridgway and Condie, 2004). This current is largely subsurface, located along the outer continental slope, and averages $\sim 50 \text{ cm s}^{-1}$. In the upper 500 m of the water column, isotherms are downwelled by $\sim 100 \text{ m}$. The resulting thermal wind shear is strong enough to cause an undercurrent (Middleton and Cirano, 1999).

Along the coast between Robe and the eastern Bight, the mean wind stress has an equatorward (upwelling favorable) component which is particularly strong between January and March. These winds can cause significant upwelling events off the Gulfs and Robe region. The deepest upwelling occurs south of Kangaroo Island where $15 \text{ }^{\circ}\text{C}$ water is upwelled from $\sim 150 \text{ m}$ depth. This is one of very few areas anywhere along the southern Australian coastline where upwelling is regularly found at the surface. Upwelling has even been observed when winds are not upwelling favorable (Middleton and Platov, 2003).

An undercurrent flows in the opposite direction from the coastal current. The undercurrent flows northward along the coast of Tasmania and then westward along the eastern South Australia coast and across the Great Australian Bight. In this area it is called the Flinders Current (Cirano and Middleton, 2004). The undercurrent continues westward from the Great Australian Bight to Cape Leeuwin where it is named the Leeuwin Undercurrent. The undercurrent flows at \sim one-third the speed of the surface current at $\sim 10 \text{ cm s}^{-1}$ (Middleton and Cirano, 1999). It has a wintertime maximum of $\sim 16 \text{ cm s}^{-1}$ at a depth of $\sim 400 \text{ m}$ (Middleton and Cirano, 2002). Two conditions are necessary for the undercurrent to form. First the thermal wind shear must be large enough to overcome the cross-shelf sea level gradient. Second, an alongshore sea level gradient must exist (Middleton and Cirano, 1999).

Ridgway and Condie (2004) suggest a standard naming convention for the current system of the southern coast (which will be used in this study) based on differences in geography, forcing mechanisms, and water masses. The flow turning around Cape Leeuwin and penetrating as far as the western Great Australian Bight should continue to be called the Leeuwin Current (LC). The section of the flow from the Bight to Bass Strait should be called the South Australia Current (SAC), a name that was found in atlases dating back as far as 1853. This section of the current contains the salty water

mass formed in the Bight. It is broader than the LC, and appears to be forced more by local winds than the pressure gradient. Finally, the Zeehan Current is that southward flowing, warm, saline current along the west coast of Tasmania. A graphical depiction of these major currents using the Ridgway and Condie (2004) naming convention is included in Figure 1.2.

There is considerable interannual variability in the Leeuwin Current along the west coast of Australia. The strength of the Leeuwin Current along the southern coast is highly dependent upon the winds. The high pressure cell over the continent (which drives the westerly winds along the southern coast) is also known to have interannual variability which could lead to large variability in the current system along the southern coast (Ridgway and Condie, 2004). The degree of variability remains unknown. The entire current system off the southern coast of Australia has been studied far less than the Leeuwin Current off the west coast and other current systems of the world (Herzfeld and Tomczak, 1997; Middleton and Cirano, 1999; Middleton and Cirano, 2002; Ridgway and Condie, 2004) and many gaps remain in our knowledge of this complex current system.

This study is both a theoretical and numerical modeling study of the current system off western and southern Australia. Chapter II provides a description of the model used throughout the study, including the data sets, preprocessing, and boundary conditions. Chapter III is a theoretical section which seeks to provide a fluid-dynamics based explanation of why eddies form at a preferential location off Cape Leeuwin. The theoretical explanations are compared against two model runs to test for consistency. A series of process-oriented experiments are conducted in Chapter IV. These experiments, arranged in the order of increasing complexity, seek to isolate which features in the current system are caused by which type of forcing. Chapter V extends the complexity of the modeling studies by adding daily varying winds to isolate the effects of temporal variability. This section also examines features generated by smaller scale wind features by using higher spatial resolution wind forcing. The effects of the features generated by the modeling studies of the two previous sections on the acoustic properties of the complex current system are explored in Chapter VI. Finally, Chapter VII provides a brief overview of results for all experiments presents in Chapters III through VI.

II. MODEL DESCRIPTION

The Princeton Ocean Model (POM), a well-documented (e.g. Blumberg and Mellor, 1987; Mellor, 1996) sigma-coordinate model was used for the modeling portions of this study. POM is a primitive equation, free surface model with a second-moment turbulence closure scheme (Mellor and Yamada, 1982) that can realistically simulate processes associated with continental shelf flows and bottom boundary layer dynamics in coastal regimes. This model has also been used successfully to simulate decadal processes in entire ocean basins (see Ezer and Mellor, 1994, 1997).

The prognostic variables of POM are potential temperature, salinity, density, the three velocity components, surface elevation, and turbulent kinetic energy (Blumberg and Mellor, 1987). The model uses a split time step interval to separately calculate external and internal modes. The external mode solves the equations for the vertically integrated momentum equations and calculates the sea surface and barotropic velocity components. The external time step is six seconds for the model runs used in Section III and twelve seconds for all other model runs. The internal mode solves the complete 3D baroclinic equations with a time step of 300 seconds for Section III experiments and 600 seconds for the other model runs.

The horizontal grid resolution varies from 3 km by 3 km to 10 km by 10 km for the experiments in Chapter III. For all other experiments the grid resolution varies from 5.7 km by 6 km to 13.7 km by 10.2 km. The varying resolution allows for more grid points in areas of larger gradients (of temperature and bottom topography) and fewer grid points in areas with smaller gradients. The finest resolution of 3 km by 3 km (5.7 km by 6 km) is located over the continental shelf and slope around Cape Leeuwin, where both the bottom slope and temperature gradient are greatest. The model uses 21 vertical sigma levels which are most closely spaced near the surface and the bottom in order to better resolve the surface and bottom boundary layers, both of which are important in coastal regions. The time constraints related to the higher vertical resolution near the surface and bottom are eliminated by using an implicit vertical time differencing scheme.

A Smagorinsky formulation (Smagorinsky et al., 1965) is used for the horizontal diffusion. The horizontal viscosity coefficients vary with the grid size, the velocity gradient and a coefficient. A coefficient value of 0.2 is used in this model, consistent with other POM studies (e.g., Ezer and Mellor, 1997).

A. DATA SETS

The model domain (Figure 2.1a for Chapter III and Figure 2.1b for Chapters IV through VI) contains most of the western and southern coasts of Australia, from 24.5°S to 39°S and 109°E to 121°E (for Chapter III model runs) and 22.5°S to 40°S and 107.5°E to 142.5°E (for all other model runs). The topographic data was obtained from the Institute of Geophysics and Planetary Physics, University of California San Diego (Smith and Sandwell, 1997). This topography data set, with a resolution of 2 minutes, was compiled from over 30-years of bottom echo sounding by ships. Gravity estimates derived from altimetry data were used to interpolate soundings in data sparse regions. The annual temperature and salinity climatology data set from the World Ocean Atlas 1994 (WOA94) (Levitus and Boyer, 1994; and Levitus et al., 1994) was used to initialize the model. The horizontal resolution of these data sets is 1 by 1 degree at standard depths.

The European Center for Medium-range Weather Forecasting (ECMWF) daily reanalysis wind fields for each day of the year from 1980 through 1989 formed the basis for the wind forcing fields used in the model runs for all experiments in Chapters III and IV and for the first two daily wind experiments in Chapter V. These winds are from the ECMWF Re-analysis (ERA-15) project which contains winds from January 1, 1979 through February 28, 1994. The winds are stored on a 2.5° by 2.5° horizontal grid (Gibson et. al., 1997). The wind fields for the higher resolution daily wind experiments were formed from the Navy's Operational Global Atmospheric Prediction System (NOGAPS) model operational analysis. This data set is provided as a part of the Global Ocean Data Assimilation Experiment (GODAE) projected hosted by the Fleet Numerical Meteorology and Oceanography Center (FNMOC) in Monterey, CA. These winds are reanalyzed to a 1° by 1° horizontal grid (Goerss and Phoebus, 1992).

B. PRE-PROCESSING

The topography data set was interpolated from its regularly spaced 2 minute resolution grid to the POM model grid with varying resolution. In the model grid used in the Chapter III model runs, the resolution varies from 10 km by 10 km offshore, 3 km by 10 km over the continental shelf and slope regions of the western and southern coasts, to 3 km by 3 km around the southwest corner of Australia where the western and southern 3 km by 10 km bands meet (and where the temperature gradient and bottom slope are greatest). This grid is represented by 252 by 226 grid points. For the model runs used in Chapters IV through VI, the resolution is 13.7 km by 10.2 km offshore, 5.7 km by 10.2 km and 13.7 km by 6 km along the western on southern coasts, and 5.7 km by 6 km around the southwest corner of the continent. This grid is represented by 233 by 298 grid points.

The slope parameter, which is defined as $\frac{|\delta H|}{2\bar{H}}$, where \bar{H} is the average depth of

two adjacent grid points and δH , is the difference in depth between those same grid points (Mellor et al., 1998). Due to the sloping sigma levels in a sigma coordinate model such as POM, pressure gradient force errors are inevitable. According to Mellor et al (1998), the slope parameter must be less than 0.2 at all locations in order to decrease the pressure gradient force error to an acceptable error (i.e., $\sim 0.5 \text{ cm s}^{-1}$). By constructing the grid such that the closest grid spacing is located over the steepest slopes of the continental slope, the slope parameter is minimized. However, some areas of the steepest bottom gradient still have a slope parameter greater than 0.2, so smoothing of the bottom topography is required in order to minimize the pressure gradient force errors. In the first model, used for the experiments in Chapter III, the topography was first smoothed with a Gaussian filter using a weighted average of 25 by 25 points and a standard deviation of eight. After the slope parameter was reduced to values less than 0.2 at all grid points, all depths greater than 2500 m were reassigned a depth of 2500m. Figure 2.2a shows the topography after smoothing for Chapter III experiments.

For the larger domain model used in Chapters IV through VI, a new topography smoothing technique (Martinho and Batteen, 2005) was used, which better preserves the

original configuration of the coastline, continental shelf break, seamounts, and islands, while still reducing the slope parameter to an acceptable value at all grid points. This smoothing technique uses an iterative, one-dimensional smoothing method. The slope parameter is first calculated between each set of adjacent grid points, then if it exceeds a threshold value (in this case, 0.2) the depth is adjusted just enough to bring the slope parameter to the threshold value. The method is first applied in a given direction, then in a direction 90 degrees to the direction of the first pass. The routine continues to calculate and adjust the slope parameter in each direction until the slope parameter is at or below the threshold value at each grid point. As before, all depths greater than 2500 m were then reassigned a depth of 2500 m. Figure 2.2b shows the topography which was smoothed using this technique. The coastline was assigned a depth of 20 m in both model domains to avoid dividing by zero.

The WOA94 annual temperature and salinity fields were used for the Chapter III experiments (Figures 2.3a and 2.4a) and for Experiments 1 through 6 (annual wind and thermohaline forcing experiments) in Chapter IV (Figures 2.3b and 2.4b). The WOA94 monthly temperature and salinity fields (for January and July) were used for all the monthly and daily wind forcing experiments for the upper 1000 m of the water column. Since the monthly data was only available for the upper 1000 m, these monthly fields were merged with quarterly (January through March and July through September) temperature and salinity fields for depths of 1000 m to 2500 m. These temperature and salinity fields were interpolated from the one degree by one degree horizontal grid at standard depths to the varying horizontal resolution model grid with its 21 vertical sigma levels using a three-dimensional linear interpolation scheme. The January temperature and salinity fields for the surface are shown in Figures 2.3c and 2.4c. The July temperature and salinity fields for the surface are shown in Figures 2.3d and 2.4d.

The European Center for Medium-range Weather Forecasting (ECMWF) daily reanalysis wind fields for each day of the year from 1980 through 1989 formed the basis for the wind forcing fields used in the model runs for all experiments in Chapters III and IV and for the first two daily wind experiments in Chapter V. These wind speeds were converted to wind stress locally. The same algorithm was used for calculating wind

stresses for all annual, seasonal, and daily wind forcing fields. In order to form the annual wind field, the winds for each day for the entire ten years were averaged together (Figures 2.5a and 2.5b). The seasonal wind fields were created by averaging together all the January winds (summer case) (Figure 2.5c) and all the July winds (winter case) (Figure 2.5d) for the ten year period. The daily winds were used with one wind file per day from the same data set for each day of December 1980 through February 1981 and June 1981 through August 1981 for the first two daily wind experiments. For the other daily wind experiments, the Navy Operational Global Atmospheric Prediction System (NOGAPS) winds were used for each day of December 2000 through February 2001 and June 2001 through August 2001. The same algorithm was used to convert the NOGAPS winds to wind stress as that used for converting the ECMWF winds. All wind fields were interpolated to the horizontal resolution of the model grid using a two dimensional linear interpolation scheme.

C. INITIALIZATION, FORCING AND BOUNDARY CONDITIONS

As discussed above, the model was initialized with annual temperature and salinity values for the Chapter III experiments and for Experiments 1 through 6 of Chapter IV and with the merged monthly/quarterly temperature and salinity fields for all other experiments. Since the model runs reached a quasi-equilibrium state in a relatively short time (~26 days), zero salinity and temperature fluxes were prescribed at the ocean surface. The annual climatological surface temperature (Figures 2.3a and 2.3b) shows a strong north-south gradient with a maximum temperature of ~24°C along the western coast of Australia at the northern end of the domain and decreasing values to the south to a minimum of ~14°C at the southern edge of the model domain. The climatological surface salinity (Figures 2.4a and 2.4b) reaches a maximum of ~35.8 at the center of the western edge of the model domain and decreases slightly to both the north and south. Model runs using horizontally averaged climatology (Chapter IV, Experiments 1 and 2) use the same initial temperature and salinity over the entire model domain (e.g., 19.8°C and 35.4 are the temperature and salinity values, respectively, for the surface) to remove any thermohaline gradient forcing.

The model was forced from rest with the annual, monthly, or daily ECMWF wind fields (or NOGAPS daily wind fields for daily wind Experiments 3 and 4), which were interpolated to the model grid. As seen in Figures 2.5a through 2.5d, southerly winds dominate the west coast region. These winds are southerly in both the annual and monthly average wind fields and during the vast majority of the days in both the ECMWF and NOGAPS daily wind fields. The southern portion of the model domain is more variable, though westerly winds dominate the offshore areas. In the coastal areas of southern Australia, the winds are weakly southerly or southeasterly in the averaged wind fields. The daily winds rotate through every direction in the coastal/littoral region with a three to six day period as weather systems pass through the area. Through this rotation in wind direction, the winds have a weak westerly component in most of the coastal region much of the time, except that the winds along the coast of the Great Australian Bight have a weak easterly component on about one-third of the days.

Although no general criteria can determine the best boundary conditions for a specific model or study, correct specification of the open boundary conditions is imperative for achieving realistic results. Otherwise reflections, spurious currents, and/or changes in the total water volume in the model can occur. For free-surface models, such as this one, it is important that the boundary conditions be transparent to the waves. In this model, a gradient boundary condition (Chapman, 1985) which allows geostrophic flow normal to the boundary is used for the elevation. For the baroclinic velocity components normal to the boundary, an explicit wave radiation scheme based on the Sommerfeld radiation condition is used. For inflow situations, the model is forced with WOA94 (Levitus and Boyer, 1994; and Levitus et al., 1994) temperature and salinity values and an advection scheme is used for outflow situations. For the barotropic velocity components, Flather (1976) developed a radiation condition, based on the Sommerfeld equation combined with the continuity equation, which allows radiation of wave energy across the boundary while allowing conservation of mass inside the model domain. Palma and Matano (1998) reformulated this scheme using the Roed and Smedstad (1984) technique, which breaks the velocity into both global and local

components. This open boundary condition, called the Flather radiation plus Roed local solution by Palma and Matano (1998), was used in these experiments.

THIS PAGE INTENTIONALLY LEFT BLANK

III. BOUNDARY CURRENT SEPARATION

As a relatively narrow and swift poleward current, the Leeuwin Current in some ways is more similar to subtropical western boundary currents than to other subtropical eastern boundary currents. The Gulf Stream detaches from the coastline at Cape Hatteras and flows into the open ocean. Likewise, all other subtropical western boundary currents detach from the coast at some point and form a gyre. The Leeuwin Current, however, even though it shares many other characteristics with western boundary currents, changes direction ninety degrees from southward to eastward around Cape Leeuwin. Since Coriolis force acts to the left in the Southern Hemisphere and the coastline is to the left of the current, it might be anticipated that the current would be turned in that direction. Indeed, previous large-scale modeling studies (e.g., Case 1 of Batteen and Butler, 1998) have depicted the current overshooting the turn (i.e., completely detaching from the coast locally) and then turning left and rejoining the southern coastline. This work seeks to explain more systematically why the current repeatedly detaches from the coastline at Cape Leeuwin, generating a continuous supply of eddies from this location, which is in agreement with available observations. In particular, a close examination of model results shows that the current does detach from the coastline at Cape Leeuwin, and then is turned to the left under the influence of Coriolis force, forming meanders which break off as eddies. The current subsequently reattaches to the coastline and, as current speed increases following the shedding of an eddy, the detachment and eddy generation cycle begins again. This process of separation and re-attachment is consistent with drifting buoy observations (e.g., Godfrey et. al., 1986). This process leads to an area of enhanced eddy generation at Cape Leeuwin.

A. THEORETICAL DEVELOPMENT

Here we first review the theory of boundary current separation used for the Gulf Stream in a flat bottom case. Next we apply the theory to the LCS and develop a scaled approximation of boundary current separation which includes the vortex stretching term. Finally, the concept of critical streamline radius of curvature is discussed.

1. Theory

In Martinho (2003), the Marshall and Tansley (2001) theory for separation of the Gulf Stream from the coastline at Cape Hatteras was applied to the Iberian Peninsula eastern boundary case to show how model resolution and bathymetry smoothing could prevent separation of submesoscale coherent vortices (Meddies) from the deep undercurrent at Cabo de Sao Vicente. In the current work, the separation theory is further applied to an anomalous eastern boundary current (poleward flow resulting in a coastline to the left of the current instead of to the right), i.e., the Leeuwin Current, in the Southern Hemisphere. The theory is used to explain how detachment of the current at Cape Leeuwin provides a location of preferential eddy generation, even though the current continues around the cape beyond the newly formed eddies instead of leaving the coastline altogether and continuing into the open ocean as the Gulf Stream does off Cape Hatteras

Boundary layer separation is necessary for the detachment of a boundary current from the coastline, or continental shelf break, along which it is flowing (Marshall and Tansley, 2001). This separation occurs when a nearly inviscid fluid lying just outside the boundary layer encounters an adverse pressure gradient and undergoes an appreciable deceleration (Batchelor, 1967). The downstream speed of a boundary current, and therefore its downstream pressure variations are determined by three large-scale dynamical processes: the beta effect, vortex stretching and changes in the streamline curvature.

To show this, consider the quasi-adiabatic, steady-state equations of motion with density as a vertical coordinate:

$$\vec{u} \cdot \nabla \vec{u} + \vec{f} \vec{k} \times \vec{u} + \frac{\nabla(M)}{\rho} = 0 \quad (1)$$

$$\nabla \cdot (h \vec{u}) = 0 \quad (2)$$

where \vec{u} is the isopycnal velocity, ∇ is the lateral gradient operator along isopycnals, f is

the Coriolis parameter, $M = p + \rho g z$ is the Montgomery potential, p is the pressure, ρ is density, g is the gravitational acceleration, z is height and $h = \frac{\partial z}{\partial \rho}$ is the isopycnal thickness. The absolute vorticity equation obtained by taking the curl of (1) is:

$$\nabla \cdot (\zeta \vec{u}) + \vec{u} \cdot \nabla f = \frac{f}{h} \vec{u} \cdot \nabla h \quad (3)$$

where ζ is the vertical component of the relative vorticity. If we assume that the coastline is to the left of the boundary current, then after the integration over a rectangular area ABCD and some scaling we obtain :

$$\left[\frac{v^2}{2} \right]_A^D = \iint_{ABCD} \beta^* v dA - \iint_{ABCD} \frac{f}{h} \vec{u} \cdot \nabla h dA + \left[\int \frac{v^2}{R} dn \right]_{BA}^{CD} \quad (4)$$

where $\beta^* = \frac{\partial f}{\partial s}$, s and n are the natural coordinates, R is the radius of curvature of the streamlines and v is the velocity in natural coordinates. (For a graphical representation of this integration area, see Figure 1 of Marshall and Tansley (2001)). The first term on the right-hand-side of Equation (4) is the beta effect, the second the vortex stretching and the third the coastline curvature.

In the Gulf Stream case studied by Marshall and Tansley (2001) (i.e., with the coast on the left side of the boundary current and an anticyclonic current (corresponding to the case of the Gulf Stream)), in order for the current to detach from the coastline, it is necessary for a significant downstream deceleration to occur, (i.e. $v_D^2 < v_A^2$, which means $\left[\frac{v^2}{2} \right]_A^D < 0$). That is

$$\iint_{ABCD} \beta^* v dA - \iint_{ABCD} \frac{f}{h} \vec{u} \cdot \nabla h dA + \left[\int \frac{v^2}{R} dn \right]_{BA}^{CD} < 0 \quad (5)$$

In this case, the beta term is always negative and works to accelerate and therefore stabilize the current and inhibit separation. In contrast, the vortex stretching acts

to decelerate the current, thus enhancing separation. For the coastline to induce separation it is necessary for the vortex stretching and curvature terms to overcome the stabilizing effects of the beta term. In the flat bottom case considered by Marshall and Tansley (2001), there is no vortex stretching so the relation between beta and curvature that gives the separation condition is:

$$R < \left(\frac{v}{\beta^*} \right)^{\frac{1}{2}} \quad (6)$$

Martinho (2003) applied this theory to the eastern boundary case. In particular, that development was done for the case of Meddy separation from the eastern boundary current system's deep undercurrent. In that case the condition for separation was that $\left[\frac{v^2}{2} \right]_A^D$ be positive because the coastline is to the right of the cyclonic boundary current.

2. Development of Scaled Approximation

Here the theory is applied to an anomalous poleward eastern boundary current in the Southern Hemisphere, i.e., to the LCS off Cape Leeuwin. Since the coastline is to the left of the current as in the Gulf Stream case, the separation condition is again $\left[\frac{v^2}{2} \right]_A^D < 0$

as in Marshall and Tansley's study, therefore inequality (5) holds for this Leeuwin Current case. The beta term is always negative and works to decelerate the boundary current, thereby enhancing separation for all eastern boundary currents. Since the current would be turning in an anticyclonic direction around Cape Leeuwin, the vortex stretching term is also negative and enhances separation of the current. In the natural coordinate system, the radius of curvature R is positive for a current turning to the left (anticyclonic in the Southern Hemisphere) (Holton, 2004). However, the streamline curvature term

$\left[\int \frac{v^2}{R} dn \right]_{BA}^{CD}$ is actually the change in $\left[\int \frac{v^2}{R} dn \right]$ from the upstream BA end of the integration area to the downstream CD end of the integration area. Assuming the downstream curvature to be infinite (a straight coastline), this term is zero at the CD end

of the integration area and $\left[\int \frac{v^2}{R} dn \right]_{BA}^{CD} = - \left[\int \frac{v^2}{R} dn \right]$. Therefore, the streamline curvature

term is also negative in this case and also acts to decelerate the current. Although, this gives the result that the separation condition is always satisfied, it is useful to study the magnitude of each of these terms because in cases with a very large radius of curvature or very small velocity, all terms on the left side of inequality (5) can sum to near zero, leading to an essentially neutral condition where separation may or may not occur.

So that the magnitude of each of these terms can be estimated and their subsequent effects on separation of the current from the coastline studied, we now expand the Marshall and Tansley (2001) methodology further to also include a scaled vortex stretching term, and a scaled approximation of inequality (5). It is important to note that from a large-scale perspective, the Leeuwin Current is always accelerating in the downstream direction on the western coast due to the constant influx of geostrophic flow resulting from the steric/thermohaline gradient. Here, however, we wish to consider only a relatively small region, i.e. the Leeuwin Current near Cape Leeuwin. In this case, once the current is in quasi-equilibrium, it tends to be trapped over the shelf break. As a result, it generally is parallel to the isobaths and effectively ∇h is zero in inequality (5). In order to consider the effect of vortex stretching, we must consider ∇h along the path of the streamline if the current were deflected slightly (say 1°) offshore from this path parallel to the isobaths. It should be noted that if the current is deflected farther offshore, a larger value of ∇h will result. Since the current flows approximately parallel to the isobaths along the continental shelf break, h is approximately constant and $O(10^2)$. The typical value of -100 m is used for h in inequality (5) as it is near the depth midpoint of the current which extends from the surface down to ~ 250 m. The term $\bar{u} \bullet \nabla h$ is approximated by multiplying a typical mean value of velocity (U) by the typical mean value of ∇h , where ∇h is the gradient of the bottom depth in the down-stream direction as described above. Since we are considering a relatively small area, such as the flow of the current around Cape Leeuwin, we can consider f to be approximately constant with an order of 10^{-4} . This typical value is used in the scaled vortex stretching term in inequality (5). Finally the integral portion of the term is estimated by multiplying the width of the

current (δ) by the downstream distance Δs , yielding the correct units, m^2s^{-2} , for the entire term.

$$\beta^* U \delta \Delta s - f U \frac{\nabla h}{h} \delta \Delta s - \frac{U^2 \delta}{R} < 0 \quad (7)$$

Here all symbols are the same as in inequality (5) except that δ is the current width, Δs is the downstream length of the current considered, and U is a typical current speed. As noted in the preceding paragraph, the sign of the streamline curvature term is reversed since $\left[\int \frac{v^2}{R} dn \right]_{BA}^{CD} = - \left[\int \frac{v^2}{R} dn \right]$.

3. Estimations of the Critical Streamline Radius of Curvature

With the addition of the scaled vortex stretching term developed in the previous section (and the resulting inequality (7)), a general inequality can be developed to quantify the critical radius of curvature which will allow separation in Marshall and Tansley's Gulf Stream case with bottom topography. By considering $\Delta s \sim R$ and solving inequality (5) for R , a general condition can be obtained for the maximum radius of curvature of a cape which allows separation to occur within the current. This condition is given by

$$R < \left(\frac{U}{f \frac{\nabla h}{h} - \beta^*} \right)^{\frac{1}{2}} \quad (8)$$

In their Gulf Stream case, the coastline curvature term had to overcome the stabilizing effect of the beta term in order to decelerate the current enough for separation to occur. In this case, where the Leeuwin Current rounds Cape Leeuwin, there is no critical radius of curvature per se beyond which the current cannot separate. However, the radius is still important because a large radius can lead to a sum for inequality (5) that is closer to zero and a current which is closer to neutral rather than a current with a strong inclination to separate from the coastline.

B. COMPARISON OF THEORETICAL RESULTS WITH MODEL RUNS

In order to test if these theoretical predictions of separation for the flat-bottom and topography cases are consistent with model simulations, two model runs were conducted and compared against the calculations in the LCS (see Figure 2.1a for the model domain). The same climatological thermohaline (Figures 2.3a and 2.4a) and wind forcing (Figure 2.5a) were used for both cases. The first run used a flat bottom and the second run used the smoothed Smith and Sandwell (1997) topography (Figure 2.2a).

In the first model run, the flat-bottom case, a relatively strong and narrow poleward surface current forms along the coast (Figure 3.1a). Consistent with the theoretical calculations, the current detaches from the coast as it passes Cape Leeuwin. This detachment from the coast has already begun by day 20 (Figure 3.1a), and by day 40 a relatively large eddy has formed in the current downstream of Cape Leeuwin (Figure 3.1b). By day 60, a relatively large meander in the current has formed at Cape Leeuwin and an eddy lies just beyond the Cape, with the main flow of the current remaining detached from the coastline. It then turns eastward along the southern coast beyond Cape Leeuwin (Figure 3.1c).

In the second model run, with bottom topography, a narrow and swift poleward surface current again forms (Figure 3.2a). The current follows the continental shelf break smoothly around Cape Leeuwin and along the southern coast at day 20 with no evidence of detachment. By day 40, however, the current has detached forming a large meander just downstream of Cape Leeuwin. The current reattaches to the continental shelf break just beyond the meander for a relatively short distance before meandering of the current occurs along the relatively straight coastline south and east of Cape Leeuwin (Figure 3.2b) consistent with baroclinic instability generated by the increasing vertical velocity shear, e.g., Batteen and Butler (1998). Consistent with the theoretical calculations, the current subsequently detaches from the coastline at Cape Leeuwin, the area predicted to be a region of enhanced eddy generation. Between days 40 and 60 (not shown) the current has reattached to the shelf break. By day 60 a new meander has begun to form just north of the Cape (Figure 3.2c).

In both model runs, detachment occurs off Cape Leeuwin, providing an area of enhanced meander/eddy generation. The smoothed topography model shows the cycle of formation which occurs beginning with the current smoothly attached to the continental shelf break. As the current velocity increases, the current becomes more unstable and detachment occurs. A meander in the current results as the current is detached and then pushed back toward the shore by the Coriolis force. The meander subsequently develops into an eddy and begins to move offshore. As the eddy is shed, the remaining current flow is much weaker and is again able to attach to the shelf break. As the current velocity increases, the cycle begins again.

C. DYNAMICAL ANALYSES

It is important to note that on a larger scale (e.g., all along the western coast), baroclinic instability plays a large role in the formation of meanders and eddies (e.g., Batteen and Rutherford, 1990; Batteen et. al., 1992), which can also result in the detachment of the boundary current from the coast. (For further discussion of the role of baroclinic instability, see Batteen (1997). This explains why meanders and eddies form in other areas along the coast, sometimes even along sections of straight coastline. As a result, the theory presented in the previous section cannot be directly proven by comparisons with the model results in Section 3 and observations. However, these comparisons can be used to show that the theory is not inconsistent with both the model results and observations. Here we show the consistency of the theory using both an Eulerian and a Lagrangian approach.

1. Eulerian Analysis

In the Eulerian analysis, the values for each term in inequality (7) are calculated for flat-bottom, smoothed model topography, and raw topography cases. Typical values of $U \sim 10^{-1} \text{ m s}^{-1}$, $\beta^* \sim -10^{-11} \text{ m}^{-1} \text{ s}^{-1}$, $f = -8 \times 10^{-5} \sim 10^{-4} \text{ s}^{-1}$, $h \sim -10^2 \text{ m}$ (near the midpoint of the current vertically), $\delta \sim 10^5 \text{ m}$, and $\Delta s \sim R$ are used for all three cases. (Note that specific values for ∇h and R , which are also used in the calculations, are listed in Table 3.1.) The results of these calculations for inequality (7) are shown in Table 3.2. For an eastern boundary current with the coastline on its left, the first term β^* is always

negative. Therefore, the beta effect always acts to decelerate the current and therefore encourages separation for eastern boundary currents (though this is not true for *western* boundary currents). Marshall and Tansley (2001) showed that vortex stretching always inhibits separation in cyclonically turning currents and always enhances separation in anticyclonically turning currents. Since the Leeuwin Current turns anticyclonically around Cape Leeuwin in this case, the vortex stretching term is negative and acts to enhance separation. For the third term, i.e., the curvature term, in natural coordinates, it is important to note that the velocity is positive definite and the radius can be positive or negative depending upon the direction of curvature. For the case considered here, the current rounds Cape Leeuwin in an anticyclonic direction so R is positive. As previously discussed, however, the sign of the streamline curvature term must be reversed

since $\left[\int \frac{v^2}{R} dn \right]_{BA}^{CD} = - \left[\int \frac{v^2}{R} dn \right]$. As a result, the streamline curvature term is also always

negative for this case, acting to decelerate the current and thereby enhance separation.

This leads to the result that for both flat bottom and topography cases, the criterion for separation is always satisfied. The curvature of the coastline is a very important influence, as the value for this term is an order of magnitude larger for the flat bottom case than for the topography case, which has a much larger radius of curvature. Another result from this analysis is that the vortex stretching is an order of magnitude larger than the combination of beta and curvature terms. As a result, in all cases, the left side of inequality (7) sums to a negative value and the condition for separation is met.

2. Lagrangian Analysis

For the Lagrangian analysis, the changes in velocity in the downstream direction in the current are examined for days 20, 40, and 60 for the flat bottom and smoothed topography cases. In this analysis, a series of points are chosen lying parallel to the coastline (for the flat bottom case) or parallel to the continental shelf break (for the smoothed topography case). Each of the analysis points is chosen to be collocated with a model grid point so that the point speed from the model output can be taken directly. The speed at each of these points is calculated and then the change in speed in the downstream direction is diagnosed. Since and points are not equally spaced in distance

and due to large differences in speed at different times and locations, a direct difference in speed from one point to the next is not meaningful. In order to normalize the data for each point and allow for a meaningful comparison, the change in speed is expressed as a percentage of the upstream speed and divided by distance between the points for an “acceleration per unit distance” measurement. While this value is not truly acceleration (since it is a change in velocity over distance rather than a change in velocity over time), it is useful in diagnosing that downstream deceleration which leads to boundary current separation as discussed by Batchelor (1967). To aid in the discussion below, Tables 3.3a and 3.3b summarize the points used for the Lagrangian analysis with corresponding speeds and percent change in speed in the downstream direction.

At day 20 in the flat bottom case, no detachment is yet evident between points 1 and 4 (Figure 3.3a). However, detachment is beginning to occur on the downstream side of Cape Leeuwin between points 4 and 5. The five points shown in Figure 3.3a and summarized in Table 3.3a show the following: The speed decreases by 0.93 %/km between points 1 and 2, then accelerates by 0.65 %/km between points 2 and 3. The speed again decreases by 0.34 %/km between points 3 and 4. As the speed decreases by 2.85 %/km between points 4 and 5, detachment is beginning to occur (Figure 3.3a). A discussion of what constitutes a significant change in speed is included in the last paragraph of this section.

At day 40, detachment from the coastline upstream of Cape Leeuwin (likely due to baroclinic instability along this relatively straight section of coastline) is apparent (Figure 3.3b). While the current is attached to the coast between points 3 and 4, Table 3.3a shows an acceleration of 4.65 %/km. As expected, the current is unable to round Cape Leeuwin without detaching as the current decelerates 2.95 %/km between points 4 and 5 and forming an eddy on the lee side of Cape Leeuwin (Figure 3.3b).

At day 60, the changes in speed are similar to those at day 40 (see Table 3.3a). The current accelerates by 2.31 %/km as it flows from point 1 to point 2 (Figure 3.3c and Table 3.3a). Between points 2 and 3 the current decelerates from 0.6 m/s to 0.31 m/s or -1.3 %/km. At this point, the current remains almost parallel to the coastline, but separation is beginning in this area. Between points 3 and 4, the speed decreases by 2.66

%/km and the current has clearly detached between these two points. In fact, the current nearest the coastline is actually flowing in the opposite direction beyond point 4 and a mesoscale anticyclonic eddy is clearly visible south of points 4 and 5 (Figure 3.3c).

At day 20 for the smoothed topography case, the current is flowing smoothly along the contour of the continental shelf break. Since the current is farther offshore, i.e., along the shelf break instead of at the coastline, analysis points are chosen just offshore of and parallel to the shelf break (Figure 3.4a). Between points 1, 2, and 3, the current accelerates slightly (see Table 3.3b). Between points 3 and 4, the current speed decreases, but only by 0.54 %/km. Between points 4 and 5 the current speed decreases by 0.84 %/km. At all locations, the current remains anchored along the shelf break with no sign of detachment.

At day 40, a meander is beginning to form in the current between points 1, 2, and 3 (Figure 3.4b). The current decelerates 1.16 %/km between points 1 and 2, then accelerates 3.20 %/km between points 2 and 3 downstream of the apex of the meander. The current appears to be reattached to the shelf break by point 3 and remains so until shortly beyond point 4 (the current accelerates by 1.14 %/km between points 3 and 4). Between points 4 and 5, the current decelerates by 2.19 %/km and the current detaches forming a large meander (Figure 3.4b). The current reattaches to the shelf break beyond the meander and continues eastward into the southern Australia coastal area where another slight meander forms along the straight coastline outside the analysis area (Figure 3.2b).

By day 60, the meander discussed above has detached as an eddy and drifted to the south-southwest where it is visible in Figure 3.2c south of Cape Leeuwin. After shedding the eddy, the current has largely reattached to the shelf break and now a new meander is just starting to form between points 2 and 3 (Figure 3.4c) as the current decelerates 1.59 %/km between these points. The current actually accelerates through points 3, 4, and 5 and the current is attached and smoothly flowing along the shelf break in these areas.

Although these six snapshots (i.e., days 20, 40, and 60 for the flat bottom and smoothed topography model runs) might be considered an insufficient number of cases to assign a critical value of deceleration which will lead to separation, we can still compare the values among these cases with each other to ensure that they are self-consistent. Overall, based on Figures 3.3a through 3.4c and Tables 3.3a and 3.3b, we can state the following: For all points where the downstream decrease in speed is less than 1 %/km, there are no indications of current detachment. At the other end of the scale, the current is clearly detached from the coastline at all points where the downstream deceleration exceeds 2 %/km (flat bottom: point 5 at day 20, point 5 at day 40, and point 4 at day 60; topography: point 5 at day 40). Note however, that there are also intermediate cases (i.e., point 3 in the flat bottom day 60 case (-1.30 %/km) and point 2 in the smoothed topography day 60 case (-1.59 %/km)). In these cases, although the current becomes much broader and the beginning of meandering is evident, the deceleration appears not to be sufficient to result in complete boundary current separation and the formation of large sweeping meanders or eddies.

D. SUMMARY OF BOUNDARY CURRENT SEPARATION RESULTS

This work has sought to explain more systematically why boundary current separation occurs at Cape Leeuwin resulting in an area of enhanced eddy generation in the Leeuwin Current off Cape Leeuwin, which is in agreement with available observations. The Leeuwin Current System (LCS) is an anomalous subtropical eastern boundary current system. With its swift and narrow poleward surface current and energetic mesoscale features such as meanders and eddies, the Leeuwin Current shares many characteristics with subtropical western boundary currents. Unlike these western boundary currents which tend to completely detach from the coastline at some point (e.g., the Gulf Stream leaves the coast off Cape Hatteras), the Leeuwin Current separates from the continental shelf break as it rounds Cape Leeuwin, shedding eddies, and is then turned left under the influence of the Coriolis force to flow eastward along the southern coast of Australia. For the Gulf Stream, a scaled approximation for the beta effect and streamline curvature was used to determine whether a current could detach from a western boundary coastline. That work was applied to the LCS eastern boundary current

and included an additional term, i.e the vortex stretching term, which acts in the presence of bottom topography. Theoretical calculations showed that this term exceeded the sum of the beta term and streamline curvature term, and strongly enhanced boundary current separation. Two model runs (with and without bottom topography) showed that the theoretical calculations were not inconsistent with model results.

A flat-bottom model was used to simulate the Leeuwin Current as it rounds Cape Leeuwin from the north where the current is turning in an anticyclonic direction. In this case, both the beta term and streamline curvature term in inequality (5) were shown to be negative and to act to enhance separation. This allowed the current to separate from the coastline forming relatively large meanders and eddies in the current.

When bottom topography was added to the model, the vortex stretching term was shown to decelerate the current downstream and to enhance separation from the coast. Since the bottom topography adds a continental shelf, a stabilizing effect was also introduced. Note that the current in this case preferentially follows the continental shelf break, rather than the coastline. As the shelf break has a much larger radius of curvature (~ 175 km) than the coastline (~ 50 km), the larger radius resulted in a smaller curvature term. However, since the effect of vortex stretching was much greater than the effect of curvature, boundary current separation still occurred, resulting in a preferential location for eddy generation off Cape Leeuwin, consistent with the theoretical calculations and in agreement with available observations.

THIS PAGE INTENTIONALLY LEFT BLANK

IV. PROCESS-ORIENTED EXPERIMENTS

A. WIND FORCING OVER A FLAT BOTTOM

In Experiment 1, the model was initialized using horizontally averaged annual temperature and salinity climatology, which removes all thermohaline forcing. A flat bottom with a uniform depth of 2500 m eliminated any topographic effects. A realistic coastline was used. The sole forcing in this experiment was from the annually averaged climatological winds. This wind field (Figure 2.5b) is southerly (i.e., equatorward) along the entire western coast of Australia and the wind increases in magnitude toward the north. Over the coastal waters of southern Australia, the winds are westerly, except inside the Great Australian Bight, where the winds are relatively weak and southerly. The stronger offshore winds decrease in strength toward the coast, resulting in a positive wind stress curl along the entire southern coastline. Table 4.1 summarizes the forcing used for each process-oriented experiment.

As expected, an equatorward surface current develops along the western coast. By day 20 (Figure 4.1), the equatorward current follows the coastline from Cape Leeuwin to the northern boundary of the model domain. The current, as expected, is strongest at $\sim 10 \text{ cm s}^{-1}$ at the northern end of the coastline where the wind is strongest. Note that throughout this discussion, when current speeds are given, that speed is the maximum in the core of the current at that location. Vertical cross-sections were constructed and the maximum current speed for that latitude or longitude is used as the current speed for that location. In addition, a weaker, westward current forms along the southern coast as far as the western end of the Great Australian Bight. Upwelling is readily apparent along the west coast from $\sim 29^\circ\text{S}$ to the northern end of the model domain.

By day 30, a continuous coastal surface current flows westward from $\sim 135^\circ\text{E}$ along the south coast and then northward along the western coast (Figure 4.2a). The current increases in strength as it flows westward to $\sim 10 \text{ cm s}^{-1}$ at Cape Leeuwin. As the current flows equatorward along the west coast, it no longer continues to intensify, but it does broaden with increased distance toward the north from $\sim 50 \text{ km}$ wide at Cape Leeuwin to $\sim 100 \text{ km}$ wide at 26°S . A weak poleward undercurrent also develops along

the western coast. For example, at 26°S, the core of the undercurrent flows at $\sim 7 \text{ cm s}^{-1}$ at a depth of $\sim 150 \text{ m}$ (Figure 4.2b). At Cape Leeuwin ($\sim 34^\circ\text{S}$), the undercurrent is weaker and deeper: $\sim 2 \text{ cm s}^{-1}$ at $\sim 350 \text{ m}$ depth (Figure 4.2c). Along the southern coast, there is no discernible undercurrent (not shown).

By day 30, both the intensity and extent of the upwelling has increased. Upwelling is clearly visible along the western coast as far south as Cape Leeuwin. For example, a pool of $\sim 16.8^\circ\text{C}$ water is upwelled to the surface along the coastline at 26°S with the band of upwelled water extending up to $\sim 50 \text{ km}$ offshore (Figure 4.2d). Farther south, near Cape Leeuwin, the upwelling is at the surface with the isotherms tilting upward toward the coast (Figure 2e). Though there is no discernible upwelling at the surface anywhere along the southern coast, the isotherms do tilt upward slightly within $\sim 30 \text{ km}$ of the coast down to $\sim 250 \text{ m}$ depth at 117°E (Figure 2f).

By day 60, a westward coastal surface current hugs the coastline along the entire length of southern Australia (Figure 4.3a). This current begins very weak ($< 2 \text{ cm s}^{-1}$ at 140°E) and strengthens as it flows toward the west. It rounds the bend of Cape Leeuwin, where it reaches a speed of $\sim 12 \text{ cm s}^{-1}$, and continues to flow equatorward along the west coast to the northern boundary of the model domain.

As in the day 30 result, the current does not continue to intensify as it moves northward along the western coast; instead it broadens from $\sim 55 \text{ km}$ at Cape Leeuwin to $\sim 130 \text{ km}$ wide at 26°S. In addition, there is a broad offshore flow along the northern third of the west coast, but no narrow, swift squirts or jets typical of other eastern boundary currents. At 26°S, Figure 4.3b shows that the equatorward surface flow has moved offshore, and that the undercurrent has surfaced yielding a 5 cm s^{-1} poleward surface flow adjacent to the coastline. The core of this current flows at $\sim 10 \text{ cm s}^{-1}$ at 150 m depth.

By day 60, the intensity and extent of the upwelling has also increased. The pool of cooler water at the surface extends to a width of $\sim 100 \text{ km}$ at 26°S (Figure 4.3c). Upwelling is apparent at the surface along the entire length of the west coast. At depths between $\sim 200 \text{ m}$ and $\sim 500 \text{ m}$, downwelling is apparent in the downward-sloping isotherms, consistent with a poleward undercurrent.

Farther south, at Cape Leeuwin, the undercurrent has intensified to $\sim 6 \text{ cm s}^{-1}$ at a depth of $\sim 150 \text{ m}$ (Figure 4.3d). The upwelling in this area is less intense than farther north, with 17.9°C water upwelled along the coast and 18.4°C water offshore (Figure 4.3e). Isotherms are sloped upward to a depth of 200 m in the 50 km nearest the coast. Between $\sim 250 \text{ m}$ and $\sim 500 \text{ m}$ depth, the isotherms are tilted downward toward the coast in the nearest 25 km due to downwelling caused by the relatively weak undercurrent.

Along the southern coast, the current broadens from the Tasman Coast to Cape Leeuwin, but, unlike the west coast current, it remains attached to the coast (Figure 4.3a). As at day 30, the undercurrent is relatively weak at $\sim 1 \text{ cm s}^{-1}$ at 117°E (Figure 4.3f). There is, however, a very slight downward tilt of isotherms toward the coast between $\sim 300 \text{ m}$ and $\sim 500 \text{ m}$, consistent with some undercurrent activity at 117°E (Figure 4.3g). Farther east, at 130°E in the middle of the Great Australian Bight, there is a very broad $1\text{--}2 \text{ cm s}^{-1}$ current flowing opposite the surface current between $\sim 1000 \text{ m}$ and the bottom (Figure 4.3h), but this is far too deep to be considered a subsurface undercurrent. There is no downward tilt to the isotherms at depth (Figure 4.3i), which supports the claim of no subsurface undercurrent.

Again there is no pool of cooler water or any other evidence of upwelling at the surface along the south coast. Below the surface, though, the isotherms do bend upwards toward the coast down to a depth of $\sim 250 \text{ m}$ within $\sim 25 \text{ km}$ nearest the coast at 117°E (Figure 4.3g). This shows that upwelling is occurring; it is just too weak to be seen at the surface. Farther east, in the Great Australian Bight, there is also no evidence of upwelling at the surface and there is only a slight upward tilt of the isotherms toward the coast (Figure 4.3i).

The resulting currents from this simulation are more characteristic of a typical eastern boundary current (EBC) system such as the California Current System than of the coastal current system off western and southern Australia. Some characteristics of the observed Australia current system did form, however. Though the observed coastal current off western Australia (the Leeuwin Current) actually flows along the continental shelf break instead of adjacent to the coastline, there is a weak equatorward current inshore of the Leeuwin Current flowing in the same direction as the wind. That weak

equatorward current along the coastline is simulated in this experiment. Along the southern coast, the South Australia Current also flows along the shelf break rather than along the coastline. A broad, weak westward current lies inshore of the South Australia Current in the Great Australian Bight similar to the current formed in the bight in this experiment. Upwelling is frequently observed in the eastern Great Australian Bight. Even though the cooler water was not visible at the surface in this experiment, the upward tilting isotherms in this area show that the model is simulating upwelling in this region.

Though some characteristics of the observed current system were correctly simulated in this experiment, there were a number of differences from the observed system. The Leeuwin Current is poleward along the western coast then turns eastward at Cape Leeuwin instead of equatorward and westward as formed in this experiment. Along the southern coast, the South Australia Current is westward where the model formed an eastward current. The modeled current speeds are much less than the observed 50 cm s^{-1} to 70 cm s^{-1} speeds observed in the Leeuwin Current. The observed undercurrent is equatorward along the western coast and westward along the southern coast where the model formed poleward and eastward undercurrents. The location of the currents is also incorrect; the observed currents flow along the continental shelf break while the currents in this experiment are adjacent to the coast. Finally, even though the observed currents along the southern coast flow in the same direction as the wind, this experiment shows that those currents are not generated by the wind and must be the result of some other type of forcing. Further investigations will attempt to produce the observed current system characteristics above which were not modeled by this wind-forcing-only experiment and isolate which types of forcing are responsible for each of the characteristics.

B. WIND FORCING OVER TOPOGRAPHY

All model parameters in Experiment 2 are the same as in Experiment 1 except that the flat bottom has been replaced with the Sandwell and Smith (1996) bottom topography which has been interpolated to match the model's grid resolution and smoothed as

described in Chapter II (Figure 2.2b). The same realistic coastline is used. The temperature and salinity climatology has again been horizontally averaged to remove all thermohaline forcing. The wind forcing (Figure 2.5b) is the same as in Experiment 1. Table 4.1 summarizes the forcing used for each process-oriented experiment.

Though it is relatively weak and not well organized east of the Great Australian Bight, a continuous coastal current develops along the entire southern and western coasts by day 20 (Figure 4.4). As in Experiment 1, the current is westward along the southern coast, then flows around the bend at Cape Leeuwin and then northward along the western coast. Unlike the current which formed directly adjacent to the coast in Experiment 1, the core of this current develops along the continental shelf break and the upper continental slope. This current is broader than the current which developed over the flat bottom, with a width of ~ 50 km at 34°S and >100 km at 26°S . The current is also stronger than the flat-bottom current, with a maximum speed of $\sim 27 \text{ cm s}^{-1}$ at 26°S . Upwelling also develops by day 20, though it is less intense and covers less area than in the flat-bottom case. The only visible evidence of upwelling at the surface is a pool of cooler water ($\sim 17.5^{\circ}\text{C}$) ~ 20 km wide between 25°S and 27°S , while offshore water in this area is $\sim 18.5^{\circ}\text{C}$ (Figure 4.4).

Along the southern coast at day 20, the location of the coastal current along the shelf break instead of adjacent to the coastline is more apparent, especially across the Great Australian Bight with its wide continental shelf. A maximum current of $\sim 10 \text{ cm s}^{-1}$ forms at the surface at 117°E . The core of this current lies just off the shelf break ~ 35 km offshore with weaker westward currents inshore over the shelf. Farther east, at the Great Australian Bight (130°E), the current is weaker with a maximum speed of $\sim 4 \text{ cm s}^{-1}$ in the core of the current over the shelf break, ~ 180 km seaward of the coastline. Again, a weaker westward current lies over the entire width of the continental shelf. There is no undercurrent anywhere along the southern coast. There is also no cool water at the surface or any other evidence of upwelling, such as upward tilting isotherms, at any location along the southern coast (Figure 4.4).

By day 30, the coastal current is continuous along the entire southern and western coast, though it is still relatively weak east of the Great Australian Bight (Figure 4.5a). It

is stronger and broader along both coasts, and as at day 20, the core of the current continues to lie over the shelf break instead of along the coast. The peak speed of the current is $\sim 29 \text{ cm s}^{-1}$ over the shelf break at 26°S (Figure 4.5b) where the current is $\sim 200 \text{ km wide}$. Farther south along the western coast, at 34°S , the current is $\sim 120 \text{ km wide}$ and has a magnitude of $\sim 21 \text{ cm s}^{-1}$ (Figure 4.5c). More upwelling is now evident along the western coast, but the extent and magnitude of upwelling are still less than developed in the flat-bottom case of Experiment 1. The greatest extent of upwelling is a $\sim 50 \text{ km wide}$ cooler pool of water between 24°S and 27°S which has a minimum temperature of $\sim 17^\circ\text{C}$ (Figures 4.5a and 4.5d). Weaker upwelling is also visible between 29°S and 30°S and just north of Cape Naturaliste, where $\sim 18.1^\circ\text{C}$ water is upwelled to the surface (Figures 4.5e and 4.5f).

Though weaker than the western coast current, the current along the southern coast is stronger than the currents of the flat-bottom experiment. As in the previous experiment, the current is weakest at the eastern end of the coast and increases in strength with distance toward the west. At the middle of the Great Australian Bight, the maximum surface current speed is $\sim 5 \text{ cm s}^{-1}$. The core of this current lies over the shelf break $\sim 180 \text{ km offshore}$ (Figure 4.5g). A weaker ($< 3 \text{ cm s}^{-1}$) westward current develops inshore of this current over the continental shelf. Farther west, at 117°E , the current increases to a speed of $\sim 12 \text{ cm s}^{-1}$ (Figure 4.5h). The current remains trapped along the shelf break, which at this location is $\sim 35 \text{ km from the shore}$. A field of weaker westward currents lies over the shelf at this location, as well. There is still no undercurrent at any location along the southern coast and no evidence of upwelling, either at the surface or at any subsurface level.

By day 60, the current has continued to intensify (Figure 4.6a), with maximum speeds of $\sim 40 \text{ cm s}^{-1}$ at 26°S (Figure 4.6b) and $\sim 32 \text{ cm s}^{-1}$ at 34°S (Figure 4.6c). The current has broadened to $\sim 200 \text{ km wide}$ along the entire western coast north of Cape Leeuwin (Figure 4.6a). The upwelling along the western coast has also increased in area to a near continuous band of cooler water along the coast from Cape Leeuwin to the northern boundary of the model domain. For example, a pool of $\sim 14.8^\circ\text{C}$ water lies along with coast at 26°S with 18.5°C offshore (Figure 4.6d). The upwelling at 34°S is weaker

with 17.3°C at the surface near the coastline (Figure 4.6e). The extent of upwelling is still much less than that produced by the flat-bottomed model run. Though a broad and slow ($< 2 \text{ cm s}^{-1}$) poleward flow exists over much of the western coast offshore area below 1000 m depth, there is still no realistic undercurrent (Figures 4.6b and 4.6c). This broad opposing flow is likely due simply to continuity in the model.

The currents along the southern coast have also intensified from day 30 to day 60. At the middle of the Great Australian Bight (130°E), the maximum surface current speed has reached $\sim 15 \text{ cm s}^{-1}$ with the core of this current remaining over the continental shelf break $\sim 180 \text{ km}$ from the shore (Figure 4.6f). Near the western end of the southern coast, at 117°E , the current has intensified to $\sim 31 \text{ cm s}^{-1}$. The current has moved slightly offshore from previous times to $\sim 45 \text{ km}$ from the coast, still over the continental slope (Figure 4.6g). The weaker, westward currents over the continental shelf remain at both locations. The broad, slow, and deep opposing flow described for the western coastal currents exists along the southern coast as well, but there is still no realistic subsurface undercurrent.

A unique feature which develops by day 60 is a relatively narrow band of slightly warmer water at the surface along the shelf break in the eastern one-third of the Great Australian Bight (Figures 4.6a and 4.6h). A temperature cross section of the upper 100 m of the water column at 125°E (Figure 4.6h) shows that this band of warmer water is $\sim 40 \text{ km}$ wide (i.e., between 34.2°S and 34°S). The maximum sea surface temperature in this band is 18.75°C while water outside the band is 18.37°C . There is no visible evidence of upwelling at any location along the southern coast, though there is a slight upward tilt of isotherms in the upper 100 m of the water column at the western end of the coastline (not shown).

The current pattern at day 90 (not shown) is little changed from day 60. The core of the westward and equatorward currents remains over the shelf break and continental slope for all locations. The upwelling along the western coast is more continuous than at day 60, but there is still no upwelling along the southern coast. The ribbon of warm water along the shelf break of the Great Australian Bight persists.

As in Experiment 1, the overall current pattern formed in this experiment was more characteristic of a typical Eastern Boundary Current system than of the current pattern in this region. However, several features which are typical of the Australian currents were correctly modeled. The addition of topography forced a change in the location of the coastal currents from the coastline to the continental shelf break, where they are observed to occur both along the western coast and the southern coast. Inshore of the main flow of the coastal current, weaker poleward currents along the western coast and westward currents along the southern coast formed (on the continental shelf) which are similar to those which are observed in the region. The slightly warmer band of surface water that formed along the shelf break of the Great Australian Bight is representative of the warm water mass which is observed to form in this area. The observed water mass is 2-3°C warmer than surrounding waters, while the modeled water mass was only ~0.5°C warmer. The areal extent of the water mass was not large enough, probably due to the modeled currents flowing in the opposite direction of the observed current which spreads the water mass along the southern coast.

Other features continue to be different from those observed. The Leeuwin Current and South Australia Current are still flowing with the wind rather than against the wind. The undercurrent formed is too broad, weak, and deep and is likely due to continuity in the model formulation rather than the formation of a true undercurrent. Though not as intense or widespread as in Experiment 1, upwelling is simulated along the western coast where no upwelling is observed. No upwelling formed along the southern coast at the eastern end of the Great Australian Bight or in the Eyre/Kangaroo Island areas where upwelling is observed to occur. Although an eddy field is observed to occur offshore of the Leeuwin Current along the western coast and offshore of the South Australia Current along the southern coast, no eddies were formed in this experiment. The next set of experiments will introduce thermohaline forcing to determine which of these features can be correctly modeled.

C. THERMOHALINE FORCING OVER A FLAT BOTTOM

Experiment 3 is the first to use the full annual temperature (Figure 2.3b) and salinity (Figure 2.4b) climatology, which models the observed density/sea height gradient and introduces thermohaline forcing into the model. There is no wind forcing in this experiment. The same coastline and 2500 m deep flat bottom from Experiment 1 are used, eliminating any topographic effects. The goal of this experiment is to isolate which features in the current system are generated by the thermohaline forcing. Table 4.1 summarizes the forcing used for each process-oriented experiment.

The relatively strong alongshore thermohaline gradient forces a broad onshore flow off the western coast, which is deflected poleward along the coast. By day 20, the current is stronger than in either of the wind-forcing-only experiments ($\sim 120 \text{ cm s}^{-1}$ maximum speed). The current is poleward along the entire length of the western coast, then turns eastward around Cape Leeuwin due to the Coriolis force, and continues eastward along the southern coast to the eastern end of the Great Australian Bight (Figure 4.7a). At 34°S , the poleward current is $\sim 70 \text{ km}$ wide and has a maximum speed of $\sim 110 \text{ cm s}^{-1}$. Underneath this surface current, the core of the $\sim 14 \text{ cm s}^{-1}$ undercurrent lies at $\sim 600 \text{ m}$ depth (Figure 4.7b). A band of warm subtropical water is advected poleward along the coast by this current. At Cape Leeuwin, the sea surface temperature in the current is $\sim 22^\circ\text{C}$, while the offshore water is $\sim 18.5^\circ\text{C}$ (Figure 4.7a). This warm band of water extends around the cape and reaches as far east as 120°E . Along the southern coast, the current becomes narrower and weaker as it moves eastward along the coast of the Great Australian Bight until it is no longer recognizable as a continuous coastal current in the Gulfs region. The maximum surface speed is $\sim 15 \text{ cm s}^{-1}$ at 130°E .

By day 30, the poleward current along the western coast reaches a maximum speed of $\sim 135 \text{ cm s}^{-1}$. The poleward advection of warm subtropical water along the coast continues and the sea surface temperature in the current at Cape Leeuwin reaches 23.2°C (Figure 4.8a). Strong downwelling is apparent within $\sim 75 \text{ km}$ of the coast in this area in the upper 500 m of the water column. Below that depth, upwelling is occurring to a depth of $\sim 1200 \text{ m}$ (Figure 4.8b). At Cape Leeuwin, at $\sim 34^\circ\text{S}$, the surface current is $\sim 100 \text{ cm s}^{-1}$ and there is a $\sim 17 \text{ cm s}^{-1}$ undercurrent centered at $\sim 600 \text{ m}$ depth (Figure 4.8c).

The strong horizontal temperature gradient at the surface along the seaward side of the current along with the large horizontal shear from the strong and narrow current result in barotropic instability. In addition, the vertical shear caused by the swift poleward current overlying a relatively strong equatorward undercurrent with its core only 600 m deep leads to baroclinic instability. As a result of these instabilities and the coastline irregularity, two \sim 100 km wide meanders form just south of Cape Leeuwin and begin to move eastward along the current (Figure 4.8a).

Along the southern coast, the band of warm water reaches across the entire width of the Great Australian Bight by day 30 (Figure 4.8a). The continuous coastal current now extends as far east as Kangaroo Island (\sim 137°E). The strong coastal current, with more quiescent waters offshore and a strong opposing undercurrent underneath, decreases the stability in this region as well.

In the Great Australian Bight, at 130°E, the eastward surface current has reached a speed of \sim 50 cm s $^{-1}$ and has an opposing undercurrent of \sim 10 cm s $^{-1}$ with its core at \sim 850 m depth (Figure 4.8d). The current is \sim 60 km wide and lies adjacent to the coastline. This is the maximum speed reached by the surface current in this area at any time during the model simulation. Between days 30 and 60, the surface current speed slowly decreases and the core of the current moves offshore as the undercurrent moves upward until it surfaces at day 60, yielding an (unrealistic) westward surface current along the coast and an eastward surface current \sim 50 km offshore. Farther west, at 117°E, the surface current had already reached a maximum speed of 67 cm s $^{-1}$ at day 20 and decreases to \sim 57 cm s $^{-1}$ by day 30. The undercurrent here has continued to increase to \sim 38 cm s $^{-1}$. The undercurrent lies right along the coast with its core at \sim 600 m depth (Figure 4.8e). By this time the surface current has broadened to \sim 200 km as the first anticyclonic meander approaches this location.

After day 30, the two meanders propagate eastward with the current. Three new meanders subsequently form and begin moving eastward around the southwest corner of the continent by day 39. By day 48, the two meanders develop into eddies and several new meanders form and begin evolving into eddies as well. During this same time period, the poleward current along the western coast continues to move offshore and

weaken as the undercurrent becomes shallower and strengthens. Along the southern coast between Cape Leeuwin and the western Great Australian Bight, the current breaks down into a field of eastward propagating eddies, so that by day 60, the coastal current as a continuous flow no longer exists in this area. In the bight, the coastal current remains, but it weakens to ~ 20 cm s $^{-1}$ while the undercurrent strengthens to ~ 15 cm s $^{-1}$ and shoals, causing an irregular flow with the eastward coastal current pushed offshore and a relative strong westward current at several locations along the shore.

By day 60, the predominant coastal current off the western coast is the equatorward current along the shore that formed from the undercurrent shoaling as the poleward surface current moved offshore (Figure 4.9). The broad geostrophic onshore flow along the thermohaline gradient still results in a poleward current, but that current now lies ~ 120 km offshore. The meanders along the southwest corner of the continent develop into eddies. The area between Cape Leeuwin and the Great Australian Bight is no longer recognizable as a coastal current; instead it is a field of eddies moving eastward. The eastward South Australia Current remains from mid-bight to Kangaroo Island, but it has been pushed 50-100 km offshore and the westward undercurrent shoals to form a westward surface current inshore of the South Australia Current in some locations.

By day 81, the current reversal is complete across the entire model domain (Figure 4.10). The undercurrent completely shoals forming a westward coastal current throughout the Great Australian Bight. The eastward current in this area no longer exists. A number of the eddies also disappear leaving a westward current along the southern coast from Kangaroo Island to Cape Leeuwin and a poleward current along the entire western coast. Several large (as wide as ~ 250 km) eddies remain at the southwest corner of the continent along the western coast.

The overall current pattern formed in this experiment, unlike those of the wind-only experiments, was more similar to the coastal current system off the western and southern coasts of Australia than to a typical eastern boundary current system. The broad onshore flow along the thermohaline gradient off the western coast was correctly represented. This onshore flow was directed southward to form a narrow and swift

poleward current along the western coast. This poleward current advected a narrow band of warm subtropical water poleward along the coast, then around Cape Leeuwin and eastward along the southern coast similar to the advection which is observed. The poleward current forced strong downwelling along the western coast, which is also observed. Finally, meanders and eddies which are frequently observed in this region were simulated in this experiment.

Though a number of features of the current system were correctly simulated in this experiment, there were still significant differences from the observed system. The coastal current along the western and southern coasts was too strong; in fact, at some times in some locations the current speed was more than double the observed speed. Even though the coastal current in this experiment flowed in the correct direction, its location was incorrect. The current formed along the shore, while the observed currents flowed along the continental shelf break. The incorrect location is related to another discrepancy: there was no weak opposing current inshore of the coastal current as observed. No upwelling was simulated anywhere along the southern coast, although upwelling is observed to frequently occur in the eastern end of the Great Australian Bight and in the Kangaroo Island area. Finally, the coastal current moved offshore as time passed, while the observed current remained trapped along the continental shelf break/continental slope. This offshore movement allowed the undercurrent to shoal and finally produce a westward and equatorward current along the coast. This resulted in a complete current reversal from the observed currents by day 81.

D. THERMOHALINE FORCING OVER TOPOGRAPHY

All model parameters in Experiment 4 are the same as in Experiment 3 except that the flat bottom has been replaced with the Sandwell and Smith (1996) bottom topography (Figure 2.2b) which has been interpolated to match the model's grid resolution and smoothed as described in Chapter II. The same realistic coastline is used. As in Experiment 3, this simulation again uses the strong thermohaline gradient (Figures 2.3b and 2.4b) unique to the Leeuwin Current System. In the absence of the opposing wind field, this thermohaline gradient will be the only forcing modeled. The addition of

topography will allow any topographic effects, which were missing from Experiment 3, to develop. Table 4.1 summarizes the forcing used for each process-oriented experiment.

Just as in Experiment 3, by day 20 the relatively strong alongshore thermohaline gradient forces a broad onshore flow off the western coast, which is then deflected toward the south as it approaches the continental shelf (Figure 4.11a). This results in a poleward current along the continental shelf break/continental slope. The addition of topography results in a much weaker current than in the flat-bottomed case of Experiment 3 ($\sim 28 \text{ cm s}^{-1}$ vice $\sim 120 \text{ cm s}^{-1}$ at 26°S) (Figure 4.11b). As before, the current is quite broad at its origin ($\sim 250 \text{ km}$ at 26°S) and becomes narrower and stronger as it flows southward along the shelf break. At Cape Leeuwin, the current has narrowed to $\sim 100 \text{ km}$ wide and strengthened to $\sim 50 \text{ cm s}^{-1}$ (Figures 4.11a and 4.11c). A continuous equatorward undercurrent lies underneath this poleward surface current, beginning at $\sim 18 \text{ cm s}^{-1}$ with a core depth of $\sim 800 \text{ m}$ at 26°S (Figure 4.11b), then slightly strengthening and shoaling to $\sim 20 \text{ cm s}^{-1}$ at $\sim 450 \text{ m}$ off Cape Leeuwin (Figure 4.11c). A band of warm subtropical water is advected southward along the entire western coast, then around the cape and eastward to $\sim 120^\circ\text{E}$ along the southern coast (Figure 4.11a).

Along the southern coast, the eastward surface current reaches its maximum strength of $\sim 55 \text{ cm s}^{-1}$ by 117°E , where the current is generally accepted as part of the Leeuwin Current (Ridgeway and Condie, 2004). The current subsequently loses strength as it flows eastward along the shelf break of the southern coast as the South Australian Current. At 130°E in the middle of the Great Australian Bight, the current speed has dropped to $\sim 20 \text{ cm s}^{-1}$ (Figure 4.11d). It is not recognizable as a continuous coastal current in the eastern Bight and beyond. Downwelling is apparent at 117°E with warm water at the surface and isotherms tilted downward at the coast in the upper 500 m of the water column (Figure 4.11e). Isotherms also tilt downward toward the coast, consistent with downwelling, in the Great Australian Bight (Figure 4.11f).

By day 25 (not shown), two meanders begin to form in the current along the southwest corner of the continent, south of Cape Leeuwin. Two additional meanders also begin to form farther north along the western coast. By day 30, all four meanders are clearly visible in Figure 4.12a. As before, the current is broad ($\sim 200 \text{ km}$) but relatively

weak ($\sim 30 \text{ cm s}^{-1}$) near its origin in the north, and then it narrows and increases in strength as it flows toward the south to a width of $\sim 75 \text{ km}$ and a speed of $\sim 45 \text{ cm s}^{-1}$ at Cape Leeuwin. At 26°S , a $\sim 15 \text{ cm s}^{-1}$ equatorward undercurrent opposes the poleward surface current with its core at $\sim 750 \text{ m}$ depth (Figure 4.12b). This undercurrent becomes stronger and shallower with distance to the south where it flows at $\sim 20 \text{ cm s}^{-1}$ at 650 m depth at Cape Leeuwin (Figure 4.12c). Downwelling is apparent along the entire western coast both in the warm band of surface water (Figure 4.12a) and the subsurface isotherms tilting downward toward the coast in the upper 500 m of the water column, for example at 26°S (Figure 4.12d).

After the surface current rounds the bend beyond Cape Leeuwin and flows eastward along the southern coast, it reaches its maximum speed of $\sim 72 \text{ cm s}^{-1}$ at 117°E (Figure 4.12e), then it weakens as it continues eastward down to $\sim 25 \text{ cm s}^{-1}$ along the Great Australian Bight at 130°E (Figure 4.12f). The current remains continuous across the entire Great Australian Bight and as far east as Kangaroo Island ($\sim 137^\circ\text{E}$). The current remains anchored to the continental shelf break/continental slope at all locations, with no indications of the broadening and moving away from the coast which occurred in Experiment 3. A westward undercurrent of $\sim 20 \text{ cm s}^{-1}$ centered at $\sim 650 \text{ m}$ depth opposes the surface flow at 117°E (Figure 4.12e). At 130°E , near the origin of the undercurrent, the undercurrent is much weaker at $\sim 5 \text{ cm s}^{-1}$ with a weak core at $\sim 850 \text{ m}$ depth adjacent to the slope (Figure 4.12f). In this area, however, the westward subsurface flow is very broad and disorganized, unlike the strong core found farther west.

Over the shelf in the Great Australian Bight, the circulation is all eastward (Figure 4.12a). There is no indication of a gyre-type circulation in the Bight or a weak westward inshore current as is observed in this area. Along with the observed gyre circulation, upwelling is frequently observed to occur in the eastern Bight. In contrast, the model produces a pool of warmer water at the surface and downward tilting subsurface isotherms (Figure 4.12g), indicating downwelling instead of upwelling.

The band of warm Leeuwin Current water extends as far along the south coast as 122°E (Figure 4.12a). There is a large temperature gradient in this area with water in the current at 19.6°C and water offshore of the current at 15.9°C . Farther east, the contrast is

not as great, but a band of slightly warmer water is advected eastward along the continental shelf break across the entire Great Australian Bight. At 130°E, the water is the current is 18.3°C and water offshore of the current at 15.5°C. Along with this band of warm water, downwelling is apparent across the southern coast (e.g., Figures 4.12h and 4.12i).

After day 30, the meanders continue to grow and more meanders form. By day 48 (not shown), an eddy dipole pair lies along the offshore side of the current south of Cape Leeuwin. A series of eddy-like warm features lie along the offshore side of the current between this eddy pair and the western Great Australian Bight.

At day 60, the Leeuwin Current along the western coast remains quite broad at its origin at the northern end of the model domain and narrows by the time it reaches the capes (Figure 4.13). It also strengthens from $\sim 20 \text{ cm s}^{-1}$ at 26°S to $\sim 50 \text{ cm s}^{-1}$ at the Cape Leeuwin. There are now five meanders/eddies along the western coast, the largest of which is $\sim 400 \text{ km}$ wide off Cape Leeuwin. Downwelling persists along the entire western coast.

After rounding the bend, the current still reaches its maximum speed of $\sim 75 \text{ cm s}^{-1}$ at 117°E. The eddy-like warm water features persist along the offshore side of the current as far east as the western Great Australian Bight. The warm Leeuwin Current water extends into the western half of the Great Australian Bight and a weaker band of warm water lies along the shelf break across the entire length of the southern coast. The westward coastal current is now continuous along the entire length of the southern coast to the eastern boundary of the model domain. The current speed decreases to the east to $\sim 25 \text{ cm s}^{-1}$ at 130°E. The current remains correctly positioned along the shelf break. The undercurrent remains similar in speed and depth to those described for day 30 at all locations. There is still no westward inshore current in the Great Australian Bight and no upwelling at any location along the southern coast. In fact, downwelling persists at all locations.

By day 72, warm-core, anticyclonic eddies have separated from the current at both 34°S and 37°S and begin to drift westward (Figure 4.14). The field of eddy-like

features offshore of the current between 115°E and 125°E persists, and meanders begin to form in the current in this area. Smaller meanders begin to form along the current across the Great Australian Bight. Otherwise, there is little discernible change in the current system through the end of the 90 day model run.

The overall current pattern formed in this experiment was more similar to the coastal current system off the western and southern coasts of Australia than those in any other experiment so far. The broad onshore flow along the thermohaline gradient off the western coast was correctly represented and correctly directed southward to form a narrow and swift poleward current along the continental shelf break off the western coast. This poleward current advected a narrow band of warm subtropical water poleward along the coast, then around Cape Leeuwin and eastward along the southern coast similar to the advection which is observed. The poleward current forced strong downwelling along the western coast, which is also observed. Meanders and eddies which are frequently observed in this region were also formed in this simulation. The greatest contrast from the previous experiment was the correct location of the current along the shelf break. The current formed in the correct location, and it also remained anchored to the continental shelf break/continental slope throughout the model run instead of broadening and moving offshore as occurred in the previous experiment.

There were still some incorrectly modeled features in this experiment. While not as strong as the currents which developed in Experiment 3, the surface coastal current was slightly too strong along the western coast and the western portion of the southern coast. There was no opposing current inshore of the coastal current on shelf as observed. Just as in the previous experiment, no upwelling was simulated anywhere along the southern coast, although upwelling is observed to frequently occur in the eastern end of the Great Australian Bight and in the Kangaroo Island area.

E. WIND AND THERMOHALINE FORCING OVER A FLAT BOTTOM

Experiment 5 uses the full annual temperature (Figure 2.3b) and salinity (Figure 2.4b) climatology which introduces thermohaline forcing into the model. The wind field (Figure 2.5b) used in Experiments 1 and 2 is also used to force the model. The same

coastline and 2500 m deep flat bottom from Experiments 1 and 3 are used, eliminating any topographic effects. The goal of this experiment is to determine which features in the current system are generated by the combination of wind and thermohaline forcing in the absence of any topographic effects. Table 4.1 summarizes the forcing used for each process-oriented experiment.

As in the previous experiments which included thermohaline forcing, the relatively strong alongshore thermohaline gradient forces a broad onshore flow off the western coast, which is deflected toward the south as it nears the coast. This results in a relatively strong and narrow poleward surface current adjacent to the coast (Figure 4.15a). By day 20, the current is $\sim 35 \text{ cm s}^{-1}$ at 26°S (Figure 4.15b) and $\sim 90 \text{ cm s}^{-1}$ at 34°S near Cape Leeuwin (Figure 4.15c). This poleward current, the Leeuwin Current, begins quite broad ($\sim 200 \text{ km}$) at its origin along the northern portion of the western coast and narrows with distance to the south to $\sim 100 \text{ km}$ at Cape Leeuwin. Below this surface current, an opposing undercurrent with a 650 m deep $\sim 15 \text{ cm s}^{-1}$ core at 34°S (Figure 4.15c) and a 600 m deep $\sim 8 \text{ cm s}^{-1}$ core at 26°S (Figure 4.15b) flows toward the equator. As before, a band of warm subtropical water is advected poleward along the coast by this current (Figure 4.15a).

As the surface current follows the coastline around the southwest corner of the continent and continues eastward along the southern coast, it weakens slightly to $\sim 65 \text{ cm s}^{-1}$ at 117°E . A continuous eastward coastal current extends across the entire Great Australian Bight, but it is narrower and weaker ($\sim 30 \text{ km wide}$ and $\sim 15 \text{ cm s}^{-1}$ at 130°E) than farther west. The current is incorrectly positioned directly adjacent to the coast at all locations where the current exists. A westward undercurrent lies underneath the eastward surface with a speed of $\sim 30 \text{ cm s}^{-1}$ and a core depth of $\sim 650 \text{ m}$ at 117°E (Figure 4.15d). Farther east, in the Great Australian Bight, no realistic undercurrent has yet formed, but there is a core of $\sim 6 \text{ cm s}^{-1}$ at $\sim 2300 \text{ m}$ depth (Figure 4.15e) probably due to continuity in the model. Warm Leeuwin Current water is advected around the Cape and eastward along the southern coast as far as $\sim 120^\circ\text{E}$ (Figure 4.15a). Downwelling is apparent at 117°E by the warm water at the surface and the downward tilting isotherms in the upper 500 m of the water column in the 50 km nearest the shore. Below 500 m, the isotherms

are tilted upward due to upwelling forced by the undercurrent (Figure 4.15f). In the Great Australian Bight, downward tilting isotherms in the upper 500 m are also apparent. The upward tilting of the deeper isotherms is very slight due to the weaker and deeper undercurrent (Figure 4.15g).

By day 25 (not shown), three meanders begin to form in the surface current in the area around Cape Leeuwin. The extent of the warm water band along the southern coast continues to move eastward. The coastal current intensifies in the Great Australian Bight and the extent of the continuous coastal current continues to move eastward.

By day 30, the current at the northern end of the western coast weakens to $\sim 17 \text{ cm s}^{-1}$ and broadens to $\sim 300 \text{ km}$ (Figure 4.16a). At 34° , near Cape Leeuwin, the current intensifies to $\sim 95 \text{ cm s}^{-1}$ and two of the three meanders in this area grow to a width of $\sim 100 \text{ km}$ each. Along much of the western coast, the current begins to drift offshore. Advection of the warm subtropical water poleward along the coast continues and downwelling is prevalent along the entire western coastline.

By day 30 along the southern coast, the southernmost meander at Cape Leeuwin has begun to drift eastward along the southern coast with the current. The warm Leeuwin Current water reaches the western Great Australian Bight. The surface current intensifies to $\sim 86 \text{ cm s}^{-1}$ at 117°E (Figure 4.16b). The current intensifies along the remainder of the southern coast as well, reaching $\sim 42 \text{ cm s}^{-1}$ in the Great Australian Bight at 130°E (Figure 4.16c). The current has not broadened appreciatively in this area. The current is now a continuous eastward surface flow as far east as Kangaroo Island. Beneath the surface, the westward undercurrent remains strong at $\sim 27 \text{ cm s}^{-1}$ at 650 m depth at 117°E (Figure 4.16b). Farther east, at 130°E , the undercurrent becomes much more organized and strengthens to $\sim 10 \text{ cm s}^{-1}$ with a $\sim 900 \text{ m}$ deep core (Figure 4.16c). Downwelling persists from the surface down to $\sim 500 \text{ m}$ depth all along the southern coast (e.g., Figure 4.16d). Below 500 m depth, strong upwelling continues at 117°E and weaker upwelling is apparent at 130°E . There is no evidence of upwelling at the surface at any location along the southern coastline.

After day 30, the meanders in the vicinity of Cape Leeuwin continue to grow and two more meanders form between Cape Leeuwin and the western Great Australian Bight. By day 42 (not shown), five meanders lie between Cape Leeuwin and the Great Australian Bight and the warm Leeuwin Current is advected into the western third of the Bight. The surface current along the western coast continues to weaken and move away from the coastline as the undercurrent intensifies and shoals. By day 45, the undercurrent has surfaced along much of the western coast resulting in a narrow and strong (up to ~ 55 cm s^{-1}) equatorward current along the coast and a weaker broad poleward current offshore (Figure 4.17). Eddy fields lies along the coast from 33°S (just north of Cape Naturaliste) around the bend and along the south coast to the Great Australian Bight.

By day 60, the equatorward current at the northern end of the western coast intensifies to ~ 85 cm s^{-1} (Figure 4.18). The two meanders in the vicinity of Cape Leeuwin become anticyclonic eddies and begin to drift away from the current. The undercurrent completely surfaces between Cape Leeuwin and the Great Australian Bight resulting in a westward surface current along the coast inshore of the eddy field in this location. The undercurrent begins to surface in the Great Australian Bight, causing the surface current to become discontinuous and disorganized, but not yet completely westward.

After day 60, eddies continue to grow and separate from the current near the southwestern corner of the continent. Meanders begin to form in the equatorward current along the western coast. The eddy field along the southern coast between Cape Leeuwin and the Great Australian Bight begins to break down, but the westward current along the coast persists. By day 72 (Figure 4.19), the undercurrent completely surfaces along the entire coastline, though still somewhat disorganized in the Great Australian Bight, resulting in a complete current reversal as occurred in Experiment 3.

The overall current pattern formed in this experiment, began quite similar to the coastal current system off the western and southern coasts of Australia. The currents which developed were more similar to those formed in the thermohaline forcing experiments than to those of the wind forcing experiments, showing that the strong thermohaline gradient has a greater effect on the currents of the region than the wind.

The broad onshore flow at the northern end of the western coast was correctly modeled. Similar to the observed currents, this onshore flow was deflected toward the south to form a poleward current which narrowed and strengthened with distance toward the south. The current continued around the cape and eastward along the southern coast. The current advected a narrow band of warm subtropical water south along the western coast and then east along the southern coast to the Great Australian Bight. Also as observed, meanders and eddies formed in the current in the vicinity of Cape Leeuwin and an eddy field formed offshore of the current along the southern coast between Cape Leeuwin and the Great Australian Bight. Downwelling was prevalent along the western coast.

As in previous experiments, the modeled current system still differed from the observed system in several ways. The coastal current along the western and southern coasts was too strong; however, its speed was less than the currents which developed in Experiment 3 with only thermohaline forcing, showing that the wind forcing does counteract the thermohaline forcing to slow the currents. As in Experiment 3, the current flowed in the correct direction, but the current was incorrectly located adjacent to the shore rather than a few kilometers offshore where the shelf break should lie. There was no weak opposing current inshore of the coastal current. No upwelling developed anywhere along the southern coast, although upwelling is observed to frequently occur in the eastern end of the Great Australian Bight and in the Kangaroo Island area. Finally, just as in Experiment 3, the coastal current moved offshore allowing the undercurrent to shoal and finally produce a westward and equatorward current along the coast. The entire current system reversed in direction from the observed current system by day 72. The only significant difference from Experiment 3 (thermohaline forcing only over flat bottom) was that the currents were weaker.

F. WIND AND THERMOHALINE FORCING OVER TOPOGRAPHY

Experiment 6 was initialized with the most complete set of annually averaged climatology possible. The ECMWF wind forcing used (Figure 2.5b) in Experiments 1, 2, and 5 was used to force the model. The full annual temperature (Figure 2.3b) and salinity

(Figure 2.4b) fields from Experiments 3, 4, and 5 provide thermohaline forcing. The Sandwell and Smith (1996) bottom topography (Figure 2.2b) allows the development of topographic effects and the same realistic coastline from the other experiments was used. Table 4.1 summarizes the forcing used for each process-oriented experiment.

As in the other experiments which incorporate thermohaline forcing, by day 20 a broad onshore flow develops along the northern end of the western coast (Figure 4.20a). This onshore flow is deflected toward the south as it approaches the continental slope and results in a poleward surface current. The current is $\sim 27 \text{ cm s}^{-1}$ and $\sim 200 \text{ km}$ wide at 26°S near its origin (Figure 4.20b) and it intensifies to $\sim 47 \text{ cm s}^{-1}$ and narrows to $\sim 100 \text{ km}$ by Cape Leeuwin (Figure 4.20c). Beneath this relatively swift and narrow current, an opposing equatorward undercurrent develops. The core of the undercurrent lies at $\sim 450 \text{ m}$ depth and moves at $\sim 20 \text{ cm s}^{-1}$ at 34°S , near Cape Leeuwin (Figure 4.20c). The undercurrent intensifies slightly to $\sim 22 \text{ cm s}^{-1}$ and deepens to $\sim 750 \text{ m}$ depth at 26°S (Figure 4.20b). A band of warm subtropical water is advected southward along the entire western coast (Figure 4.20a).

The Leeuwin Current follows the continental shelf break around the southwest corner of the continent and continues eastward along the southern coast where it reaches its maximum speed of $\sim 51 \text{ cm s}^{-1}$ and narrows to $\sim 60 \text{ km}$ wide at 117°E . The opposing westward $\sim 19 \text{ cm s}^{-1}$ undercurrent with a $\sim 600 \text{ m}$ deep core lies underneath this surface current (Figure 4.20d). The weaker South Australia Current continues eastward across the width of the Great Australian Bight. This current is also $\sim 60 \text{ km}$ wide and reaches a speed $\sim 18 \text{ cm s}^{-1}$ at 130°E in the middle of the Bight. There is a $\sim 5 \text{ cm s}^{-1}$ undercurrent with a core $\sim 1000 \text{ m}$ deep core, but a broad weak and disorganized westward current extends all the way to the bottom at 2500 m (Figure 4.20e). Along its entire length, the surface coastal current is correctly positioned along the continental shelf break. The current is weak and disorganized over the broad Great Australian Bight shelf inshore of the South Australia Current.

Leeuwin Current water is advected around the cape and eastward to $\sim 119^\circ\text{E}$. A second band of warm water begins to form and move eastward from the west Great Australian Bight from $\sim 123^\circ\text{E}$ and extends across the western third of the bight. As

observed, this warm water is a different water mass from the Leeuwin Current water and is identifiable by its slightly lower salinity (Figure 4.20f). With no inshore current, no upwelling has formed along the eastern Great Australian Bight. In fact, weak downwelling is apparent in the upper 500 m of the water column at 134.5°E where upwelling should occur (Figure 4.20g).

At day 30, the Leeuwin Current along the western coast is ~200 km wide at its origin at the northern end of the western coast (Figure 4.21a). Its speed increases slightly to $\sim 30 \text{ cm s}^{-1}$. The current narrows to ~100 km and strengthens to $\sim 41 \text{ cm s}^{-1}$ at Cape Leeuwin (Figure 4.21b). The equatorward undercurrent lies around a $\sim 21 \text{ cm s}^{-1}$ core at ~750 m at the cape (Figure 4.21b) and strengthens slightly to $\sim 23 \text{ cm s}^{-1}$ as it shoals to ~450 m depth by 26°S (Figure 4.21c). The surface current still lies along the continental shelf break, with no apparent broadening or offshore drift, as occurred in all the flat bottom experiments. Two meanders begin to form at $\sim 28^\circ\text{S}$ and $\sim 30^\circ\text{S}$. Warm water continues to be advected southward along the entire length of the coast and downwelling is prevalent at all locations (e.g., at 26°S, Figure 4.21d).

The relatively strong Leeuwin Current continues around the shelf break of the cape and eastward along the southern coast to reach $\sim 62 \text{ cm s}^{-1}$ at 117°E (Figure 4.21e). Two meanders begin to form in the current to the south and east of Cape Leeuwin as the current moves around the bend (Figure 4.21a). The surface current is stronger than at previous times across much of the southern coast. The speed reaches $\sim 22 \text{ cm s}^{-1}$ at 130°E (Figure 4.21f), then weakens as it continues east. There is now a continuous surface coastal current beyond Kangaroo Island. The South Australia Current still lies along the shelf break of the broad Great Australian Bight continental shelf. On the shelf, the inshore current remains weak and disorganized, flowing eastward in some locations and westward in other locations (Figure 4.21a).

The warm Leeuwin Current water now extends east to $\sim 122^\circ\text{E}$ (Figure 4.21a) and a second, lower salinity, warm water mass extends eastward from the western Great Australian Bight (Figures 4.21a and 4.21g). As expected, downwelling is apparent at both 117°E (Figure 4.21h) and off the mid-Great Australian Bight at 130°E (Figure 4.21i), both by the pool of warmer water at the surface and by the isotherms tilting

downward toward the coast in the upper 500 m of the water column. Downwelling is also occurring at 134.5°E in the eastern end of the Great Australian Bight where upwelling is observed to occur (Figure 4.21j) .

After day 30, the two meanders in the Leeuwin Current at ~28°S and ~30°S continue to grow and a new meander begins to form just north of Cape Leeuwin. The two meanders south and east of Cape Leeuwin continue to grow and by day 42 (not shown) have become eddies, though not yet detached from the current. The extent of the Leeuwin Current warm water mass along the southern coast continues to grow. By day 42, the band of warm water reaches across the Great Australian Bight. From temperature alone, there appears to be only one continuous warm water mass in a narrow band along the shelf break, but the waters across the western Great Australian Bight are still slightly less saline than those farther west (Figure 4.22). By day 51, one of the eddies south of Cape Leeuwin detaches from the current and begins to drift westward (Figure 4.23).

At day 60, the meanders in the Leeuwin Current along the western coast continue to grow. The meander at ~28°S develops into a ~160 km diameter anticyclonic eddy, though not yet detached from the current (Figure 4.24a). Although meanders/eddies form, the basic flow of the poleward surface current remains anchored along the continental shelf break. The current remains relatively strong, ~43 cm s⁻¹ at 30°S (Figure 4.24b) and intensifies to ~75 cm s⁻¹ by 34.5°S (Figure 4.24c). An equatorward surface current develops on the continental shelf inshore of the poleward coastal current along the entire western coast (e.g., at 30°S, Figure 4.24b), though it is quite weak along the southern half of the coast.

The eddy which detached from the current south of Cape Leeuwin on day 51 is ~200 km wide and its center lies ~350 km west of the current (Figure 4.24a). It continues to drift westward. A field of meanders lies along the offshore side of the current along the southern coast between Cape Leeuwin and the Great Australian Bight, with an associated series of wave-like warm water features in the temperature structure. A continuous surface coastal current now spans the entire length of the southern coast to the eastern boundary of the model domain (Figure 4.24a). The current has strengthened slightly across the Great Australian Bight to ~25 cm s⁻¹ at 130°E (Figure 4.24d). The

current remains attached to the continental shelf break along its entire path. The surface current weakens slightly ($\sim 56 \text{ cm s}^{-1}$ at 117°E , Figure 4.24e) from previous times at the western end of the coastline as the eddy field develops in that area. The opposing westward undercurrent has a $\sim 700 \text{ m}$ deep $\sim 7 \text{ cm s}^{-1}$ core at 130°E (Figure 4.24d) and intensifies and shoals slightly as it moves west to $\sim 17 \text{ cm s}^{-1}$ and $\sim 550 \text{ m}$ depth at 117°E (Figure 4.24e). There is still no discernible gyre or westward inshore current over the Great Australian Bight shelf. The entire current pattern over the shelf remains very disorganized (Figure 4.24a). With no westward current along the shore, no upwelling has developed. Downwelling is prevalent along the entire southern coast, even in the eastern Great Australian Bight where upwelling should occur (Figure 4.24f).

After day 60, more west coast meanders develop into eddies, with one detaching from the current at $\sim 28^\circ\text{S}$ at day 75 (Figure 4.25). Meanders also become eddies at 32°S and just north of Cape Leeuwin at $\sim 34^\circ\text{S}$. The eddy south of Cape Leeuwin which detached from the current on day 51 continues to drift westward. The second eddy in that area is now also detached and drifting westward and a third eddy has formed in its place. The eddy field along the southern coast between Cape Leeuwin and the western Great Australian Bight becomes more well defined. Weak meanders form offshore of the current across the Great Australian Bight. The current remains continuous to the eastern boundary of the model domain. Eddies continue to form and detach from the current along the western coast and the southwest corner of the continent, the eddy field between Cape Leeuwin and the Great Australian Bight strengthens slightly, and small meanders persist across the Bight. No real change occurs through the end of the 90 day model run. The gyre/westward inshore current in the Great Australian Bight never forms and upwelling never develops.

As expected, this experiment using the most realistic forcing produced the most realistic results. The broad onshore flow along the thermohaline gradient at the northern end of the western coast was deflected toward the south to form a relatively strong and narrow poleward surface coastal current, the Leeuwin Current. This current correctly narrowed and intensified at its southern end and then followed the continental shelf break around the cape and continued eastward along the southern coast. The coastal current

continued eastward with the formation of the South Australia Current along the Great Australian Bight and farther east, forming a continuous current all the way to the eastern boundary of the model domain. The opposing undercurrent was eastward along the southern coast and equatorward along the western coast. The current was correctly positioned along the shelf break instead of adjacent to the coast. A weak opposing equatorward current formed inshore of the coastal current along the western coast as observed, but not along the southern coast. A narrow band of warm subtropical water was advected poleward and then eastward and a second, more saline water mass originated at the western end of the Great Australian Bight and was carried eastward as well. Meanders and eddies formed in the Leeuwin Current of the western coast and around Cape Leeuwin at the southwestern corner of the continent. The eddy field developed on the offshore side of the current between Cape Leeuwin and the Great Australian Bight and a field of weak meanders formed along the Great Australian Bight.

Though most aspects of the current system modeled by this experiment were qualitatively correct, the gyre/westward flow along the shore never developed on the Great Australian Bight shelf inshore of the South Australia Current. This is likely an artifact of the annual averaging of the wind forcing. Since the easterly wind in the Great Australian Bight is relatively weak, when averaged together with winds from other directions which occur during storm passages, it is hypothesized that the resultant wind field is not sufficiently strong to produce a westward current. With no westward current, the upwelling expected in this region also should not develop.

G. SEASONAL WIND (JANUARY) AND THERMOHALINE FORCING OVER TOPOGRAPHY

Experiment 7 was the first of the seasonal wind cases. Daily winds for January were extracted from the same ten-year ECMWF wind set as used in the previous experiments. These winds were averaged to form a January monthly wind field (Figure 2.5c). The WOA94 monthly temperature (Figure 2.3c) and salinity (Figure 2.4c) for January were used for the upper 1000m and were merged with the January through March seasonal climatology for depths below 1000m. The same bottom topography

(Figure 2.2b) and coastline from the previous experiments were used. Table 4.1 summarizes the forcing used for each process-oriented experiment.

Along the western coast of Australia, the winds are generally southerly throughout the year. The strength of these winds varies with season. During Austral summer (November through February), the southerly winds are strongest in the area between 20°S and 35°S (Figure 2.5c). The winds begin to decrease in March as the monsoon over northern Australia reverses and reach a minimum in May. By July, the winds are still much weaker than in summer (Figure 2.5d). Throughout both seasons, the winds are westerly below ~35°S (Godfrey and Ridgway, 1985). As these winds oppose the alongshore steric sea-level slope, they are thought to be responsible for the Leeuwin Current being strongest in winter (when winds are weakest) and weakest in summer (when winds are strongest) (e.g., Godfrey and Ridgway, 1985; Smith et. al., 1991). Experiments 7 and 8 are forced with both full seasonal temperature and salinity climatology and seasonal winds for January and July in order to isolate these seasonal effects on the current system.

As expected, a broad onshore flow develops off the northern end of the western coast by day 20 and is deflected toward the south as it approaches the coast, forming the poleward Leeuwin Current along the continental shelf break (Figure 4.26a). For the first time, however, an equatorward shelf current lies inshore of the Leeuwin Current along the coastline along much of the western coast. At 26°S the poleward surface current is ~150 km wide with a maximum speed of ~30 cm s⁻¹. Inshore of this current, an equatorward current of ~30 cm s⁻¹ lies adjacent to the coast on the shelf (Figure 4.26b). At 34°S (Cape Leeuwin), the Leeuwin Current narrows to ~100 km and strengthens slightly to ~37 cm s⁻¹. Here where the shelf is quite narrow (~38 km), the poleward Leeuwin Current extends all the way to the coast and there is no equatorward shelf current (Figure 4.26c). Farther north, the equatorward shelf current is clearly visible near 32°S and then continuously from ~30°S up to ~24°S. Beneath the poleward Leeuwin Current lies an opposing undercurrent with a ~23 cm s⁻¹ core near 450 m depth off Cape Leeuwin (Figure 4.26c). The undercurrent strengthens and deepens as it flows toward the equator, reaching ~33 cm s⁻¹ with a core depth of ~600 m at 26°S (Figure 4.26b). As in

all the previous experiments which incorporated thermohaline forcing, a narrow band of warm water is advected southward along the coast. The warm water is carried around Cape Leeuwin and as far east as $\sim 118^{\circ}\text{E}$ along the southern coast (Figure 4.26a).

Along the southern coast, the eastward coastal current lies along the continental shelf break for most of the distance of the coastline, but there is a break in it from $\sim 126^{\circ}\text{E}$ to $\sim 132^{\circ}\text{E}$ across the middle of the Great Australian Bight. This current is very well-defined along the western portion of the southern coast (from Cape Leeuwin to the western Great Australian Bight) with a $\sim 37 \text{ cm s}^{-1}$ core along the shelf break over a $\sim 25 \text{ cm s}^{-1}$ opposing undercurrent centered near 500 m depth at 117°E (Figure 4.26d). In this area, the eastward coastal current extends all the way to the coast with no opposing shelf current. There is a weak ($\sim 11 \text{ cm s}^{-1}$ at 130°E) westward current on the shelf adjacent to the coast in the eastern half of the Great Australian Bight (Figure 4.26e).

At day 30, the poleward Leeuwin Current continues as before along the western coast with an equatorward shelf current inshore of it along much of the western coast (Figure 4.27a). Meanders form near 30°S , near 31°S , and just south of Cape Leeuwin. The current continues to flow around Cape Leeuwin and the advected band of warm water is now clearly visible to $\sim 120^{\circ}\text{E}$. A weaker warm band of water extends across much of the Great Australian Bight.

A continuous eastward coastal current follows the continental shelf break along the entire southern coast. The current is $\sim 38 \text{ cm s}^{-1}$ at 117°E and lies over a $\sim 28 \text{ cm s}^{-1}$ opposing undercurrent centered at ~ 500 m (Figure 4.27b). There is no westward shelf current in this area between Cape Leeuwin and the Great Australian Bight where the shelf is narrow and the Leeuwin Current extends all the way to the coast. Farther east, the current weakens to $\sim 21 \text{ cm s}^{-1}$ at 130°E where it lies over an $\sim 11 \text{ cm s}^{-1}$ undercurrent centered near 700 m depth (Figure 4.27c). In this area in the Great Australian Bight the shelf current is westward at $\sim 12 \text{ cm s}^{-1}$ on the 40 km of the shelf nearest the shore. As observed, the current flow in the Great Australian Bight is a weak gyre with the eastward South Australian Current along the shelf break, northward flow in the eastern bight, and a westward flow adjacent to the coast. Wave-like features in the sea surface temperature

structure begin to form offshore of the current south of Cape Leeuwin and offshore of the South Australia Current along the Great Australian Bight continental shelf break (Figures 4.27a and 4.27d).

After day 30, the meanders in the Leeuwin Current along the western coast continue to develop and grow. Meanders also begin to form offshore of the coastal current along the western end of the southern coast between 115°E and 120°E by day 39 (Figure 4.28). The continuous coastal current along the entire length of the southern continental shelf break persists.

By day 60, eddies form in the Leeuwin Current at ~28°S and just north of Cape Leeuwin (~33.5°S) with large meanders at 31°S and southwest of Cape Leeuwin (Figure 4.29a). A pool of cooler surface water upwelled by the equatorward shelf current is visible at the surface in Geographe Bay, just north of Cape Leeuwin (see Figure 1.1 for geographical location). Along the southern coast, wave-like features in the sea surface temperature structure are visible between Cape Leeuwin and the western end of the Great Australian Bight (Figure 4.29b). A continuous South Australian Current persists across the Great Australian Bight continental shelf break and a meander/eddy field is now setting up offshore of this current as observed. The surface current has intensified slightly to $\sim 24 \text{ cm s}^{-1}$ at 130°E (Figure 4.29c). The gyre remains in place on the shelf of the Great Australian Bight with a westward shelf current near the beach where small patches of cooler upwelled water are now barely visible in the eastern end of the bight. A slightly larger pool of upwelled water is also visible along the northern and southern coasts of Kangaroo Island (Figure 4.29d).

After day 60, the meanders and eddies along the western coast in the Leeuwin Current continue to form and grow. By day 81 (Figure 4.30), the continuous poleward current has broken down into a series of eddies and all but disappeared as a coherent coastal current. As the Leeuwin Current feeding into the western end of the southern coast diminishes, the coastal current along the remainder of the southern coast also diminishes and eventually reverses direction. Although the reversal of the current along the southern coast was not expected, the breakdown of the Leeuwin Current along the

west coast is consistent with observational studies. Such studies show that the current is weak during spring (September-December) and almost vanishes completely during early summer (January) (Smith et. al., 1991).

The current system modeled by this experiment was the most realistic of any experiment in the process-oriented section of this study and most aspects of the current system were qualitatively correct. This was the only experiment to develop an equatorward current on the shelf inshore of the Leeuwin Current along the western coast. The gyre/westward flow along the shore on the Great Australian Bight shelf inshore of the South Australia Current was also modeled, though it was quite weaker ($\sim 11 \text{ cm s}^{-1}$) than observed values of $\sim 50 \text{ cm s}^{-1}$ (Godfrey et. al., 1986). As is earlier experiments, this is likely an artifact of the averaging of the wind forcing. With such a weak westward current, the resultant upwelling was barely discernible at the surface.

H. SEASONAL WIND (JULY) AND THERMOHALINE FORCING OVER TOPOGRAPHY

Experiment 8 was the second seasonal wind cases. Daily winds for July were extracted from the same ten-year ECMWF wind set as used in the previous experiments. These winds were averaged to form a July monthly wind field (Figure 2.5d). The WOA94 monthly temperature (Figure 2.3d) and salinity (Figure 2.4d) for July were used for the upper 1000 m and were merged with the July through September seasonal climatology for depths below 1000 m. The same bottom topography (Figure 2.2b) and coastline from the previous experiments were used. Table 4.1 summarizes the forcing used for each process-oriented experiment.

As in previous experiments using thermohaline forcing, a broad onshore flow develops off the northern end of the western coast by day 20 and is deflected toward the south as it approaches the coast, forming the poleward Leeuwin Current along the continental shelf break (Figure 4.31a). At 26°S the current is $\sim 22 \text{ cm s}^{-1}$ and $\sim 110 \text{ km}$ wide (Figure 4.31b). It intensifies to $\sim 40 \text{ cm s}^{-1}$ and narrows to $\sim 60 \text{ km}$ wide at Cape Leeuwin (Figure 4.31c). An opposing equatorward undercurrent lies below this current with a $\sim 35 \text{ cm s}^{-1}$ core at $\sim 350 \text{ m}$ at 34°S (Figure 4.31c), which deepens and slows

slightly to $\sim 26 \text{ cm s}^{-1}$ at 500 m by the time it reaches 26°S (Figure 4.31b). As in the cases with annually averaged thermohaline forcing, the current advects a narrow band of warm water poleward along the entire western coast, then around Cape Leeuwin and eastward as far as 120°E along the southern coast (Figure 4.31a). As before, the current rounds the bend in the coastline at Cape Leeuwin to flow eastward along the southern coast. The eastward coastal current is 35 cm s^{-1} and $\sim 60 \text{ km}$ wide at 117°E with an undercurrent of $\sim 13 \text{ cm s}^{-1}$ centered at $\sim 300\text{m}$ depth (Figure 4.31d). The current is quite coherent until it reaches the western Great Australian Bight, where it becomes weaker and more diffuse. The current weakens to $\sim 17 \text{ cm s}^{-1}$ at 125°E (Figure 4.31e) and $\sim 13 \text{ cm s}^{-1}$ at 130°E (Figure 4.31f) near the middle of the bight. At this time the current is eastward, or has an eastward component, over most of the continental shelf of the Great Australian Bight. Beyond the Great Australian Bight, a narrower ($\sim 60 \text{ km}$ wide) coastal current is again evident along the shelf break offshore of Kangaroo Island (Figure 4.31a).

At day 30, the broad inflow toward the coast on the northern end of the western coast persists, still resulting in a poleward coastal current (Figure 4.32a). At $\sim 16 \text{ cm s}^{-1}$ at 26°S (Figure 4.32b), the strength of the current has actually decreased slightly from day 20. It is also somewhat broader. As before (and as expected) the current intensifies and narrows as it approaches Cape Leeuwin to $\sim 40 \text{ cm s}^{-1}$ and 60 km wide at 34°S (Figure 4.32c). An opposing equatorward undercurrent lies below this current with a $\sim 39 \text{ cm s}^{-1}$ core at $\sim 350 \text{ m}$ at 34°S (Figure 4.32c), which deepens and slows slightly to $\sim 25 \text{ cm s}^{-1}$ at 600 m by the time it reaches 26°S (Figure 4.31b). As before, the band of warm water is advected southward, then around Cape Leeuwin and eastward along the southern coast as far as $\sim 125^\circ\text{E}$ in the western Great Australian Bight. Two anticyclonic meanders/eddies begin to form offshore of the current just south of Cape Leeuwin. A coherent continuous current is visible at the surface along the continental shelf break to $\sim 130^\circ\text{E}$ and the again from $\sim 133^\circ\text{E}$ and continuing eastward. The surface coastal current is strongest along the western end of the southern coast at $\sim 42 \text{ cm s}^{-1}$ at 117°E (Figure 4.32d) and decreases as it flows eastward along the coast to $\sim 17 \text{ cm s}^{-1}$ at 125°E (Figure 4.32e) and $\sim 18 \text{ cm s}^{-1}$ at 130°E (Figure 4.32f). An opposing westward undercurrent lies beneath this coastal current which increases in strength as it flows westward from $\sim 13 \text{ cm s}^{-1}$ at 117°E to $\sim 15 \text{ cm s}^{-1}$ at 125°E and $\sim 17 \text{ cm s}^{-1}$ at 130°E .

s^{-1} at 130°E (Figure 4.32f) to $\sim 15 \text{ cm s}^{-1}$ at 125°E (Figure 4.32e). As the undercurrent reaches 117°E , beneath the strongest surface current, it has intensified to $\sim 19 \text{ cm s}^{-1}$ (Figure 4.32d). As before, there is an eastward component to the shelf current over the entire Great Australian Bight. Wave-like features in the sea surface temperature structure develop offshore of the coastal current along the continental slope of the bight. These wave-like features also occur in the sea surface temperature pattern between 115°E and 120°E offshore of the relative strong current along the western end of the southern coast (Figure 4.32a).

By day 39 (not shown), an eddy detaches from the current south of Cape Leeuwin. In addition to the wave-like features in the sea surface temperature, meandering in the surface current becomes visible between Cape Leeuwin and the western Great Australian Bight.

The poleward surface current and advection of warm water along the western coast continues at day 60 (Figure 4.33a). The eddy which detached south of Cape Leeuwin at day 39 drifts toward the northwest and meanders form at 31°S and at 33°S . Weaker than at previous times, the surface current is now $\sim 16 \text{ cm s}^{-1}$ at 26°S (Figure 4.33b) and $\sim 30 \text{ cm s}^{-1}$ at 34°S (Figure 4.33c). The undercurrent is $\sim 26 \text{ cm s}^{-1}$ at 26°S and $\sim 30 \text{ cm s}^{-1}$ at 34°S . The undercurrent extended up to the surface at 34°S just offshore of the poleward coastal current to form the eastern side of the eddy there (Figure 4.33c). Another shallow poleward current (the western side of the eddy) is visible offshore of this current. The current continues to follow the shelf break around Cape Leeuwin and eastward. A continuous surface coastal current is now visible along the shelf break along the entire southern coast. The band of advected warm water also continues around Cape Leeuwin and eastward into the Great Australian Bight. The wave-like features in the sea surface temperature persist on the seaward side of the current between Cape Leeuwin and the western Great Australian Bight. The eastward current continues to lie over the entire continental shelf of the Great Australian Bight as before. The maximum speed of this current at 125°E is $\sim 20 \text{ cm s}^{-1}$ (Figure 4.33d) and at 130°E it is $\sim 19 \text{ cm s}^{-1}$ (Figure 4.33e). The wave-like sea surface temperature features also continue offshore of the coastal current along the shelf break of the Great Australian Bight.

After day 60, the formation of eddies along the western coast and off Cape Leeuwin continues (e.g., day 72, Figure 4.34). The wave-like sea surface temperature features and meanders in the surface current between Cape Leeuwin and the western Great Australian Bight persist. Likewise, the wave-like sea surface temperature features persist offshore of the bight. The continuous coastal current along the continental shelf break remains along the entire southern coastline. The overall pattern of the current flow remains unchanged through the end of the model run.

Similar to the annually averaged wind with thermohaline forcing case (Experiment 6), most aspects of the current system modeled by this experiment were qualitatively correct, but the gyre/westward flow along the shore never developed on the Great Australian Bight shelf inshore of the South Australia Current. This is likely an artifact of the annual averaging of the wind forcing. Since the easterly wind in the Great Australian Bight is relatively weak, when averaged together with winds from other directions which occur during storm passages, the resultant wind field is not sufficiently strong to produce a westward current. With no westward current, the upwelling expected in this region also did not develop.

I. SUMMARY OF PROCESS-ORIENTED EXPERIMENT RESULTS

In Experiment 1, the model was initialized using horizontally averaged annual temperature and salinity climatology, which removed all thermohaline forcing. The model was run over a flat bottom with a uniform depth of 2500 m, eliminating any topographic effects, and a realistic coastline. The only forcing was from the annually averaged climatological winds

The resulting currents were more characteristic of a typical eastern boundary current (EBC) system than of the coastal current system off western and southern Australia. Some characteristics of the observed Australia current system did form, however. A weak equatorward current has been observed on the continental shelf inshore of the Leeuwin Current flowing in the same direction as the wind. A similar weak equatorward current along the coastline did form in this experiment. Along the southern coast, the South Australia Current also flows along the shelf break with a broad, weak

westward current inshore of the South Australia Current in the Great Australian Bight similar to the current formed in the bight in this experiment. Upwelling, frequently observed in the eastern Great Australian Bight, was evident in the upward tilting isotherms in this area, though quite weak.

There were also a number of differences from the observed system. The currents along the southern coast were westward and the Leeuwin Current along the western coast was equatorward, rather than the observed eastward and poleward currents. The undercurrent also flowed in the opposite direction from the observed undercurrent. The location of the currents was also incorrect with currents adjacent to the coast instead along the continental shelf break as observed.

In Experiment 2, the model was again initialized using horizontally averaged annual temperature and salinity climatology. This time, the flat bottom was replaced with the smoothed Sandwell and Smith (1996) bottom topography as described in Chapter II. The same realistic coastline was used. The only forcing was from the annually averaged climatological winds used in Experiment 1.

As in Experiment 1, the overall current pattern formed in this experiment was more characteristic of a typical Eastern Boundary Current system than of the current pattern in this region. However, several features which are typical of the Australian currents were correctly modeled. The addition of topography moved the coastal currents from the coastline to the continental shelf break, where they are observed to occur both along the western coast and the southern coast. Weaker, poleward currents along the western coast and westward currents along the southern coast formed inshore of the coastal currents. The slightly warmer band of surface water that formed along the shelf break of the Great Australian Bight is representative of the warm water mass which is observed to form in this area. The observed water temperature and areal extent of the water mass were less than observed.

Other features continue to be different from those observed. The Leeuwin Current and South Australia Current are still flowing with the wind rather than against the wind. The undercurrent formed is too broad, weak, and deep and is likely due to

continuity in the model formulation rather than the formation of a true undercurrent. Upwelling was again modeled along the western coast where no upwelling is observed. No upwelling formed along the southern coast at the eastern end of the Great Australian Bight or in the Eyre/Kangaroo Island areas where upwelling is observed.

Experiment 3 was the first to use the full annual temperature and salinity climatology, introducing thermohaline forcing into the model. There was no wind forcing in this experiment. The same coastline and 2500 m flat bottom from Experiment 1 were used, eliminating any topographic effects.

The overall current pattern formed in this experiment, was more similar to the coastal current system off the western and southern coasts of Australia than to a typical eastern boundary current system. The broad onshore flow along the thermohaline gradient off the western coast was correctly represented, and that onshore flow was directed southward to form a narrow and swift poleward current along the western coast. This poleward current advected a narrow band of warm subtropical water poleward along the coast, then around Cape Leeuwin and eastward along the southern coast similar to the advection which is observed. The poleward current forced strong downwelling along the western coast, which is also observed. The observed meanders and eddies were also simulated in this experiment.

There were still significant differences from the observed system. The coastal current along the western and southern coasts was stronger than observed current speeds. Even though the coastal current in this experiment flowed in the correct direction, it was incorrectly located along the shore rather than along the continental shelf break. With the coastal current along the shore, no weak opposing current inshore of the coastal current could form. No upwelling was simulated anywhere along the southern coast. Finally, the coastal current moved offshore as time passed, while the observed current remains trapped along the continental shelf break/continental slope. This offshore movement allowed the undercurrent to shoal and finally produce a westward and equatorward current along the coast. This resulted in a complete current reversal from the observed currents by day 81.

Experiment 4 again used the full annual temperature and salinity climatology, to allow thermohaline forcing. There was no wind forcing in this experiment. All model parameters in Experiment 4 are the same as in Experiment 3 except that the flat bottom has been replaced with the smoothed Sandwell and Smith (1996) bottom topography as described in Chapter II. The same realistic coastline was used.

The overall current pattern formed in this experiment was more similar to the coastal current system off the western and southern coasts of Australia than in any previous experiment. The broad onshore flow along the thermohaline gradient off the western coast was correctly represented and correctly directed southward to form a narrow and swift poleward current along the continental shelf break of the western coast. This poleward current advected a narrow band of warm subtropical water poleward along the coast, then around Cape Leeuwin and eastward along the southern coast similar to the advection which is observed. The poleward current forced strong downwelling along the western coast, which is also observed. Meanders and eddies which are frequently observed in this region were also formed in this simulation. The greatest contrast from the previous experiment was the correct location of the current along the shelf break. The current formed in the correct location and it also remained anchored to the continental shelf break/continental slope throughout the model run instead of broadening and moving offshore as occurred in the previous experiment.

There were still some incorrectly modeled features in this experiment. Though slowed somewhat by the addition of topography, the surface coastal current was still too strong as in Experiment 3. There was no opposing shelf current developed inshore of the coastal current. Just as in the previous experiment, no upwelling was simulated anywhere along the southern coast, even in areas where upwelling is observed to frequently occur in the eastern end of the Great Australian Bight and near Kangaroo Island.

Experiment 5 used both thermohaline forcing from the full annual temperature and salinity climatology and the wind forcing used in Experiments 1 and 2. The 2500 m deep flat bottom eliminated any topographic effects.

The overall current pattern formed in this experiment, began quite similar to the coastal current system off the western and southern coasts of Australia with currents similar to those formed in the thermohaline forcing experiments, showing that the strong thermohaline gradient has a greater effect on the currents of the region than the wind. The broad onshore flow at the northern end of the western coast was correctly modeled, along with the poleward current which narrowed and strengthened with distance toward the south. The current continued around the cape and eastward along the southern coast. The current advected a narrow band of warm subtropical water south along the western coast and then east along the southern coast to the Great Australian Bight. Also as observed, meanders and eddies formed in the current in the vicinity of Cape Leeuwin and an eddy field formed offshore of the current along the southern coast between Cape Leeuwin and the Great Australian Bight. Downwelling was prevalent along the western coast.

As in previous experiments, the modeled current system still differed from the observed system in several ways. The coastal current along the western and southern coasts was too strong; however, its speed was less than the currents which developed in Experiment 3 with only thermohaline forcing, showing that the wind forcing does counteract the thermohaline forcing to slow the currents. As in Experiment 3, the current flowed in the correct direction, but the current was incorrectly located adjacent to the shore rather than a few kilometers offshore where the shelf break should lie. There was no weak opposing current inshore of the coastal current. No upwelling developed anywhere along the southern coast, although upwelling is observed to frequently occur in the eastern end of the Great Australian Bight and in the Kangaroo Island area. Finally, just as in Experiment 3, the coastal current moved offshore allowing the undercurrent to shoal and finally produce a westward and equatorward current along the coast. The entire current system reversed in direction from the observed current system by day 72. The only significant difference from Experiment 3 (thermohaline forcing only over flat bottom) was that the currents were weaker.

Experiment 6 was initialized with the most complete set of annually averaged climatology possible. The model was run with thermohaline forcing from the full annual

temperature and salinity fields and the annually averaged wind forcing. The Sandwell and Smith (1996) bottom topography allowed the development of topographic effects and the same realistic coastline from the other experiments was used.

As expected, this experiment produced the most realistic results of all the annual forcing cases. The broad onshore flow along the thermohaline gradient at the northern end of the western was deflected toward the south to form a relatively strong and narrow poleward surface coastal current, the Leeuwin Current, which correctly narrowed and intensified at its southern end and then followed the continental shelf break around the cape and continued eastward along the southern coast. The coastal current continued eastward with the formation of the South Australia Current along the Great Australian Bight and farther east, forming a continuous current all the way to the eastern boundary of the model domain. The opposing undercurrent was eastward along the southern coast and equatorward along the western coast. The current was correctly positioned along the shelf break, with a weak opposing equatorward current inshore of the coastal current along the western coast as observed, but not along the southern coast. A narrow band of warm subtropical water was advected poleward and then eastward and a second, more saline water mass originated at the western end of the Great Australian Bight and was carried eastward as well. Meanders and eddies formed in the Leeuwin Current of the western coast and around Cape Leeuwin at the southwestern corner of the continent. The eddy field developed on the offshore side of the current between Cape Leeuwin and the Great Australian Bight and a field of weak meanders formed along the Great Australian Bight.

Although most aspects of the current system modeled by this experiment were qualitatively correct, the gyre/westward flow along the shore never developed on the Great Australian Bight shelf inshore of the South Australia Current, likely due to the averaging of the wind forcing. Since the easterly wind in the Great Australian Bight is relatively weak, when averaged together with winds from other directions which occur during storm passages, the resultant wind field is not sufficiently strong to produce a westward current. With no westward current, the upwelling expected in this region also did not develop.

Experiment 7 was the first of the seasonal wind cases, which used averaged January winds to represent the summer seasonal case. The WOA94 monthly temperature and salinity for January were used for the upper 1000m and were merged with the January through March seasonal climatology for depths below 1000m. The same bottom topography and coastline from the previous experiments were used.

The current system modeled by this experiment was the most realistic of any experiment in the process-oriented section of this study and most aspects of the current system were qualitatively correct. This was the only experiment to develop an equatorward current on the shelf inshore of the Leeuwin Current along the western coast. The gyre/westward flow along the shore on the Great Australian Bight shelf inshore of the South Australia Current was also modeled, though it was weaker ($\sim 11 \text{ cm s}^{-1}$) than observed values of $\sim 50 \text{ cm s}^{-1}$ (Godfrey et. al., 1986). As in earlier experiments, this is likely an artifact of the averaging of the wind forcing. With such a weak westward current, the resultant upwelling was barely discernible at the surface.

Experiment 8 was the second seasonal wind case, which used averaged July winds to represent the winter seasonal case. The WOA94 monthly temperature and salinity for July were used for the upper 1000m and were merged with the July through September seasonal climatology for depths below 1000m. The same bottom topography and coastline from the previous experiments were used.

Similar to the annually averaged wind with thermohaline forcing case (Experiment 6), most aspects of the current system modeled by this experiment were qualitatively correct, but the gyre/westward flow along the shore never developed on the Great Australian Bight shelf inshore of the South Australia Current. This is likely an artifact of the annual averaging of the wind forcing. Since the easterly wind in the Great Australian Bight is relatively weak, when averaged together with winds from other directions which occur during storm passages, the resultant wind field is not sufficiently strong to product a westward current. With no westward current, the upwelling expected in this region also did not develop.

The purpose of the process-oriented experiments was to isolate which features in the current system were caused by which type of forcing by applying each forcing individually and in various combinations. Table 4.2 summarizes each of the features and forcing which appears to cause them. The current direction is a result of thermohaline forcing. When no thermohaline forcing was applied, the current flowed in the opposite direction. The poleward advection of warm water is a result of the current direction and, therefore, was also caused by this thermohaline gradient. Topography is responsible for the location of the current along the shelf break. In all flat-bottom experiments, the current formed adjacent to the coast and then broadened and moved offshore late in the model runs. The narrow width of the current appears to be caused by interaction between the opposing thermohaline forcing and wind. The current strength is a factor of thermohaline forcing, wind, and topography. When thermohaline forcing is used alone, the current is too strong. Both wind and topography act to slow the current to a more realistic speed. The opposing inshore current over the continental shelf is caused by the wind along the western coast, but only forms with summertime winds along the southern coast. Meanders and eddies are a factor of the opposing thermohaline and wind forcing. In addition, as discussed in Chapter III, the coastline direction and radius of curvature and vortex stretching imposed by the continental slope influence the locations at which the eddies can form. Finally, the gyre and resultant upwelling in the Great Australian Bight are caused by the change in the direction of the winds during austral summer.

THIS PAGE INTENTIONALLY LEFT BLANK

V. DAILY WIND EXPERIMENTS

All previous experiments in this study have used a model forced with averaged annual or monthly winds which do not change with time in the model run. Using averaged and unchanging wind forcing is useful for isolating the types of forcing associated with various features formed in the the current system, as studied in Chapter IV. However, there is considerable temporal variability in the coastal current system of western and southern Australia and a model using non-time-varying wind forcing is unable to simulate this temporal variability. The strength of the Leeuwin Current, especially along the western coast, but also along the southern coast is highly dependent upon the winds. The high pressure cell over the continent (which drives the westerly winds along the southern coast) is also known to have interannual variability which could lead to large variability in the current system along the southern coast (Ridgway and Condie, 2004). In addition, Herzfeld and Tomczak (1997) found that sea surface temperature distribution in the Great Australian Bight depends upon seasonal, and even smaller scale, variability in the winds.

Averaging the winds over time can be effective at capturing a representative forcing field for areas where there is little variation in the direction of the wind such as the western Australia region. Along the western coast of Australia between 20°S and 35°S the winds are generally southerly throughout the year. The strength of these winds varies with season, with the strongest winds during Austral summer (November through February) and the weakest winds during May through July (Godfrey and Ridgway, 1985). Temporally averaging these winds produces a wind field that is a true average in speed since the direction is always essentially the same. A comparison of the annual (Figure 2.5b), January monthly (Figure 2.5b), and July monthly (Figure 2.5b) wind forcing fields shows that they are qualitatively quite similar in this region, only varying in intensity. Throughout both seasons, the winds are westerly below ~35°S (Godfrey and Ridgway, 1985). In this area, temporal averaging also produces representative forcing fields. However, the winds rotate through every direction in the region between the southern coastline and ~35°S as weather systems pass through the area (Middleton and Cirano,

2002). In the Great Australian Bight, the wind has a westerly component about a third of the time and an easterly component about two-thirds of the time. Averaging these winds in time produces a resultant field that has the direction of the prevailing wind but a much smaller speed than observed winds. This unrealistically weak wind forcing is likely responsible for the absence of the Great Australian Bight gyre and upwelling in the previous experiments.

It has been shown that when a free-surface regional ocean model is initialized and forced with high temporal and spatial resolution forcing fields, many combinations of boundary conditions will not remain stable (Martinho, 2003). For this reason, two different sets of daily wind experiments were accomplished. In the first two experiments the model is forced with daily winds from the same ECMWF data set (and interpolated from the same $2.5^\circ \times 2.5^\circ$ spatial resolution) as the annually and seasonally averaged wind fields. When interpolated to the model grid, the resulting forcing wind fields are smoothly varying in space, but the temporal resolution is increased to daily.

After verification that using daily varying wind forcing does not adversely affect boundary condition stability, the spatial resolution of the wind forcing is also increased. Experiments 3 and 4 are forced with NOGAPS $1^\circ \times 1^\circ$ resolution wind fields. In all daily wind experiments, after the wind stress fields are calculated, they are interpolated to the model's spatial grid, producing one wind file per day. As the model runs, it also interpolates the wind stresses in time for each time step (Jayne and Tokmakian, 1997). This temporal interpolation produces a smoothly varying forcing field that is less likely to excite inertial oscillations in the model solution as the forcing changes from one field to the next. The same boundary conditions from the annual wind forcing experiments, described in Chapter II, were used for both summer and winter daily wind forcing experiments.

A. JANUARY DAILY ECMWF WIND FORCING

This experiment is the first of the daily wind cases. Daily winds for December 1980 through February 1981 were used to force the model. The model was started from rest on December 1, 1980, and the daily winds for December were used to spin up the

model. The analysis period of the model run is days 30 through 60, when the January, 1981 winds are used to force the model. These winds are from the same ECMWF wind set which were averaged together to form annual or monthly forcing for the process-oriented experiments of the previous chapter. The WOA94 monthly temperature (Figure 2.3c) and salinity (Figure 2.4c) for January were used for the upper 1000 m and were merged with the January through March seasonal climatology for depths below 1000 m. The same bottom topography (Figure 2.2b) and coastline from the previous experiments were used.

By day 20 (December 21, 1980), the broad onshore flow at the northern end of the model domain along the western coast has developed. As in previous experiments, this onshore flow is deflected to the south as it approaches the continental shelf, resulting in a relatively narrow and swift poleward coastal current, the Leeuwin Current (Figure 5.1). As expected, the band of warm water is advected southward. The current rounds Cape Leeuwin and flows eastward along the southern coast as far as Esperance ($\sim 124^{\circ}\text{E}$). The ribbon of warm water is visible as far east as $\sim 118^{\circ}\text{E}$. No organized current is yet evident in the Great Australian Bight or farther east (Figure 5.1).

By day 30 (December 31, 1980), the current has continued to develop as expected along the western coast with a swift poleward surface current advecting warm water southward (Figure 5.2a). An equatorward current has developed on the shelf inshore of the coastal current in the embayment between Cape Leeuwin and Perth. Cooler water at the surface in this area is indicative of upwelling. Upwelling in this location has been observed (Gersbach et. al., 1999). The maximum speed of this shelf current is $\sim 12 \text{ cm s}^{-1}$ (Figure 5.2b). Offshore at this location (33.25°S) just north of Cape Leeuwin, the surface coastal current has reached a speed of $\sim 43 \text{ cm s}^{-1}$ and the undercurrent is $\sim 21 \text{ cm s}^{-1}$ (Figure 5.2b).

The surface current rounds Cape Leeuwin and flows along the southern coast beyond Esperance and follows the shelf break across the width of the Great Australian Bight. At 130°E in the middle of the Great Australian Bight, the surface current is $\sim 21 \text{ cm s}^{-1}$ and the undercurrent, centered at $\sim 650 \text{ m}$ depth, is $\sim 12 \text{ cm s}^{-1}$ (Figure 5.2c). The inshore current on the broad Great Australian Bight shelf is westward at $\sim 7 \text{ cm s}^{-1}$

(Figures 5.2a and 5.2c). Though this weak gyre has developed in the Great Australian Bight, with the coastal current flowing eastward along the shelf break and the inshore current flowing westward near the shore, no upwelling is evident. In particular, the isotherms are sloping slightly downward toward the coast (Figure 5.2d).

The pattern at day 45 (January 15, 1981) is similar to previous day shown, i.e., with a swift poleward current along the western coast rounding Cape Leeuwin and flowing eastward to the eastern end of the Great Australian Bight (Figure 5.3a). However, several meanders have begun to form in the Leeuwin Current along the northern portion of the western coast. In addition, a meander lies just beyond Cape Leeuwin. Several wave-like features in the sea surface temperature structure lie between Cape Leeuwin and $\sim 120^{\circ}\text{E}$. The surface poleward current has reached $\sim 35 \text{ cm s}^{-1}$ at 33.25°S near Cape Leeuwin with a $\sim 12 \text{ cm s}^{-1}$ equatorward undercurrent centered at $\sim 500 \text{ m}$ depth (Figure 5.3b). Inshore of this current, the inshore equatorward current has reached a speed of $\sim 12 \text{ cm s}^{-1}$ over the shelf. A pool of cooler water is still visible at the surface of this embayment between Cape Leeuwin and Perth (Figure 5.3a), but it is smaller than at day 30. Along the Great Australian Bight, the coastal current still follows the shelf break and its speed has reached $\sim 25 \text{ cm s}^{-1}$ at 130°E . Beneath this current, at a depth of $\sim 700 \text{ m}$, a $\sim 10 \text{ cm s}^{-1}$ flows westward (Figure 5.3c). The weak gyre on the Great Australian Bight shelf is still in place with a westward shelf current of $\sim 5 \text{ cm s}^{-1}$ adjacent to the shore (Figures 5.3a and 5.3c), but there is still no evidence of upwelling (Figure 5.3d).

By day 60 (January 30, 1981), the Leeuwin Current along the western coast has developed several broad meanders and the current has moved slightly offshore allowing the undercurrent to surface in some places (Figure 5.4a). This result is not unexpected when compared to January observations of the region (Smith, et. al., 1991). At 33.25°S near Cape Leeuwin, the surface current has moved $\sim 50 \text{ km}$ offshore of the shelf break and flows poleward at $\sim 34 \text{ cm s}^{-1}$ (Figure 5.4b). The undercurrent has a maximum speed of $\sim 28 \text{ cm s}^{-1}$ in a core at $\sim 500 \text{ m}$ depth and its upper edge broaches the surface along the shelf break. The undercurrent also appears to have surfaced along the western portion of the southern coast, resulting in an apparent reversal in the current in this area. Across the

Great Australian Bight, the current is westward and has strengthened to $\sim 20 \text{ cm s}^{-1}$ over the entire continental shelf (Figures 5.4a and 5.4c). The eastward coastal current remains in place over the continental slope, though the core of its maximum speed is now $\sim 40 \text{ m}$ beneath the surface (Figure 5.4c). The $\sim 10 \text{ cm s}^{-1}$ westward undercurrent still lies beneath the coastal current at $\sim 700 \text{ m}$ depth (Figure 5.4c). A very thin band of cooler water is discernible adjacent to the shore in the eastern Great Australian Bight, but there is no upward tilt in the isotherms below this area (Figures 5.4a and 5.4d).

The current system which formed in this experiment was qualitatively correct in most respects. The resulting development of the currents was also quite similar to that of the monthly January wind case explored in Chapter IV, though current speeds in this daily wind case were slightly higher during the early times in the model run. The meander and eddy development were comparable to those in the earlier model run and the breakdown of the Leeuwin Current, which is observed (Smith et. al., 1991), occurred in both model runs. Throughout the model run, there appeared to be no unrealistic currents or temperature features which could be attributed to unstable boundary conditions. Note also that the model was run for an additional month beyond the analysis period and the flow appeared to remain stable with no unrealistic current or temperature features during that time as well.

B. JULY DAILY ECMWF WIND FORCING

This experiment is the austral wintertime daily wind forcing case using the ECMWF winds. Daily winds for June 1981 through August 1981 were used to force the model. The model was started from rest on June 1, 1981, and the daily winds for June were used to spin up the model. The analysis period of the model run is days 30 through 60, when the July, 1981 winds are used to force the model. These winds are from the same ECMWF wind set which were averaged together to form annual or monthly forcing for the process-oriented experiments of the previous chapter. The WOA94 monthly temperature (Figure 2.3d) and salinity (Figure 2.4d) for July were used for the upper 1000

m and were merged with the July through September seasonal climatology for depths below 1000 m. The same bottom topography (Figure 2.2b) and coastline from the previous experiments were used.

As before, by day 20 (June 21, 1981), the broad onshore flow at the northern section of the western coastal region has been deflected to the south to form a relatively narrow poleward coastal current along the continental shelf break (Figure 5.5). This current, the Leeuwin Current, advects a band of warm water southward, then rounds the bend at Cape Leeuwin and flows eastward along the southern coast. The warm water advection is visible beyond Esperance into the western edge of the Great Australian Bight. The eastward current continues all the way to the eastern end of the model domain. Unlike previous experiments, however, the coastal current is not confined to a narrow band along the continental slope, but rather a broad eastward surface current lies over the entire Great Australian Bight shelf all the way to the shore (Figure 5.5).

At day 30 (July 1, 1981) the poleward Leeuwin Current remains along the shelf break for the length of the western coast and around the bend at Cape Leeuwin to flow eastward along the southern coast (Figure 5.6a). An opposing equatorward shelf current lies over most of the continental shelf of the western coast. At 33.25°S just north of Cape Leeuwin, the poleward coastal current has reached at speed of $\sim 48 \text{ cm s}^{-1}$ (Figure 5.6b). The equatorward undercurrent is $\sim 38 \text{ cm s}^{-1}$ with a core centered at $\sim 300 \text{ m}$ depth. The upper edge of this undercurrent reaches the surface offshore of the surface coastal current. Inshore of the coastal current, an equatorward shelf current of $\sim 28 \text{ cm s}^{-1}$ (Figure 5.6b) is over twice as fast as in any previous experiment but is still less than the $\sim 50 \text{ cm s}^{-1}$ observed speeds (Godfrey et. al., 1986).

Along the southern coast, the current is eastward along the entire coastline. The warm water is advected into the western one-fourth of the Great Australian Bight. A meander has begun to form at Cape Leeuwin and there are several wave-like features in the sea surface temperature structure between Cape Leeuwin and $\sim 120^\circ\text{E}$ (Figure 5.6a). Along the entire southern coast, the current is eastward over the entire shelf. In the middle of the Great Australian Bight at 130°E , the maximum current speed is $\sim 54 \text{ cm s}^{-1}$ over the shelf break, but the surface current is in excess of 50 cm s^{-1} at all locations from

the shelf break to the shore (Figure 5.6c). A broad area of opposing flow with a maximum speed of $\sim 8 \text{ cm s}^{-1}$ extends from the surface (offshore of the coastal current) to below 1000 m beneath the coastal surface current, but there is no realistic organized undercurrent (Figure 5.6c). In response to the intense eastward surface current in the Great Australian Bight, downwelling is evident in the downward sloping isotherms (Figure 5.6d).

At day 45 (July 16, 1981), the poleward Leeuwin Current begins relatively broad at its origin in the Cape Inscription area and it narrows and strengthens as it flows to the south reaching $\sim 48 \text{ cm s}^{-1}$ off Cape Leeuwin at 33.25°S (Figure 5.7a and 5.7b). Beneath this surface current a $\sim 22 \text{ cm s}^{-1}$ undercurrent has double cores at $\sim 250 \text{ m}$ and $\sim 500 \text{ m}$ depth. The poleward shelf current has weakened to $\sim 12 \text{ cm s}^{-1}$ (Figure 5.7b). An eddy has formed off Cape Leeuwin and the wave-like features in the sea surface temperature structure between Cape Leeuwin and $\sim 120^\circ\text{E}$ remain (Figure 5.7a). The eastward advected warm water covers the entire western half of the Great Australian Bight shelf and is visible in a narrow band along the shelf break beyond Kangaroo Island. The coastal current still extends in width from the shelf break to the shore, but it has weakened to $\sim 23 \text{ cm s}^{-1}$ (Figure 5.7c). Beneath and offshore of this coastal current, the westward undercurrent has strengthened to $\sim 20 \text{ cm s}^{-1}$ and now has a more well-defined core at $\sim 300 \text{ m}$ depth (Figure 5.7c). As before, downwelling is evident across this region (Figure 5.7d).

The western coastal surface current at day 60 (July 31, 1981) is similar to that of day 45. The poleward surface current is again broad ($> 250 \text{ km}$) off Cape Inscription and narrows and intensifies as it flows to the south (Figure 5.8a). Figure 5.8b shows a cross-section through an eddy just north of Cape Leeuwin with a poleward current speed of $\sim 44 \text{ cm s}^{-1}$ and an equatorward current speed of $\sim 34 \text{ cm s}^{-1}$. Inshore and beneath this eddy, a $\sim 14 \text{ cm s}^{-1}$ undercurrent lies along the continental slope centered at $\sim 500 \text{ m}$ depth (Figure 5.8b). The advected warm water continues to cover the western half of the Great Australian Bight shelf and the narrow band along the shelf break is now visible to the eastern edge of the model domain (Figure 5.8a). The field of wave-like features in the sea surface temperature structure still begins at Cape Leeuwin and has now grown

eastward to the western end of the Great Australian Bight. The current remains eastward from the shelf break to the shore, but its structure has changed from previous times. Now a swift ($\sim 38 \text{ cm s}^{-1}$) and narrow coastal current lies over the shelf break and the inshore current is much weaker at $< 10 \text{ cm s}^{-1}$ (Figure 5.8c). The westward $\sim 19 \text{ cm s}^{-1}$ undercurrent is centered at $\sim 450 \text{ m}$ depth. Downwelling continues to dominate the region (Figure 5.8d).

Daily wind Experiments 1 and 2 clearly highlight several aspects of the seasonal variability of this current system. Under the influence of stronger winds, the Leeuwin Current off the western coast was weaker in summer ($34\text{--}43 \text{ cm s}^{-1}$) (Figures 5.2b, 5.3b, and 5.4b) than in winter ($44\text{--}48 \text{ cm s}^{-1}$) (Figures 5.4b, 5.5b, and 5.6b) and even broke apart in later model times (Figure 5.4a), in agreement with available observations (e.g., Smith et. al., 1991). There was also a significant difference in the currents over the shelf of the Great Australian Bight. In summer, the variable January winds allowed a weak gyre to form over the shelf, though the model did not simulate any significant upwelling. In winter, the current remained eastward across the entire shelf. Day to day variability was also simulated in this area where the shelf current varied from 50 cm s^{-1} to 10 cm s^{-1} (Figures 5.6c and 5.8c).

As in Experiment 1, the current system which formed in this experiment was qualitatively correct. Current speeds were comparable to observed values, and the current and temperature feature structures were quite realistic. Throughout the model run, there appeared to be no unrealistic currents or temperature features which could be attributed to unstable boundary conditions. As in the previous experiment the model was run for an additional month beyond the analysis period and the flow appeared to remain stable with no unrealistic current or temperature features during that time as well.

C. JANUARY DAILY NOGAPS WIND FORCING

This experiment is the first in this study to use the higher spatial resolution of the NOGAPS daily wind forcing. This change represents an increase in resolution from $2.5^\circ \times 2.5^\circ$ of the ECMWF data set to $1^\circ \times 1^\circ$ for the NOGAPS data set. The wind field structure is quite similar in both direction and strength to the ECMWF wind field off the

western coast of Australia where there is little variability in the direction of the wind. Along the southern coast and especially in the Great Australian Bight, however, the NOGAPS wind field provides greater detail in the wind structure. If possible, NOGAPS winds would have been used for the same time period as the previous experiments using ECMWF winds. However, the NOGAPS winds were not available for those dates. Daily winds for December 2000 through February 2001 were used to force the model. The model was started from rest on December 1, 2000, and the daily winds for December were used to spin up the model. The analysis period of the model run is days 30 through 60, when the January, 2001 winds are used to force the model. The WOA94 monthly temperature (Figure 2.3c) and salinity (Figure 2.4c) for January were used for the upper 1000 m and were merged with the January through March seasonal climatology for depths below 1000 m. The same bottom topography (Figure 2.2b) and coastline from the previous experiments were used.

By day 20 (December 21, 2000), the broad onshore flow at the northern end of the model domain along the western coast has developed and is deflected to the south to produce a relatively narrow and swift poleward coastal current, the Leeuwin Current (Figure 5.9a) along the continental shelf break. The current is already relatively strong, reaching speeds of $\sim 37 \text{ cm s}^{-1}$ off Cape Inscription near its origin (Figure 5.9b) and increasing in speed to $\sim 48 \text{ cm s}^{-1}$ as it approaches Cape Leeuwin (Figure 5.9c). Beneath this poleward surface current lies an equatorward undercurrent flowing to $\sim 18 \text{ cm s}^{-1}$ off Cape Leeuwin (Figure 5.9c) and strengthening slightly to $\sim 20 \text{ cm s}^{-1}$ off Cape Inscription (Figure 5.9b). As in previous experiments, the band of warm water is advected southward. The current rounds Cape Leeuwin and flows eastward along the southern coast. The current broadens as the South Australia Current as it reaches the Great Australian Bight and eastward surface flow is visible over much of the Bight (Figure 5.9a). The current is quite strong at the western end of the southern coast with a surface current of $\sim 49 \text{ cm s}^{-1}$ and an undercurrent of $\sim 27 \text{ cm s}^{-1}$ at $\sim 600 \text{ m}$ depth (Figure 5.9d). The ribbon of warm water is visible as far east as $\sim 119^\circ\text{E}$.

At day 27 (December 28, 2000), a gyre in the surface current in the Great Australian Bight as formed with the South Australian Current flowing eastward along the

continental shelf break and a westward flowing shelf current along the shore (Figure 5.10a). The speed of both the coastal current and the opposing inshore current is $\sim 25 \text{ cm s}^{-1}$. A close examination of the temperature structure in the middle of the Great Australian Bight (Figure 5.10b) shows that the isotherms slope slightly downward from offshore to mid-shelf, under the influence of the downwelling-favorable South Australian Current. Then the isotherms flatten over the middle of the shelf, then slope slightly upward between $\sim 32.2^\circ\text{E}$ and $\sim 31.9^\circ\text{E}$. The 19.2°C and 19.4°C isotherms are plotted in magenta on Figure 5.10b to make this slope more readily apparent. Even though this isotherm slope is visible, the short duration of the easterly winds and resulting westward surface current along the shore is apparently not enough to drive any significant upwelling. There is no indication of cooler water at the surface and the upward slope of these isotherms is confined to a very small area. Farther east, at 134.5°E , the temperature profile shows no evidence of upwelling (Figure 5.10c).

By day 30 (December 31, 2000), the broad onshore flow at the northern end of the western coast continues to produce an energetic poleward Leeuwin Current (Figure 5.11a) along the continental shelf break. The current narrows and intensifies as it flows toward the south. It builds from $\sim 35 \text{ cm s}^{-1}$ near its origin off Cape Inscription (Figure 5.11b) to $\sim 54 \text{ cm s}^{-1}$ off Cape Leeuwin (Figure 5.11c). In the same distance, it narrows from over 300 km wide to $\sim 120 \text{ km}$ wide (Figures 5.11b and 5.11c). The undercurrent remains relatively constant in speed at $\sim 15 \text{ cm s}^{-1}$ but it deepens from $\sim 500 \text{ m}$ depth at Cape Leeuwin (Figure 5.11c) to $\sim 650 \text{ m}$ depth off Cape Inscription (Figure 5.11b). There is no appreciable opposing inshore current yet and there is no evidence of upwelling in the embayment just north of Cape Leeuwin (Figure 5.11d). Meanders have begun to develop in the surface current south of Cape Inscription and north of Perth, both along relatively straight sections of coastline (Figure 5.11a). As before, the band of warm water is advected southward, then around Cape Leeuwin and eastward along the southern coast.

The surface coastal current is continuous along the continental shelf break along the entire length of the southern coast to the eastern edge of the model domain (Figure 5.11a). A field of wave-like features in the sea surface temperature structure is visible

from Cape Leeuwin east to $\sim 120^{\circ}\text{E}$. In this area, the surface current has weakened slightly from its maximum off Cape Leeuwin to $\sim 38 \text{ cm s}^{-1}$ at 117°E (Figure 5.11e). Beneath this eastward surface current lies a $\sim 30 \text{ cm s}^{-1}$ westward undercurrent centered at $\sim 600 \text{ m}$ depth. Though the surface current gyre forced by transient weather systems in the Great Australian Bight was present at day 27, it has disappeared by day 30 as the inshore current has reversed. Note that the current is westward from the South Australian Current, which has a core speed of $\sim 25 \text{ cm s}^{-1}$ over the continental slope, all the way to the shore and a second core $< 20 \text{ cm s}^{-1}$ lies over the shelf near the shore (Figure 5.11f). Note that there is no evidence of upwelling in the Bight (Figure 5.11g).

After day 30, the Leeuwin Current pattern along the western coast remains similar (Figure 5.12a). At day 45 (January 15, 2001), the $\sim 27 \text{ cm s}^{-1}$ current off Cape Inscription (Figure 5.12b) strengthens to $\sim 59 \text{ cm s}^{-1}$ off Cape Leeuwin (Figure 5.12c). The opposing inshore current still has not developed and there is no upwelling north of Cape Leeuwin (Figure 5.12d). Meanders in the surface current persist between Cape Inscription and Perth. An eddy has separated from the current south of Cape Leeuwin centered at 36.1°S and 114.5°E and another eddy is forming just off Cape Leeuwin (Figure 5.12a).

During the first two weeks of January, the field of wave-like sea surface temperature features continue to develop between Cape Leeuwin and Esperance (Figure 5.12a). The surface current in this area has strengthened to $\sim 54 \text{ cm s}^{-1}$ (Figure 5.12e). The current along the shore in the western half of the Great Australian Bight is again westward, forming a partial gyre. At 130°E the South Australian Current flows eastward at $\sim 33 \text{ cm s}^{-1}$, but the inshore current is westward at less than 10 cm s^{-1} (Figure 5.12f). With such a weak and intermittent flow, as before no upwelling is produced (Figure 5.12g).

At day 60 (January 30, 2001) the current continues to be swift and narrow along the western coast (Figure 5.13a). The current has weakened to $\sim 17 \text{ cm s}^{-1}$ off Cape Inscription (Figure 5.13b) but reaches a maximum of $\sim 63 \text{ cm s}^{-1}$ off Cape Leeuwin (Figure 5.13c). An eddy has formed south of Cape Inscription and the meander persists north of Perth. The inshore current remains poleward and there is no upwelling in the embayment north of Cape Leeuwin (Figure 5.13d).

The maximum current speed for any time in the model run is $\sim 73 \text{ cm s}^{-1}$ along the continental slope at 117°E (Figure 5.13e). Farther east the current weakens considerably to $\sim 39 \text{ cm s}^{-1}$ at 130°E (Figure 5.13f), but it is continuous along the entire southern coast to the eastern edge of the model domain. The eddy fields off the southern coast between Cape Leeuwin and Esperance persist but do not appear to be intensifying. A westward inshore current flows along the shore across much of the Great Australian Bight, but there is no convincing evidence of upwelling (Figure 5.13g).

With numerous meanders, eddies, and other small-scale features in the current system, the level of mesoscale activity in this model run is quite significant, consistent with available observations (e.g., Thompson, 1984; Smith et. al., 1991; Batteen and Butler, 1998; Fang and Morrow, 2003). Figures 5.14a-5.14h document the development of a typical eddy which develops south and east of Cape Leeuwin. At day 54 (January 24, 2001), the feature is still attached to the current as a meander (Figure 5.14a). Figure 5.14b shows that, at this early time in the development of the eddy, the current is relatively deep with the southward current on the western side of the meander extending beyond 1000 m depth. After the feature has detached from the current, its maximum depth stays between $\sim 600 \text{ m}$ and 1000 m depth.

The eddy subsequently drifts $\sim 63 \text{ km}$ to the south-southwest over a period of 9 days for a speed of $\sim 7 \text{ km/day}$ or $\sim 8.1 \text{ cm s}^{-1}$. This movement is consistent with observational studies. For example, Cresswell and Golding (1980) used drifting buoys to track three eddies south of Cape Leeuwin which moved westward at 6, 6.5, and 7.4 km/day. Observations by Fang and Morrow (2003) found an average drift speed of $\sim 5 \text{ cm s}^{-1}$ for eddies south of 27S.

Fang and Morrow (2003) reported that the radius of observed eddies along the southern portion of Australia was $\sim 100\text{-}150 \text{ km}$ with the radius decreasing with higher latitude as the Rossby radius decreases. The Fang and Morrow observations also showed growth in the radius of eddies during the development phase. Slightly less than these observed sizes, the modeled southern Australia eddy depicted in Figures 5.14a through 5.14h grows from $\sim 56 \text{ km}$ to $\sim 92 \text{ km}$ radius over a period of nine days.

Since the westward current along the shore in the Great Australian Bight was only weak and intermittent and no upwelling developed during this model run, another summertime daily wind model run was done for a different year. Experiment 3a was run for December 1999 through February 2000. By day 30 (December 31, 1999), the westward current is already in place in the Great Australian Bight, with a thin ribbon of cooler upwelled water along the shore in the eastern end of the bight. There is also cooler water at the surface at the western end of Kangaroo Island and south of Kangaroo Island between 138°E and 140°E (Figure 5.15a). After day 30, the westward current over the Great Australian Bight shelf remains through day 39, then appears again at day 45 and again for days 57 through 60. Even though the current is reversing direction at day 42 (January 12, 2000), cooler water is visible at the surface along the eastern end of the bight, along the western and northern shores of Kangaroo Island, and south of Kangaroo Island (Figure 5.15b). Isotherms slope upward toward the shore in the eastern Great Australian Bight (Figure 5.15c). South of Kangaroo Island, the upwelled pool is centered at ~37°N and the isotherms slope upward toward this pool from both the north and south (Figure 5.15d). At day 60 (January 30, 2000), the extent of upwelled water in the eastern Great Australian Bight is greater than before and the upwelled water remains in both locations near Kangaroo Island (Figure 5.15e). As before, the isotherms slope upward toward the shore in the eastern bight (Figure 5.15f) and slope upward towards the cool surface water at 37°N from both directions (Figure 5.15g).

Even though satellite SST imagery has not been able to resolve the exact structure of the circulation due to the complexity of the SST structure (Ridgway and Condie, 2004), it is useful to compare the model results with satellite imagery to form a qualitative assessment of model results. For this comparison, the model results are compared with Multi-Channel Sea Surface Temperature (MCSST) satellite imagery provided by the Naval Oceanographic Office (NAVO). MCSST temperatures are calculated by NAVO from the radiance values from the National Oceanic and Atmospheric Administration's (NOAA) polar orbiting Advanced Very High Resolution Radiometer sensor (McClain et. al., 1985). The imagery is a composite of data from the seven days preceding the date of the imagery. The original resolution of the AVHRR

data is 4.4 km and the calculated MCSST temperatures are interpolated to a regular grid of 10 km resolution for presentation of the MCSST imagery.

First the surface current pattern and sea surface temperature produced for Experiment 3 at day 45, January 15, 2001 (Figure 5.12a) is compared to the MCSST imagery for January 15, 2001 (Figure 5.16a). The model results are qualitatively similar to the satellite imagery. The current is broad near its origin and narrows as it flows toward the south in the model run and satellite imagery. The meander simulated at $\sim 28^{\circ}\text{S}$ is also present in the satellite imagery and a diffuse area of warm water offshore of the current off Cape Leeuwin is not inconsistent with the eddy formed in that location in the model. The temperatures compare closely at the northern end of the west coast where the modeled temperature in the core of the current is $\sim 25^{\circ}\text{C}$ and the MCSST temperature is $\sim 25.5^{\circ}\text{C}$. Farther south, the temperatures are also similar but not as close with a 1.3°C difference off Cape Leeuwin where the model temperature is $\sim 23^{\circ}\text{C}$ and the MCSST temperature is $\sim 21.7^{\circ}\text{C}$. The warm water is also advected too far east along the southern coast.

In the modeled results for January 15, 2001 (Figure 5.12a), no upwelling develops in the eastern Great Australian Bight. A very thin ribbon of slightly cooler water along the shore is visible in the MCSST imagery (Figure 5.16a), consistent with very little upwelling. Farther east and south, both the model and the MCSST images show a cool pool south of Kangaroo Island. In Experiment 3a (summer 2000), upwelling does develop and is similar to the satellite imagery both in intensity and location. At day 42, January 12, 2000 (Figure 5.15b), the model upwelled $\sim 16^{\circ}\text{C}$ water in the eastern Great Australian Bight. At the same time, the MCSST imagery (Figure 5.16b) shows $\sim 16.5^{\circ}\text{C}$ water in the same location, $\sim 132.5^{\circ}\text{E}$ to $\sim 135.5^{\circ}\text{E}$. The Kangaroo Island pool is also similar to the imagery with modeled temperature of $\sim 15^{\circ}\text{C}$ and satellite temperature of $\sim 14.4^{\circ}\text{C}$. Between these pools of cooler water, the Spencer Gulf is warmer with $\sim 20^{\circ}\text{C}$ water in both the model results and satellite imagery. These results showing intermittent upwelling are also in agreement with recent CTD observations which show that the upwelling is intermittent with an average of two or three upwelling events per summer (some ref, 2006).

The current system which formed in this summertime daily wind model run was quite realistic. Mesoscale features formed along the western coast as expected. An analysis of a typical eddy showed that it was consistent with observations (e.g., Cresswell and Golding, 1980 and Fang and Morrow, 2003) in development, movement, and size. Even though the intermittent observed upwelling along the eastern Great Australian Bight and Kangaroo Island did not form in the 2001 model run, it did form when 2000 winds were used to force the model. This result is not unexpected, considering reports of significant interannual variability in the system (Ridgway and Condie, 2004).

D. JULY DAILY NOGAPS WIND FORCING

This experiment uses the higher spatial resolution wintertime NOGAPS daily wind forcing. As in the summertime case, the wind field structure is quite similar to the ECMWF wind field off the western coast of Australia where there is little variability in the direction of the wind, but along the southern coast and especially in the Great Australian Bight, the NOGAPS wind field provides greater detail in the wind structure. Daily winds for June 2001 through August 2001 were used to force the model. The model was started from rest on June 1, 2001, and the daily winds for June were used to spin up the model. The analysis period of the model run is days 30 through 60, when the July, 2001 winds are used to force the model. The WOA94 monthly temperature (Figure 2.3d) and salinity (Figure 2.4d) for January were used for the upper 1000 m and were merged with the January through March seasonal climatology for depths below 1000 m. The same bottom topography (Figure 2.2b) and coastline from the previous experiments were used.

By day 20 (June 21, 2001), the broad onshore flow at the northern end of the model domain along the western coast has developed and is deflected to the south to produce a relatively narrow and swift poleward coastal current, the Leeuwin Current (Figure 5.17a) along the continental shelf break. The current is already stronger than the summertime case of Experiment 3, reaching speeds of $\sim 50 \text{ cm s}^{-1}$ off Cape Inscription near its origin (Figure 5.17b) and $\sim 41 \text{ cm s}^{-1}$ as it approaches Cape Leeuwin (Figure 5.17c). Beneath this poleward surface current lies an equatorward undercurrent flowing

with speeds of $\sim 23 \text{ cm s}^{-1}$ off Cape Leeuwin (Figure 5.17c) and strengthening to $\sim 30 \text{ cm s}^{-1}$ off Cape Inscription (Figure 5.17b). As in previous experiments, the band of warm water is advected southward. The current rounds Cape Leeuwin and flows eastward along the southern coast. The current is quite strong at the western end of the southern coast with a surface current of $\sim 45 \text{ cm s}^{-1}$ and an undercurrent of $\sim 9 \text{ cm s}^{-1}$ at $\sim 600 \text{ m}$ depth (Figure 5.17d), but it weakens to $\sim 20 \text{ cm s}^{-1}$ at 130°E midway across the Great Australian Bight (not shown). The current direction is quite disorganized across the shelf of the Great Australian Bight and no coastal current has yet developed along the shelf break east of the bight. The advection of warm water is visible beyond Esperance and into the western end of the bight near 125°E (Figure 5.17a).

By day 30 (July 1, 2001), the relatively swift and narrow Leeuwin Current continues along the western coast (Figure 5.18a). The surface current is $\sim 31 \text{ cm s}^{-1}$ off Cape Inscription near its origin (Figure 5.18b) and strengthens to $\sim 58 \text{ cm s}^{-1}$ as it reaches Cape Leeuwin (Figure 5.18c). Beneath this poleward surface current an opposing equatorward undercurrent of $\sim 25 \text{ cm s}^{-1}$ is centered at $\sim 500 \text{ m}$ depth at 33.25°S (Figure 5.18c). The undercurrent strengthens slightly to $\sim 29 \text{ cm s}^{-1}$ and deepens to $\sim 600 \text{ m}$ depth off Cape Inscription (Figure 5.18b). The inshore current is equatorward over the southern end of the western coast (Figure 5.18c) and some upwelling is present in the embayment just north of Cape Leeuwin (Figures 5.18a and 5.18d).

As before, the current rounds the bend at Cape Leeuwin and flows eastward along the southern coast (Figure 5.18a). The current remains relatively strong at the western end of the coast at $\sim 39 \text{ cm s}^{-1}$ at 117°E (Figure 5.18e). At the Great Australian Bight, the surface current weakens and broadens to cover the entire continental shelf. The current is $\sim 24 \text{ cm s}^{-1}$ at 130°E , midway across the bight (Figure 5.18f). The westward flowing undercurrent is $\sim 12 \text{ cm s}^{-1}$ at $\sim 500 \text{ m}$ depth at 130°E (Figure 5.18f) and $\sim 13 \text{ cm s}^{-1}$ at $\sim 600 \text{ m}$ depth at 117°E (Figure 5.18e). The warm water is again advected beyond Esperance and into the western quarter of the bight (Figure 5.18a). A meander is developing off Cape Leeuwin and there are several wave-like features in the sea surface

temperature structure between Cape Leeuwin and Esperance (Figure 5.18a). With the westward current extending all the way to the shore, there is no upwelling in the Great Australian Bight (Figure 5.18g).

The broad onshore flow at the northern end of the western coast which results in the Leeuwin Current continues at day 45 (July 16, 2001) (Figure 5.19a). The surface is $\sim 35 \text{ cm s}^{-1}$ off Cape Inscription (Figure 5.19b) and strengthens to $\sim 50 \text{ cm s}^{-1}$ off Cape Leeuwin (Figure 5.19c). Two meanders lie between Cape Inscription and Perth. There is an eddy between Perth and Cape Leeuwin and a second eddy below Cape Leeuwin (Figure 5.19a). A velocity cross-section at 33.25°S (Figure 5.19c) cuts through the northern eddy and the coastal current. The southward flow on the offshore side of the eddy extends to a depth of $\sim 400 \text{ m}$ and the northward flow on the onshore side of the eddy joins together with the undercurrent beneath it (Figure 5.19c). The inshore current on the shelf at the southern end of the western coast has now reversed to flow poleward along with the Leeuwin Current (Figure 5.19c). There is no longer any upwelling on the northern side of Cape Leeuwin (Figure 5.19d).

As before the current continues to round Cape Leeuwin and flow eastward along the southern coast. It is strongest near the western end of the coast at $\sim 37 \text{ cm s}^{-1}$ at 117°E (Figure 5.19e). The current broadens and slows upon reaching the Great Australian Bight, with a maximum speed of $\sim 17 \text{ cm s}^{-1}$ at mid-bight (Figure 5.19f). As before, the eastward flow extends from the shelf break to the shore and there is no upwelling (Figure 5.19g). The wave-like features in the sea surface temperature structure persist between Cape Leeuwin and Esperance (Figure 5.19a).

At day 60 (July 31, 2001) the current continues to be swift and narrow along the western coast (Figure 5.20a). The current speed is $\sim 45 \text{ cm s}^{-1}$ off Cape Inscription near its origin (Figure 5.20b) and it increases to a maximum of $\sim 65 \text{ cm s}^{-1}$ off Cape Leeuwin (Figure 5.20c). One meander remains south of Cape Inscription and an eddy lies north of Perth. The eddy which was off Cape Leeuwin at day 45 has drifted to the northwest and lies between Cape Leeuwin and Perth. The inshore current remains poleward and there is no upwelling in the embayment north of Cape Leeuwin (Figure 5.20d).

Along the southern coast the current speed is $\sim 31 \text{ cm s}^{-1}$ at 117°E (Figure 5.20e). At the Great Australian Bight the current still broadens to cover the entire shelf with eastward flow. The current has weakened to a maximum of $\sim 22 \text{ cm s}^{-1}$ at 130°E (Figure 5.20f). The extent of the warm water advection has not increased beyond the western quarter of the bight. The wave-like features in the sea surface temperature between Cape Leeuwin and Esperance remain. The inshore current along the shore in the Great Australian Bight is relatively weak and eastward no upwelling is produced (Figure 5.20g).

The results of this model run were similar to the MCSST satellite imagery. The model run for day 60, July 31, 2001 (Figure 5.20a) are compare against the MCSST imagery for July 31, 2001 (Figure 5.21). The location of the current along the western coast is similare. The satellite imagery shows an offshore bulge in the warm water near the model develops an eddy north of Cape Leeuwin, the the eddy is approximately one degree south of the feature in the imagery. The path of the current along the shelf break in the western Great Australian Bight is the same in the model and the imagery. The extent of warm water advection ($\sim 127^\circ\text{E}$) is approximately the same and the offshore features between 115°E and 120°E are present in both the model and the imagery. The temperature comparison is also similar with a 0.5°C difference between the model and imagery at the northern end of the western coast and a $\sim 1.3^\circ\text{C}$ difference near Cape Leeuwin.

The current system which formed in this experiment was qualitatively correct. Current speeds were comparable to observed values, and the current and temperature feature structures were quite realistic. Throughout the model run, realistic mesoscale features such as meanders and eddies formed along the western coast. With the less variable wintertime winds, the more benign features along the southern coast were as expected.

E. SUMMARY OF DAILY WIND RESULTS

Since previous experiments in this study have used a model forced with averaged annual or monthly winds which do not change with time in the model run, they are not

able to truly capture the effects of temporal variability in forcing. There is considerable temporal variability in the coastal current system of western and southern Australia and a model using non-time-varying wind forcing is unable to simulate this temporal variability. The strength of the Leeuwin Current, especially along the western coast, but also along the southern coast is highly dependent upon the winds. There is also considerable interannual, seasonal, and smaller scale variability in the winds along the southern coast of Australia which can lead to variability in the currents and sea surface temperature distribution (Ridgway and Condie, 2004 and Herzfeld and Tomczak, 1997).

Since it has been shown that increasing the temporal and spatial resolution of the forcing fields may cause boundary conditions of the model to become unstable (Martinho, 2003), two different sets of daily wind experiments were accomplished. In the first two experiments the model was forced with daily winds from the same ECMWF data set (and interpolated from the same $2.5^\circ \times 2.5^\circ$ spatial resolution) as the annually and seasonally averaged wind fields. When interpolated to the model grid, the resulting forcing wind fields were smoothly varying in space, but the temporal resolution was increased to daily.

After verification that using daily varying wind forcing had no adverse effect on boundary condition stability, the spatial resolution was then increased. Experiments 3 and 4 were forced with NOGAPS $1^\circ \times 1^\circ$ resolution wind fields. In all daily wind experiments, after the wind stress fields were calculated they were interpolated to the model's spatial grid, producing one wind file per day. The wind stresses were also interpolated in time for each time step to produce a smoothly varying forcing field, which should be less likely to excite inertial oscillations in the model solution as the forcing changes from one field to the next (Jayne and Tokmakian, 1997).

Experiment 1 used daily winds for December 1980 through February 1981 from the ECMWF data set to force the model. The model was started from rest on December 1, 1980, and the daily winds for December were used to spin up the model. The analysis period of the model run was days 30 through 60, when the January, 1981 winds were used to force the model. These winds were from the same ECMWF wind set which were averaged together to form annual or monthly forcing for the process-oriented experiments

of the previous chapter. The WOA94 monthly temperature (Figure 2.3c) and salinity (Figure 2.4c) for January were used for the upper 1000 m and were merged with the January through March seasonal climatology for depths below 1000 m. The same bottom topography (Figure 2.2b) and coastline from the previous experiments were used.

In most respects this experiment produced quite realistic results. The narrow and swift surface current (the Leeuwin Current) along the west coast advected warm water south and around Cape Leeuwin to the southern coast. An opposing inshore current on the shelf produced upwelling in the embayment north of Cape Leeuwin. Realistic mesoscale features such as meanders and eddies were produced along the western coast. A very weak ($\sim 7 \text{ cm s}^{-1}$) westward current along the shore in the Great Australian Bight formed, but was never strong enough to generate upwelling. By day 60, the Leeuwin Current almost disappeared, consistent with observations (Smith et. al., 1991).

Experiment 2 used wintertime daily wind forcing for June 1981 through August 1981 to force the model. The model was started from rest on June 1, 1981, and the daily winds for June were used to spin up the model. The analysis period of the model run was days 30 through 60, when the July, 1981 winds were used to force the model. These winds were from the same ECMWF wind set which were averaged together to form annual or monthly forcing for the process-oriented experiments of the previous chapter. The WOA94 monthly temperature (Figure 2.3d) and salinity (Figure 2.4d) for July were used for the upper 1000 m and were merged with the July through September seasonal climatology for depths below 1000 m. The same bottom topography (Figure 2.2b) and coastline from the previous experiments were used.

This model also produced quite realistic results with the broad onshore flow at the northern section of the western coast region deflected to the south to form a relatively narrow poleward coastal current along the continental shelf break. This current, the Leeuwin Current, advected a band of warm water southward, then it rounded the bend at Cape Leeuwin to flow eastward along the southern coast. The warm water was advected beyond Esperance and into the Great Australian Bight. Unlike in previous experiments, the coastal current was not confined to a narrow band along the continental slope, but rather was a broad eastward surface current over the entire Great Australian Bight shelf

all the way to the shore. As expected for this winter season, the eastward flow on the Great Australian Bight shelf produced downwelling rather than upwelling.

Experiment 3 was the first to use the higher spatial resolution of the NOGAPS daily wind forcing. This change increased the resolution from $2.5^\circ \times 2.5^\circ$ of the ECMWF data set to $1^\circ \times 1^\circ$ for the NOGAPS data set. The structure of the NOGAPS wind field was quite similar to the ECMWF wind field off the western coast of Australia where there is little variability in the direction of the wind, but it provided greater detail in the wind structure along the southern coast. Daily winds for December 2000 through February 2001 were used to force the model. The model was started from rest on December 1, 2000, and the daily winds for December were used to spin up the model. The analysis period of the model run was days 30 through 60, when the January, 2001 winds were used to force the model. The WOA94 monthly temperature (Figure 2.3c) and salinity (Figure 2.4c) for January were used for the upper 1000 m and were merged with the January through March seasonal climatology for depths below 1000 m. The same bottom topography (Figure 2.2b) and coastline from the previous experiments were used.

As in the previous experiments, the broad onshore flow at the northern end of the model domain along the western coast developed and was deflected to the south to produce a relatively narrow and swift poleward coastal current, the Leeuwin Current along the continental shelf break of the western coast. The current was quite broad near its origin and it narrowed and increased in speed as it approached Cape Leeuwin. As in previous experiments, the band of warm water was advected southward then eastward as the current rounded Cape Leeuwin and flowed eastward along the southern coast. The current broadened as it reached the Great Australian Bight and eastward surface flow covered much of the continental shelf in the bight. Intermittently the flow near the shore in the Great Australian Bight was westward, as expected, but it was never persistent or strong enough to produce upwelling.

The development of a typical eddy which formed off Cape Leeuwin was followed and analyzed over a period of nine days. Its growth, movement, and size were all consistent with observations (e.g., Cresswell and Golding, 1980 and Fang and Morrow, 2003). After the gyre in the Great Australian Bight was weak and intermittent and no

upwelling was produced, the model was run for the 2000 summertime case. In this model run the gyre formed from days 30 through 39, day 45, and days 57 through 60. Upwelling formed and persisted along the shore in the eastern Great Australian Bight, along the western and northern coasts of Kangaroo Island, and south of Kangaroo Island. This highlighted the significant interannual variability in the system (Ridgway and Condie, 2004).

Experiment 4 also used the higher spatial resolution NOGAPS daily wind forcing, this time for the wintertime case. Daily winds for June 2001 through August 2001 were used to force the model. The model was started from rest on June 1, 2001, and the daily winds for June were used to spin up the model. The analysis period of the model run was days 30 through 60, when the July, 2001 winds were used to force the model. The WOA94 monthly temperature (Figure 2.3d) and salinity (Figure 2.4d) for January were used for the upper 1000 m and were merged with the January through March seasonal climatology for depths below 1000 m. The same bottom topography (Figure 2.2b) and coastline from the previous experiments were used.

The broad onshore flow at the northern end of the model domain along the western coast was deflected to the south to produce a relatively narrow and swift poleward coastal current, the Leeuwin Current along the continental shelf break. The current was slightly stronger than the summertime case of Experiment 3. As in previous experiments, the band of warm water was advected southward and around Cape Leeuwin to the southern coast. The current remained westward across the entire Great Australian Bight continental shelf for the duration of the model run and no upwelling was produced.

This set of experiments highlights both the seasonal and interannual variability of this complex current system. The Leeuwin Current along the western coast was slightly stronger in winter (July) than summer (January). There was much greater mesoscale activity in January when the opposing winds are strongest. Along the southern coast, a gyre formed intermittently in the Great Australian Bight in summer, but the flow was constantly eastward across the entire shelf in winter. The production of upwelling during the 2000 summer but not during the 2001 summer is an indication of the importance of interannual variability.

VI. EFFECTS OF THE CURRENT SYSTEM FEATURES ON SOUND SPEED STRUCTURE

In this final section, the effects of the modeled features of this complex current system on the acoustic structure of the region are examined. With the U.S. Navy now frequently operating in coastal and littoral areas, accurate acoustical predictions are more important than ever in these regions. While the sound speed structure in the open ocean is well known, the small-scale and often complex features of the coastal and littoral regions can complicate the acoustics picture. Chapter V highlighted the variability of this current system, both in time and space, and it is hypothesized that this variability in currents and temperature structure will also lead to variability in sound speed. While many Navy leaders and operators already seem to be aware of the complications in sound speed and sonar performance across major western boundary currents such as the Gulf Stream and Kuroshio and their rings, the effects of other current systems such as the one considered here do not seem to be so well known. It is the goal of this section of the study to demonstrate that the features of this current system (and other similar current systems) can have a significant impact on the sound speed structure. Quantifying the impact on sound speed is the first step toward improving acoustical prediction in areas such as this, and therefore improving sonar effectiveness.

The sound speed structure in a region is affected by two general processes: vertical displacement of ocean layers and horizontal advection of water masses (Lurton, 2002). The region in this study is affected by downwelling and upwelling which both displace water vertically. The Leeuwin Current advects warm water southward along the western coast and eastward along the southern coast, while the undercurrent advects cool water in the opposite direction. Meanders in the current carry warmer water offshore and eddies detach from the current, especially off Cape Leeuwin, transporting large volumes of warm water. In addition, all of these processes which act to change the sound speed are variable in time, as shown in Chapter V. Temporal variability further complicates the acoustic picture.

In this study the sound speed structure and changes in the sound speed structure are examined. First the sound speed is calculated and plotted for horizontal levels such as the surface. Then features in the current system, such as eddies, upwelling, and warm water advection are identified for further examination. Sound speed and sound speed change are calculated and plotted for vertical cross sections across the features. Each of these are studied to determine where the greatest changes occur and to identify which features cause the greatest changes.

Sound speed is a complex function of temperature, salinity, and pressure (Fofonoff and Millard, 1983). In this study the UNESCO international algorithm (equation) is used to calculate the speed of sound in seawater. This sound speed equation is based on the equation of Chen and Millero (1977) with the coefficients recalculated by Wong and Zhu (1995). This equation is far more complicated than most others in use and it uses pressure as a variable while most simpler forms use depth.

Note that a number of other equations have been published for calculating the sound speed in seawater based on laboratory measurements (e.g., Wilson, 1960; Del Grosso, 1974; Coppens, 1981; and Mackenzie, 1981). Each of these are different and there is much debate over the accuracy and range of applicability of each. In particular, Dushaw et. al. (1993) has shown that there is a difference of 0.6 m/s at 5000 bar between these equations (e.g., the Del Grosso equation and the Chen and Millero equation). Since the model results in these experiments extend to 2500 m depth, the Chen and Millero equation was chosen due to its international acceptance and greater range of applicability (i.e., applicable to shallow and deep depth as opposed to only a limited range for the simpler equations).

The model results from the NOGAPS daily wind experiments were chosen as the basis for analysis in this chapter because they were run with the most complete and realistic forcing of any of the model runs. Both experiments 3a (summer 2000) and 4 (winter 2001) were used to allow analysis of a range of current system features. Analysizing the results in opposite seasons also allows for an assessment of seasonal variability in the sound speed structure. Warm water advection by the current, warm core eddies, and upwelling are all analyzed to determine how much they change the sound

speed. It is hypothesized that these features will affect the sound speed more than other features because they change the temperature or salinity through horizontal advection of water masses or vertical displacement of water layers. In this analysis the sound speed is calculated at the time of analysis and the change in sound speed is the difference in sound speed from the initial time (climatology) to the analysis time.

A. WARM CORE EDDY

At day 45 (July 16, 2001) of daily wind Experiment 4, the Leeuwin Current is a swift and narrow poleward flow along the continental shelf break of the western coast (Figure 6.1a). Warm water is being advected southward with the current and various mesoscale features such as meanders and eddies are present along the coast. The surface sound speed (Figure 6.1b) closely mirrors the temperature field with highest sound speeds in the warm water of the Leeuwin Current. An anticyclonic, warm-core eddy lies offshore of the current southeast of Cape Leeuwin. The current speeds in the eddy reach $\sim 53 \text{ cm s}^{-1}$ on the inshore side and $\sim 58 \text{ cm s}^{-1}$ on the offshore side (Figure 6.1c). The eddy extends below 200 m depth on the offshore side and it joins the undercurrent beneath it on the inshore side. The surface sound speed is higher in the eddy than in the surrounding waters (Figure 6.1b) and this elevated sound speed extends to a depth of $\sim 250 \text{ m}$ (Figure 6.1d), the full vertical extent of the warm eddy. The increase in sound speed from the initial time is $\sim 11 \text{ m s}^{-1}$ in the eddy (Figure 6.1e). Note that the sound speed increase is even greater (i.e., $\sim 12 \text{ m s}^{-1}$) in the core of the eddy where the strongest poleward advection of warm water is occurring. The sound speed decreases by $\sim 5 \text{ m s}^{-1}$ in the counter flowing cooler water between 600 m and 1000 m depth.

B. POLEWARD ADVECTION OF WARM WATER

As the Leeuwin Current flows poleward along the western coast, it carries a band of warm subtropical water southward along the coast. Upon reaching Cape Leeuwin, the current flows around the continental shelf break and then along the southern coast (Figure 6.1a). By day 45 (July 16, 2001), this warm water extends across the western quarter of the Great Australian Bight, and as along the western coast, the fastest surface sound

speeds are collocated with the warmest water (Figure 6.1b). At 117°E (Figure 6.2a) the $\sim 37 \text{ cm s}^{-1}$ surface current lies over the shelf break. The undercurrent extends from ~ 200 m depth down to ~ 1000 m depth with a maximum speed of $\sim 24 \text{ cm s}^{-1}$ at ~ 300 m depth. The warm water of the surface current is evident by the downward sloping isotherms in the upper 200 m of the water column (Figure 6.2b). The isotherms slope upward below 600 m depth, consistent with cooler water advected westward by the undercurrent. As expected, the fastest sound speeds are in the warm water of the surface current while the slowest speeds are in the cooler water beneath (Figure 6.2c). The greatest increase in sound speed is $\sim 13 \text{ m s}^{-1}$ in the core of the surface current. The sound speed is increased over the entire shelf and the offshore extent of the surface current (Figure 6.2d). The greatest decrease in sound speed is $\sim 7 \text{ m s}^{-1}$ in the undercurrent below 600 m depth.

C. UPWELLING IN THE GREAT AUSTRALIAN BIGHT

There is significant variability in the upwelling in the Great Australian Bight. It appears in austral summer but not winter. It also varies in strength from year to year and even from week to week. During the summertime daily wind Experiment 4, no upwelling appears (e.g., Figure 6.3a). In this case the sound speed is greatest near the surface at the shelf break where the warm surface current lies (Figure 6.3b). Even though there is a $\sim 9 \text{ m s}^{-1}$ increase in sound speed in the warm advected waters over the shelf break, there is not a significant change in sound speed over the shelf. The sound speed increases by $\sim 2 \text{ m s}^{-1}$ near the shore and decreases by $\sim 2 \text{ m s}^{-1}$ near the shelf break (Figure 6.3c).

In daily wind Experiment 3a, the summertime 2000 case, upwelling develops in the Great Australian Bight. A thin band of cooler water is visible along the shore at the surface at the eastern end of the Bight (Figure 6.4a). As expected, the surface sound speed closely resembles the temperature plot with the slowest sound speeds in areas such as this where temperatures are lower (Figure 6.4b). The upward sloping isotherms over the shelf also show that upwelling is present (Figure 6.4c). There is also an upward slope

in the sound speed structure with slower speeds in the areas with cooler water (Figure 6.4d). There is a $\sim 7 \text{ m s}^{-1}$ decrease in sound speed near the shore in the area with the coolest upwelled water (Figure 6.4e).

This comparison shows how the variability in formation of mesoscale (and smaller) features leads to variability in the sound speed structure. During the period when no upwelling develops, the sound speed change is insignificant at $\pm 2 \text{ m s}^{-1}$, but when upwelling occurs the sound speed decreases by $\sim 7 \text{ m s}^{-1}$. This level of change, if not correctly predicted, could significantly impact Navy sonar operations.

D. UPWELLING SOUTH OF KANGAROO ISLAND

Cooler water is also visible at the surface as upwelling develops south of Kangaroo Island in daily wind Experiment 3a at day 45 (January 15, 2000) (Figure 6.4a). The pool of cooler water at the surface lies between $\sim 37.5^\circ\text{S}$ and $\sim 36.5^\circ\text{S}$ and the isotherms slope upward towards this region from both the north and south (Figure 6.5a). The sound speed is noticeably slower at the surface in this area (Figure 6.5b). Similar to the upwelling in the Great Australian Bight, the sound speed decrease in this area of cooler water is $\sim 7 \text{ m s}^{-1}$.

E. SUMMARY OF ACOUSTIC RESULTS

Numerous mesoscale features develop along the western and southern coasts of Australia including upwelling, warm and cold water advection, meanders, and eddies. Each of these features can cause changes in sound speed through vertical displacement of water layers or horizontal advection of water masses. The greatest increase in sound speed was $\sim 13 \text{ m s}^{-1}$ caused by the advection of warm water by the surface current along the western portion of the southern coastline. Similarly the warm current just south of Cape Leeuwin increased the sound speed by $\sim 12 \text{ m s}^{-1}$, while the eddy offshore of that location caused an $\sim 11 \text{ m s}^{-1}$ increase. Upwelling, both on the shelf of the Great Australian Bight and south of Kangaroo Island, caused $\sim 7 \text{ m s}^{-1}$ decreases in sound speed. Advection of cooler water by the undercurrent decreased the sound speed by $\sim 5 \text{ m s}^{-1}$ (south of Cape Leeuwin at 35°S) to $\sim 7 \text{ m s}^{-1}$ (along the southern coast at 117°E). The

variability in the sound speed produced by variability in temperature structure was highlighted by a comparison of daily wind Experiment 4 (winter) with Experiment 3a (summer). In the summer case when upwelling developed in the Great Australian Bight, the sound speed was decreased by $\sim 7 \text{ m s}^{-1}$, but in the winter case with no upwelling the sound speed change of $\pm 2 \text{ m s}^{-1}$ was not significant. These results show that the eastern and southern current systems such as that along western and southern Australia can produce significant variability in the sound speed structure which could impact Navy sonar operations.

VII. SUMMARY AND CONCLUSIONS

A. SUMMARY

This study was both a theoretical and numerical modeling study of the current system off western and southern Australia. Chapter II provided a description of the model used throughout the study, including the data sets, preprocessing, and boundary conditions. Chapter III sought to provide a fluid-dynamics based explanation for why eddies form at a preferential location off Cape Leeuwin. The theoretical explanations were compared against two model runs to test for consistency. A series of process-oriented experiments were conducted in Chapter IV. These experiments, arranged in the order of increasing complexity, sought to isolate which features in the current system are caused by which type of forcing. Chapter V extended the complexity of the modeling studies by adding daily varying winds to isolate the effects of temporal variability. This section also examined features generated by smaller scale wind features by using higher spatial resolution wind forcing. The effects of the features generated by the modeling studies of the two previous sections on the acoustic properties of the complex current system are explored in Chapter VI. Here we provide a brief overview of results for all experiments presented in Chapters III through VI.

The boundary current separation section (Chapter III) sought to explain more systematically why boundary current separation occurs at Cape Leeuwin resulting in an area of enhanced eddy generation in the Leeuwin Current off Cape Leeuwin, which is in agreement with available observations. The Leeuwin Current System (LCS) is an anomalous subtropical eastern boundary current system. With its swift and narrow poleward surface current and energetic mesoscale features such as meanders and eddies, the Leeuwin Current shares many characteristics with subtropical western boundary currents. Unlike these western boundary currents which tend to completely detach from the coastline at some point (e.g., the Gulf Stream leaves the coast off Cape Hatteras), the Leeuwin Current separates from the continental shelf break as it rounds Cape Leeuwin, shedding eddies, and is then turned left under the influence of the Coriolis force to flow eastward along the southern coast of Australia. For the Gulf Stream, a scaled

approximation for the beta effect and streamline curvature was used to determine whether a current could detach from a western boundary coastline. That work was applied to the LCS eastern boundary current and included an additional term, i.e the vortex stretching term, which acts in the presence of bottom topography. Theoretical calculations showed that this term exceeded the sum of the beta term and streamline curvature term, and strongly enhanced boundary current separation. A model (in this case the Princeton Ocean Model (POM)) was run with and without bottom topography to show that the calculations were not inconsistent with the model results.

When a flat-bottom model was used to simulate the Leeuwin Current as it rounds Cape Leeuwin from the north where the current is turning in an anticyclonic direction, both the beta term and streamline curvature term in inequality (5) were shown to be negative and to act to enhance separation. This allowed the current to separate from the coastline forming relatively large meanders and eddies in the current.

When bottom topography was added to the model, the vortex stretching term was shown to decelerate the current downstream and to enhance separation from the coast. Since the bottom topography adds a continental shelf, a stabilizing effect was also introduced. Note that the current in this case preferentially follows the continental shelf break, rather than the coastline. As the shelf break has a much larger radius of curvature (~175 km) than the coastline (~50 km), the larger radius resulted in a smaller curvature term. However, since the effect of vortex stretching was much greater than the effect of curvature, boundary current separation still occurred, resulting in a preferential location for eddy generation off Cape Leeuwin, consistent with the theoretical calculations and in agreement with available observations.

In the process-oriented experiments (Chapter IV), a series of model runs of increasing complexity were conducted using various forcing mechanisms and combinations of forcing mechanisms (see below). The goal of this series of experiments was to isolate which type of forcing or combination of forcing is responsible for producing each of the major features of the current system off western and southern Australia.

In Experiment 1, the model was initialized using horizontally averaged annual temperature and salinity climatology, which removed all thermohaline forcing. The model was run over a flat bottom with a uniform depth of 2500 m, eliminating any topographic effects, and a realistic coastline. The only forcing was from the annually averaged climatological winds

The resulting currents were more characteristic of a typical eastern boundary current (EBC) system than of the coastal current system off western and southern Australia. Some characteristics of the observed Australia current system did form, however. A weak equatorward current has been observed on the continental shelf inshore of the Leeuwin Current flowing in the same direction as the wind. A similar weak equatorward current along the coastline did form in this experiment. Along the southern coast, the South Australia Current also flows along the shelf break with a broad, weak westward current inshore of the South Australia Current in the Great Australian Bight similar to the current formed in the bight in this experiment. Upwelling, frequently observed in the eastern Great Australian Bight, was evident in the upward tilting isotherms in this area, though quite weak.

There were also a number of differences from the observed system. The currents along the southern coast were westward and the Leeuwin Current along the western coast was equatorward, rather than the observed eastward and poleward currents. The undercurrent also flowed in the opposite direction from the observed undercurrent. The location of the currents was also incorrect with currents adjacent to the coast instead along the continental shelf break as observed.

In Experiment 2, the model was again initialized using horizontally averaged annual temperature and salinity climatology. This time, the flat bottom was replaced with the smoothed Sandwell and Smith (1996) bottom topography as described in Chapter II. The same realistic coastline was used. The only forcing was from the annually averaged climatological winds used in Experiment 1.

As in Experiment 1, the overall current pattern formed in this experiment was more characteristic of a typical Eastern Boundary Current system than of the current

pattern in this region. However, several features which are typical of the Australian currents were correctly modeled. The addition of topography moved the coastal currents from the coastline to the continental shelf break, where they are observed to occur both along the western coast and the southern coast. Weaker, poleward currents along the western coast and westward currents along the southern coast formed inshore of the coastal currents. The slightly warmer band of surface water that formed along the shelf break of the Great Australian Bight is representative of the warm water mass which is observed to form in this area. The observed water temperature and areal extent of the water mass were less than observed.

Other features continue to be different from those observed. The Leeuwin Current and South Australia Current are still flowing with the wind rather than against the wind. The undercurrent formed is too broad, weak, and deep and is likely due to continuity in the model formulation rather than the formation of a true undercurrent. Upwelling was again modeled along the western coast where no upwelling is observed. No upwelling formed along the southern coast at the eastern end of the Great Australian Bight or in the Eyre/Kangaroo Island areas where upwelling is observed.

Experiment 3 was the first to use the full annual temperature and salinity climatology, introducing thermohaline forcing into the model. There was no wind forcing in this experiment. The same coastline and 2500 m flat bottom from Experiment 1 were used, eliminating any topographic effects.

The overall current pattern formed in this experiment, was more similar to the coastal current system off the western and southern coasts of Australia than to a typical eastern boundary current system. The broad onshore flow along the thermohaline gradient off the western coast was correctly represented, and that onshore flow was directed southward to form a narrow and swift poleward current along the western coast. This poleward current advected a narrow band of warm subtropical water poleward along the coast, then around Cape Leeuwin and eastward along the southern coast similar to the advection which is observed. The poleward current forced strong downwelling along the western coast, which is also observed. The observed meanders and eddies were also simulated in this experiment.

There were still significant differences from the observed system. The coastal current along the western and southern coasts was stronger than observed current speeds. Even though the coastal current in this experiment flowed in the correct direction, it was incorrectly located along the shore rather than along the continental shelf break. With the coastal current along the shore, no weak opposing current inshore of the coastal current could form. No upwelling was simulated anywhere along the southern coast. Finally, the coastal current moved offshore as time passed, while the observed current remains trapped along the continental shelf break/continental slope. This offshore movement allowed the undercurrent to shoal and finally produce a westward and equatorward current along the coast. This resulted in a complete current reversal from the observed currents by day 81.

Experiment 4 again used the full annual temperature and salinity climatology, to allow thermohaline forcing. There was no wind forcing in this experiment. All model parameters in Experiment 4 are the same as in Experiment 3 except that the flat bottom has been replaced with the smoothed Sandwell and Smith (1996) bottom topography as described in Chapter II. The same realistic coastline was used.

The overall current pattern formed in this experiment was more similar to the coastal current system off the western and southern coasts of Australia than in any previous experiment. The broad onshore flow along the thermohaline gradient off the western coast was correctly represented and correctly directed southward to form a narrow and swift poleward current along the continental shelf break of the western coast. This poleward current advected a narrow band of warm subtropical water poleward along the coast, then around Cape Leeuwin and eastward along the southern coast similar to the advection which is observed. The poleward current forced strong downwelling along the western coast, which is also observed. Meanders and eddies which are frequently observed in this region were also formed in this simulation. The greatest contrast from the previous experiment was the correct location of the current along the shelf break. The current formed in the correct location and it also remained anchored to the continental shelf break/continental slope throughout the model run instead of broadening and moving offshore as occurred in the previous experiment.

There were still some incorrectly modeled features in this experiment. Though slowed somewhat by the addition of topography, the surface coastal current was still too strong as in Experiment 3. There was no opposing shelf current developed inshore of the coastal current. Just as in the previous experiment, no upwelling was simulated anywhere along the southern coast, even in areas where upwelling is observed to frequently occur in the eastern end of the Great Australian Bight and near Kangaroo Island.

Experiment 5 used both thermohaline forcing from the full annual temperature and salinity climatology and the wind forcing used in Experiments 1 and 2. The 2500 m deep flat bottom eliminated any topographic effects.

The overall current pattern formed in this experiment, began quite similar to the coastal current system off the western and southern coasts of Australia with currents similar to those formed in the thermohaline forcing experiments, showing that the strong thermohaline gradient has a greater effect on the currents of the region than the wind. The broad onshore flow at the northern end of the western coast was correctly modeled, along with the poleward current which narrowed and strengthened with distance toward the south. The current continued around the cape and eastward along the southern coast. The current advected a narrow band of warm subtropical water south along the western coast and then east along the southern coast to the Great Australian Bight. Also as observed, meanders and eddies formed in the current in the vicinity of Cape Leeuwin and an eddy field formed offshore of the current along the southern coast between Cape Leeuwin and the Great Australian Bight. Downwelling was prevalent along the western coast.

As in previous experiments, the modeled current system still differed from the observed system in several ways. The coastal current along the western and southern coasts was too strong; however, its speed was less than the currents which developed in Experiment 3 with only thermohaline forcing, showing that the wind forcing does counteract the thermohaline forcing to slow the currents. As in Experiment 3, the current flowed in the correct direction, but the current was incorrectly located adjacent to the shore rather than a few kilometers offshore where the shelf break should lie. There was

no weak opposing current inshore of the coastal current. No upwelling developed anywhere along the southern coast, although upwelling is observed to frequently occur in the eastern end of the Great Australian Bight and in the Kangaroo Island area. Finally, just as in Experiment 3, the coastal current moved offshore allowing the undercurrent to shoal and finally produce a westward and equatorward current along the coast. The entire current system reversed in direction from the observed current system by day 72. The only significant difference from Experiment 3 (thermohaline forcing only over flat bottom) was that the currents were weaker.

Experiment 6 was initialized with the most complete set of annually averaged climatology possible. The model was run with thermohaline forcing from the full annual temperature and salinity fields and the annually averaged wind forcing. The Sandwell and Smith (1996) bottom topography allowed the development of topographic effects and the same realistic coastline from the other experiments was used.

As expected, this experiment produced the most realistic results of all the annual forcing cases. The broad onshore flow along the thermohaline gradient at the northern end of the western was deflected toward the south to form a relatively strong and narrow poleward surface coastal current, the Leeuwin Current, which correctly narrowed and intensified at its southern end and then followed the continental shelf break around the cape and continued eastward along the southern coast. The coastal current continued eastward with the formation of the South Australia Current along the Great Australian Bight and farther east, forming a continuous current all the way to the eastern boundary of the model domain. The opposing undercurrent was eastward along the southern coast and equatorward along the western coast. The current was correctly positioned along the shelf break, with a weak opposing equatorward current inshore of the coastal current along the western coast as observed, but not along the southern coast. A narrow band of warm subtropical water was advected poleward and then eastward and a second, more saline water mass originated at the western end of the Great Australian Bight and was carried eastward as well. Meanders and eddies formed in the Leeuwin Current of the western coast and around Cape Leeuwin at the southwestern corner of the continent. The

eddy field developed on the offshore side of the current between Cape Leeuwin and the Great Australian Bight and a field of weak meanders formed along the Great Australian Bight.

Although most aspects of the current system modeled by this experiment were qualitatively correct, the gyre/westward flow along the shore never developed on the Great Australian Bight shelf inshore of the South Australia Current, likely due to the averaging of the wind forcing. Since the easterly wind in the Great Australian Bight is relatively weak, when averaged together with winds from other directions which occur during storm passages, the resultant wind field is not sufficiently strong to produce a westward current. With no westward current, the upwelling expected in this region also did not develop.

Experiment 7 was the first of the seasonal wind cases, which used averaged January winds to represent the summer seasonal case. The WOA94 monthly temperature and salinity for January were used for the upper 1000m and were merged with the January through March seasonal climatology for depths below 1000m. The same bottom topography and coastline from the previous experiments were used.

The current system modeled by this experiment was the most realistic of any experiment in the process-oriented section of this study and most aspects of the current system were qualitatively correct. This was the only experiment to develop an equatorward current on the shelf inshore of the Leeuwin Current along the western coast. The gyre/westward flow along the shore on the Great Australian Bight shelf inshore of the South Australia Current was also modeled, though it was weaker ($\sim 11 \text{ cm s}^{-1}$) than observed values of $\sim 50 \text{ cm s}^{-1}$ (Godfrey et. al., 1986). As is earlier experiments, this is likely an artifact of the averaging of the wind forcing. With such a weak westward current, the resultant upwelling was barely discernable at the surface.

Experiment 8 was the second seasonal wind case, which used averaged July winds to represent the winter seasonal case. The WOA94 monthly temperature and salinity for July were used for the upper 1000m and were merged with the July through

September seasonal climatology for depths below 1000m. The same bottom topography and coastline from the previous experiments were used.

Similar to the annually averaged wind with thermohaline forcing case (Experiment 6), most aspects of the current system modeled by this experiment were qualitatively correct, but the gyre/westward flow along the shore never developed on the Great Australian Bight shelf inshore of the South Australia Current. This is likely an artifact of the annual averaging of the wind forcing. Since the easterly wind in the Great Australian Bight is relatively weak, when averaged together with winds from other directions which occur during storm passages, the resultant wind field is not sufficiently strong to produce a westward current. With no westward current, the upwelling expected in this region also did not develop.

The purpose of the process-oriented experiments was to isolate which features in the current system were caused by which type of forcing by applying each forcing individually and in various combinations. Table 4.2 summarizes each of the features and forcing which appears to cause them. The current direction is a result of thermohaline forcing. When no thermohaline forcing was applied, the current flowed in the opposite direction. The poleward advection of warm water was also caused by this thermohaline gradient. Topography is responsible for the location of the current along the shelf break. In all flat-bottom experiments, the current formed adjacent to the coast and then broadened and moved offshore late in the model runs. The narrow width of the current appears to be caused by interaction between the opposing thermohaline forcing and wind. The current strength is a factor of thermohaline forcing, wind, and topography. When thermohaline forcing is used alone, the current is too strong. Both wind and topography act to slow the current to a more realistic speed. The opposing inshore current over the continental shelf is caused by the wind along the western coast, but only forms with summertime winds along the southern coast. Meanders and eddies are a factor of the opposing thermohaline and wind forcing. In addition, as discussed in Chapter 3, the coastline direction and radius of curvature and vortex stretching imposed by the

continental slope influence the locations at which the eddies can form. Finally, the gyre and resultant upwelling in the Great Australian Bight are caused by the summertime winds.

The daily wind forcing experiments (Chapter V) sought to isolate the effects of interannual and smaller scale temporal variability on the current system. Model runs using higher spatial resolution wind forcing than used in previous experiments were also conducted in order to examine the effects of smaller scale wind features on the current system. Since previous experiments in this study used a model forced with averaged annual or monthly winds which do not change with time in the model run, they are not able to truly capture the effects of temporal variability in forcing. There is considerable temporal variability in the coastal current system of western and southern Australia and a model using non-time-varying wind forcing is unable to simulate this temporal variability. The strength of the Leeuwin Current, especially along the western coast, but also along the southern coast is highly dependent upon the winds. There is also considerable interannual, seasonal, and smaller scale variability in the winds along the southern coast of Australia which can lead to variability in the currents and sea surface temperature distribution (Ridgway and Condie, 2004 and Herzfeld and Tomczak, 1997).

Since it has been shown that increasing the temporal and spatial resolution of the forcing fields may cause boundary conditions of the model to become unstable (Martinho, 2003), the first two experiments used daily winds from the same ECMWF data set (and interpolated from the same $2.5^\circ \times 2.5^\circ$ spatial resolution) as the annually and seasonally averaged wind fields. When interpolated to the model grid, the resulting forcing wind fields were smoothly varying in space, but the temporal resolution was increased to daily.

After verification that using daily varying wind forcing had no adverse effect on boundary condition stability, the spatial resolution was then increased. Experiments 3 and 4 were forced with NOGAPS $1^\circ \times 1^\circ$ resolution wind fields. In all daily wind experiments, after the wind stress fields were calculated they were interpolated to the model's spatial grid, producing one wind file per day. The wind stresses were also

interpolated in time for each time step to produce a smoothly varying forcing field, which should be less likely to excite inertial oscillations in the model solution as the forcing changes from one field to the next.

Experiment 1 used daily winds for December 1980 through February 1981 from the ECMWF data set to force the model. The model was started from rest on December 1, 1980, and the daily winds for December were used to spin up the model. The analysis period of the model run was days 30 through 60, when the January, 1981 winds were used to force the model. These winds were from the same ECMWF wind set which were averaged together to form annual or monthly forcing for the process-oriented experiments of the previous chapter. The WOA94 monthly temperature (Figure 2.3c) and salinity (Figure 2.4c) for January were used for the upper 1000 m and were merged with the January through March seasonal climatology for depths below 1000 m. The same bottom topography (Figure 2.2b) and coastline from the previous experiments were used.

In most respects this experiment produced quite realistic results. The narrow and swift surface current (the Leeuwin Current) along the west coast advected warm water south and around Cape Leeuwin to the southern coast. An opposing inshore current on the shelf produced upwelling in the embayment north of Cape Leeuwin. Realistic mesoscale features such as meanders and eddies were produced along the western coast. A very weak ($\sim 7 \text{ cm s}^{-1}$) westward current along the shore in the Great Australian Bight formed, but was never strong enough to generate upwelling. By day 60, the Leeuwin Current almost disappeared, consistent with observations (Smith et. al., 1991).

Experiment 2 used wintertime daily wind forcing for June 1981 through August 1981 were used to force the model. The model was started from rest on June 1, 1981, and the daily winds for June were used to spin up the model. The analysis period of the model run was days 30 through 60, when the July, 1981 winds were used to force the model. These winds were from the same ECMWF wind set which were averaged together to form annual or monthly forcing for the process-oriented experiments of the previous chapter. The WOA94 monthly temperature (Figure 2.3d) and salinity (Figure 2.4d) for July were used for the upper 1000 m and were merged with the July through September

seasonal climatology for depths below 1000 m. The same bottom topography (Figure 2.2b) and coastline from the previous experiments were used.

This model also produced quite realistic results with the broad onshore flow at the northern section of the western coast region deflected to the south to form a relatively narrow poleward coastal current along the continental shelf break. This current, the Leeuwin Current, advected a band of warm water southward, then it rounded the bend at Cape Leeuwin to flow eastward along the southern coast. The warm water was advected beyond Esperance and into the Great Australian Bight. Unlike in previous experiments, the coastal current was not confined to a narrow band along the continental slope, but rather was a broad eastward surface current over the entire Great Australian Bight shelf all the way to the shore. As expected for this winter season, the eastward flow on the Great Australian Bight shelf produced downwelling rather than upwelling.

Experiment 3 was the first to use the higher spatial resolution of the NOGAPS daily wind forcing. This change increased the resolution from $2.5^\circ \times 2.5^\circ$ of the ECMWF data set to $1^\circ \times 1^\circ$ for the NOGAPS data set. The structure of the NOGAPS wind field was quite similar to the ECMWF wind field off the western coast of Australia where there is little variability in the direction of the wind, but it provided greater detail in the wind structure along the southern coast. Daily winds for December 2000 through February 2001 were used to force the model. The model was started from rest on December 1, 2000, and the daily winds for December were used to spin up the model. The analysis period of the model run was days 30 through 60, when the January, 2001 winds were used to force the model. The WOA94 monthly temperature (Figure 2.3c) and salinity (Figure 2.4c) for January were used for the upper 1000 m and were merged with the January through March seasonal climatology for depths below 1000 m. The same bottom topography (Figure 2.2b) and coastline from the previous experiments were used.

As in the previous experiments, the broad onshore flow at the northern end of the model domain along the western coast developed and was deflected to the south to produce a relatively narrow and swift poleward coastal current, the Leeuwin Current along the continental shelf break of the western coast. The current was quite broad near its origin and it narrowed and increased in speed as it approached Cape Leeuwin. As in

previous experiments, the band of warm water was advected southward then eastward as the current rounded Cape Leeuwin and flowed eastward along the southern coast. The current broadened as it reached the Great Australian Bight and eastward surface flow covered much of the continental shelf in the Bight. Intermittently the flow near the shore in the Great Australian Bight was westward, as expected, but it was never persistent or strong enough to produce upwelling.

The development of a typical eddy which form off Cape Leeuwin was followed and analyzed over a period of nine days. Its growth, movement, and size were all consistent with observations (e.g., Cresswell and Golding, 1980 and Fang and Morrow, 2003). After the gyre in the Great Australian Bight was weak and intermittent and no upwelling was produced, the model was run for the 2000 summertime case. In this model run the gyre formed from days 30 through 39, day 45, and days 57 through 60. Upwelling formed and persisted along the shore in the eastern Great Australian Bight, along the western and northern coasts of Kangaroo Island, and south of Kangaroo Island. This highlights the significant interannual variability in the system (Ridgway and Condie, 2004).

Experiment 4 also used the higher spatial resolution NOGAPS daily wind forcing, this time for the wintertime case. Daily winds for June 2001 through August 2001 were used to force the model. The model was started from rest on June 1, 2001, and the daily winds for June were used to spin up the model. The analysis period of the model run was days 30 through 60, when the July, 2001 winds were used to force the model. The WOA94 monthly temperature (Figure 2.3d) and salinity (Figure 2.4d) for January were used for the upper 1000 m and were merged with the January through March seasonal climatology for depths below 1000 m. The same bottom topography (Figure 2.2b) and coastline from the previous experiments were used.

The broad onshore flow at the northern end of the model domain along the western coast was deflected to the south to produce a relatively narrow and swift poleward coastal current, the Leeuwin Current along the continental shelf break. The current was slightly stronger than the summertime case of Experiment 3. As in previous experiments, the band of warm water was advected southward and around Cape Leeuwin

to the southern coast. The current remained westward across the entire Great Australian Bight continental shelf for the duration of the model run and no upwelling was produced.

This set of experiments highlights both the seasonal and interannual variability of this complex current system. The Leeuwin Current along the western coast was slightly stronger in winter (July) than summer (January). There was much greater mesoscale activity in January when the opposing winds are strongest. Along the southern coast, a gyre formed intermittently in the Great Australian Bight in summer, but the flow was constantly eastward across the entire shelf in winter. The production of upwelling during the 2000 summer but not during the 2001 summer is an indication of the interannual variability.

In the final chapter, the effects of the modeled features of this complex current system on the acoustic structure of the region were examined. With the U.S. Navy now frequently operating in coastal and littoral areas, accurate acoustical predictions are more important than ever in these regions. While the sound speed structure in the open ocean is well known, the sound speed structure in the coastal and littoral regions also needs to be determined because the smaller scale and often complex features of the coastal and littoral regions can complicate the acoustics picture.

Numerous mesoscale features develop along the western and southern coasts of Australia including upwelling, warm and cold water advection, meanders, and eddies. Each of these features can cause changes in sound speed through vertical displacement of water layers or horizontal advection of water masses. The greatest increase in sound speed was $\sim 13 \text{ m s}^{-1}$ caused by the advection of warm water by the surface current along the western portion of the southern coastline. Similarly the warm current just south of Cape Leeuwin increased the sound speed $\sim 12 \text{ m s}^{-1}$ and the eddy offshore of that location cause an $\sim 11 \text{ m s}^{-1}$ increase. Upwelling, both on the shelf of the Great Australian Bight and south of Kangaroo Island, caused $\sim 7 \text{ m s}^{-1}$ decreases in sound speed. Advection of cooler water by the undercurrent decreased the sound speed by $\sim 5 \text{ m s}^{-1}$ (south of Cape Leeuwin at 35°S) to $\sim 7 \text{ m s}^{-1}$ (along the southern coast at 117°E). The variability in the sound speed produced by variability in temperature structure was highlighted by a comparison of daily wind Experiment 4 (winter) with Experiment 3a (summer). In the

summer case when upwelling developed in the Great Australian Bight, the sound speed was decreased $\sim 7 \text{ m s}^{-1}$, but in the winter case with no upwelling the sound speed change of $\sim 2 \text{ m s}^{-1}$ was not significant. These results show that even relatively weak current systems such as that along southern Australia can produce variability in the sound speed structure which may affect Navy sonar operations.

B. CONCLUSIONS

The boundary current separation study sought to explain from a fluid dynamics theoretical framework why boundary current separation occurs off Cape Leeuwin creating an area of enhanced eddy generation. Separation has been shown to occur when a current undergoes downstream deceleration due to adverse downstream pressure gradient. This pressure gradient is affected by beta effect, vortex stretching, and streamline curvature. Previous work was expanded by the introduction of a scale vortex stretching term. It was shown that all three processes act to decelerate the current and to enhance separation. After separation occurs, the current is turned left under the influence of Coriolis force and forms a meander which can subsequently detach from the current as an eddy.

In the process-oriented experiments, a series of model runs of increasing complexity were run in order to isolate which forcing mechanisms are responsible for which features in the current system. It was shown that the current direction, and the resultant advection of warm water, are caused by the thermohaline gradient. Topography is responsible for the location of the current along the shelf break, and topographic beta due to the continental slope prevents the current from becoming broader and drifting westward away from the shelf break. The swift current forced by thermohaline gradient is slowed to realistic speeds by the opposing wind and topography. The opposing inshore current over the continental shelf is forced by the wind. Meanders and eddies result from the opposition of the thermohaline and wind forcing. The gyre in the Great Australian Bight and the resultant upwelling are caused by the change in wind direction in summer.

The daily wind experiments captured the seasonal and interannual variability of the current system. The Leeuwin Current along the western coast was stronger in winter

than in summer. The mesoscale activity was highest in January (summer) when opposing winds are greatest. The gyre in the Great Australian Bight and upwelling in the bight and along Kangaroo Island were shown to appear only in summer. In addition, the interannual variability was demonstrated by the formation of upwelling in the summer of 2000 but not in 2001.

The final chapter examines the effects of these mesoscale features in the current system on the acoustic structure in the region. It was shown that the greatest changes in sound speed of $\sim 13 \text{ m s}^{-1}$ (from the initial state) resulted from the advection of warm water onto the southern coast by the Leeuwin Current. Advection of cooler water by the undercurrent, transport of warmer water in anticyclonic eddies, and upwelling were also shown to cause significant changes in sound speed. The difference in sound speed change in the eastern Great Australian Bight and Kangaroo Island region during upwelling events ($\sim 7 \text{ m s}^{-1}$) and non-upwelling events ($\pm 2 \text{ m s}^{-1}$) highlight the variability in sound speed. All these results demonstrate that even relatively weak current systems can produce variability in sound speed which can adversely impact Navy sonar operations.

LIST OF REFERENCES

Batchelor, G.K. An Introduction to Fluid Dynamics, *Cambridge University Press*, 615p., 1967.

Batteen, M. L. Wind-forced modeling studies of currents, meanders, and eddies in the California Current System. *J. Geophys. Res.*, **102(C1)**, 985-1010, 1997.

Batteen, M. L. and C. L. Butler. Modeling studies of the Leeuwin Current off western and southern Australia. *J. Phys. Oceanogr.*, **28 (11)**, 2199-2221, 1998.

Batteen, M. L., and M. J. Huang. The effect of salinity on density in the Leeuwin Current System. *J. Geophys. Res.*, **103(C11)**, 24,693-24,721, 1998.

Batteen, M. L., and M. J. Rutherford. Modeling studies of eddies in the Leeuwin Current: The role of thermal forcing. *J. Phys. Oceanogr.*, **20 (9)**, 1484-1520, 1990.

Batteen, M. L., M. J. Rutherford, and E. J. Bayler. A numerical study of wind- and thermal-forcing effects on the ocean circulation off western Australia. *J. Phys. Oceanogr.*, **22 (12)**, 1406-1433, 1992.

Blumberg, A. F., and G. L. Mellor. A Description of a Three-Dimensional Coastal Ocean Circulation Model, *Three-Dimensional Coastal Ocean Models, Coastal Estuarine Sciences*. 4: edited by N. Heaps, pp 1-16, AGU, Washington, D. C., 1987.

Chapman, D. C. Numerical Treatment of Cross-Shelf Open Boundaries in a Barotropic Coastal Ocean Model, *Journal of Physical Oceanography*, **25**, 1060-1075, 1985.

Chen, C. T., and F. J. Millero. Speed of sound in seawater at high pressures, *J. Acoust. Soc. Am.*, **62(5)**, 1129-1135, 1977.

Cirano, M. and J. F. Middleton, Aspects of the mean wintertime circulation along Australia's southern shelves: Numerical studies, *J. Phys. Oceanogr.*, **33(3)**, 668-684, 2004.

Coppens, A. B. Simple equations for the speed of sound in Neptunian waters, *J. Acoust. Soc. Am.*, **69(3)**, 862-863, 1981.

Cresswell, G. R. and T. J. Golding. Observations of a south-flowing current in the southeastern Indian Ocean, *Deep-sea Res.*, **27**, 449-466, 1980.

Del Grosso, V. A. New equation for the speed of sound in natural waters (with comparisons to other equations), *J. Acoust. Soc. Am.*, **56**(4), 1084-1091, 1974.

Ezer, T. and G. L. Mellor, Diagnostic and prognostic Calculations of the North Atlantic circulation and sea level using a sigma coordinate ocean model, *J. Geophys. Res.*, **99**(C7), 14159-14171, 1994.

Ezer, T. and G. L. Mellor, Simulations of the Atlantic Ocean with a free surface sigma coordinate ocean model, *J. Geophys. Res.*, **102**(C7), 15647-15657, 1997.

Flather, R. A. A tidal model of the northwest European continental shelf. *Mem. Soc. R. Sci. Liege, Ser. 6, 10*, 141-164, 1976.

Gersbach, G. H., C. B. Pattiarchi, G. N. Ivey, and G. R. Cresswell. Upwelling on the southwest coast of Australia – Source of the Capes Current? *Continental Shelf Res.*, **19**, 363-400, 1999.

Gibson, J. K., P. Kallberg, S. Uppala, A. Nomura, A. Hernandez, E. Serrano. ERA Description. *ECMWF Re-Analysis Project Report Series*, **1**, 1997.

Godfrey, J. S. and K. R. Ridgway. The large-scale environment of the poleward-flowing Leeuwin Current, Western Australia: Longshore steric height gradients, wind Stress and geostrophic flow, *J. Phys. Oceanogr.*, **15**(5), 481-495, 1985.

Godfrey, J. S., D. J. Vaudrey, and S. D. Hahn. Observations of the shelf-edge current south of Australia, Winter 1982, *J. Phys. Oceanogr.*, **16**(4), 668-679, 1986.

Goerss, J. S. and P. A. Phoebus. The Navy's operational atmospheric analysis. *Weather and Forecasting*, **7**, 232-249, 1992.

Griffiths, R. W. and A. F. Pierce. Instability and eddy pairs on the Leeuwin Current south of Australia, *Deep-sea Research* **32** (12), 1511, 1985.

Herzfeld, M. and M. Tomczak. Numerical modeling of sea surface temperature and circulation in the Great Australian Bight, *Prog. Oceanogr.*, **39**, 29-78 1997.

Holton, J.R. An introduction to dynamic meteorology, fourth edition, *Elsevier Academic Press*, 535pp, 2004.

Jayne, S. R. and R. Tokmakian. Forcing and sampling of ocean general circulation models: Impact of high-frequency motions. *J. Phys. Oceanogr.*, **27**(6), 1173-1179, 1998.

Levitus, S., and T. P. Boyer, World Ocean Atlas 1994, Vol. 4: Temperature, *NOAA Atlas NESDI 4*, 117 pp., U. S. Dept. of Commerce, Washington, D.C., 1994.

Levitus, S., R. Burgett, and T. P. Boyer, World Ocean Atlas 1994, Vol. 3: Salinity, *NOAA Atlas NESDI 3*, 99 pp., U. S. Dept. of Commerce, Washington, D.C., 1994.

Marshall, D. P. and C.E. Tansley. An Implicit Formula for Boundary Current Separation, *J. Phys. Oceanogr.* 1633-1638, 2001.

Martinho, A. S. Sensitivity studies using multi-region and open boundary conditions for terrain bottom following ocean models, Ph.D dissertation in Physical Oceanography, Naval Postgraduate School, Monterey, CA, 210 p., 2003.

Martinho, A. S. and M. L. Batten. On reducing the slope parameter in terrain-following numerical ocean models. *Ocean Modeling*, **13**, 166-175, 2006.

McClain, E. P., W. G. Pichel, and C. C. Walton. Comparative performance of AVHRR based multichannel sea surface temperatures, *J. Geophys. Res.*, 90, 11587-11601, 1985.

McCreary, J. P. Jr., S. R. Shetye, and P. K. Kundu. Thermohaline forcing of eastern boundary currents: With application to the circulation off the west coast of Australia, *J. Mar. Res.*, **44**, 71-92, 1986.

Mellor, G.L. User's Guide for a Three-Dimensional, Primitive Equation, Numerical Ocean Model, 40 pp, Program in Atmospheric and Ocean Sciences Report, Princeton Univ., Princeton, N. J., 1996.

Mellor, G.L., L.-Y. Oey, and T. Ezer. Sigma Coordinate Pressure Gradient Errors and the Seamount Problem. *Journal of Atmospheric and Ocean Technology*, **15**, 1122-1131, 1998.

Mellor, G. L., and T. Yamada, Development of a turbulence closure model for geophysical fluid problems, *Rev. Geophys. Space Phys.*, 20, 851-875, 1982.

Middleton, J. F. and M. Cirano. Wind-forced downwelling slope currents: A numerical study, *J. Phys. Oceanogr.*, **29(8)**, 1723-1743, 1999.

Middleton, J. F. and M. Cirano. A northern boundary current along Australia's southern shelves: The Flinders Current, *J. Geophys. Res.*, **107(C9)**, Art. No. C03129, 2002.

Middleton, J. F. and G. Platov. The mean summertime circulation along Australia's southern shelves: A numerical study, *J. Phys. Oceanogr.*, **33(11)**, 2270-2287, 2003.

Morrow, R., F. Fang, M. Fieux, and R. Molcard. Anatomy of three warm-core Leeuwin Current eddies, *Deep-Sea Res.*, **50**, 2229-2243, 2003.

Palma E.D., and R. P. Matano. On the Implementation of Passive Open Boundary Conditions for a General Circulation Model: the Barotropic Mode, *Journal of Geophysical Research*. **103 (C1)**, 1319-1341, 1998.

Palma, E. D., and R. P. Matano, On the implementation of passive open boundary conditions for a general circulation model: The three-dimensional case, *J. Geophys. Res.*, 105(C4), 8605-8627, 2000.

Pearce, A. F., and C. B. Pattiarchi. The Capes Current: A summer countercurrent flowing past Cape Leeuwin and Cape Naturaliste, Western Australia, *Continental Shelf Res.*, **19**, 401-420, 1999.

Richardson, P. L. and A. Tychensky. Meddy Trajectories in the Canary Basin Measured During the SEMAPHORE Experiment, 1993-1995, *Journal of Geophysical Research*. 103:25029-25045, 1998.

Ridgway, K. R. and S. A. Condie, The 5500-km-long boundary flow off western and southern Australia, *J. Geophys. Res.*, **109(C4)**, Art. No. C04017, 2004.

Rochford, D. J. Seasonal changes in the distribution of Leeuwin Current waters off southern Australia. *Australian Journal of Marine and Freshwater Research*, **37(1)**, 1-10, 1986.

Roed, L. P. and O. M. Smedstad. Open boundary conditions for forced waves in a rotating fluid, *SIAM J. Sci. Stat. Comput.*, **5**, 414-426, 1984.

Schott, F. A. and J. P. McCreary. The monsoon circulation of the Indian Ocean. *Progress in Oceanography*, **51 (1)**, 1-123, 2001.

Smagorinsky, J., S. Manabe, and J. L. Holloway, Numerical results from a nine-level general circulation model of the atmosphere, *Mon. Weather Rev.*, 93, 727-768, 1965.

Smith, R. L., A. Huyer, J. S. Godfrey, and J. A. Church. The Leeuwin Current off Western Australia, 1986-1987, *J. Phys. Oceanogr.*, **21(2)**, 323-345, 1991.

Smith, W. H. F., and D. T. Sandwell, Global seafloor topography from satellite altimetry and ship depth soundings, *Science*, **277**, 1956-1962, 1997.

Thompson, R. O. R. Y. Observations of the Leeuwin Current off Western Australia, *J. Phys. Oceanogr.*, **14(3)**, 623-628, 1984.

Thompson, R. O. R. Y. Continental-shelf-scale model of the Leeuwin Current, *J. Mar. Res.*, **45**, 813-827, 1987.

Trenberth, K. E., W. G. Large, J. G. Olsen. The mean annual cycle in global ocean wind stress, *J. Phys. Oceanogr.* **20(11)**, 1742-1760, 1990.

THIS PAGE INTENTIONALLY LEFT BLANK

APPENDIX. TABLES AND FIGURES

This appendix contains all tables and figures referred to throughout the text. The tables and figures are captioned according to the chapter from which they are referred. The first digit of the table number or figure number is the chapter from which that table or figure is referred.

Case	∇h	$R (km)$
Flat Bottom	N/A	50
Smoothed Topo	0.0005	155
Raw Topo	0.0007	185

Table 3.1. Summary of gradient and radius of curvature values for the cases of flat bottom, smoothed model topography, and the raw topography as the Leeuwin Current approaches Cape Leeuwin. Note that the curvature values for smoothed topography and raw topography are the curvature of the 100m isobath (along the path of the current).

Term	Beta	Vortex Stretching	Curvature	Sum	Separation	
					Theoretical	Model/ Observed Result
Analytical Terms in (5)	$\iint_{ABCD} \beta^* v dA$	$- \iint_{ABCD} \frac{f}{h} \vec{u} \bullet \nabla h dA$	$\left[\int \frac{v^2}{R} dn \right]_{BA}^{CP}$			
Scaled Terms in (7)	$\beta^* U \delta s$	$- fU \frac{\nabla h}{h} \delta s$	$- \frac{U^2 \delta}{R}$			
Flat Bottom	-0.005	N/A	-0.02	-0.025	Yes	Yes
Smoothed Topo	-0.016	-0.16	-0.006	-0.182	Yes	Yes
Raw Topo	-0.019	-0.259	-0.005	-0.283	Yes	Yes

Table 3.2. Summary of separation calculations for the cases in Table 3.1.

Flat Bottom, Day 20				
Point	Latitude	Longitude	Speed (m/s)	% Change in Speed per km
1	33.27°S	115.15°E	0.33	N/A
2	33.60°S	115.02°E	0.61	-0.93
3	33.94°S	114.88°E	0.76	0.65
4	34.27°S	114.88°E	0.66	-0.34
5	34.52°S	115.15°E	0.15	-2.85
Flat Bottom, Day 40				
1	33.27°S	115.15°E	0.01	N/A
2	33.60°S	115.02°E	0.07	43.65
3	33.94°S	114.88°E	0.25	6.26
4	34.27°S	114.88°E	0.67	4.65
5	34.52°S	115.15°E	0.13	-2.95
Flat Bottom, Day 60				
Point	Latitude	Longitude	Speed (m/s)	% Change in Speed per km
1	33.27°S	115.15°E	0.32	N/A
2	33.60°S	115.02°E	0.60	2.31
3	33.94°S	114.88°E	0.31	-1.30
4	34.27°S	114.88°E	0.01	-2.66
5	34.52°S	115.15°E	0.10	44.57

Table 3.3a. Summary of points used for Lagrangian analysis with corresponding speeds and percent change in speed in the downstream direction for flat bottom at days 20, 40, and 60.

Smoothed Topography, Day 20				
Point	Latitude	Longitude	Speed (m/s)	% Change in Speed per km
1	33.27°S	114.75°E	0.31	N/A
2	33.60°S	114.62°E	0.38	0.64
3	33.94°S	114.62°E	0.46	0.57
4	34.27°S	114.75°E	0.37	-0.54
5	34.60°S	114.95°E	0.25	-0.84
Smoothed Topography, Day 40				
Point	Latitude	Longitude	Speed (m/s)	% Change in Speed per km
1	33.27°S	114.75°E	0.23	N/A
2	33.60°S	114.62°E	0.13	-1.16
3	33.94°S	114.62°E	0.29	3.20
4	34.27°S	114.75°E	0.41	1.14
5	34.60°S	114.95°E	0.08	-2.19
Smoothed Topography, Day 60				
Point	Latitude	Longitude	Speed (m/s)	% Change in Speed per km
1	33.27°S	114.75°E	0.47	N/A
2	33.60°S	114.62°E	0.19	-1.59
3	33.94°S	114.62°E	0.22	0.30
4	34.27°S	114.75°E	0.69	5.95
5	34.60°S	114.95°E	0.81	0.48

Table 3.3b. Summary of points used for Lagrangian analysis with corresponding speeds and percent change in speed in the downstream direction for smoothed topography at days 20, 40, and 60.

Experiment	Climatology	Wind	Bottom
1	Horizontally averaged annual	Annual	Flat bottom
2	Horizontally averaged annual	Annual	Smoothed topo
3	Full annual	None	Flat bottom
4	Full annual	None	Smoothed topo
5	Full annual	Annual	Flat bottom
6	Full annual	Annual	Smoothed topo
7	Full summertime	Summertime	Smoothed topo
8	Full wintertime	Wintertime	Smoothed topo

Table 4.1. Summary of experimental design for process-oriented experiments showing climatology (temperature and salinity forcing), wind forcing, and bottom type for each experiment.

Current System Feature	Forcing Responsible
Current direction	Thermohaline
Current location along shelf break	Topo
Current width	Thermohaline/wind (and topo prevents broadening)
Current strength	Thermohaline/wind/topo
Opposing inshore current	Wind (west coast) Seasonality (south coast)
Meanders/eddies	Thermohaline (enhanced by wind)
Gyre/upwelling in GAB	Seasonality of wind

Table 4.2. Summary of current system features and the type forcing which appears to be responsible for each feature.

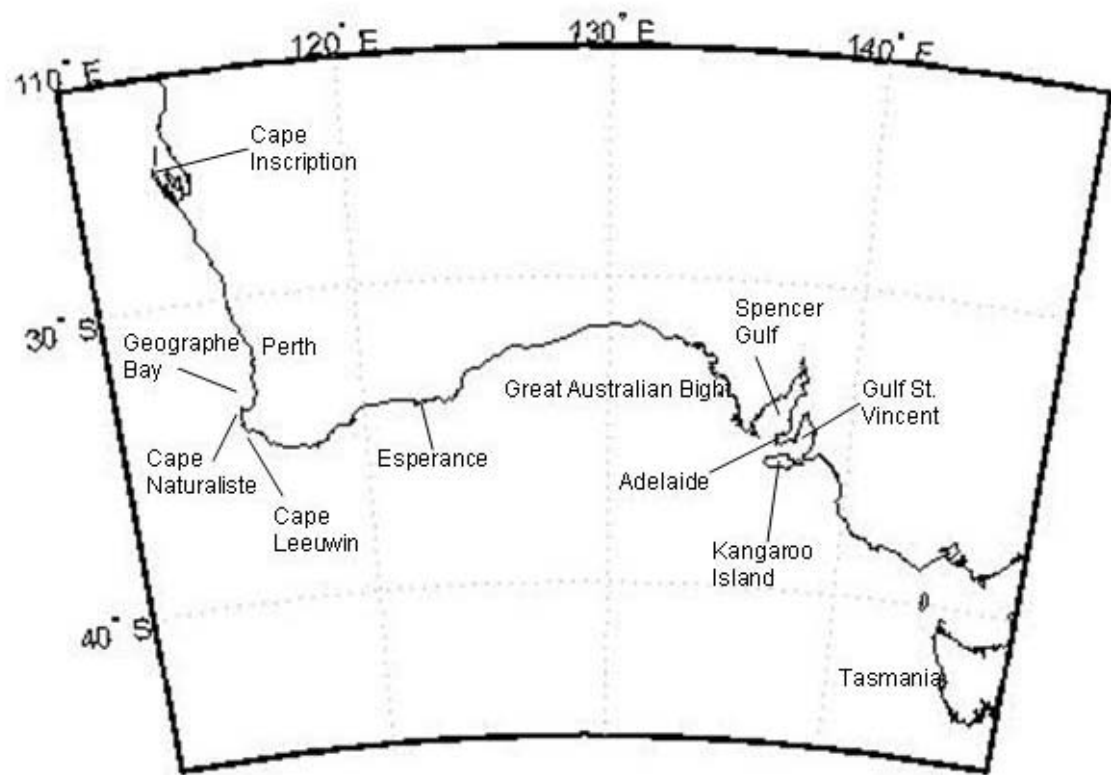


Figure 1.1. Geographical names for locations in the study area.

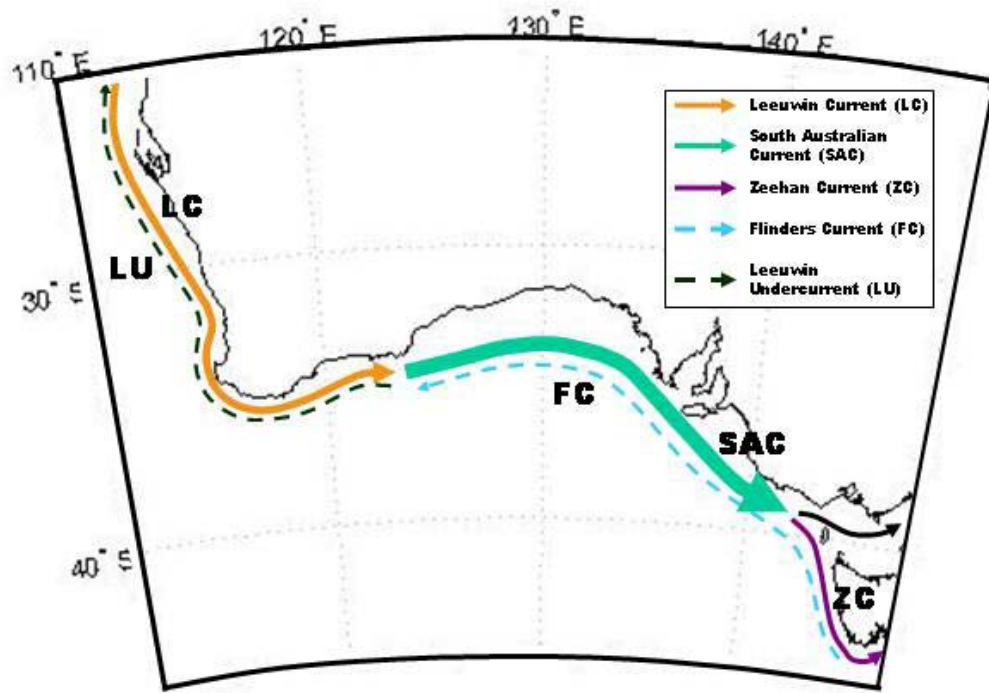


Figure 1.2. System of naming the currents and undercurrents off the western and southern coasts of Australia presented by Ridgway and Condie (2004).

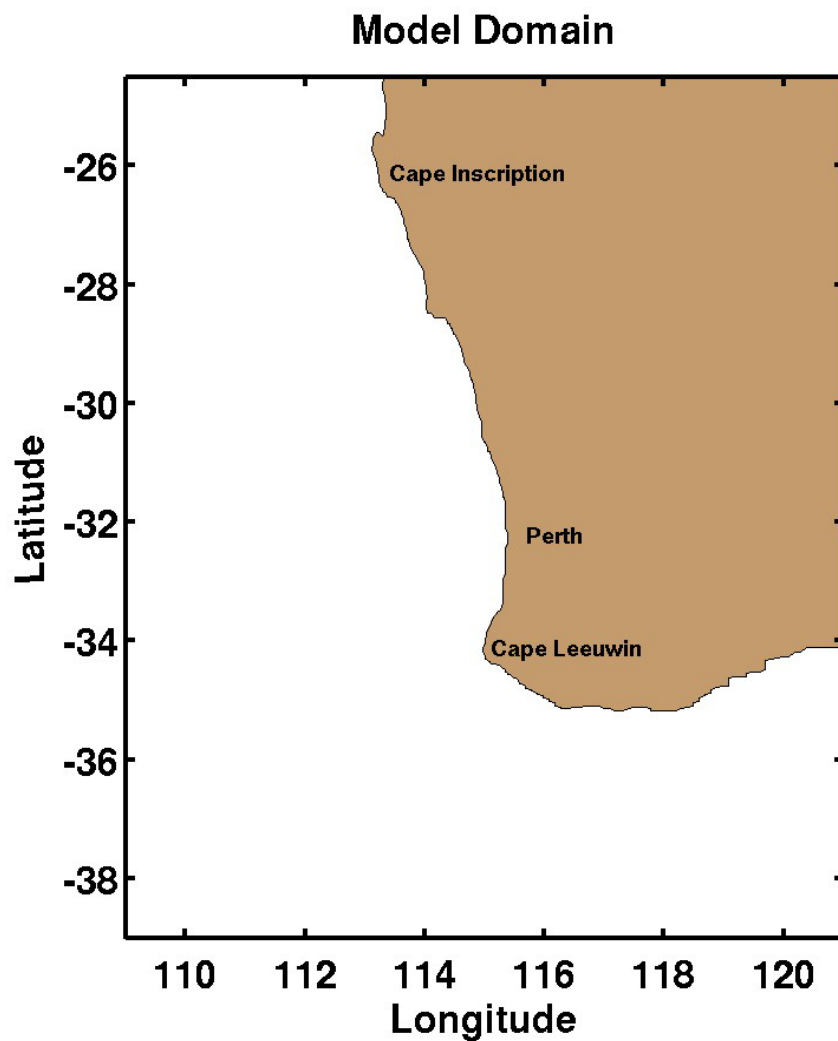


Figure 2.1a. The model domain used for Chapter III experiments extends from 24.5°S to 39°S and from 109°E to 121°E.

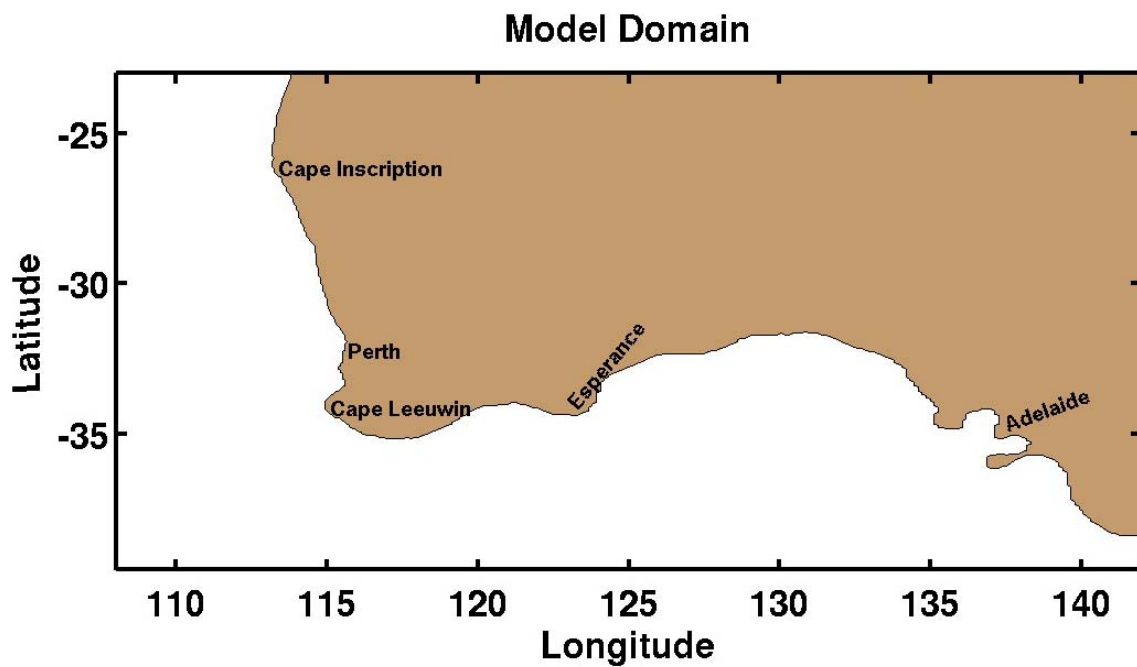


Figure 2.1b. The model domain used for Chapter IV through VI experiments extends from 22.5°S to 40°S and from 107.5°E to 142.5°E.

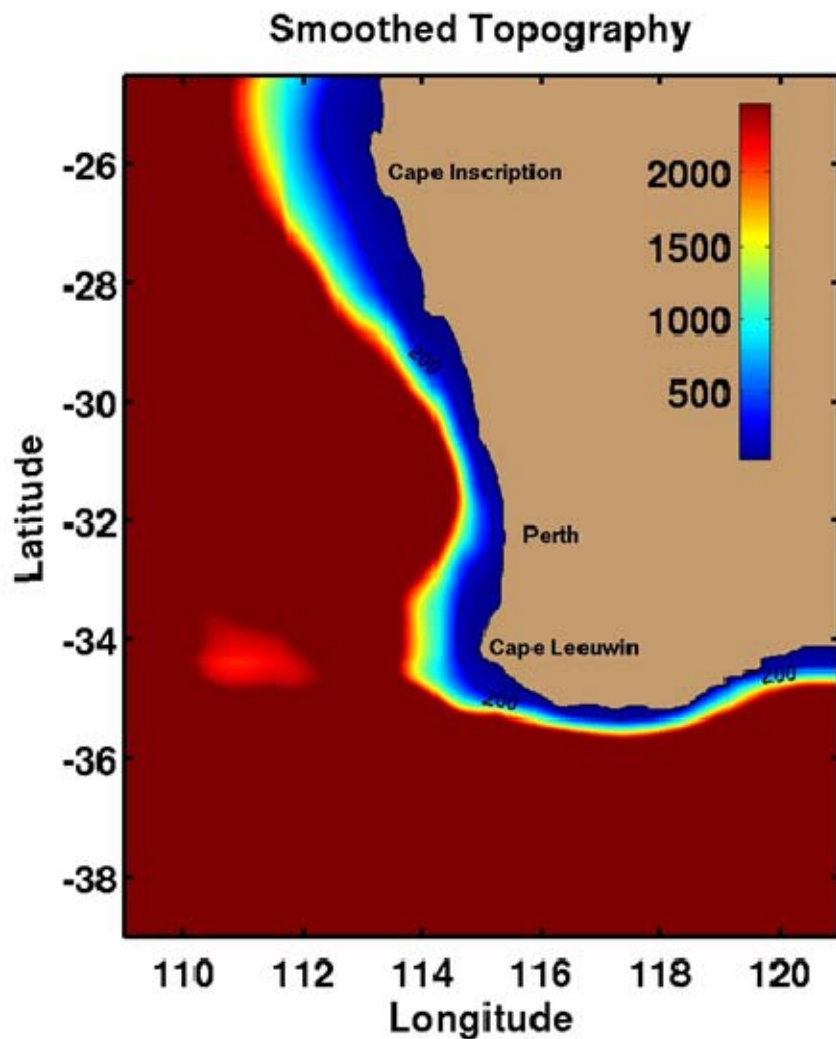


Figure 2.2a. The topography for Chapter III experiments was first smoothed with a Gaussian filter using a weighted average of 25 by 25 points and a standard deviation of eight, then all depths greater than 2500 m were reassigned a depth of 2500m.

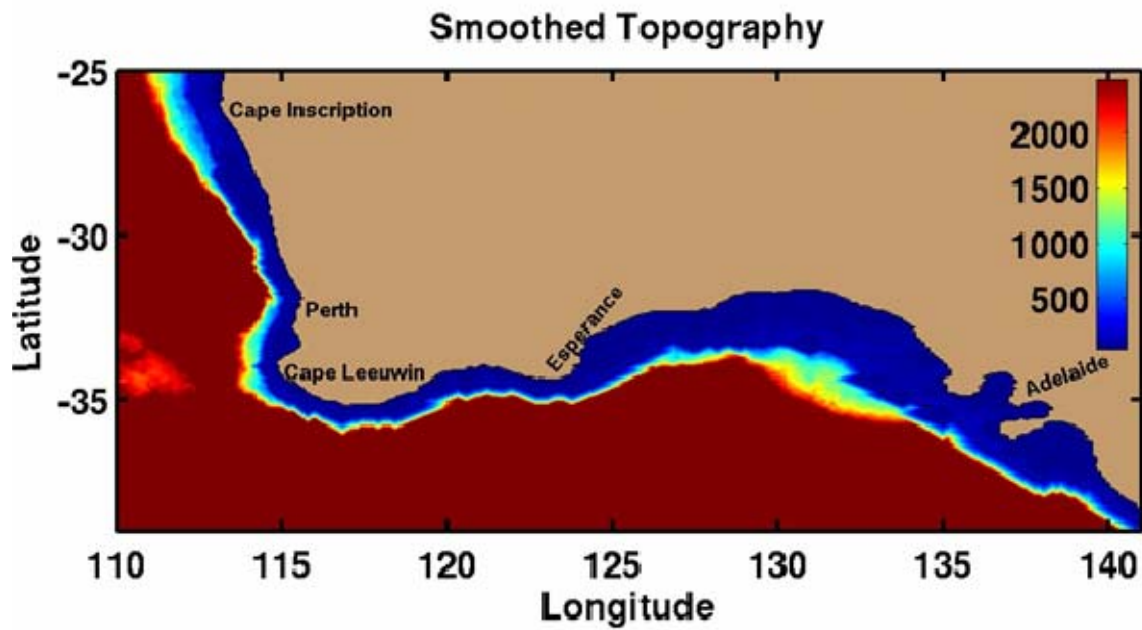


Figure 2.2b. The topography for experiments in Chapters IV through VI was first smoothed with a one-dimensional direct-iterative smoothing method, then all depths greater than 2500 m were reassigned a depth of 2500m.

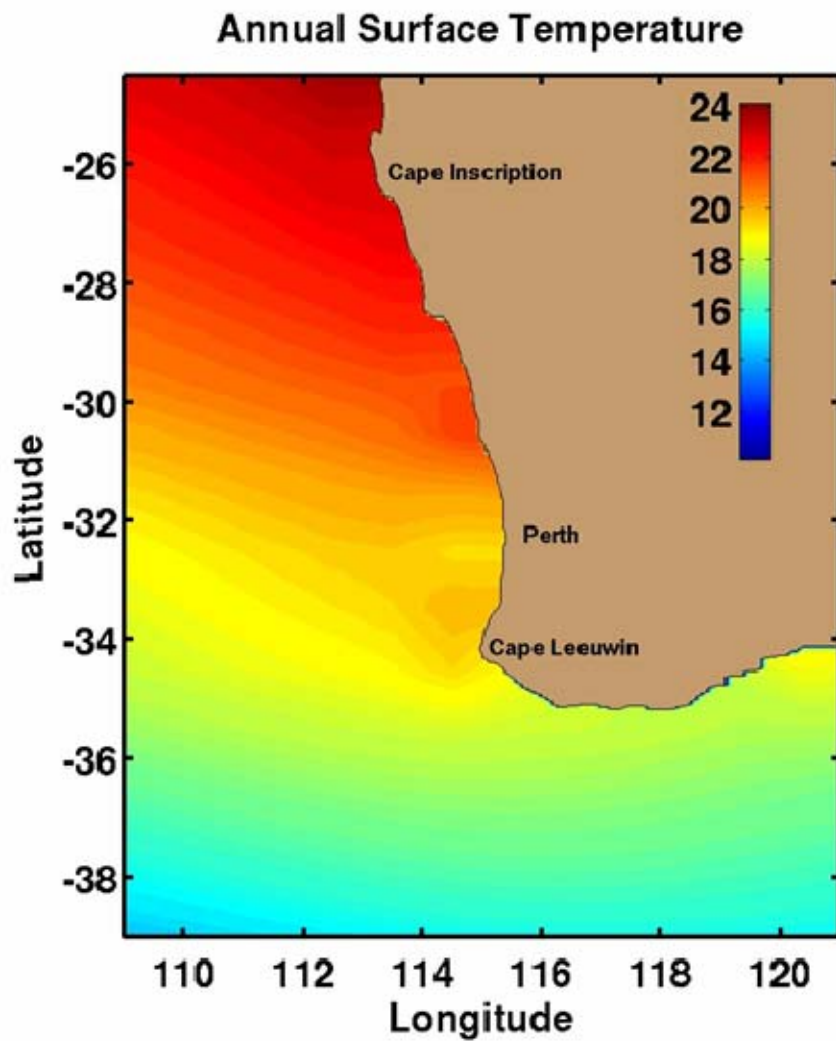


Figure 2.3a. Annual climatological surface temperature ($^{\circ}\text{C}$) obtained from Levitus and Boyer (1994) used in Chapter III experiments.

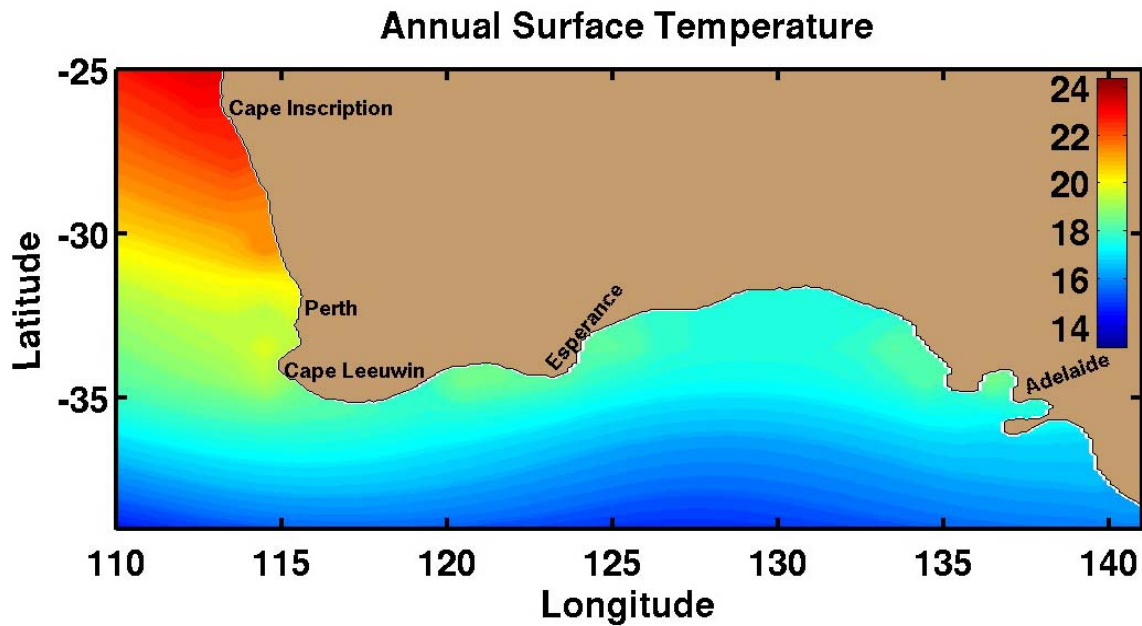


Figure 2.3b. Annual climatological surface temperature (°C) obtained from Levitus and Boyer (1994) used in Chapter IV annual forcing experiments.

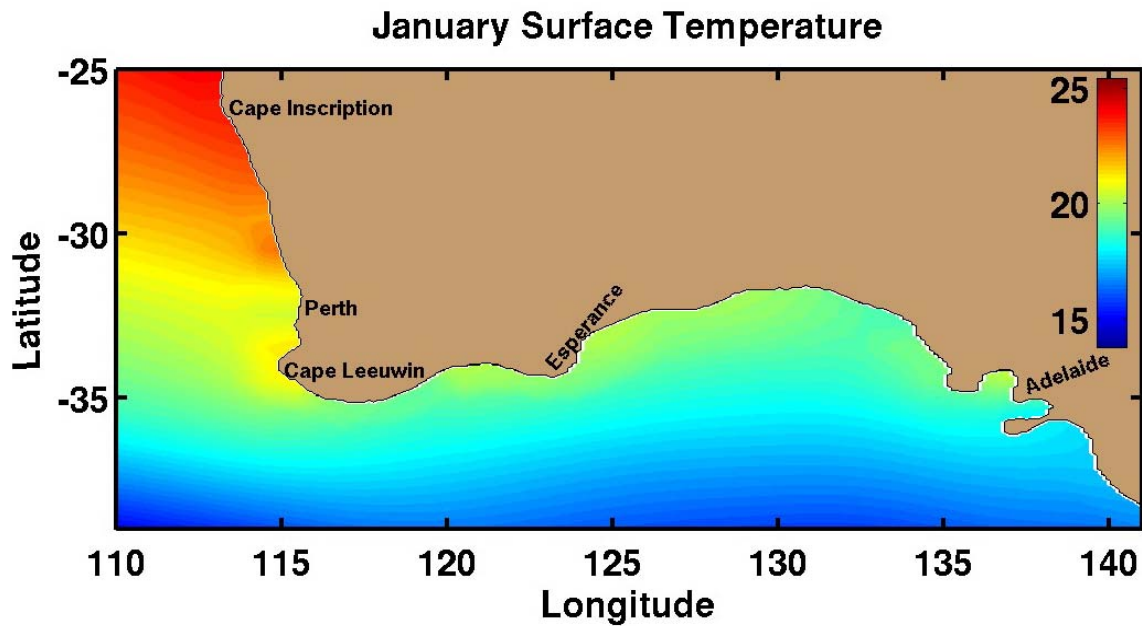


Figure 2.3c. January climatological surface temperature ($^{\circ}\text{C}$) obtained from Levitus and Boyer (1994) used in Experiment 7 of Chapter IV.

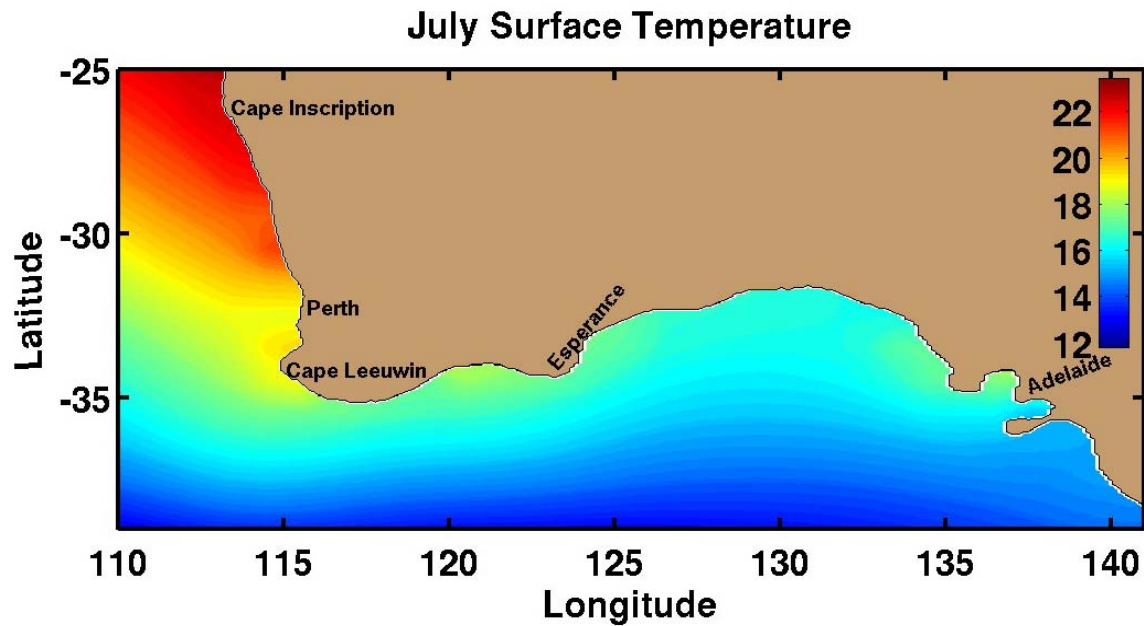


Figure 2.3d. July climatological surface temperature ($^{\circ}\text{C}$) obtained from Levitus and Boyer (1994) used in Experiment 8 of Chapter IV.

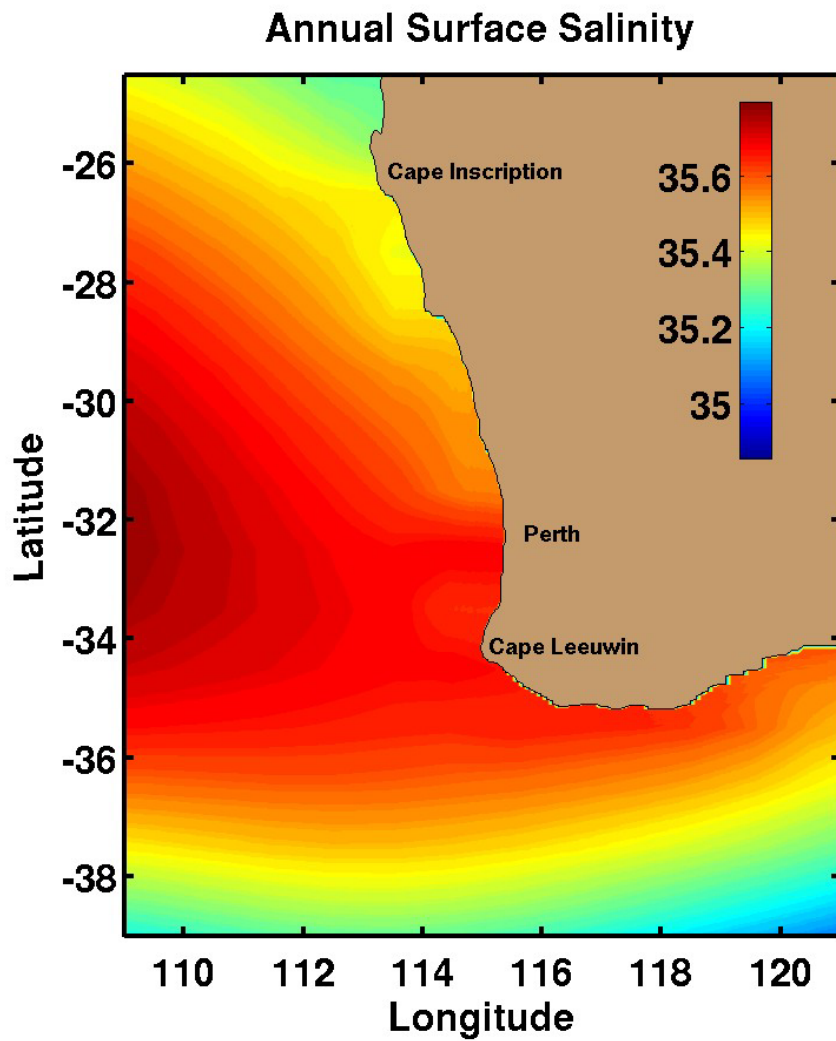


Figure 2.4a. Annual climatological surface salinity obtained from Levitus and Boyer (1994) used in Chapter III experiments.

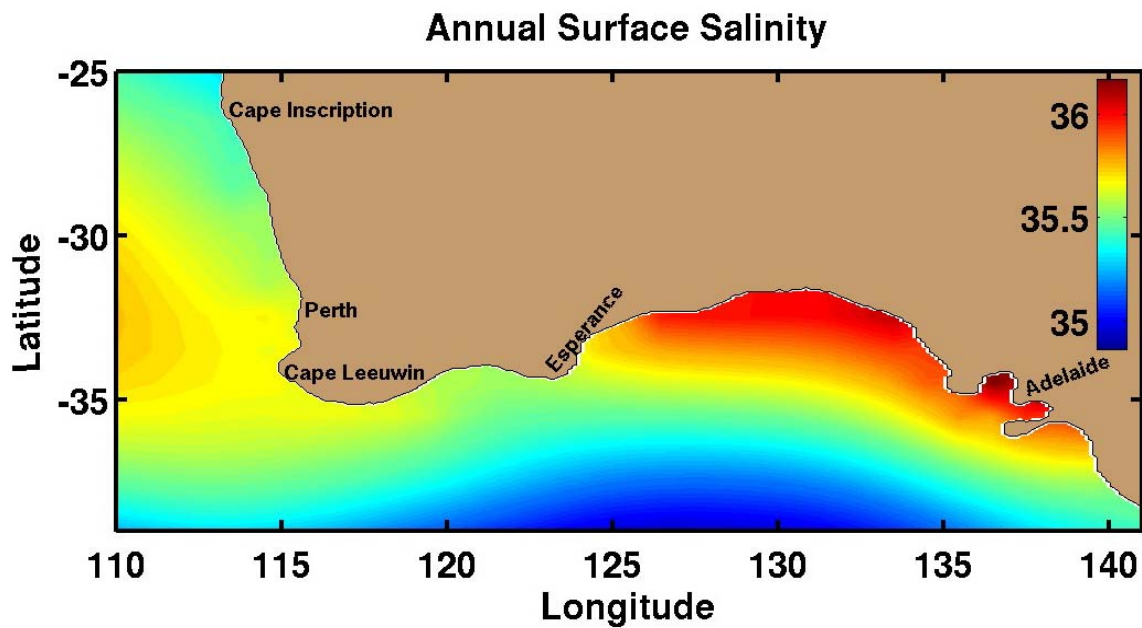


Figure 2.4b. Annual climatological surface salinity obtained from Levitus and Boyer (1994) used in Chapter IV annual forcing experiments.

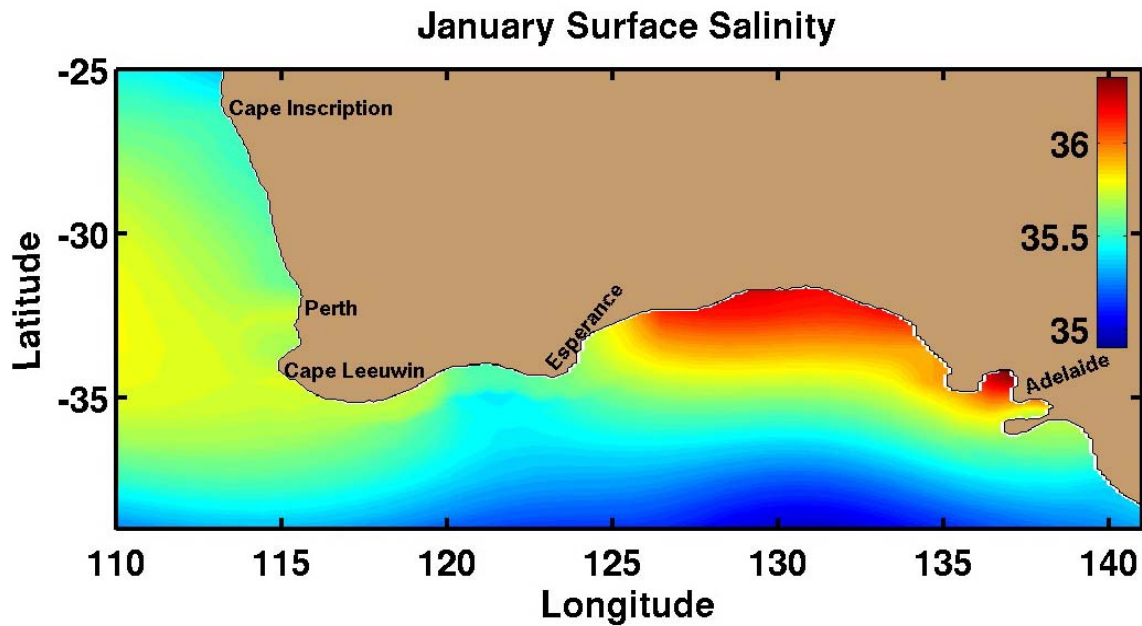


Figure 2.4c. January climatological surface salinity obtained from Levitus and Boyer (1994) used in Experiment 7 of Chapter IV.

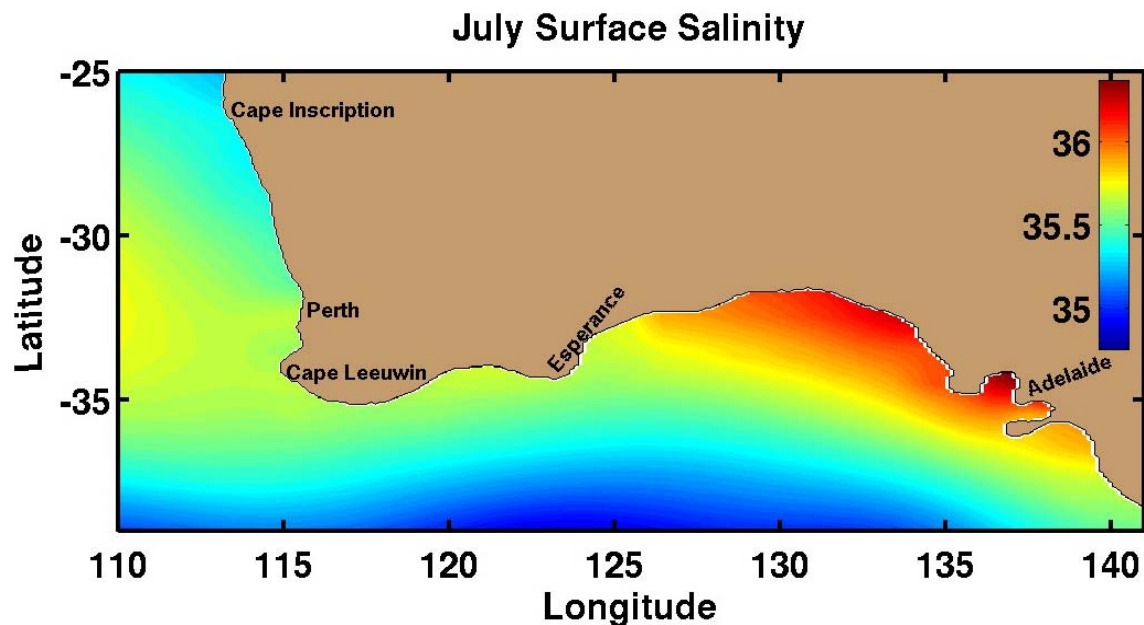


Figure 2.4d. July climatological surface salinity obtained from Levitus and Boyer (1994) used in Experiment 8 of Chapter IV.

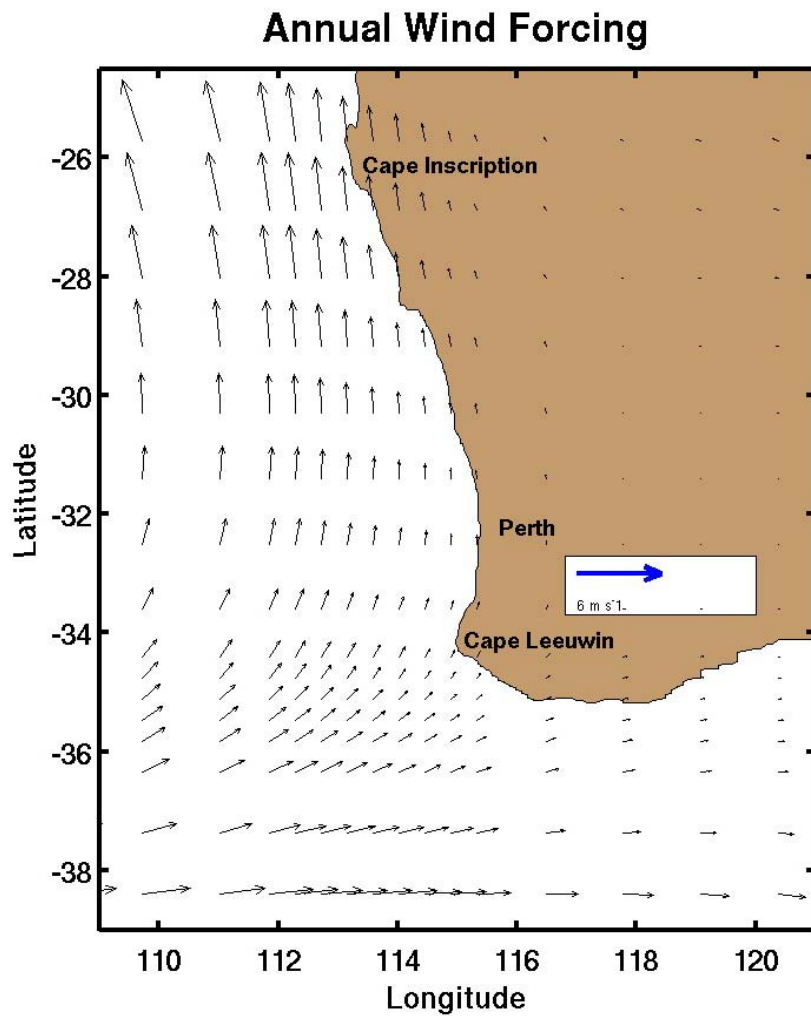


Figure 2.5a. Annual average wind in m/s from climatological ECMWF winds obtained from Trenberth et al., 1990 used in Chapter III experiments.

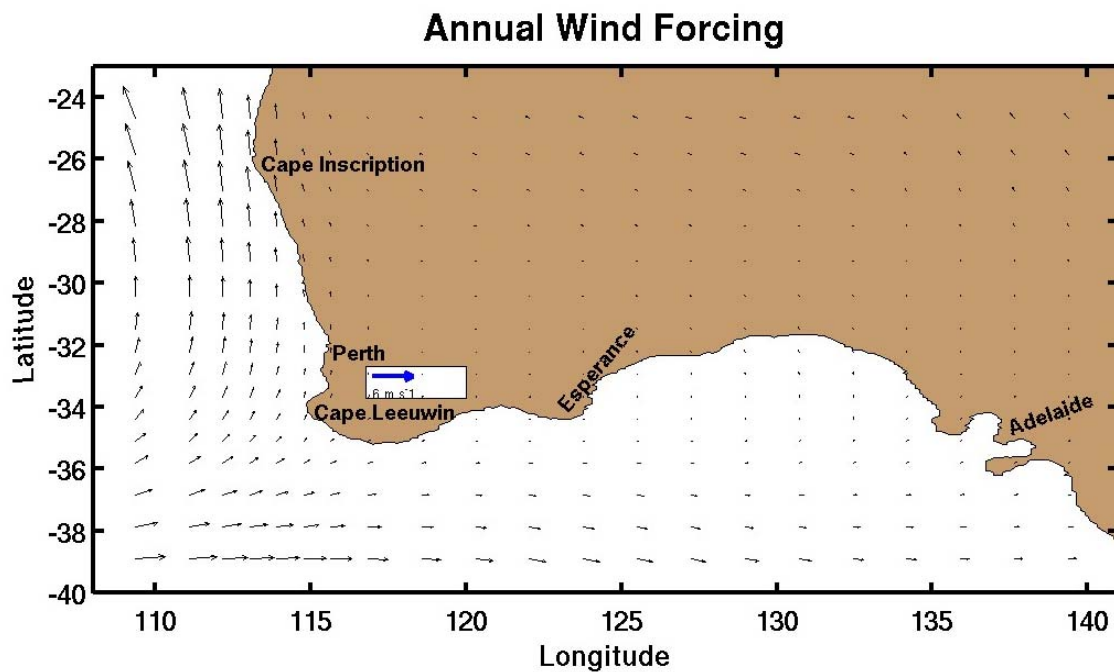


Figure 2.5b. Annual average wind in m/s from climatological ECMWF winds obtained from Trenberth et al., 1990 used in Experiments 1, 2, 5, and 6 of Chapter IV.

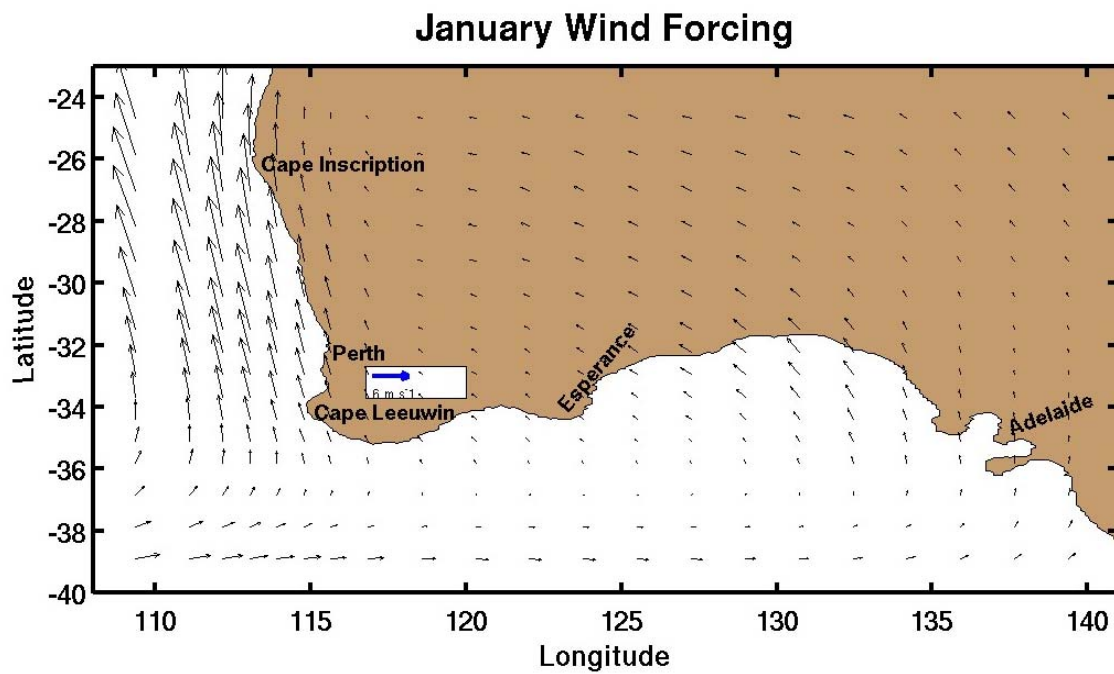


Figure 2.5c. January average wind in m/s from climatological ECMWF winds obtained from Trenberth et al., 1990 used in Experiment 7 of Chapter IV.

July Wind Forcing

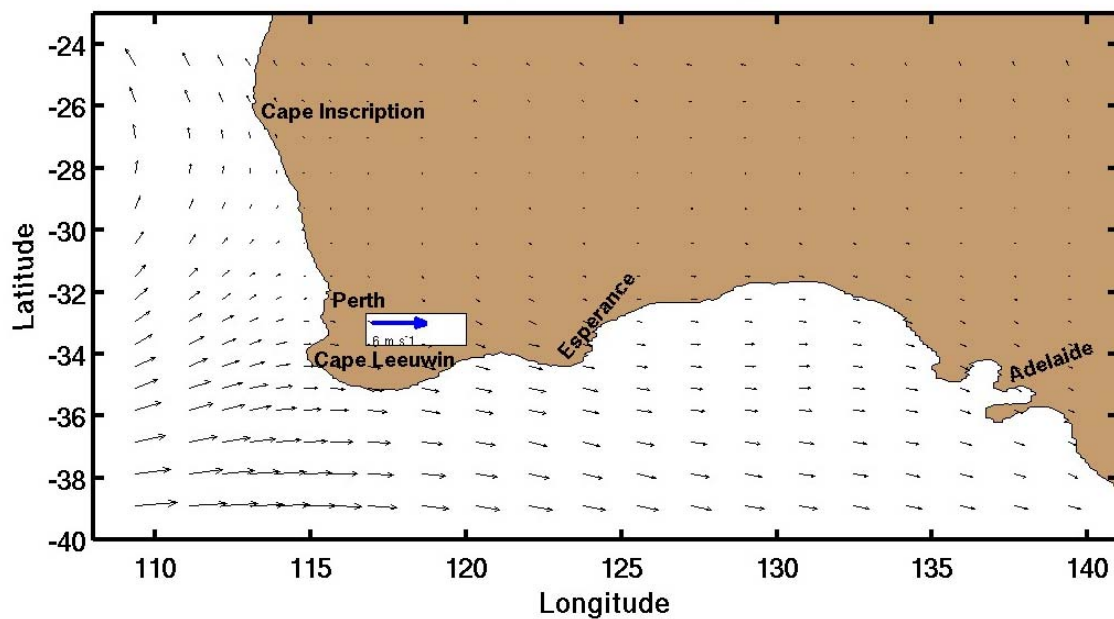


Figure 2.5d. July average wind in m/s from climatological ECMWF winds obtained from Trenberth et al., 1990 used in Experiment 8 of Chapter IV.

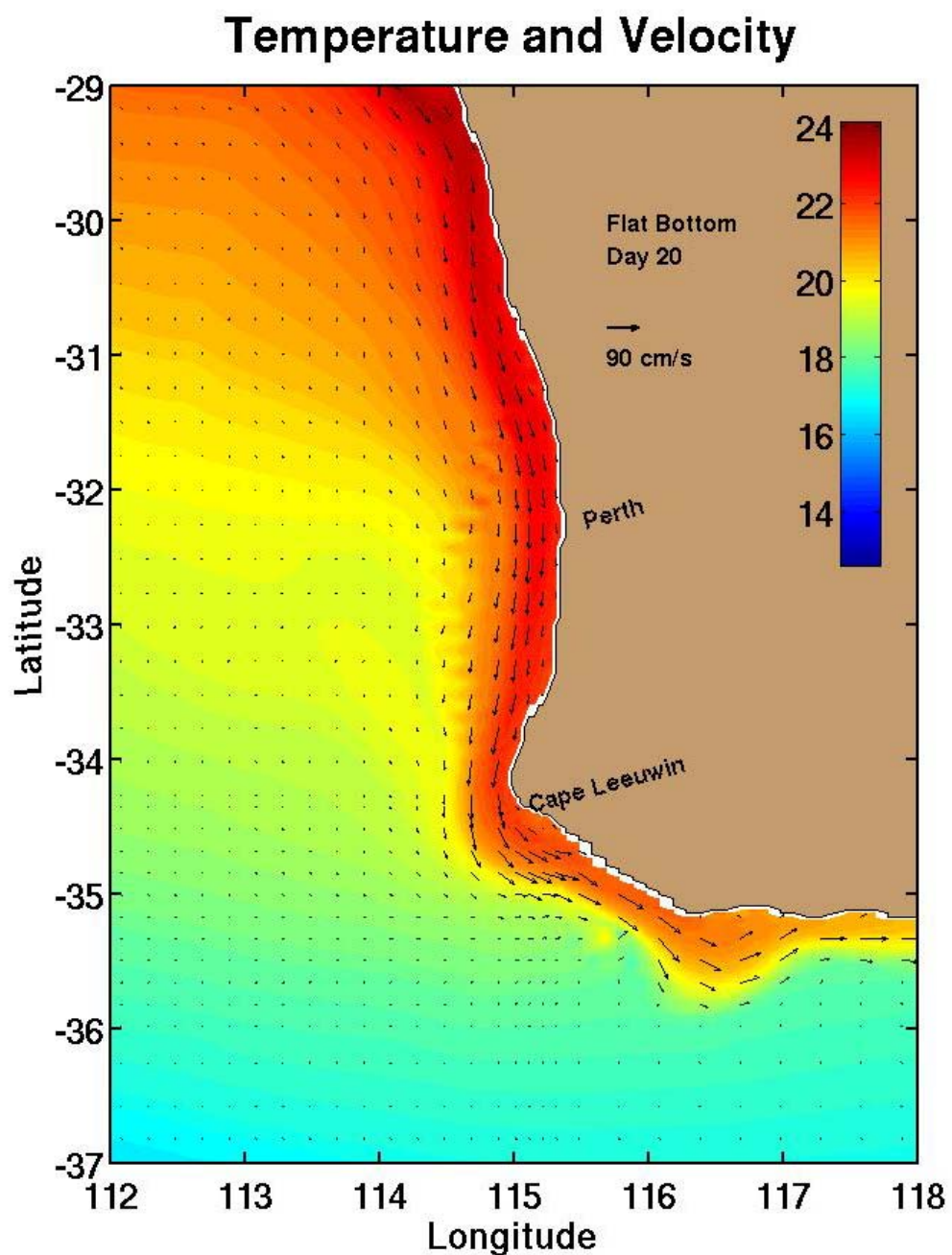


Figure 3.1a. Surface velocity vectors and color-shaded sea surface temperature for day 20 for the flat-bottom model run.

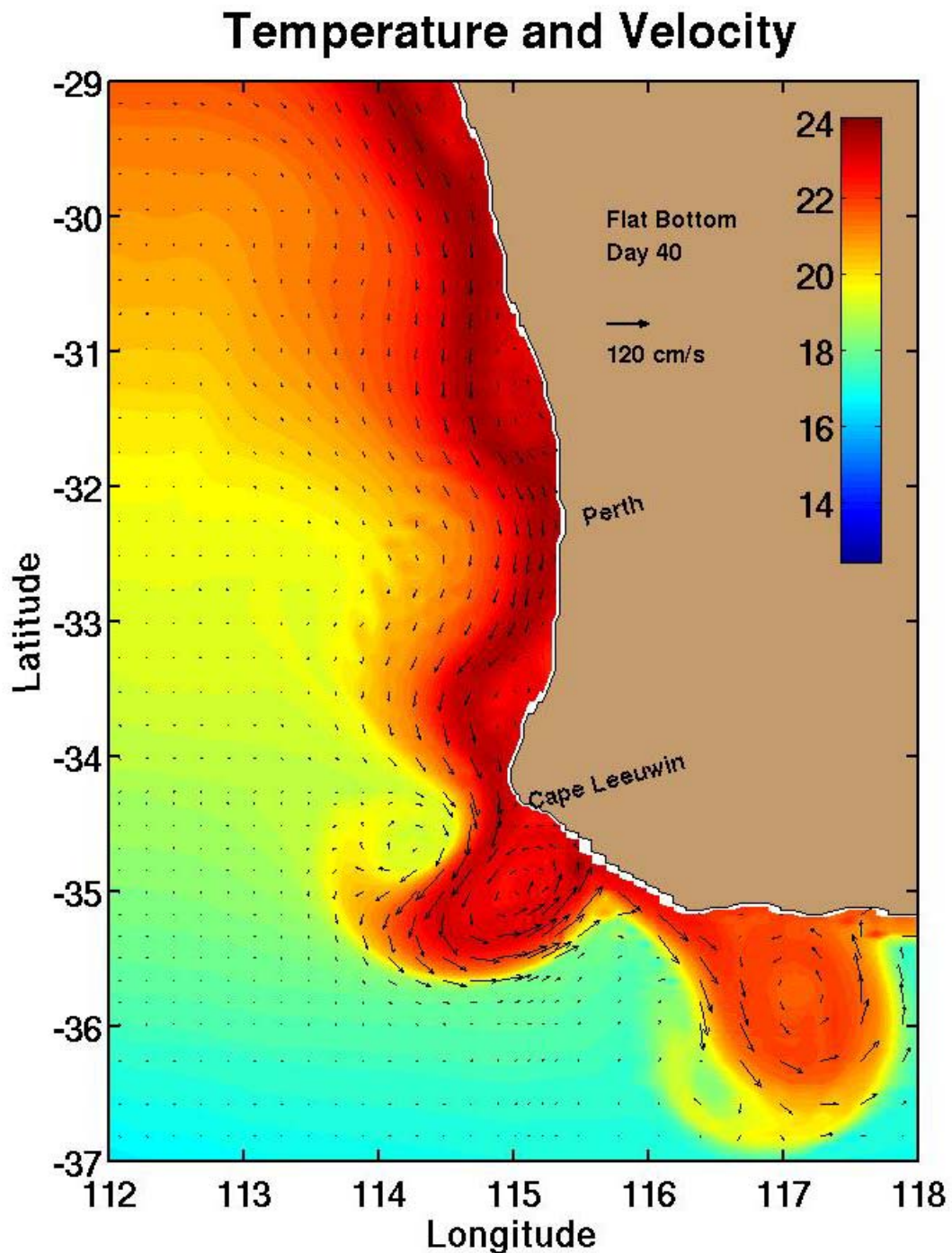


Figure 3.1b. Surface velocity vectors and color-shaded sea surface temperature for day 40 for the flat-bottom model run.

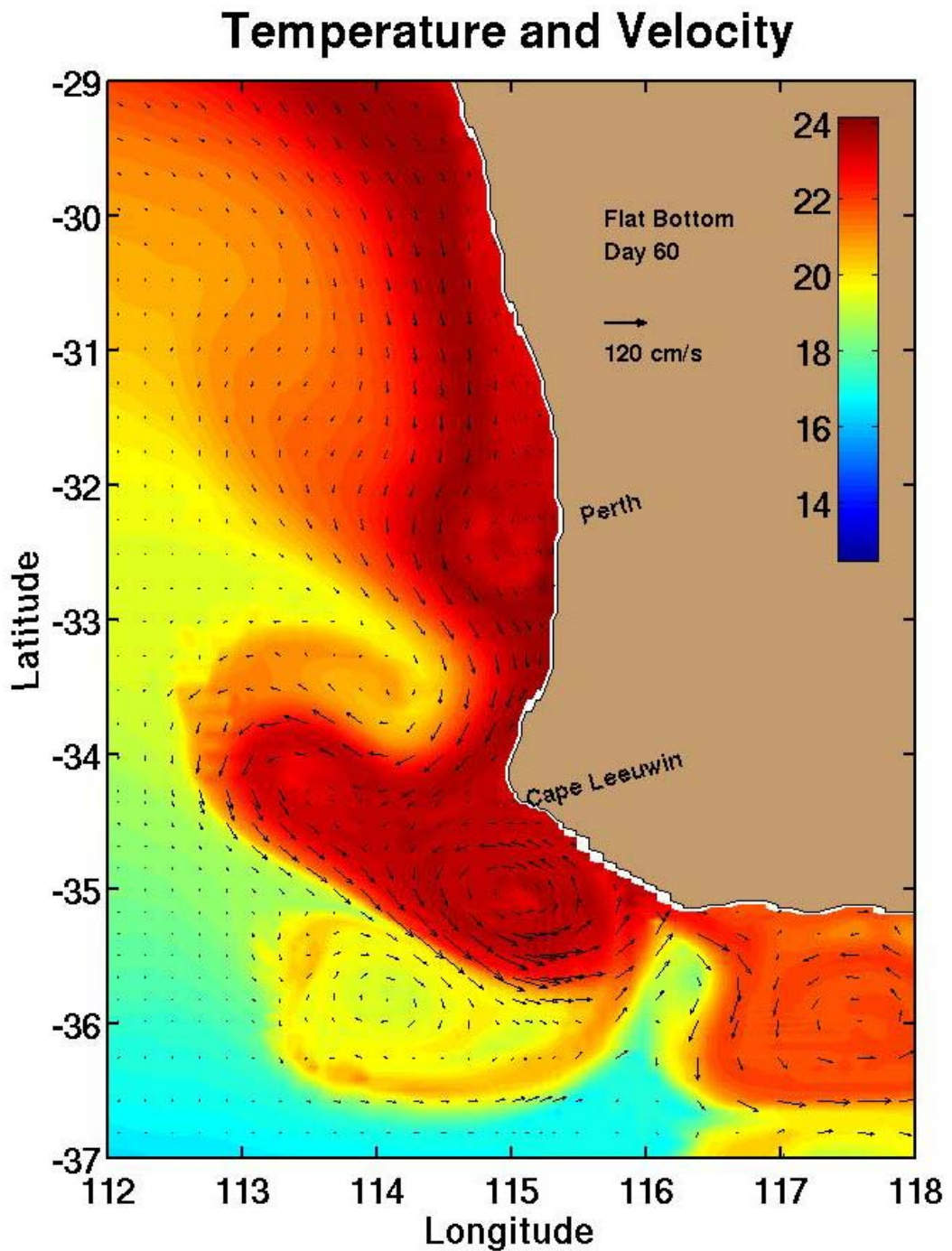


Figure 3.1c. Surface velocity vectors and color-shaded sea surface temperature for day 60 for the flat-bottom model run.

Temperature and Velocity

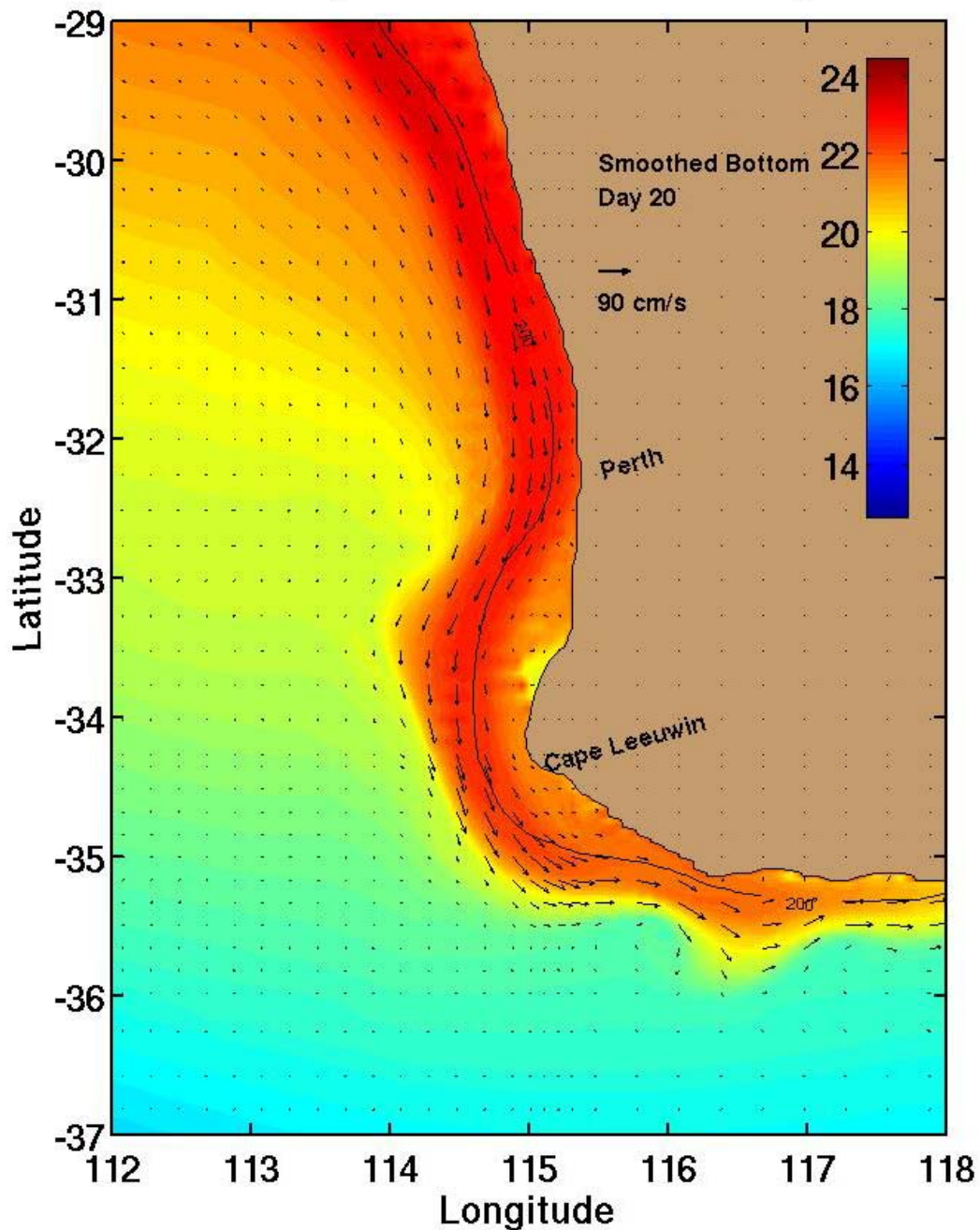


Figure 3.2a. Surface velocity vectors and color-shaded sea surface temperature for day 20 for the model run with topography. The solid line depicts the 200 m isobath, the approximate location of the shelf break.

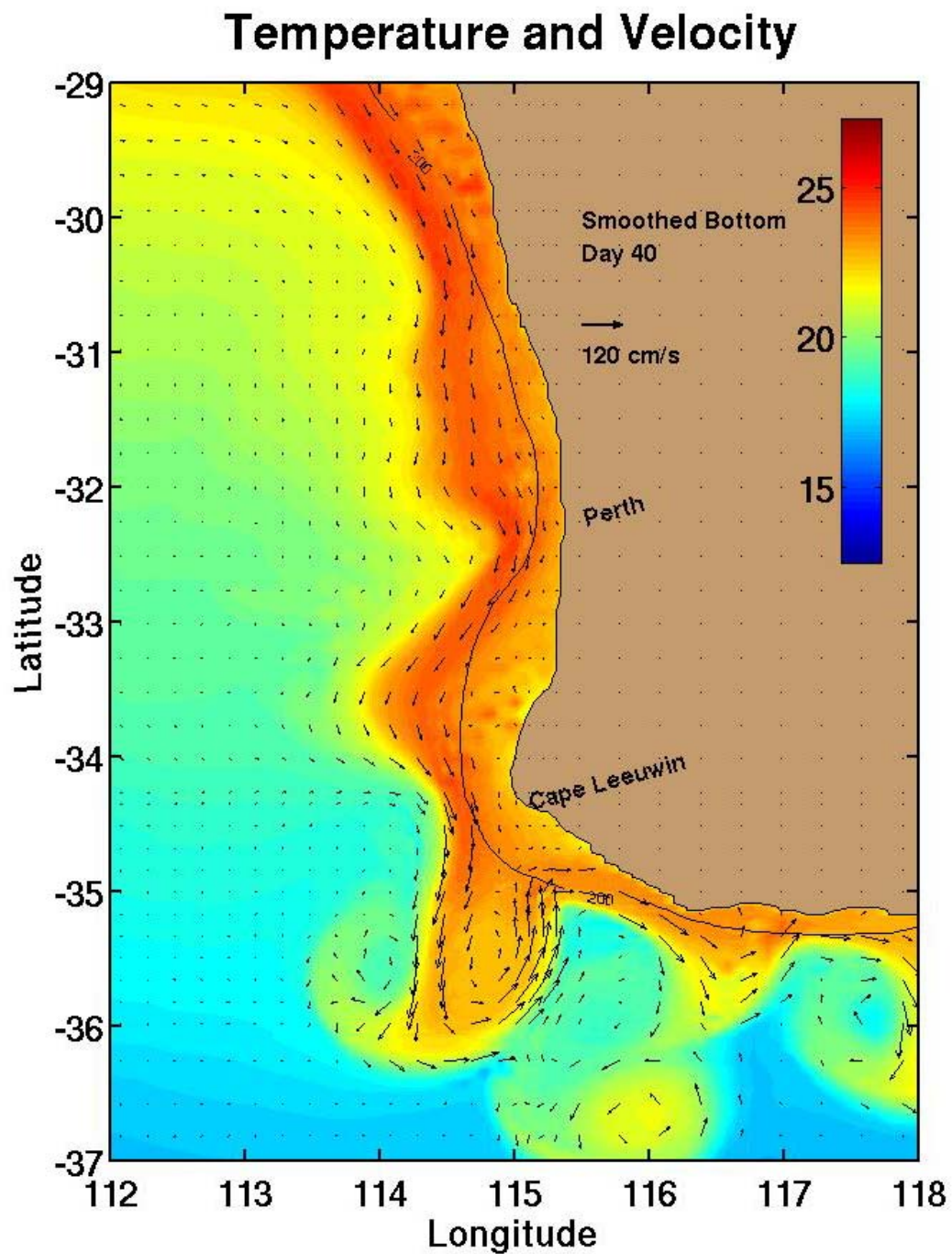


Figure 3.2b. Surface velocity vectors and color-shaded sea surface temperature for day 40 for the model run with topography). The solid line depicts the 200 m isobath, the approximate location of the shelf break.

Temperature and Velocity

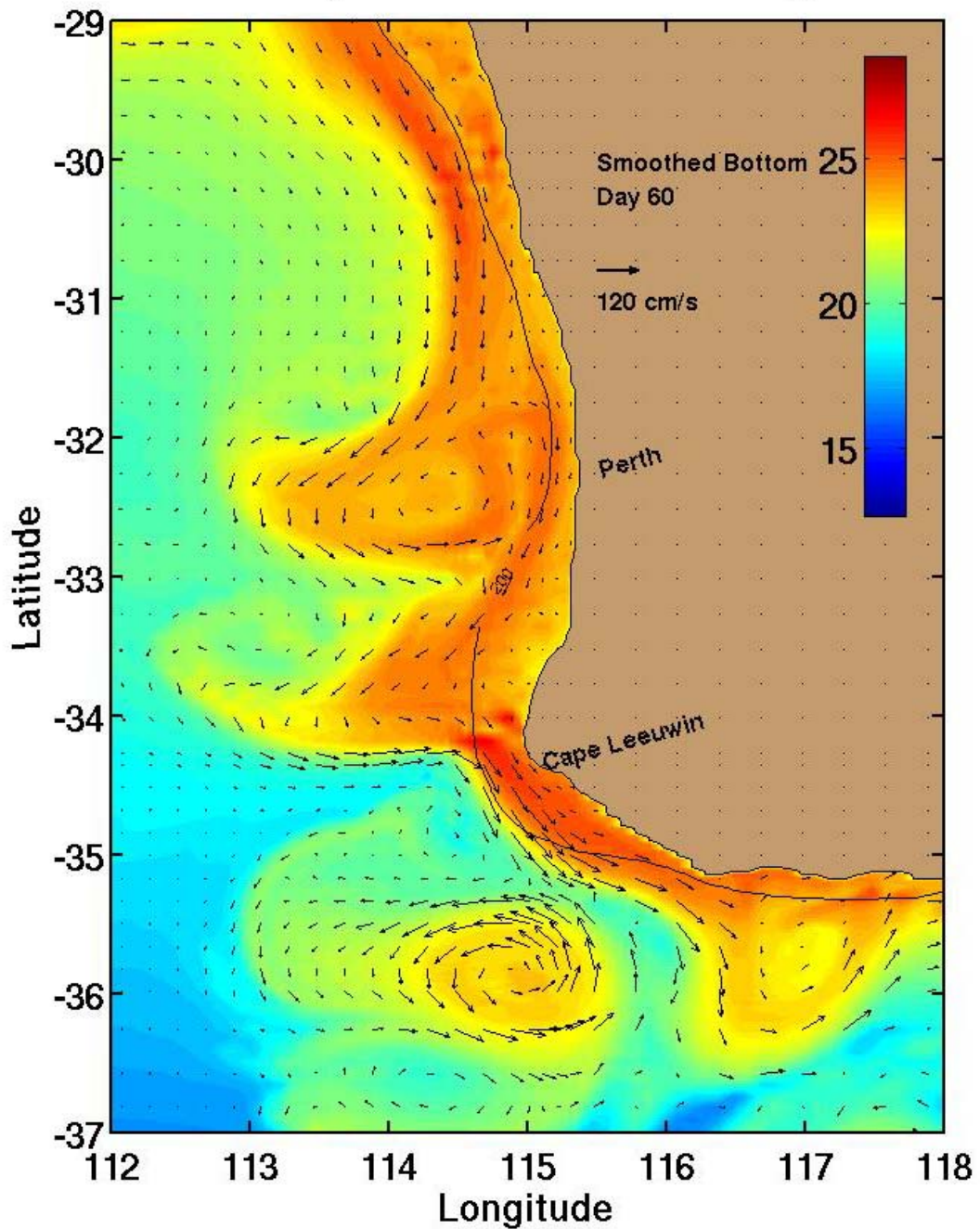


Figure 3.2c. Surface velocity vectors and color-shaded sea surface temperature for day 60 for the model run with topography. The solid line depicts the 200 m isobath, the approximate location of the shelf break.

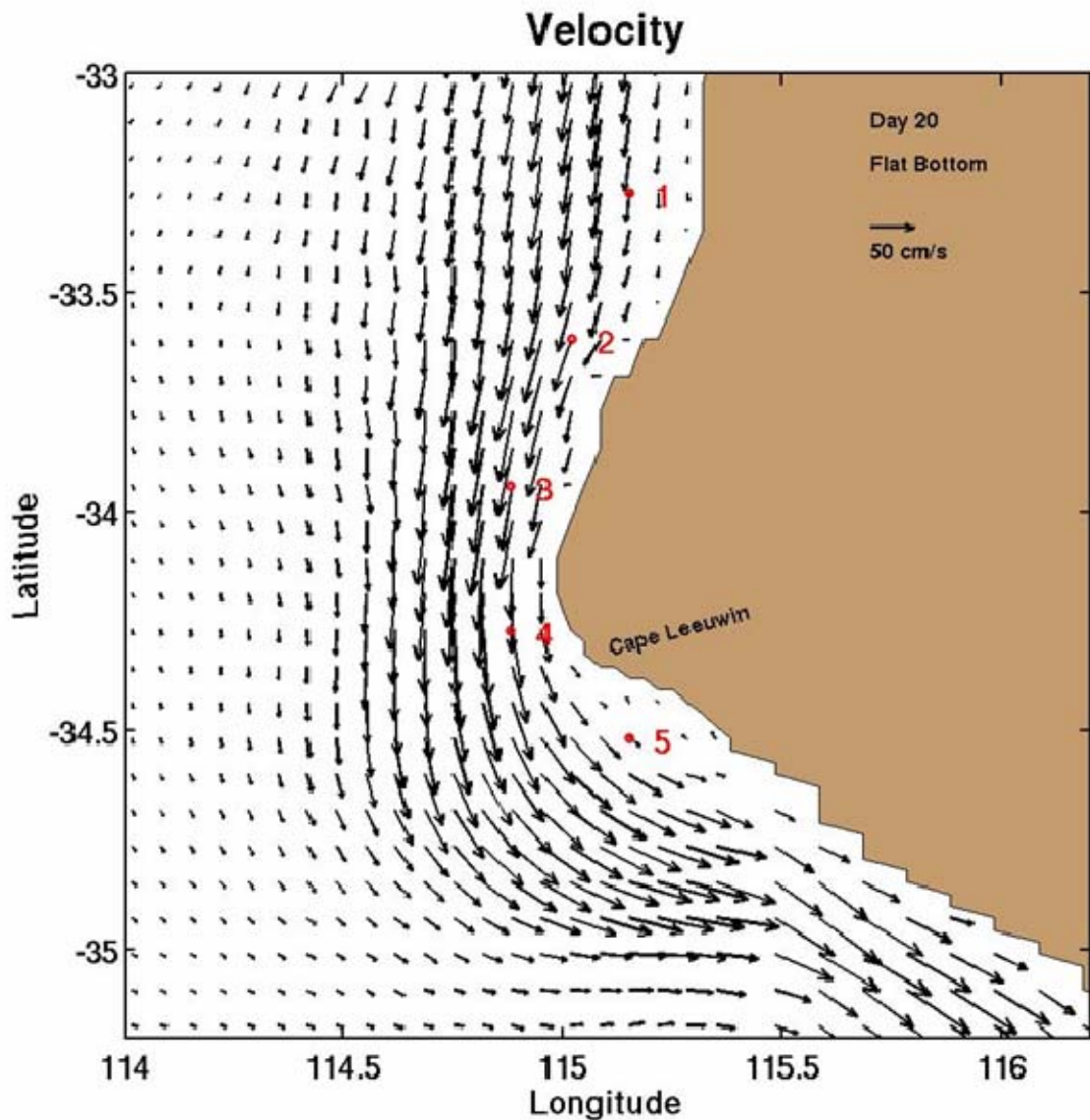


Figure 3.3a. Surface velocity vectors depicting the Leeuwin Current approaching and rounding Cape Leeuwin at day 20 for the flat bottom model run. The red circles which are numbered in red show the locations of the analysis points used in the Lagrangian dynamical analysis.

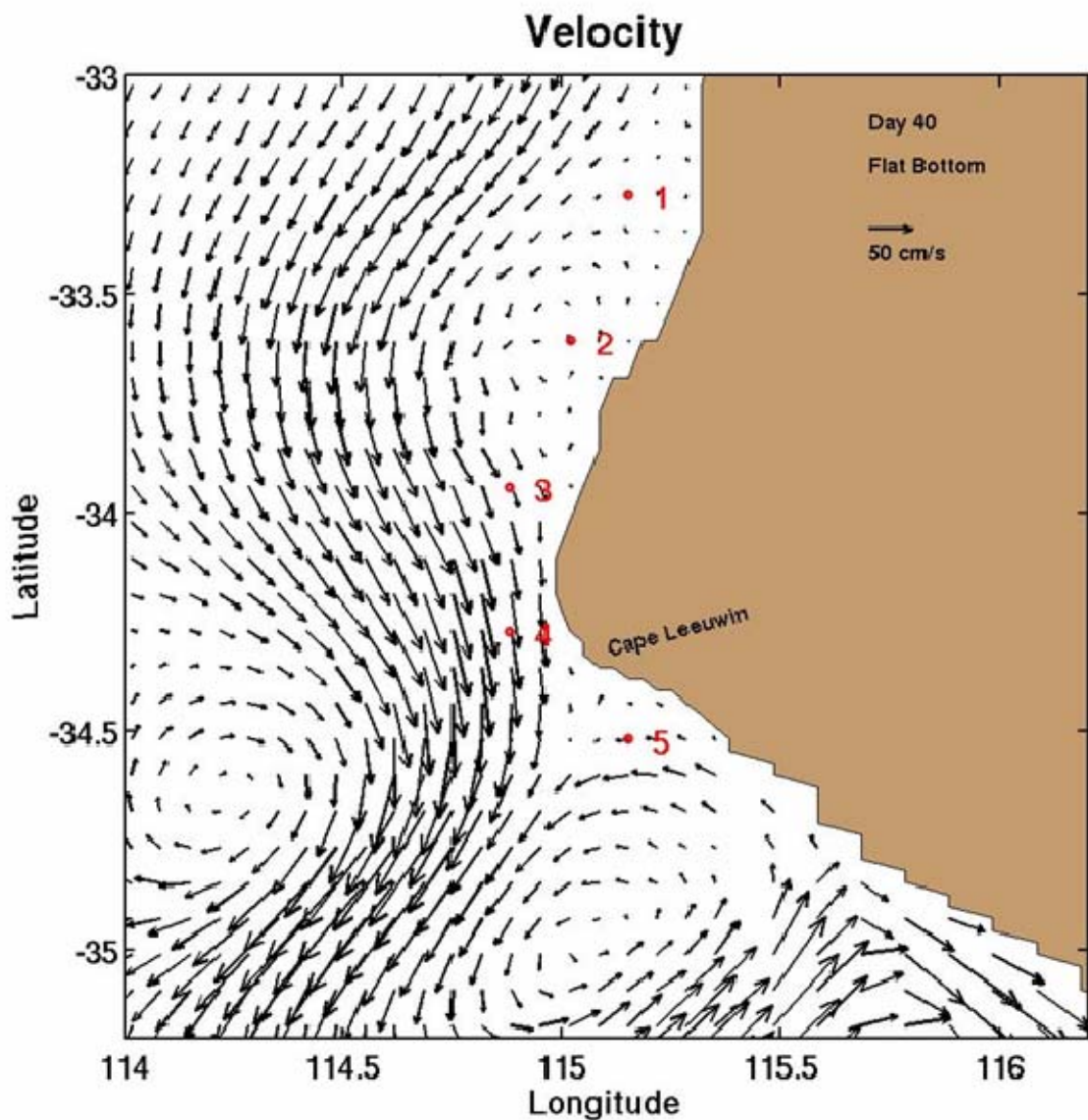


Figure 3.3b. Surface velocity vectors depicting the Leeuwin Current approaching and rounding Cape Leeuwin at day 40 for the flat bottom model run. The red circles which are numbered in red show the locations of the analysis points used in the Lagrangian dynamical analysis.

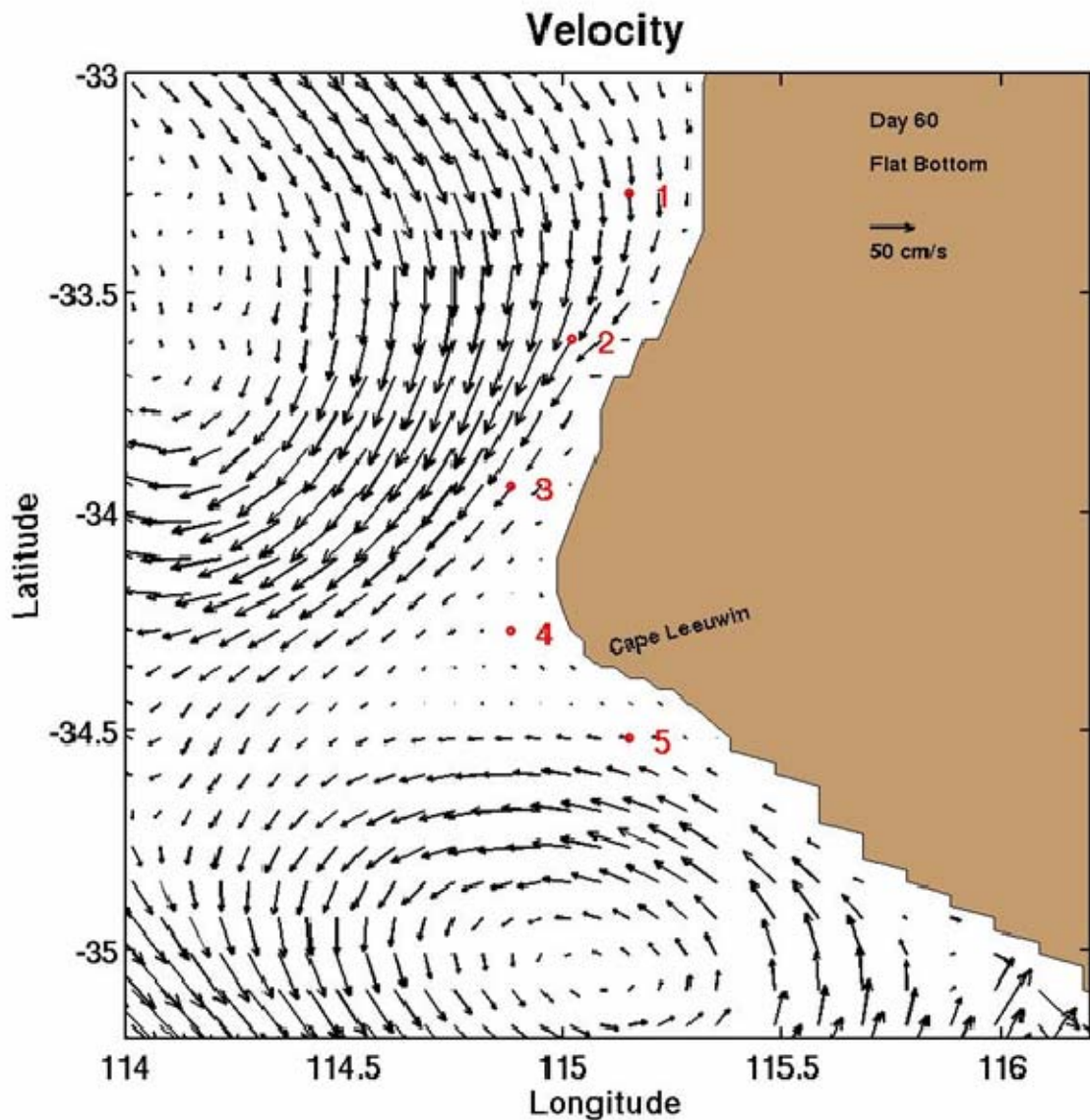


Figure 3.3c. Surface velocity vectors depicting the Leeuwin Current approaching and rounding Cape Leeuwin at day 60 for the flat bottom model run. The red circles which are numbered in red show the locations of the analysis points used in the Lagrangian dynamical analysis.

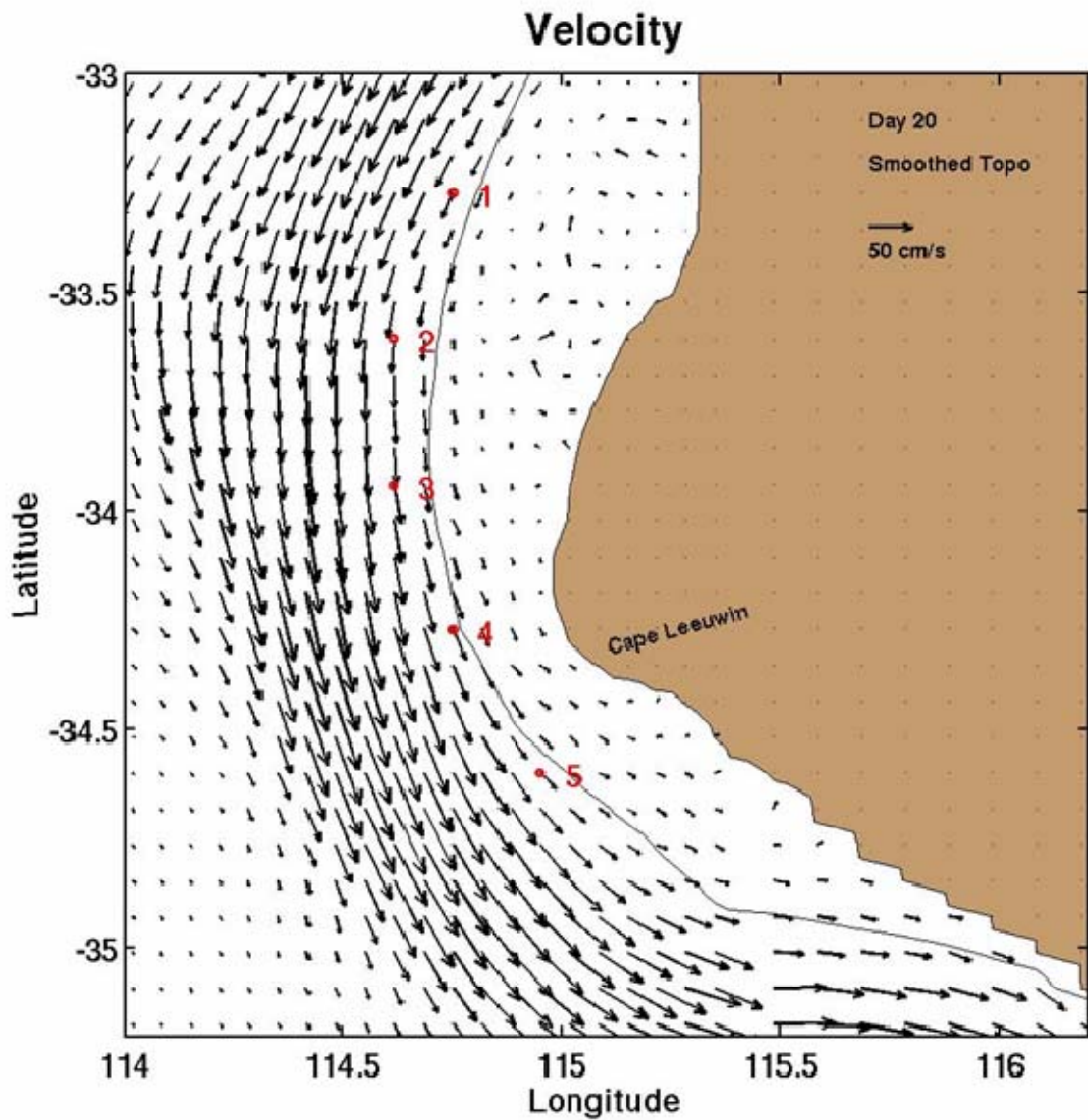


Figure 3.4a. Surface velocity vectors depicting the Leeuwin Current approaching and rounding Cape Leeuwin at day 20 for the smoothed topography model run. The red circles which are numbered in red show the locations of the analysis points used in the Lagrangian dynamical analysis. The solid line depicts the 200 m isobath, the approximate location of the shelf break.

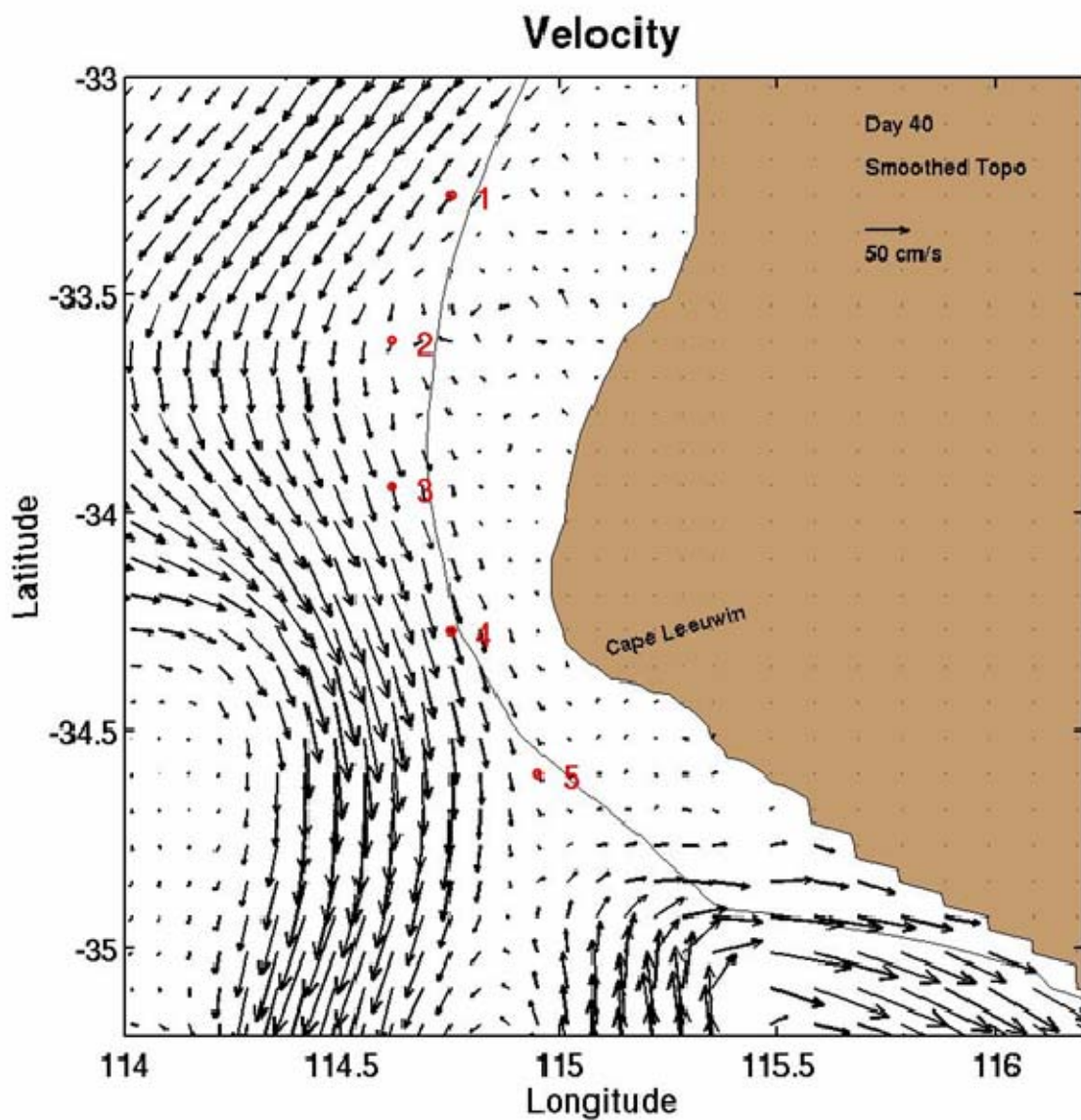


Figure 3.4b. Surface velocity vectors depicting the Leeuwin Current approaching and rounding Cape Leeuwin at day 40 for the smoothed topography model run. The red circles which are numbered in red show the locations of the analysis points used in the Lagrangian dynamical analysis. The solid line depicts the 200 m isobath, the approximate location of the shelf break.

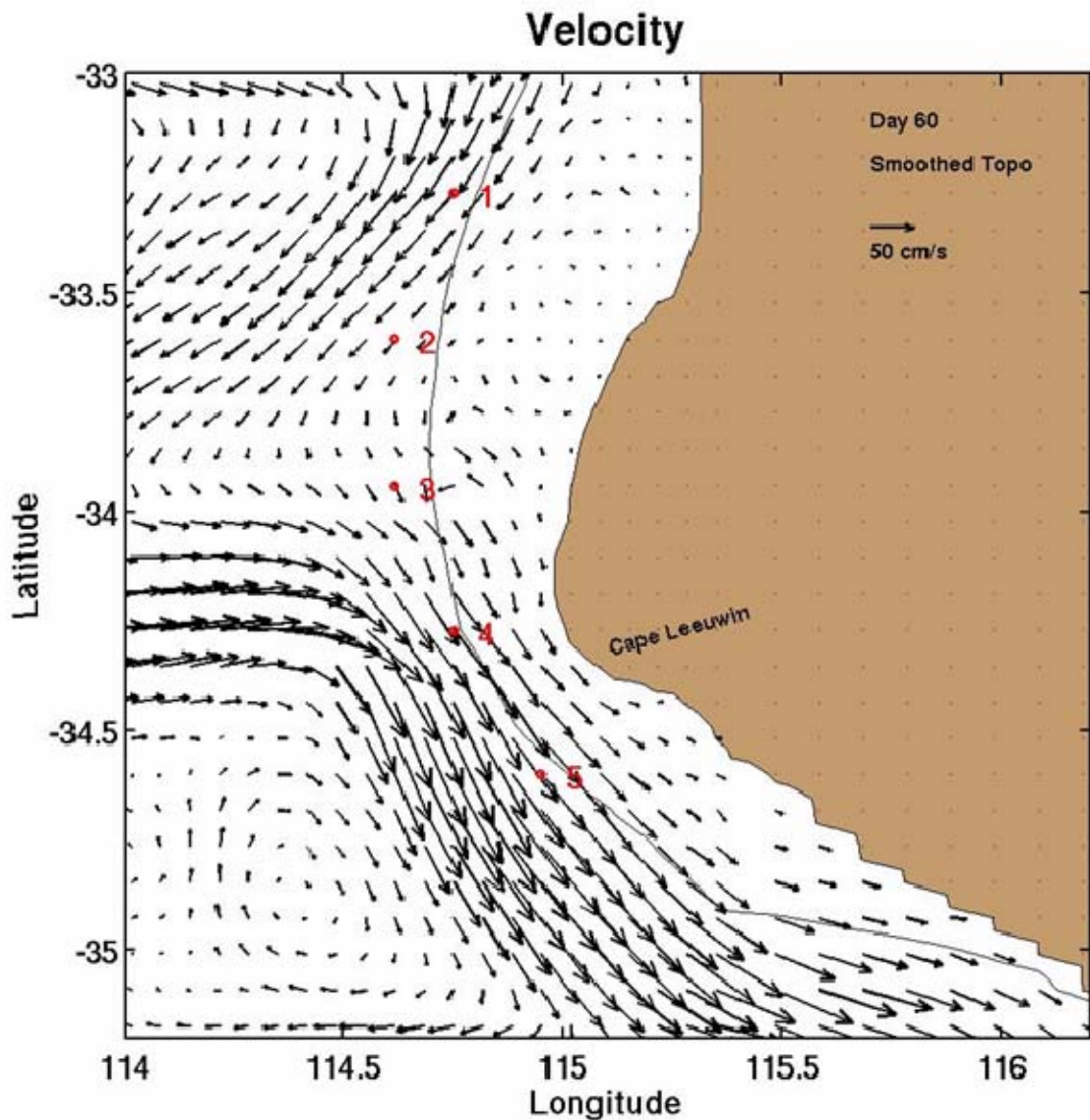


Figure 3.4c. Surface velocity vectors depicting the Leeuwin Current approaching and rounding Cape Leeuwin at day 60 for the smoothed topography model run. The red circles which are numbered in red show the locations of the analysis points used in the Lagrangian dynamical analysis. The solid line depicts the 200 m isobath, the approximate location of the shelf break.

Experiment 1, Day 20, Surface.

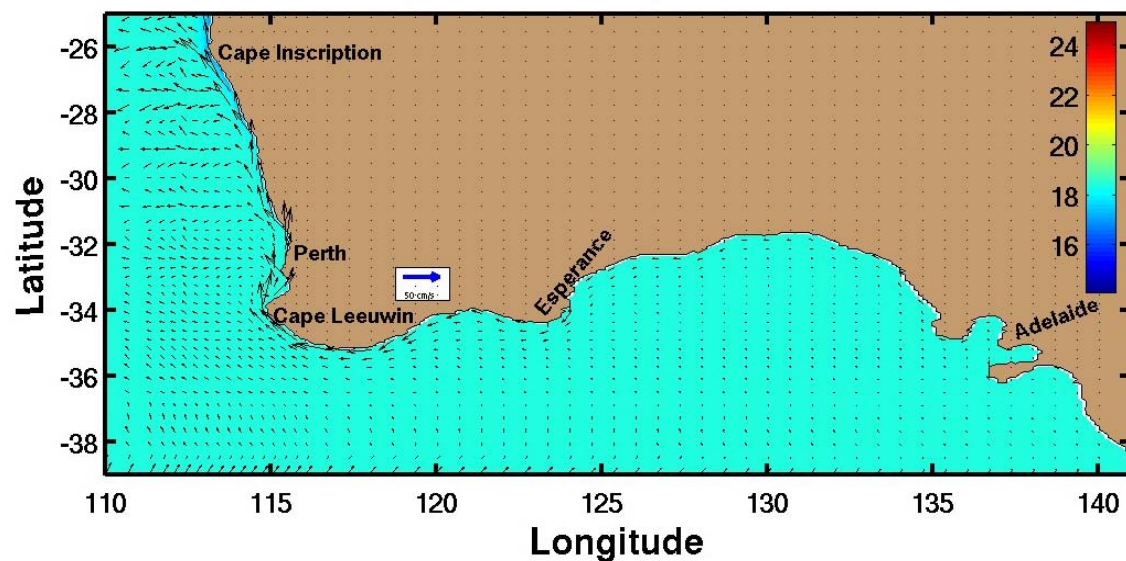


Figure 4.1. Sea surface temperature ($^{\circ}\text{C}$) and velocity vectors for Experiment 1 on day 20.

Experiment 1, Day 30, Surface.

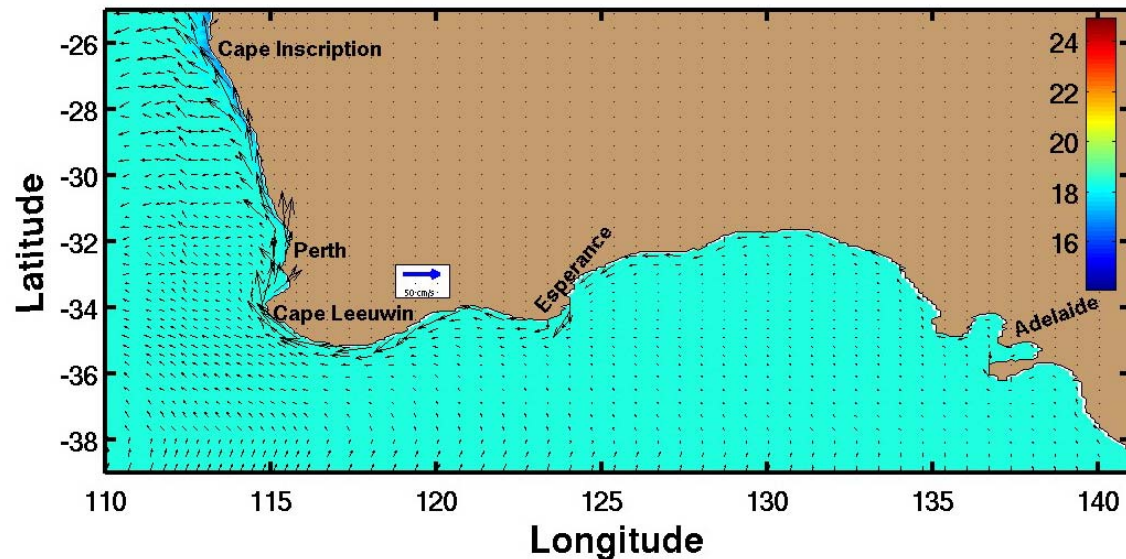


Figure 4.2a. Sea surface temperature ($^{\circ}\text{C}$) and velocity vectors for Experiment 1 on day 30.

Experiment 1, v Cross-section at 26S, Day 30.

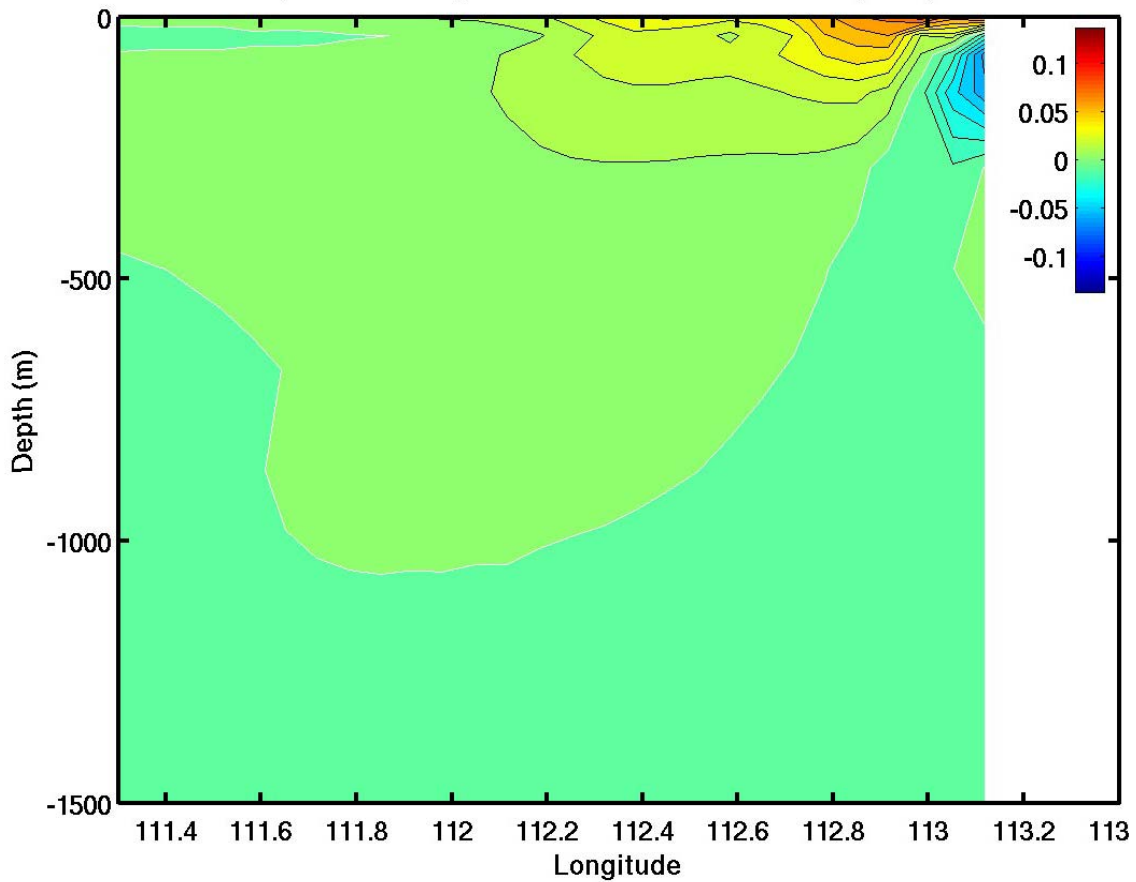


Figure 4.2b. Cross-section of meridional velocity component (m s^{-1}) at 26°S for Experiment 1 on day 30. Red is equatorward (north) and blue is poleward (south). The white contour is zero.

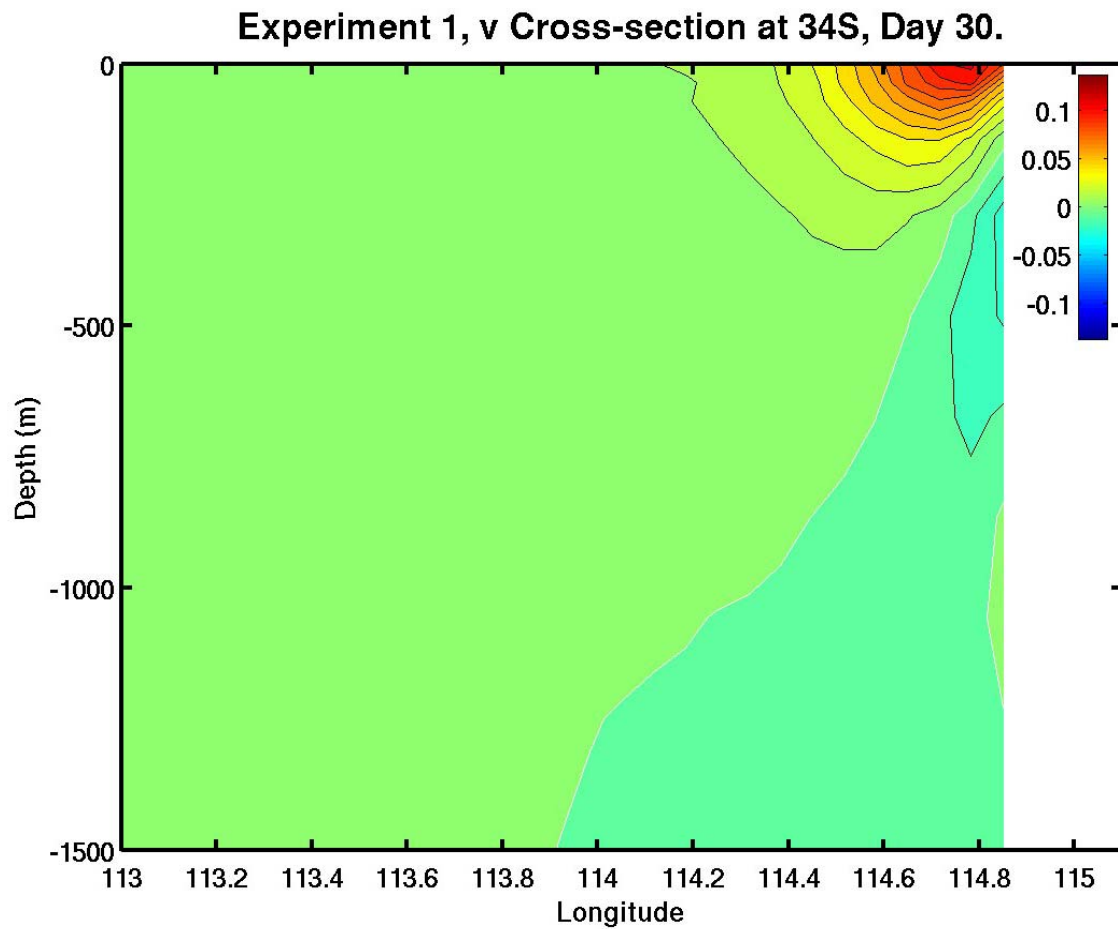


Figure 4.2c. Cross-section of meridional velocity component (m s^{-1}) near Cape Leeuwin (34°S) for Experiment 1 on day 30. Red is equatorward (north) and blue is poleward (south). The white contour is zero.

Experiment 1, Temp Cross-section at 26S, Day 30.

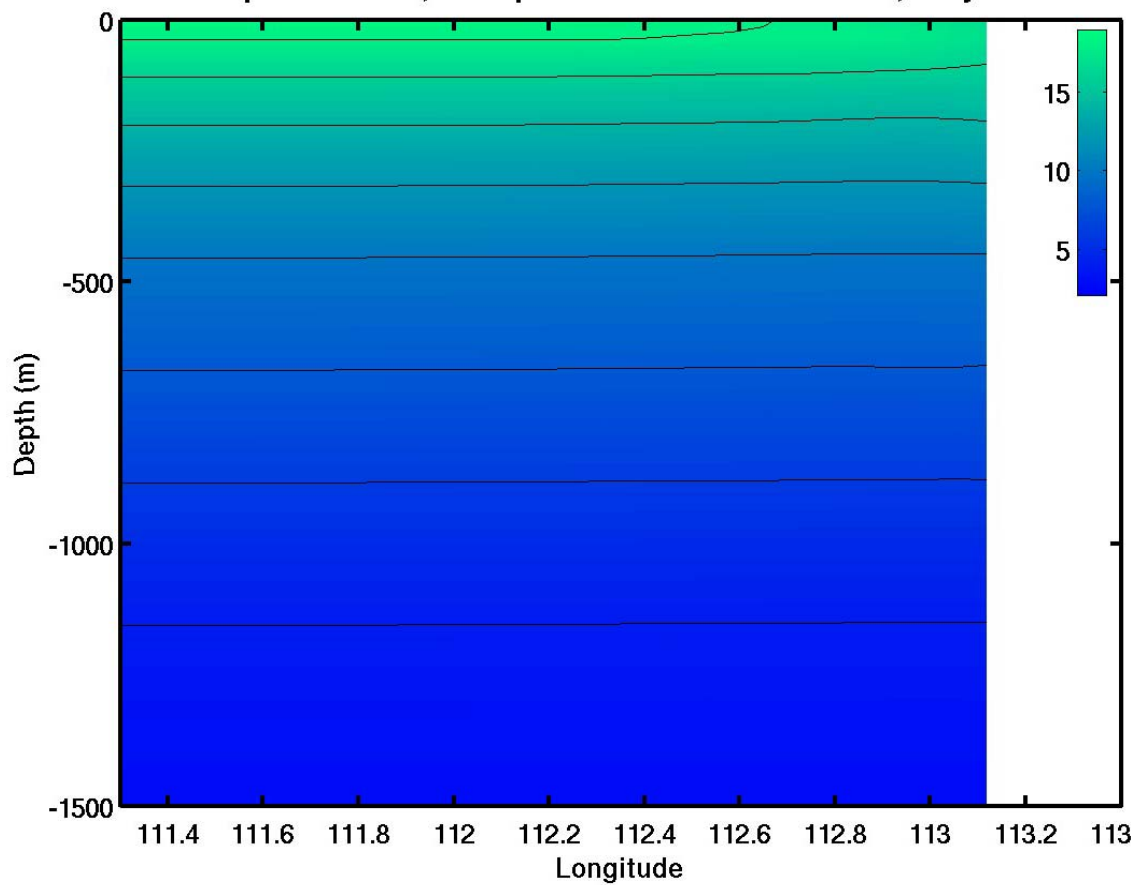


Figure 4.2d. Cross-section of temperature (°C) along an east-west transect at 26°S for Experiment 1 on day 30.

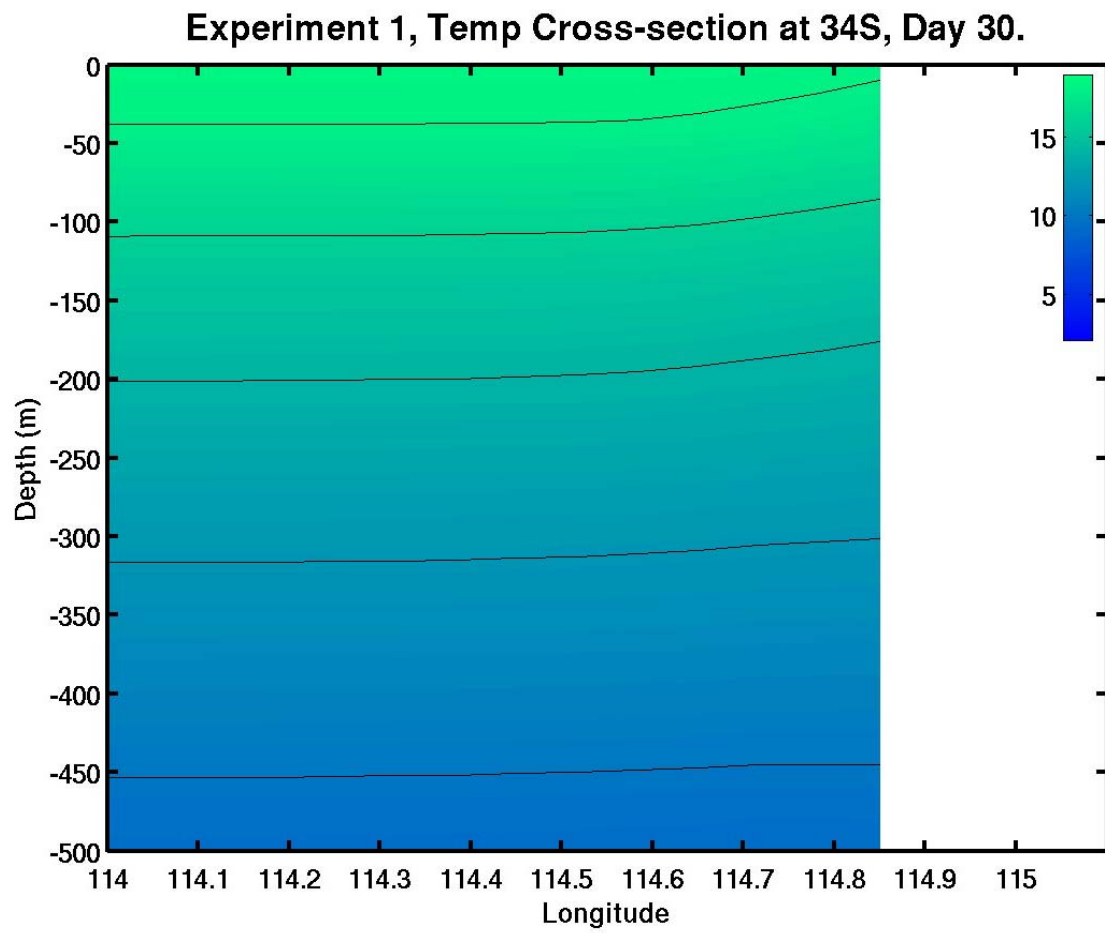


Figure 4.2e. Cross-section of temperature ($^{\circ}\text{C}$) along an east-west transect near Cape Leeuwin (34°S) for Experiment 1 on day 30.

Experiment 1, Temp Cross-section at 117E, Day 30.

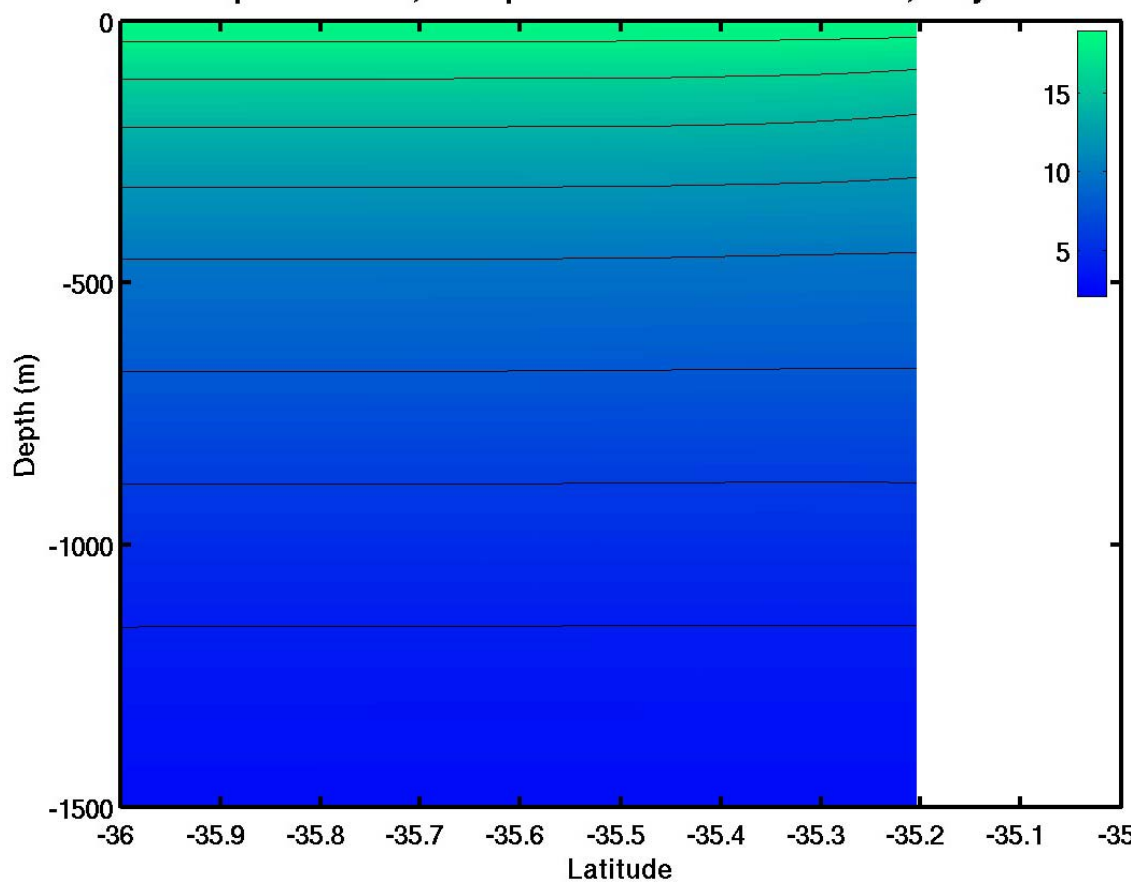


Figure 4.2f. Cross-section of temperature (°C) along a north-south transect at 117°E for Experiment 1 on day 30.

Experiment 1, Day 60, Surface.

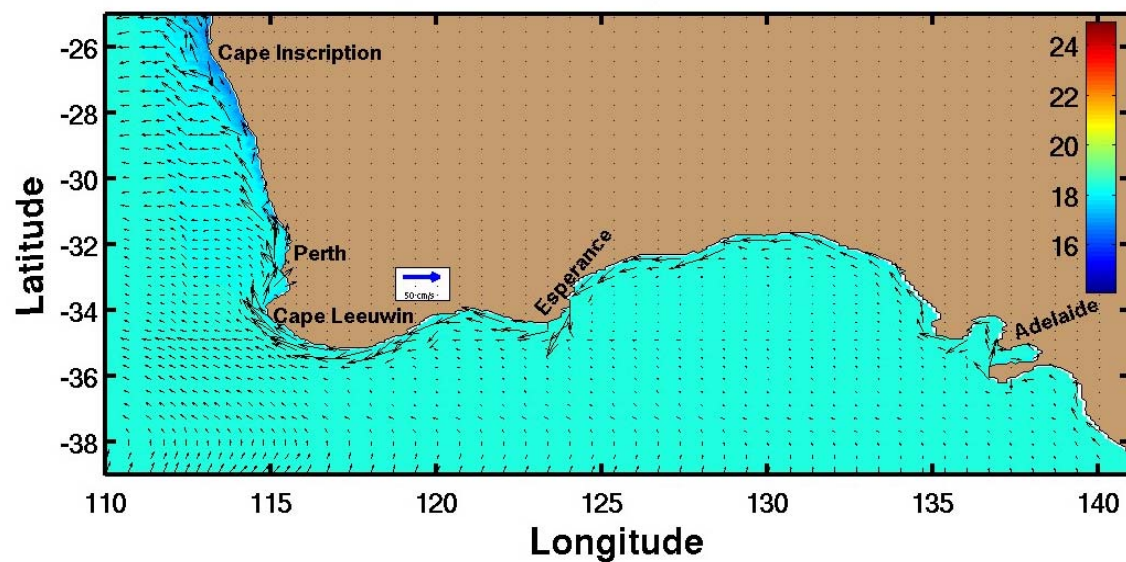


Figure 4.3a. Sea surface temperature ($^{\circ}\text{C}$) and velocity vectors for Experiment 1 on day 60.

Experiment 1, v Cross-section at 26S, Day 60.

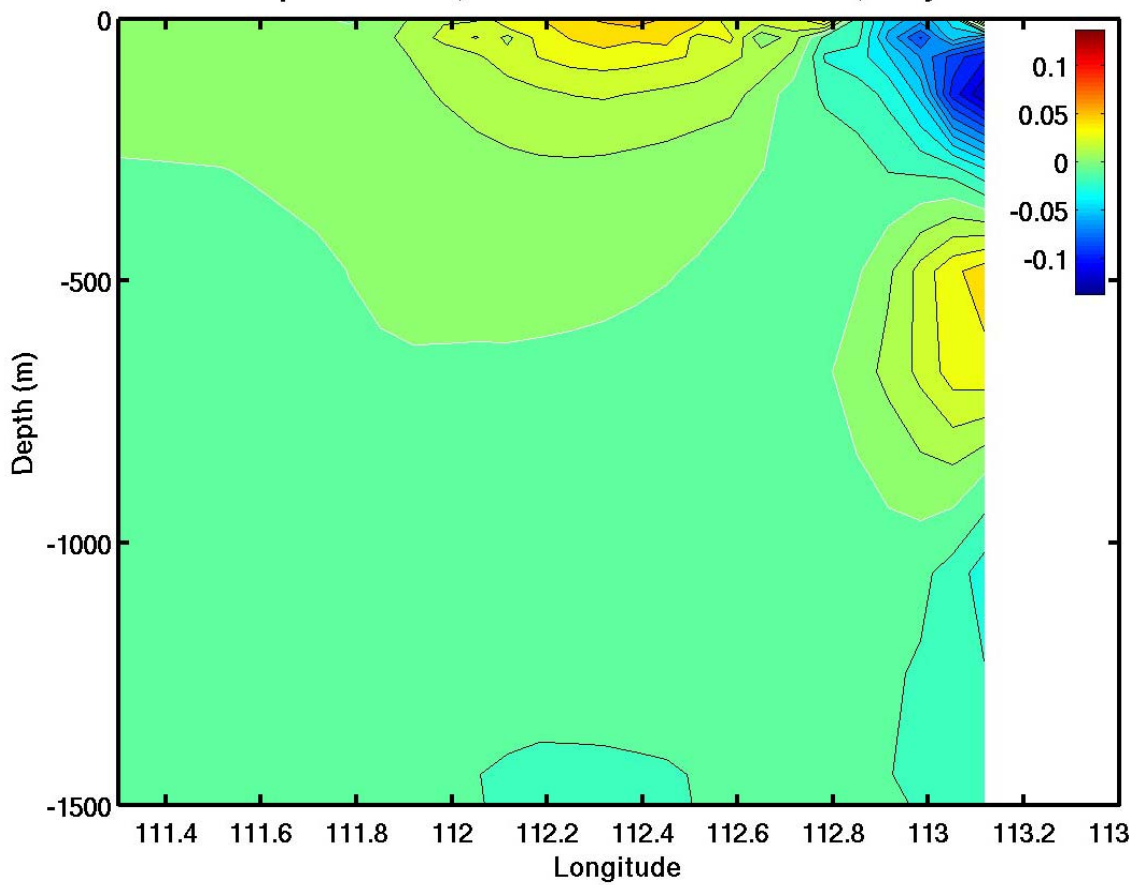


Figure 4.3b. Cross-section of meridional velocity component (m s^{-1}) at 26°S for Experiment 1 on day 60. Red is equatorward (north) and blue is poleward (south). The white contour is zero.

Experiment 1, Temp Cross-section at 26S, Day 60.

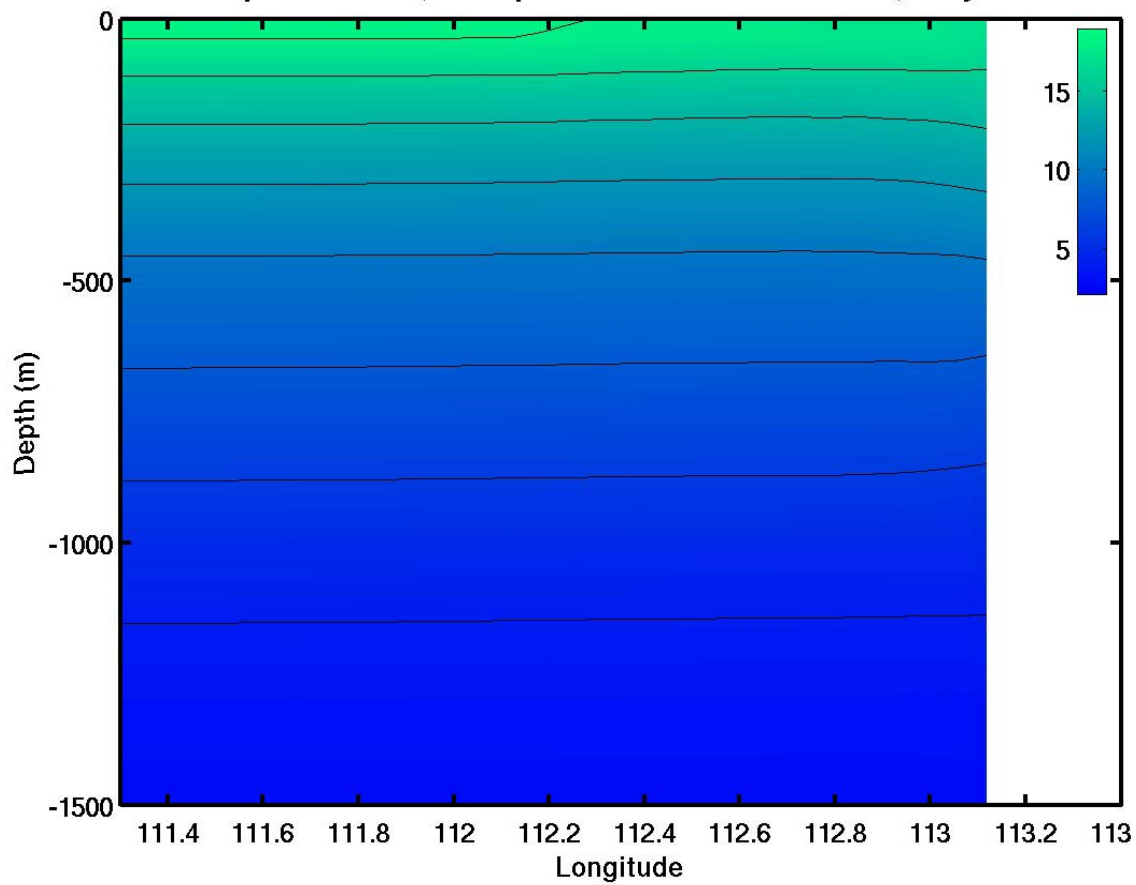


Figure 4.3c. Cross-section of temperature (°C) along an east-west transect at 26°S for Experiment 1 on day 60.

Experiment 1, v Cross-section at 34S, Day 60.

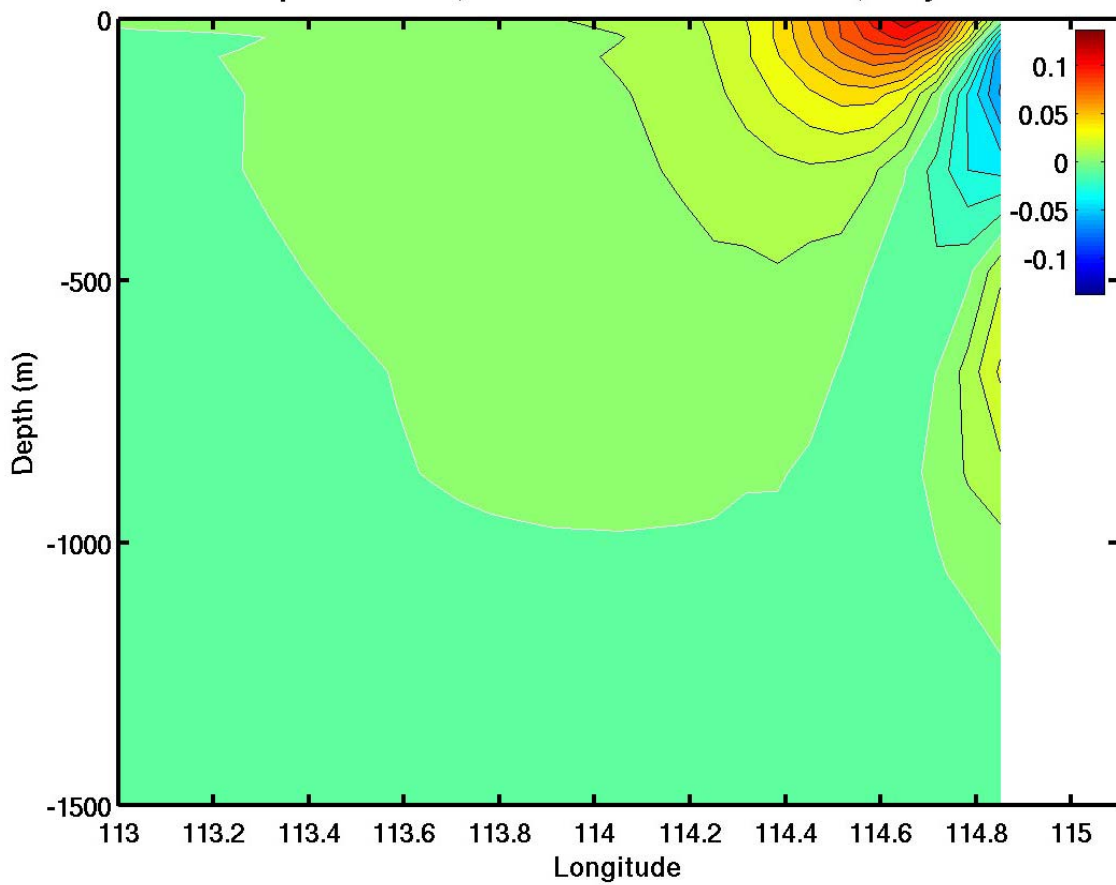


Figure 4.3d. Cross-section of meridional velocity component (m s^{-1}) near Cape Leeuwin (34°S) for Experiment 1 on day 60. Red is equatorward (north) and blue is poleward (south). The white contour is zero.

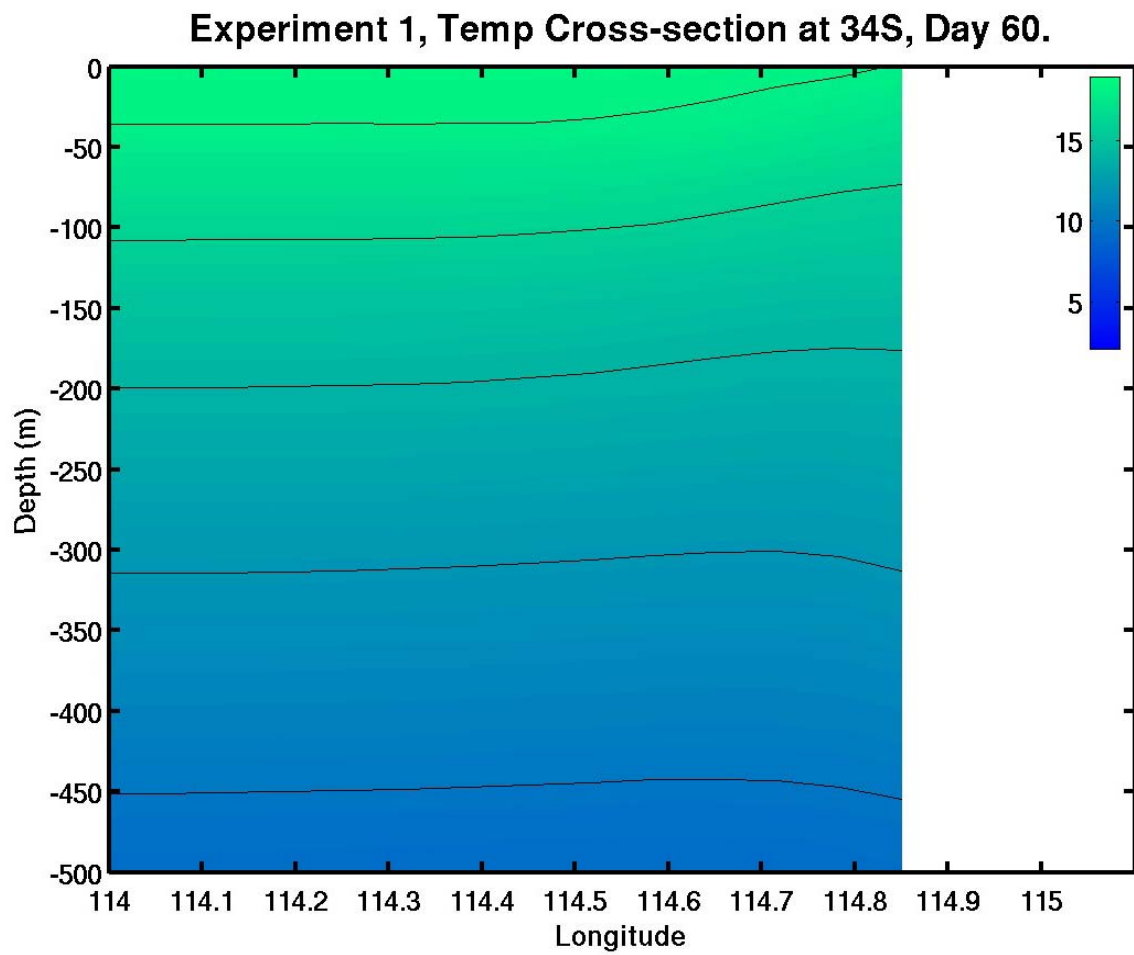


Figure 4.3e. Cross-section of temperature ($^{\circ}\text{C}$) along an east-west transect near Cape Leeuwin (34°S) for Experiment 1 on day 60.

Experiment 1, u Cross-section at 117E, Day 60.

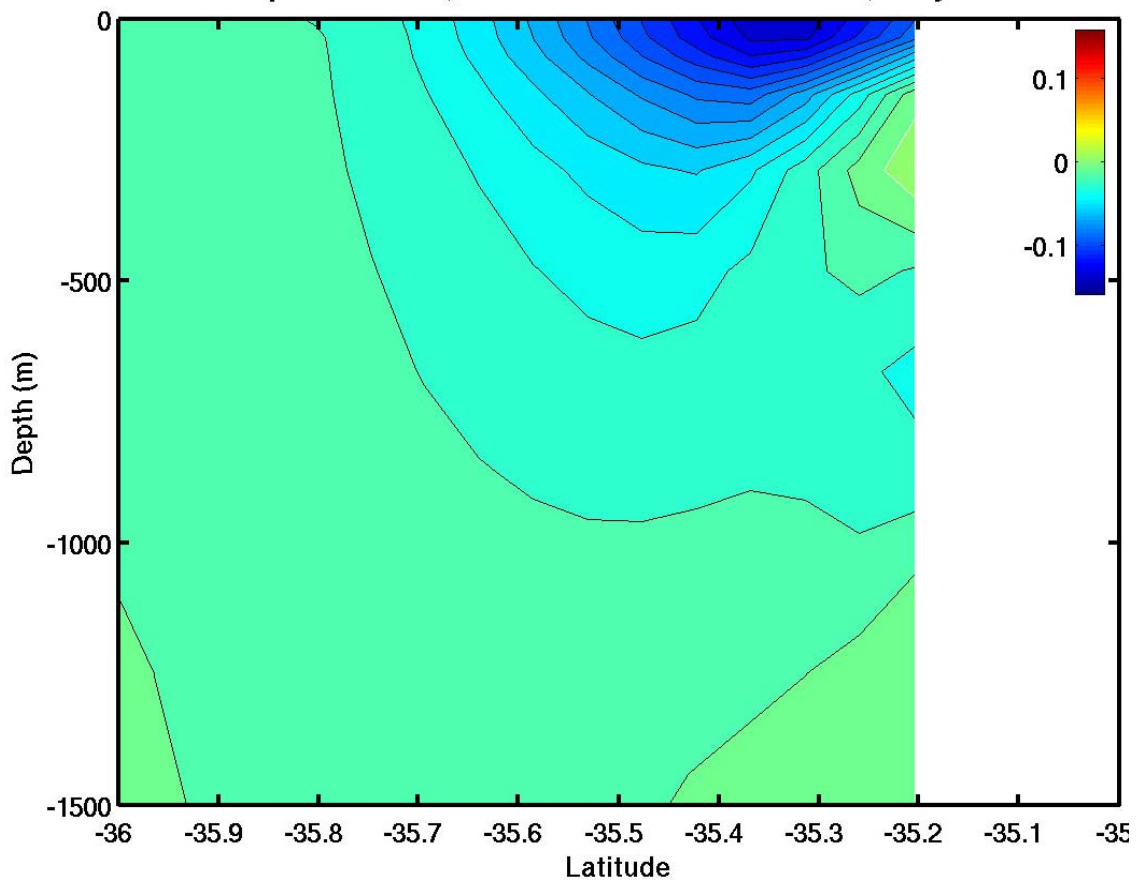


Figure 4.3f. Cross-section of zonal velocity component (m s^{-1}) at 117°E for Experiment 1 on day 60. Red is eastward and blue is westward. The white contour is zero.

Experiment 1, Temp Cross-section at 117E, Day 60.

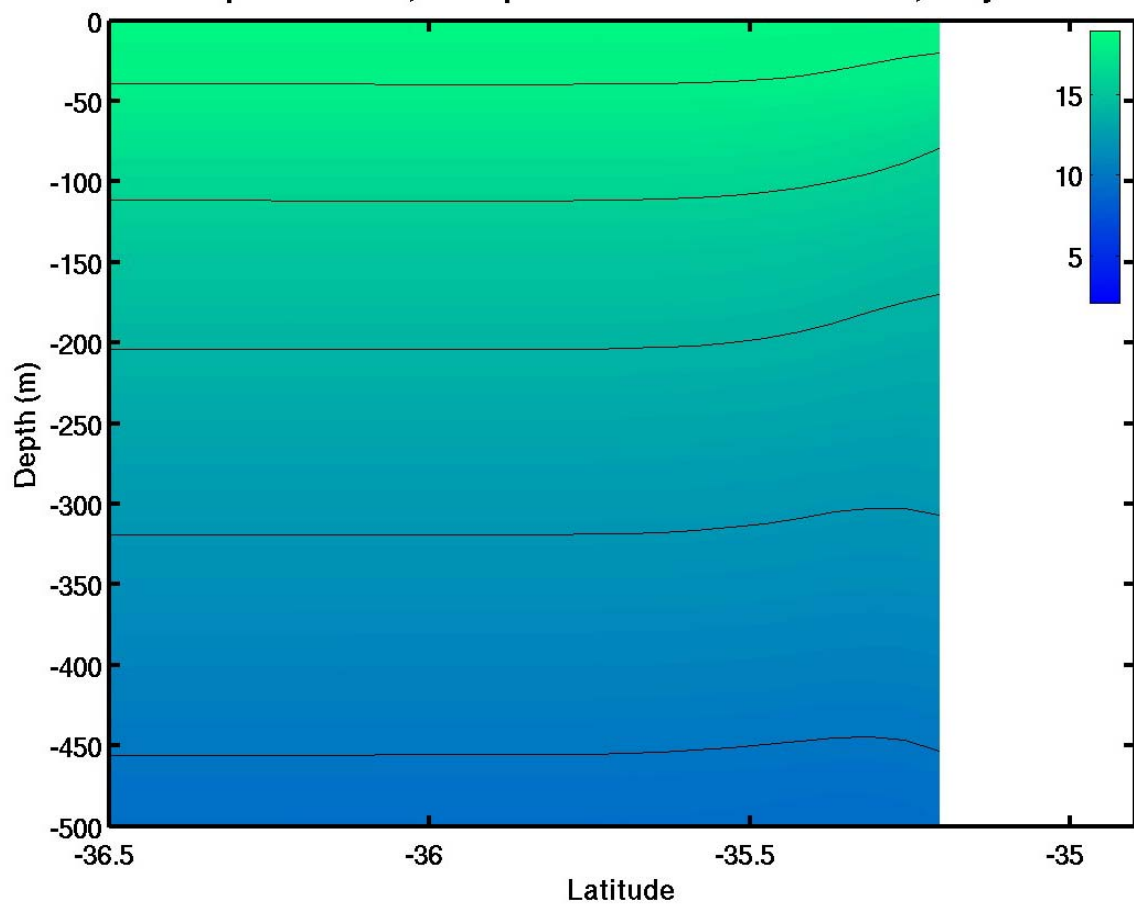


Figure 4.3g. Cross-section of temperature (°C) along a north-south transect at 117°E for Experiment 1 on day 60.

Experiment 1, u Cross-section at 130E, Day 60.

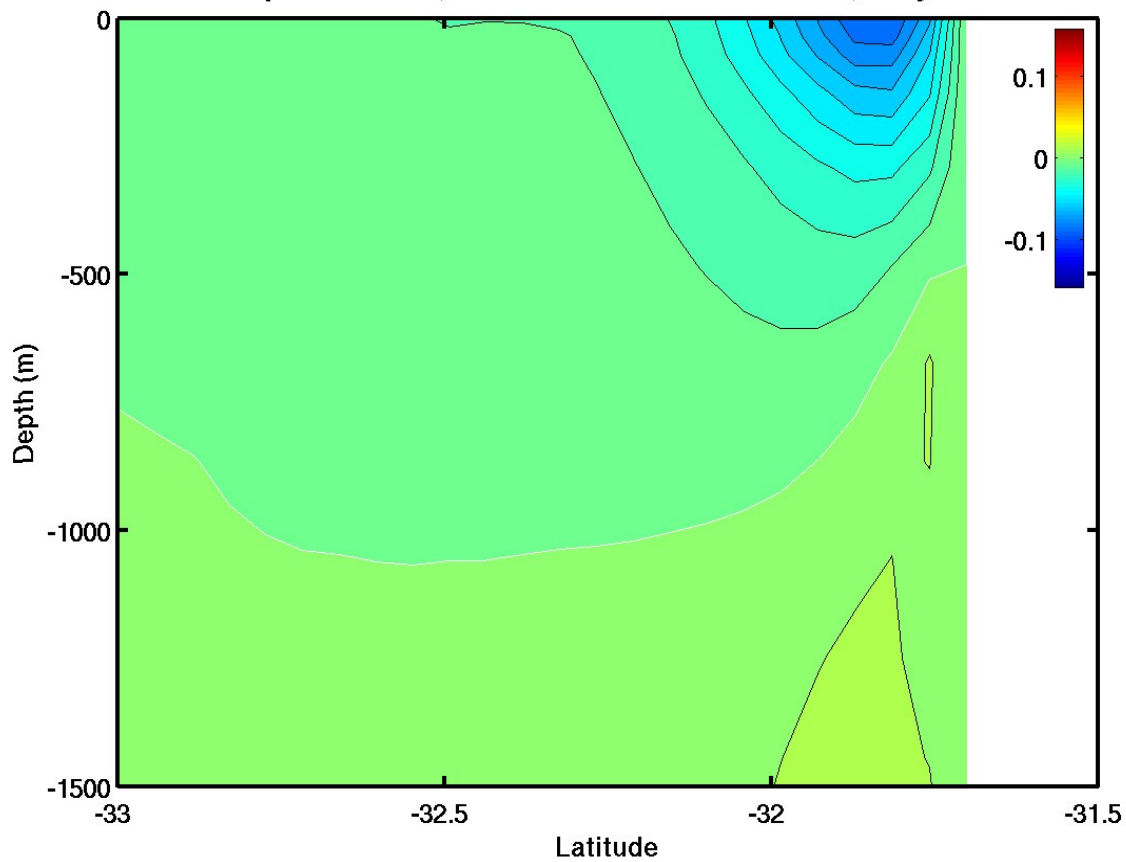


Figure 4.3h. Cross-section of zonal velocity component (m s^{-1}) in the Great Australian Bight (130°E) for Experiment 1 on day 60. Red is eastward and blue is westward. The white contour is zero.

Experiment 1, Temp Cross-section at 130E, Day 60.

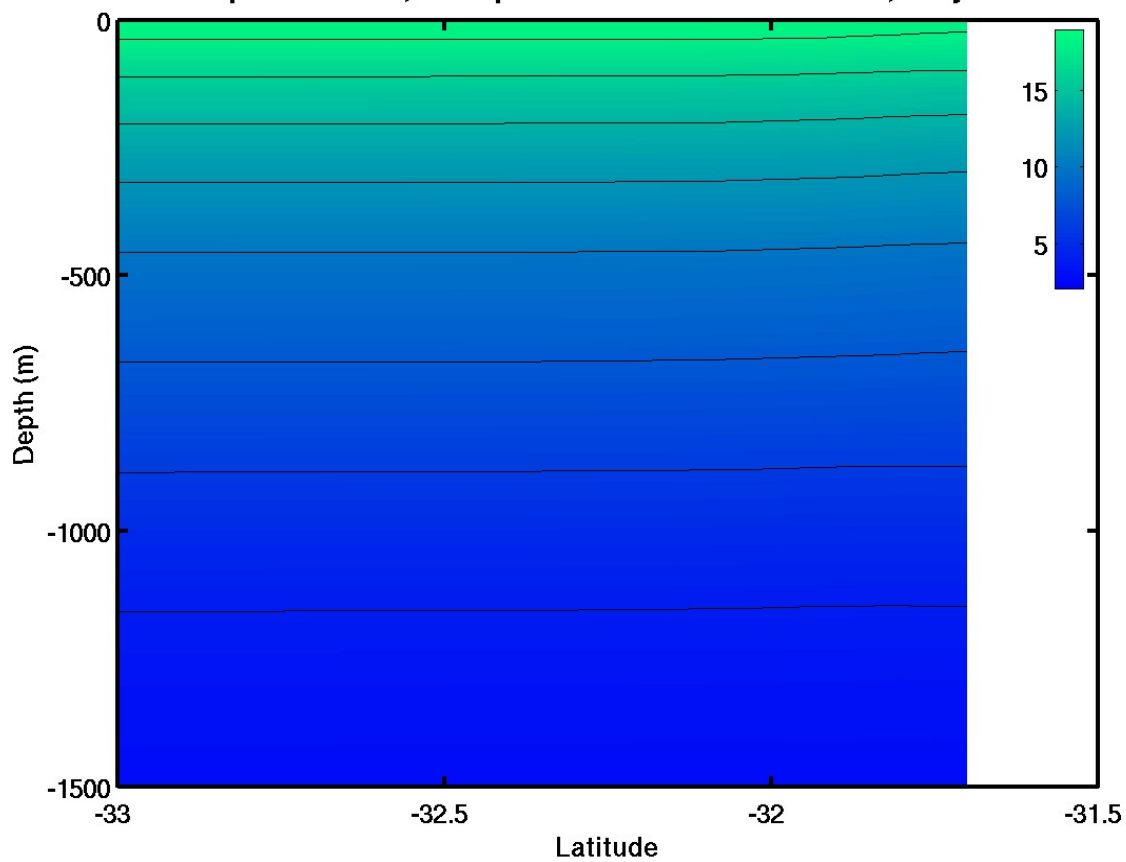


Figure 4.3i. Cross-section of temperature (°C) along a north-south transect in the Great Australian Bight (130°E) for Experiment 1 on day 60.

Experiment 2, Day 20, Surface.

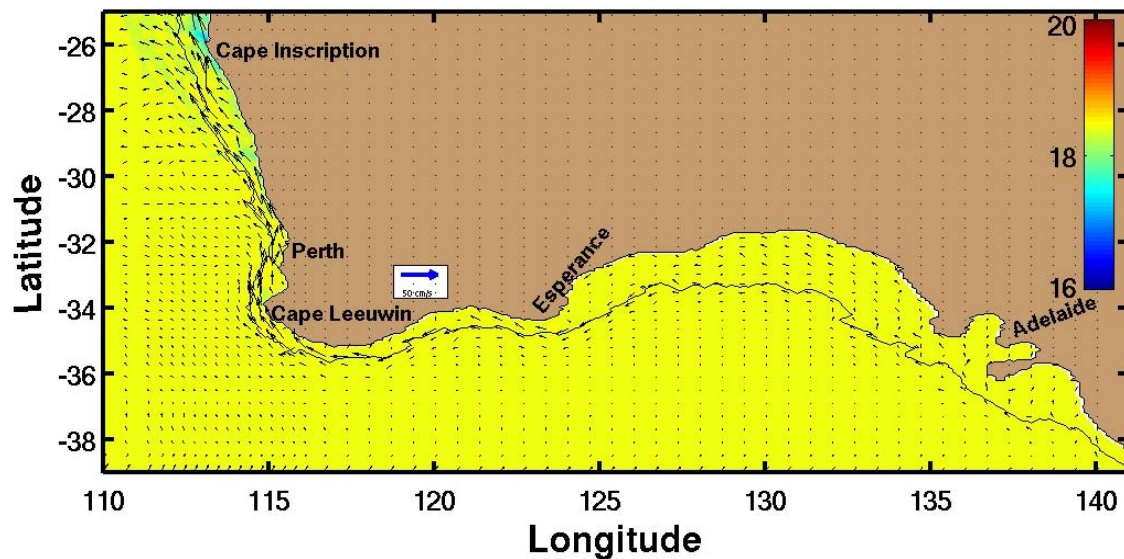


Figure 4.4. Sea surface temperature ($^{\circ}\text{C}$) and velocity vectors for Experiment 2 on day 20.

Experiment 2, Day 30, Surface.

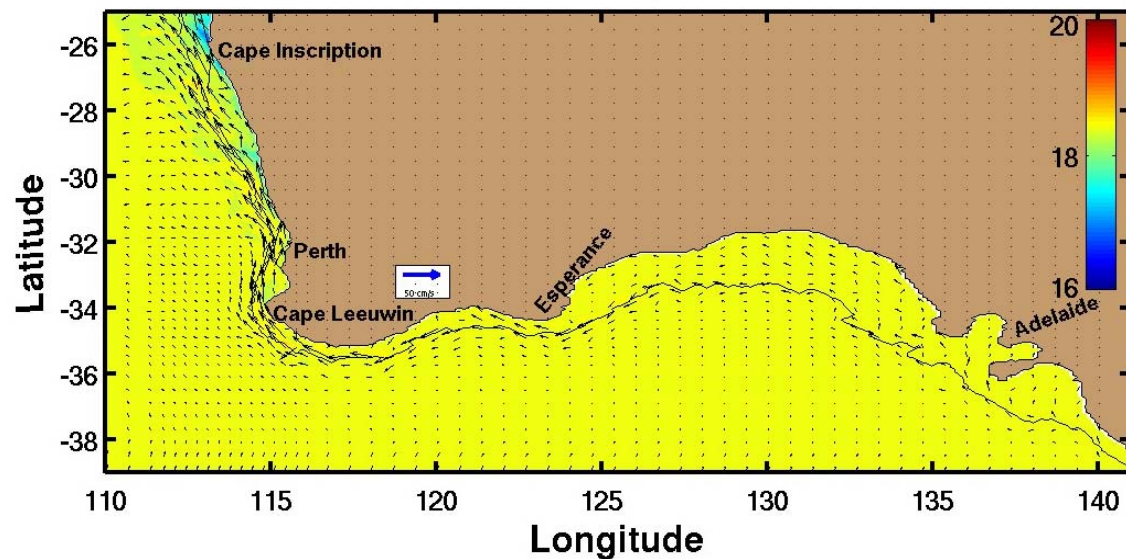


Figure 4.5a. Sea surface temperature ($^{\circ}\text{C}$) and velocity vectors for Experiment 2 on day 30.

Experiment 2, v Cross-section at 26S, Day 30.

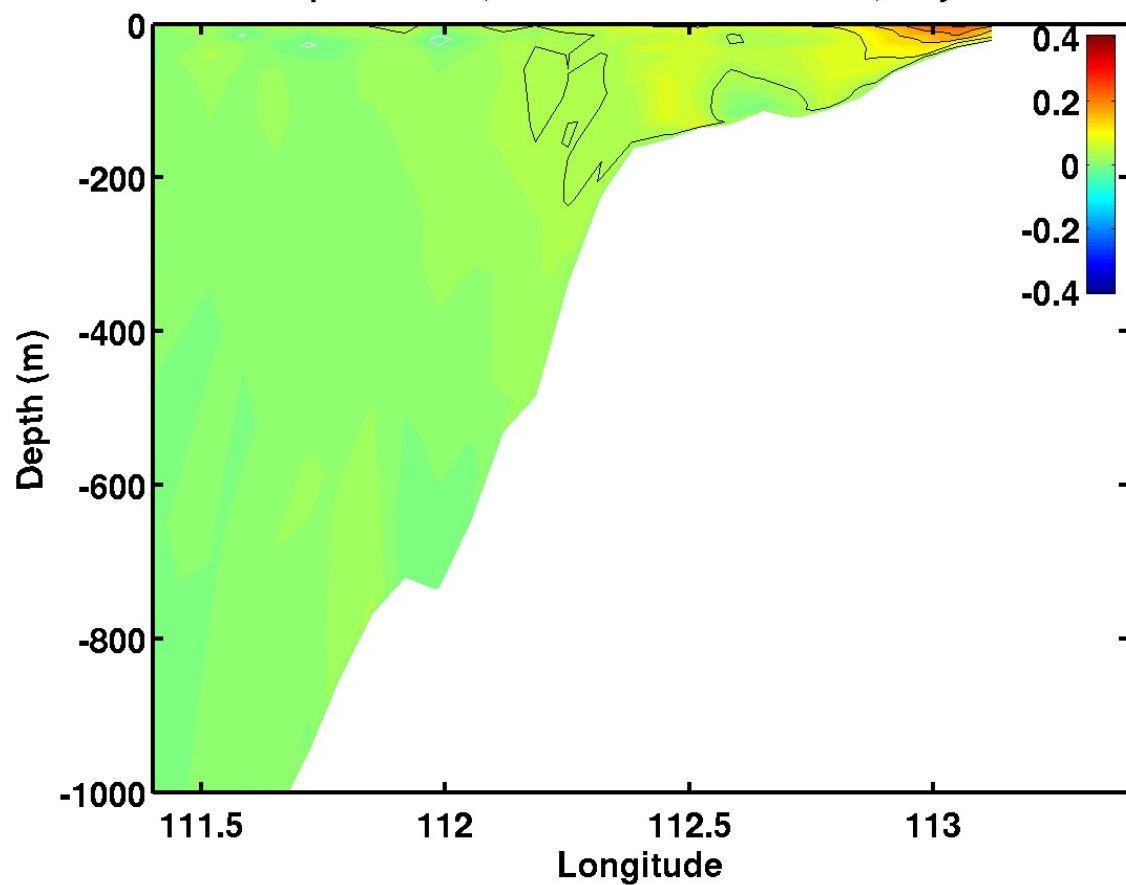


Figure 5b. Cross-section of meridional velocity component (m s^{-1}) at 26°S for Experiment 2 on day 30. Red is equatorward (north) and blue is poleward (south). The white contour is zero.

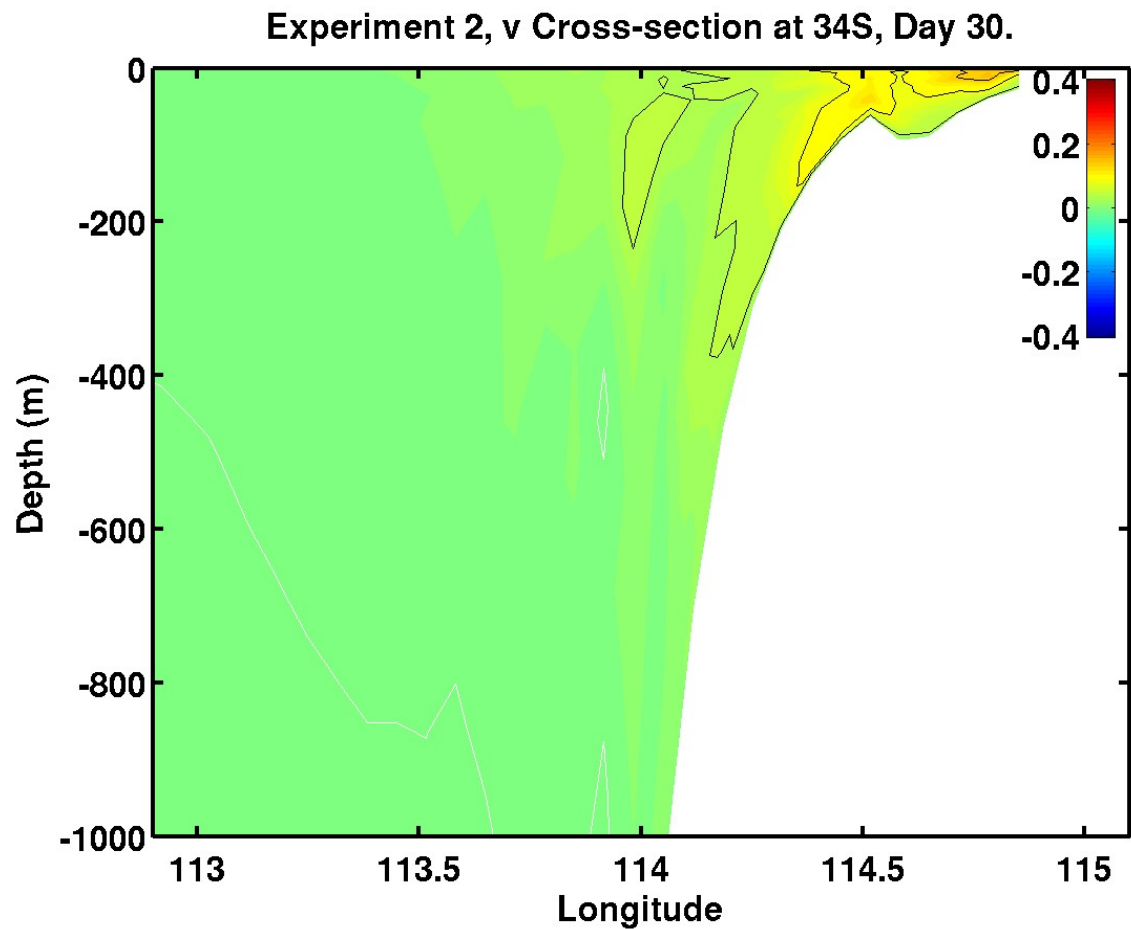


Figure 4.5c. Cross-section of meridional velocity component (m s^{-1}) near Cape Leeuwin (34°S) for Experiment 2 on day 30. Red is equatorward (north) and blue is poleward (south). The white contour is zero.

Experiment 2, Temp Cross-section at 26S, Day 30.

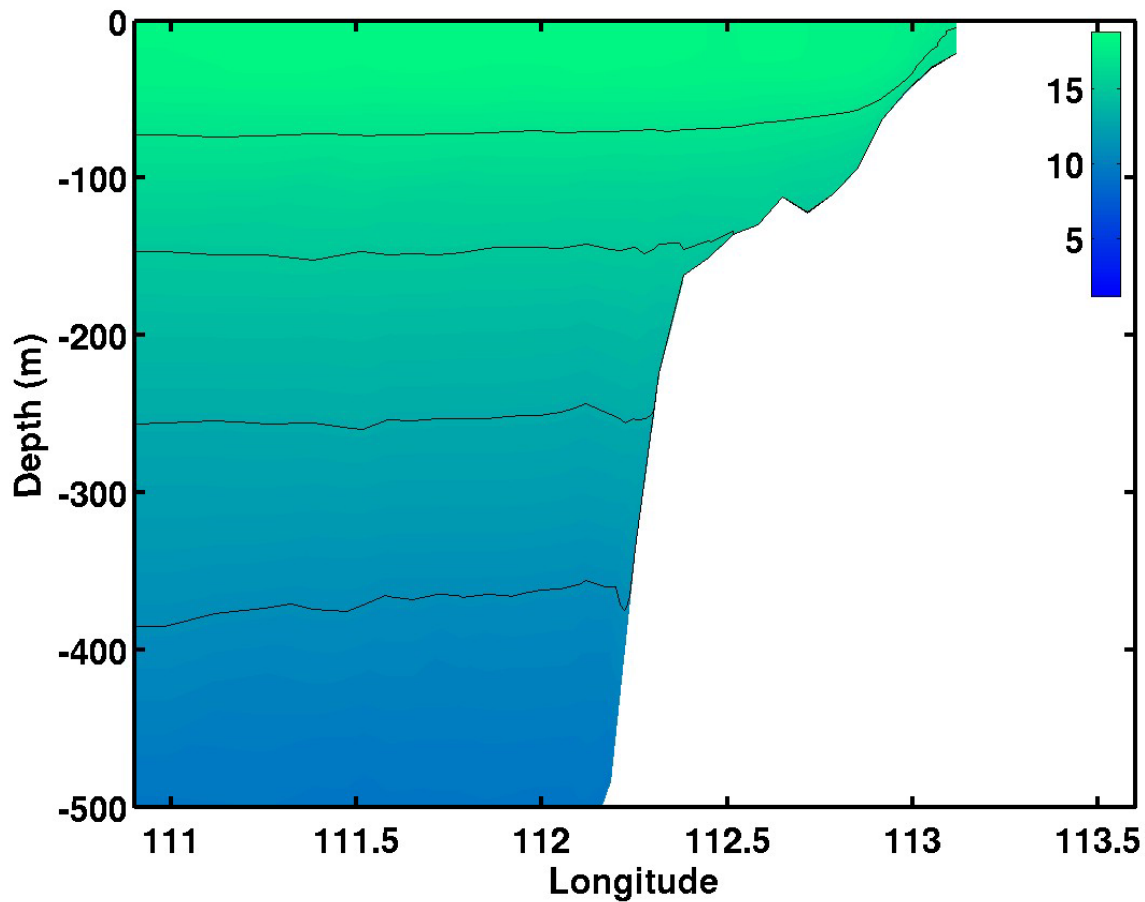


Figure 4.5d. Cross-section of temperature (°C) along an east-west transect at 26°S for Experiment 2 on day 30.

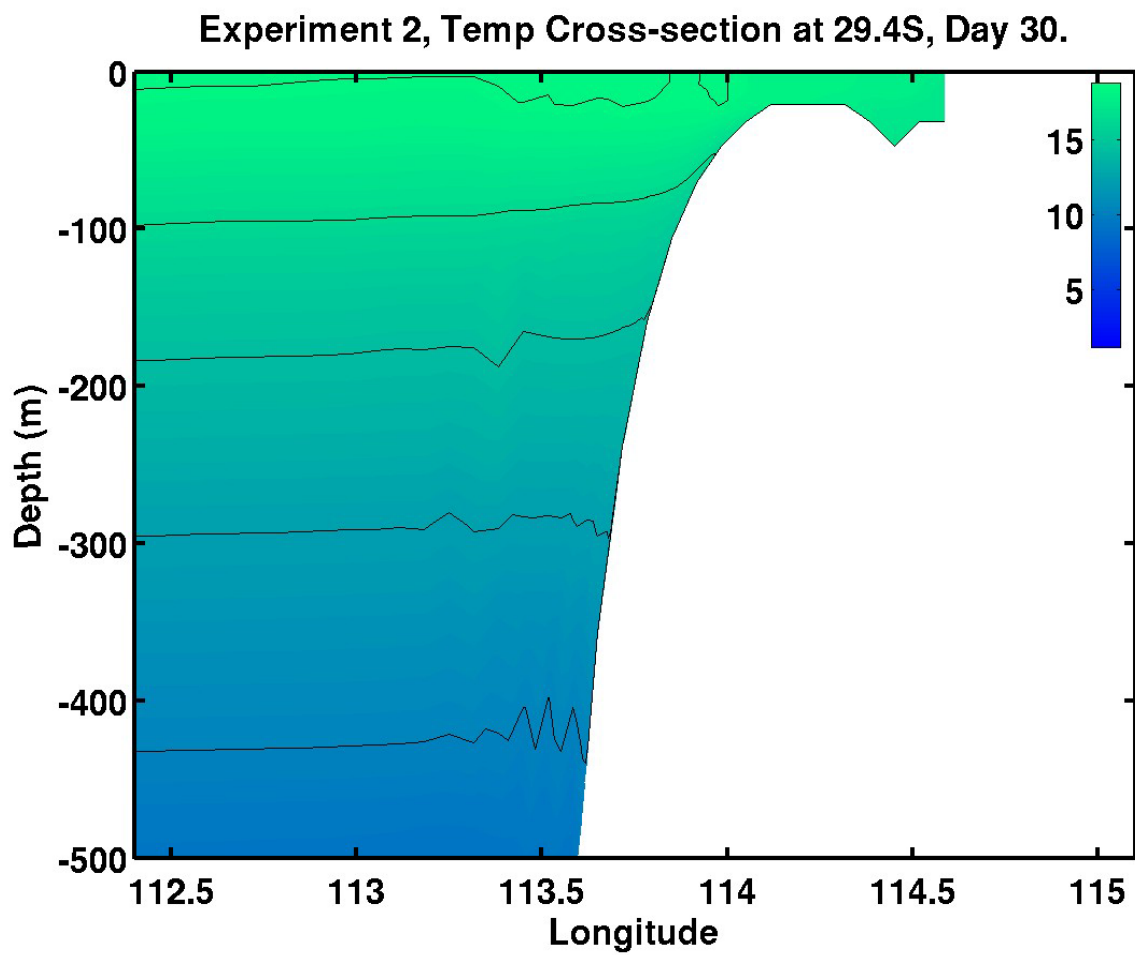


Figure 4.5e. Cross-section of temperature ($^{\circ}\text{C}$) along an east-west transect at 29.4°S for Experiment 2 on day 30.

Experiment 2, Temp Cross-section at 34S, Day 30.

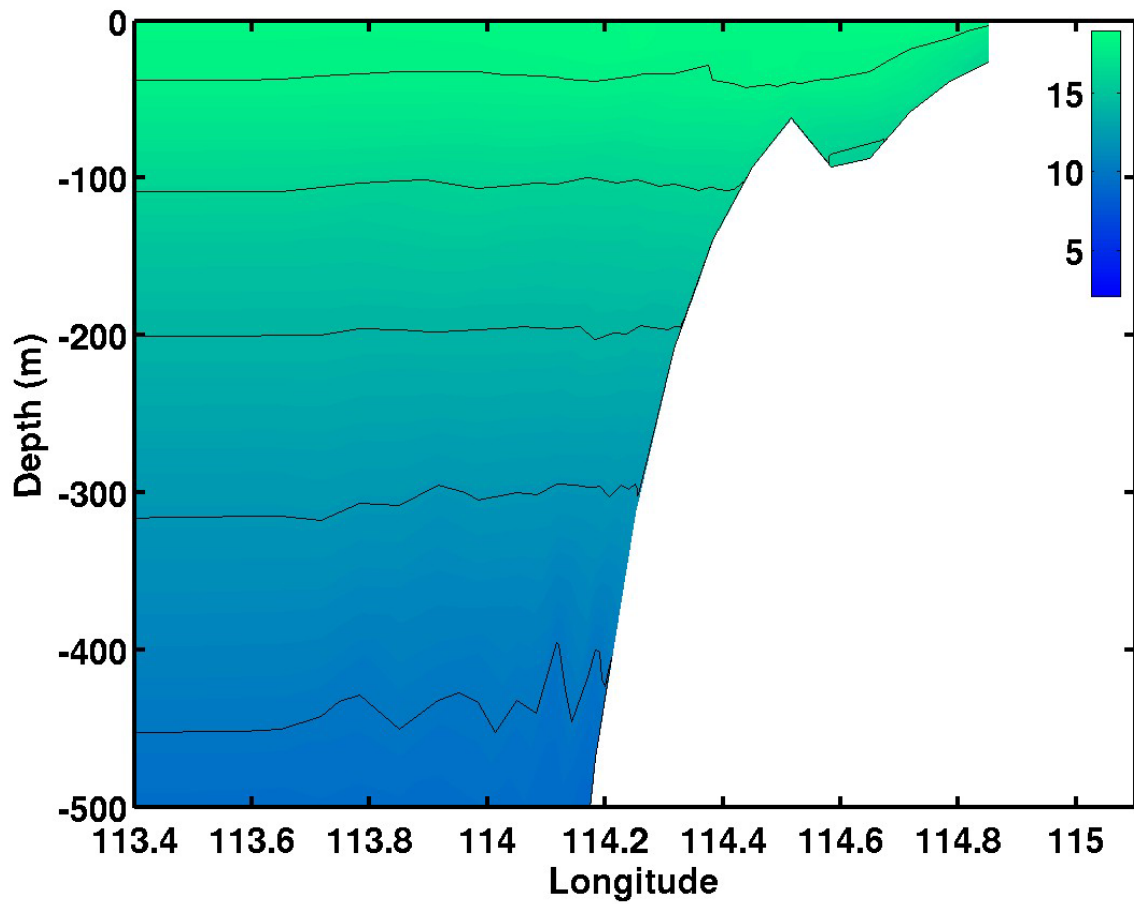


Figure 4.5f. Cross-section of temperature (°C) near Cape Leeuwin (34°S) for Experiment 2 on day 30.

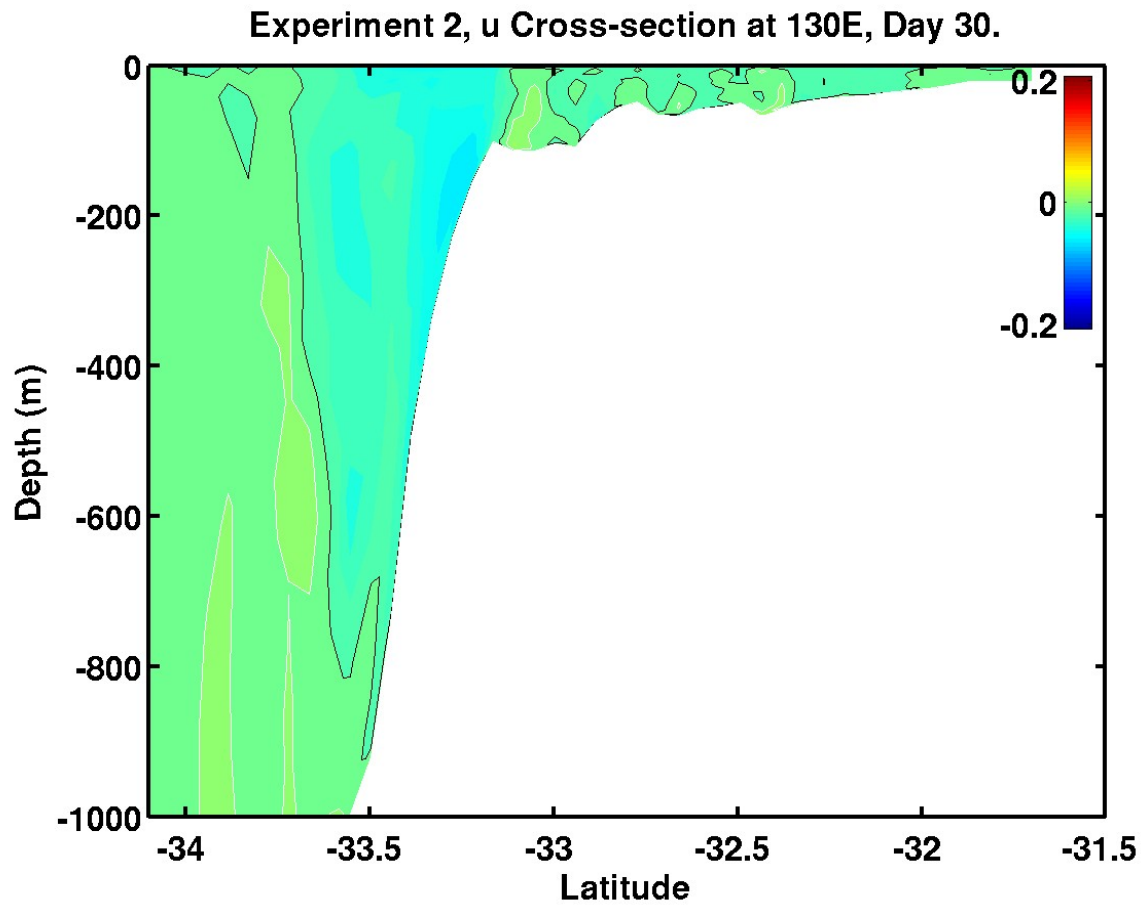


Figure 4.5g. Cross-section of zonal velocity component (m s^{-1}) in the Great Australian Bight (130°E) for Experiment 2 on day 30. Red is eastward and blue is westward. The white contour is zero.

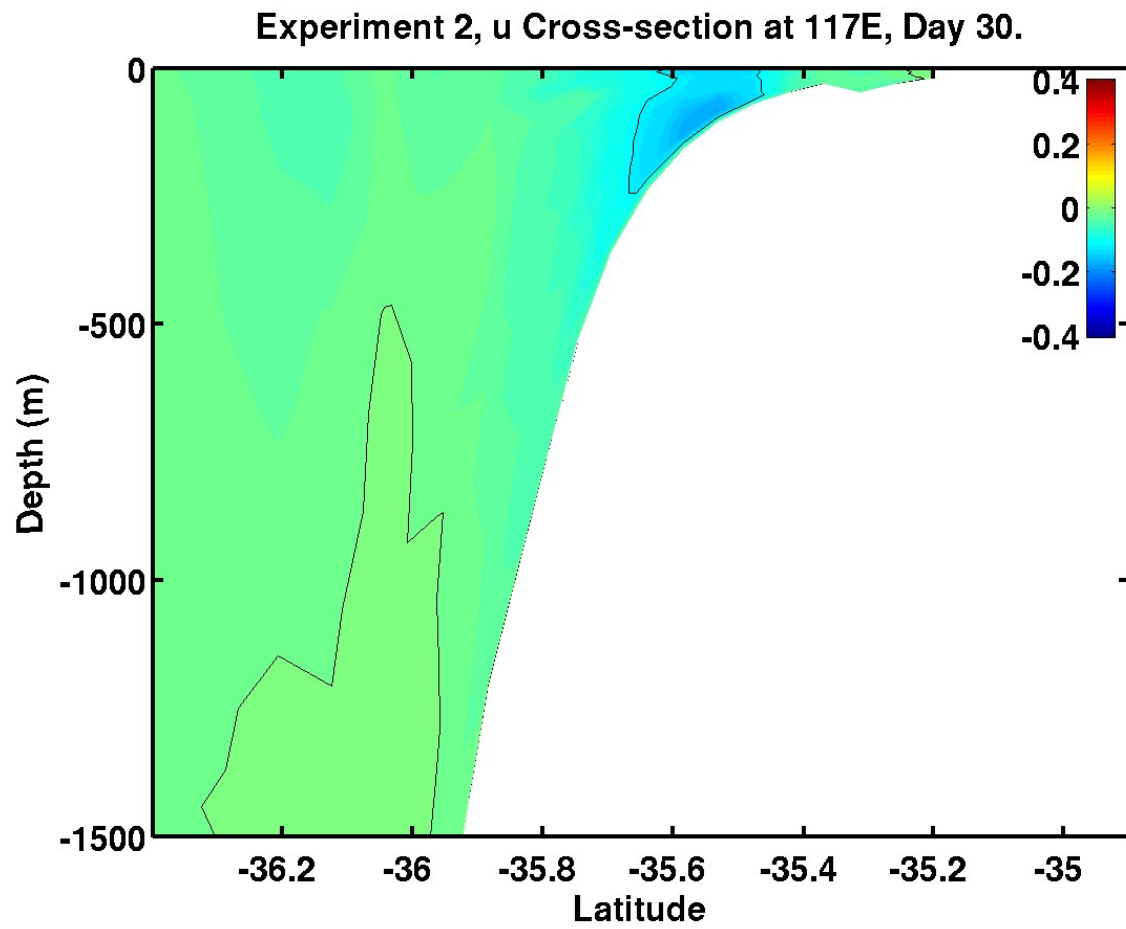


Figure 4.5h. Cross-section of zonal velocity component (m s^{-1}) at 117°E for Experiment 2 on day 30. Red is eastward and blue is westward. The white contour is zero.

Experiment 2, Day 60, Surface.

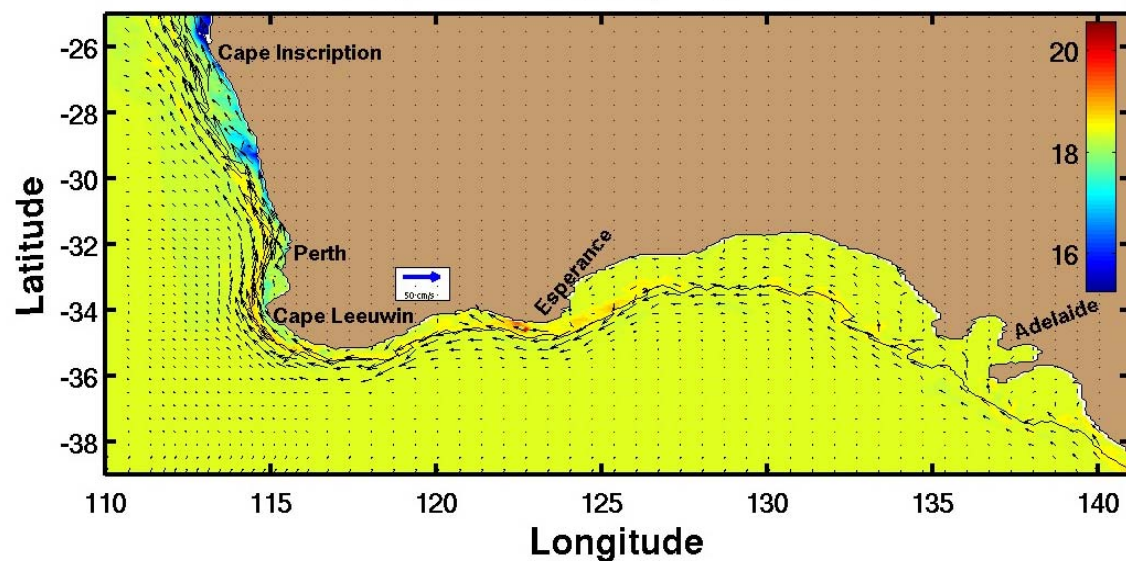


Figure 4.6a. Sea surface temperature ($^{\circ}\text{C}$) and velocity vectors for Experiment 2 on day 60.

Experiment 2, v Cross-section at 26S, Day 60.

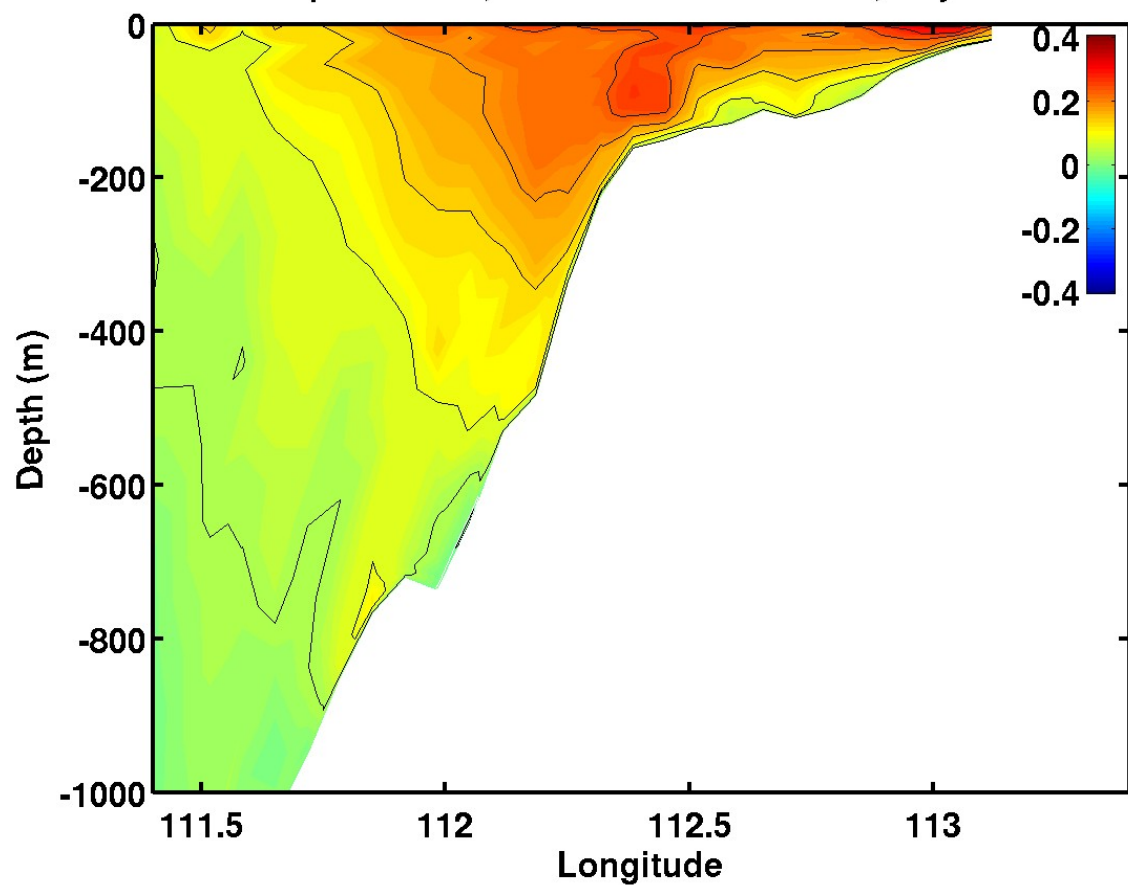


Figure 4.6b. Cross-section of meridional velocity component (m s^{-1}) at 26°S for Experiment 2 on day 60. Red is equatorward (north) and blue is poleward (south). The white contour is zero.

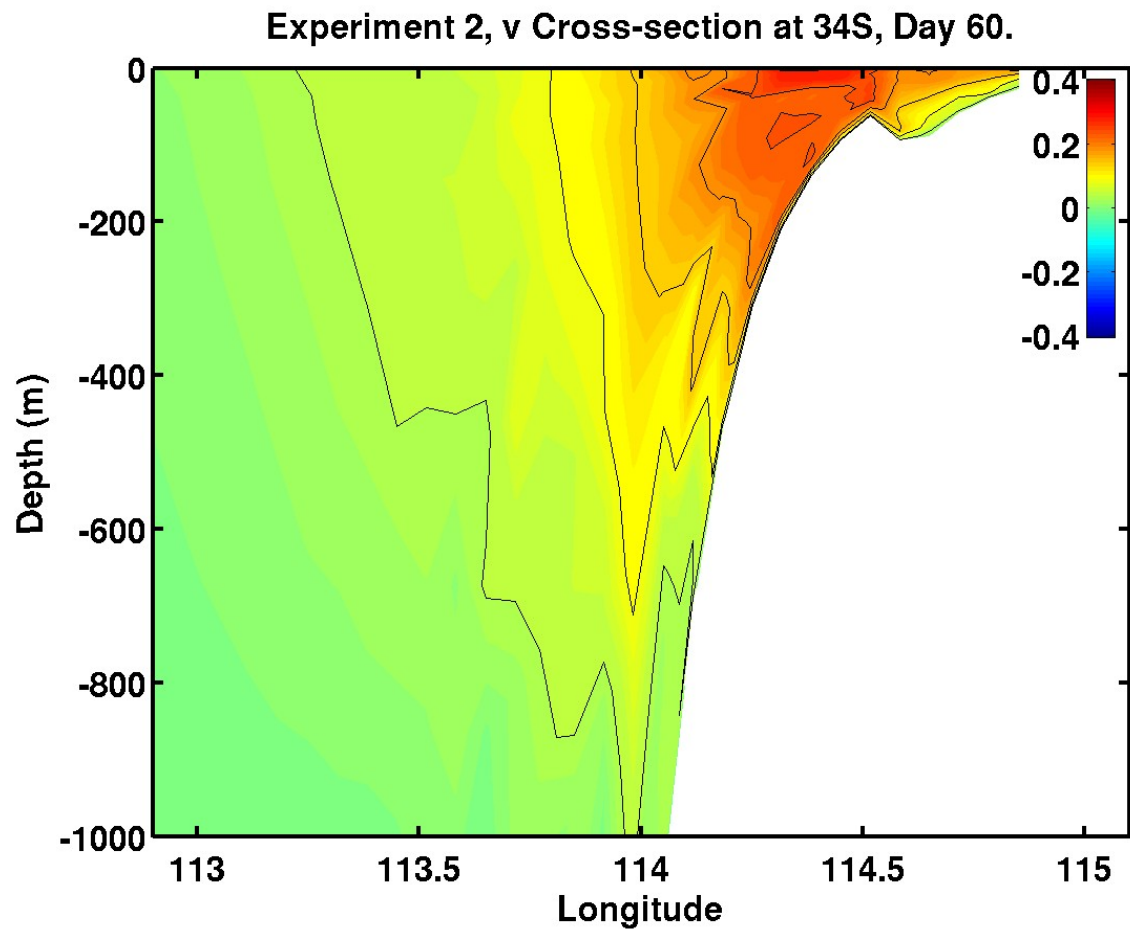


Figure 4.6c. Cross-section of meridional velocity component (m s^{-1}) near Cape Leeuwin (34°S) for Experiment 2 on day 60. Red is equatorward (north) and blue is poleward (south). The white contour is zero.

Experiment 2, Temp Cross-section at 26S, Day 60.

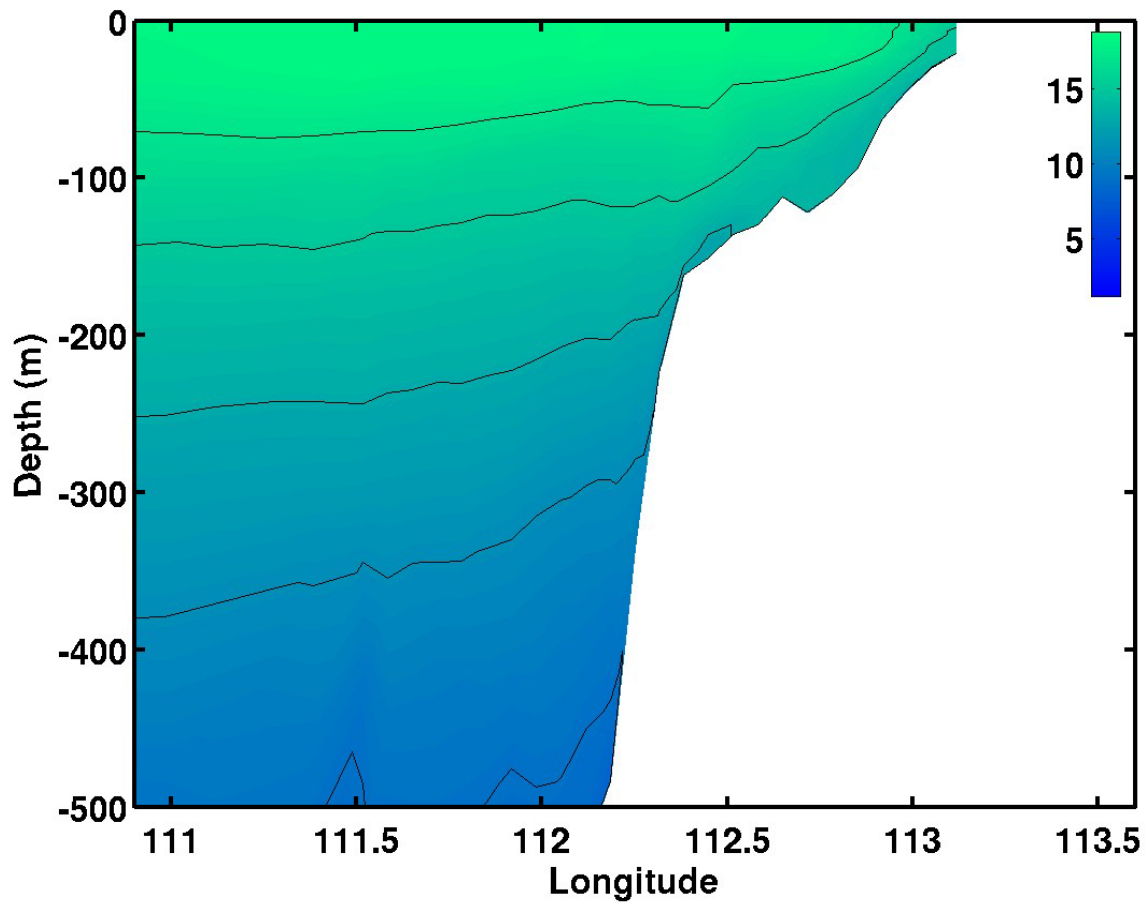


Figure 4.6d. Cross-section of temperature (°C) along an east-west transect at 26°S for Experiment 2 on day 60.

Experiment 2, Temp Cross-section at 34S, Day 60.

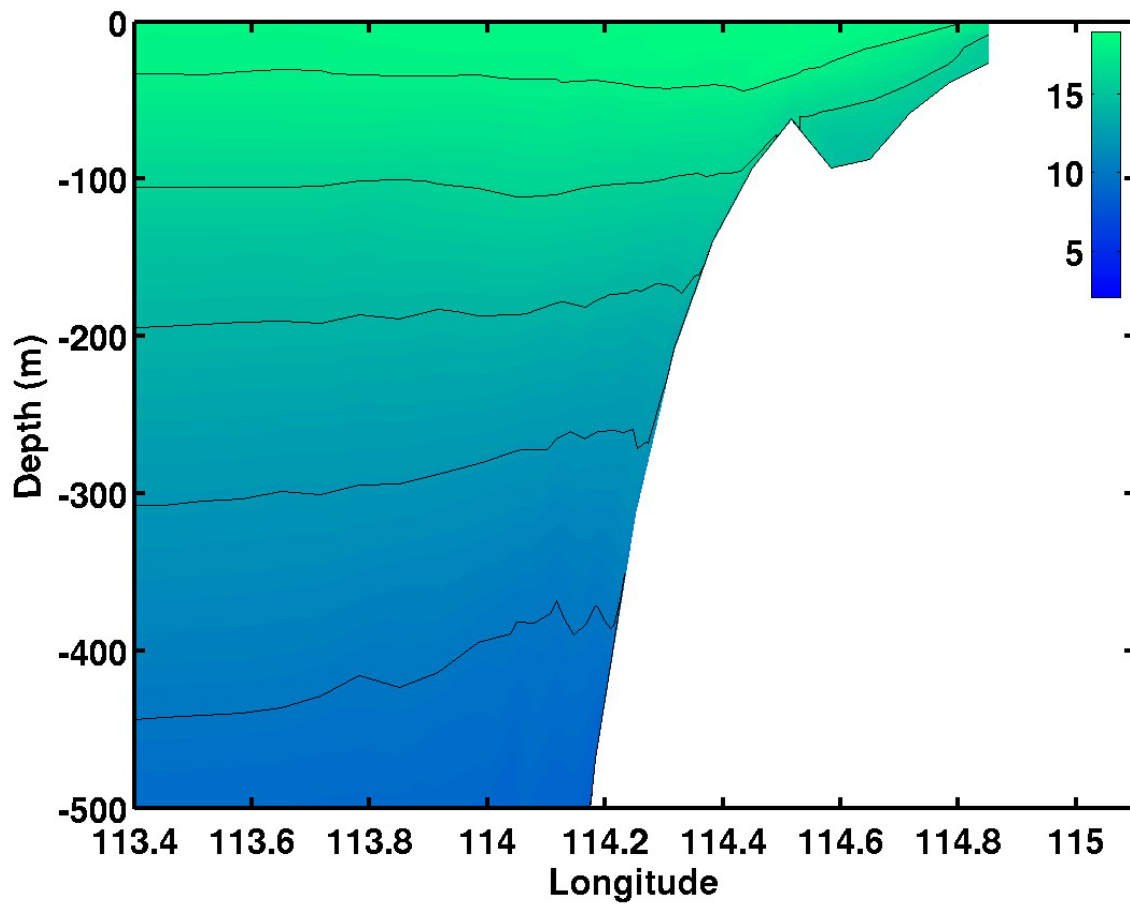


Figure 4.6e. Cross-section of temperature (°C) along an east-west transect near Cape Leeuwin (34°S) for Experiment 2 on day 60.

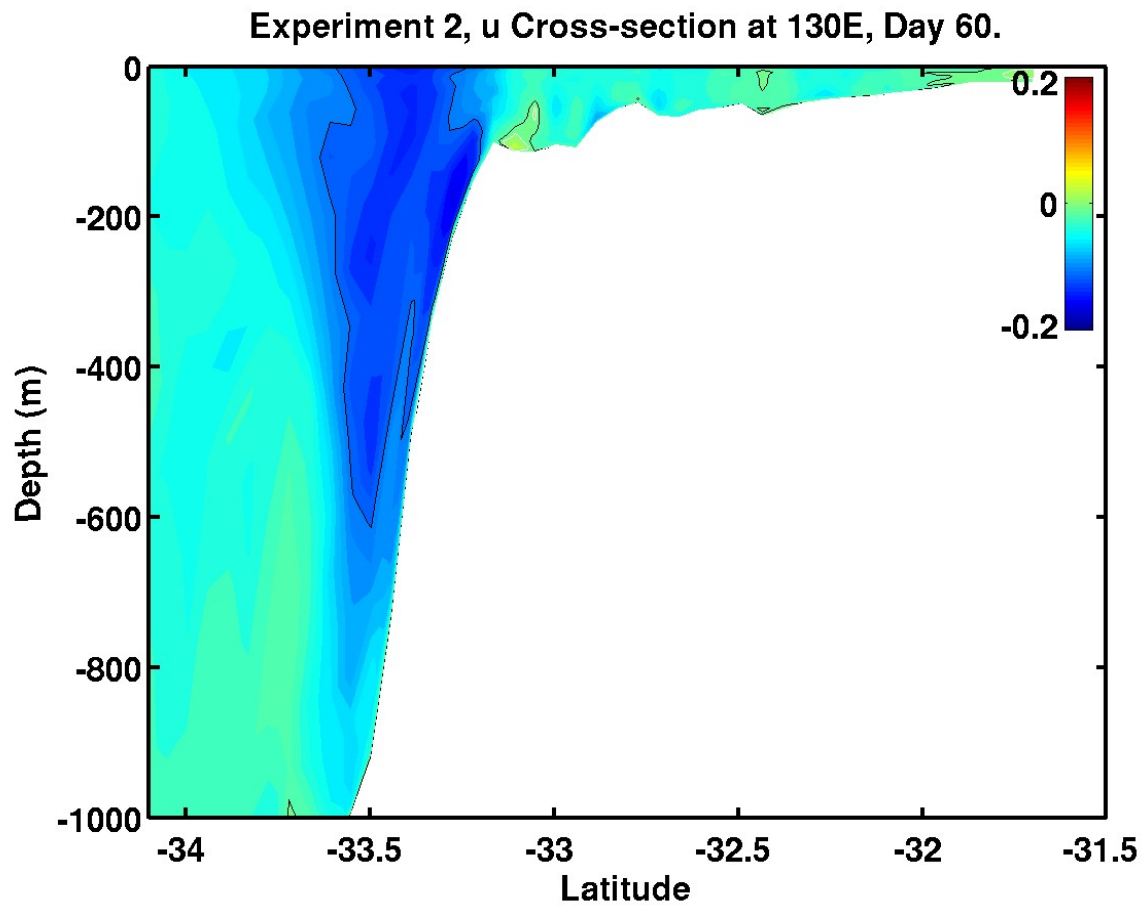


Figure 4.6f. Cross-section of zonal velocity component (m s^{-1}) in the Great Australian Bight (130°E) for Experiment 2 on day 60. Red is eastward and blue is westward. The white contour is zero.

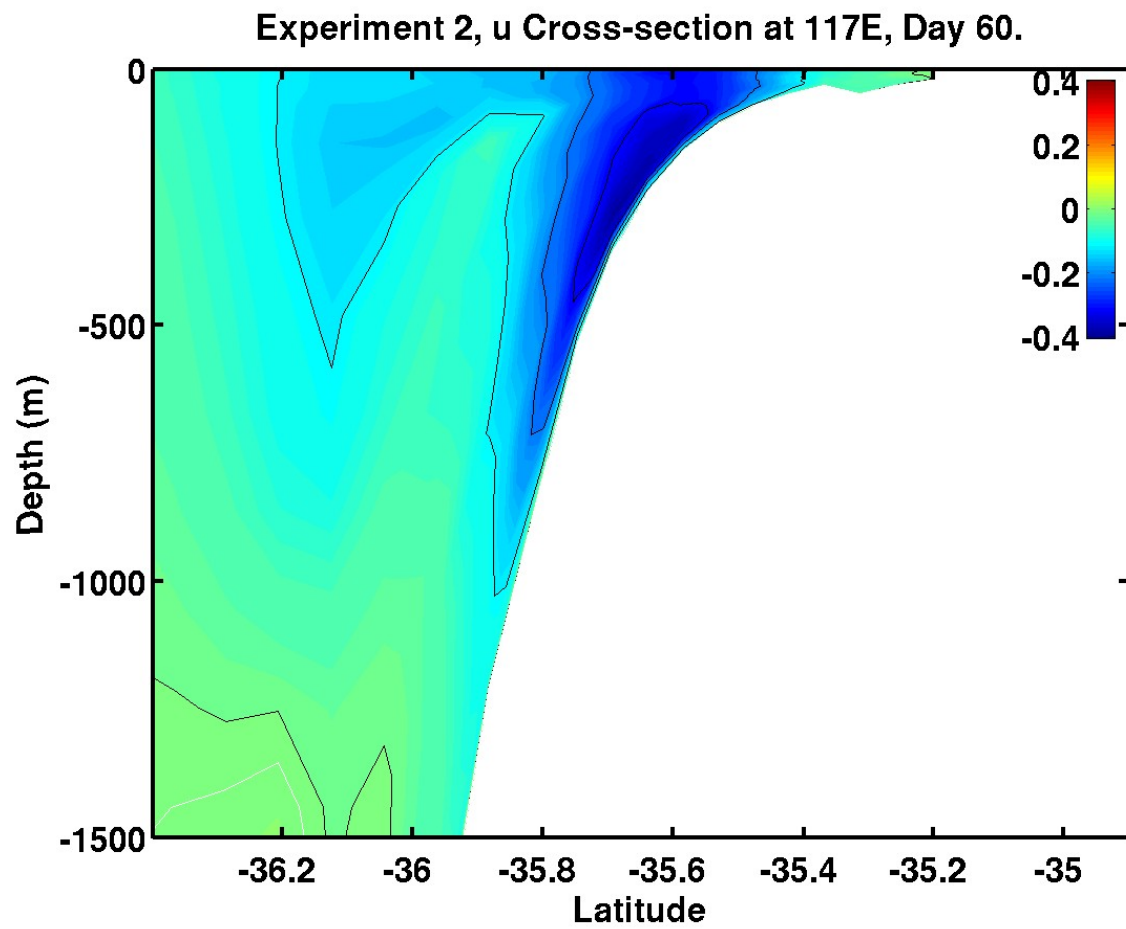


Figure 4.6g. Cross-section of zonal velocity component (m s^{-1}) at 117°E for Experiment 2 on day 60. Red is eastward and blue is westward. The white contour is zero.

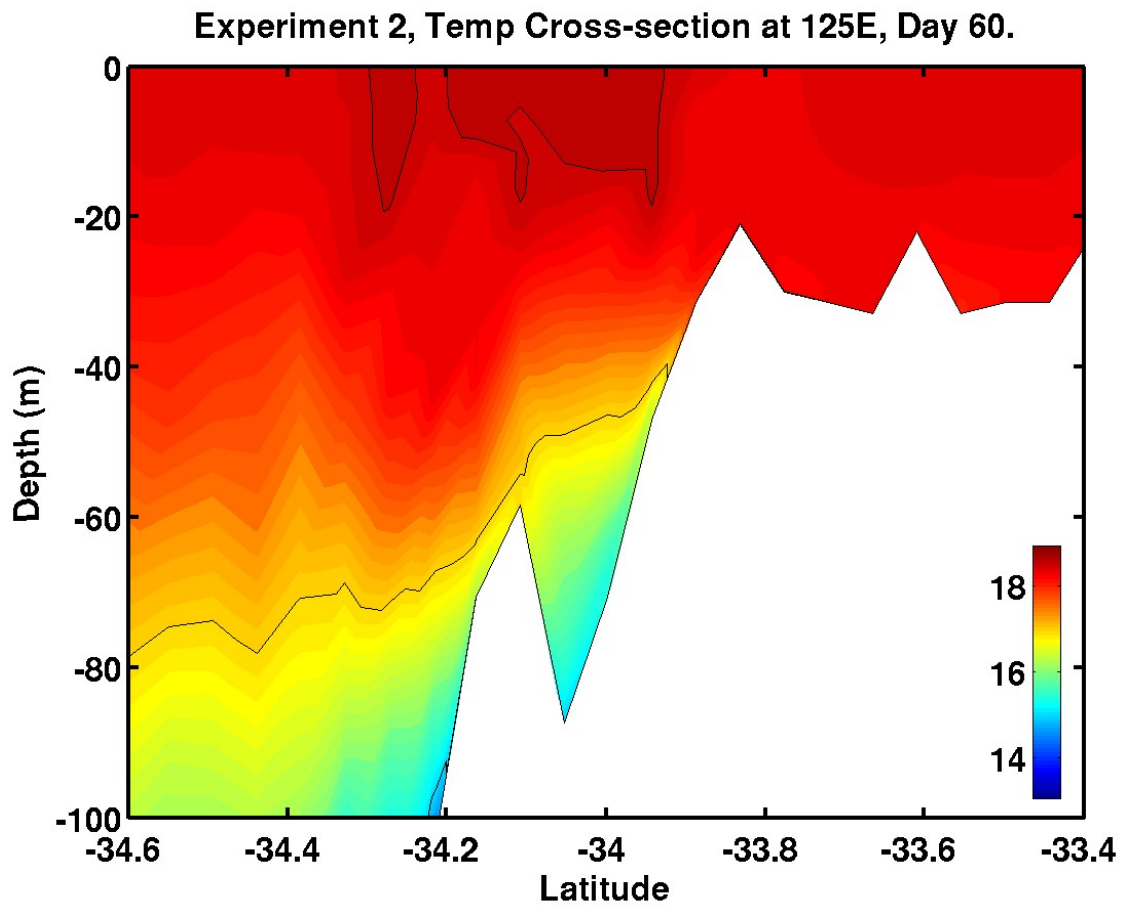


Figure 4.6h. Cross-section of temperature ($^{\circ}\text{C}$) along a north-south transect in the western Great Australian Bight (125°E) for Experiment 2 on day 60.

Experiment 3, Day 20, Surface.

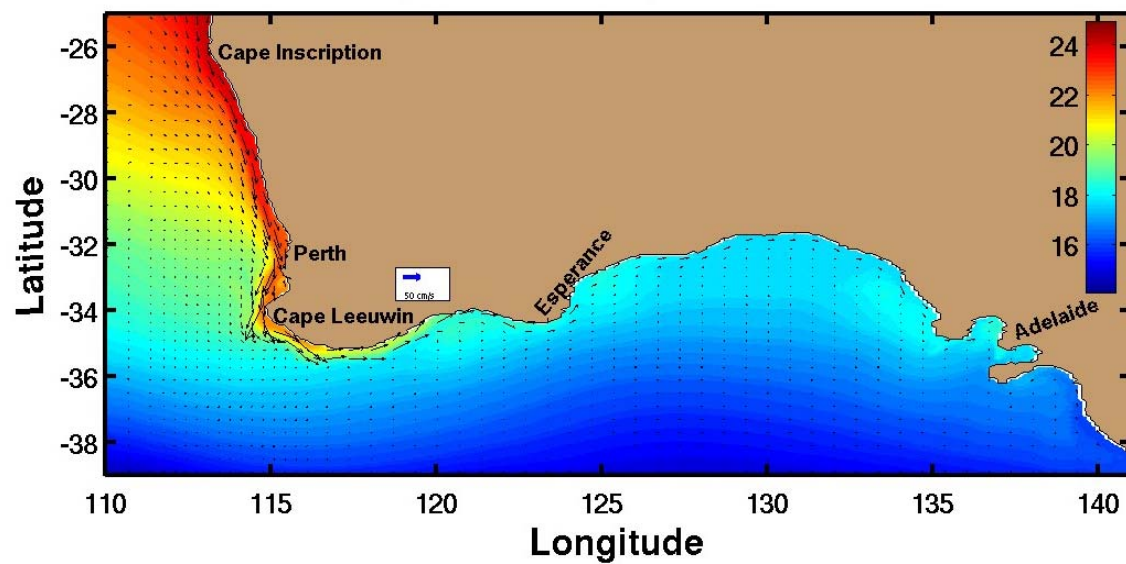


Figure 4.7a. Sea surface temperature ($^{\circ}\text{C}$) and velocity vectors for Experiment 3 on day 20.

Experiment 3, v Cross-section at 34S, Day 20.

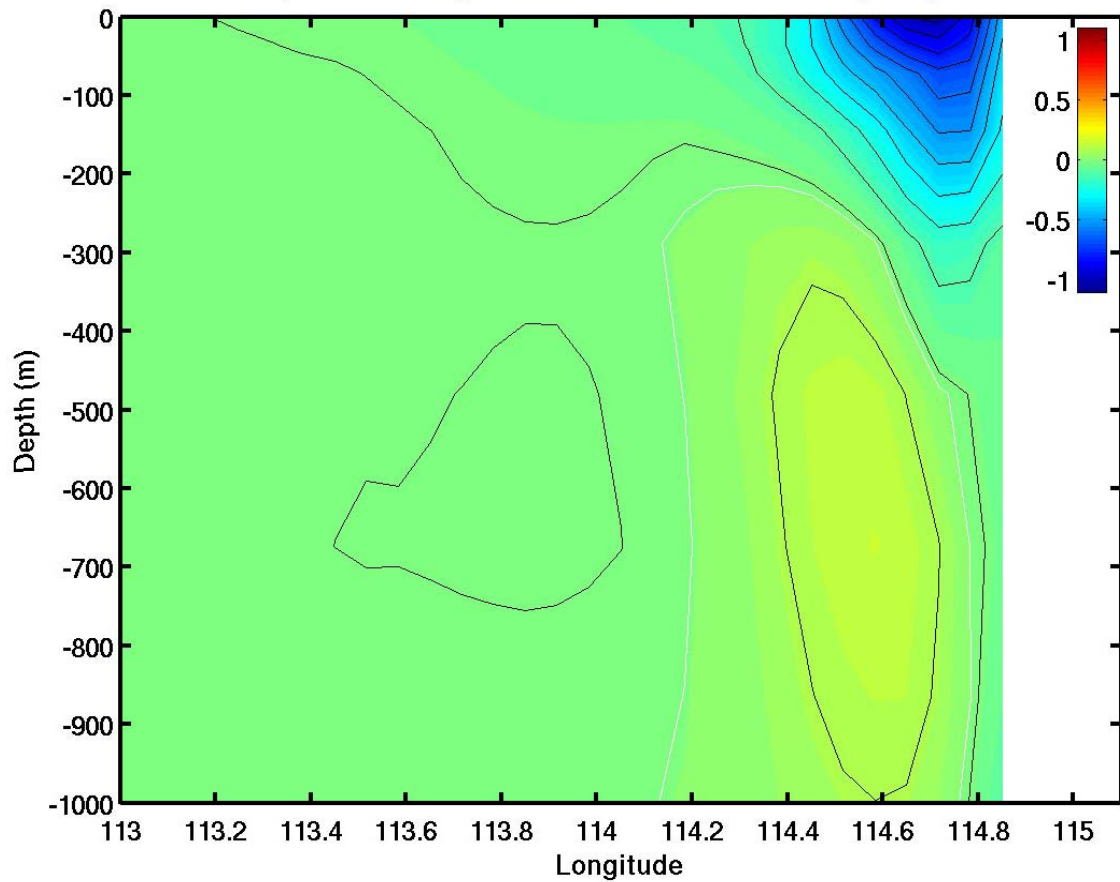


Figure 4.7b. Cross-section of meridional velocity component (m s^{-1}) near Cape Leeuwin (34°S) for Experiment 3 on day 20. Red is equatorward (north) and blue is poleward (south). The white contour is zero.

Experiment 3, Day 30, Surface.

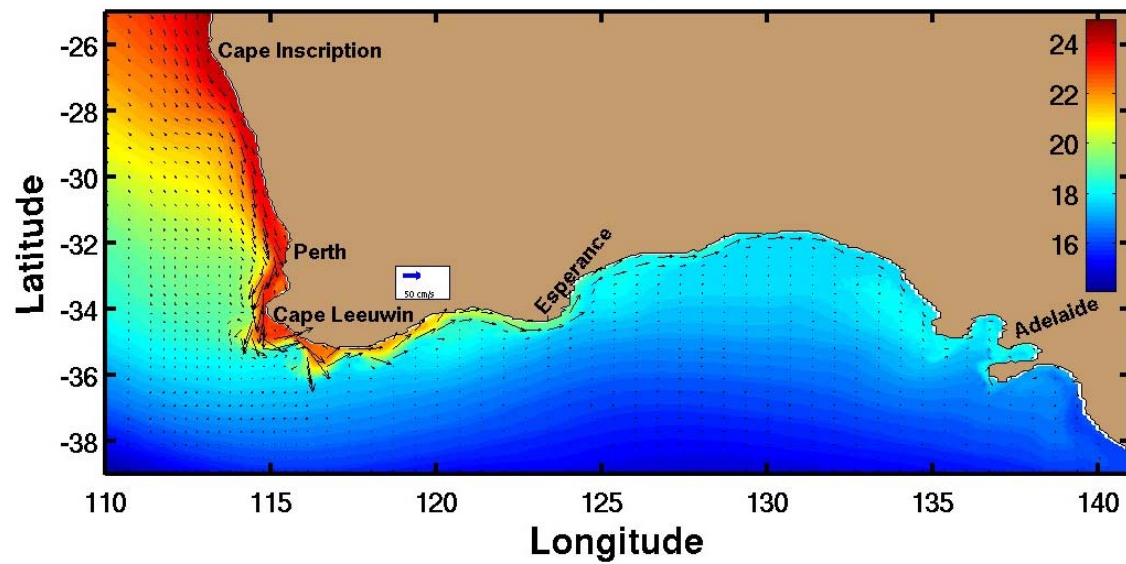


Figure 4.8a. Sea surface temperature ($^{\circ}\text{C}$) and velocity vectors for Experiment 3 on day 30.

Experiment 3, Temp Cross-section at 34S, Day 30.

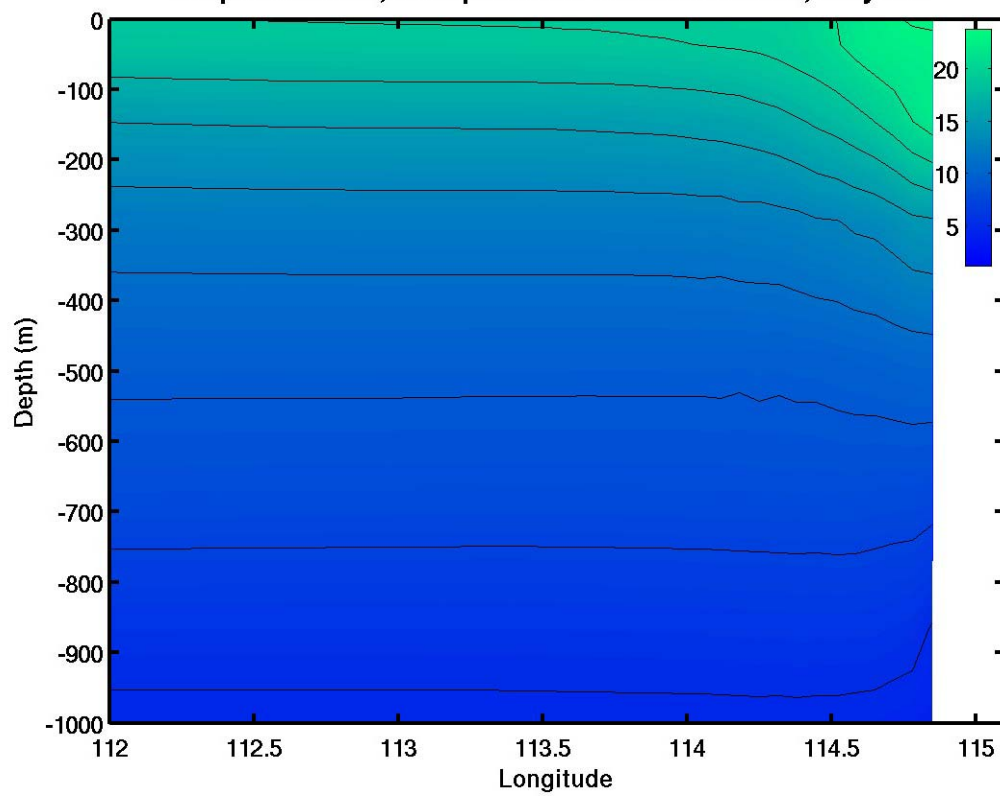


Figure 4.8b. Cross-section of temperature (°C) along an east-west transect near Cape Leeuwin (34°S) for Experiment 3 on day 30.

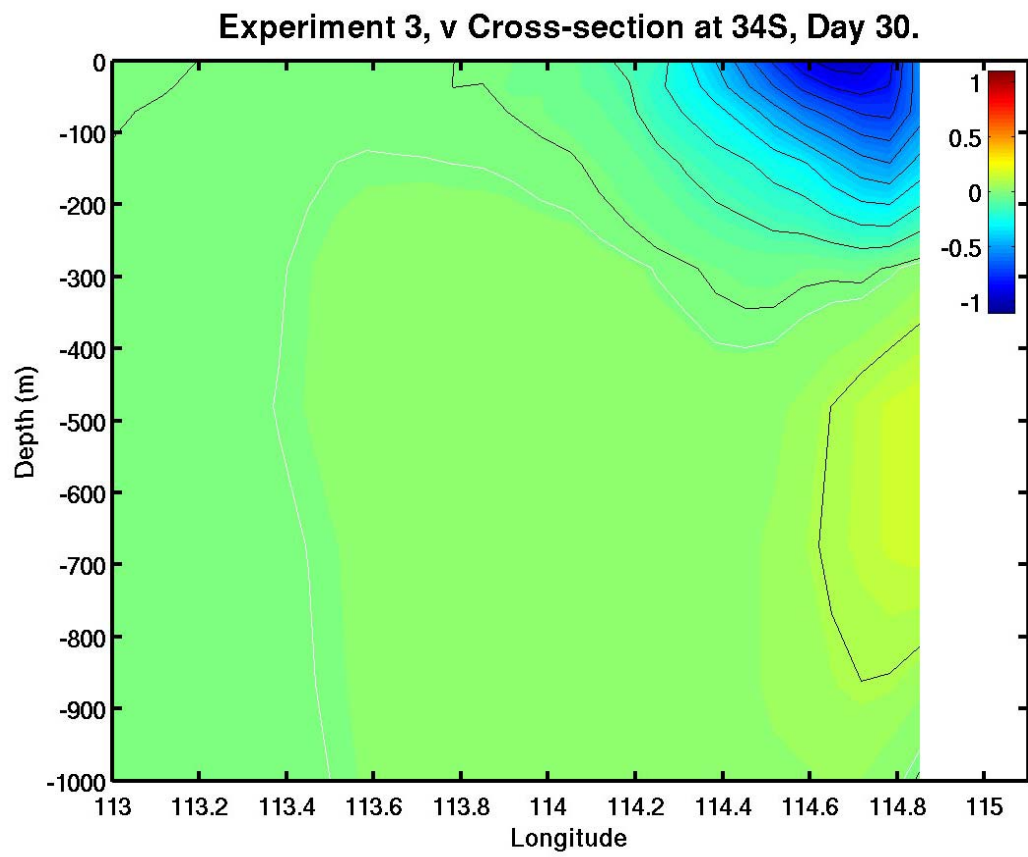


Figure 4.8c. Cross-section of meridional velocity component (m s^{-1}) near Cape Leeuwin (34°S) for Experiment 3 on day 30. Red is equatorward (north) and blue is poleward (south). The white contour is zero.

Experiment 3, u Cross-section at 130E, Day 30.

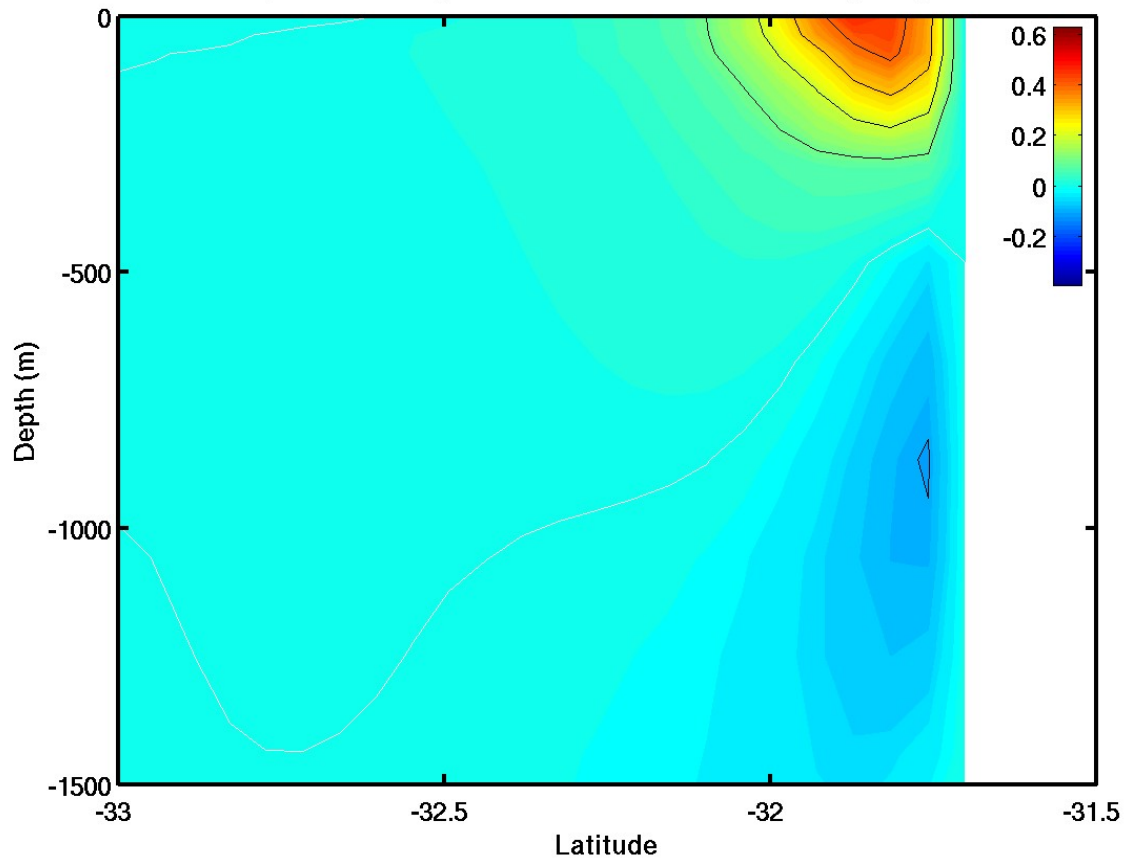


Figure 4.8d. Cross-section of temperature ($^{\circ}\text{C}$) along an north-south transect in the Great Australian Bight (130°E) for Experiment 3 on day 30.

Experiment 3, u Cross-section at 117E, Day 30.

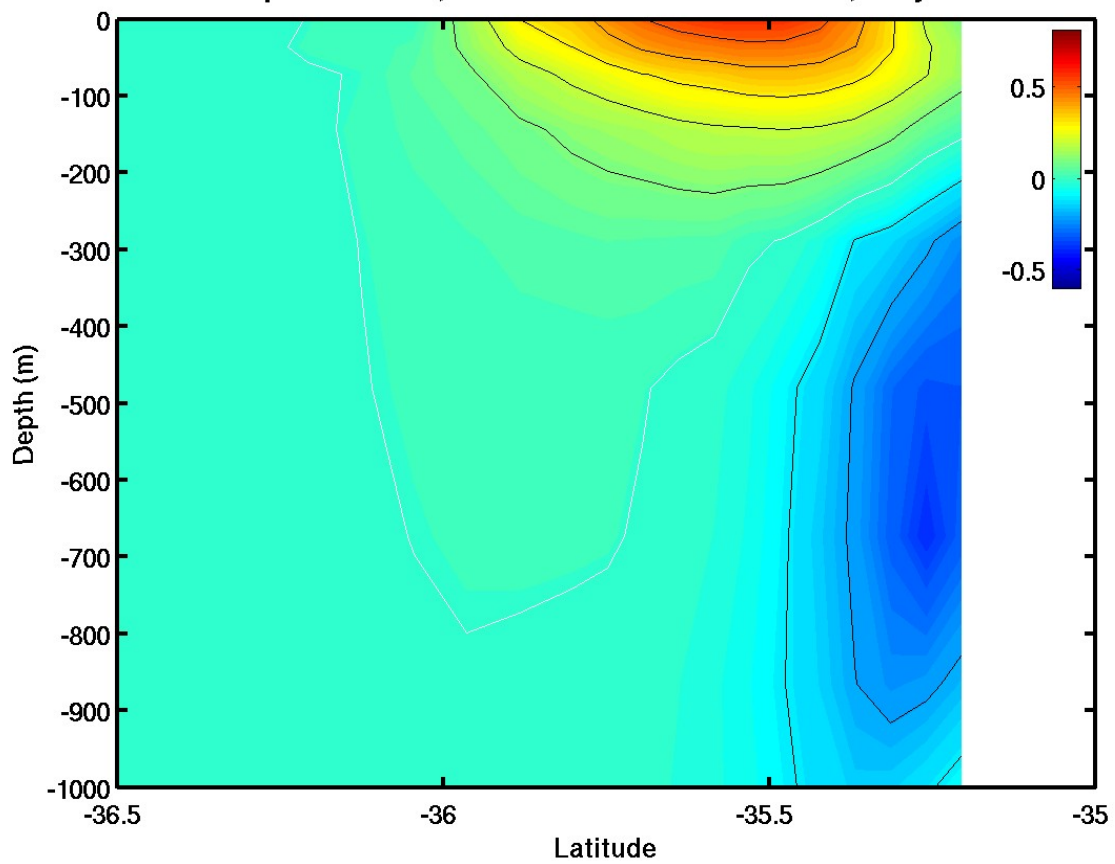


Figure 4.8e. Cross-section of zonal velocity component (m s^{-1}) at 117°E for Experiment 3 on day 30. Red is eastward and blue is westward. The white contour is zero.

Experiment 3, Day 60, Surface.

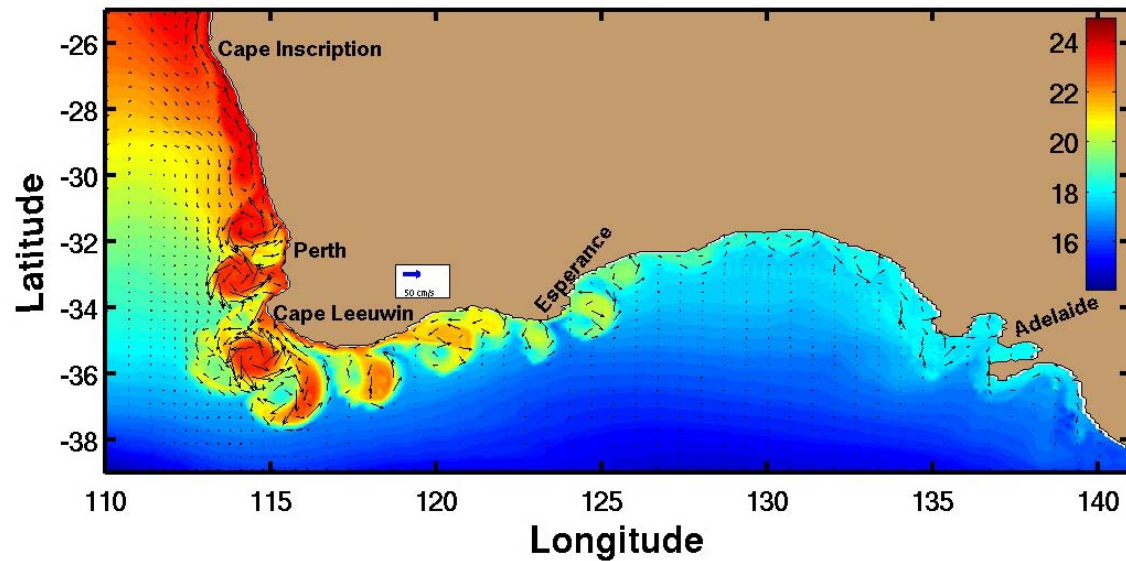


Figure 4.9. Sea surface temperature ($^{\circ}\text{C}$) and velocity vectors for Experiment 3 on day 60.

Experiment 3, Day 81, Surface.

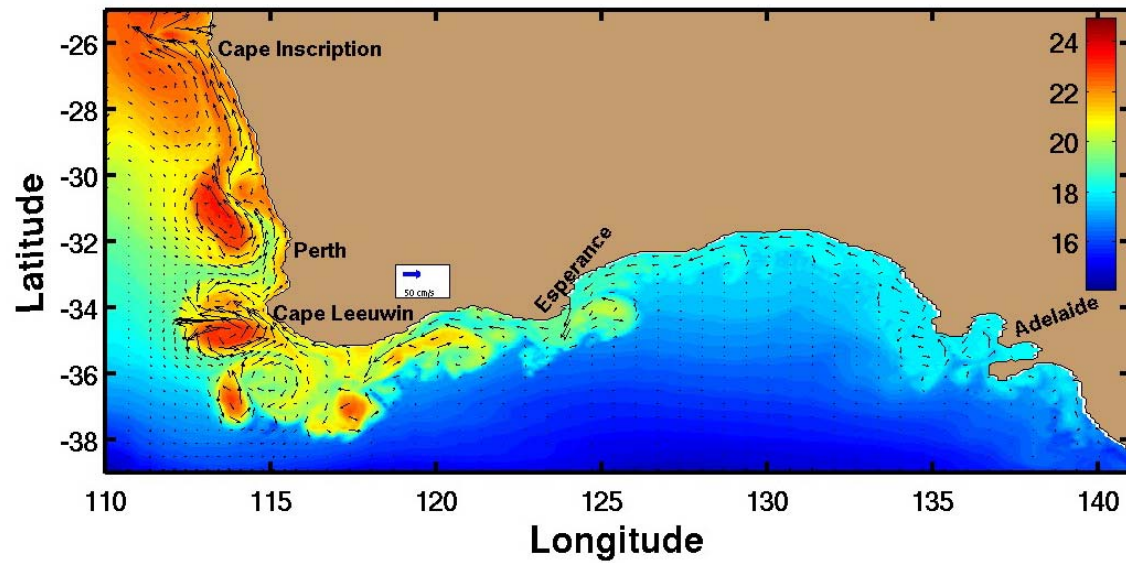


Figure 4.10. Sea surface temperature ($^{\circ}\text{C}$) and velocity vectors for Experiment 3 on day 81.

Experiment 4, Day 20, Surface.

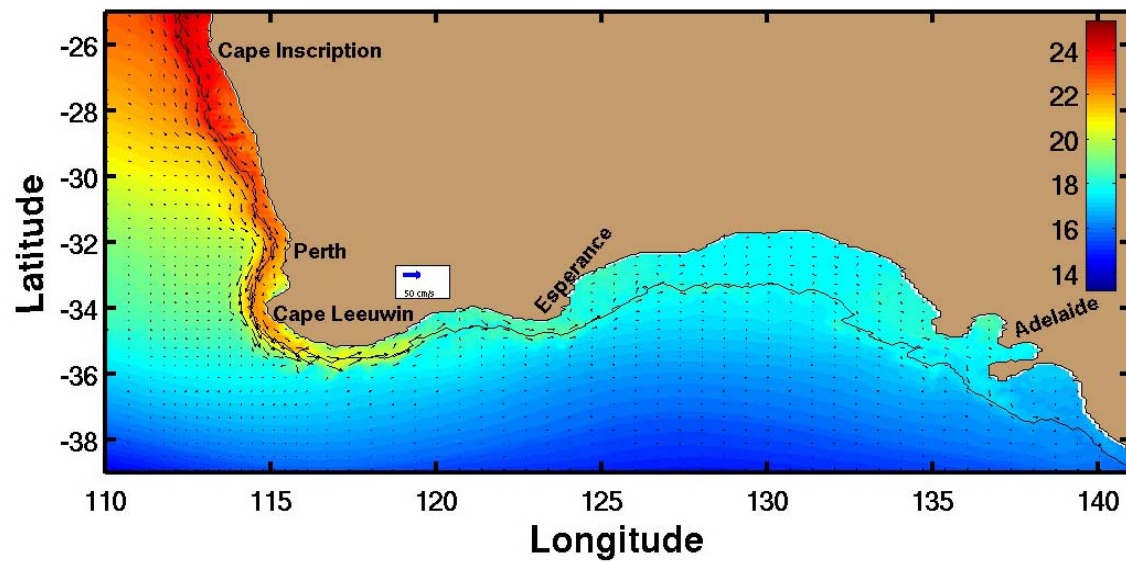


Figure 4.11a. Sea surface temperature ($^{\circ}\text{C}$) and velocity vectors for Experiment 4 on day 20.

Experiment 4, v Cross-section at 26S, Day 20.

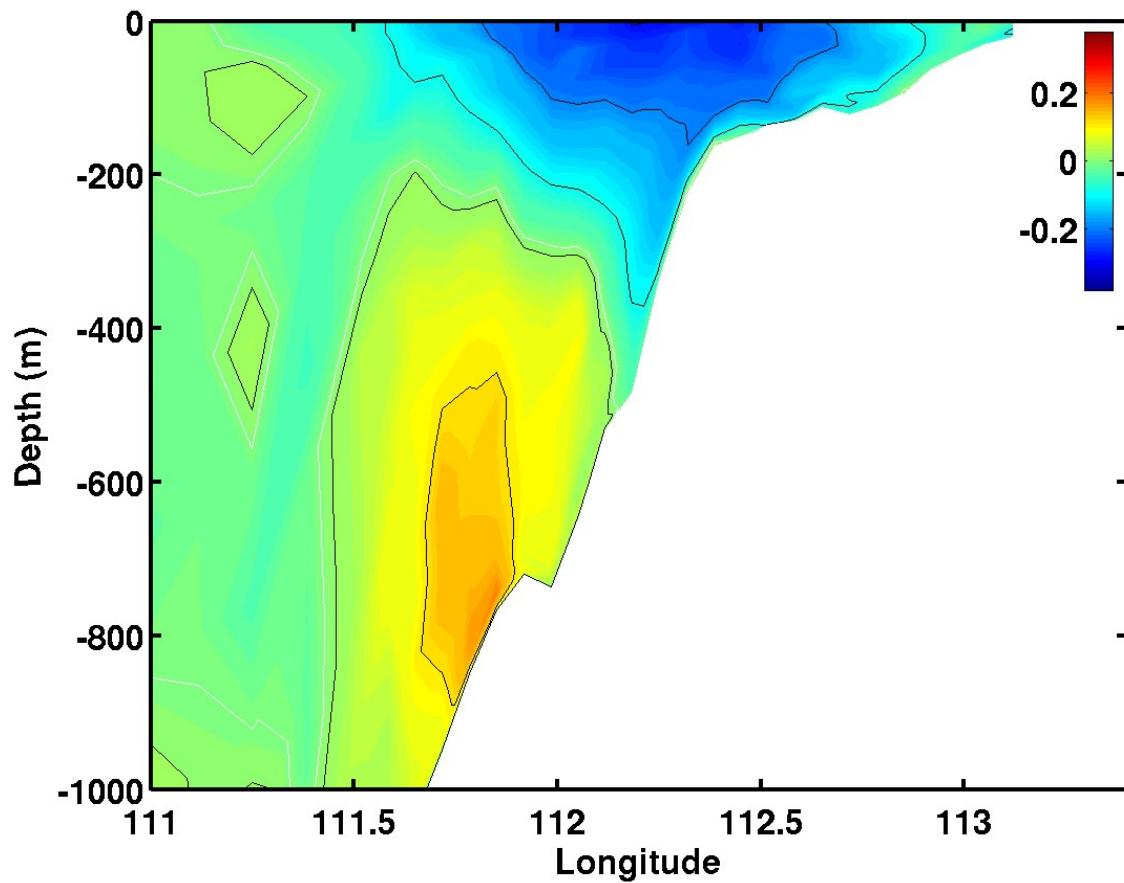


Figure 4.11b. Cross-section of meridional velocity component (m s^{-1}) at 26°S for Experiment 4 on day 20. Red is equatorward (north) and blue is poleward (south). The white contour is zero.

Experiment 4, v Cross-section at 34S, Day 20.

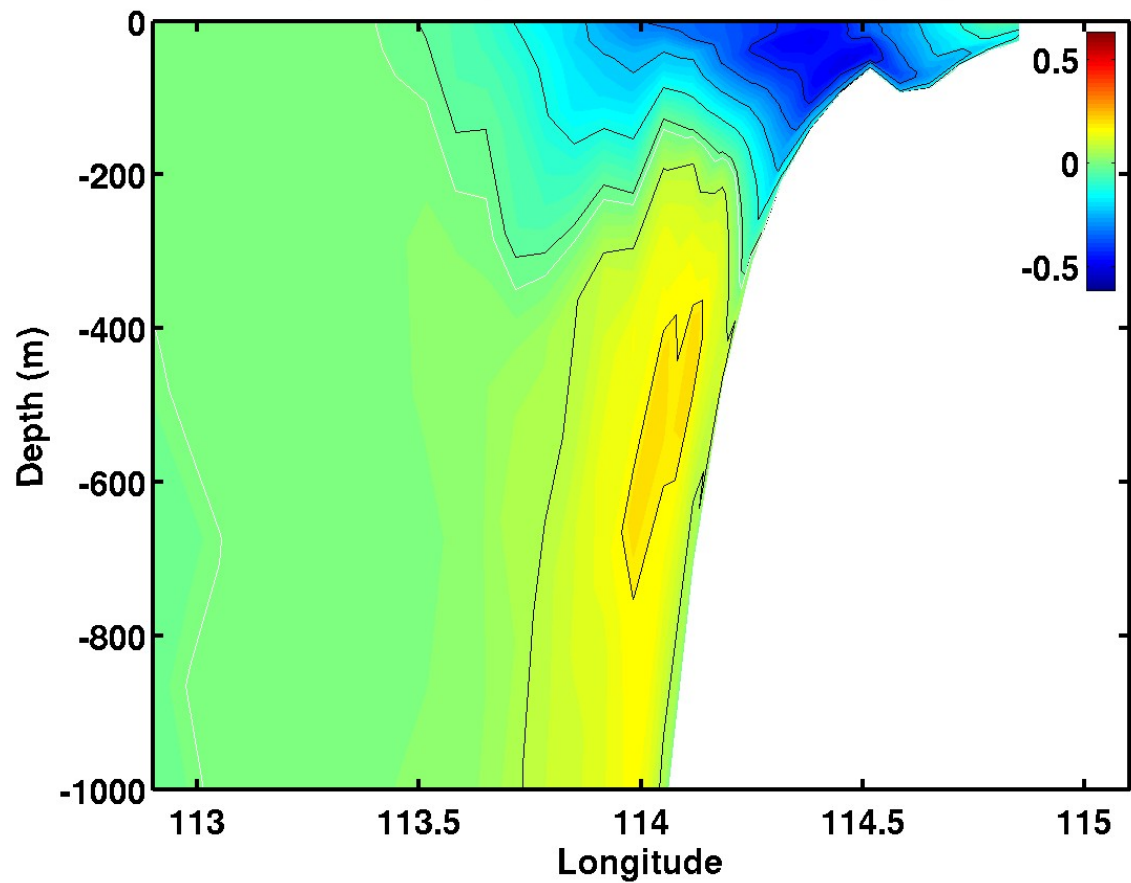


Figure 4.11c. Cross-section of meridional velocity component (m s^{-1}) near Cape Leeuwin (34°S) for Experiment 4 on day 20. Red is equatorward (north) and blue is poleward (south). The white contour is zero.

Experiment 4, u Cross-section at 130°E, Day 20.

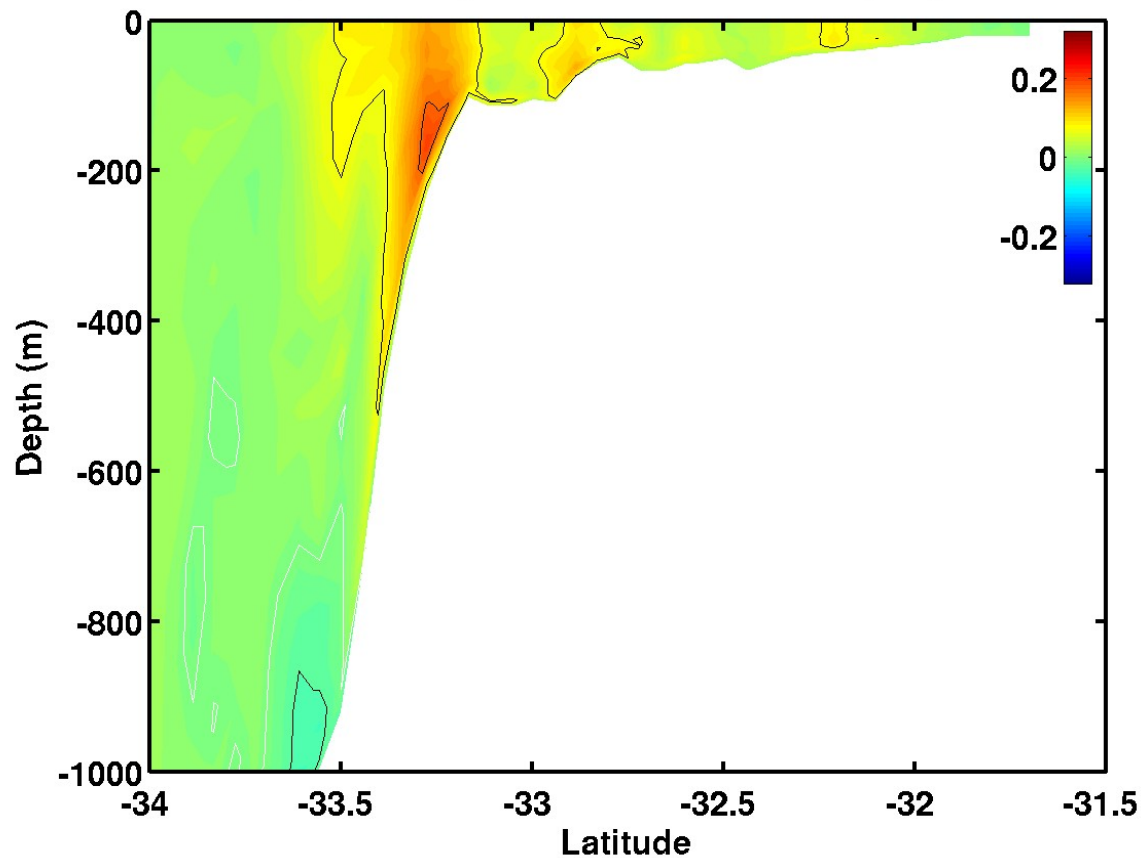


Figure 4.11d. Cross-section of zonal velocity component (m s^{-1}) in the Great Australian Bight (130°E) for Experiment 4 on day 20. Red is eastward and blue is westward. The white contour is zero.

Experiment 4, Temp Cross-section at 117E, Day 20.

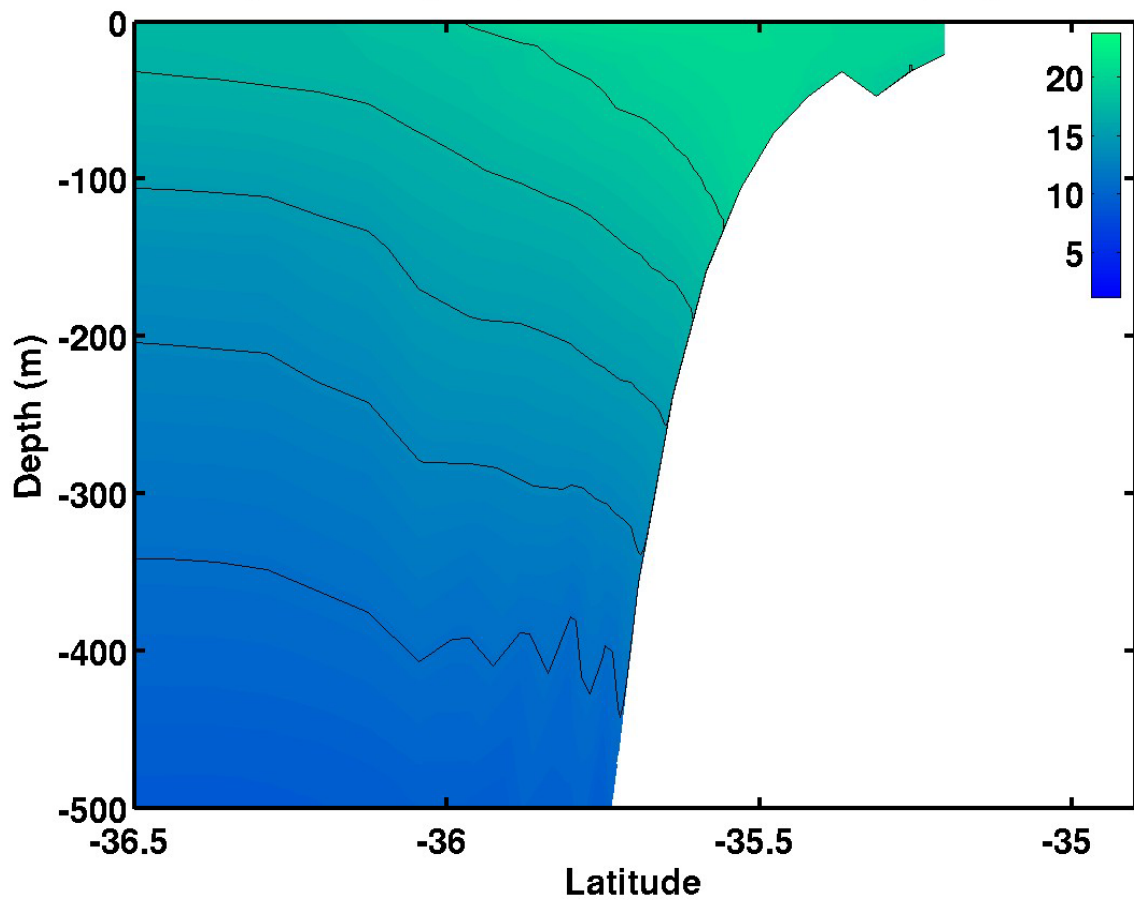


Figure 4.11e. Cross-section of temperature (°C) along a north-south transect at 117°E for Experiment 4 on day 20.

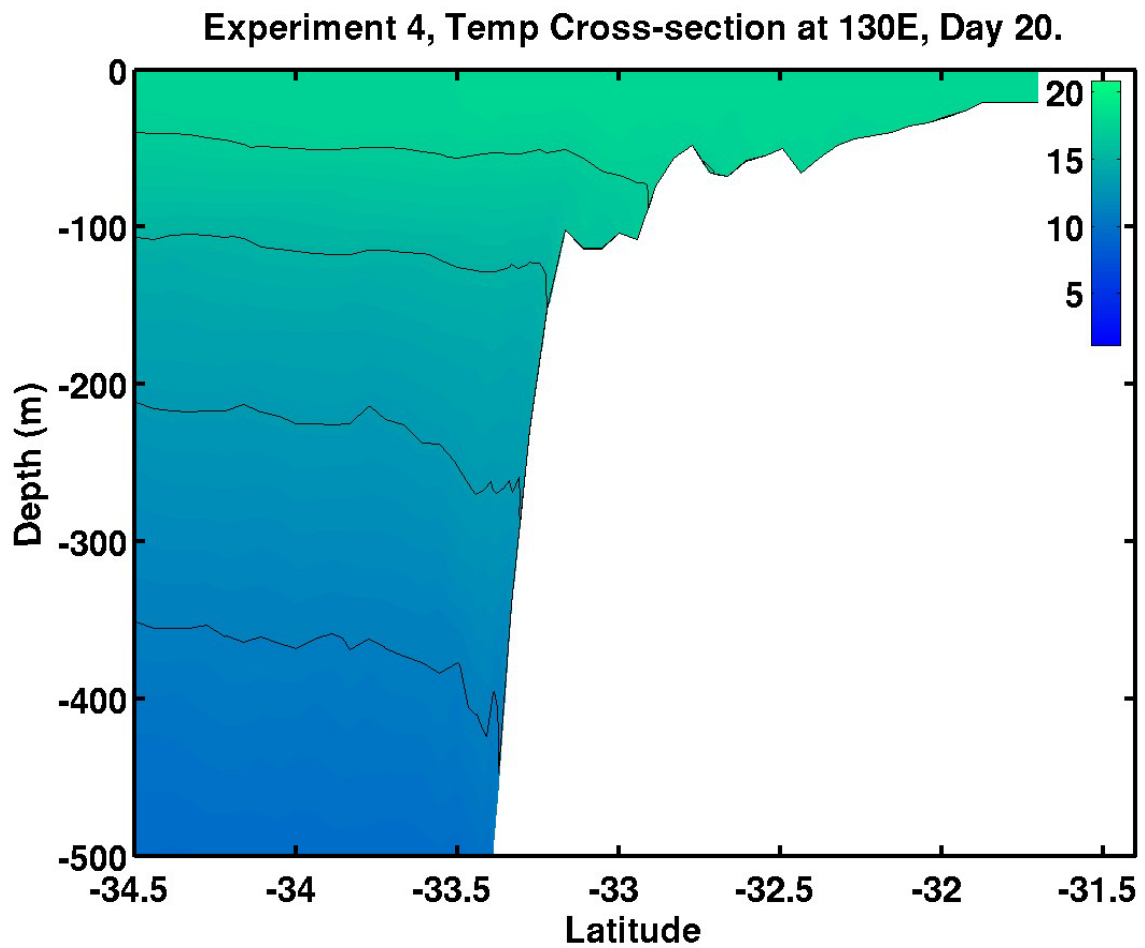


Figure 4.11f. Cross-section of temperature ($^{\circ}\text{C}$) along an north-south transect in the Great Australian Bight (130°E) for Experiment 4 on day 20.

Experiment 4, Day 30, Surface.

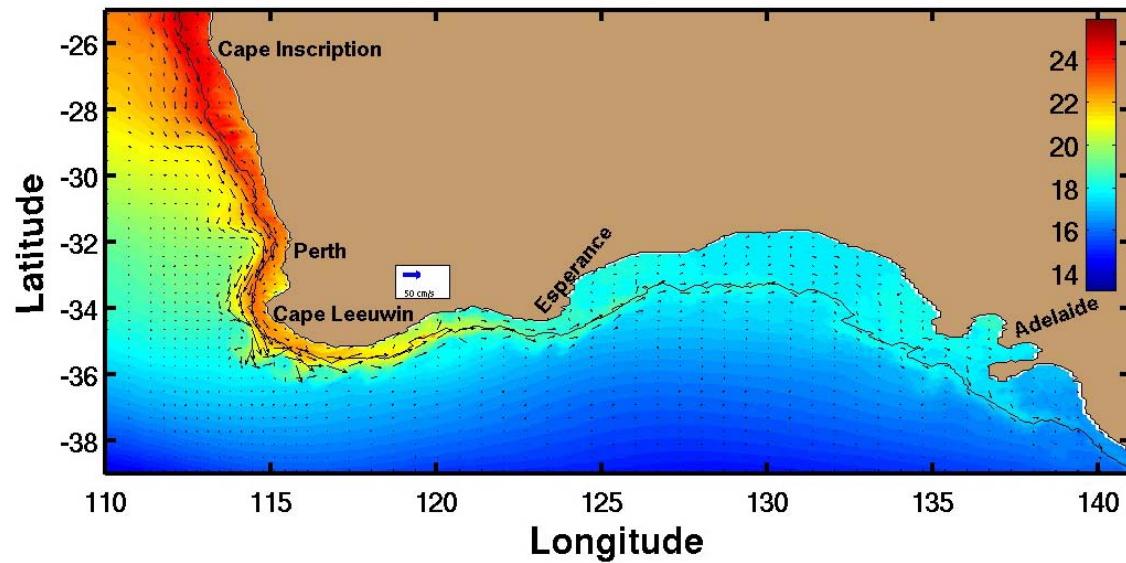


Figure 4.12a. Sea surface temperature ($^{\circ}\text{C}$) and velocity vectors for Experiment 4 on day 30.

Experiment 4, v Cross-section at 26S, Day 30.

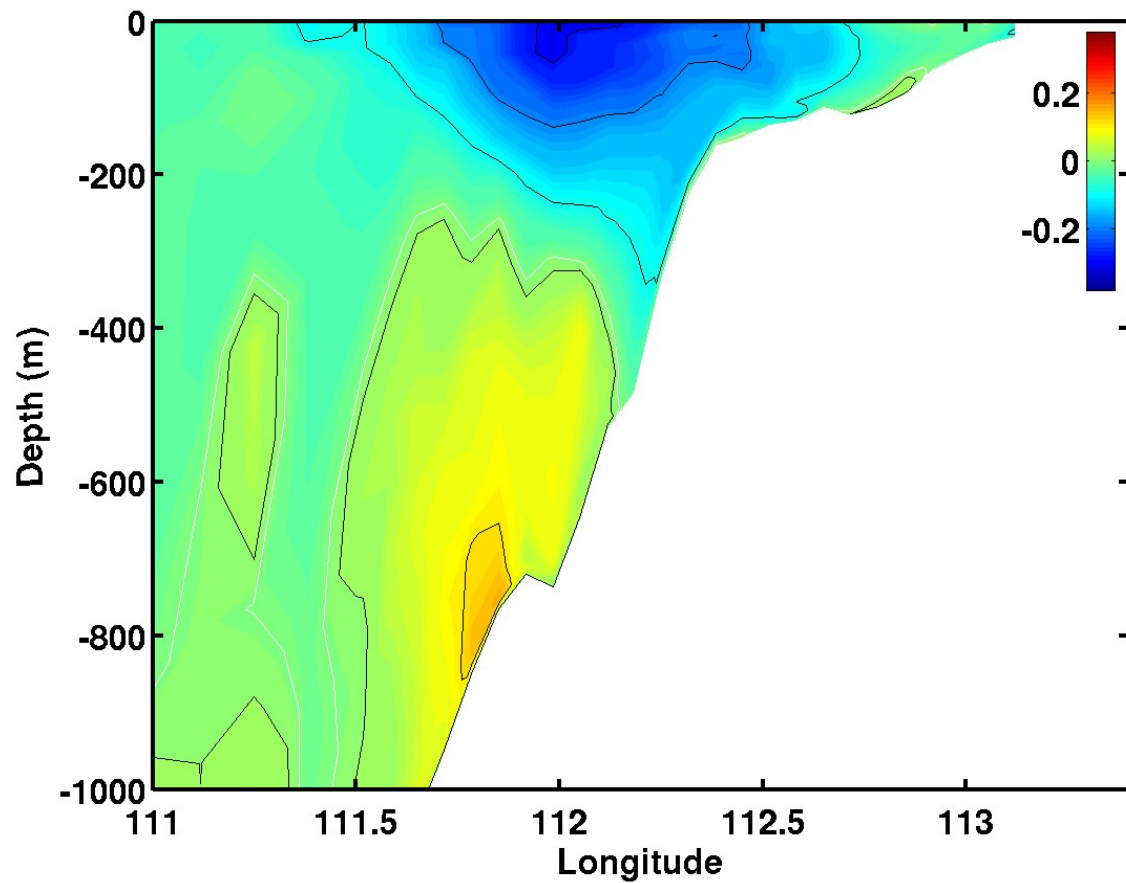


Figure 4.12b. Cross-section of meridional velocity component (m s^{-1}) at 26°S for Experiment 4 on day 30. Red is equatorward (north) and blue is poleward (south). The white contour is zero.

Experiment 4, v Cross-section at 34S, Day 30.

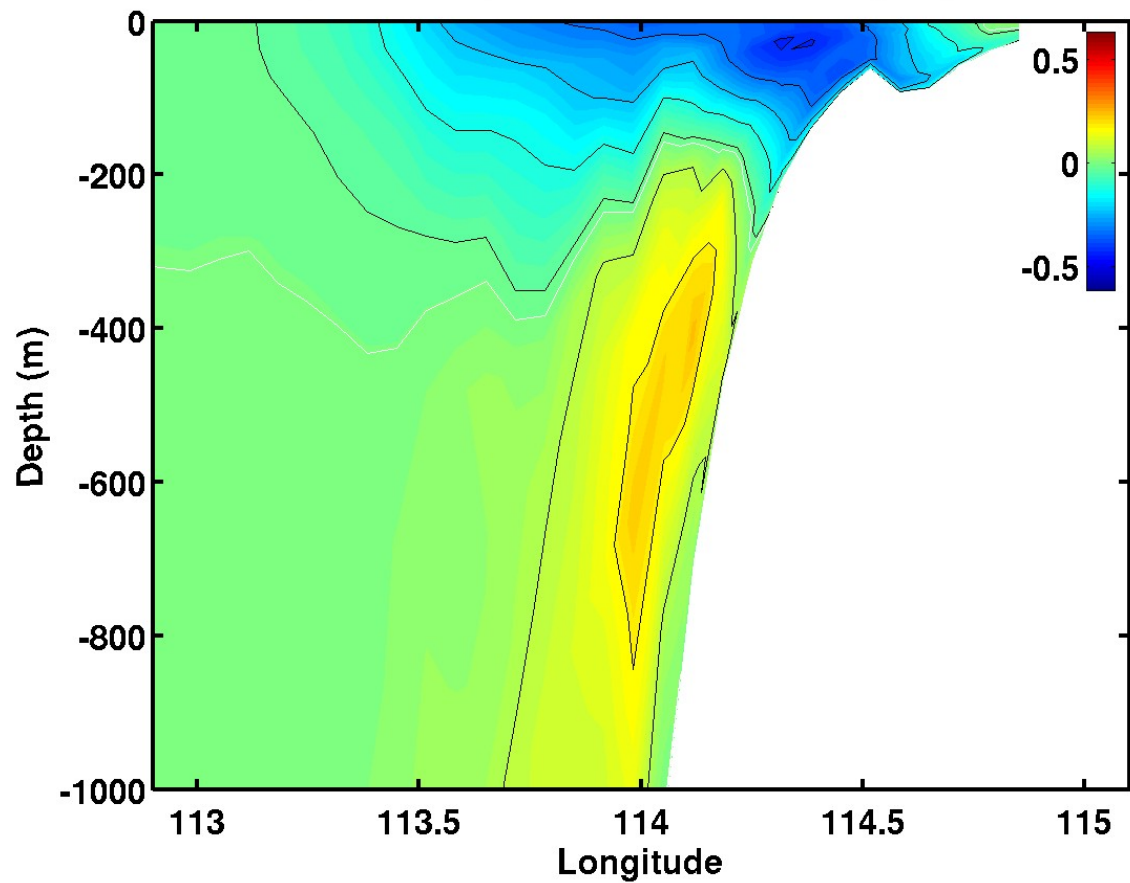


Figure 4.12c. Cross-section of meridional velocity component (m s^{-1}) near Cape Leeuwin (34°S) for Experiment 4 on day 30. Red is equatorward (north) and blue is poleward (south). The white contour is zero.

Experiment 4, Temp Cross-section at 26S, Day 30.

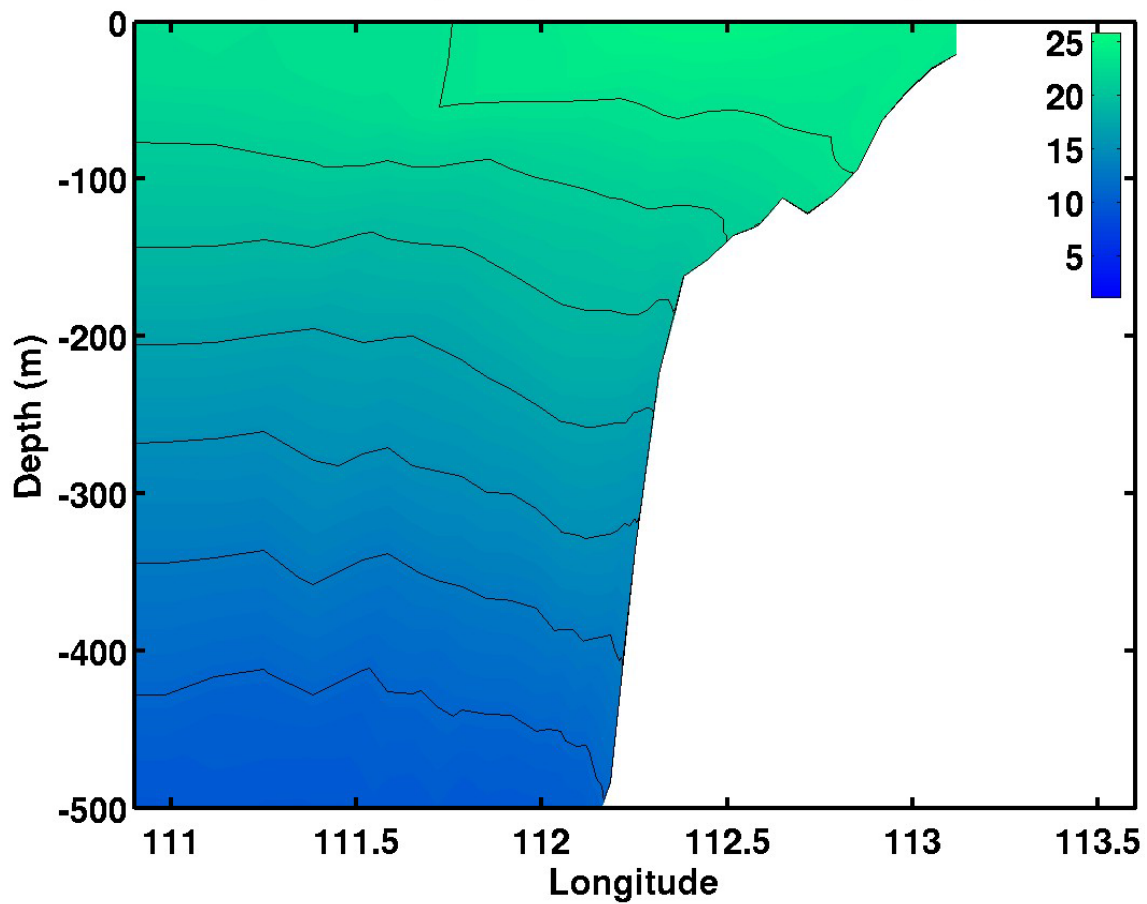


Figure 4.12d. Cross-section of temperature (°C) along an east-west transect at 26°S for Experiment 4 on day 30.

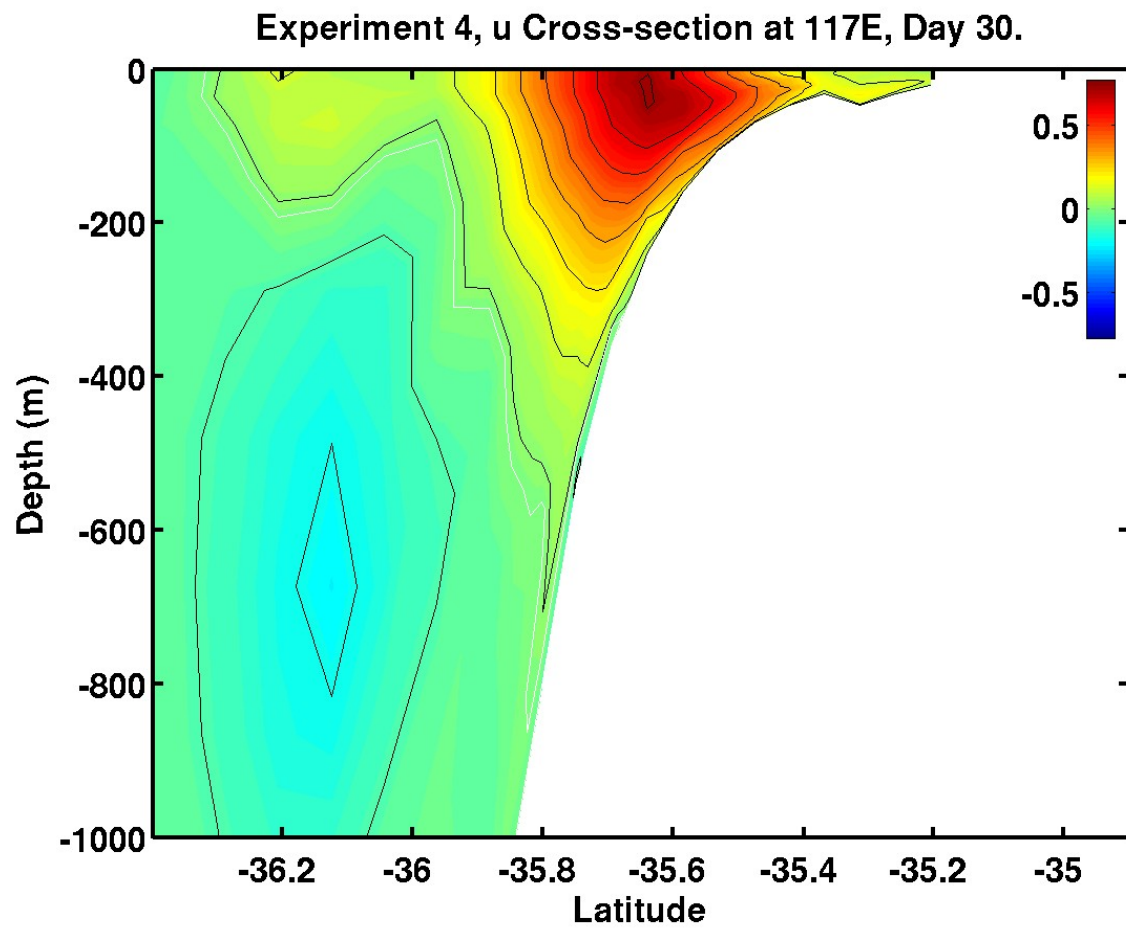


Figure 4.12e. Cross-section of zonal velocity component (m s^{-1}) at 117°E for Experiment 4 on day 30. Red is eastward and blue is westward. The white contour is zero.

Experiment 4, u Cross-section at 130E, Day 30.

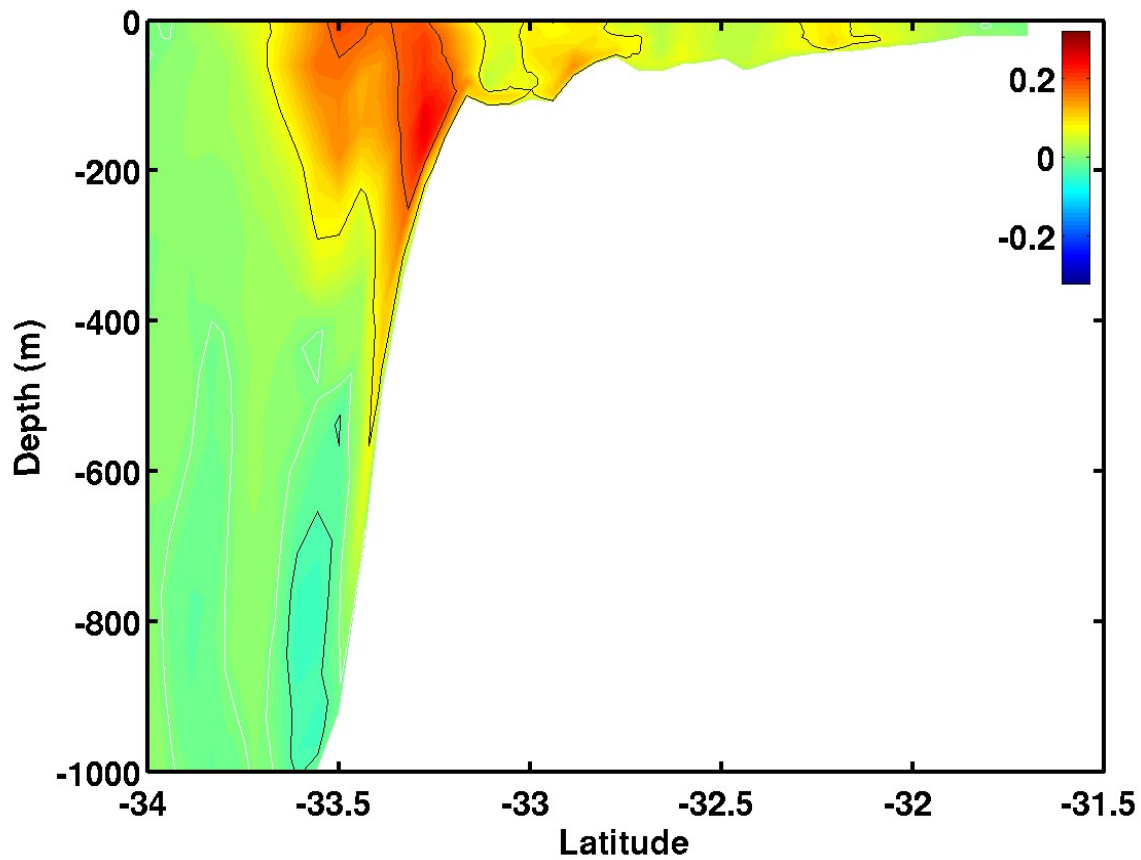


Figure 4.12f. Cross-section of zonal velocity component (m s^{-1}) in the Great Australian Bight (130°E) for Experiment 4 on day 30. Red is eastward and blue is westward. The white contour is zero.

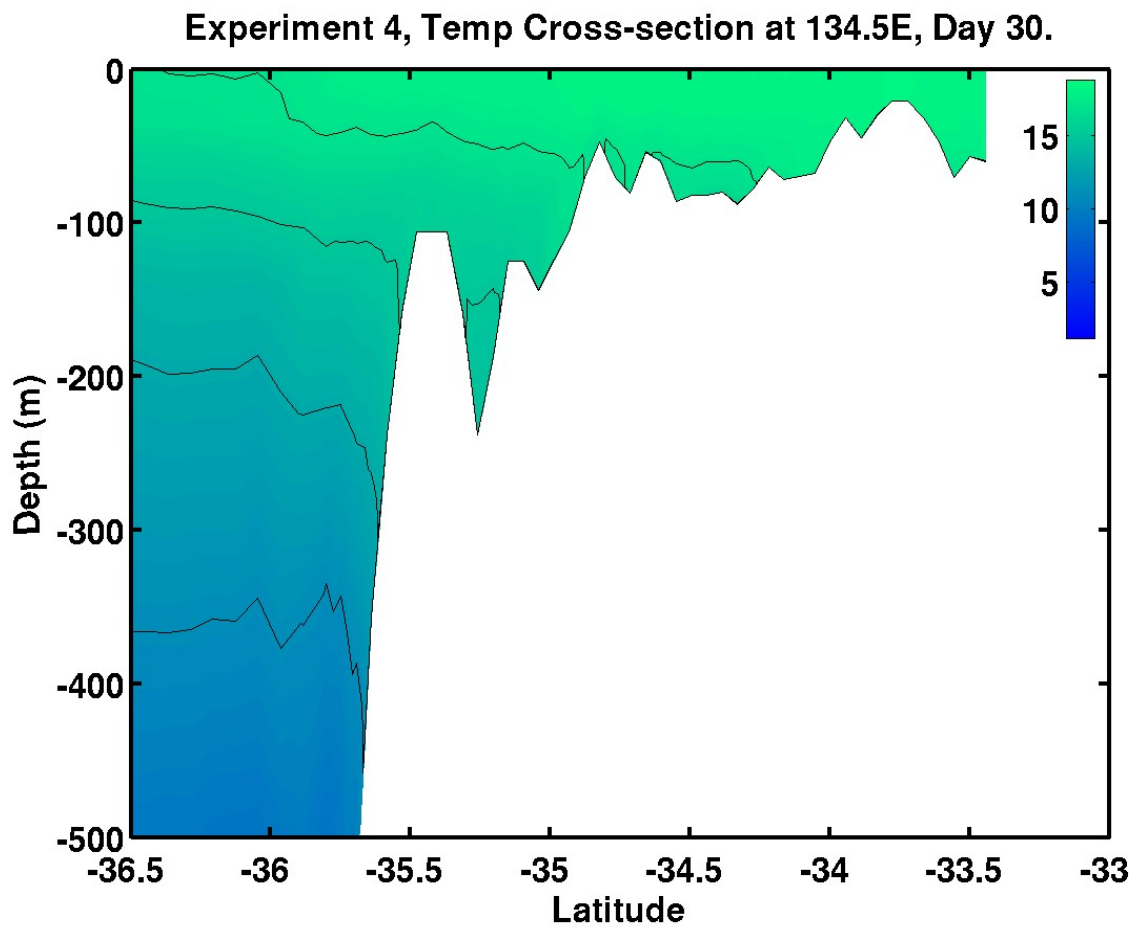


Figure 4.12g. Cross-section of temperature ($^{\circ}\text{C}$) along a north-south transect in the eastern Great Australian Bight (134.5°E) for Experiment 4 on day 30.

Experiment 4, Temp Cross-section at 117E, Day 30.

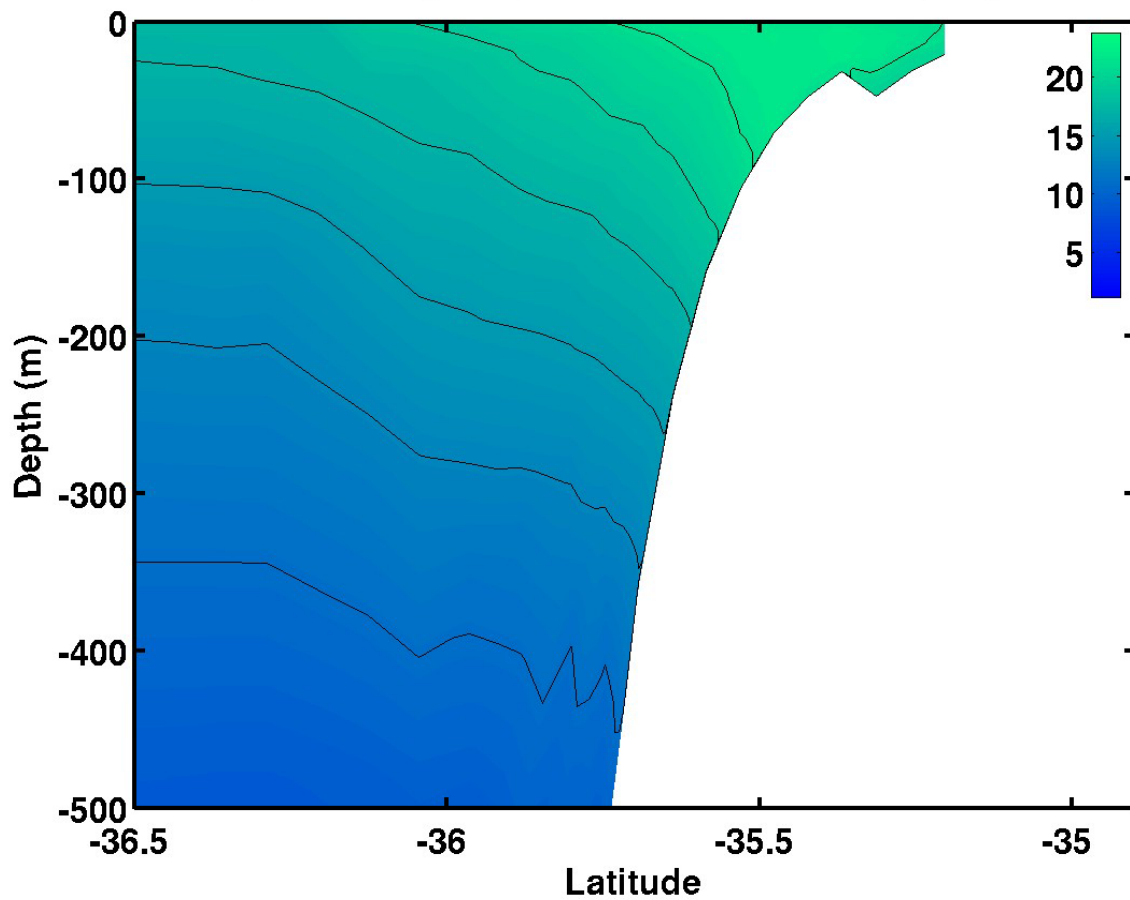


Figure 4.12h. Cross-section of temperature (°C) along a north-south transect at 117°E for Experiment 4 on day 30.

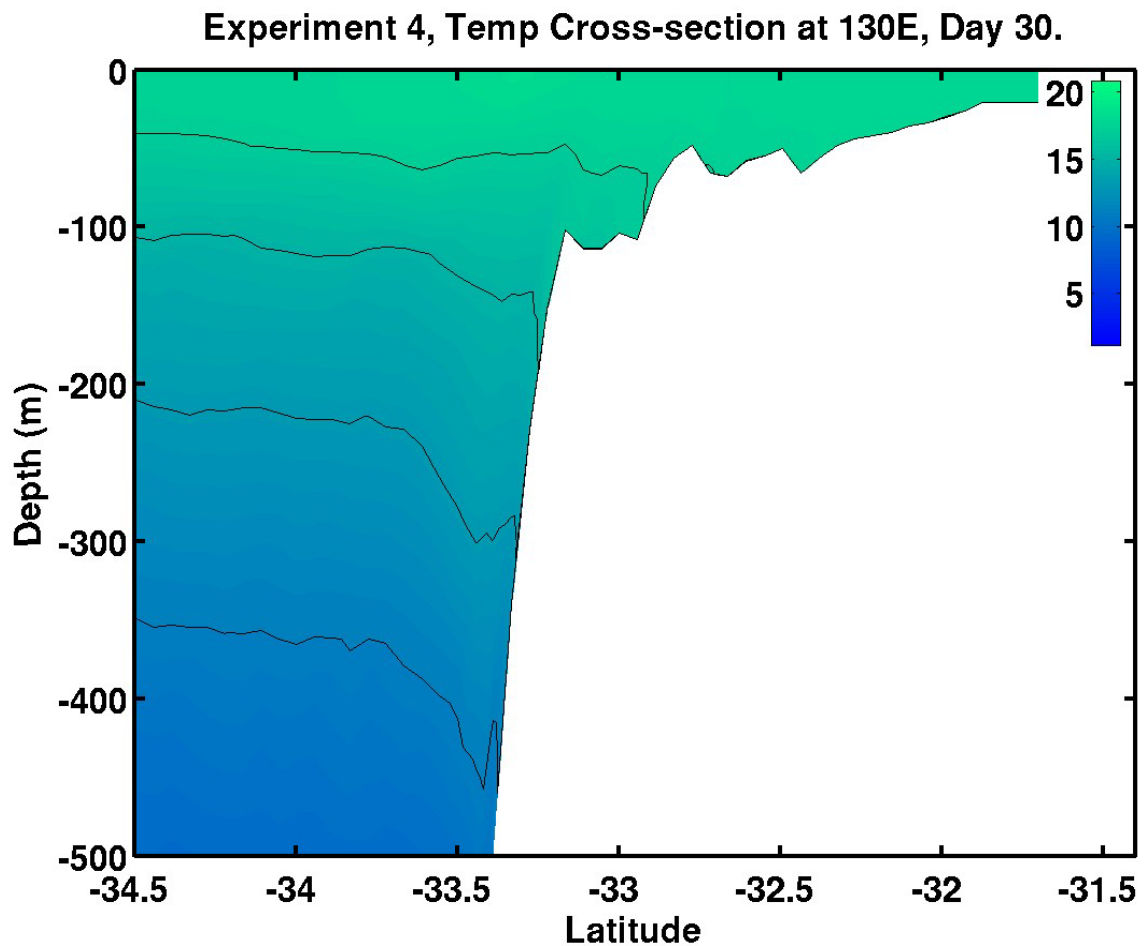


Figure 4.12i. Cross-section of temperature ($^{\circ}\text{C}$) along a north-south transect in the Great Australian Bight (130°E) for Experiment 4 on day 30.

Experiment 4, Day 60, Surface.

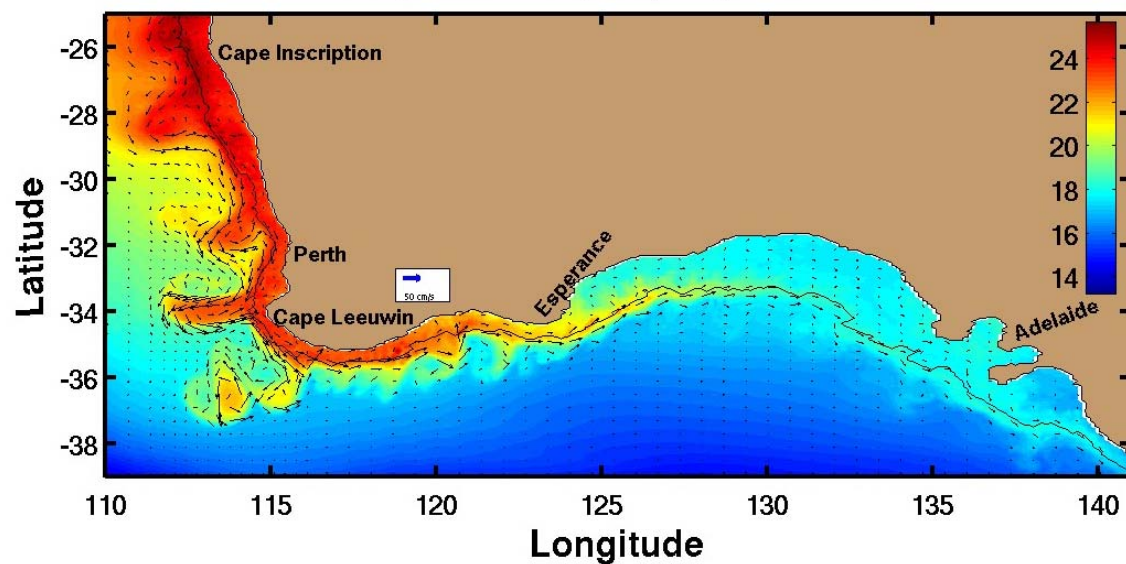


Figure 4.13. Sea surface temperature ($^{\circ}\text{C}$) and velocity vectors for Experiment 4 on day 60.

Experiment 4, Day 72, Surface.

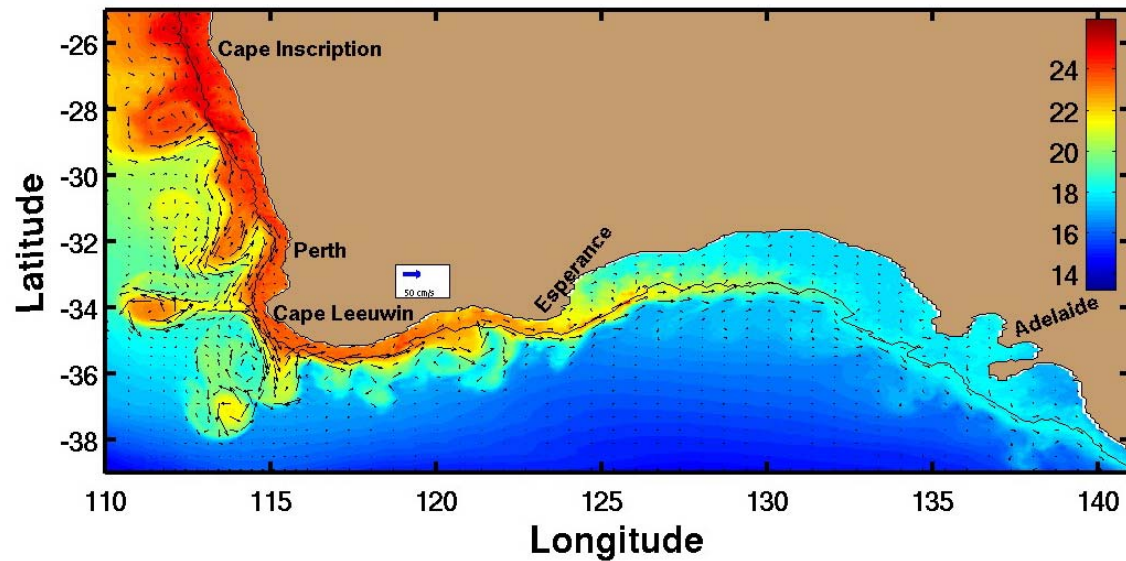


Figure 4.14. Sea surface temperature ($^{\circ}\text{C}$) and velocity vectors for Experiment 4 on day 72.

Experiment 5, Day 20, Surface.

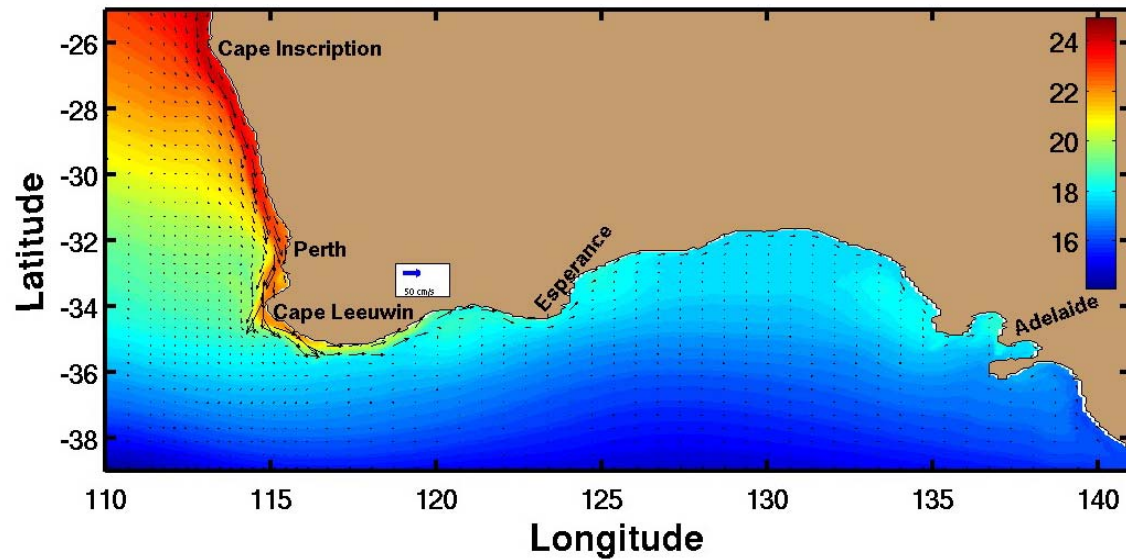


Figure 4.15a. Sea surface temperature ($^{\circ}\text{C}$) and velocity vectors for Experiment 5 on day 20.

Experiment 5, v Cross-section at 26S, Day 20.

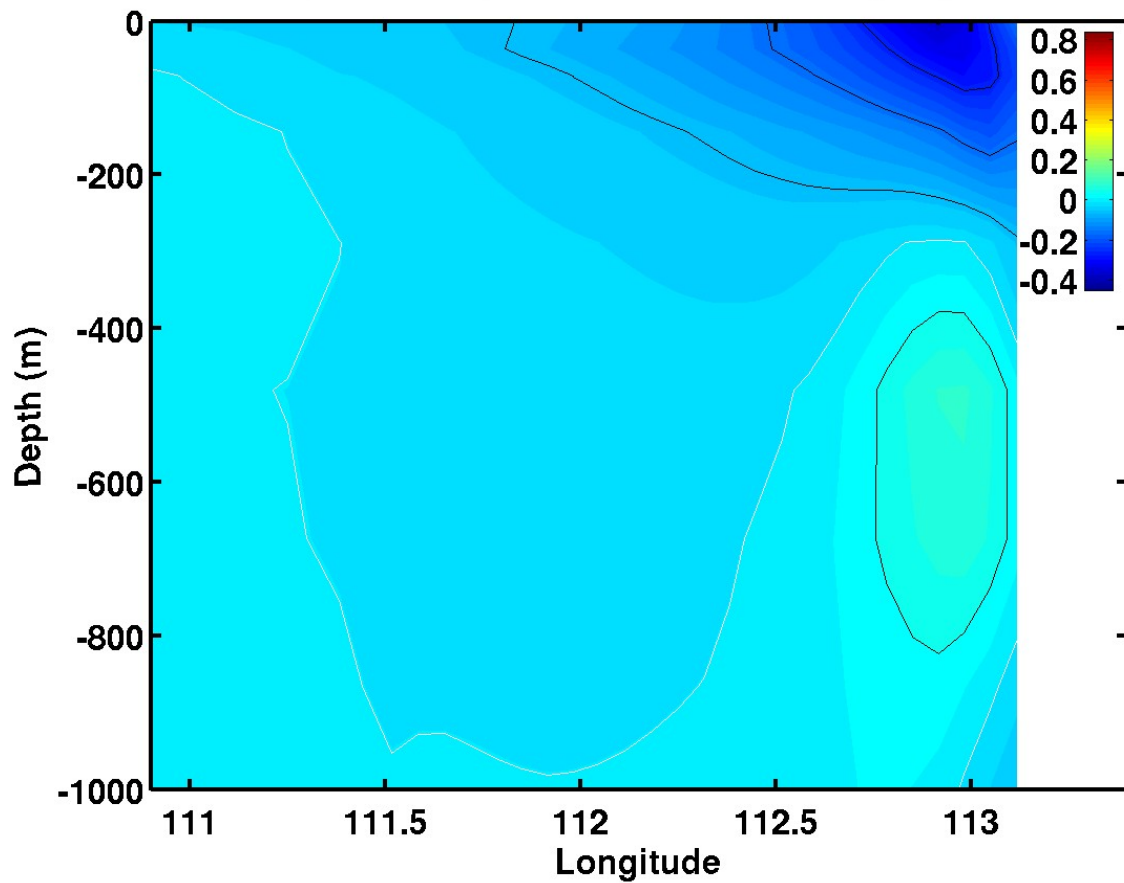


Figure 4.15b. Cross-section of meridional velocity component (m s^{-1}) at 26°S for Experiment 5 on day 20. Red is equatorward (north) and blue is poleward (south). The white contour is zero.

Experiment 5, v Cross-section at 34S, Day 20.

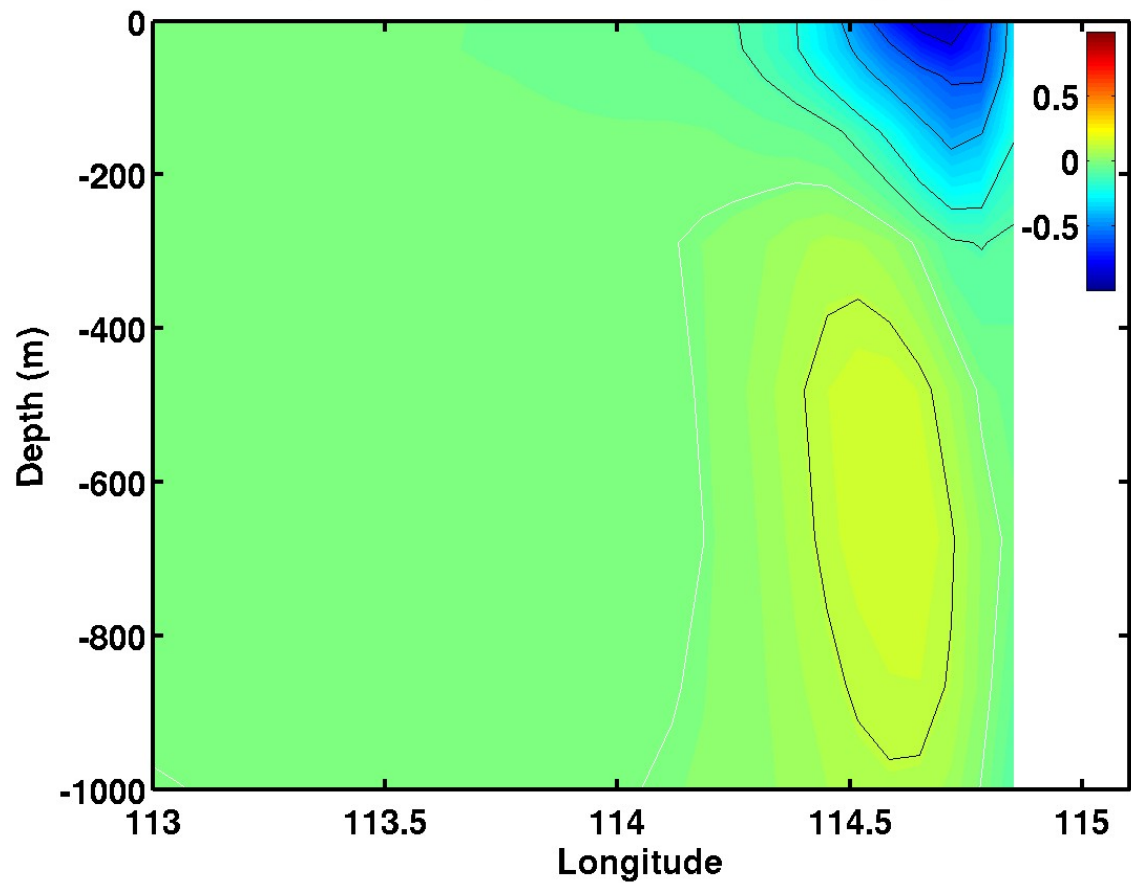


Figure 4.15c. Cross-section of meridional velocity component (m s^{-1}) near Cape Leeuwin (34°S) for Experiment 5 on day 20. Red is equatorward (north) and blue is poleward (south). The white contour is zero.

Experiment 5, u Cross-section at 117E, Day 20.

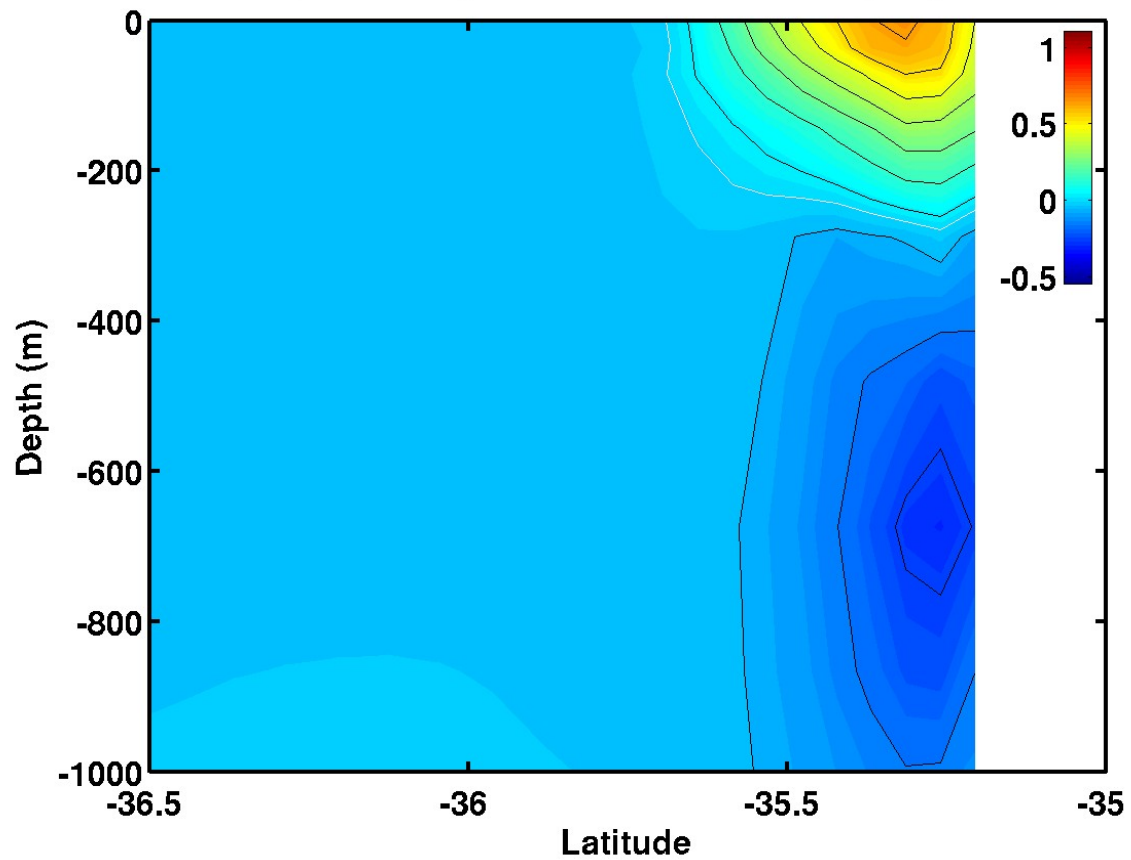


Figure 4.15d. Cross-section of temperature ($^{\circ}\text{C}$) along a north-south transect at 117°E for Experiment 5 on day 20.

Experiment 5, u Cross-section at 130E, Day 20.

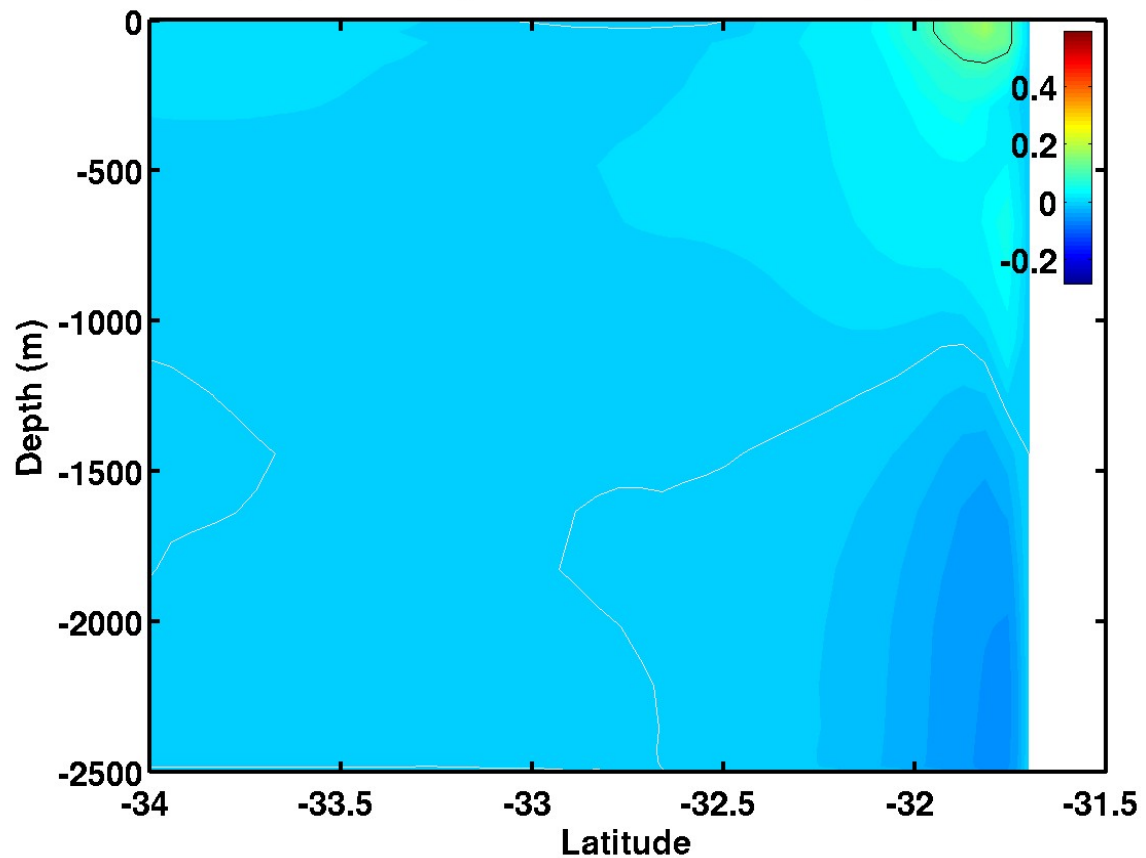


Figure 4.15e. Cross-section of zonal velocity component (m s^{-1}) in the Great Australian Bight (130°E) for Experiment 5 on day 20. Red is eastward and blue is westward. The white contour is zero.

Experiment 5, Temp Cross-section at 117E, Day 20.

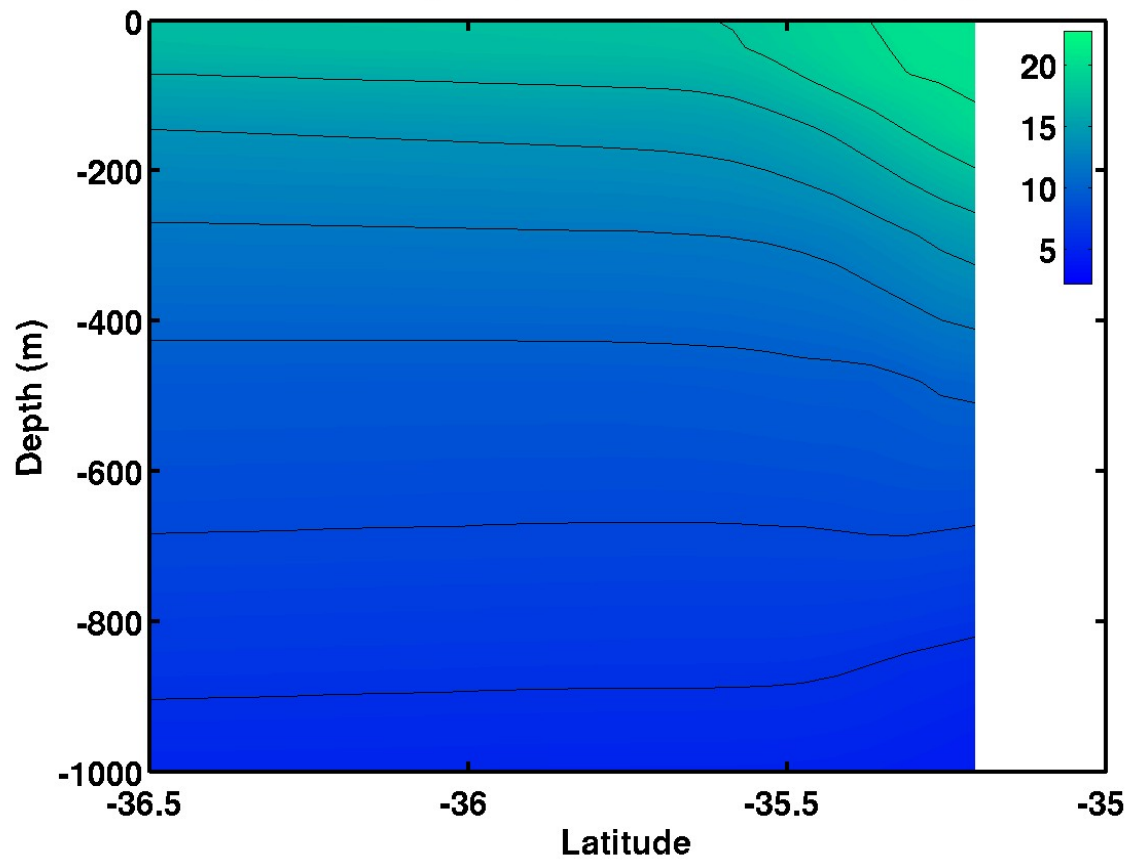


Figure 4.15f. Cross-section of temperature ($^{\circ}\text{C}$) along a north-south transect at 117°E for Experiment 5 on day 20.

Experiment 5, Temp Cross-section at 130E, Day 20.

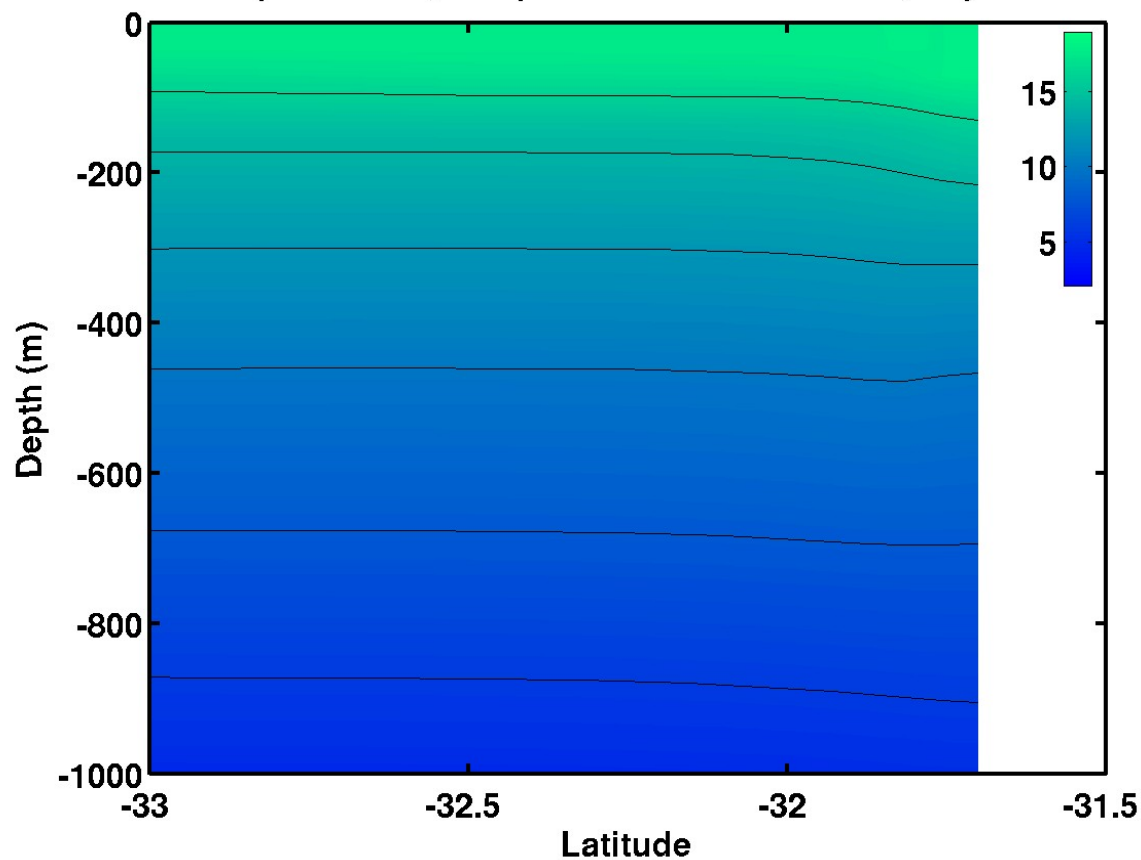


Figure 4.15g. Cross-section of temperature ($^{\circ}\text{C}$) along a north-south transect in the Great Australian Bight (130°E) for Experiment 5 on day 20.

Experiment 5, Day 30, Surface.

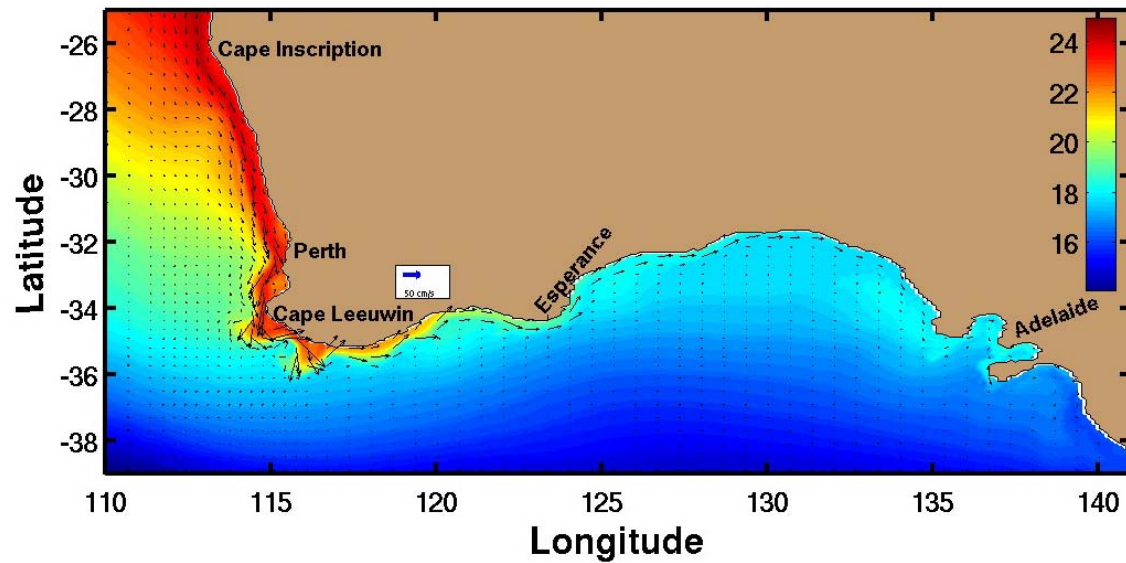


Figure 4.16a. Sea surface temperature ($^{\circ}\text{C}$) and velocity vectors for Experiment 5 on day 30.

Experiment 5, u Cross-section at 117°E, Day 30.

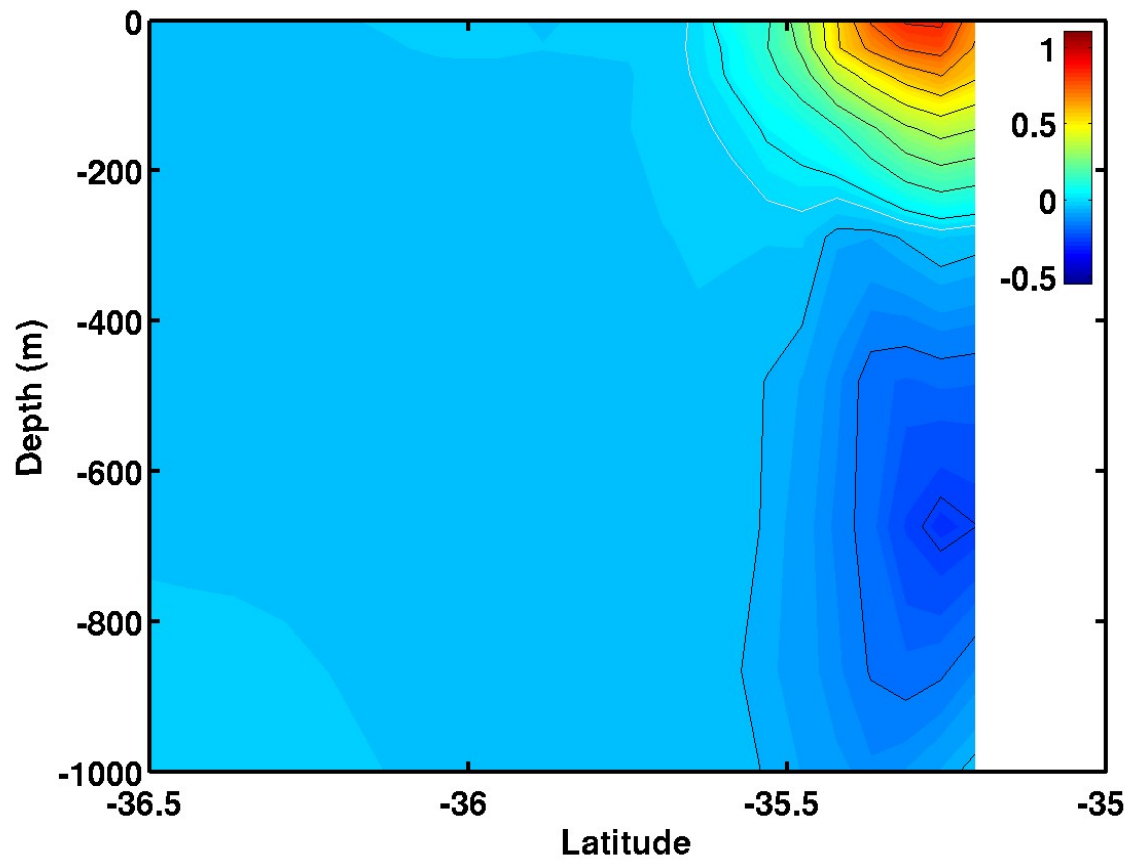


Figure 4.16b. Cross-section of zonal velocity component (m s^{-1}) at 117°E for Experiment 5 on day 30. Red is eastward and blue is westward. The white contour is zero.

Experiment 5, u Cross-section at 130E, Day 30.

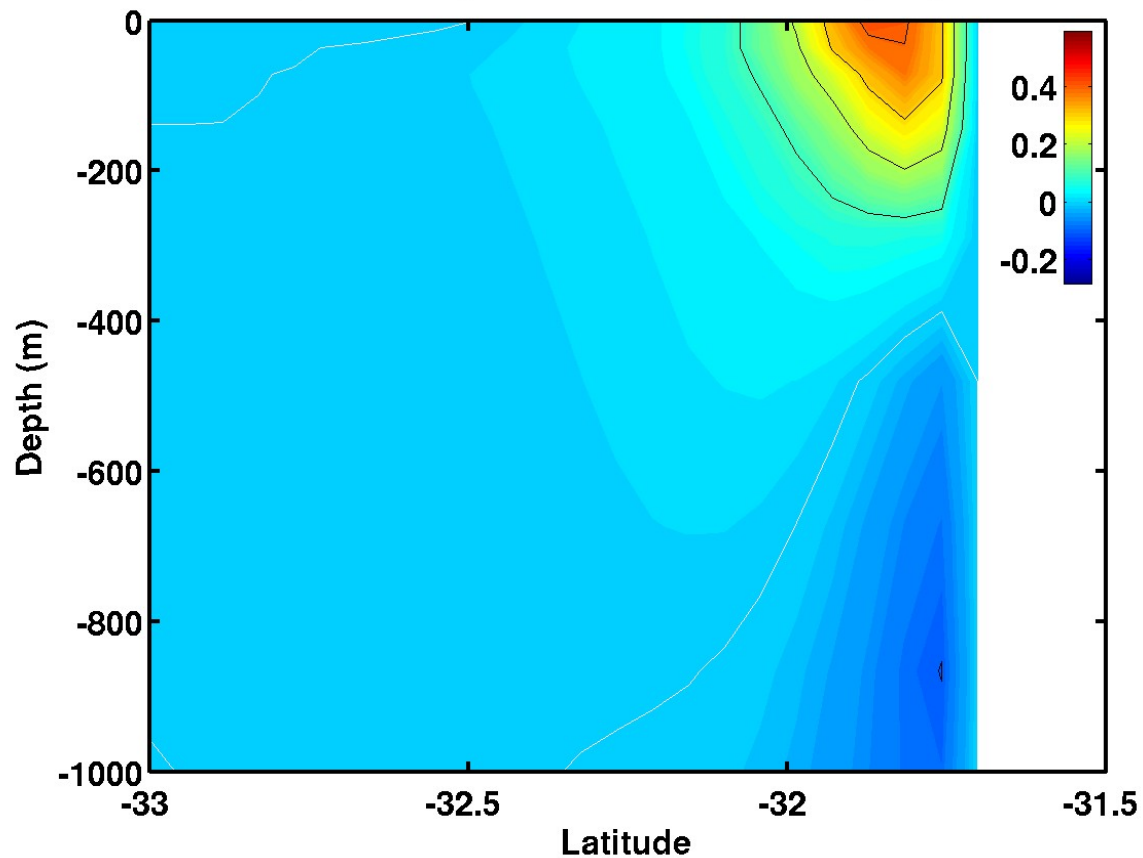


Figure 4.16c. Cross-section of zonal velocity component (m s^{-1}) in the Great Australian Bight (130°E) for Experiment 5 on day 30. Red is eastward and blue is westward. The white contour is zero.

Experiment 5, Temp Cross-section at 117E, Day 30.

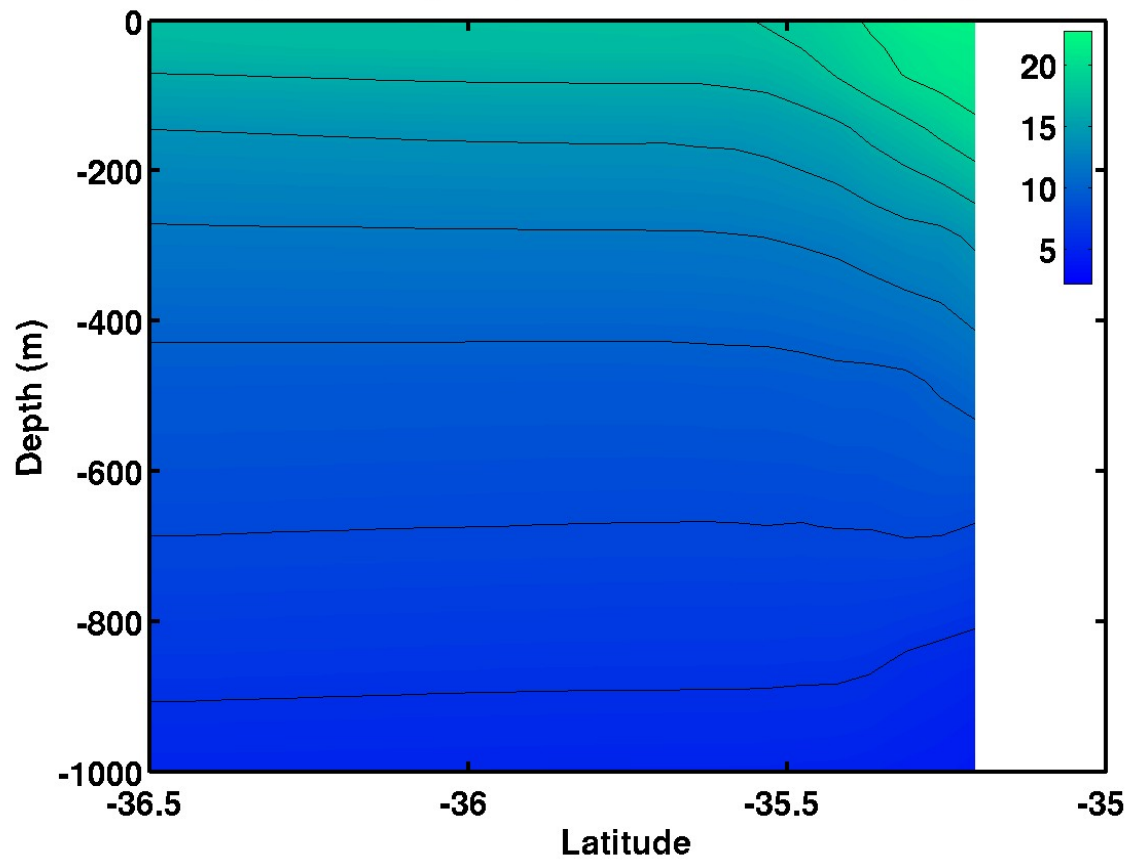


Figure 4.16d. Cross-section of temperature (°C) along a north-south transect at 117°E for Experiment 5 on day 30.

Experiment 5, Day 45, Surface.

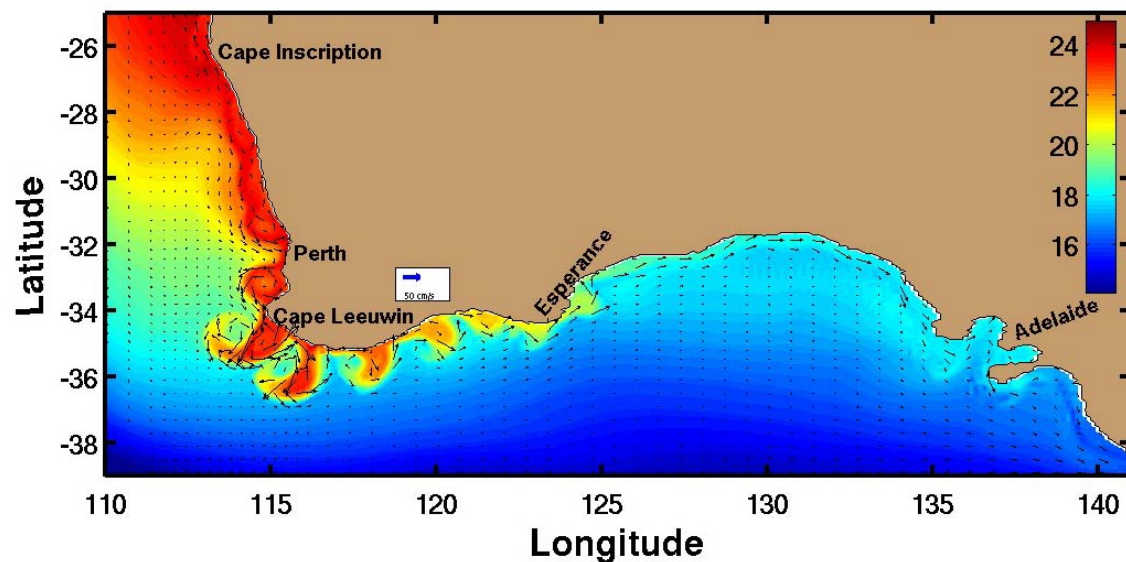


Figure 4.17. Sea surface temperature (°C) and velocity vectors for Experiment 5 on day 45.

Experiment 5, Day 60, Surface.

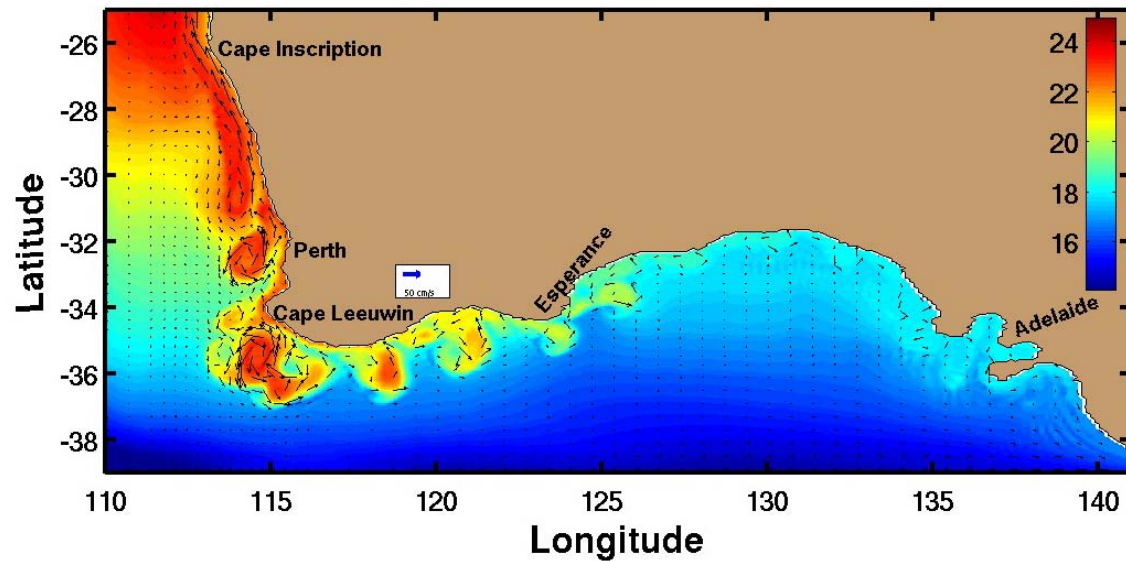


Figure 4.18. Sea surface temperature (°C) and velocity vectors for Experiment 5 on day 60.

Experiment 5, Day 72, Surface.

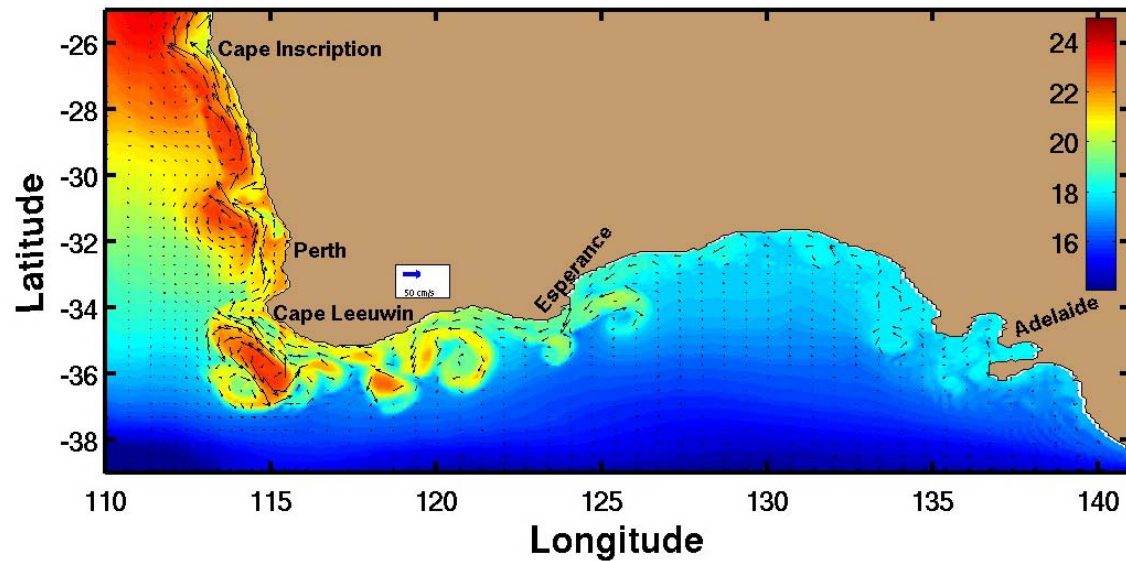


Figure 4.19. Sea surface temperature ($^{\circ}\text{C}$) and velocity vectors for Experiment 5 on day 72.

Experiment 6, Day 20, Surface.

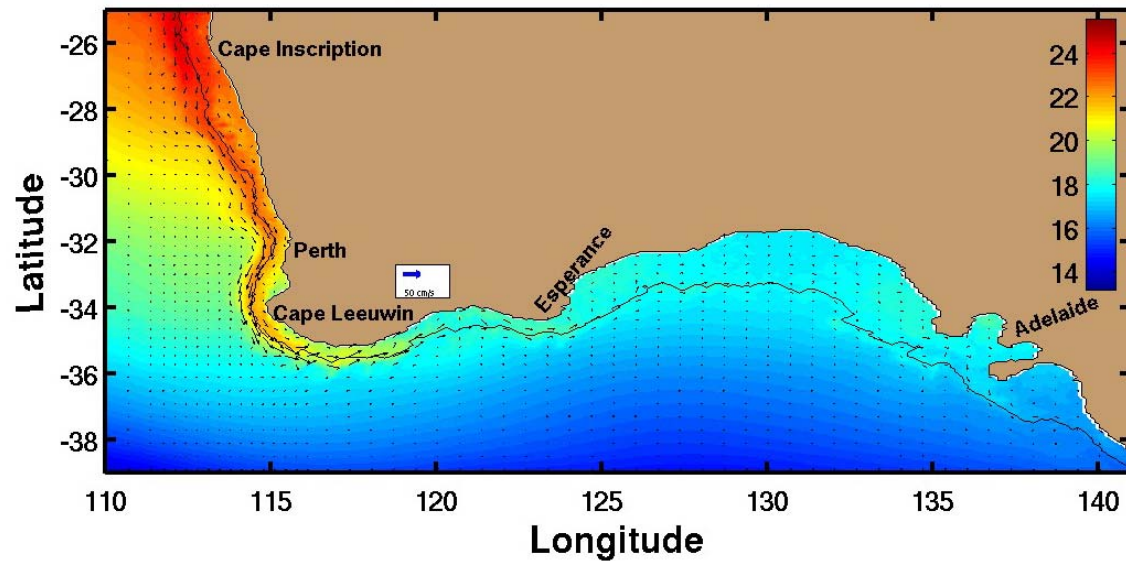


Figure 4.20a. Sea surface temperature ($^{\circ}\text{C}$) and velocity vectors for Experiment 6 on day 20.

Experiment 6, v Cross-section at 26S, Day 20.

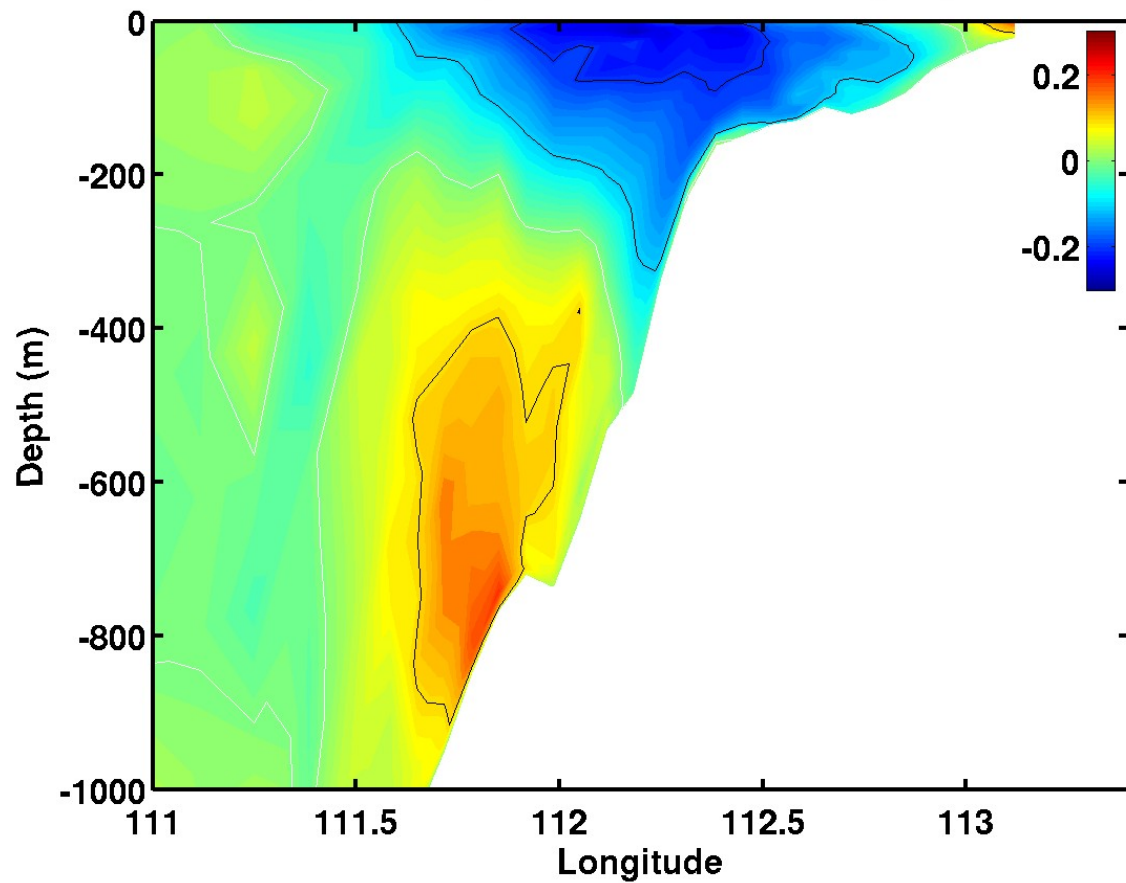


Figure 4.20b. Cross-section of meridional velocity component (m s^{-1}) at 26°S for Experiment 6 on day 20. Red is equatorward (north) and blue is poleward (south). The white contour is zero.

Experiment 6, v Cross-section at 34S, Day 20.

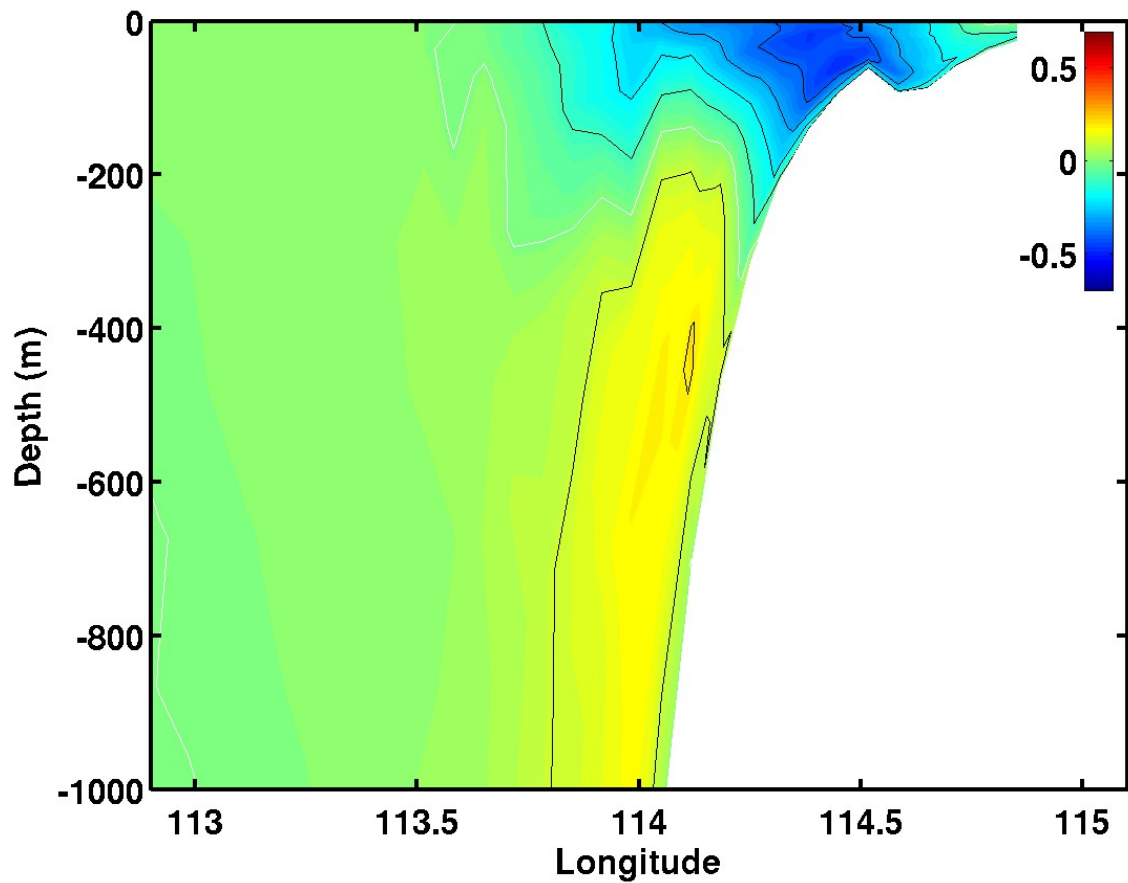


Figure 4.20c. Cross-section of meridional velocity component (m s^{-1}) near Cape Leeuwin (34°S) for Experiment 1 on day 60. Red is equatorward (north) and blue is poleward (south). The white contour is zero.

Experiment 6, u Cross-section at 117°E, Day 20.

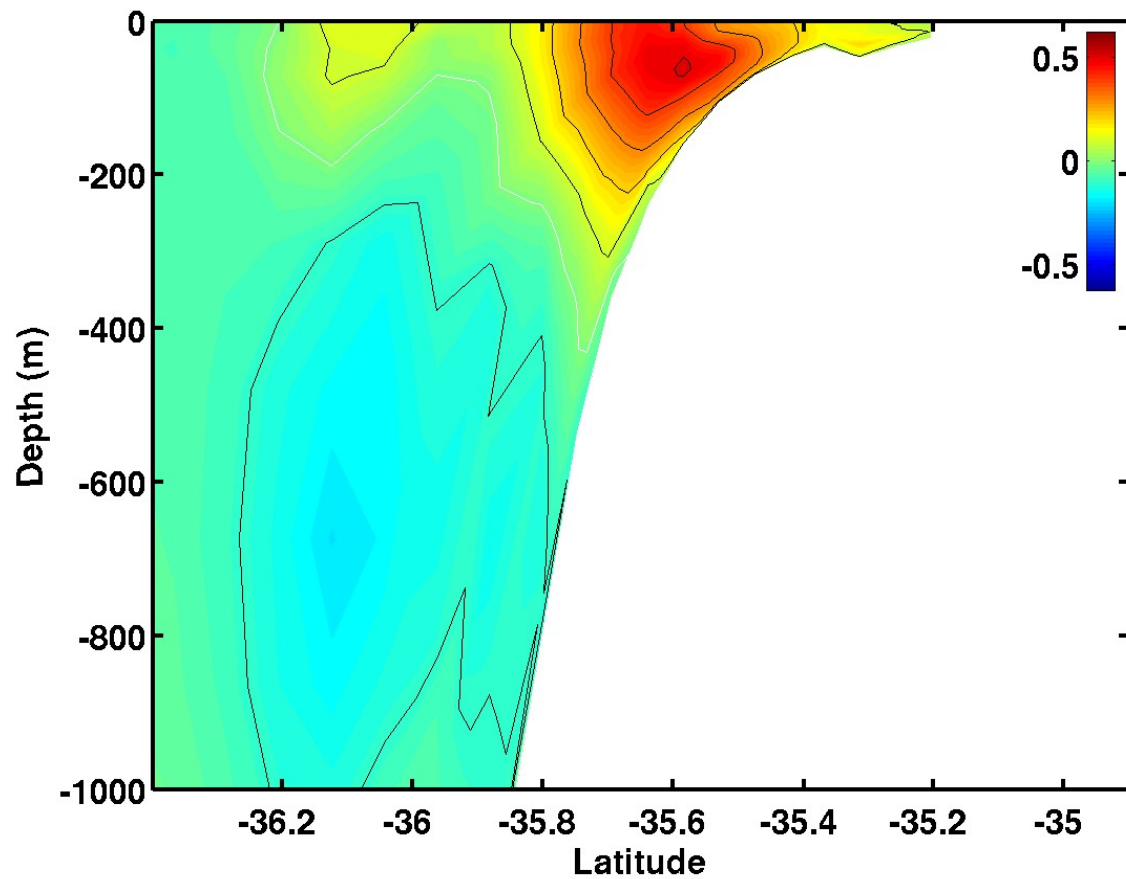


Figure 4.20d. Cross-section of zonal velocity component (m s^{-1}) at 117°E for Experiment 6 on day 20. Red is eastward and blue is westward. The white contour is zero.

Experiment 6, u Cross-section at 130E, Day 20.

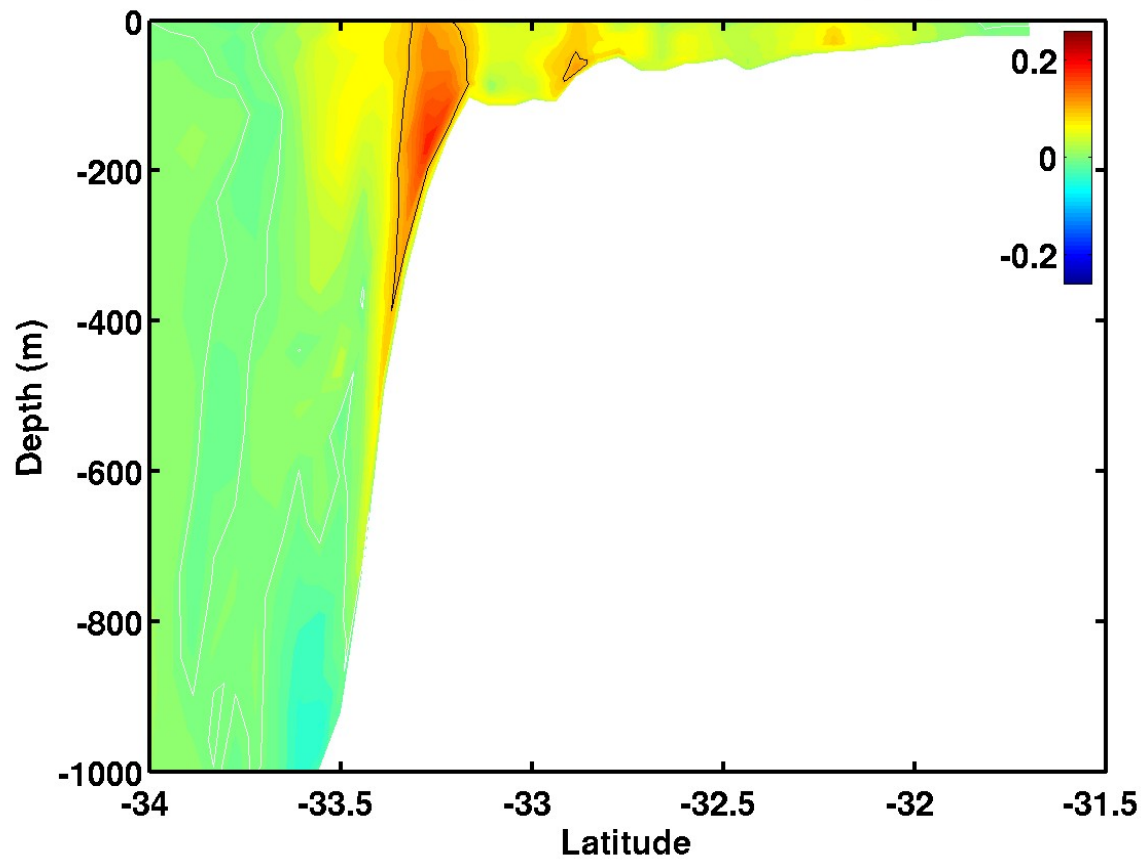


Figure 4.20e. Cross-section of zonal velocity component (m s^{-1}) in the Great Australian Bight (130°E) for Experiment 6 on day 20. Red is eastward and blue is westward. The white contour is zero.

Experiment 6, Day 20, Surface Salinity.

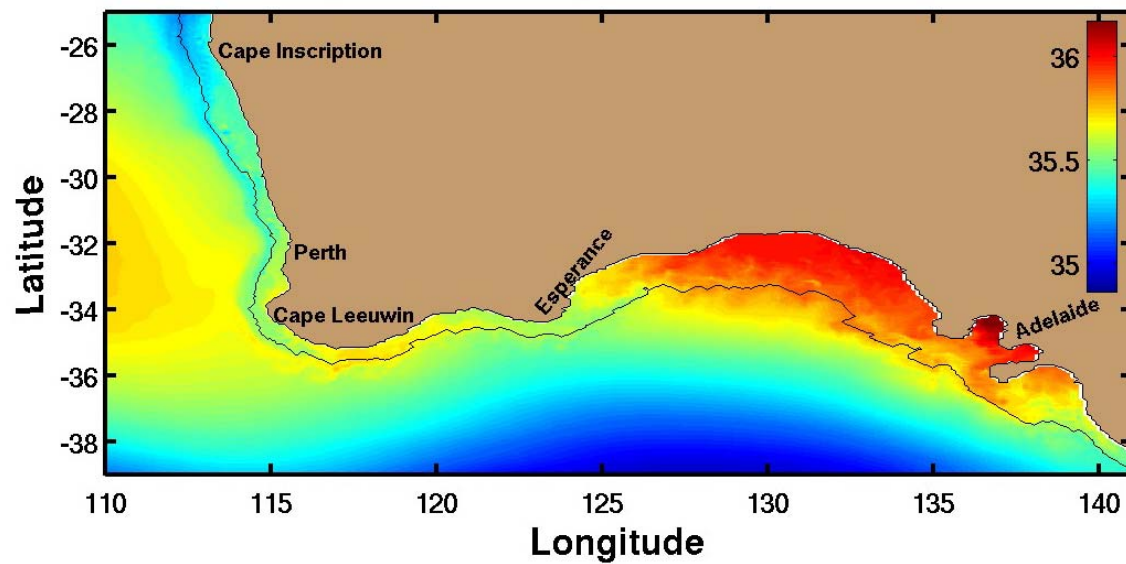


Figure 4.20f. Sea surface salinity for Experiment 6 on day 20.

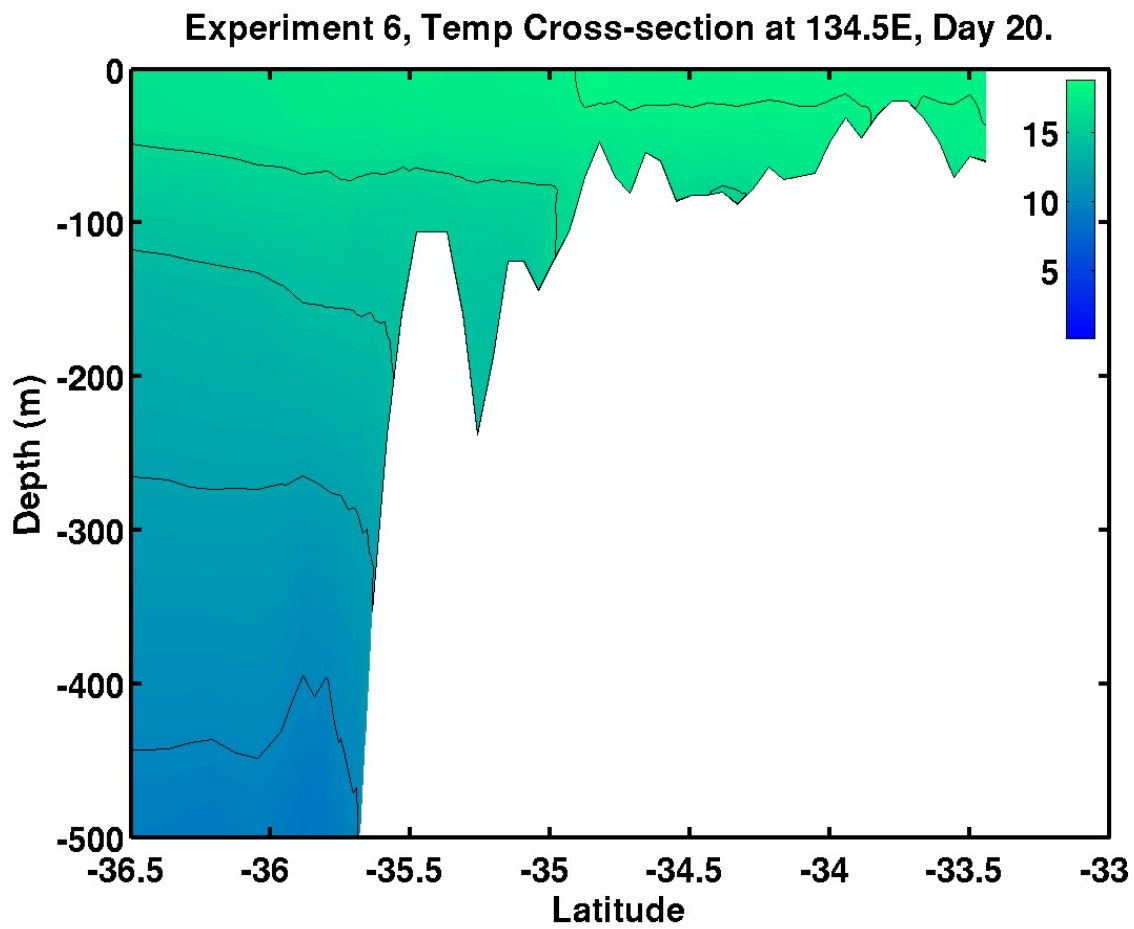


Figure 4.20g. Cross-section of temperature ($^{\circ}\text{C}$) along a north-south transect in the eastern Great Australian Bight (134.5°E) for Experiment 6 on day 20.

Experiment 6, Day 30, Surface.

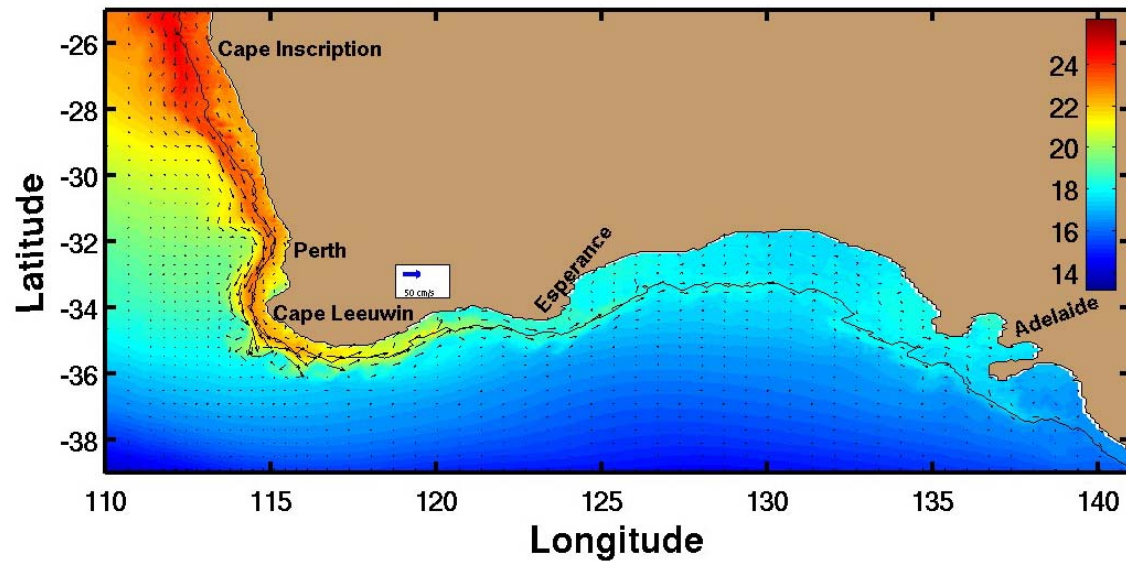


Figure 4.21a. Sea surface temperature (°C) and velocity vectors for Experiment 6 on day 30.

Experiment 6, v Cross-section at 34S, Day 30.

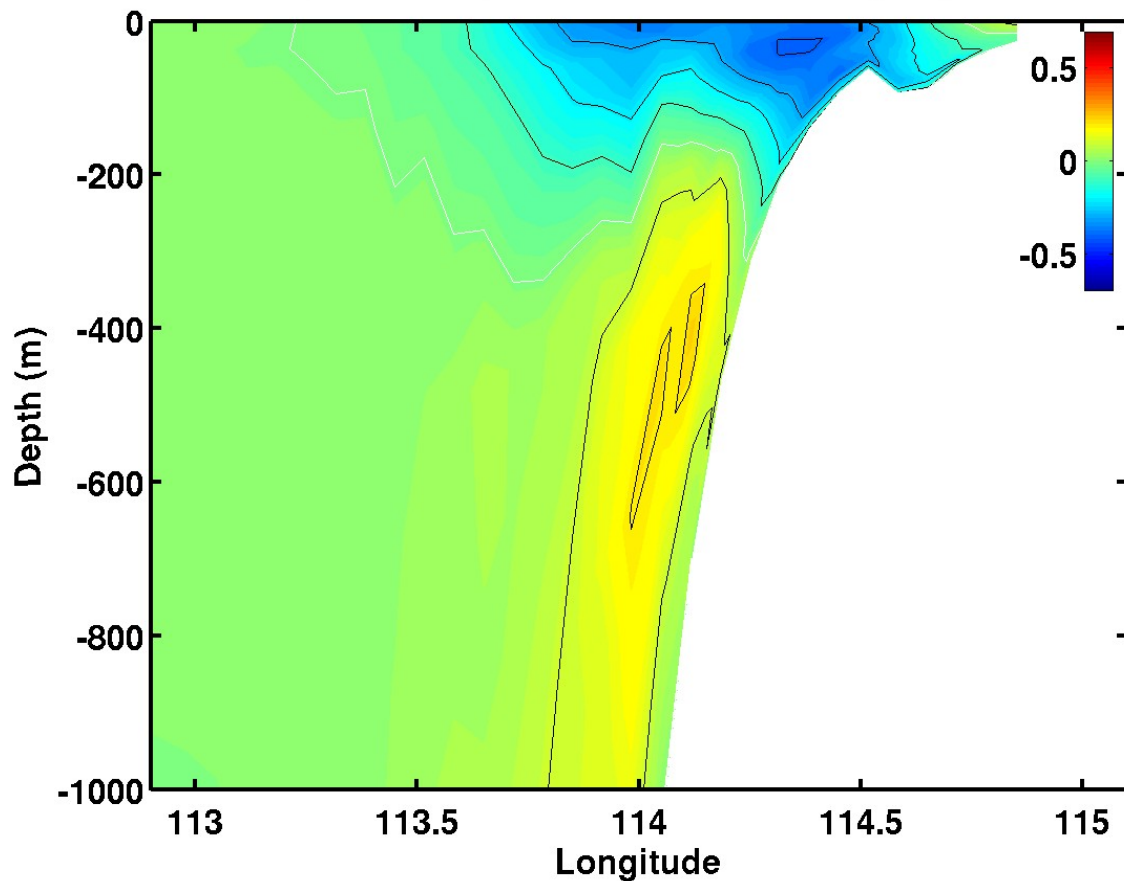


Figure 4.21b. Cross-section of meridional velocity component (m s^{-1}) near Cape Leeuwin (34°S) for Experiment 6 on day 30. Red is equatorward (north) and blue is poleward (south). The white contour is zero.

Experiment 6, v Cross-section at 26S, Day 30.

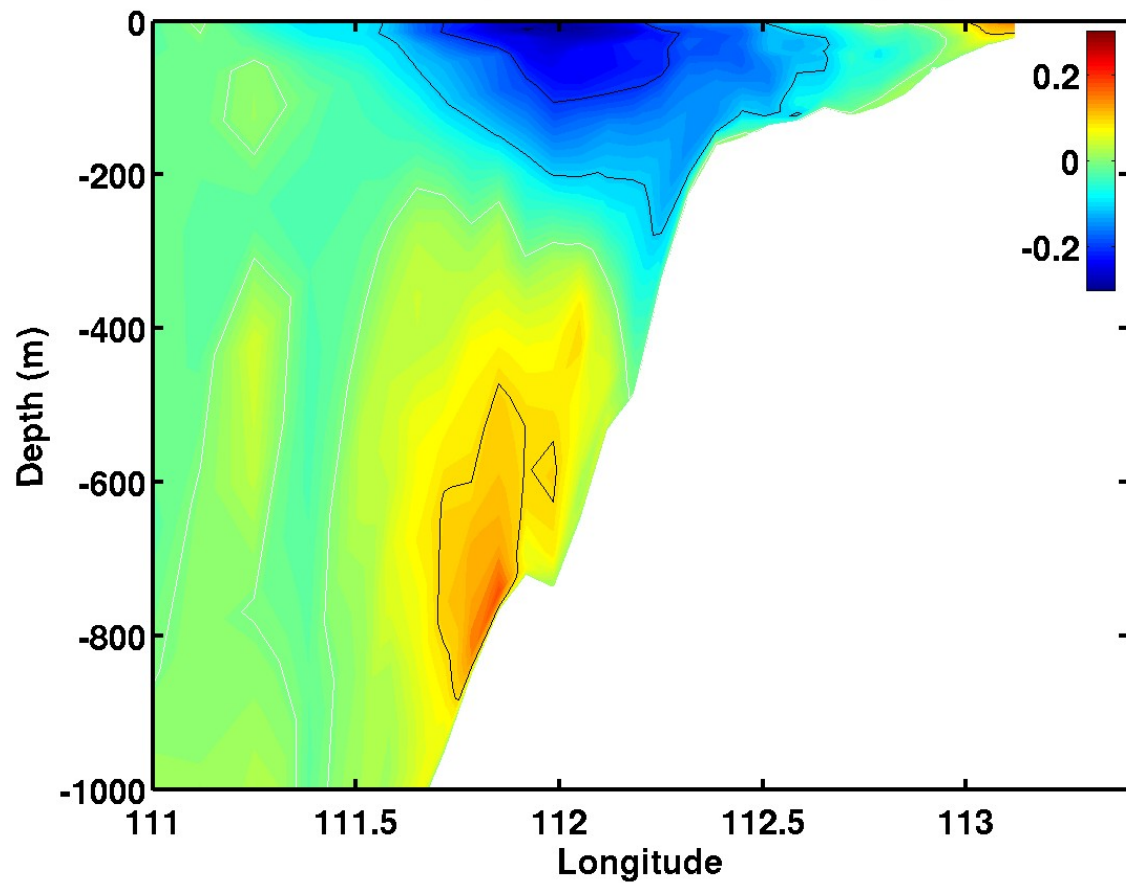


Figure 4.21c. Cross-section of meridional velocity component (m s^{-1}) at 26°S for Experiment 6 on day 30. Red is equatorward (north) and blue is poleward (south). The white contour is zero.

Experiment 6, Temp Cross-section at 26S, Day 30.

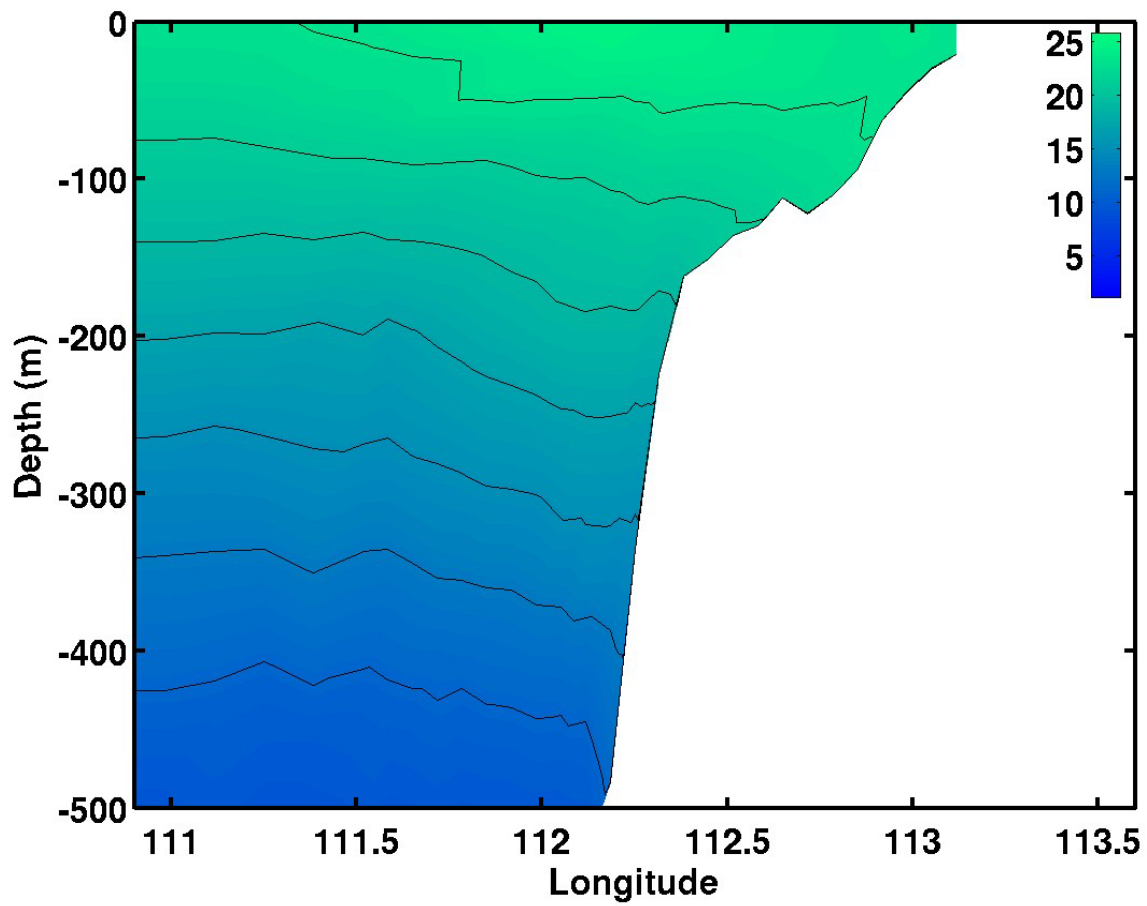


Figure 4.21d. Cross-section of temperature (°C) along an east-west transect at 26°S for Experiment 6 on day 30.

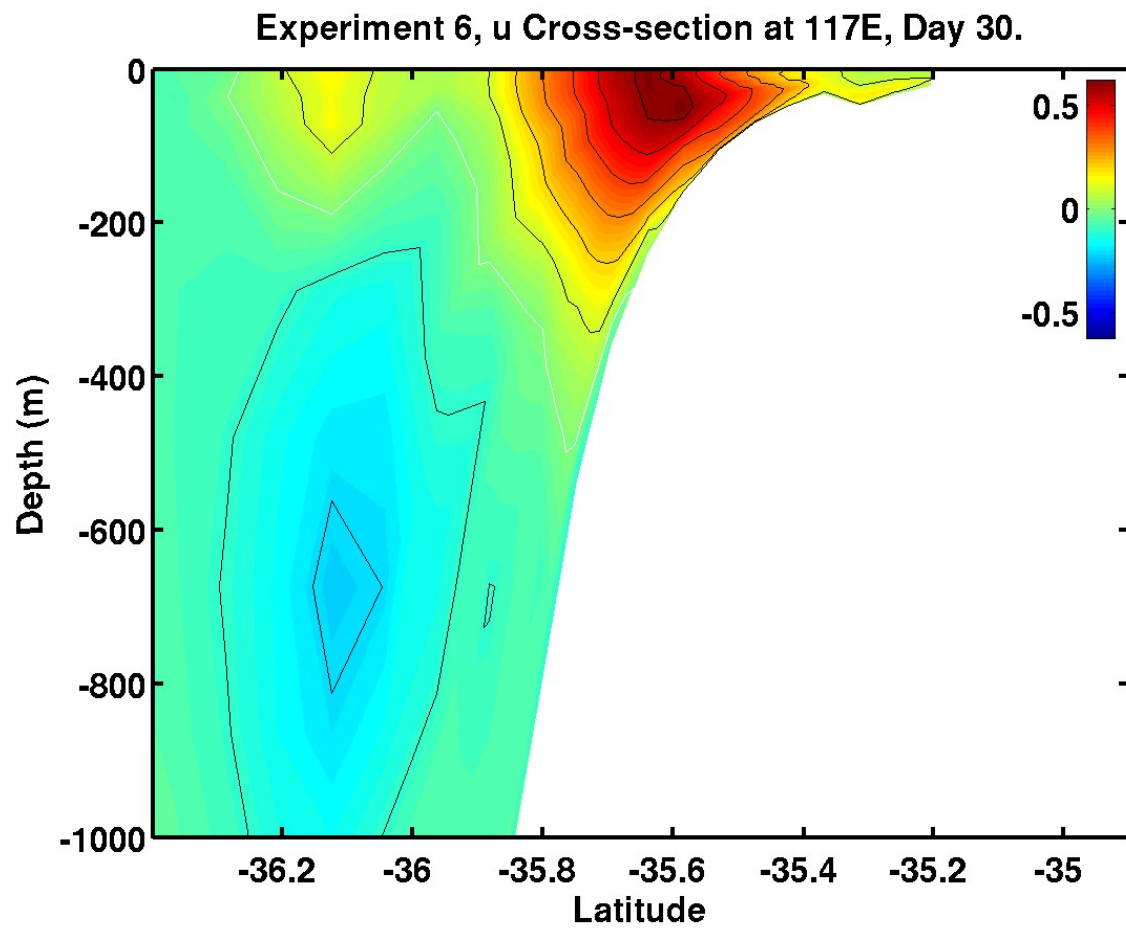


Figure 4.21e. Cross-section of zonal velocity component (m s^{-1}) at 117°E for Experiment 6 on day 30. Red is eastward and blue is westward. The white contour is zero.

Experiment 6, u Cross-section at 130E, Day 30.

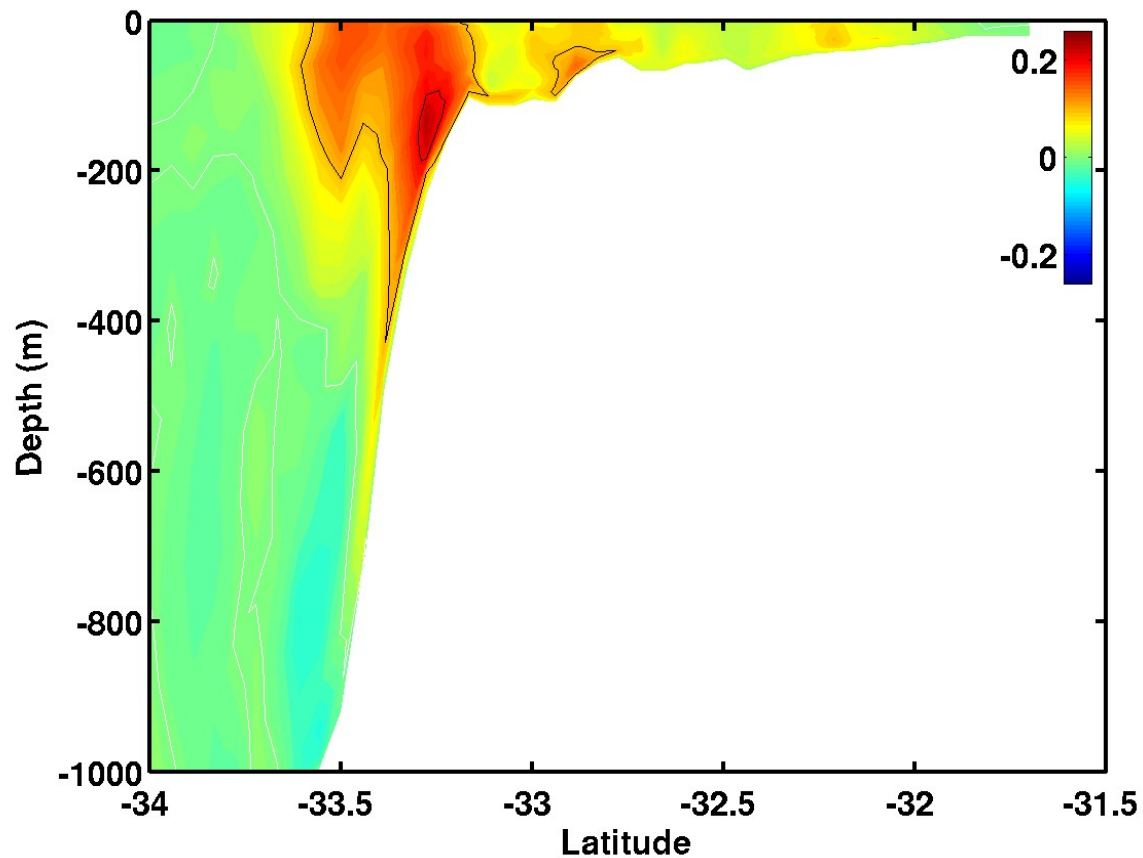


Figure 4.21f. Cross-section of zonal velocity component (m s^{-1}) in the Great Australian Bight (130°E) for Experiment 6 on day 30. Red is eastward and blue is westward. The white contour is zero.

Experiment 6, Day 30, Surface Salinity.

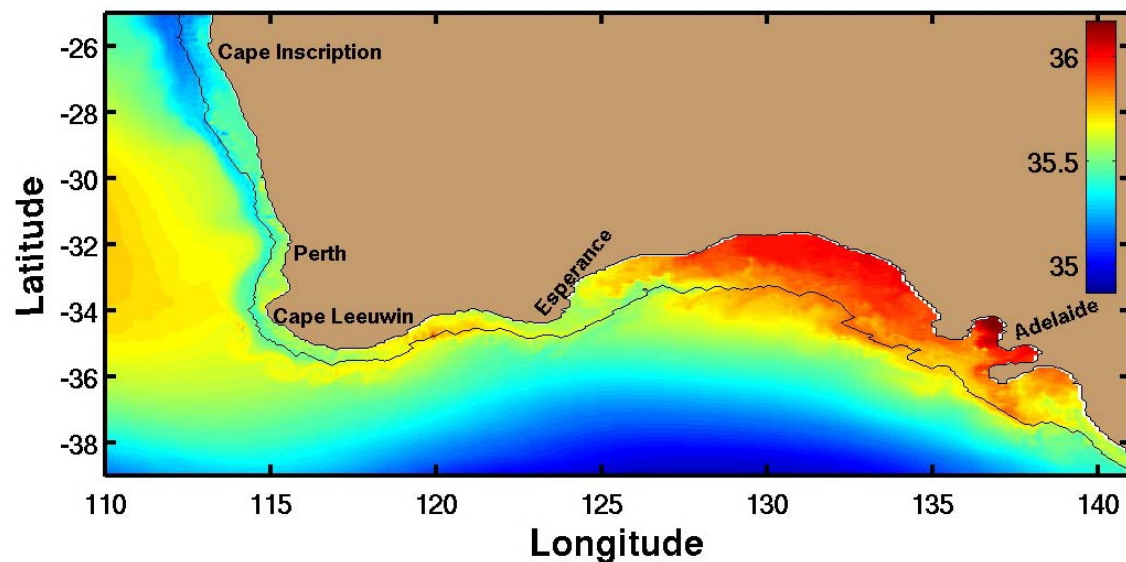


Figure 4.21g. Sea surface salinity for Experiment 6 on day 30.

Experiment 6, Temp Cross-section at 117E, Day 30.

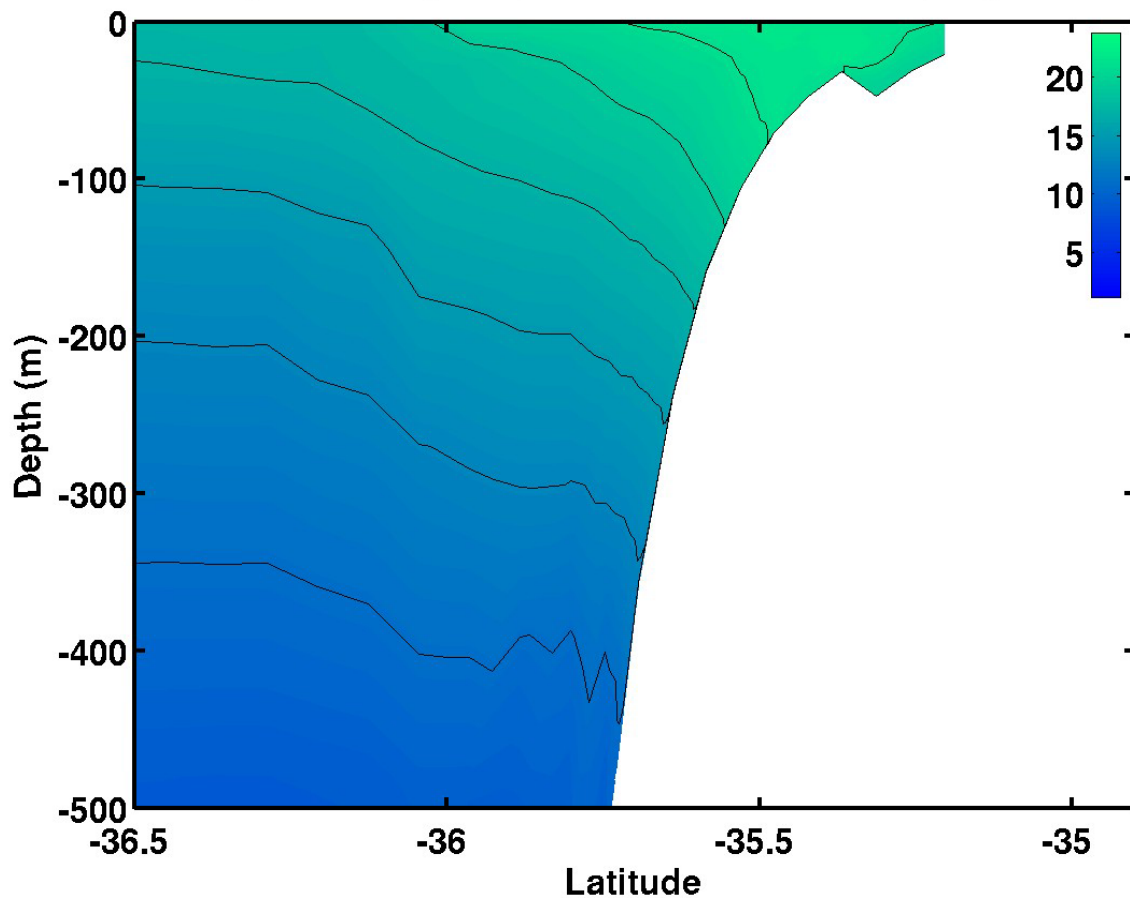


Figure 4.21h. Cross-section of temperature (°C) along a north-south transect at 117°E for Experiment 6 on day 30.

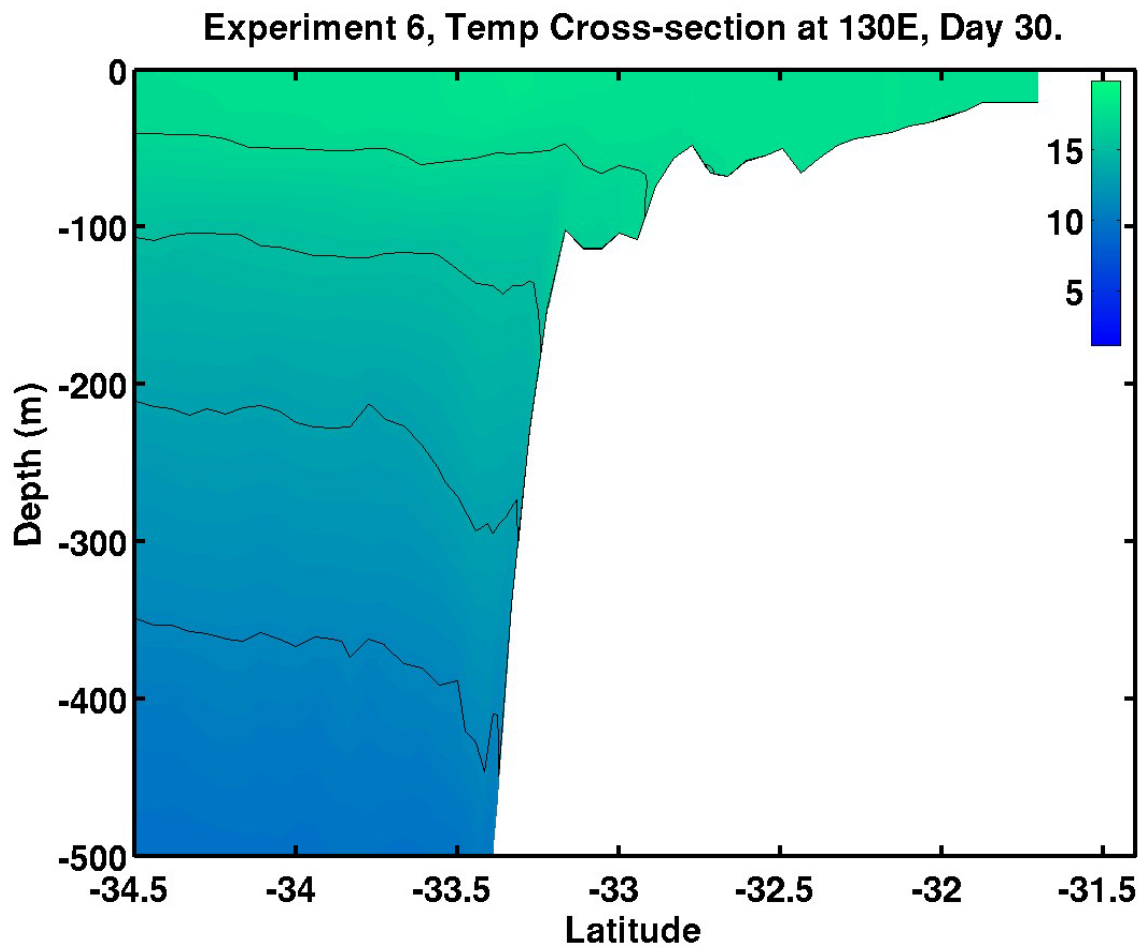


Figure 4.21i. Cross-section of temperature ($^{\circ}\text{C}$) along an north-south transect in the Great Australian Bight (130°E) for Experiment 6 on day 30.

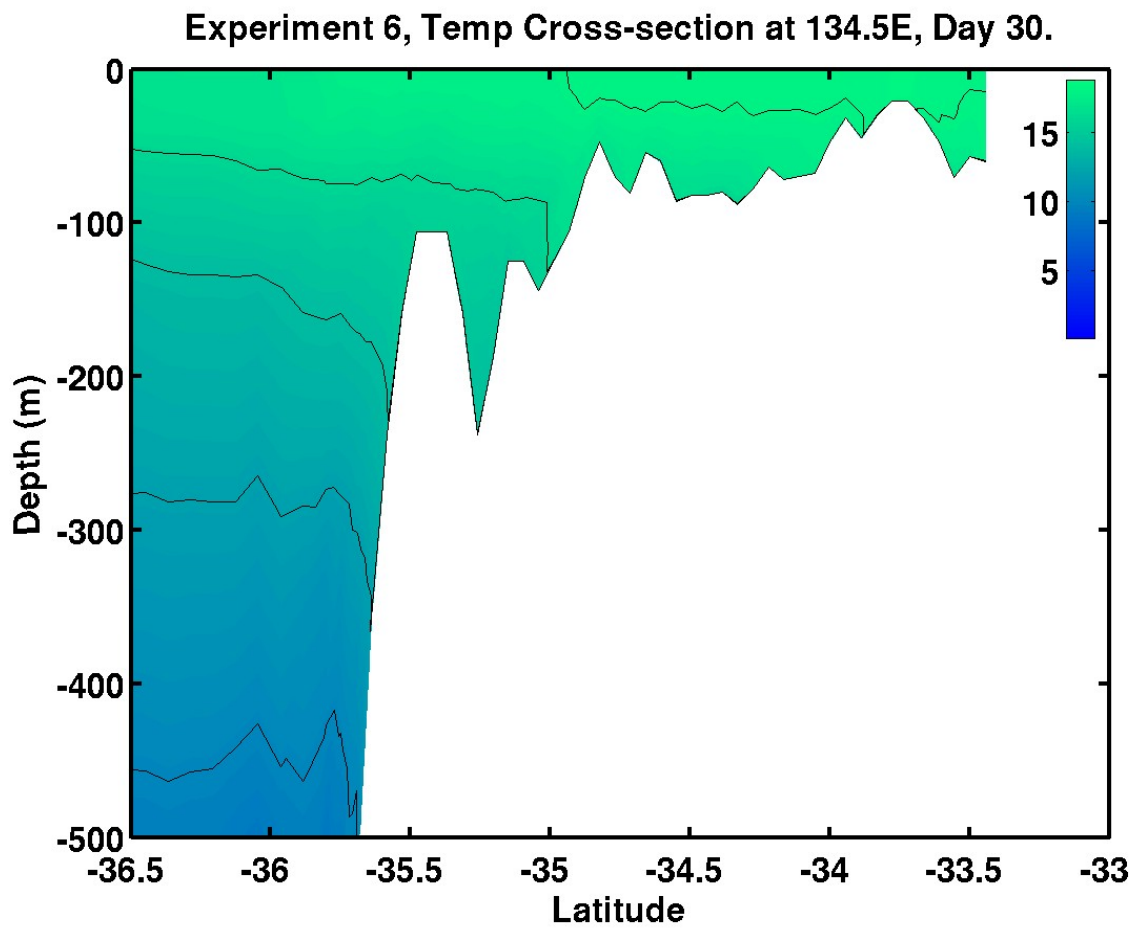


Figure 4.21j. Cross-section of temperature ($^{\circ}\text{C}$) along an north-south transect in the eastern Great Australian Bight (134.5°E) for Experiment 6 on day 30.

Experiment 6, Day 42, Surface Salinity.

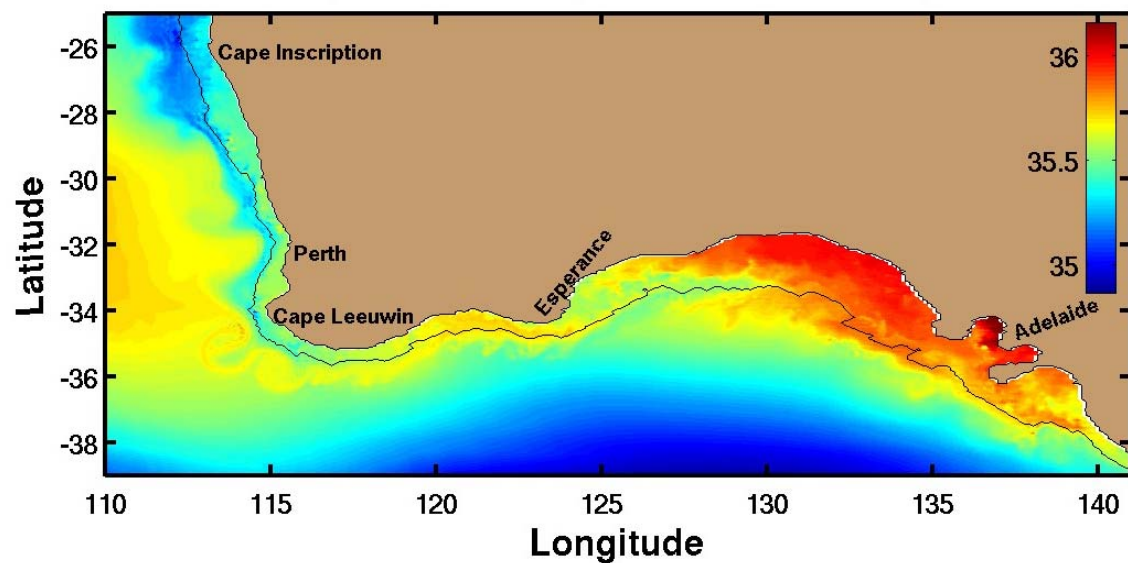


Figure 4.22. Sea surface salinity for Experiment 6 on day 42.

Experiment 6, Day 51, Surface.

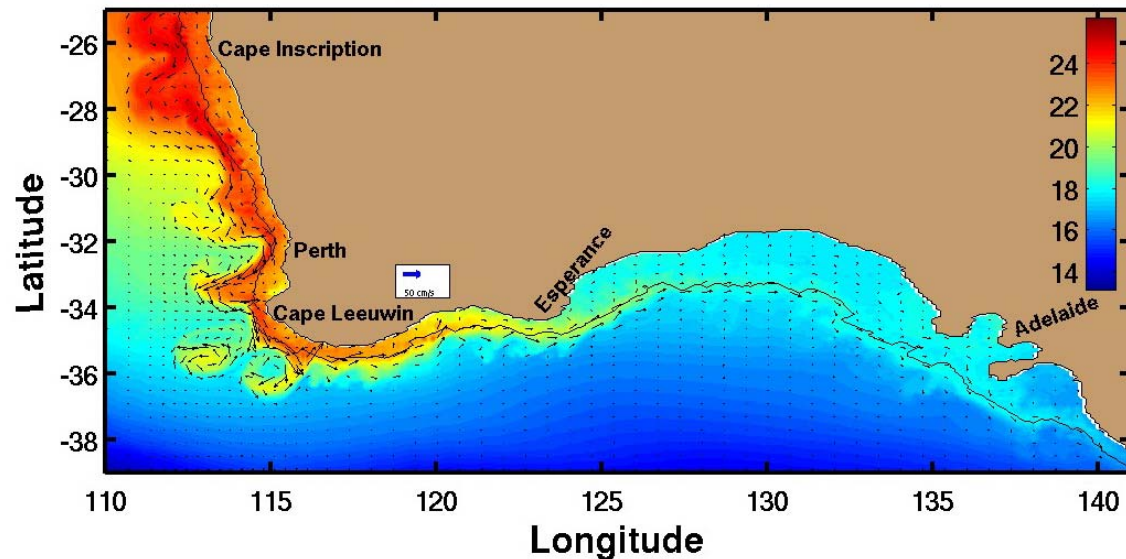


Figure 4.23. Sea surface temperature ($^{\circ}\text{C}$) and velocity vectors for Experiment 6 on day 51.

Experiment 6, Day 60, Surface.

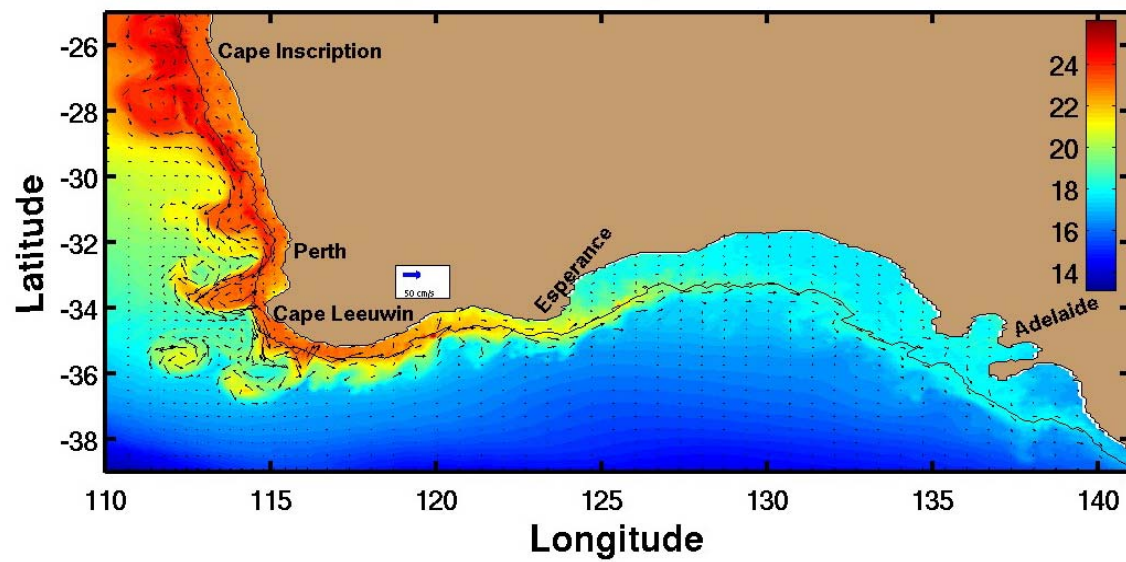


Figure 4.24a. Sea surface temperature ($^{\circ}\text{C}$) and velocity vectors for Experiment 6 on day 60.

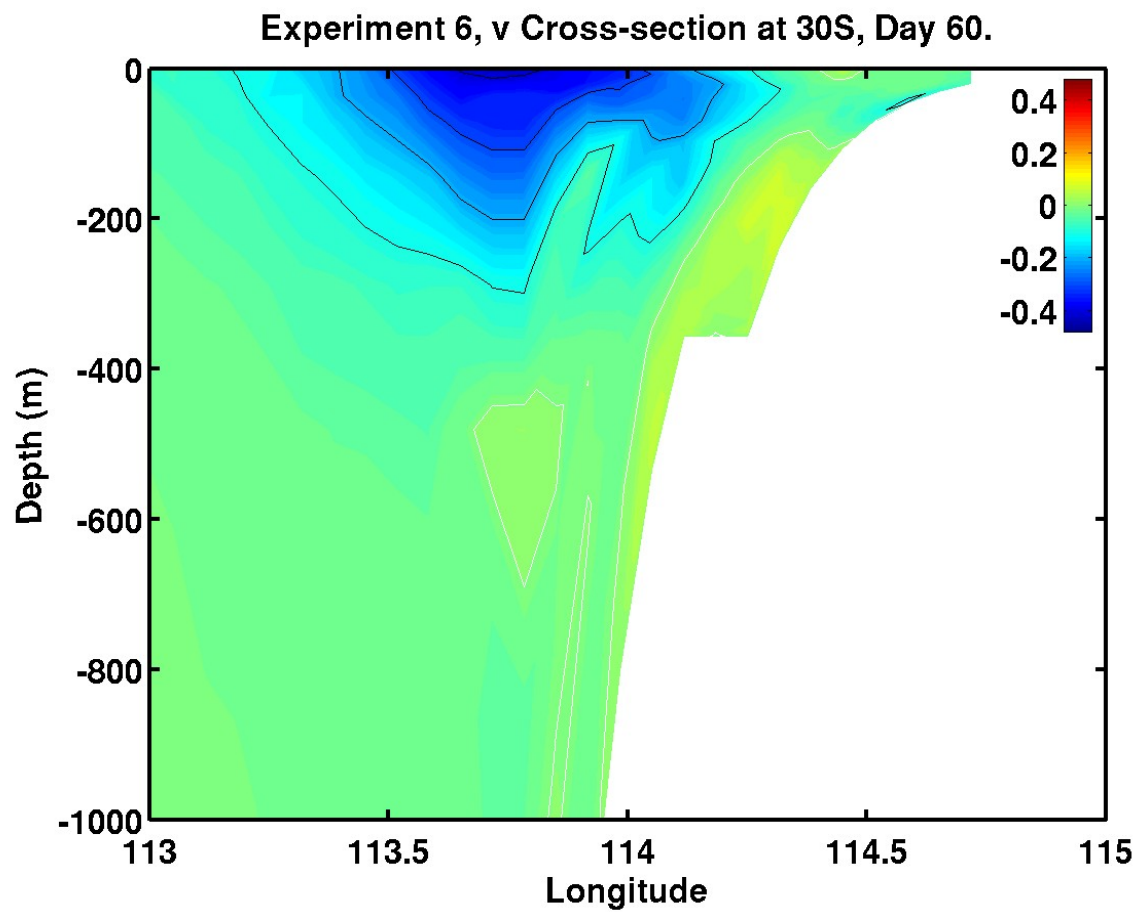


Figure 4.24b. Cross-section of temperature ($^{\circ}\text{C}$) along an east-west transect at 30°S for Experiment 6 on day 60.

Experiment 6, v Cross-section at 34.5S, Day 60.

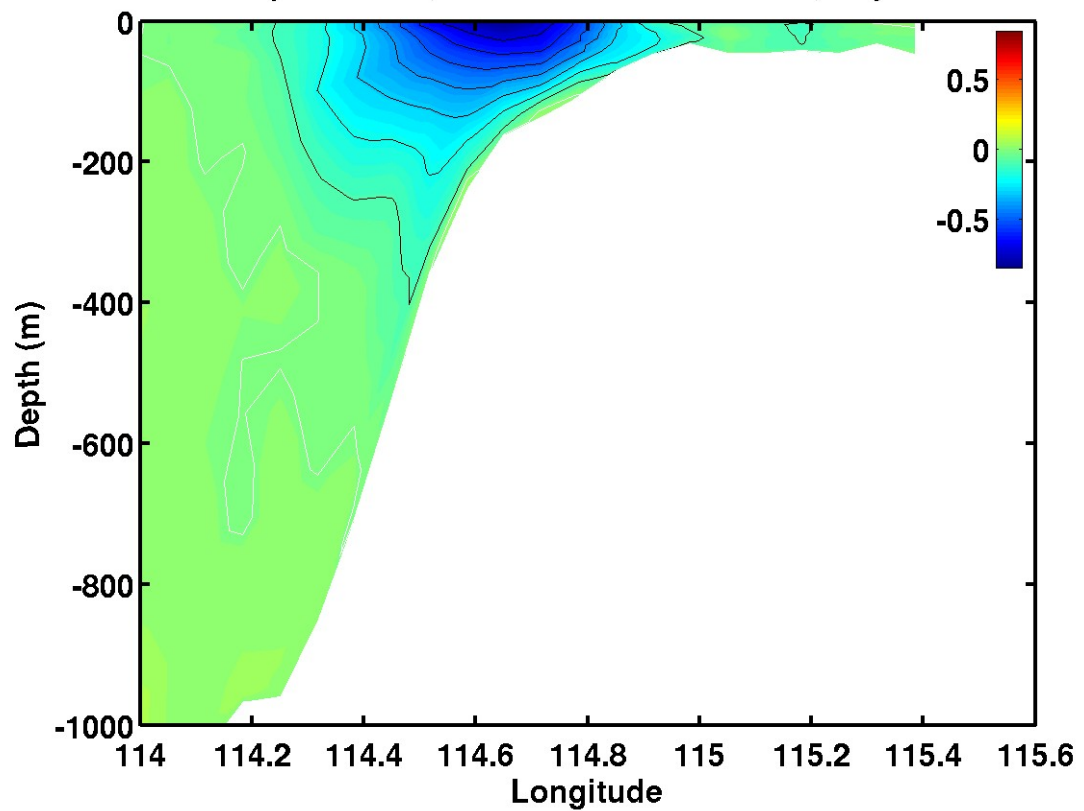


Figure 4.24c. Cross-section of meridional velocity component (m s^{-1}) near Cape Leeuwin (34.5°S) for Experiment 6 on day 60. Red is equatorward (north) and blue is poleward (south). The white contour is zero.

Experiment 6, u Cross-section at 130E, Day 60.

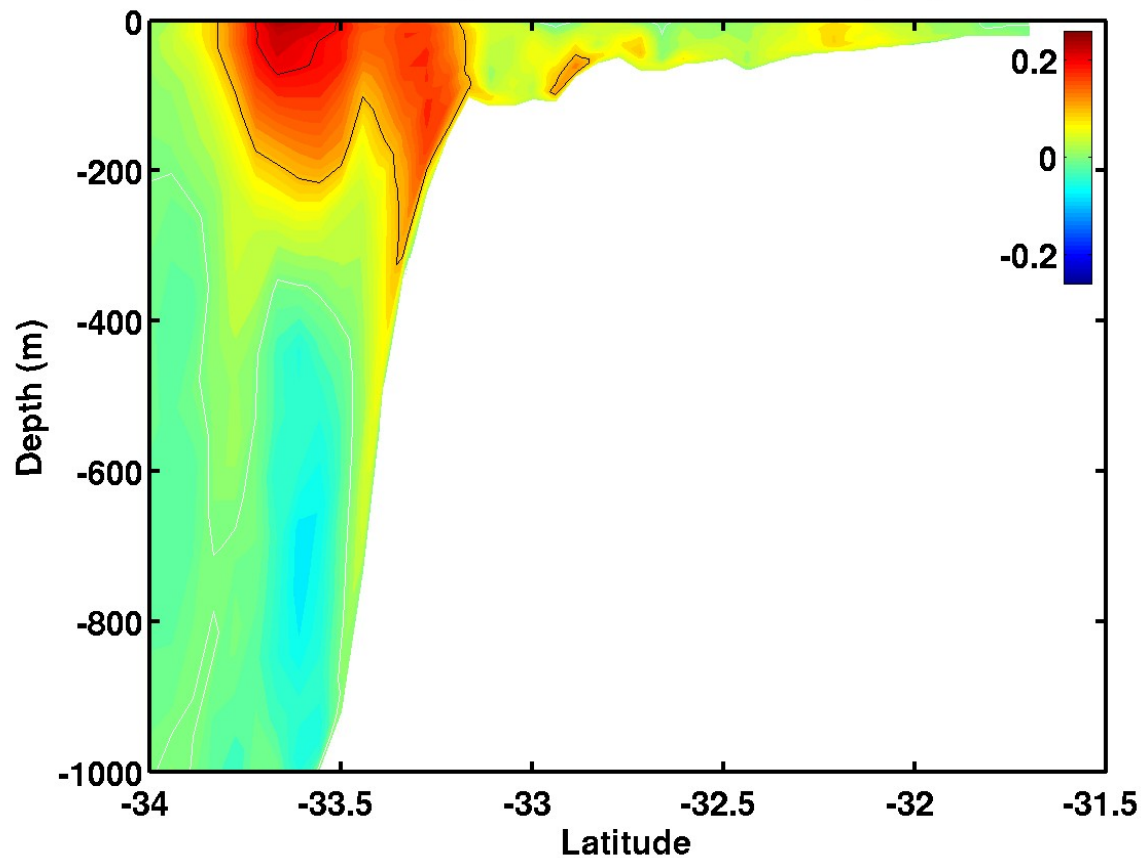


Figure 4.24d. Cross-section of zonal velocity component (m s^{-1}) in the Great Australian Bight (130°E) for Experiment 6 on day 60. Red is eastward and blue is westward. The white contour is zero.

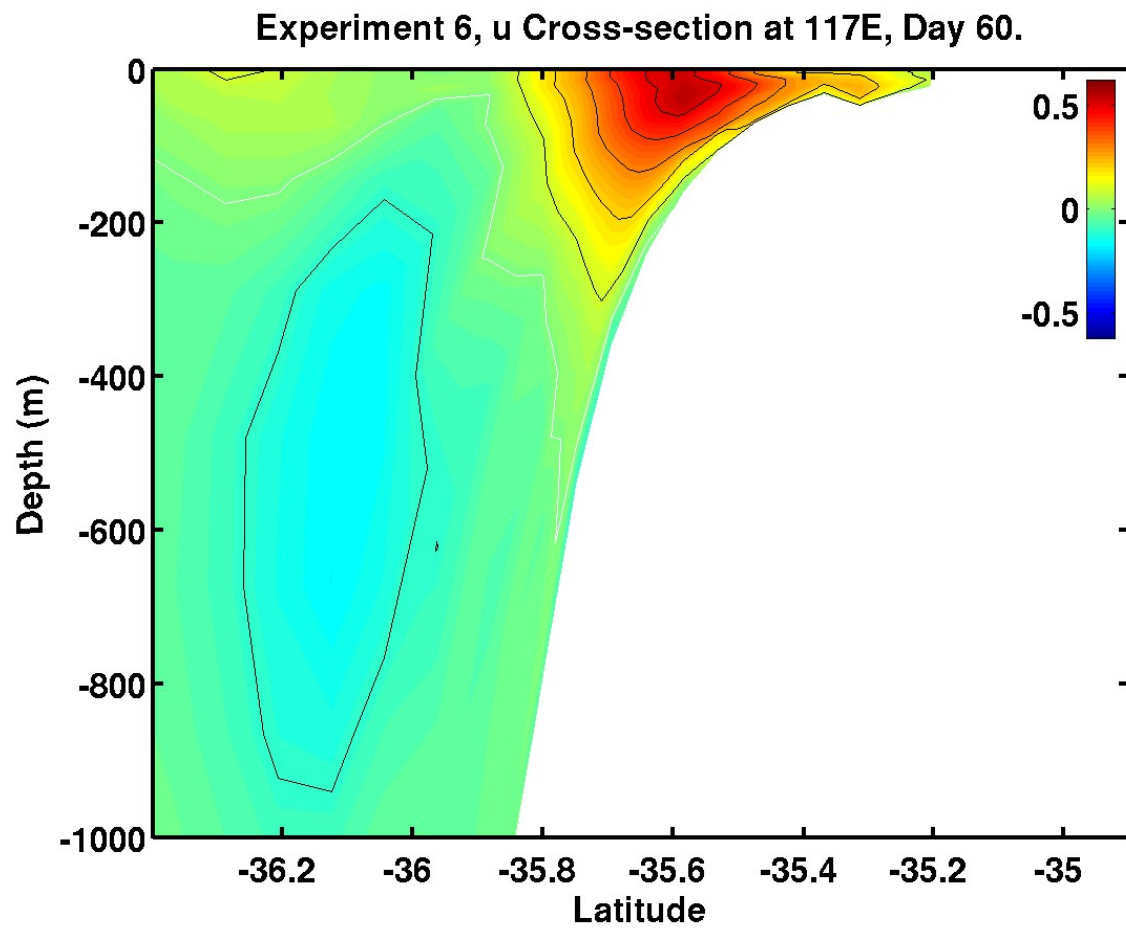


Figure 4.24e. Cross-section of zonal velocity component (m s^{-1}) at 117°E for Experiment 6 on day 60. Red is eastward and blue is westward. The white contour is zero.

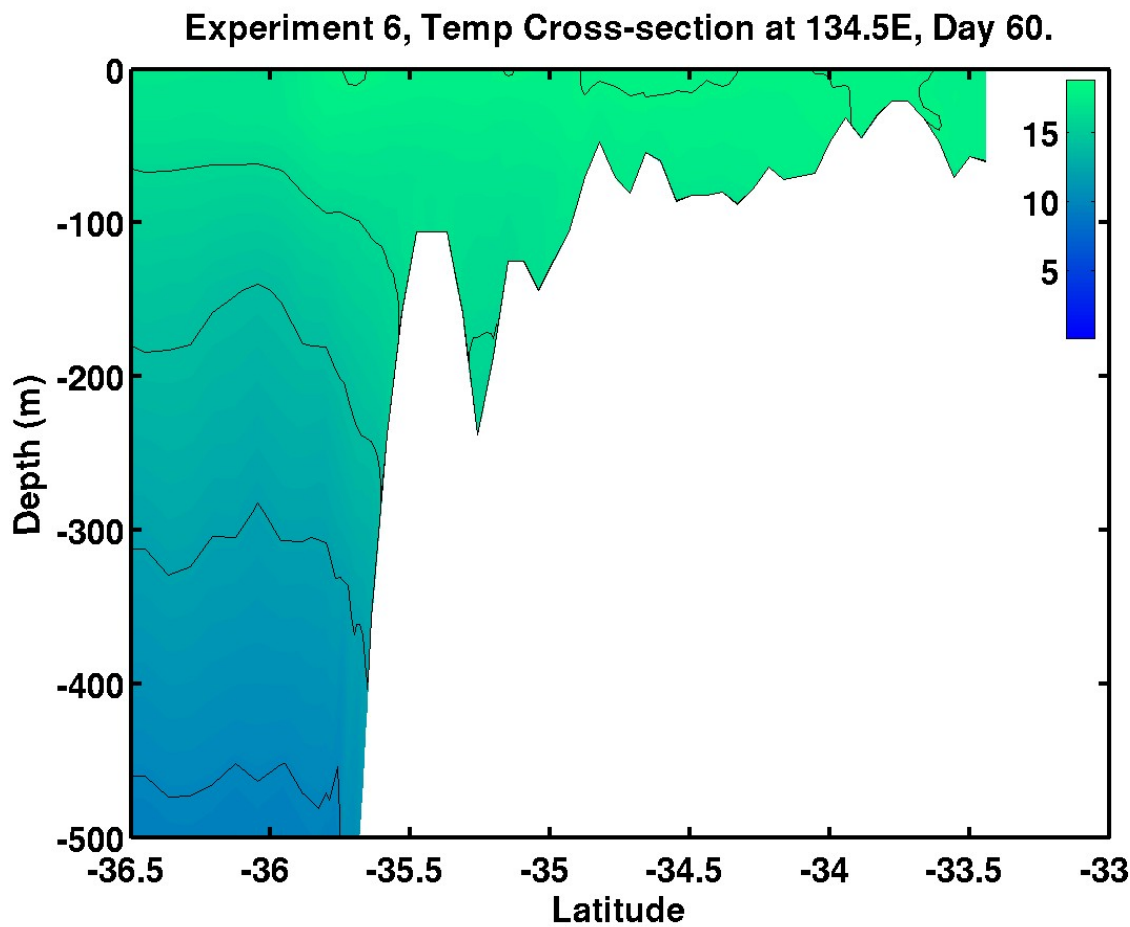


Figure 4.24f. Cross-section of temperature ($^{\circ}\text{C}$) along a north-south transect in the eastern Great Australian Bight (134.5°E) for Experiment 6 on day 60.

Experiment 6, Day 75, Surface.

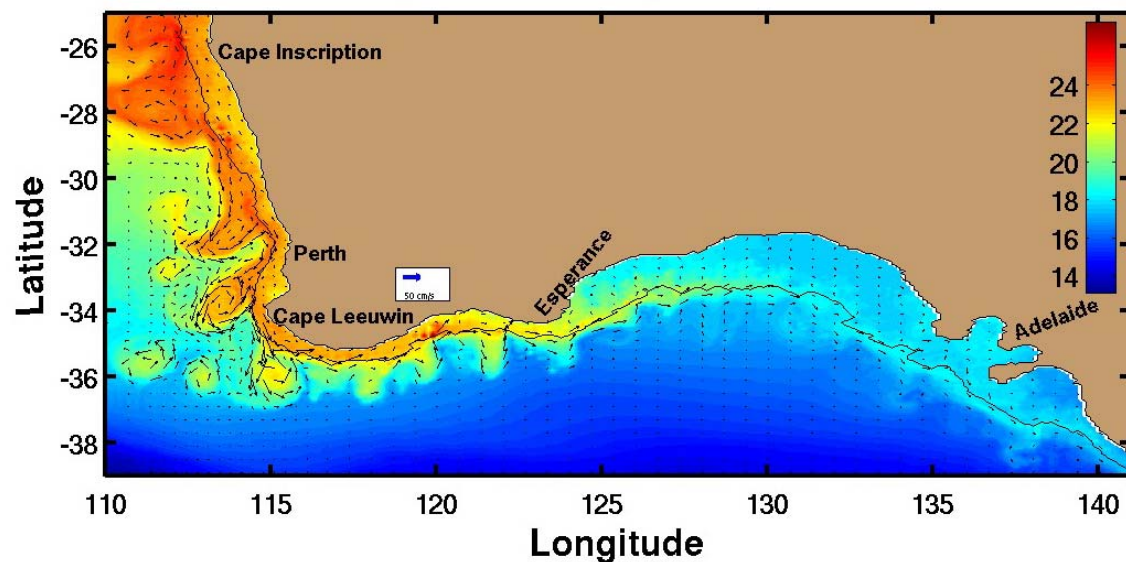


Figure 4.25. Sea surface temperature ($^{\circ}\text{C}$) and velocity vectors for Experiment 6 on day 75.

Experiment 7, Day 20, Surface.

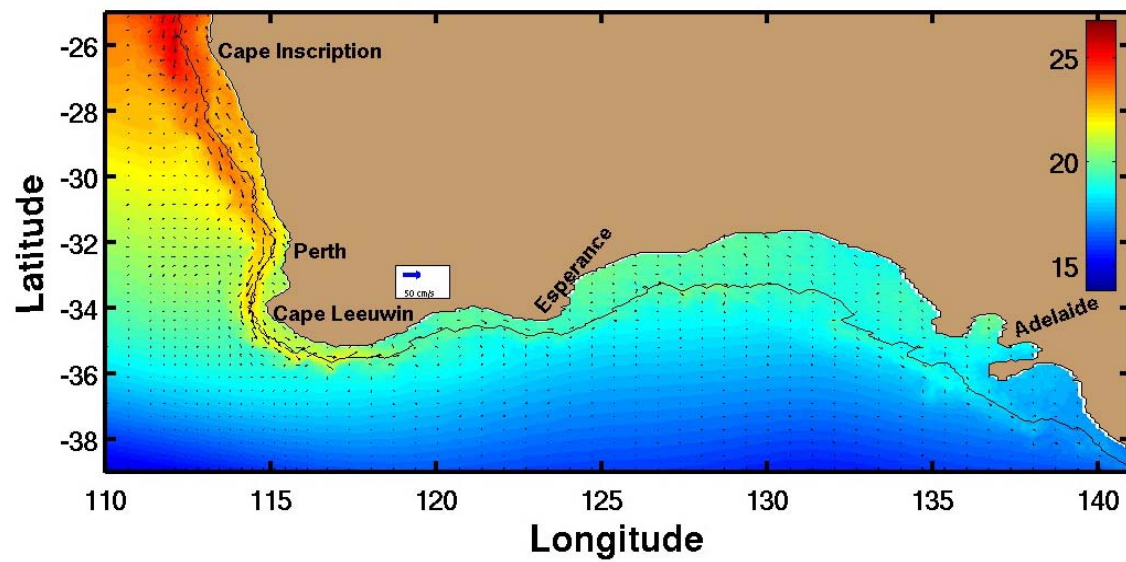


Figure 4.26a. Sea surface temperature ($^{\circ}\text{C}$) and velocity vectors for Experiment 7 on day 20.

Experiment 7, v Cross-section at 26S, Day 20.

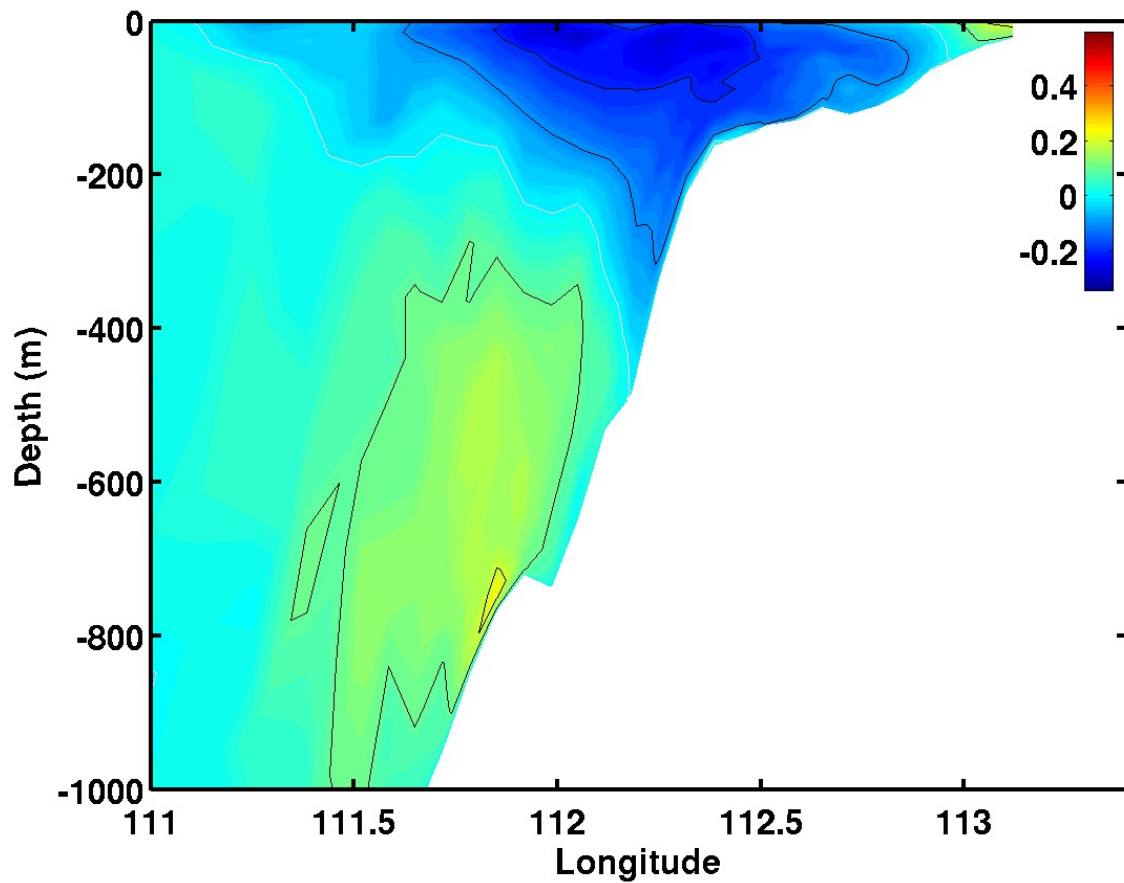


Figure 4.26b. Cross-section of meridional velocity component (m s^{-1}) at 26°S for Experiment 7 on day 20. Red is equatorward (north) and blue is poleward (south). The white contour is zero.

Experiment 7, v Cross-section at 34S, Day 20.

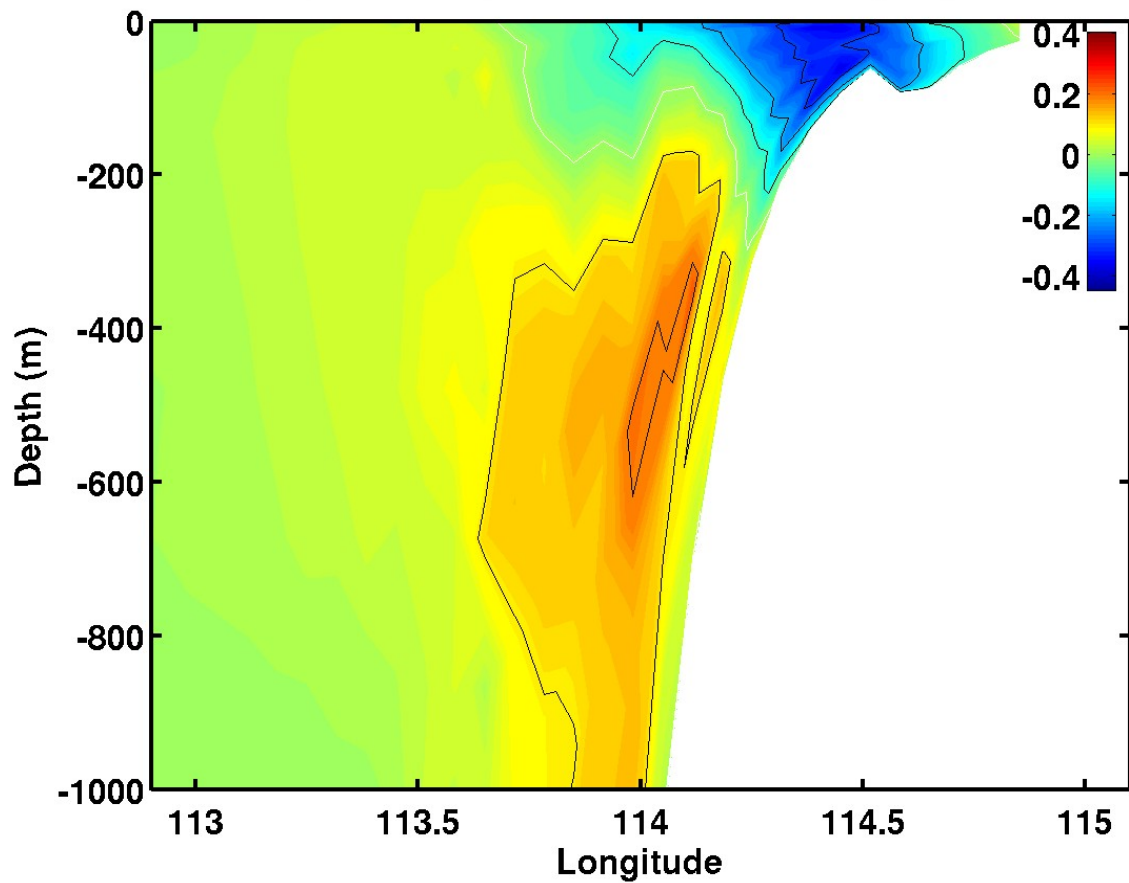


Figure 4.26c. Cross-section of meridional velocity component (m s^{-1}) near Cape Leeuwin (34°S) for Experiment 7 on day 30. Red is equatorward (north) and blue is poleward (south). The white contour is zero.

Experiment 7, u Cross-section at 117E, Day 20.

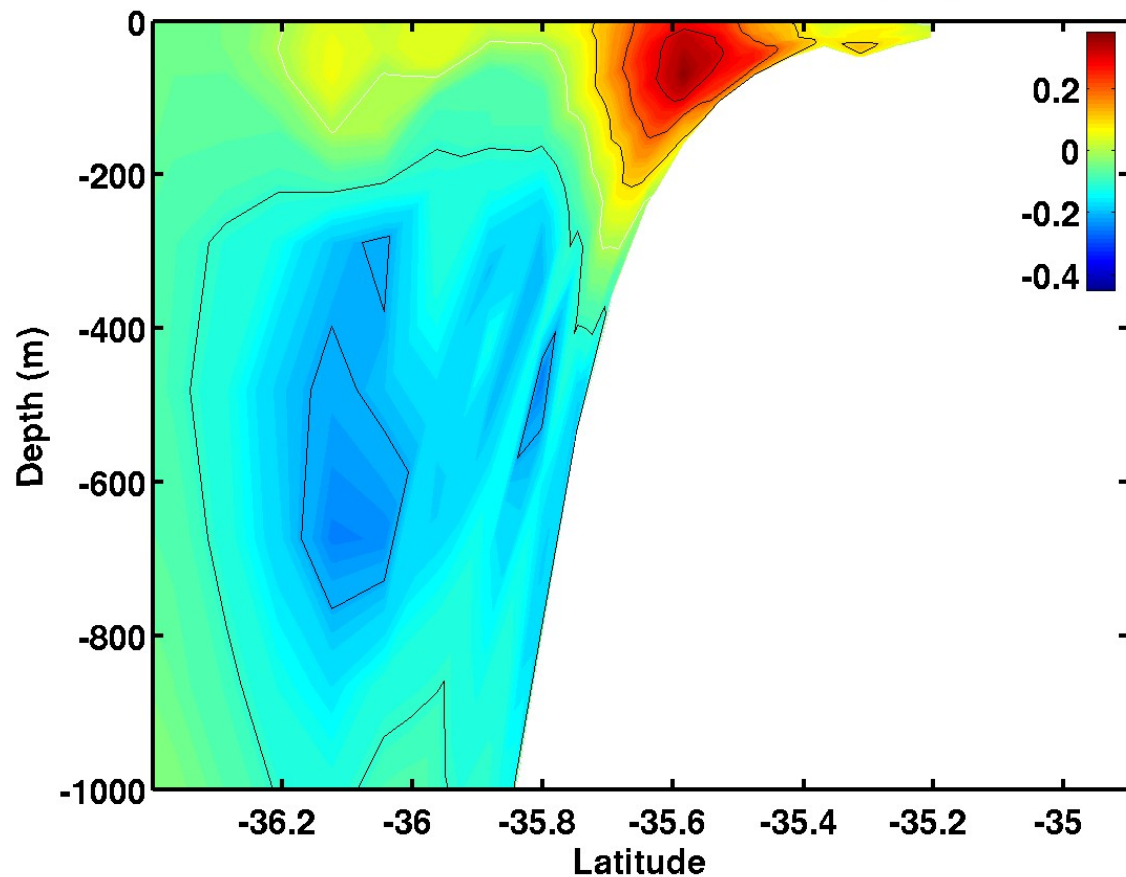


Figure 4.26d. Cross-section of zonal velocity component (m s^{-1}) at 117°E for Experiment 7 on day 20. Red is eastward and blue is westward. The white contour is zero.

Experiment 7, u Cross-section at 130E, Day 20.

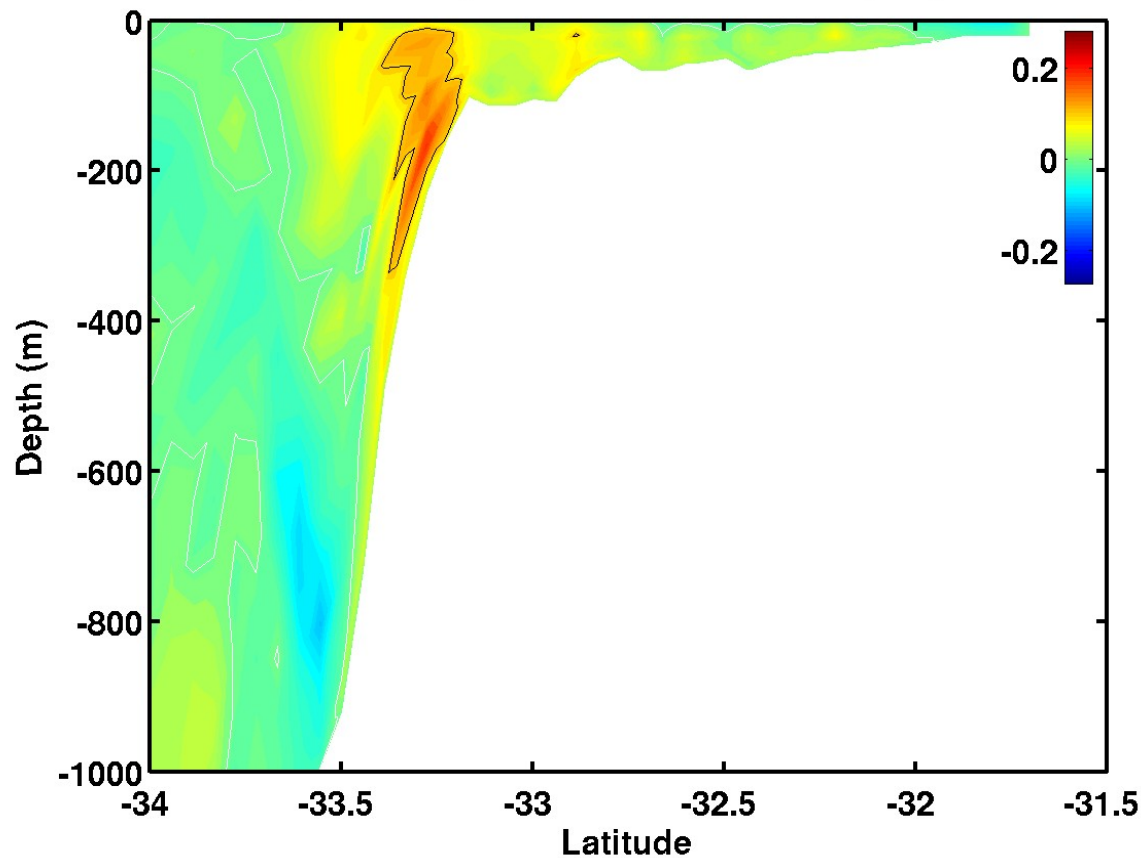


Figure 4.26e. Cross-section of zonal velocity component (m s^{-1}) in the Great Australian Bight (130°E) for Experiment 7 on day 20. Red is eastward and blue is westward. The white contour is zero.

Experiment 7, Day 30, Surface.

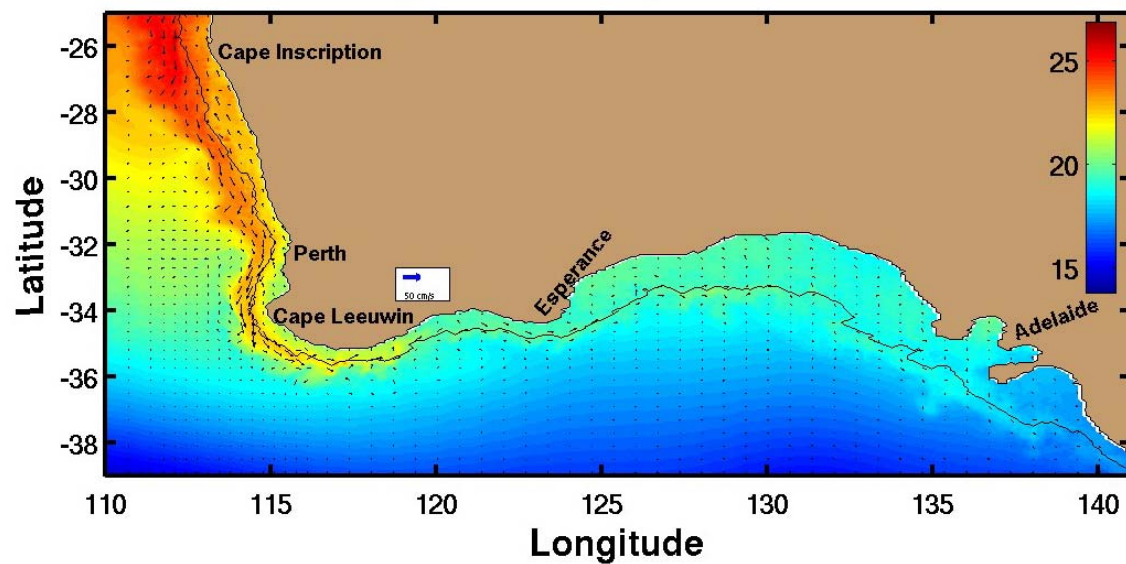


Figure 4.27a. Sea surface temperature ($^{\circ}\text{C}$) and velocity vectors for Experiment 7 on day 30.

Experiment 7, u Cross-section at 117°E, Day 30.

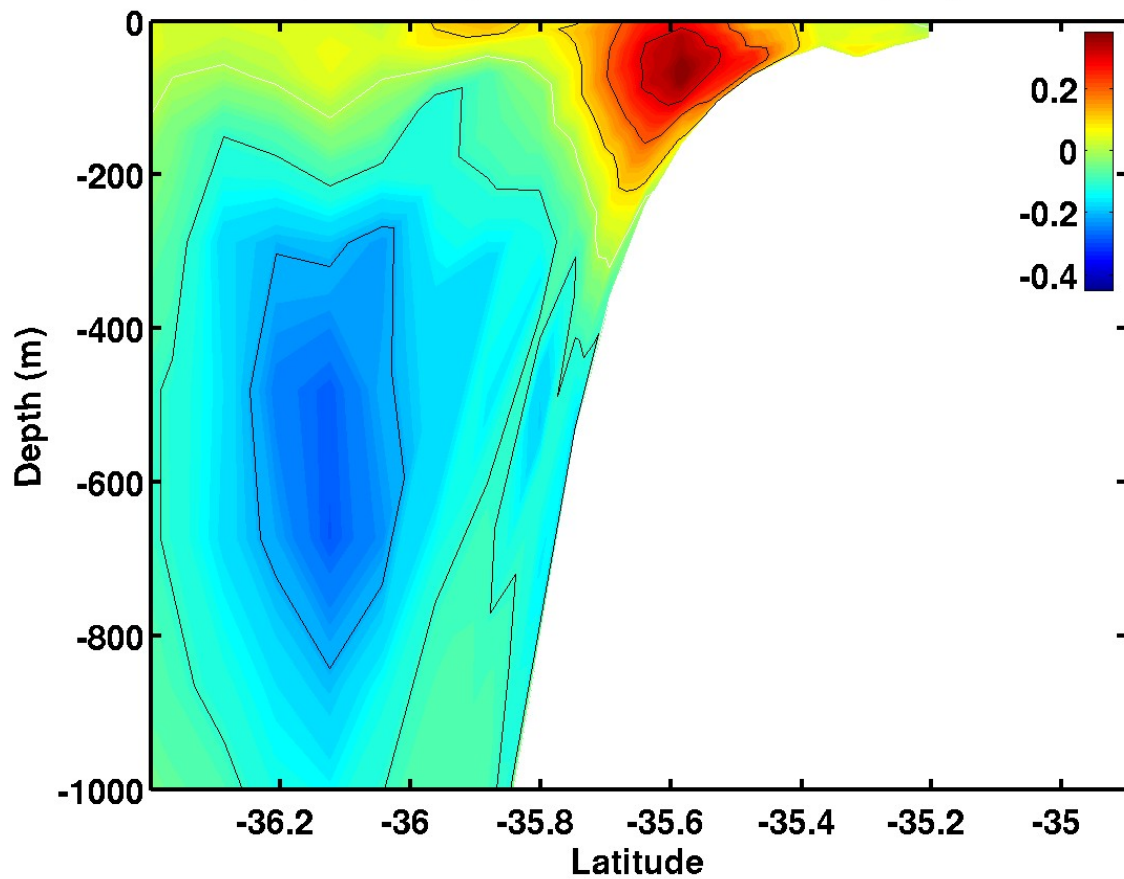


Figure 4.27b. Cross-section of zonal velocity component (m s^{-1}) at 117°E for Experiment 7 on day 30. Red is eastward and blue is westward. The white contour is zero.

Experiment 7, u Cross-section at 130E, Day 30.

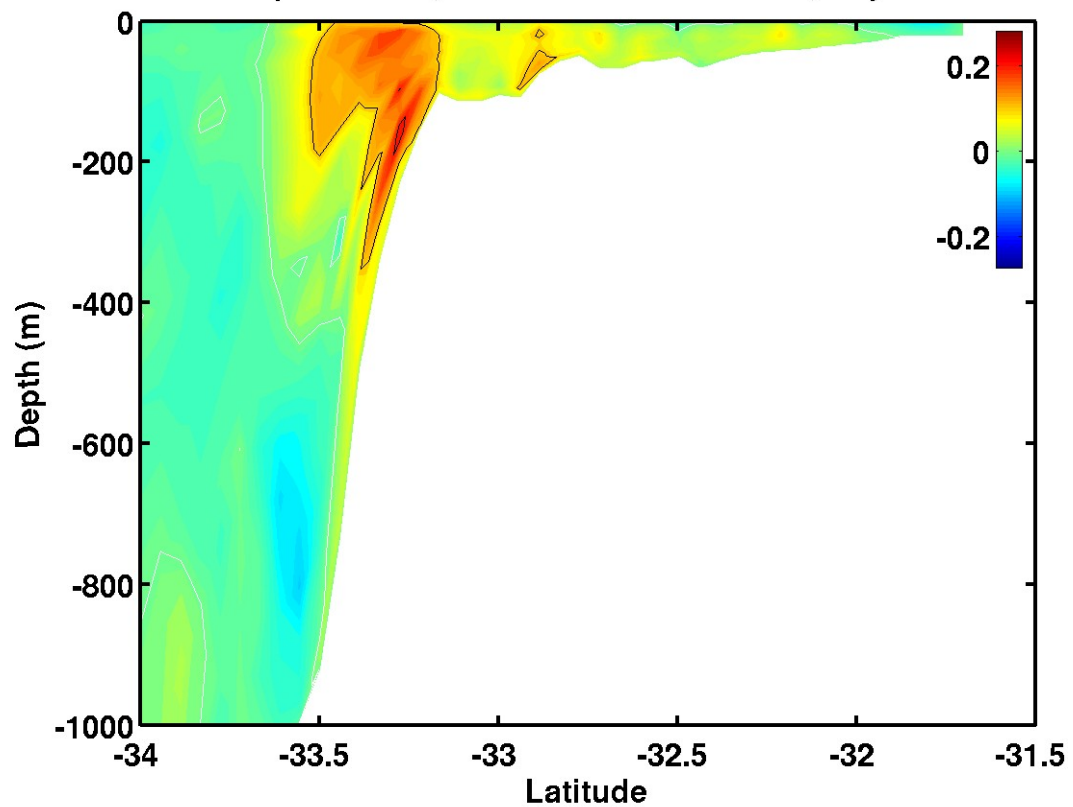


Figure 4.27c. Cross-section of zonal velocity component (m s^{-1}) in the Great Australian Bight (130°E) for Experiment 7 on day 30. Red is eastward and blue is westward. The white contour is zero.

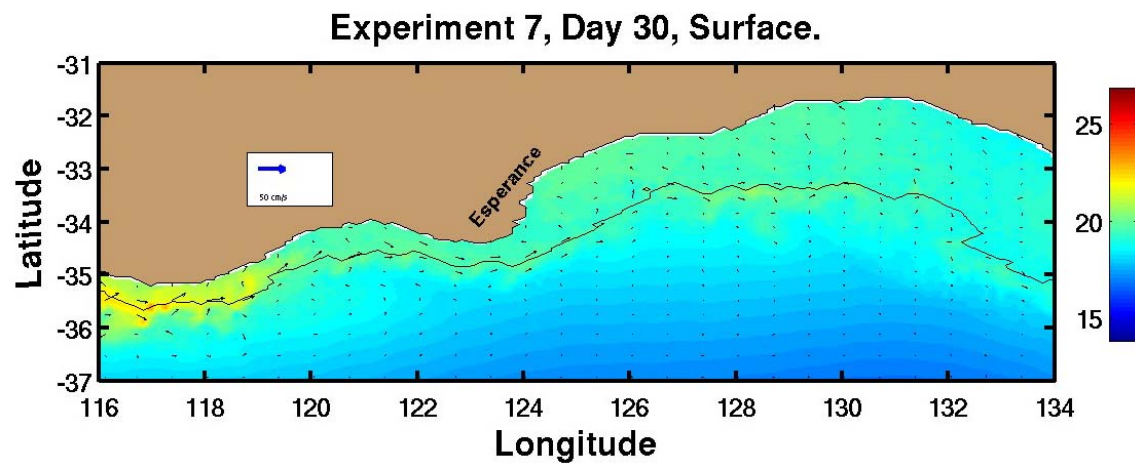


Figure 27d. Sea surface temperature ($^{\circ}\text{C}$) and velocity vectors along the southwestern coast and Great Australian Bight for Experiment 7 on day 30.

Experiment 7, Day 39, Surface.

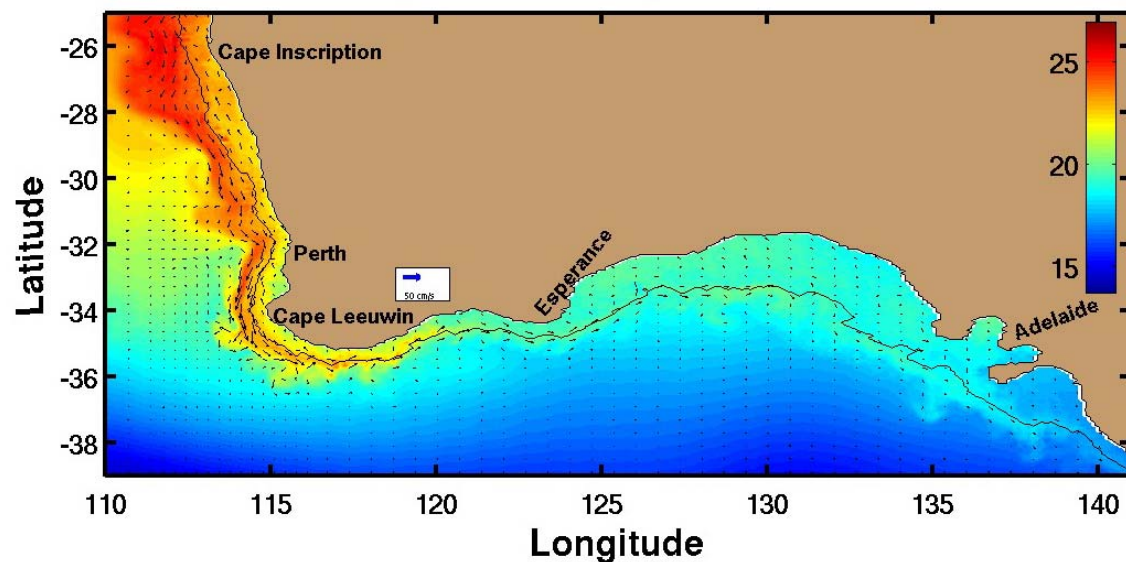


Figure 4.28. Sea surface temperature ($^{\circ}\text{C}$) and velocity vectors for Experiment 7 on day 39.

Experiment 7, Day 60, Surface.

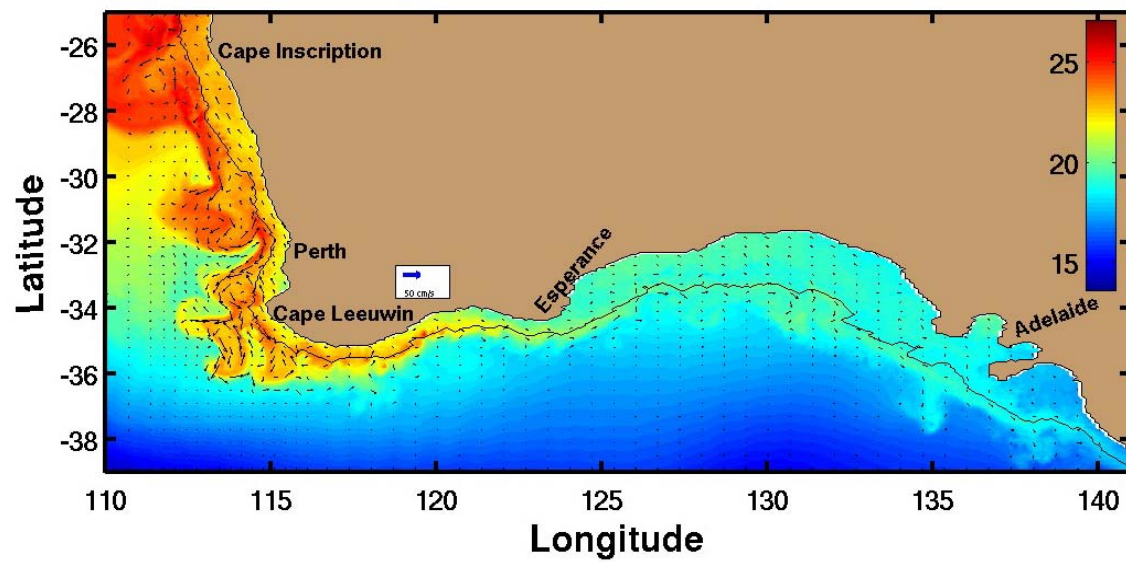


Figure 4.29a. Sea surface temperature ($^{\circ}\text{C}$) and velocity vectors for Experiment 7 on day 60.

Experiment 7, Day 60, Surface.

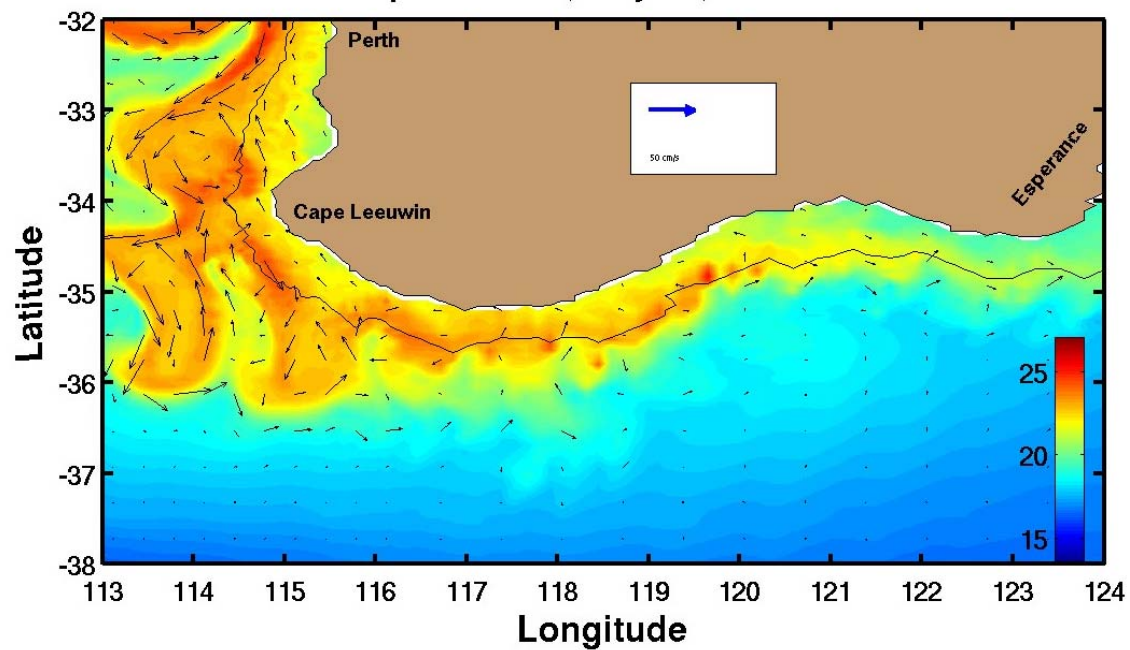


Figure 4.29b. Sea surface temperature ($^{\circ}\text{C}$) and velocity vectors along the southwestern coast for Experiment 7 on day 30.

Experiment 7, u Cross-section at 130E, Day 60.

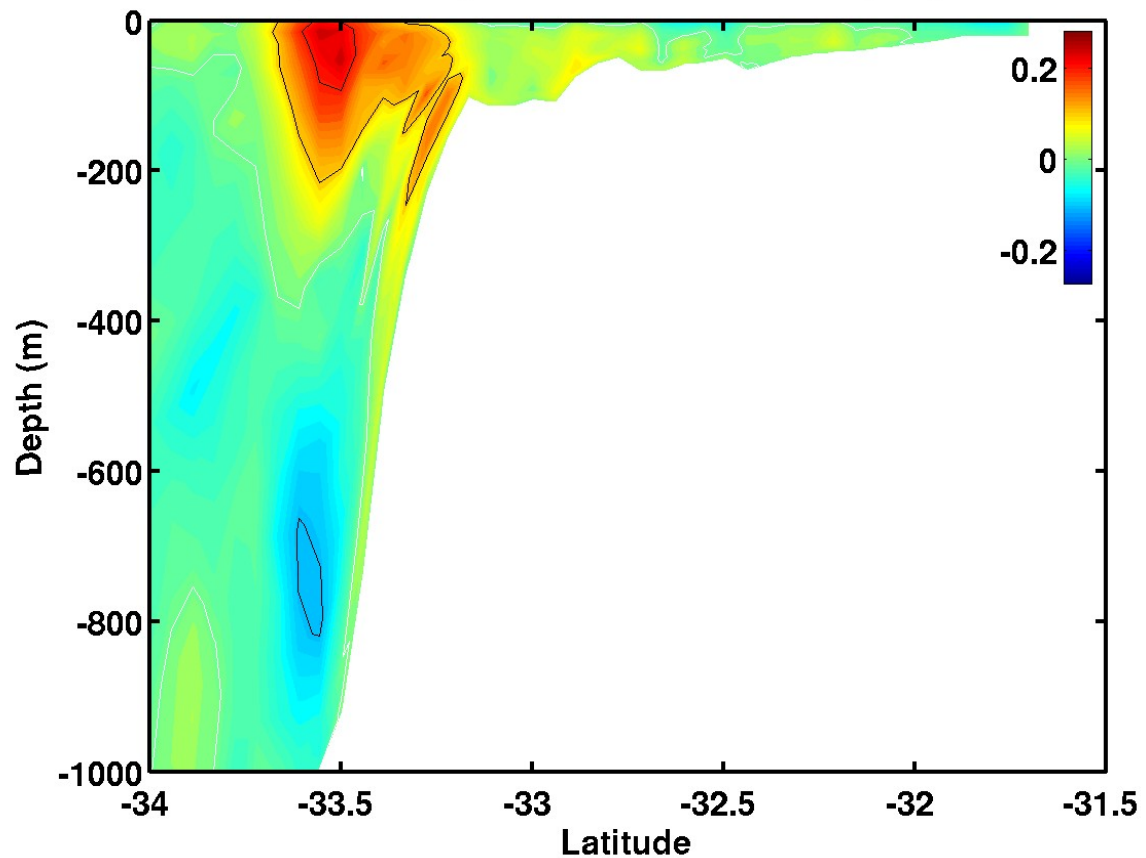


Figure 4.29c. Cross-section of zonal velocity component ($m s^{-1}$) in the Great Australian Bight ($130^{\circ}E$) for Experiment 7 on day 60. Red is eastward and blue is westward. The white contour is zero.

Experiment 7, Day 60, Surface.

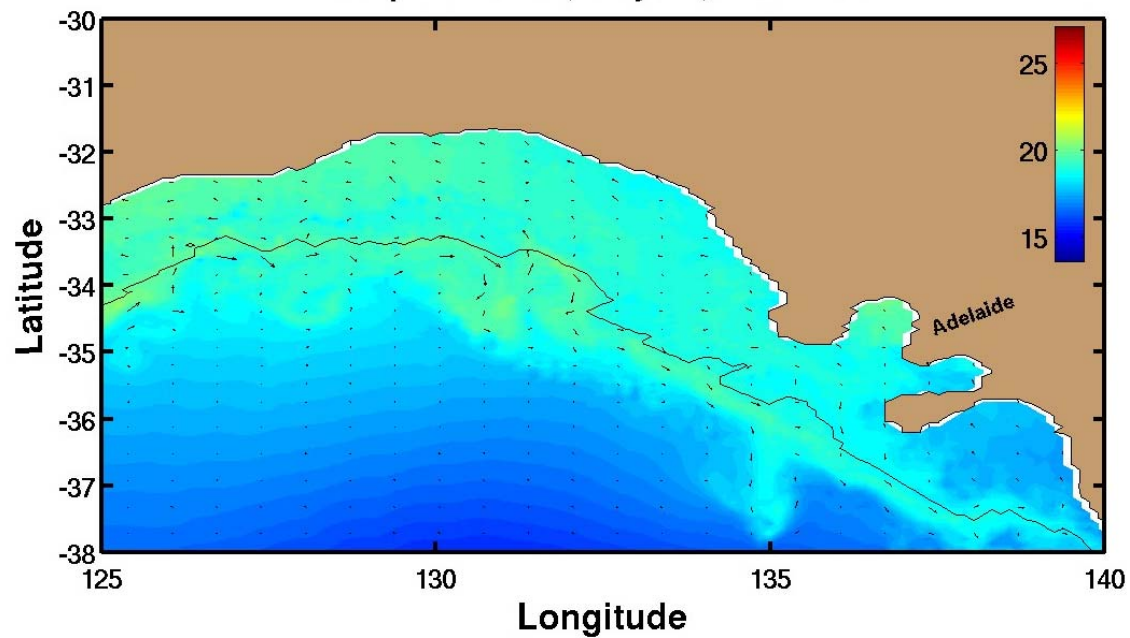


Figure 4.29d. Sea surface temperature ($^{\circ}\text{C}$) and velocity vectors for the Great Australian Bight for Experiment 7 on day 60.

Experiment 7, Day 81, Surface.

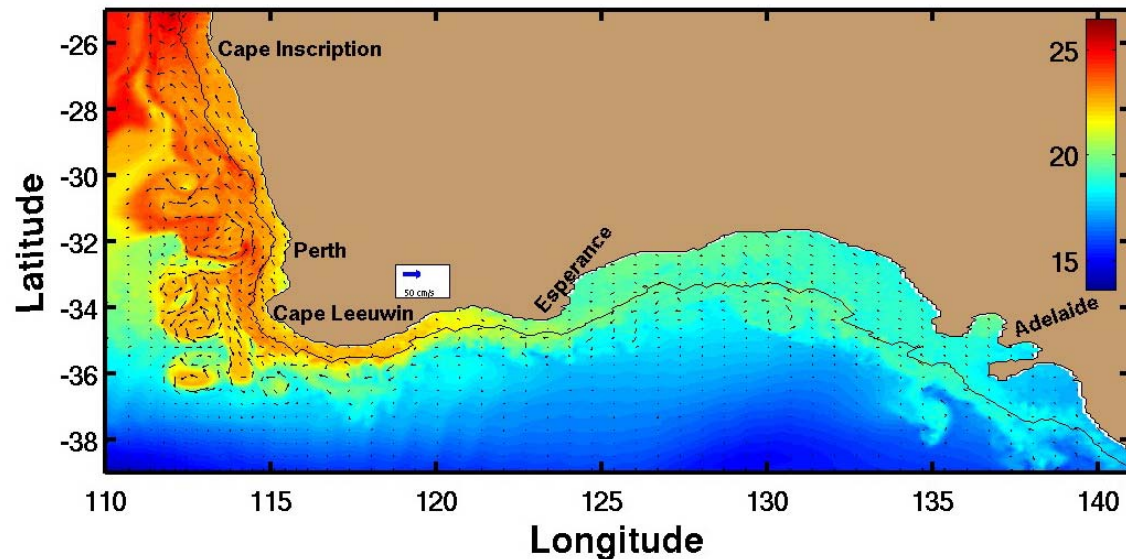


Figure 4.30. Sea surface temperature ($^{\circ}\text{C}$) and velocity vectors for Experiment 7 on day 81.

Experiment 8, Day 20, Surface.

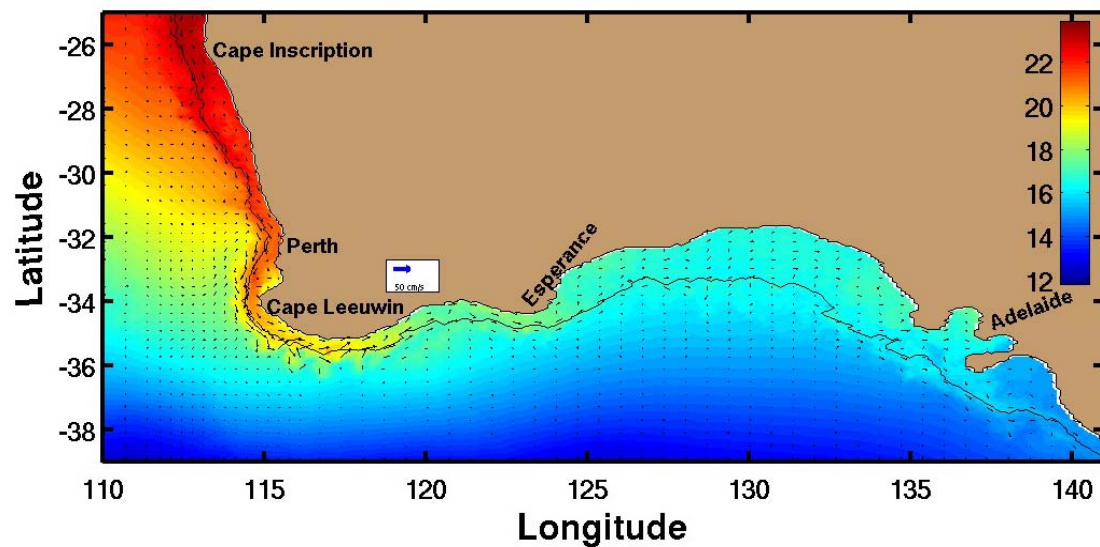


Figure 4.31a. Sea surface temperature ($^{\circ}\text{C}$) and velocity vectors for Experiment 8 on day 20.

Experiment 8, v Cross-section at 26S, Day 20.

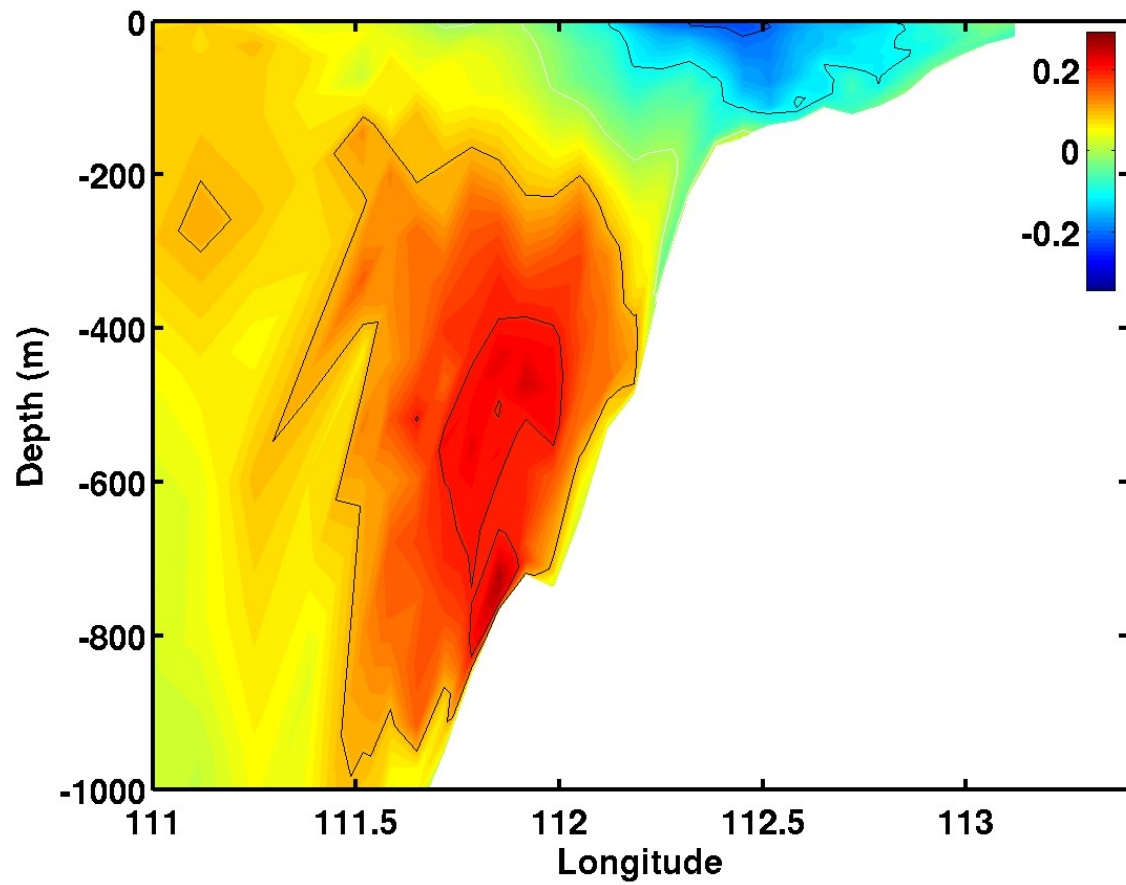


Figure 4.31b. Cross-section of temperature ($^{\circ}\text{C}$) along an east-west transect at 26 $^{\circ}\text{S}$ for Experiment 8 on day 20.

Experiment 8, v Cross-section at 34S, Day 20.

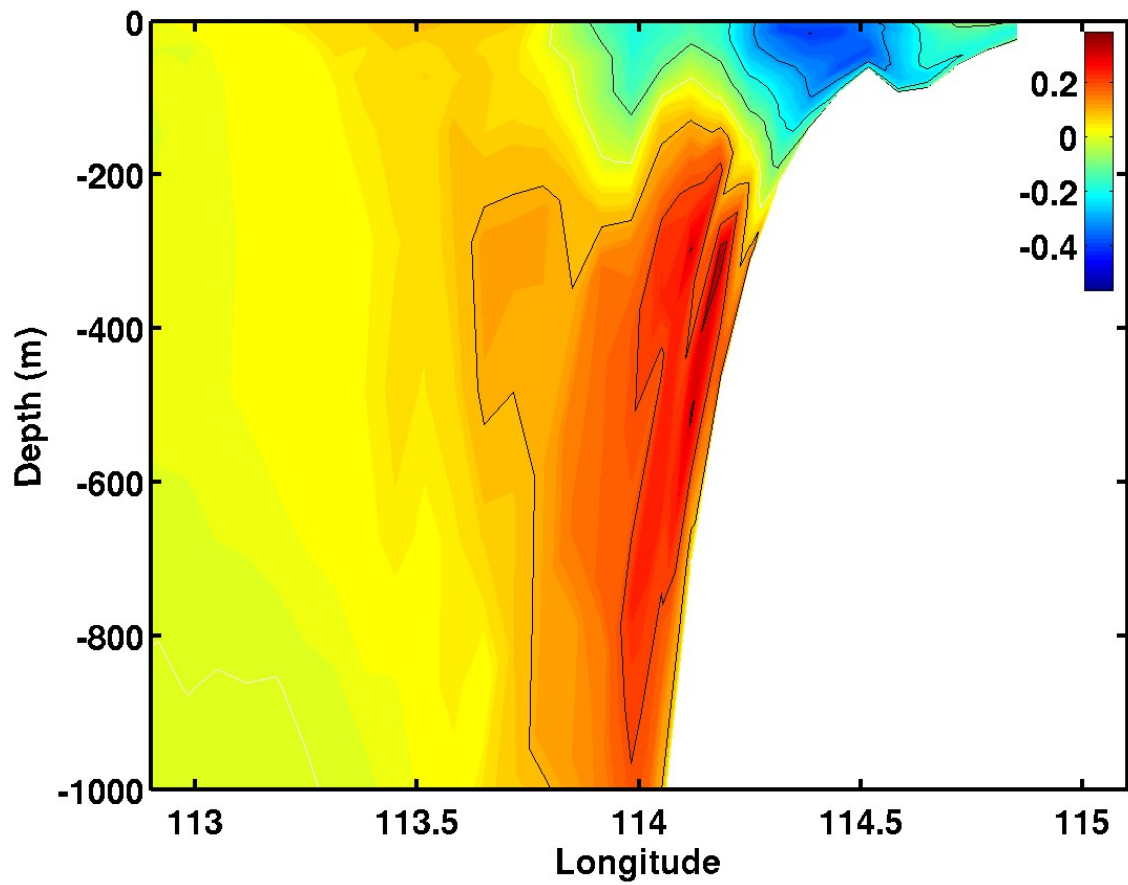


Figure 4.31c. Cross-section of temperature (°C) along an east-west transect near Cape Leeuwin (34°S) for Experiment 8 on day 20.

Experiment 8, u Cross-section at 117°E, Day 20.

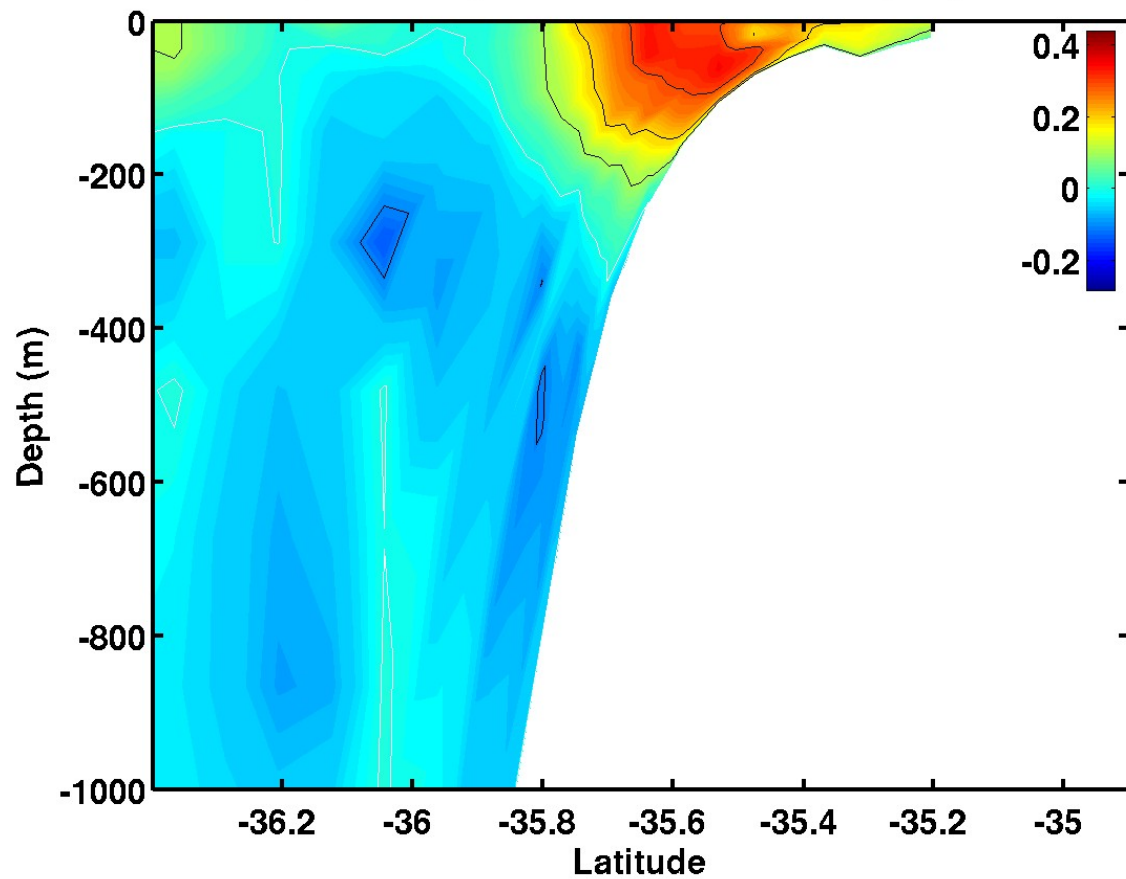


Figure 4.31d. Cross-section of zonal velocity component ($m s^{-1}$) at 117°E for Experiment 8 on day 20. Red is eastward and blue is westward. The white contour is zero.

Experiment 8, u Cross-section at 125E, Day 20.

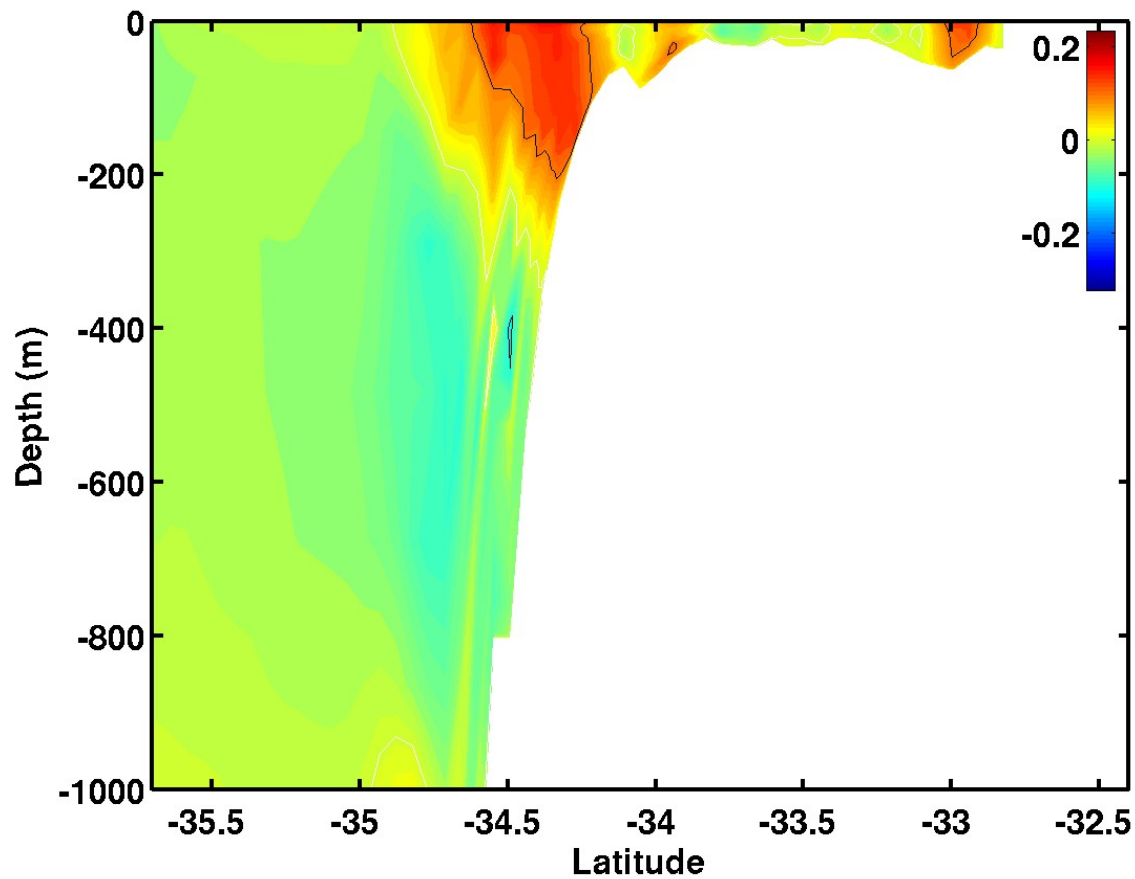


Figure 4.31e. Cross-section of zonal velocity component (m s^{-1}) along a north-south transect in the western Great Australian Bight (125°E) for Experiment 8 on day 20. Red is eastward and blue is westward. The white contour is zero.

Experiment 8, u Cross-section at 130°E, Day 20.

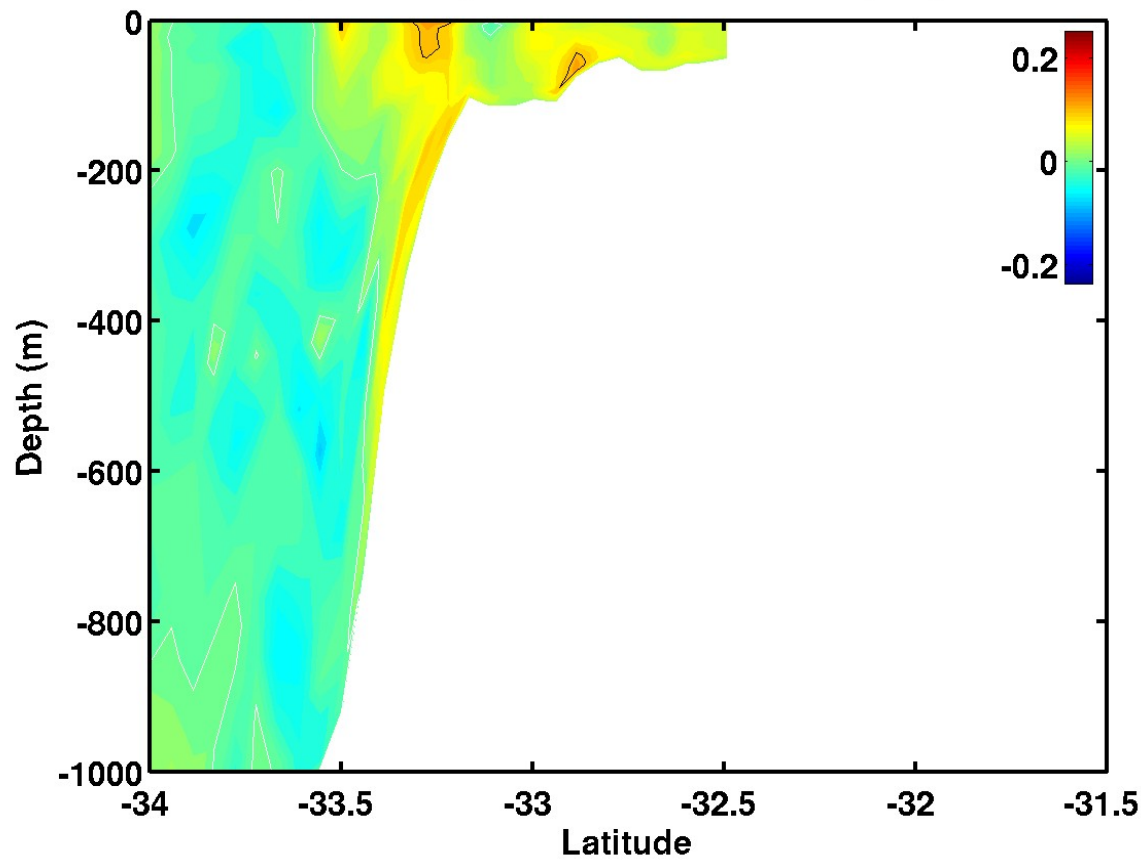


Figure 4.31f. Cross-section of zonal velocity component (m s^{-1}) in the Great Australian Bight (130°E) for Experiment 8 on day 20. Red is eastward and blue is westward. The white contour is zero.

Experiment 8, Day 30, Surface.

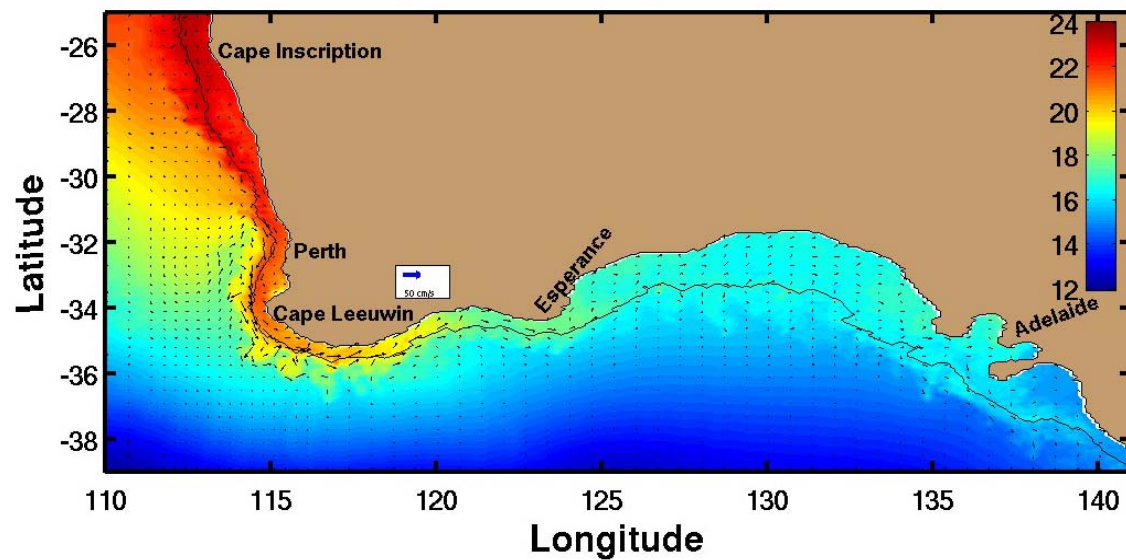


Figure 4.32a. Sea surface temperature ($^{\circ}\text{C}$) and velocity vectors for Experiment 8 on day 30.

Experiment 8, v Cross-section at 26S, Day 30.

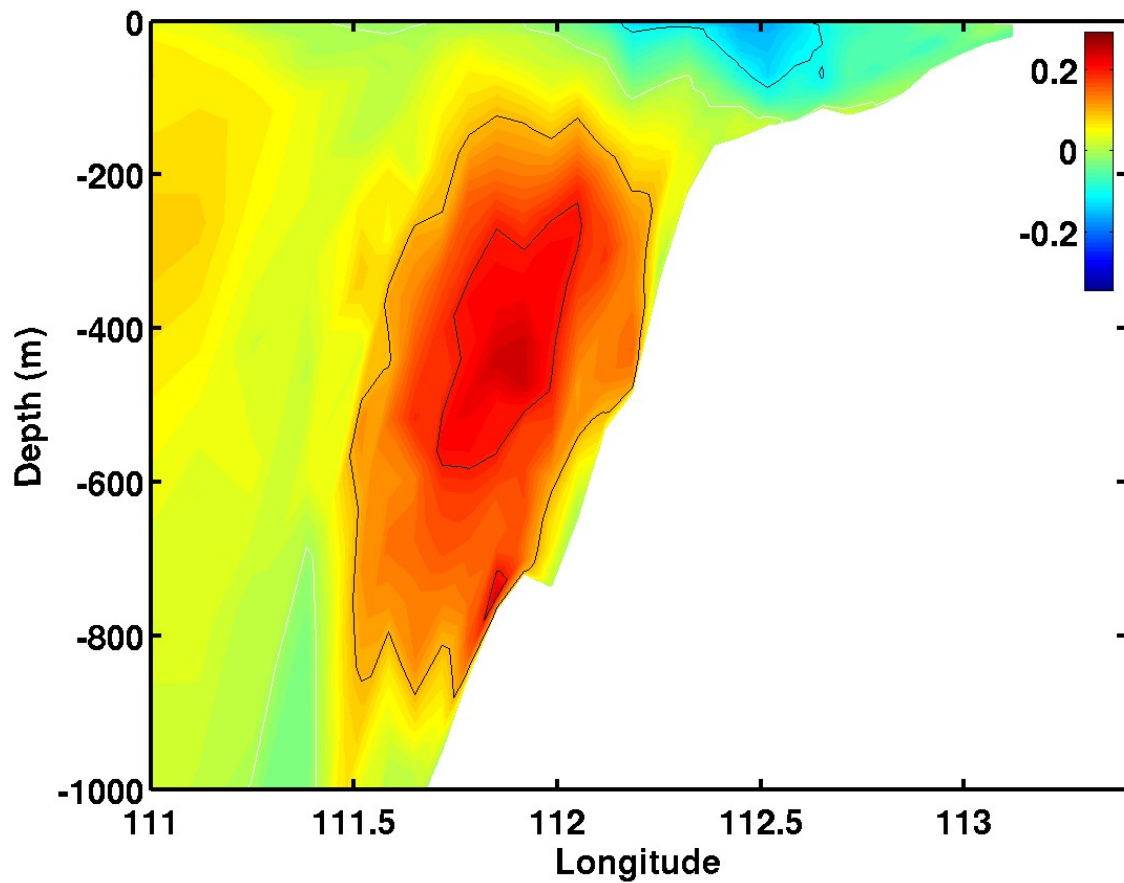


Figure 4.32b. Cross-section of meridional velocity component (m s^{-1}) at 26°S for Experiment 8 on day 30. Red is equatorward (north) and blue is poleward (south). The white contour is zero.

Experiment 8, v Cross-section at 34S, Day 30.

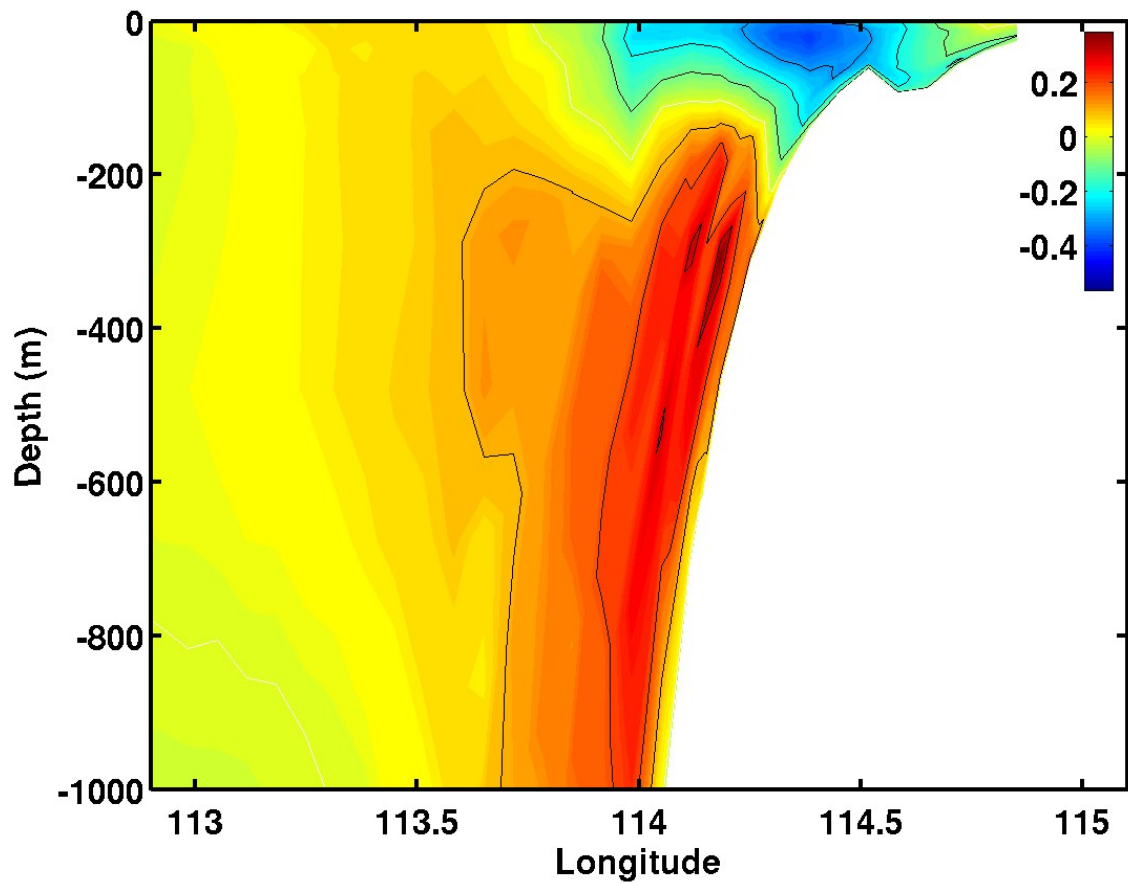


Figure 4.32c. Cross-section of meridional velocity component (m s^{-1}) near Cape Leeuwin (34°S) for Experiment 8 on day 30. Red is equatorward (north) and blue is poleward (south). The white contour is zero.

Experiment 8, u Cross-section at 117°E, Day 30.

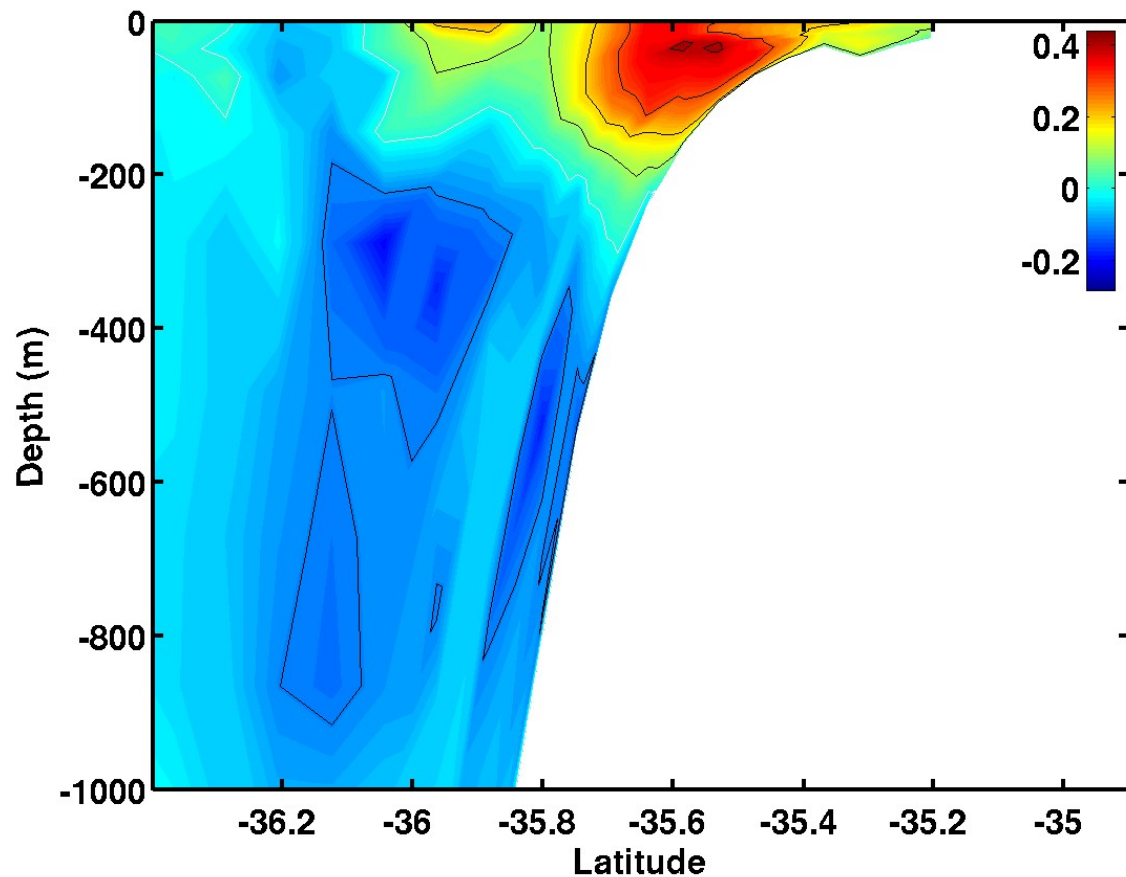


Figure 4.32d. Cross-section of zonal velocity component (m s^{-1}) at 117°E for Experiment 8 on day 30. Red is eastward and blue is westward. The white contour is zero.

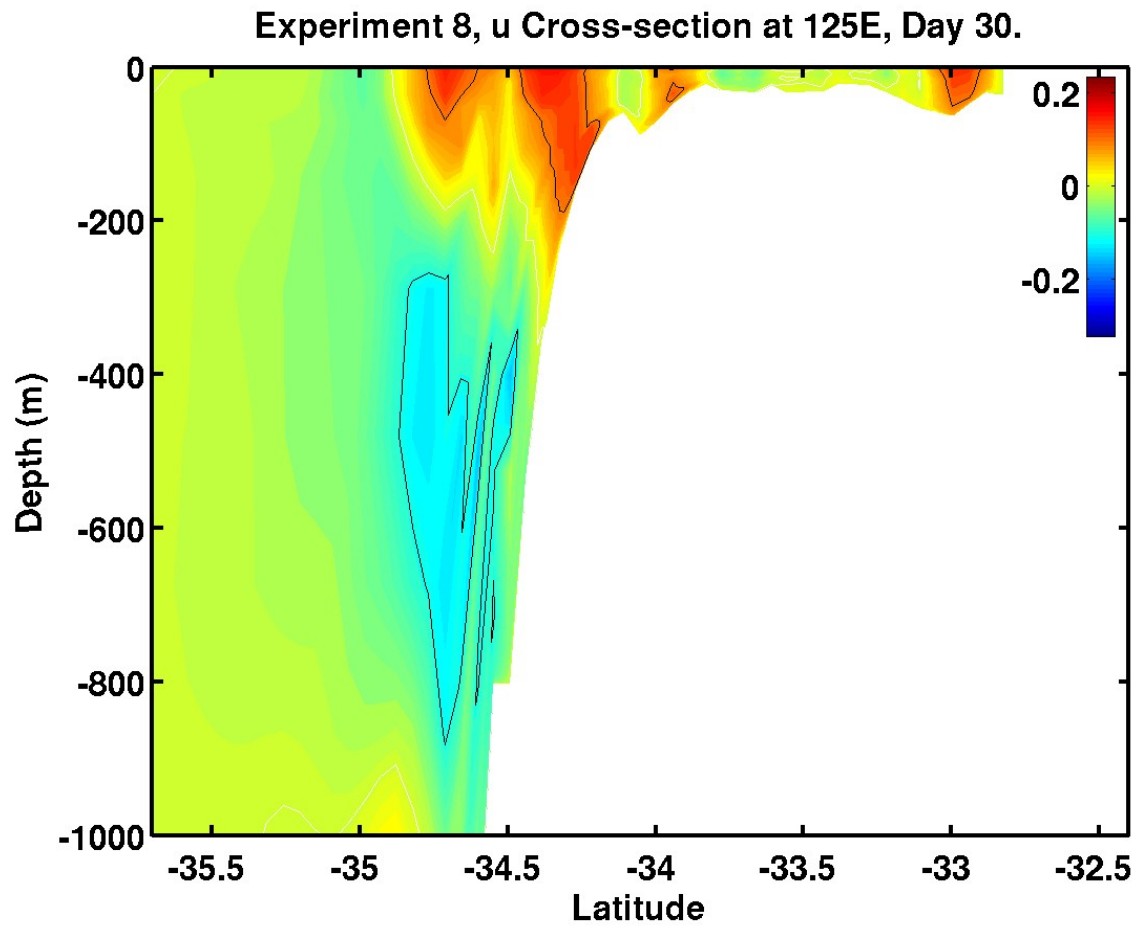


Figure 4.32e. Cross-section of zonal velocity component (m s^{-1}) in the Great Australian Bight (125°E) for Experiment 8 on day 30. Red is eastward and blue is westward. The white contour is zero.

Experiment 8, u Cross-section at 130E, Day 30.

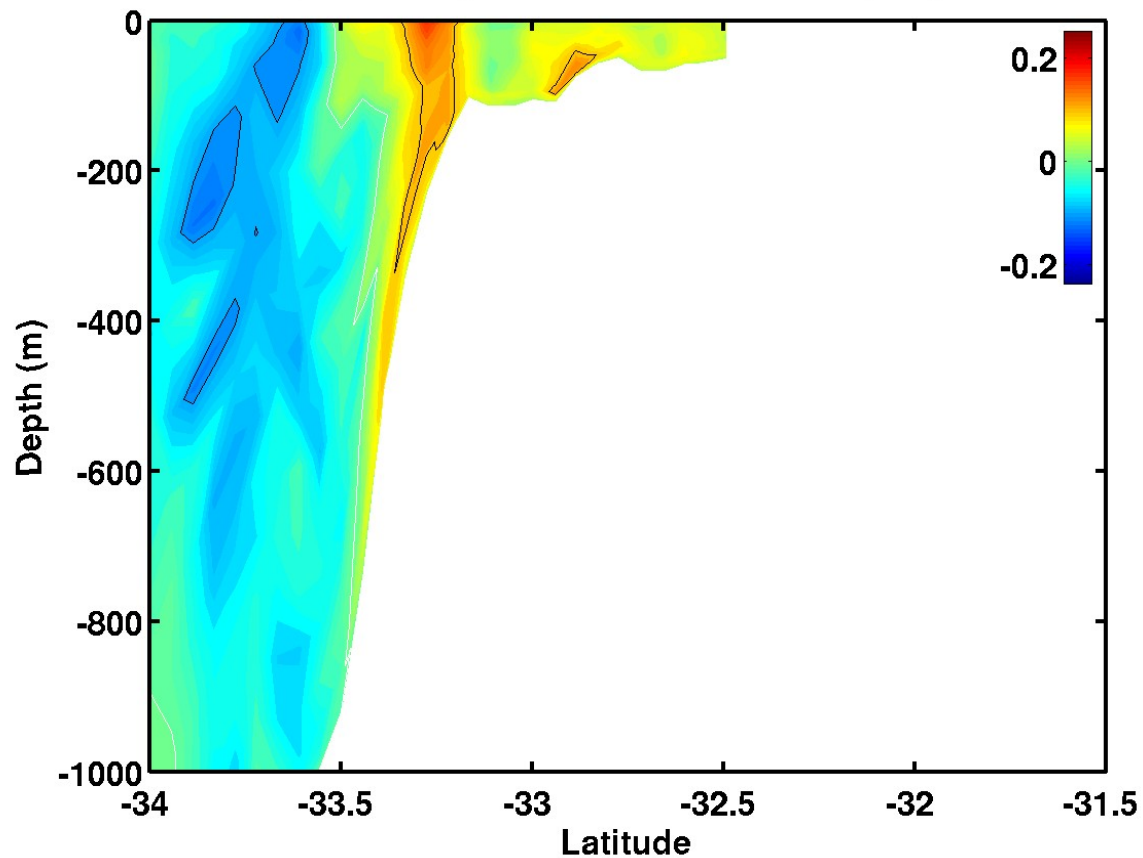


Figure 4.32f. Cross-section of zonal velocity component (m s^{-1}) in the Great Australian Bight (130°E) for Experiment 8 on day 30. Red is eastward and blue is westward. The white contour is zero.

Experiment 8, Day 60, Surface.

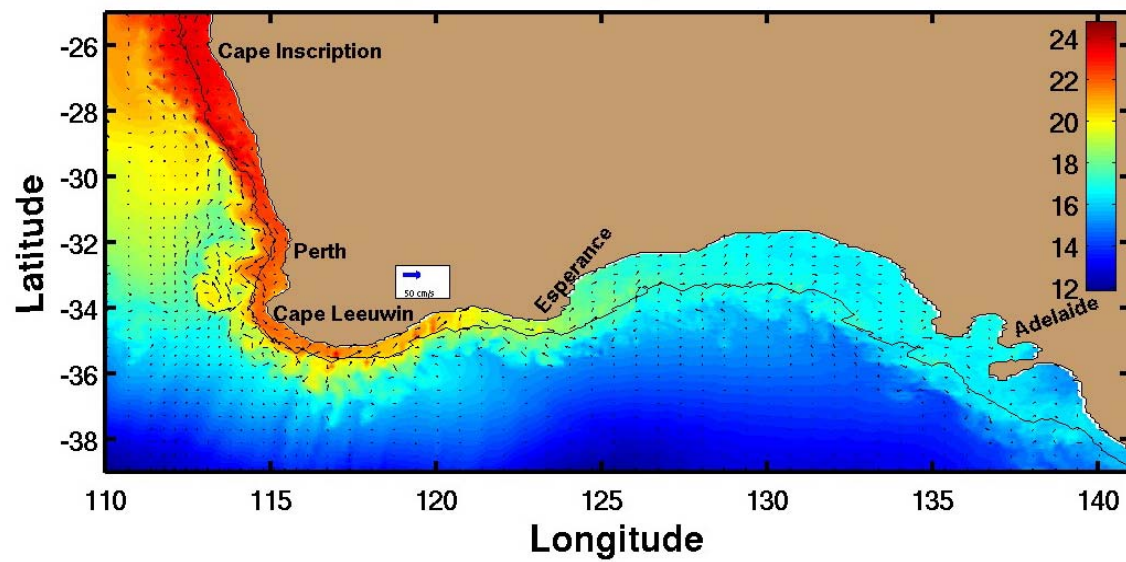


Figure 4.33a. Sea surface temperature ($^{\circ}\text{C}$) and velocity vectors for Experiment 8 on day 60.

Experiment 8, v Cross-section at 26S, Day 60.

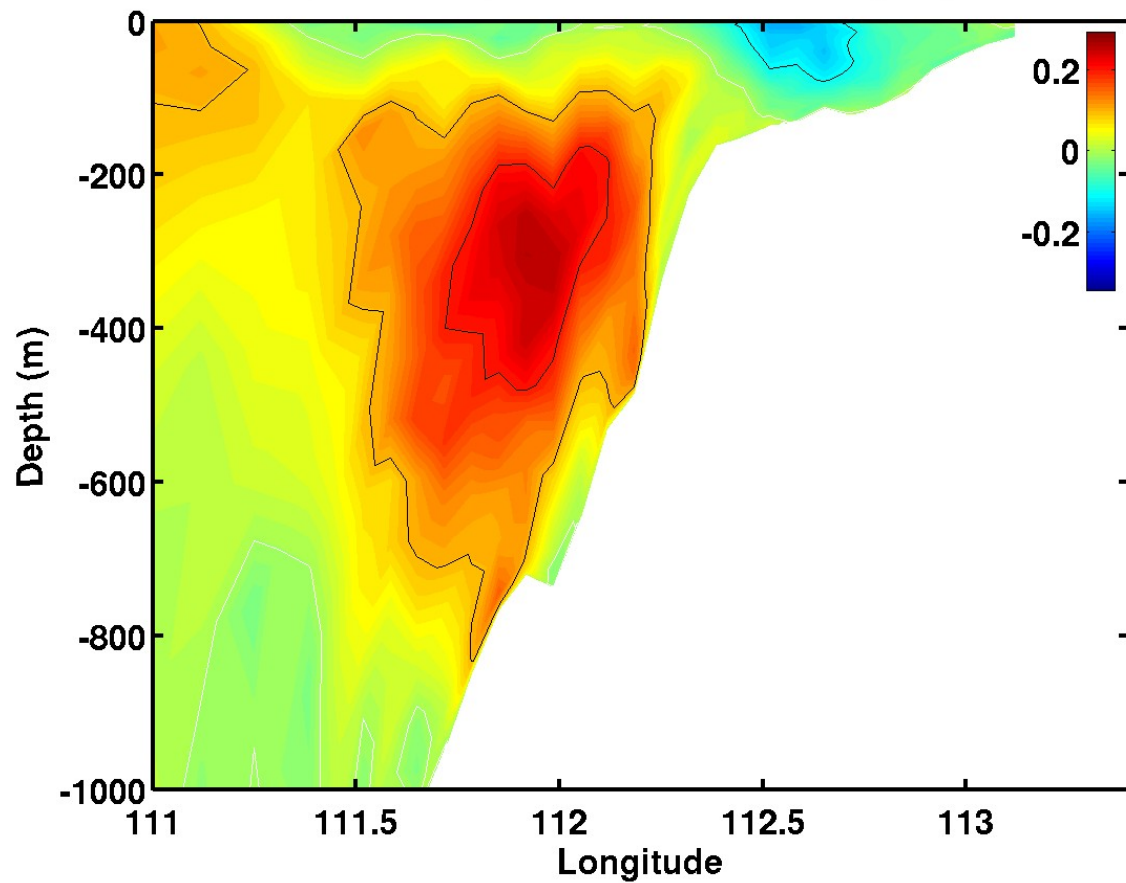


Figure 4.33b. Cross-section of meridional velocity component (m s^{-1}) at 26°S for Experiment 8 on day 60. Red is equatorward (north) and blue is poleward (south). The white contour is zero.

Experiment 8, v Cross-section at 34S, Day 60.

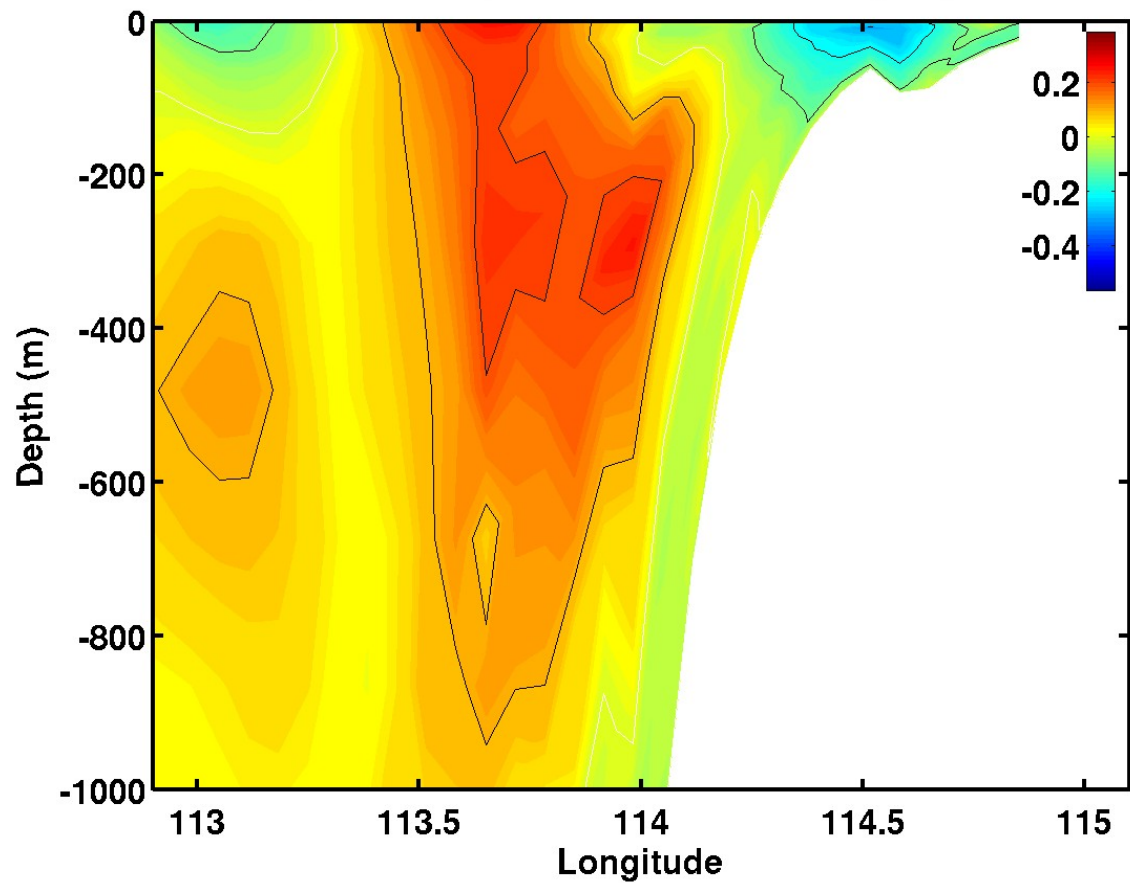


Figure 4.33c. Cross-section of meridional velocity component (m s^{-1}) near Cape Leeuwin (34°S) for Experiment 8 on day 60. Red is equatorward (north) and blue is poleward (south). The white contour is zero.

Experiment 8, u Cross-section at 125E, Day 60.

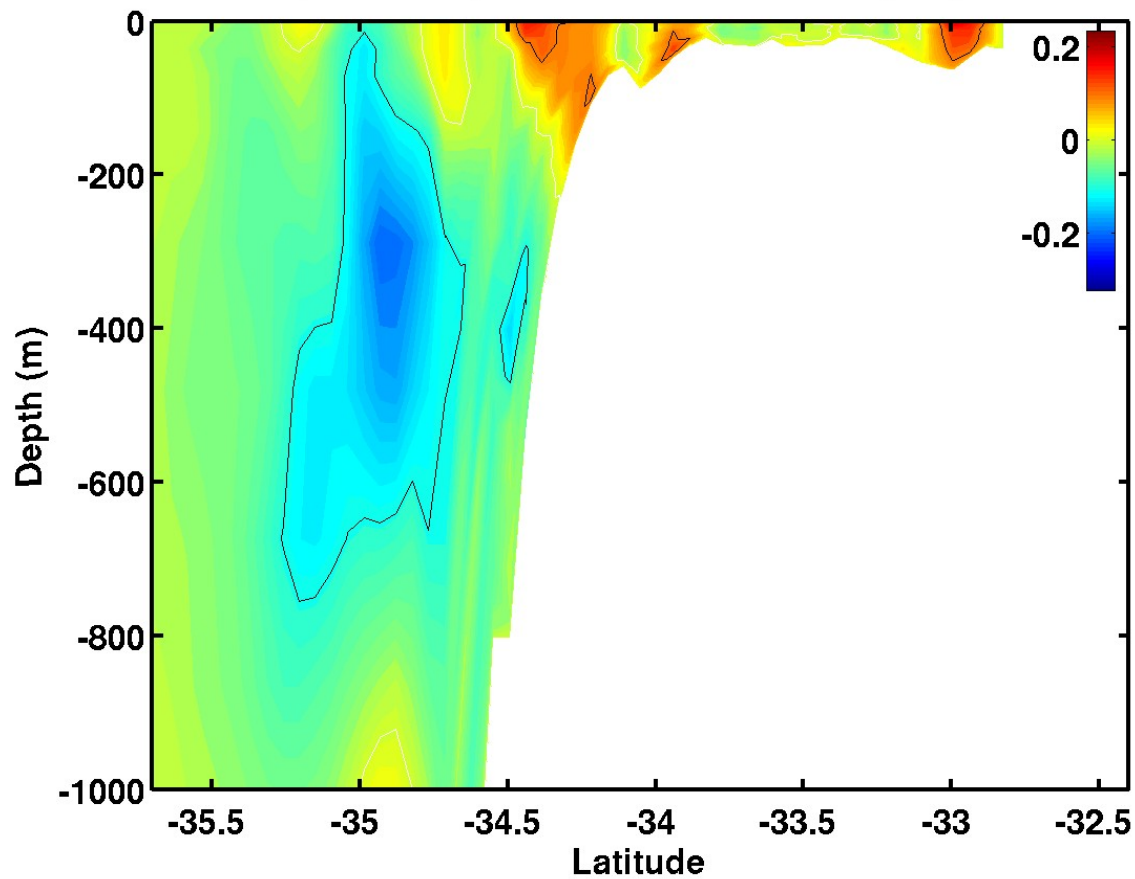


Figure 4.33d. Cross-section of zonal velocity component (m s^{-1}) along a north-south transect in the western Great Australian Bight (125°E) for Experiment 8 on day 60. Red is eastward and blue is westward. The white contour is zero.

Experiment 8, u Cross-section at 130E, Day 60.

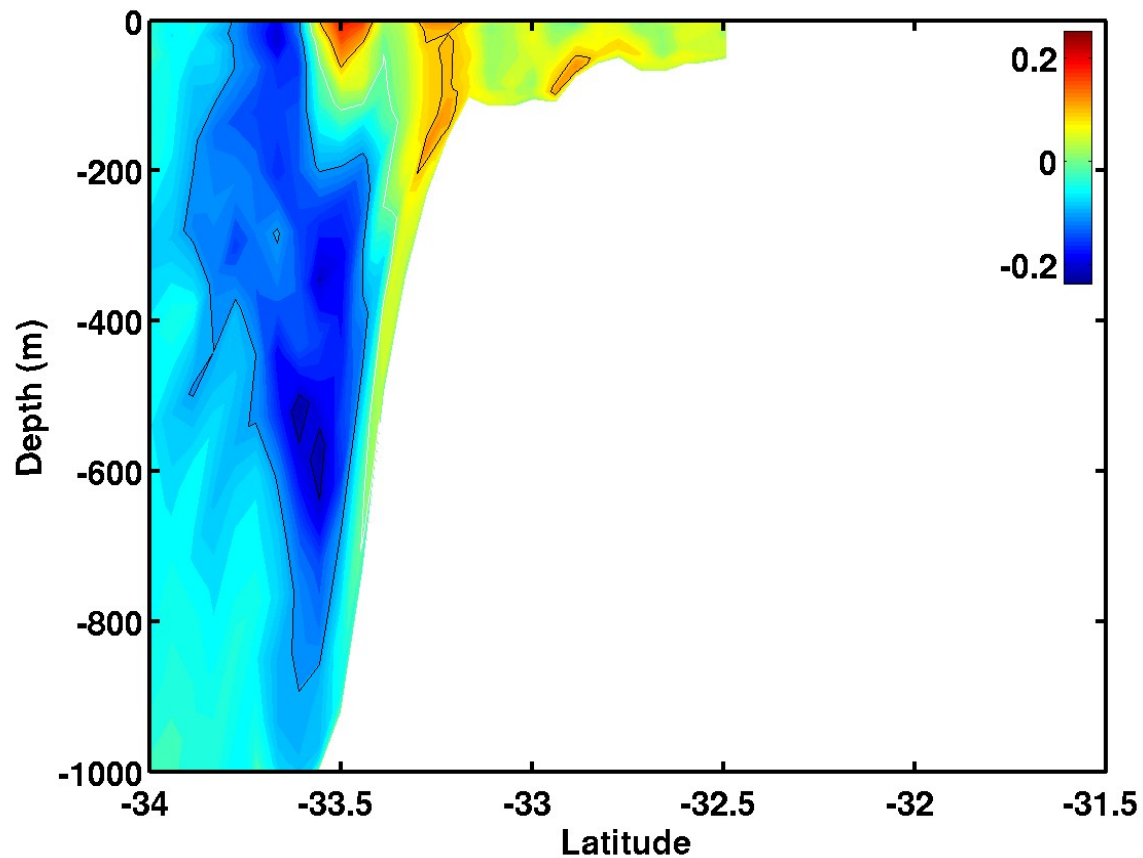


Figure 4.33e. Cross-section of zonal velocity component (m s^{-1}) in the Great Australian Bight (130°E) for Experiment 8 on day 60. Red is eastward and blue is westward. The white contour is zero.

Experiment 8, Day 72, Surface.

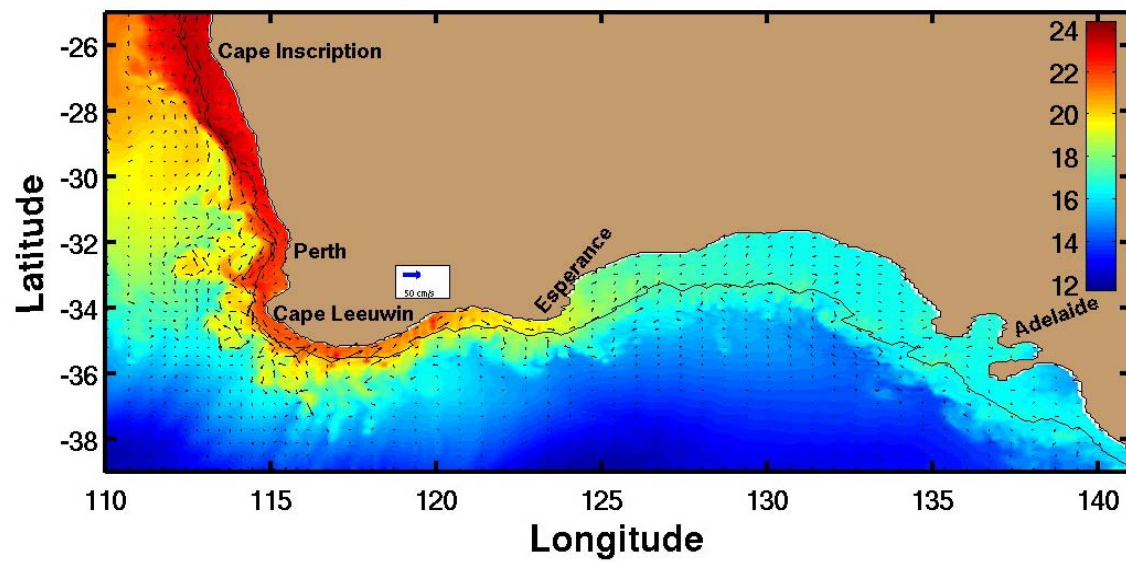


Figure 4.34. Sea surface temperature ($^{\circ}\text{C}$) and velocity vectors for Experiment 8 on day 72.

Surface Temperature and Velocity, Day 20, December 21, 1980

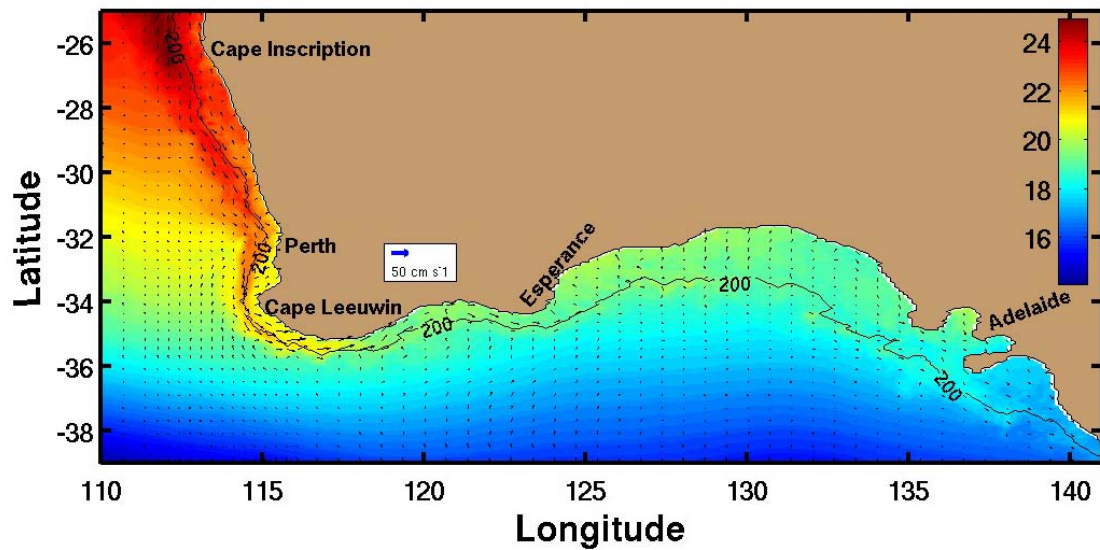


Figure 5.1. Sea surface temperature ($^{\circ}\text{C}$) and velocity vectors for daily wind Experiment 1 on day 20, December 21, 1980.

Surface Temperature and Velocity, Day 30, December 31, 1980

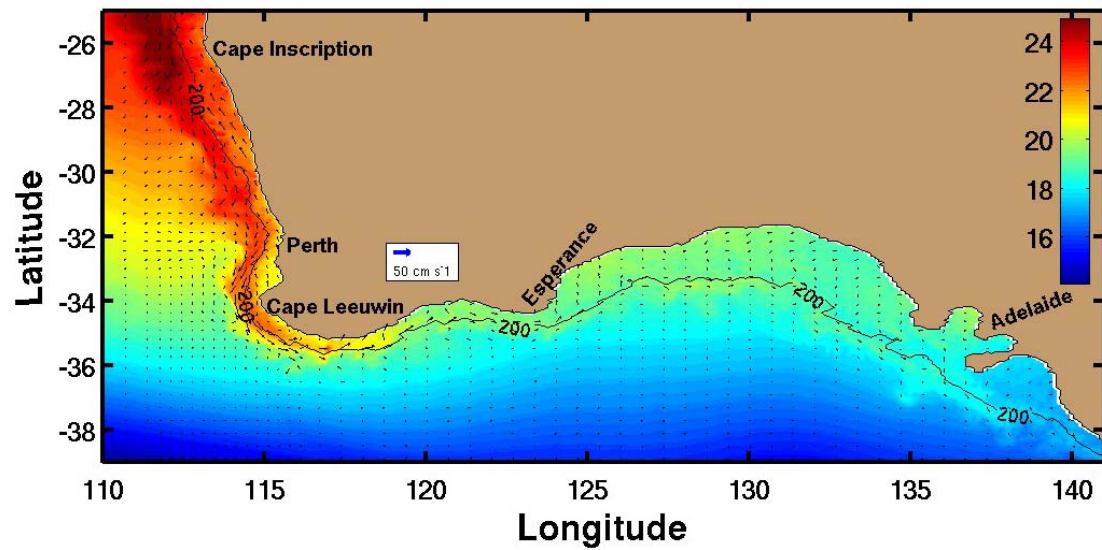


Figure 5.2a. Sea surface temperature ($^{\circ}\text{C}$) and velocity vectors for daily wind Experiment 1 on day 30, December 31, 1980.

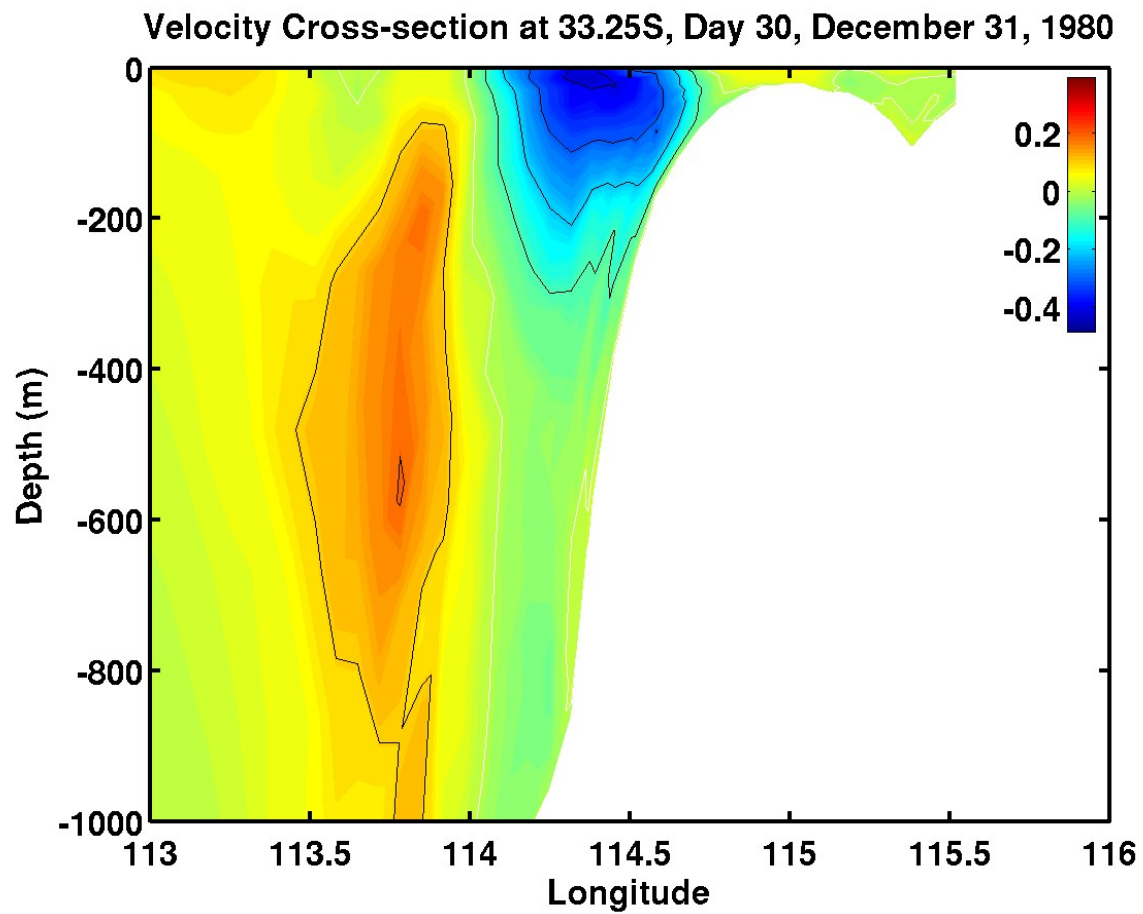


Figure 5.2b. Cross-section of meridional velocity component (m s^{-1}) 33.25°S for daily wind Experiment 1 on day 30, December 31, 1980. Red is equatorward (north) and blue is poleward (south). The white contour is zero.

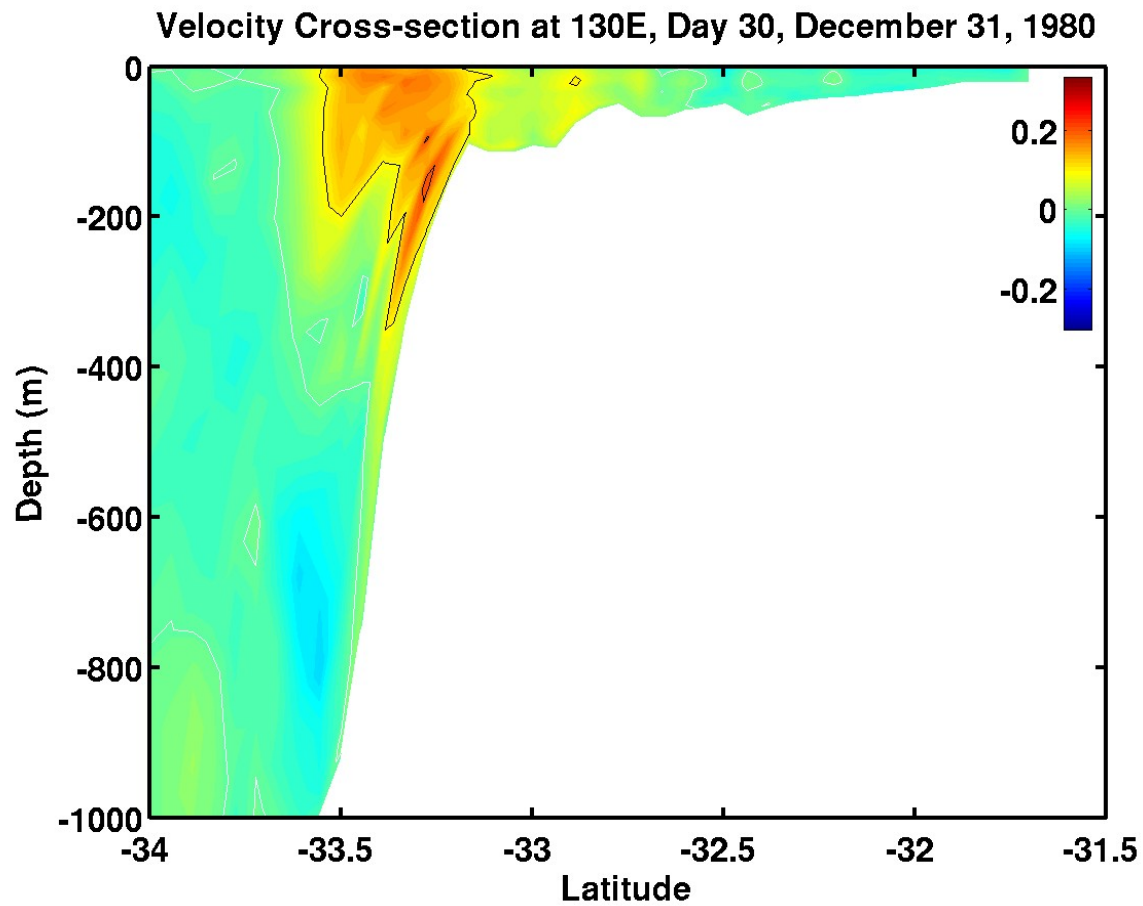


Figure 5.2c. Cross-section of zonal velocity component (m s^{-1}) in the Great Australian Bight (130°E) for daily wind Experiment 1 on day 30, December 31, 1980. Red is eastward and blue is westward. The white contour is zero.

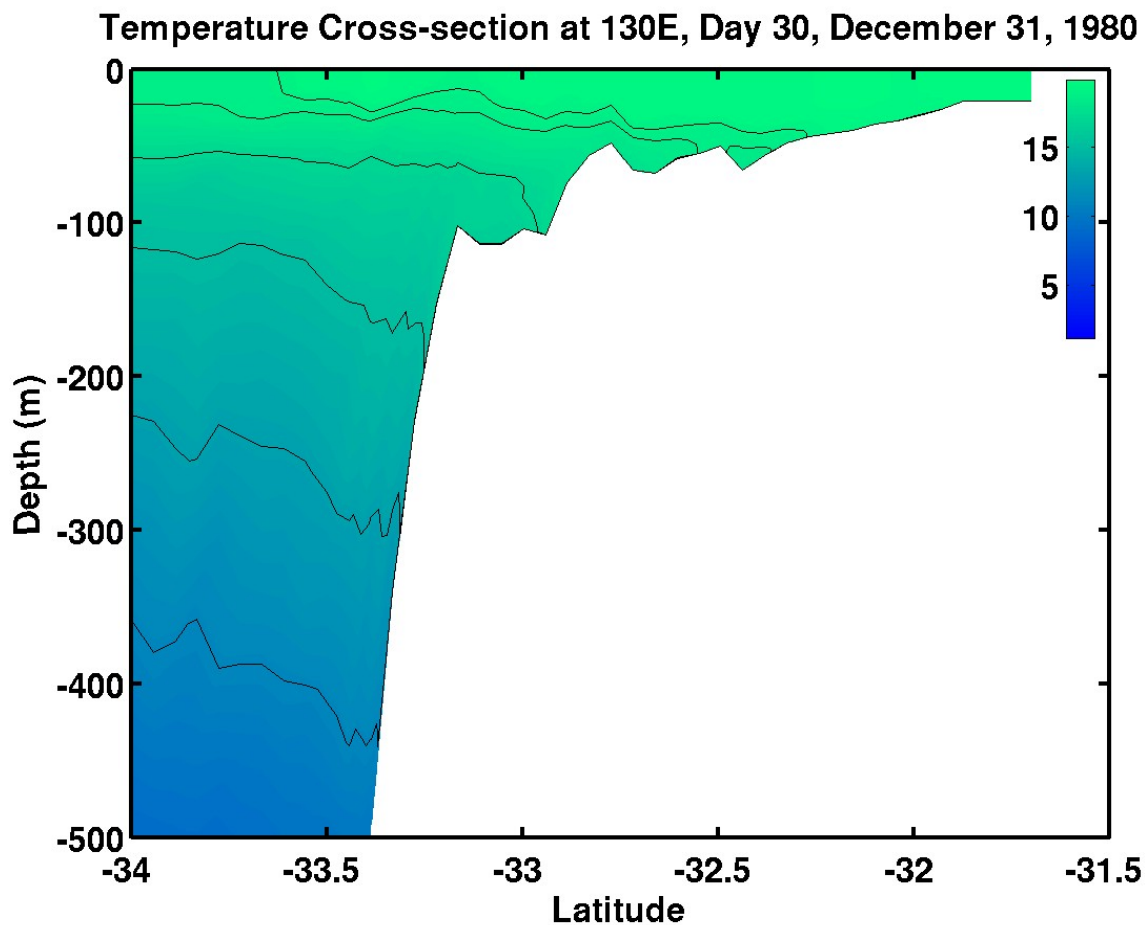


Figure 5.2d. Cross-section of temperature ($^{\circ}\text{C}$) along a north-south transect in the Great Australian Bight (130°E) for daily wind Experiment 1 on day 30, December 31, 1980.

Surface Temperature and Velocity, Day 45, January 15, 1981

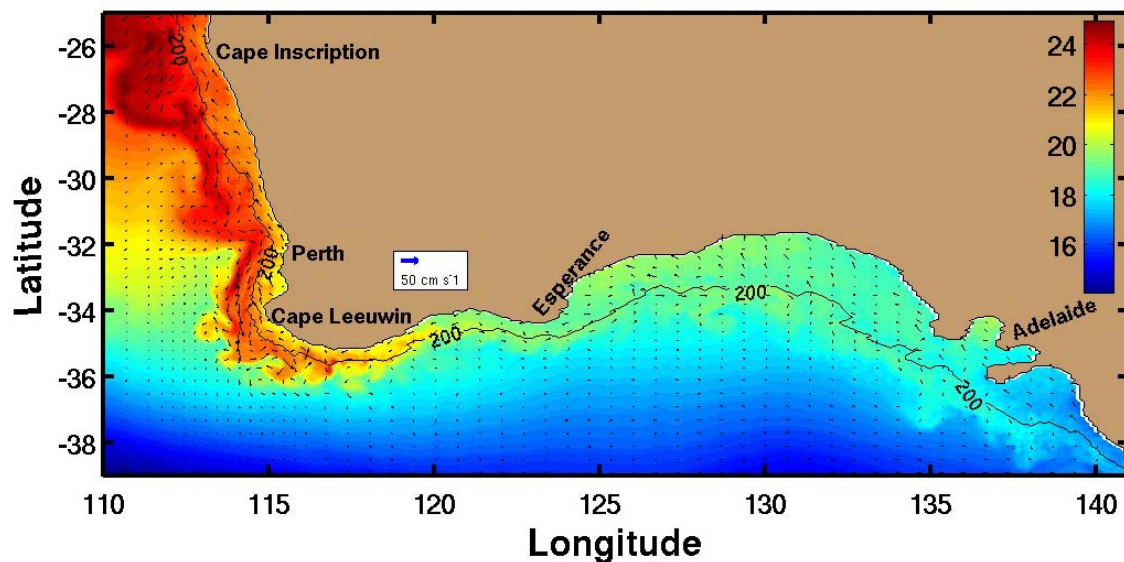


Figure 5.3a. Sea surface temperature ($^{\circ}\text{C}$) and velocity vectors for daily wind Experiment 1 on day 45, January 15, 1981.

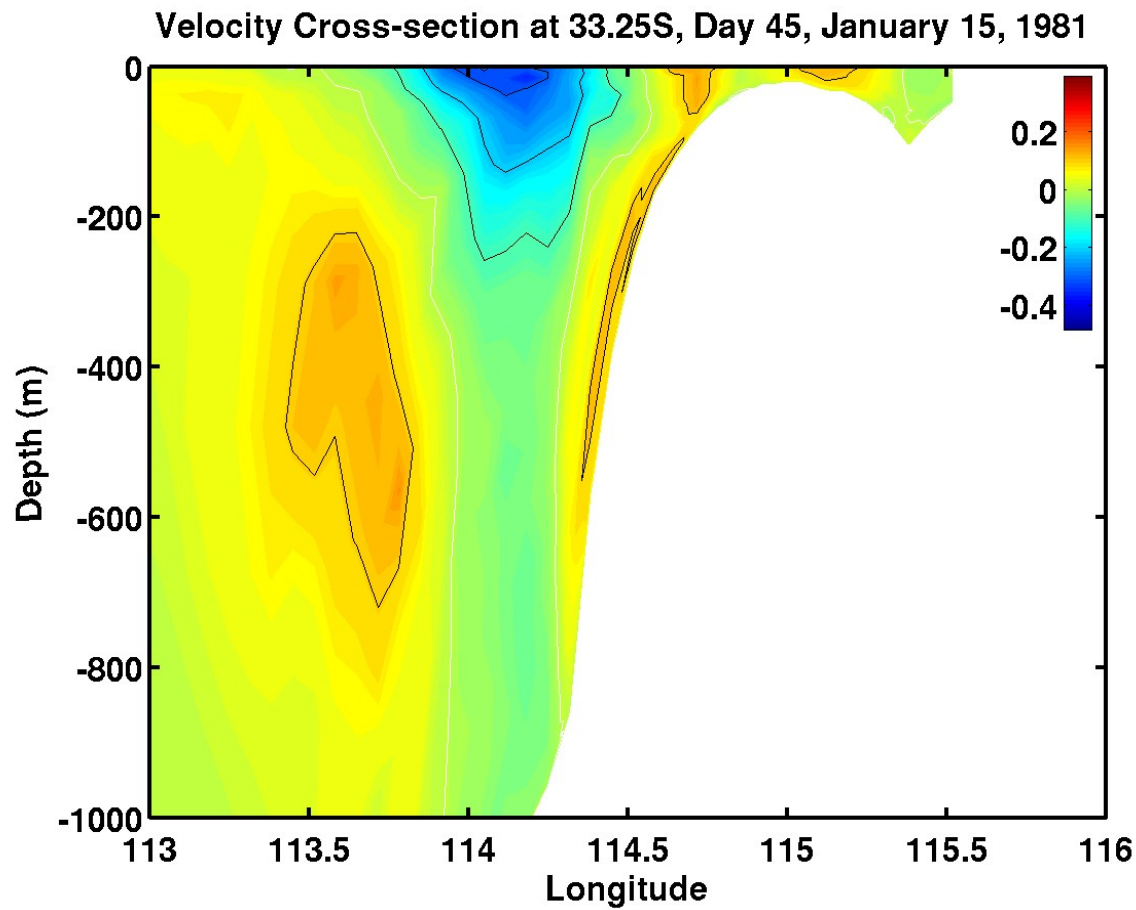


Figure 5.3b. Cross-section of meridional velocity component (m s^{-1}) 33.25°S for daily wind Experiment 1 on day 45, January 15, 1981. Red is equatorward (north) and blue is poleward (south). The white contour is zero.

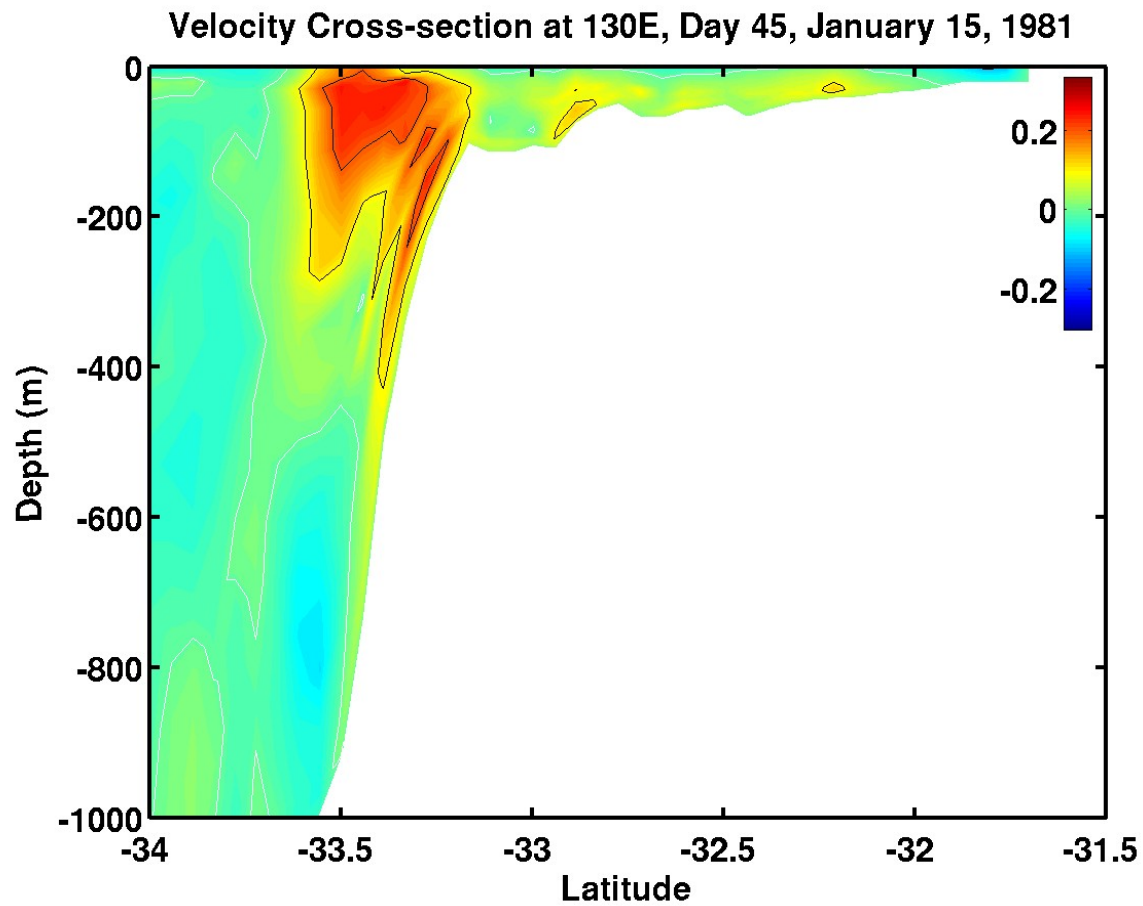


Figure 5.3c. Cross-section of zonal velocity component (m s^{-1}) in the Great Australian Bight (130°E) for daily wind Experiment 1 on day 45, January 15, 1981. Red is eastward and blue is westward. The white contour is zero.

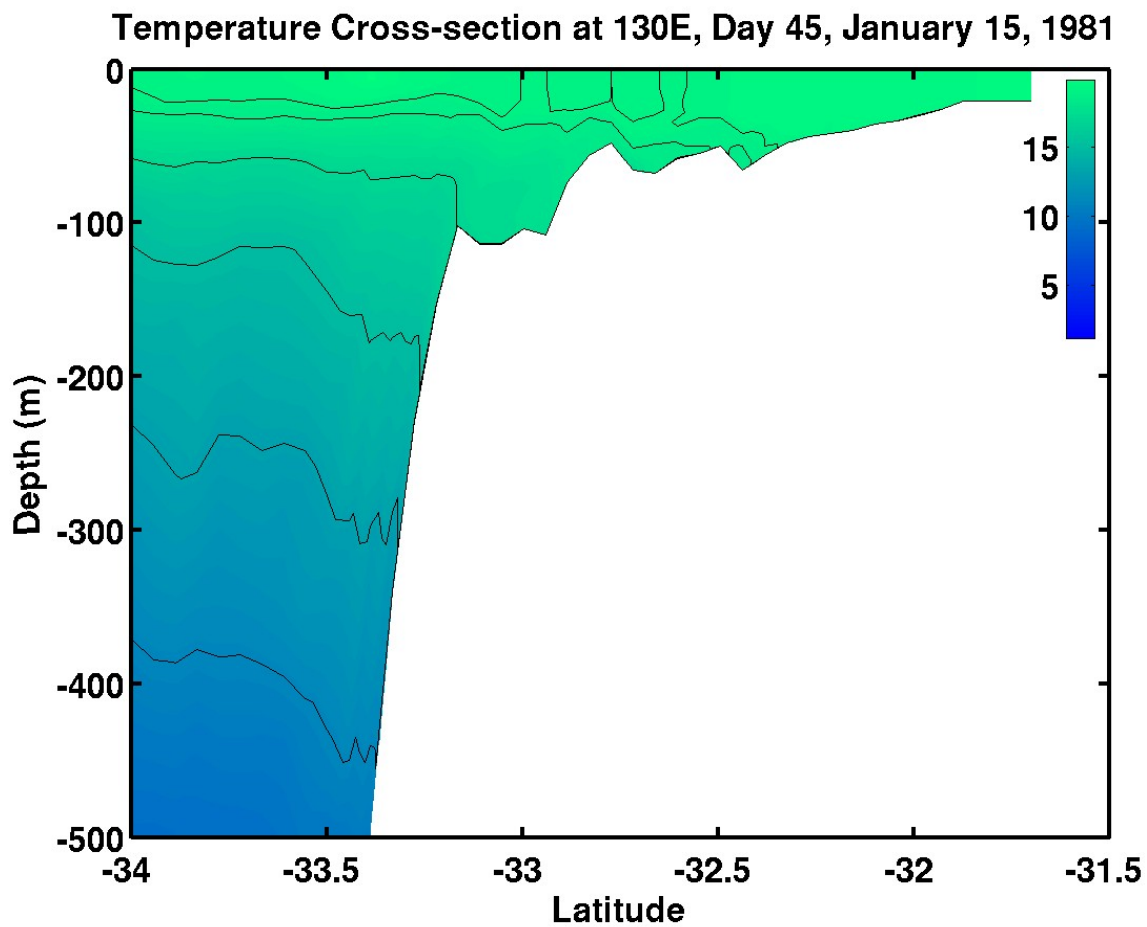


Figure 5.3d. Cross-section of temperature ($^{\circ}\text{C}$) along a north-south transect in the Great Australian Bight (130°E) for daily wind Experiment 1 on day 45, January 15, 1981.

Surface Temperature and Velocity, Day 60, January 30, 1981

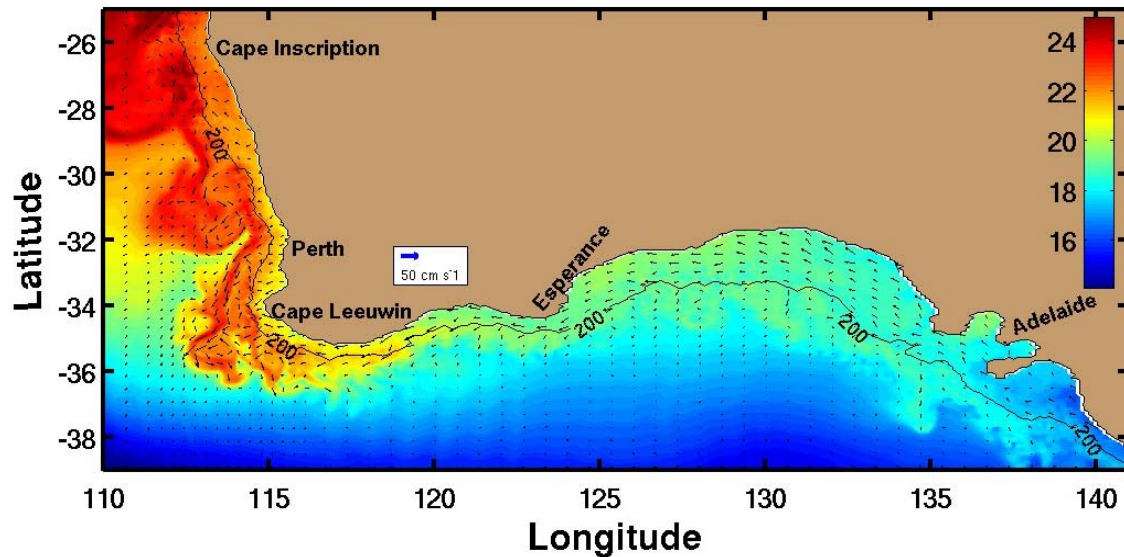


Figure 5.4a. Sea surface temperature ($^{\circ}\text{C}$) and velocity vectors for daily wind Experiment 1 on day 60, January 30, 1981.

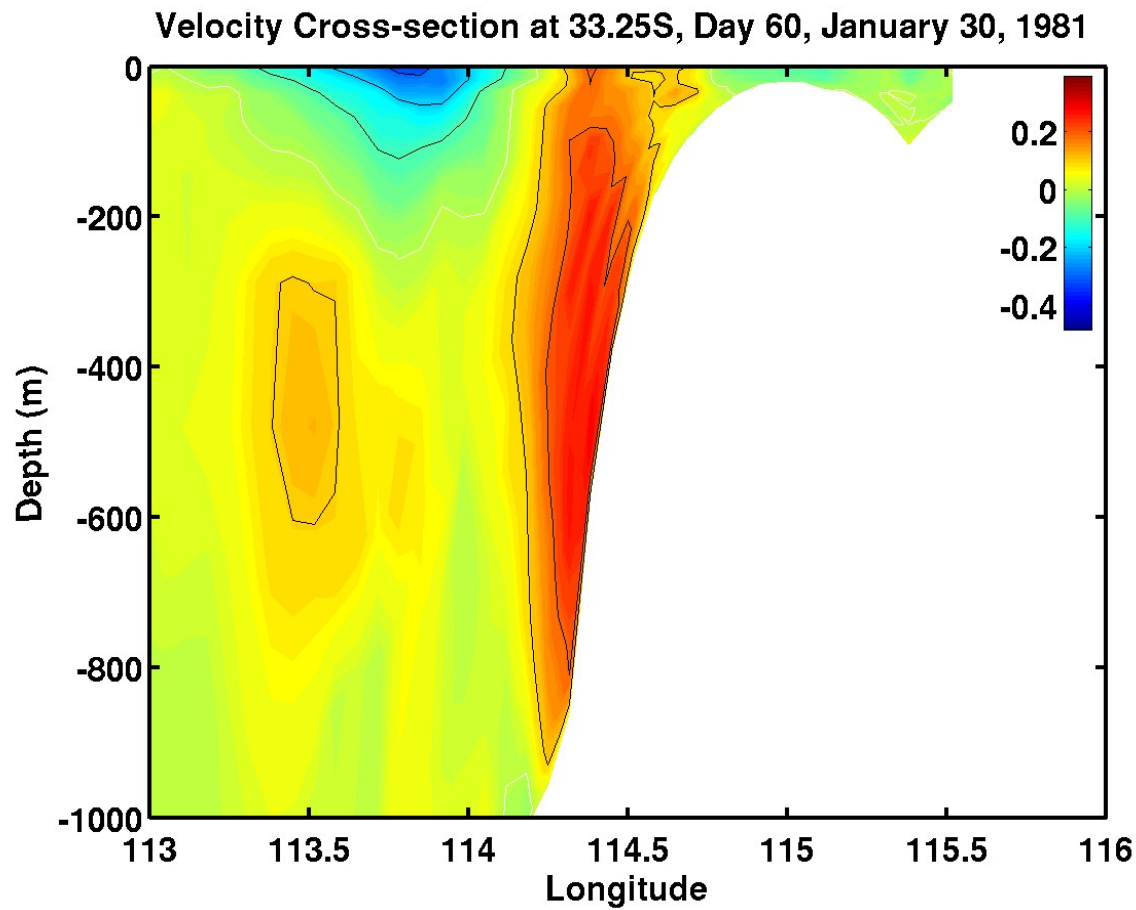


Figure 5.4b. Cross-section of meridional velocity component (m s^{-1}) 33.25°S for daily wind Experiment 1 on day 60, January 30, 1981. Red is equatorward (north) and blue is poleward (south). The white contour is zero.

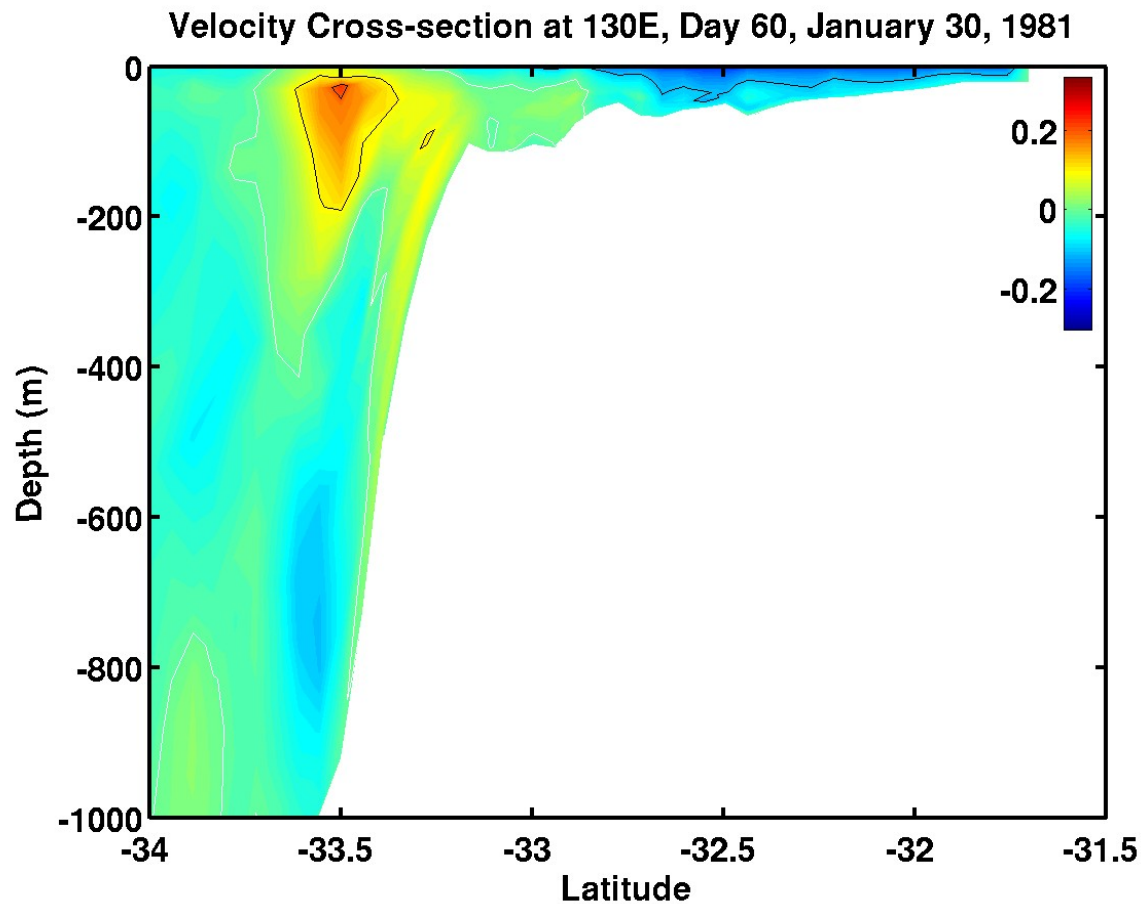


Figure 5.4c. Cross-section of zonal velocity component (m s^{-1}) in the Great Australian Bight (130°E) for daily wind Experiment 1 on day 60, January 30, 1981. Red is eastward and blue is westward. The white contour is zero.

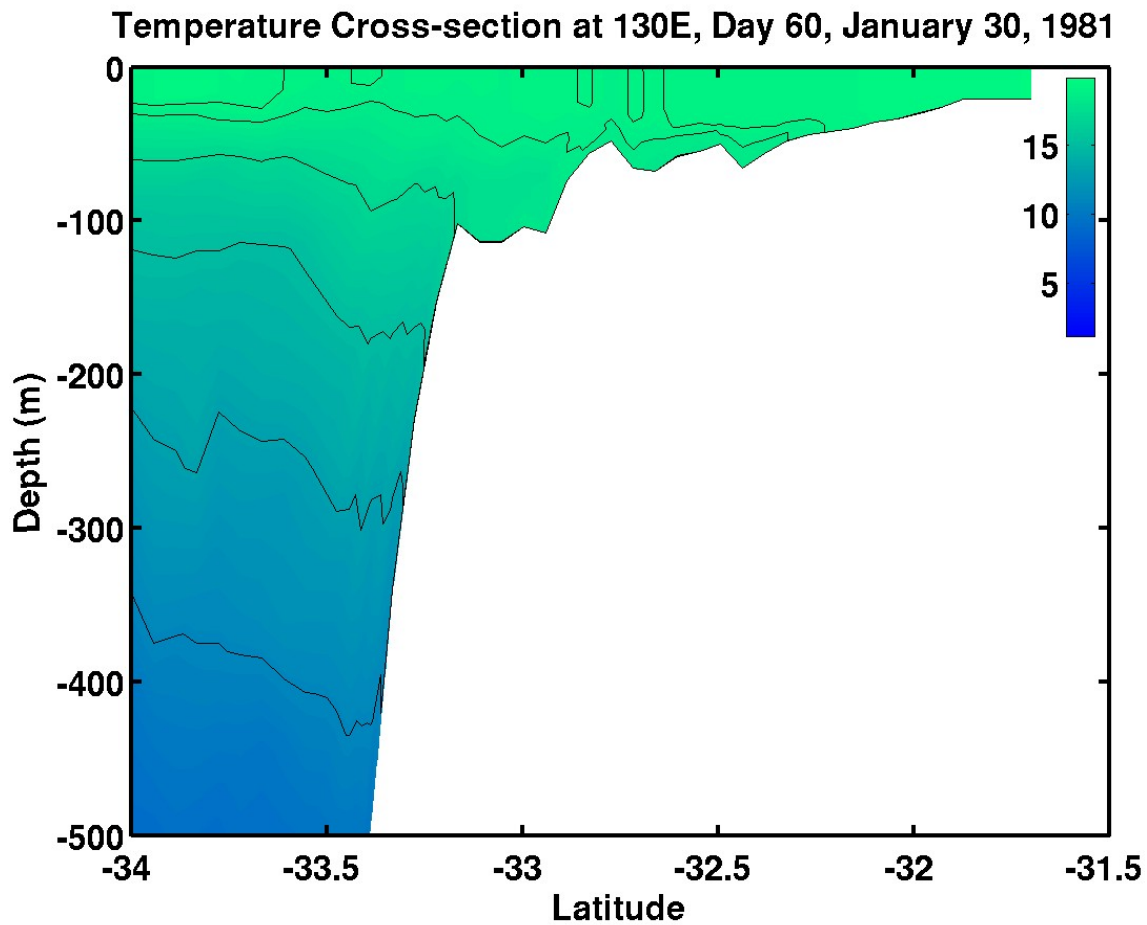


Figure 5.4d. Cross-section of temperature ($^{\circ}\text{C}$) along a north-south transect in the Great Australian Bight (130°E) for daily wind Experiment 1 on day 60, January 30, 1981.

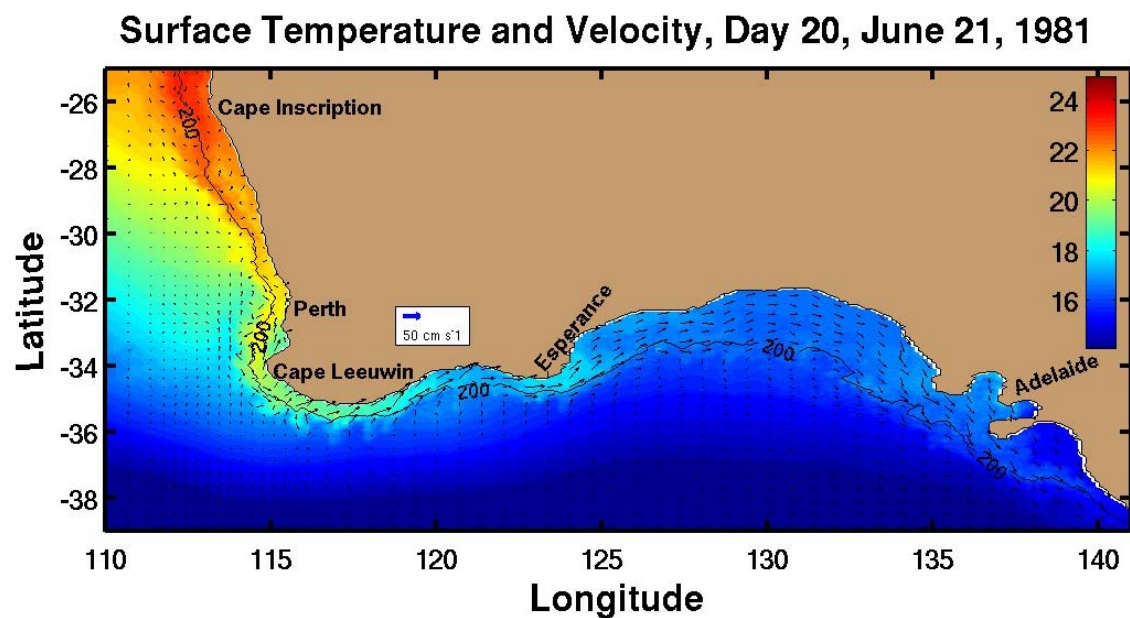


Figure 5.5. Sea surface temperature ($^{\circ}\text{C}$) and velocity vectors for daily wind Experiment 2 on day 20, June 21, 1981.

Surface Temperature and Velocity, Day 30, July 01, 1981

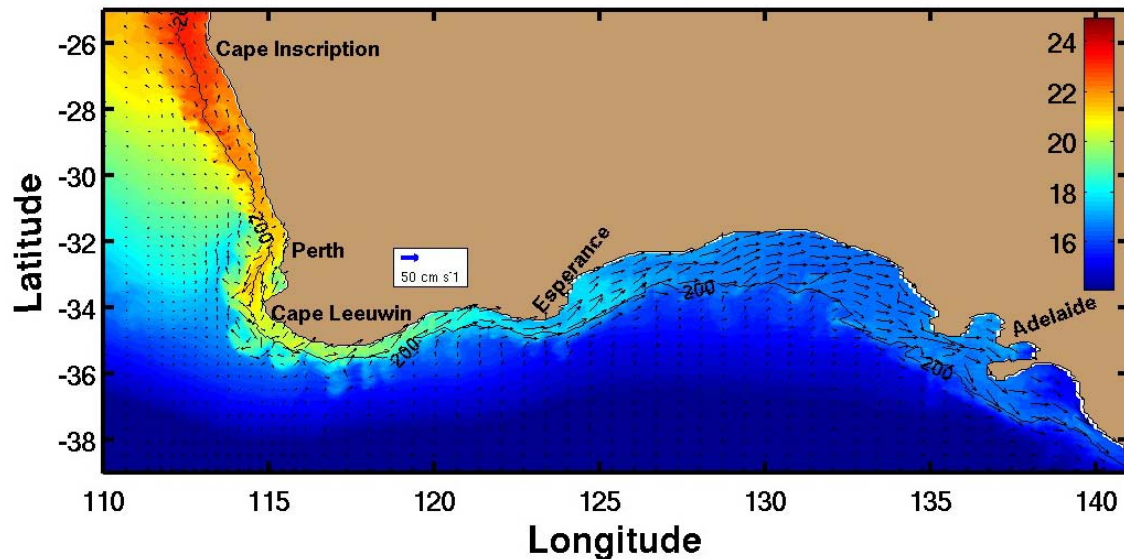


Figure 5.6a. Sea surface temperature (°C) and velocity vectors for daily wind Experiment 2 on day 30, July 1, 1981.

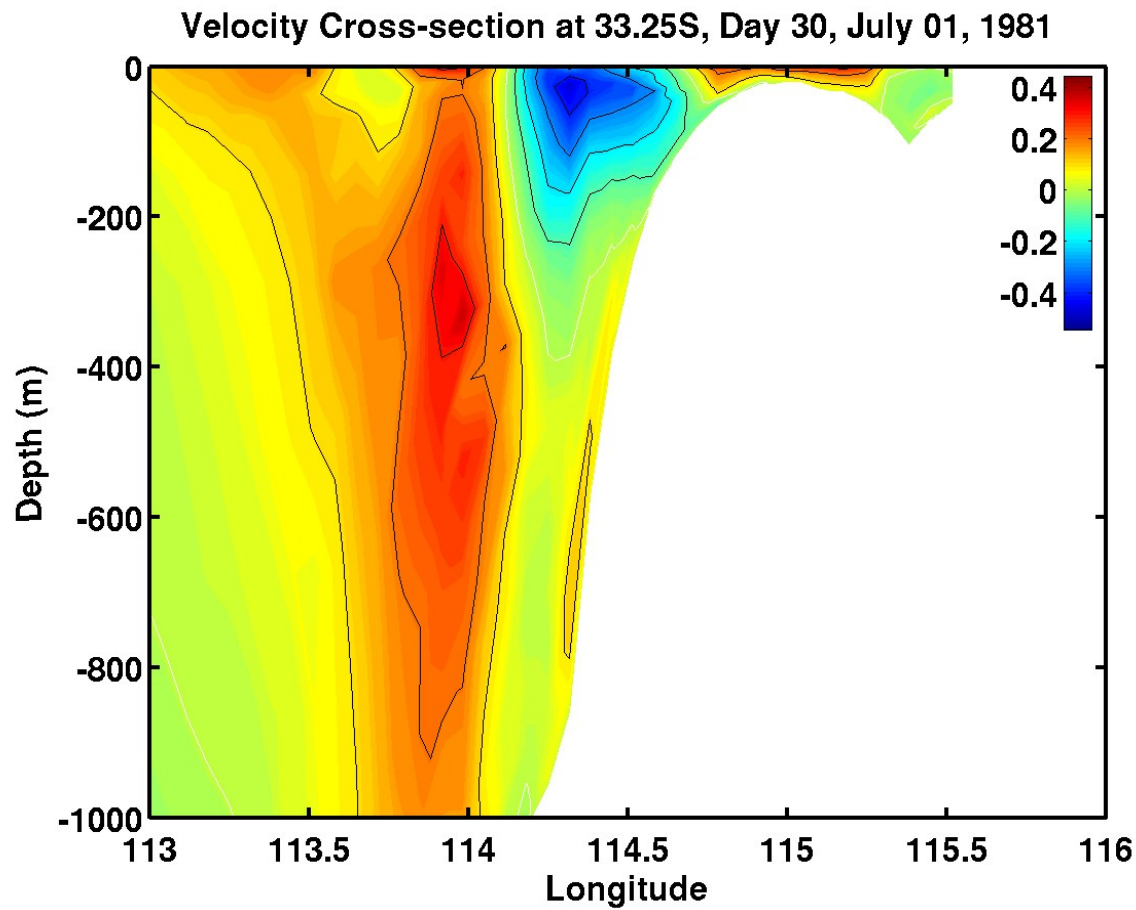


Figure 5.6b. Cross-section of meridional velocity component (m s^{-1}) 33.25°S for daily wind Experiment 2 on day 30, July 1, 1981. Red is equatorward (north) and blue is poleward (south). The white contour is zero.

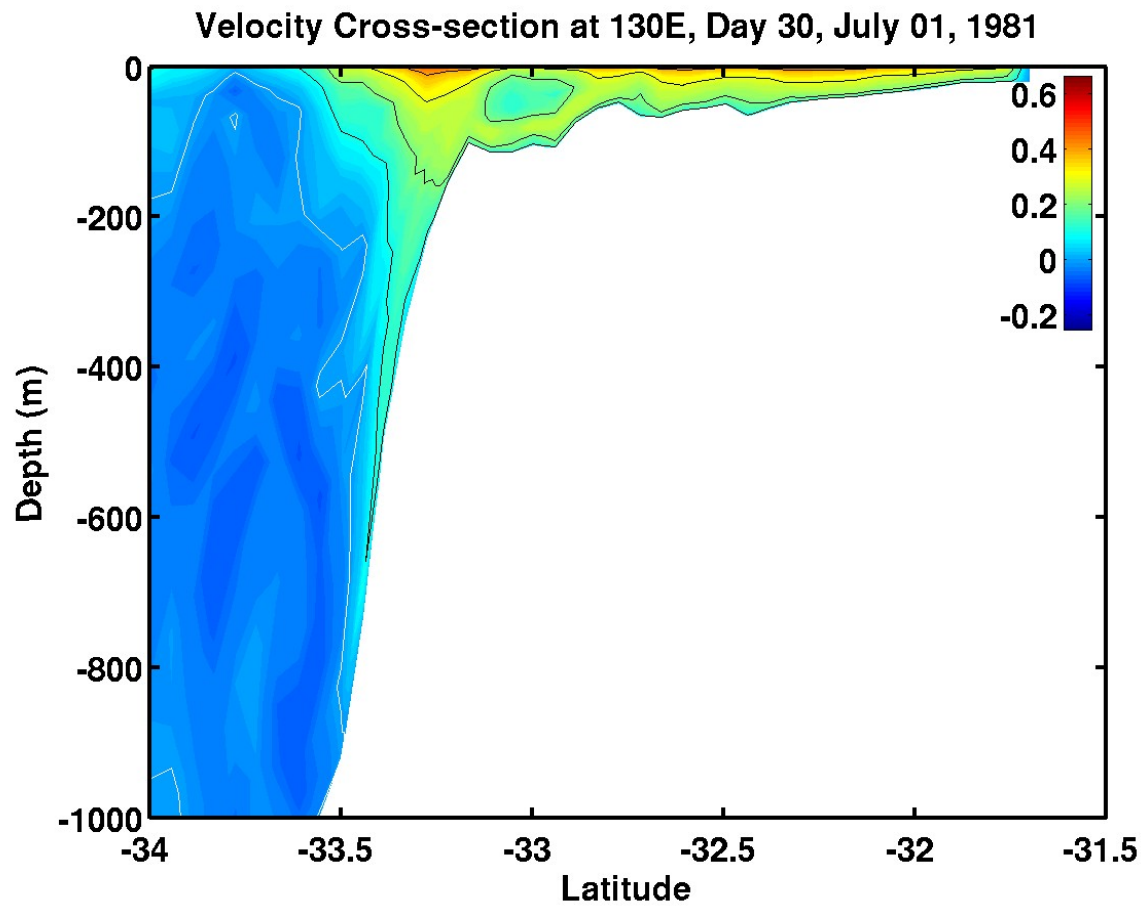


Figure 5.6c. Cross-section of zonal velocity component (m s^{-1}) in the Great Australian Bight (130°E) for daily wind Experiment 2 on day 30, July 1, 1981. Red is eastward and blue is westward. The white contour is zero.

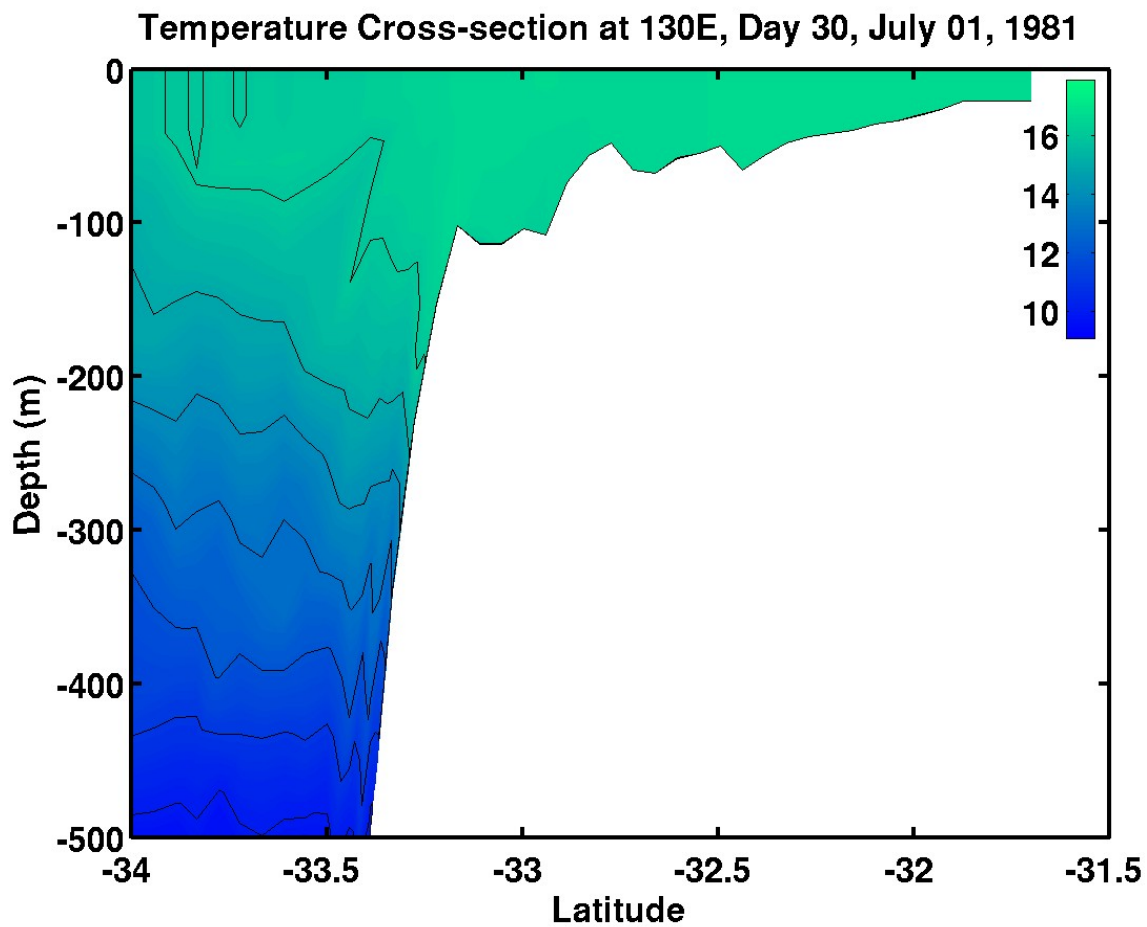


Figure 5.6d. Cross-section of temperature ($^{\circ}\text{C}$) along a north-south transect in the Great Australian Bight (130°E) for daily wind Experiment 2 on day 30, July 1, 1981.

Surface Temperature and Velocity, Day 45, July 16, 1981

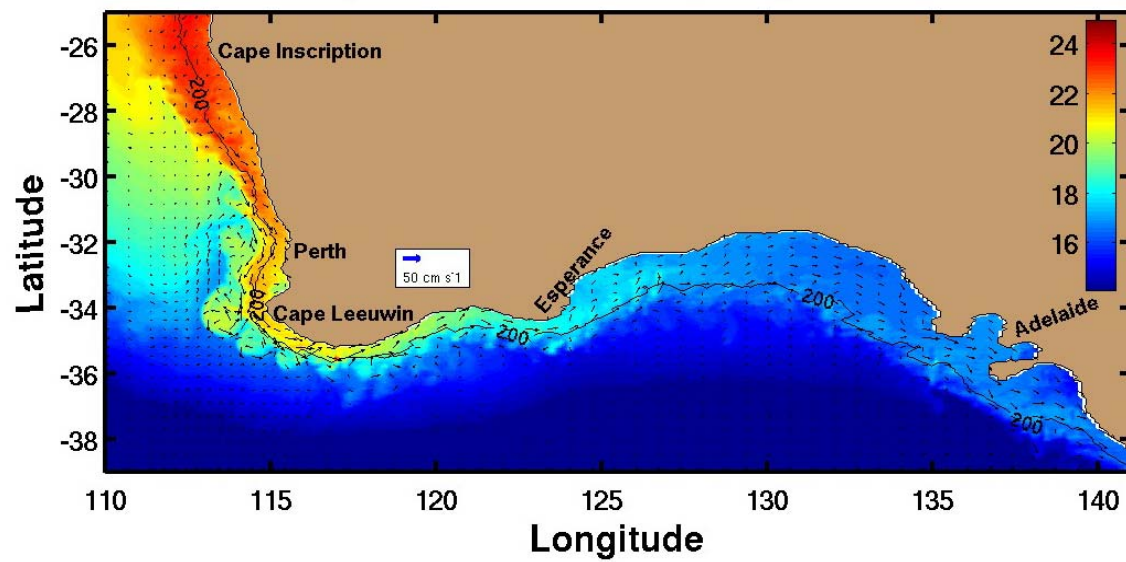


Figure 5.7a. Sea surface temperature ($^{\circ}\text{C}$) and velocity vectors for daily wind Experiment 2 on day 45, July 16, 1981.

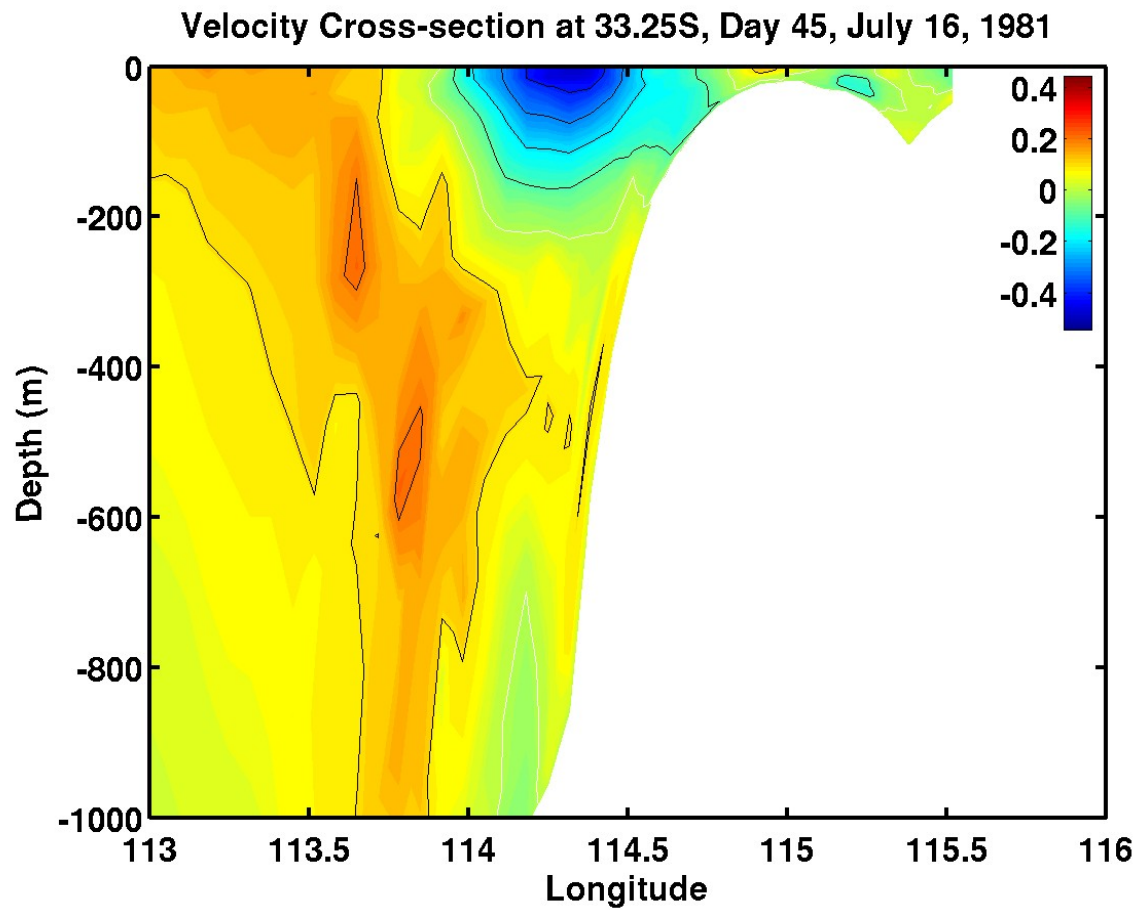


Figure 5.7b. Cross-section of meridional velocity component (m s^{-1}) 33.25°S for daily wind Experiment 2 on day 45, July 16, 1981. Red is equatorward (north) and blue is poleward (south). The white contour is zero.

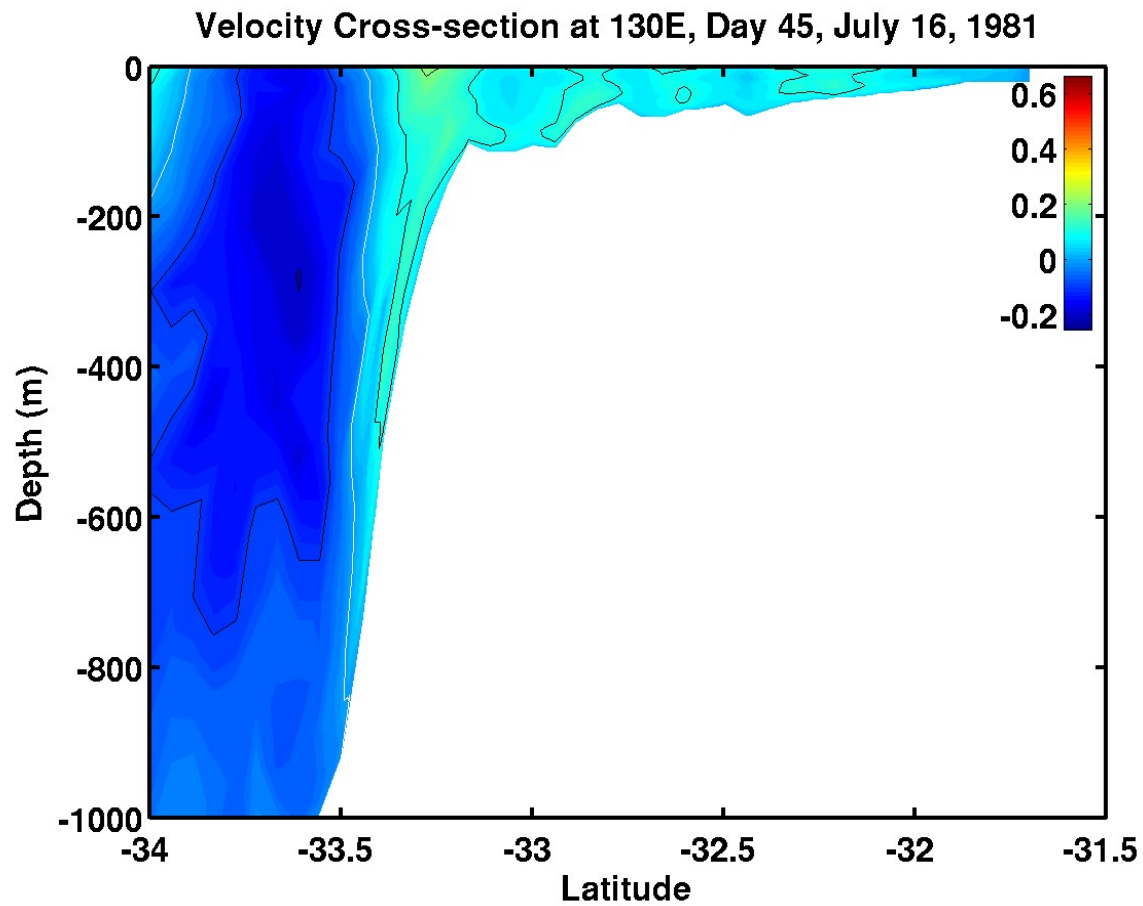


Figure 5.7c. Cross-section of zonal velocity component (m s^{-1}) in the Great Australian Bight (130°E) for daily wind Experiment 2 on day 45, July 16, 1981. Red is eastward and blue is westward. The white contour is zero.

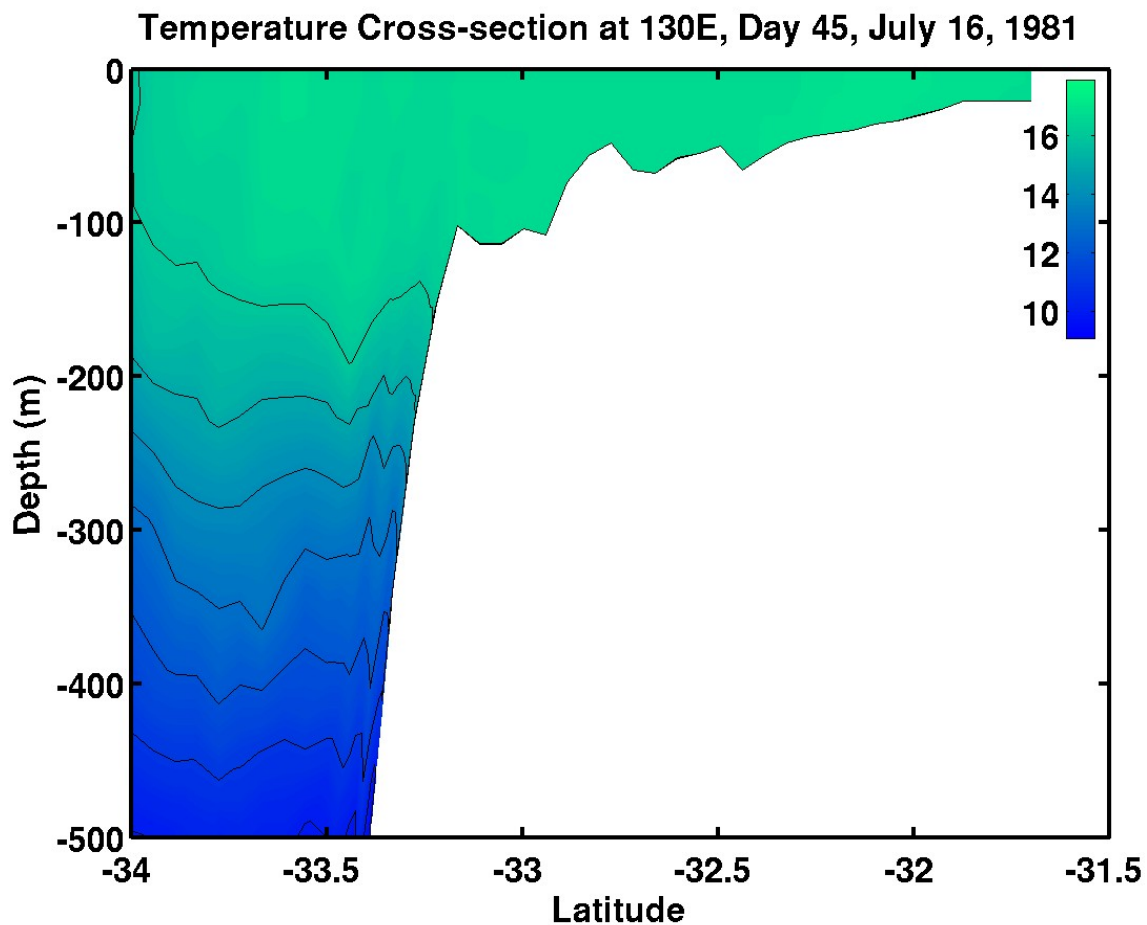


Figure 5.7d. Cross-section of temperature ($^{\circ}\text{C}$) along a north-south transect in the Great Australian Bight (130°E) for daily wind Experiment 2 on day 45, July 16, 1981.

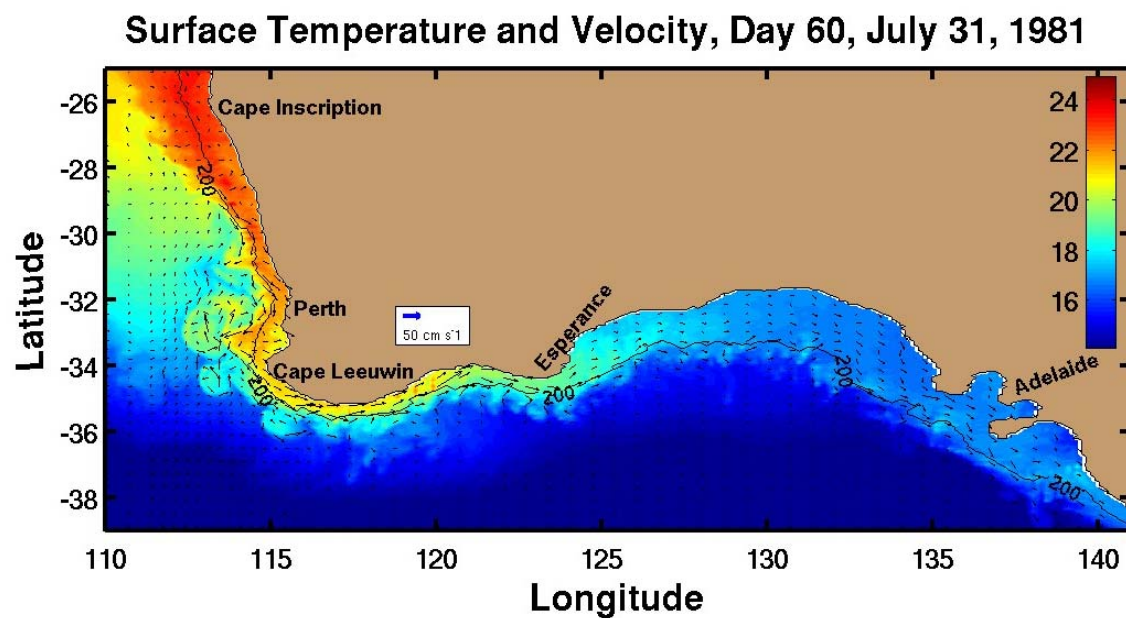


Figure 5.8a. Sea surface temperature ($^{\circ}\text{C}$) and velocity vectors for daily wind Experiment 2 on day 60, July 31, 1981.

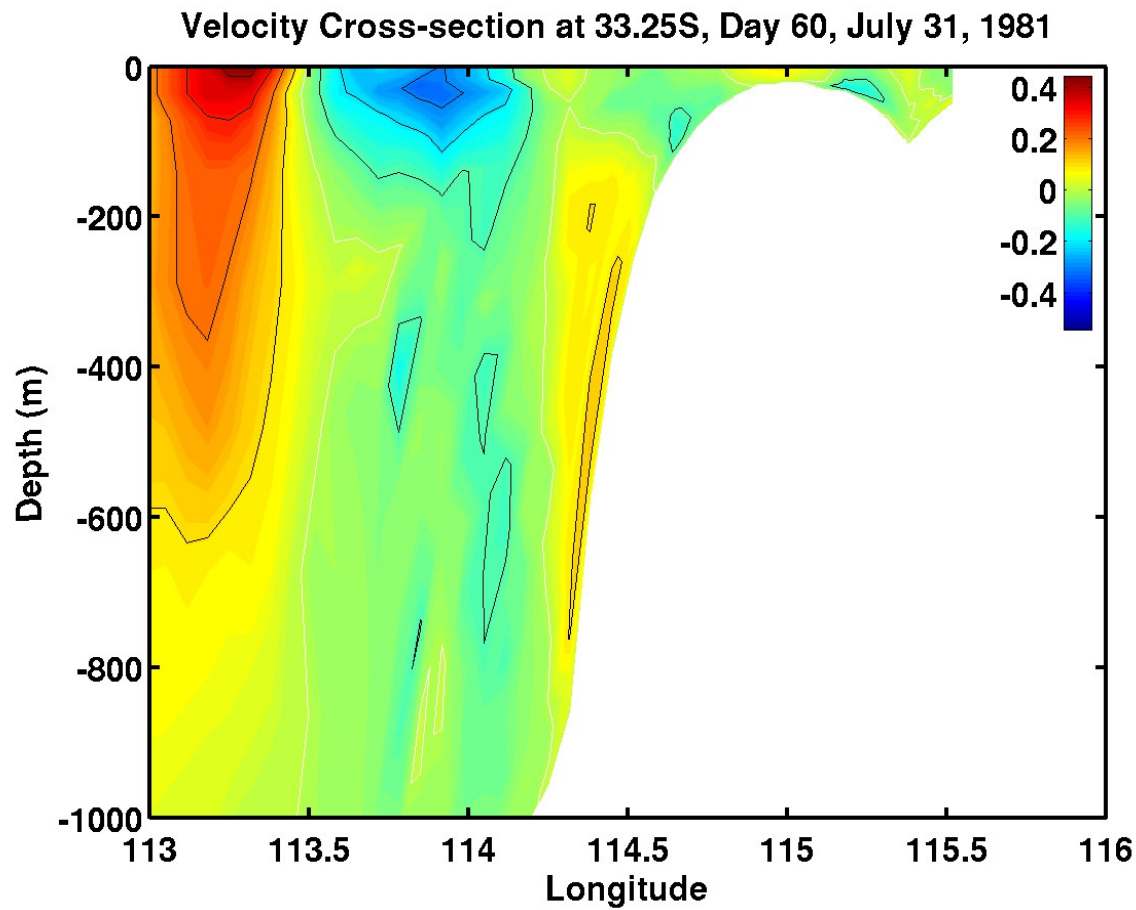


Figure 5.8b. Cross-section of meridional velocity component (m s^{-1}) 33.25°S for daily wind Experiment 2 on day 60, July 31, 1981. Red is equatorward (north) and blue is poleward (south). The white contour is zero.

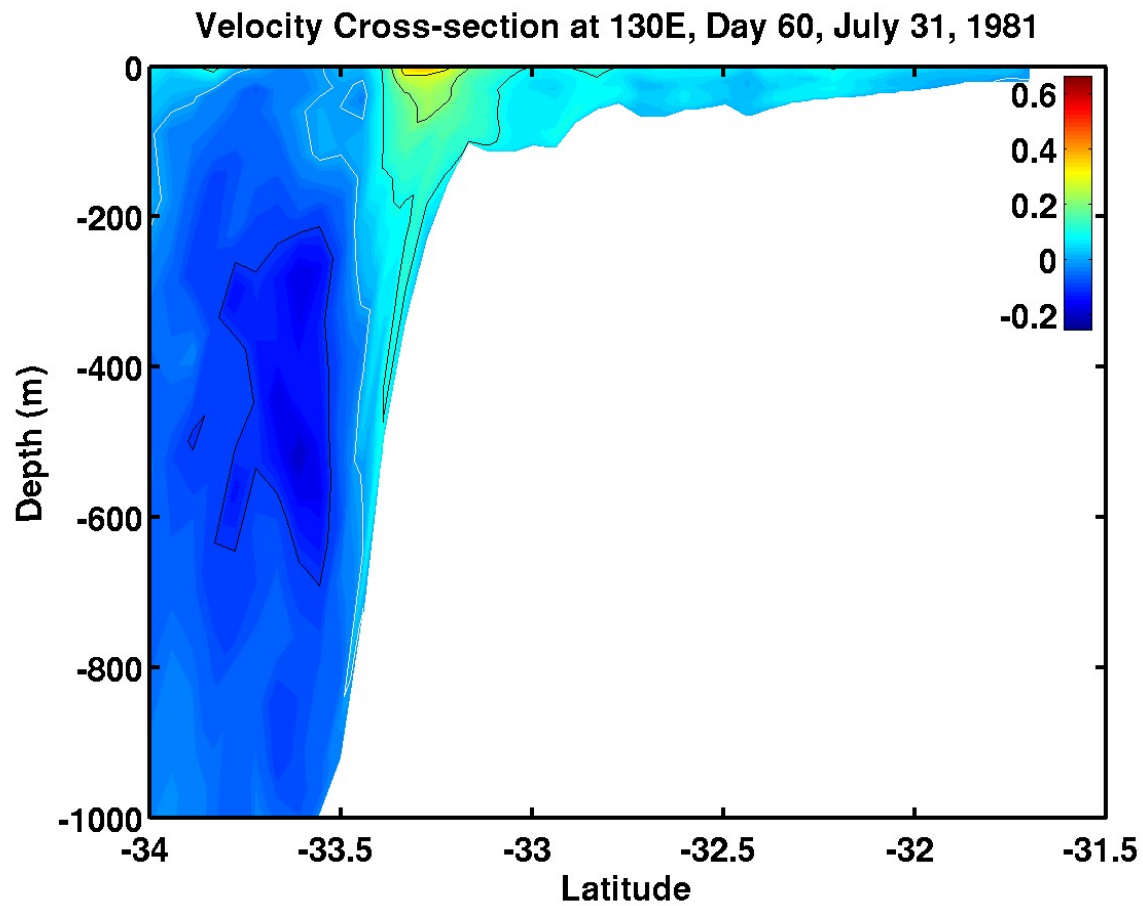


Figure 5.8c. Cross-section of zonal velocity component (m s^{-1}) in the Great Australian Bight (130°E) for daily wind Experiment 2 on day 60, July 31, 1981. Red is eastward and blue is westward. The white contour is zero.

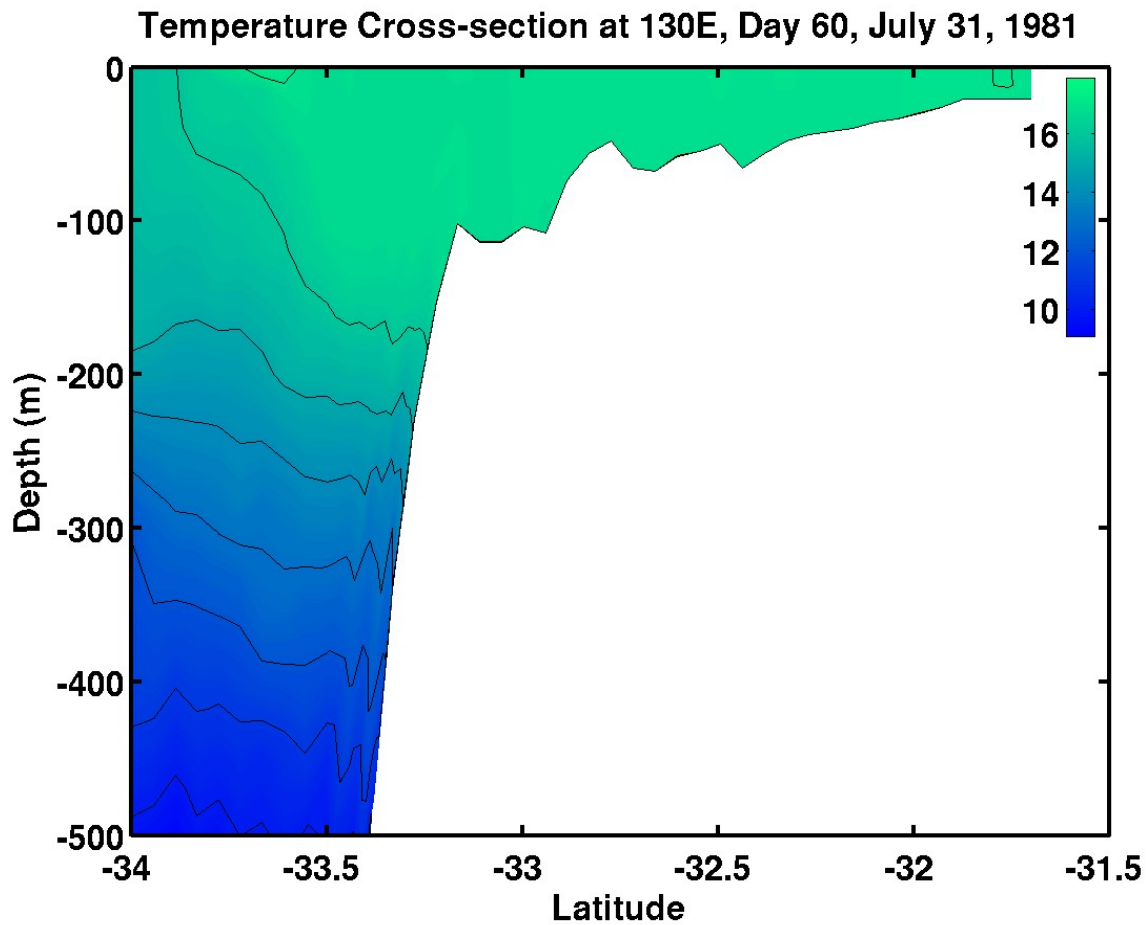


Figure 5.8d. Cross-section of temperature ($^{\circ}\text{C}$) along a north-south transect in the Great Australian Bight (130°E) for daily wind Experiment 2 on day 60, July 31, 1981.

Surface Temperature and Velocity, Day 20, December 21, 2000

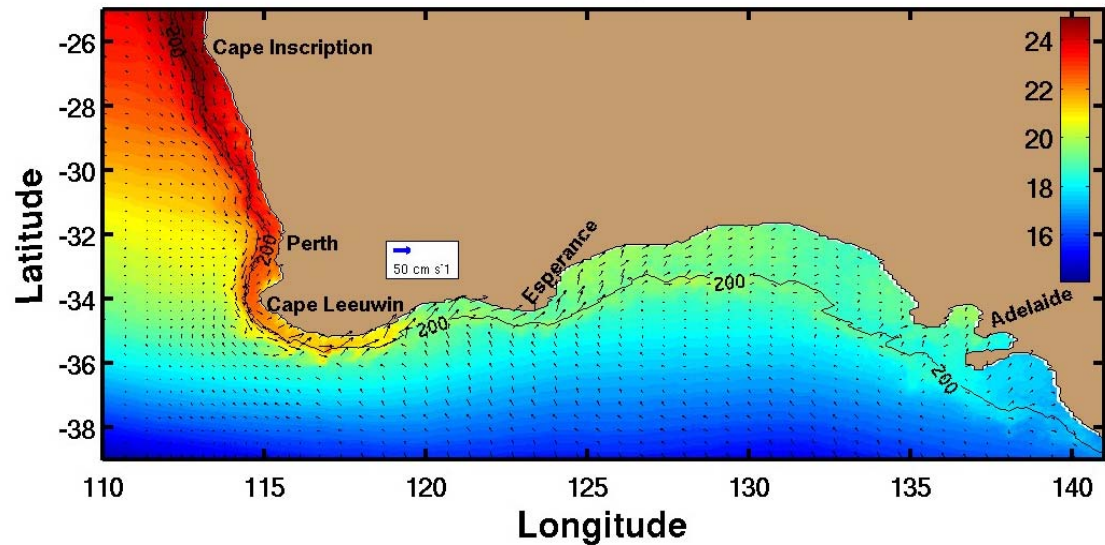


Figure 5.9a. Sea surface temperature ($^{\circ}\text{C}$) and velocity vectors for daily wind Experiment 3 on day 20, December 21, 2000.

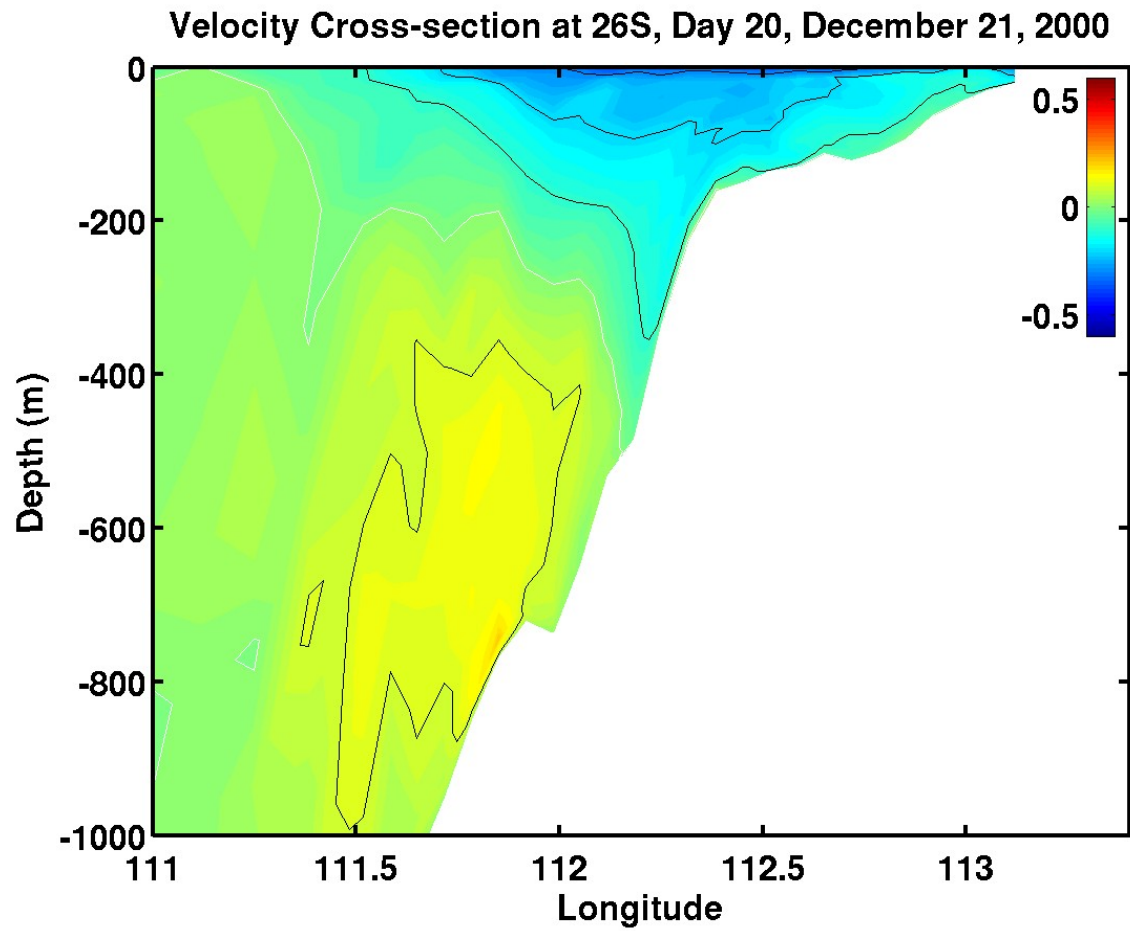


Figure 5.9b. Cross-section of meridional velocity component (m s^{-1}) at 26°S for daily wind Experiment 3 on day 20, December 21, 2000. Red is equatorward (north) and blue is poleward (south). The white contour is zero.

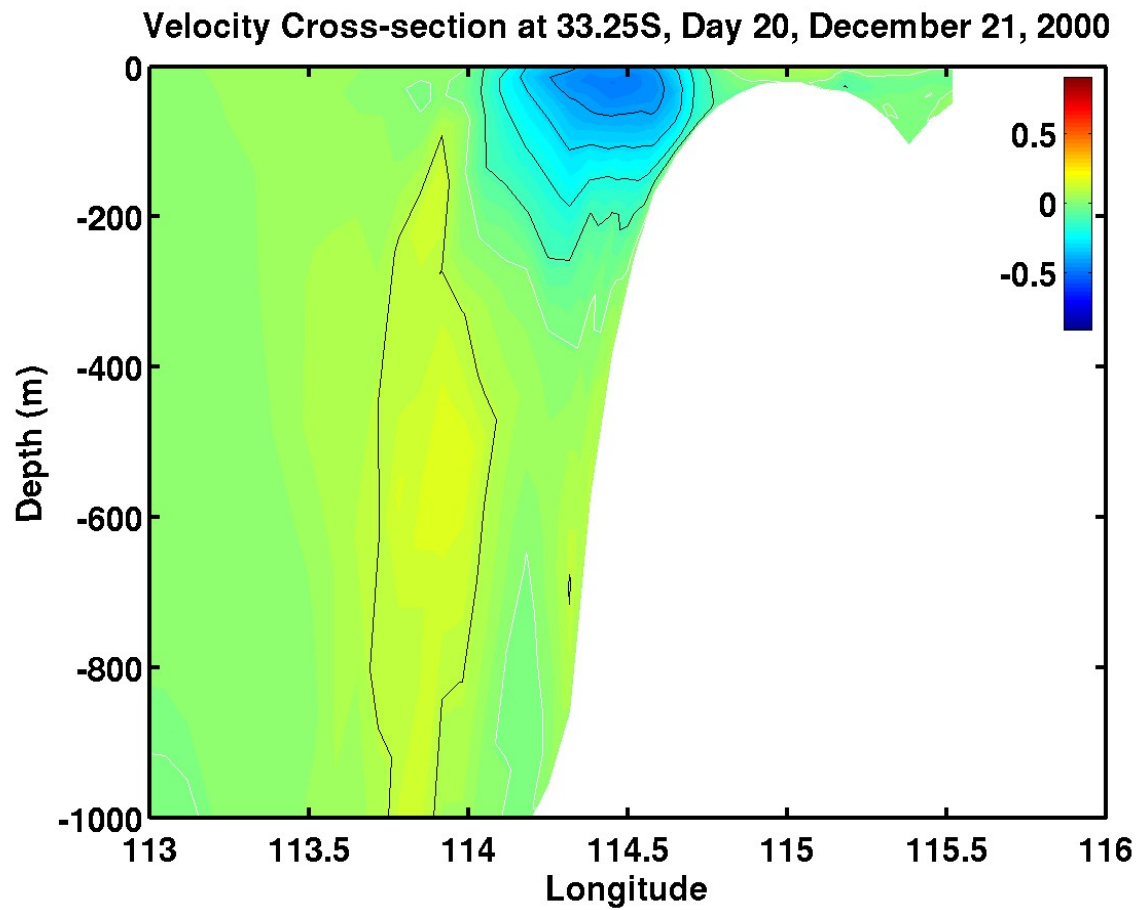


Figure 5.9c. Cross-section of meridional velocity component (m s^{-1}) 33.25°S for daily wind Experiment 3 on day 20, December 21, 2000. Red is equatorward (north) and blue is poleward (south). The white contour is zero.

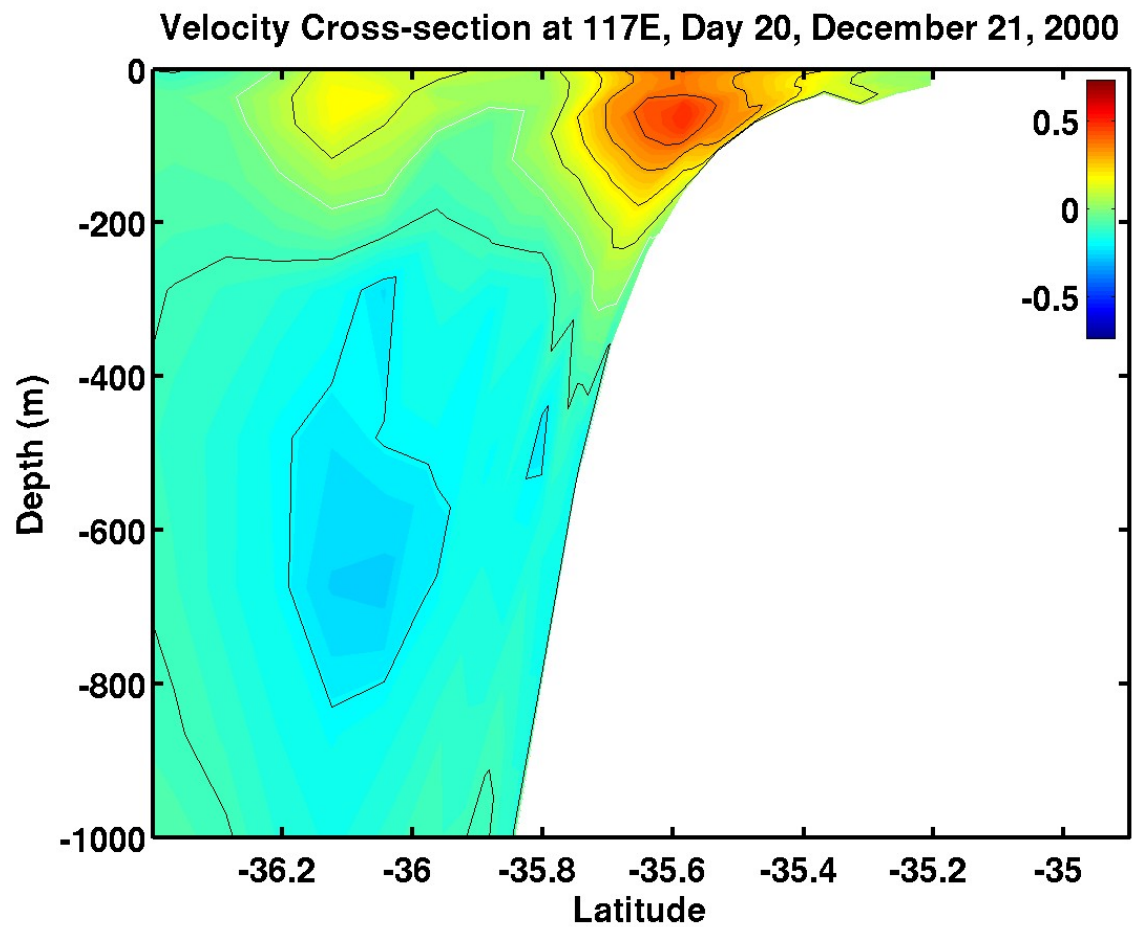


Figure 5.9d. Cross-section of zonal velocity component (m s^{-1}) at 117°E for daily wind Experiment 3 on day 30, December 31, 2000. Red is eastward and blue is westward. The white contour is zero.

Surface Temperature and Velocity, Day 27, December 28, 2000

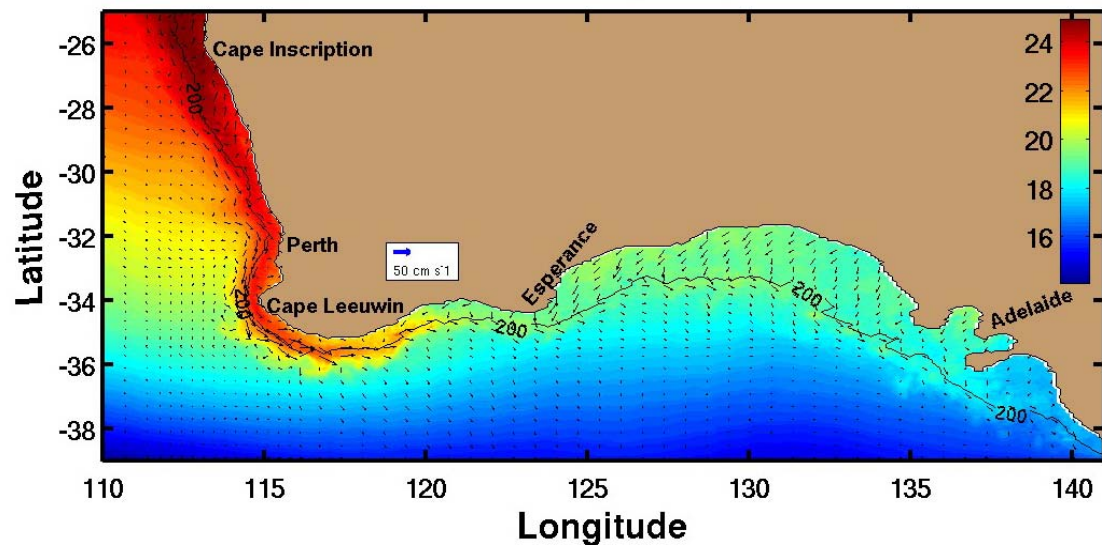


Figure 5.10a. Sea surface temperature ($^{\circ}\text{C}$) and velocity vectors for daily wind Experiment 3 on day 27, December 28, 2000.

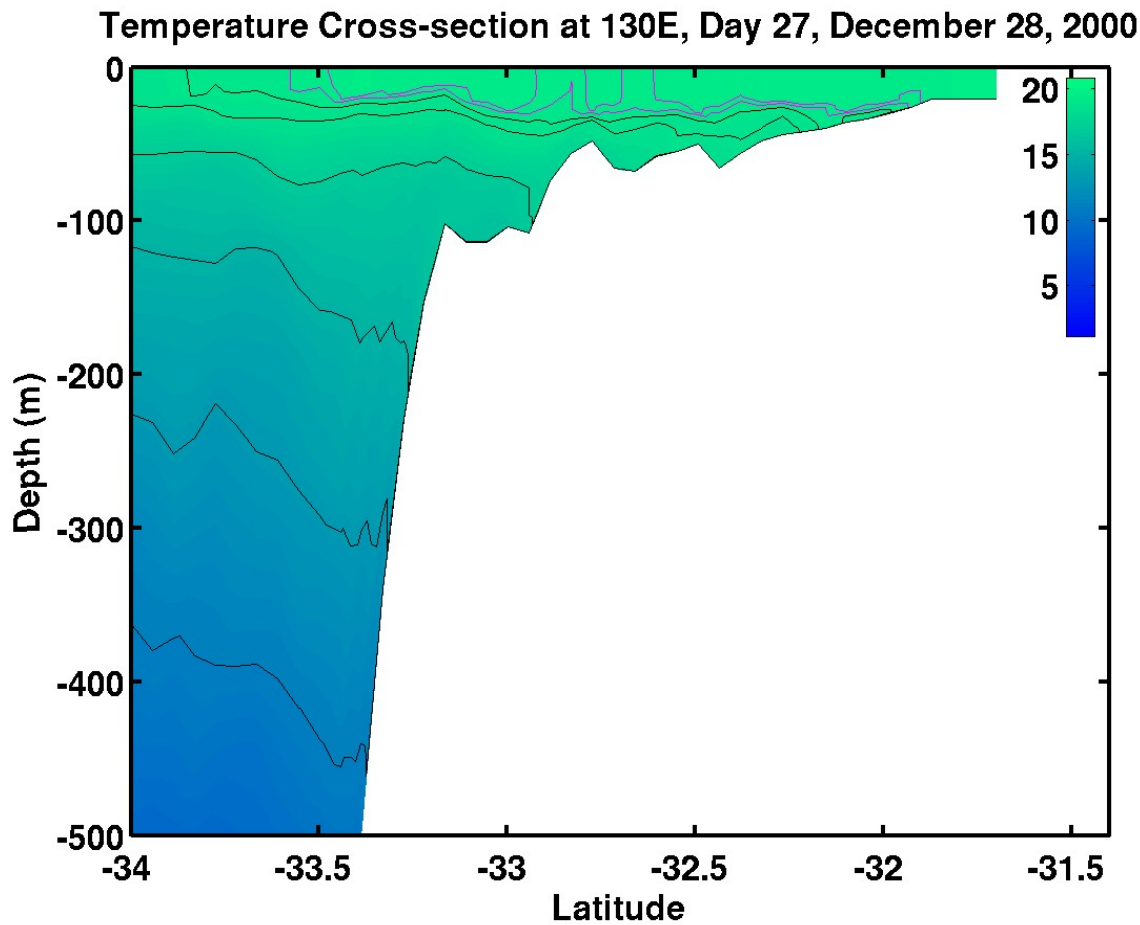


Figure 5.10b. Cross-section of temperature ($^{\circ}\text{C}$) along a north-south transect in the Great Australian Bight (130°E) for daily wind Experiment 3 on day 27, December 28, 2000. The upper magenta contour is the 19.4°C isotherm and the lower magenta contour is the 19.2°C isotherm.

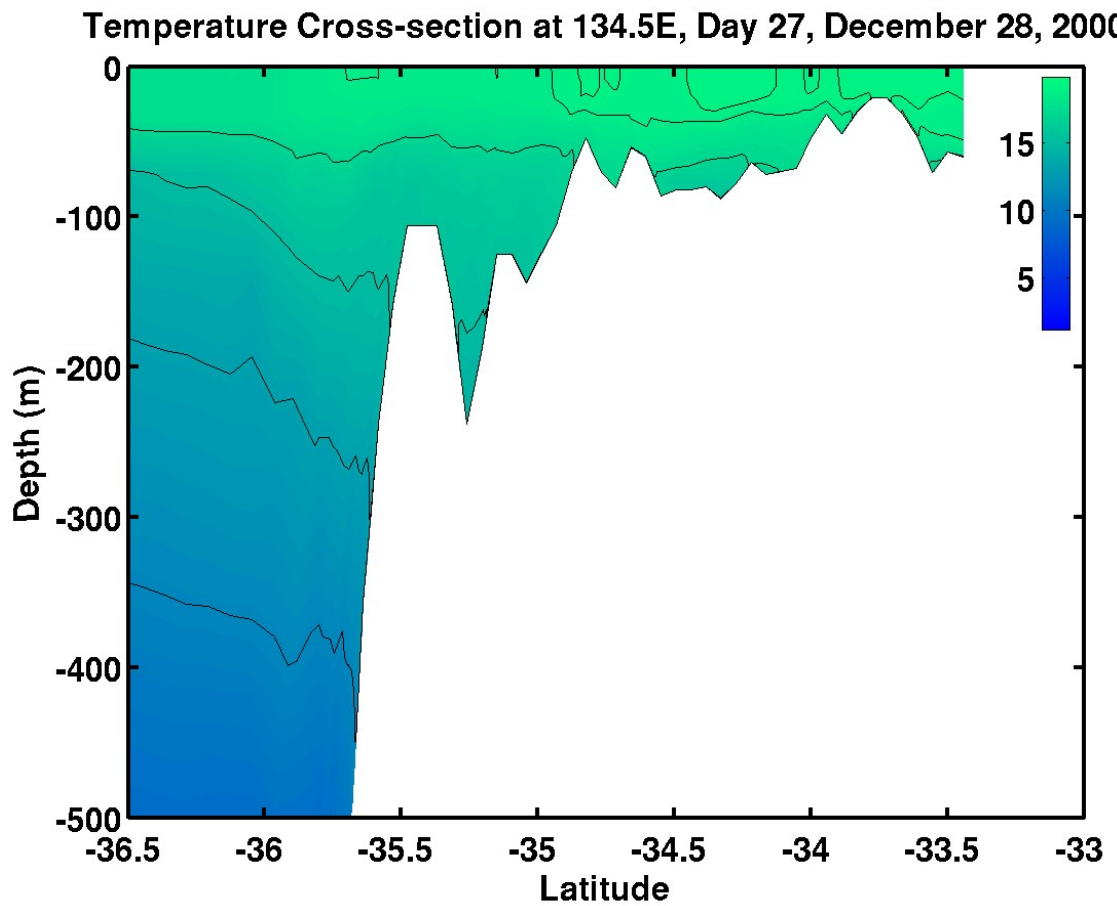


Figure 5.10c. Cross-section of temperature ($^{\circ}\text{C}$) along a north-south transect in the eastern Great Australian Bight (134.5°E) for daily wind Experiment 3 on day 27, December 28, 2000.

Surface Temperature and Velocity, Day 30, December 31, 2000

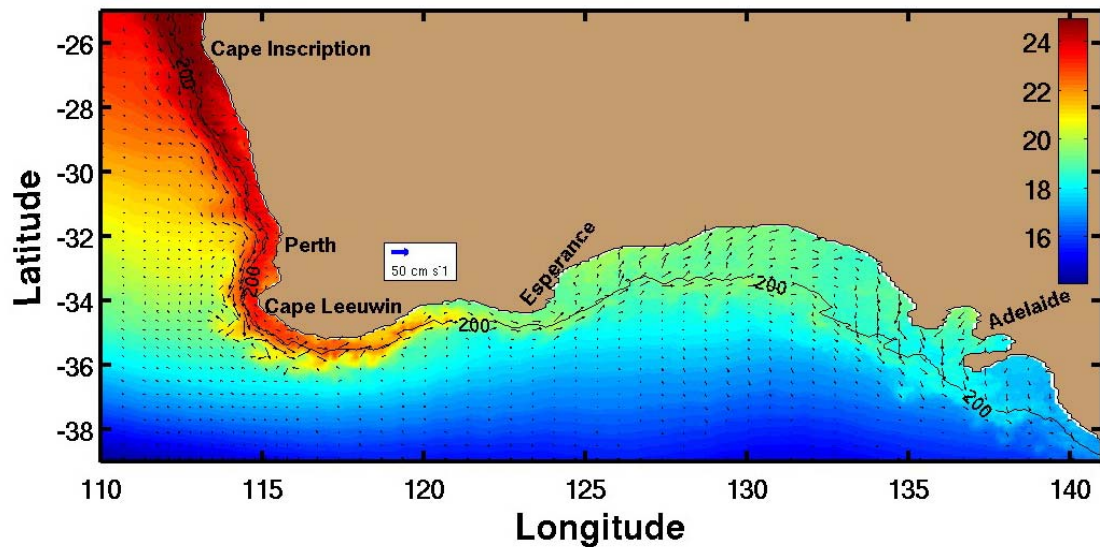


Figure 5.11a. Sea surface temperature (°C) and velocity vectors for daily wind Experiment 3 on day 30, December 31, 2000.

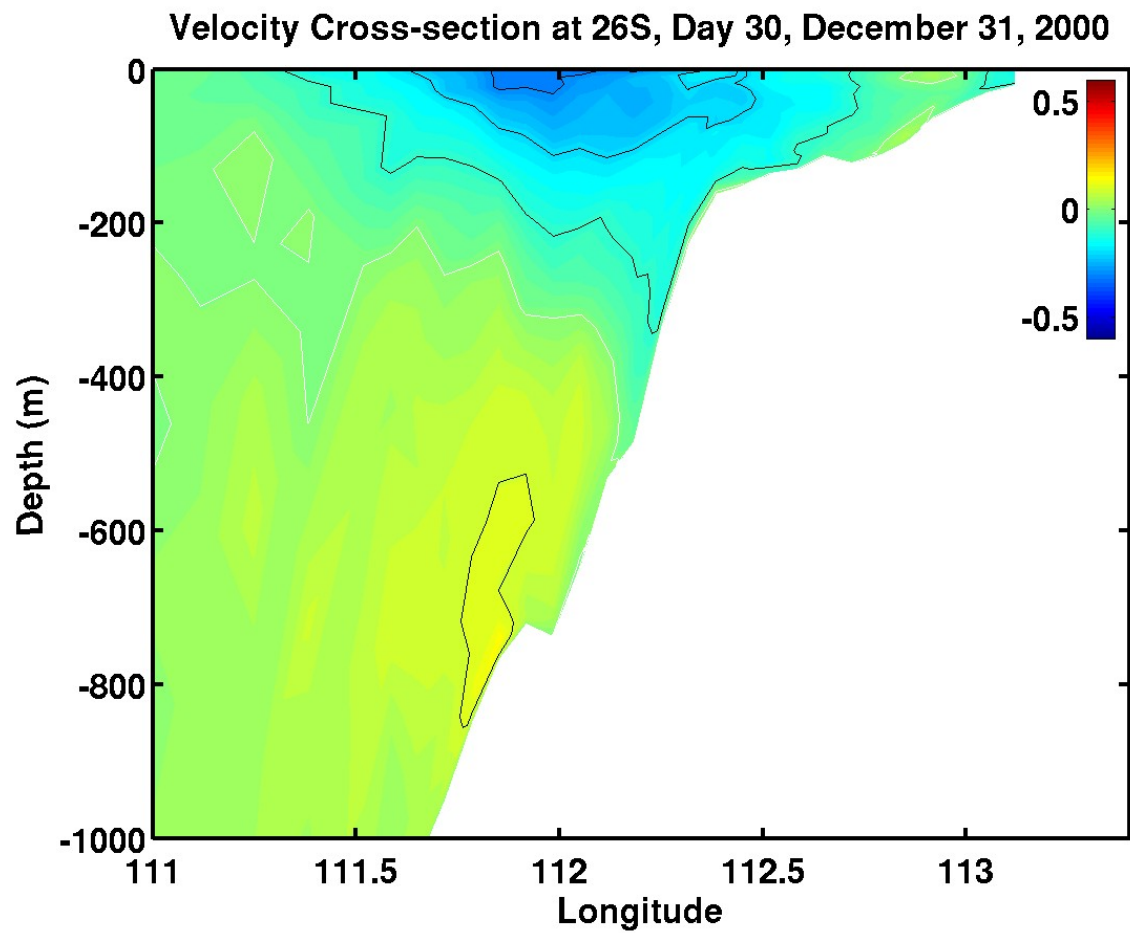


Figure 5.11b. Cross-section of meridional velocity component (m s^{-1}) at 26°S for daily wind Experiment 3 on day 30, December 31, 2000. Red is equatorward (north) and blue is poleward (south). The white contour is zero.

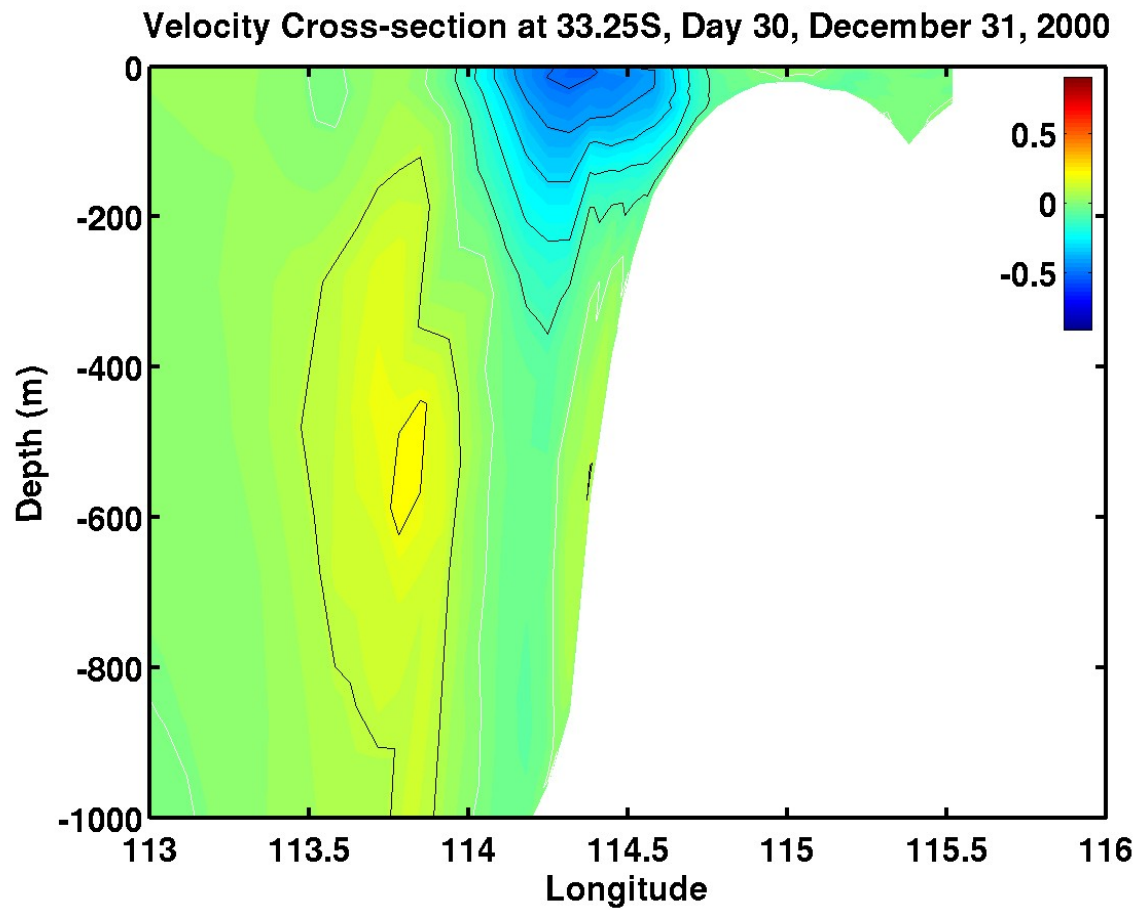


Figure 5.11c. Cross-section of meridional velocity component (m s^{-1}) just north of Cape Leeuwin at 33.25°S for daily wind Experiment 3 on day 30, December 31, 2000. Red is equatorward (north) and blue is poleward (south). The white contour is zero.

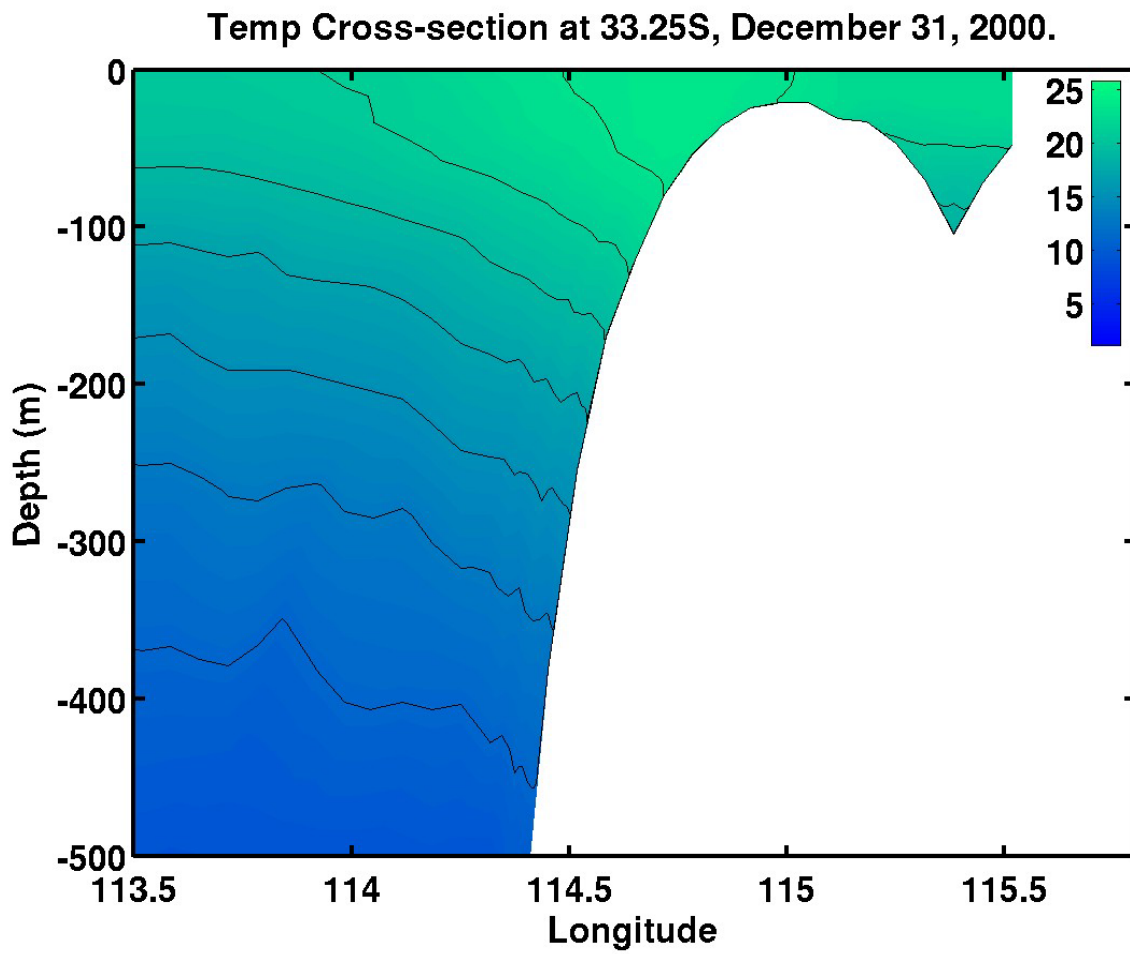


Figure 5.11d. Cross-section of temperature (°C) along an east-west transect just north of Cape Leeuwin at 33.25°S for daily wind Experiment 3 on day 30, December 31, 2000.

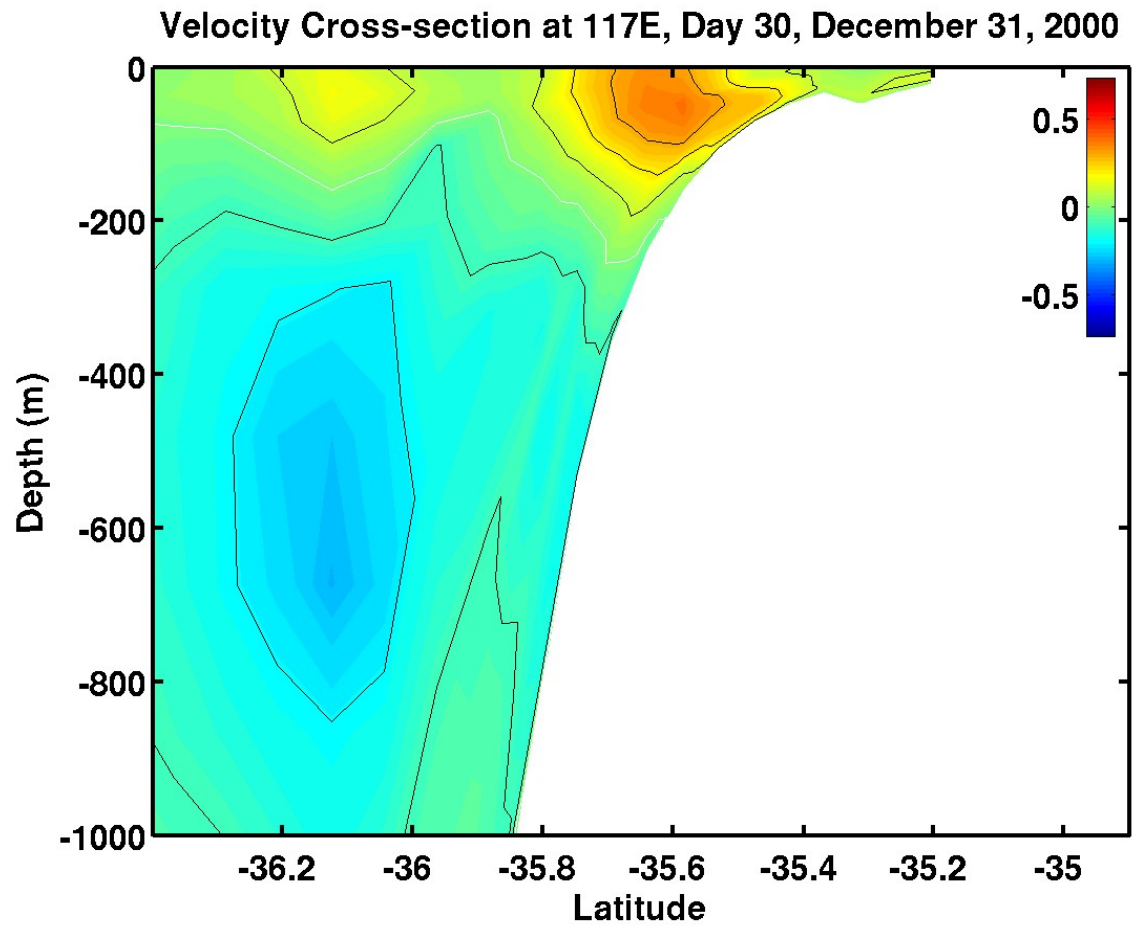


Figure 5.11e. Cross-section of zonal velocity component (m s^{-1}) at 117°E for daily wind Experiment 3 on day 30, December 31, 2000. Red is eastward and blue is westward. The white contour is zero.

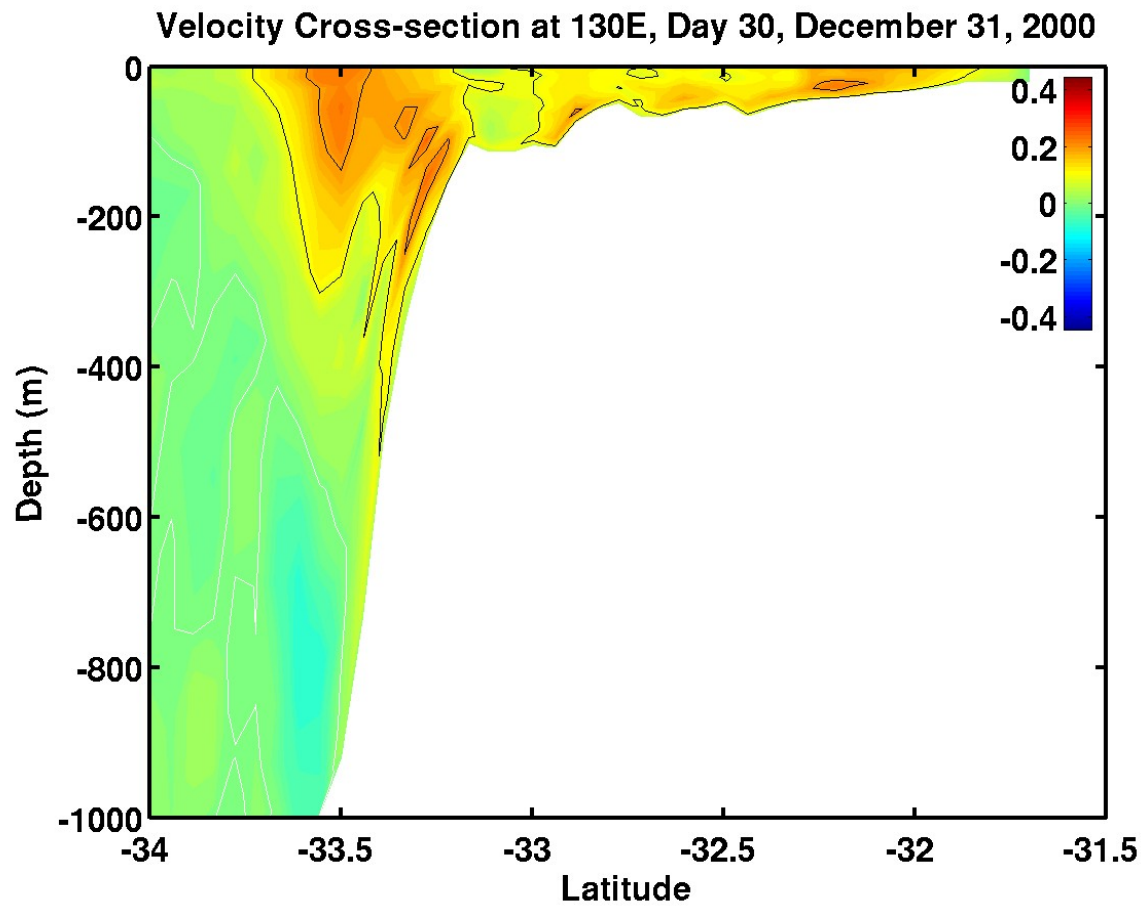


Figure 5.11f. Cross-section of zonal velocity component (m s^{-1}) in the Great Australian Bight (130°E) for daily wind Experiment 3 on day 30, December 31, 2000. Red is eastward and blue is westward. The white contour is zero.

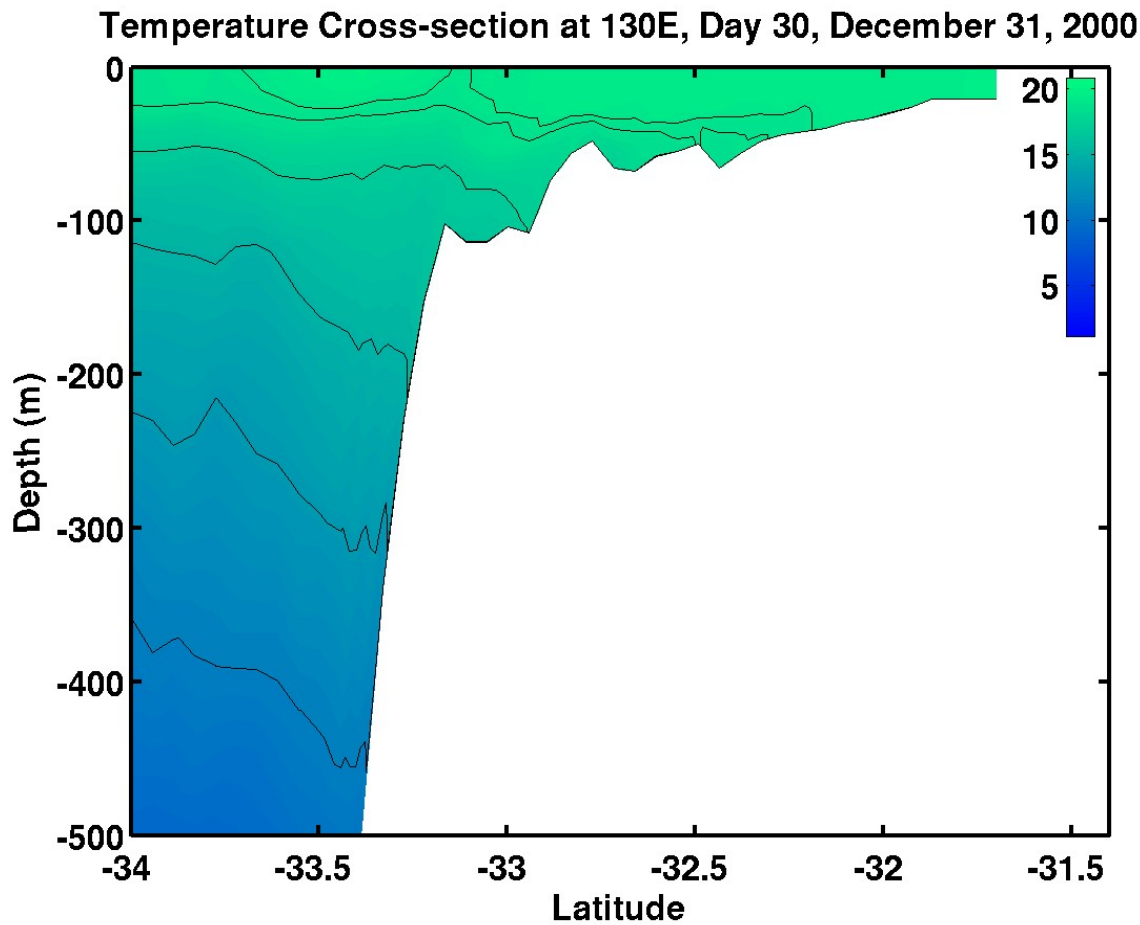


Figure 5.11g. Cross-section of temperature ($^{\circ}\text{C}$) along a north-south transect in the Great Australian Bight (130°E) for daily wind Experiment 3 on day 30, December 31, 2000.

Surface Temperature and Velocity, Day 45, January 15, 2001

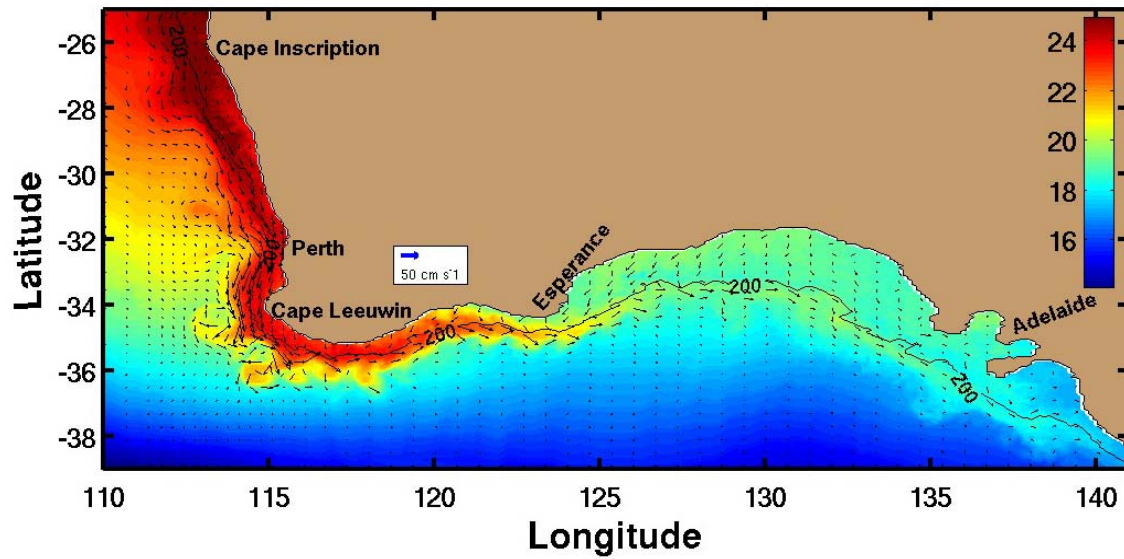


Figure 5.12a. Sea surface temperature ($^{\circ}\text{C}$) and velocity vectors for daily wind Experiment 3 on day 45, January 15, 2001.

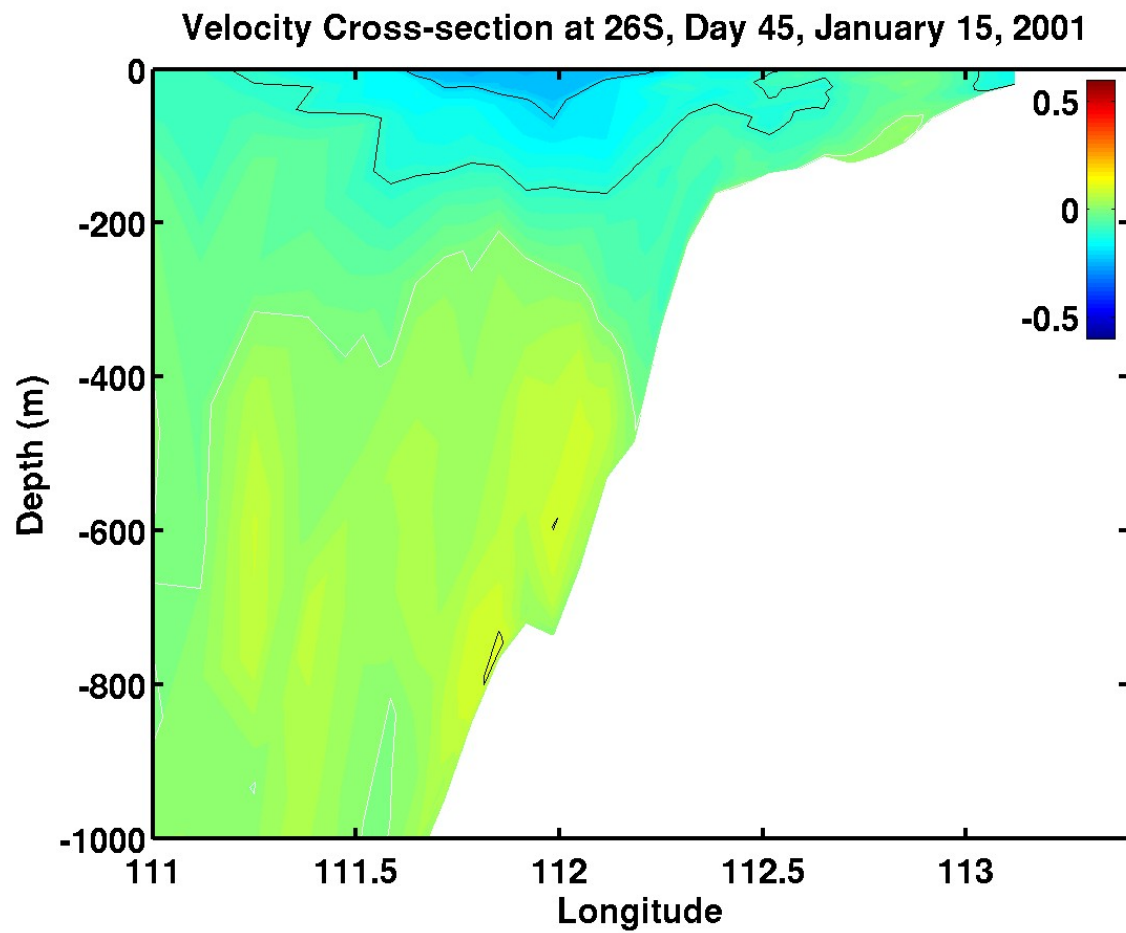


Figure 5.12b. Cross-section of meridional velocity component (m s^{-1}) at 26°S for daily wind Experiment 3 on day 45, January 15, 2001. Red is equatorward (north) and blue is poleward (south). The white contour is zero.

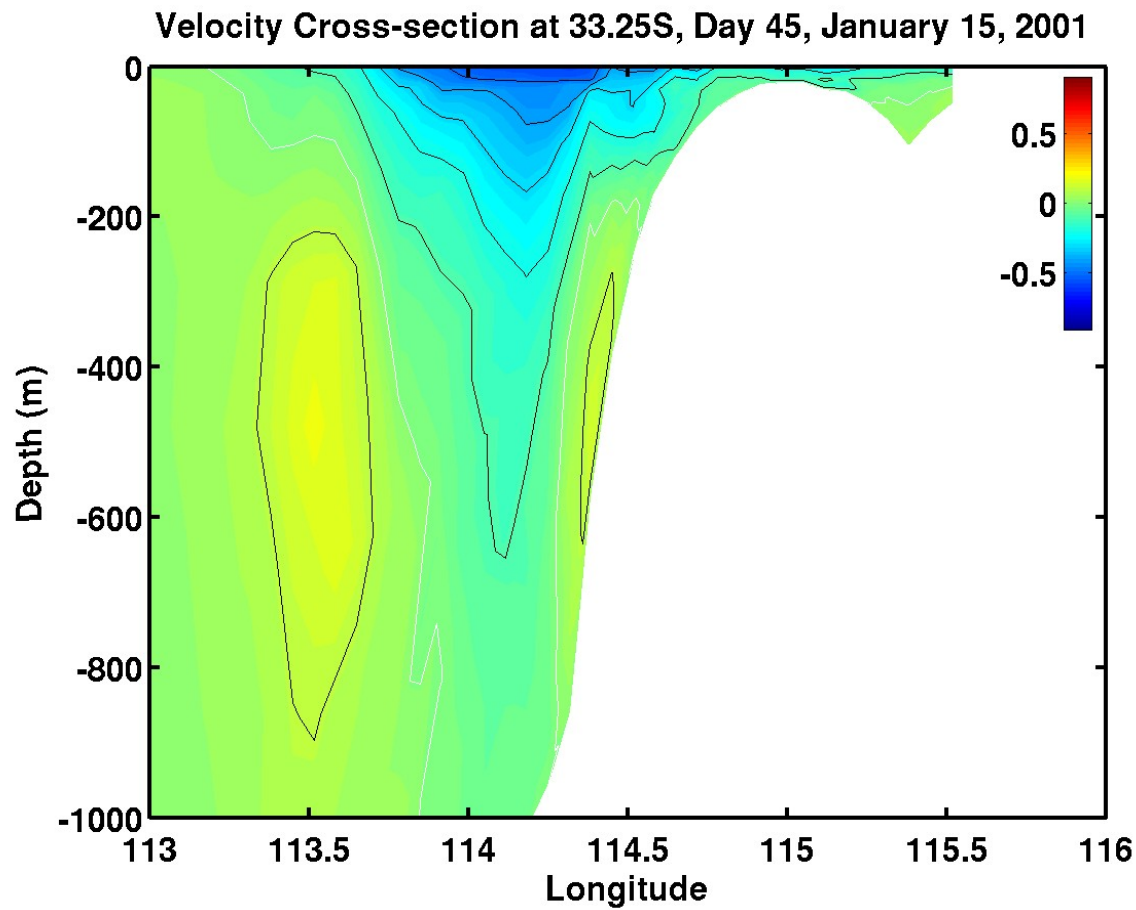


Figure 5.12c. Cross-section of meridional velocity component (m s^{-1}) just north of Cape Leeuwin at 33.25°S for daily wind Experiment 3 on day 45, January 15, 2001. Red is equatorward (north) and blue is poleward (south). The white contour is zero.

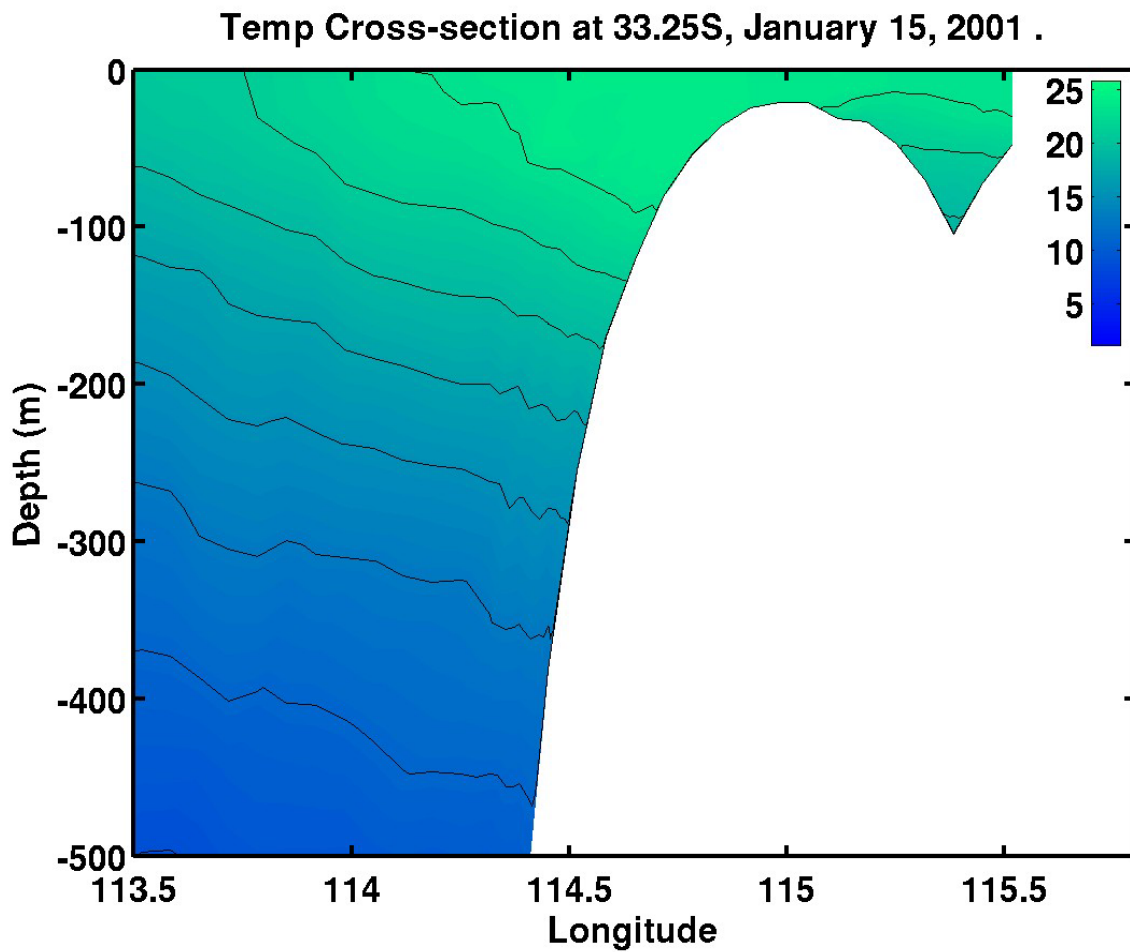


Figure 5.12d. Cross-section of temperature (°C) along an east-west transect just north of Cape Leeuwin at 33.25°S for daily wind Experiment 3 on day 45, January 15, 2001.

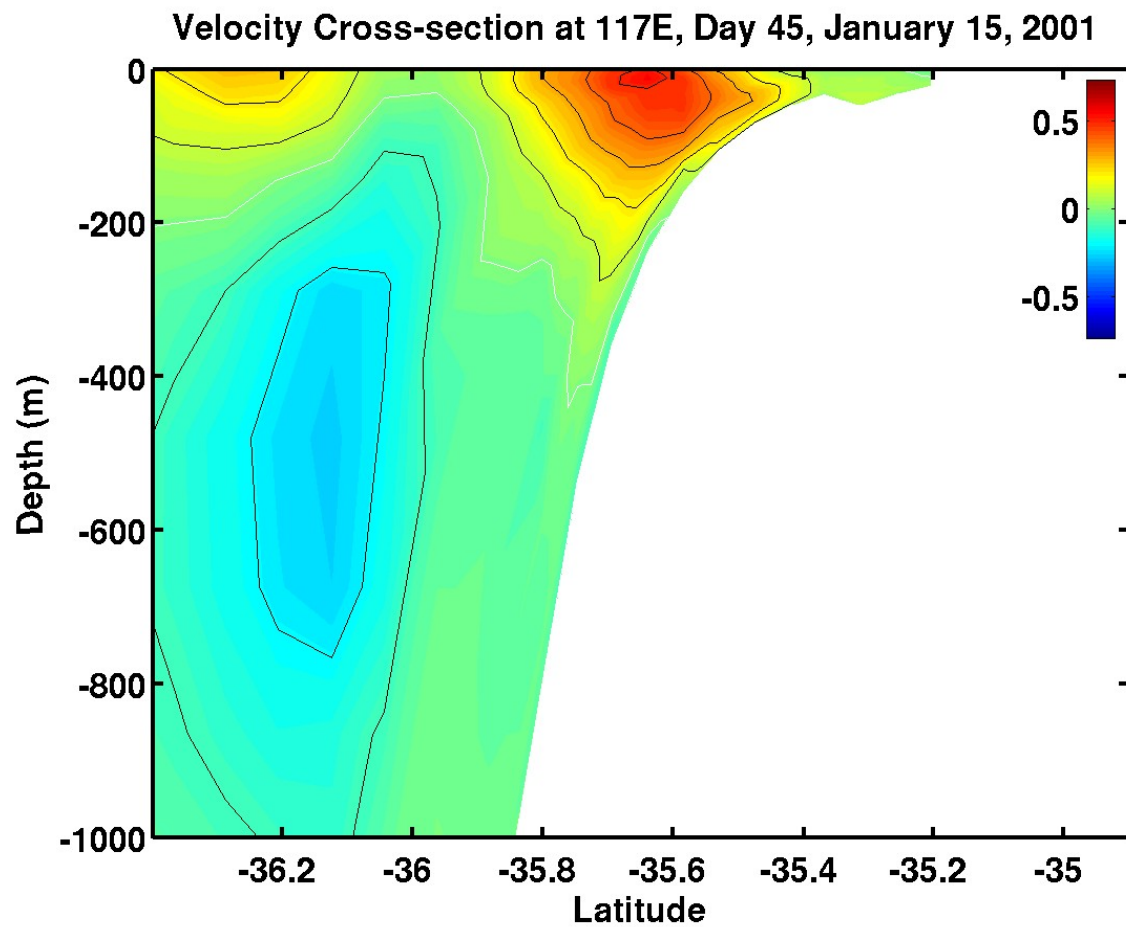


Figure 5.12e. Cross-section of zonal velocity component (m s^{-1}) at 117°E for daily wind Experiment 3 on day 45, January 15, 2001. Red is eastward and blue is westward. The white contour is zero.

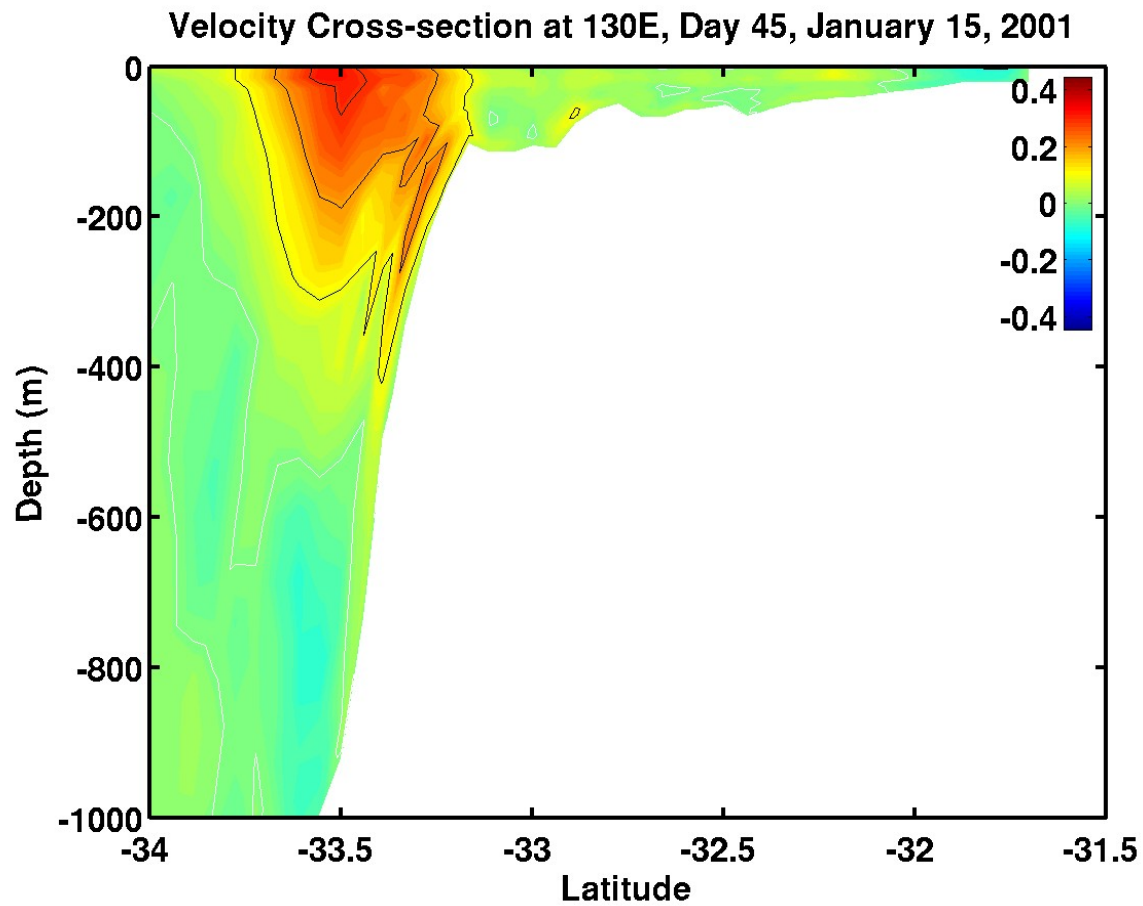


Figure 5.12f. Cross-section of zonal velocity component (m s^{-1}) in the Great Australian Bight (130°E) for daily wind Experiment 3 on day 45, January 15, 2001. Red is eastward and blue is westward. The white contour is zero.

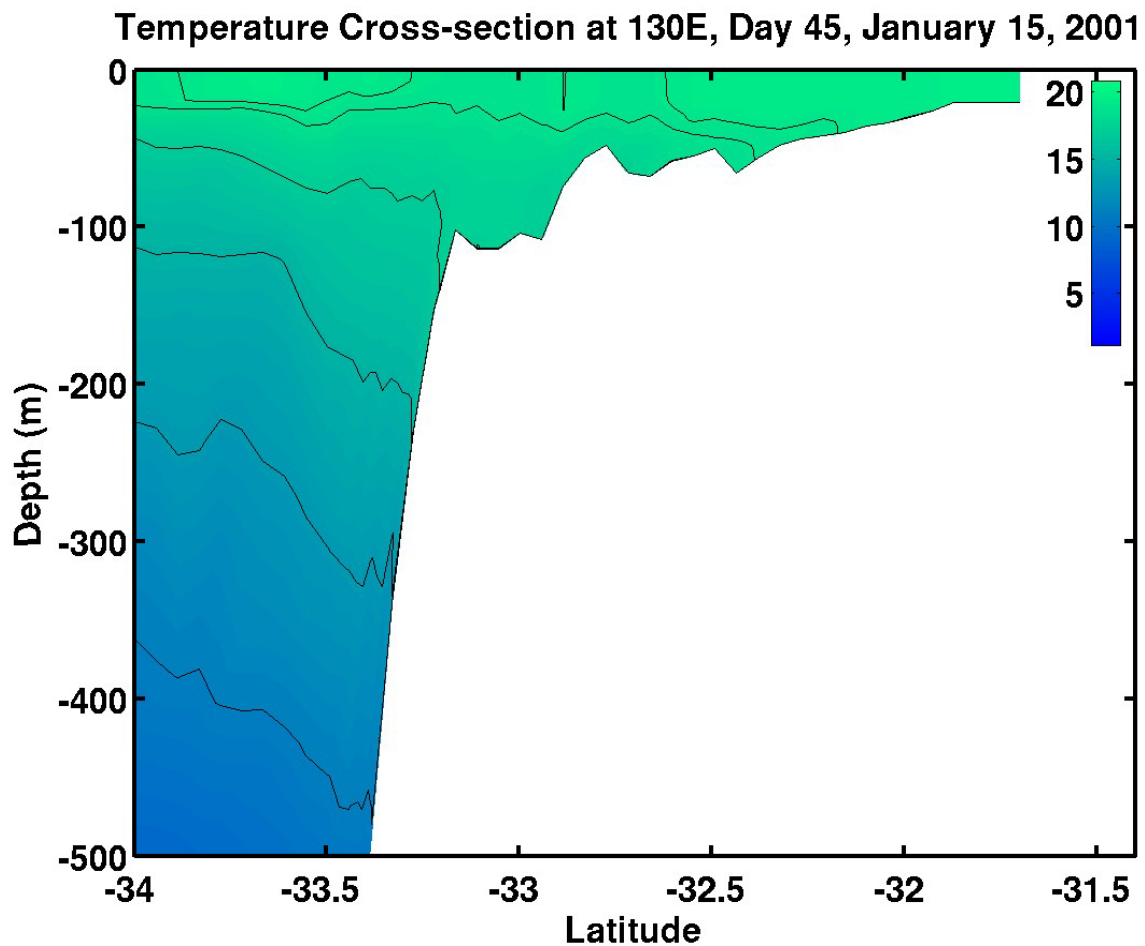


Figure 5.12g. Cross-section of temperature ($^{\circ}\text{C}$) along a north-south transect in the Great Australian Bight (130°E) for daily wind Experiment 3 on day 45, January 15, 2001.

Surface Temperature and Velocity, Day 60, January 30, 2001

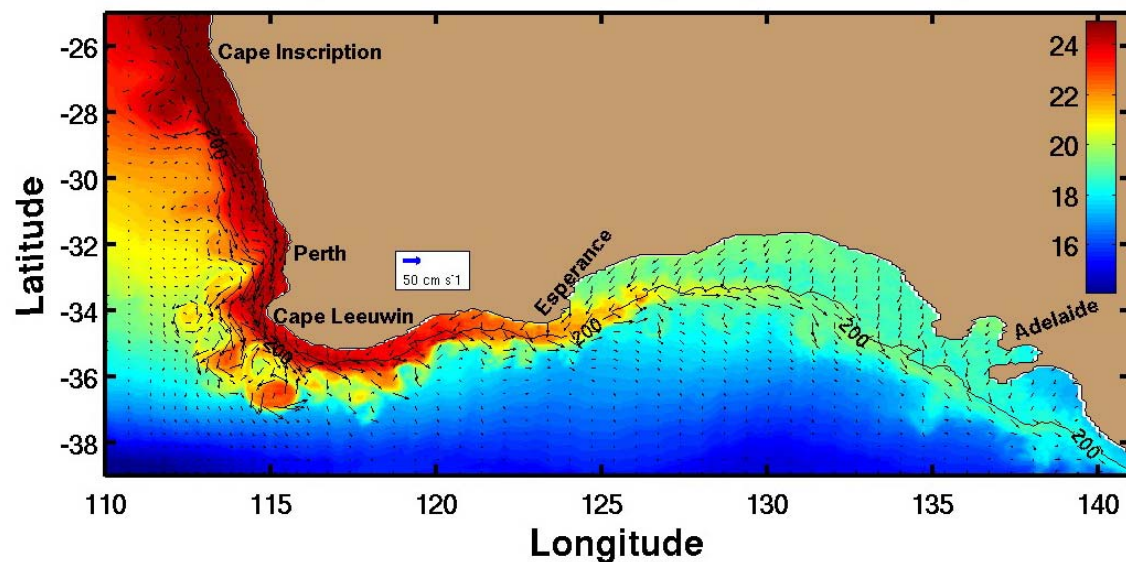


Figure 5.13a. Sea surface temperature ($^{\circ}\text{C}$) and velocity vectors for daily wind Experiment 3 on day 60, January 30, 2001.

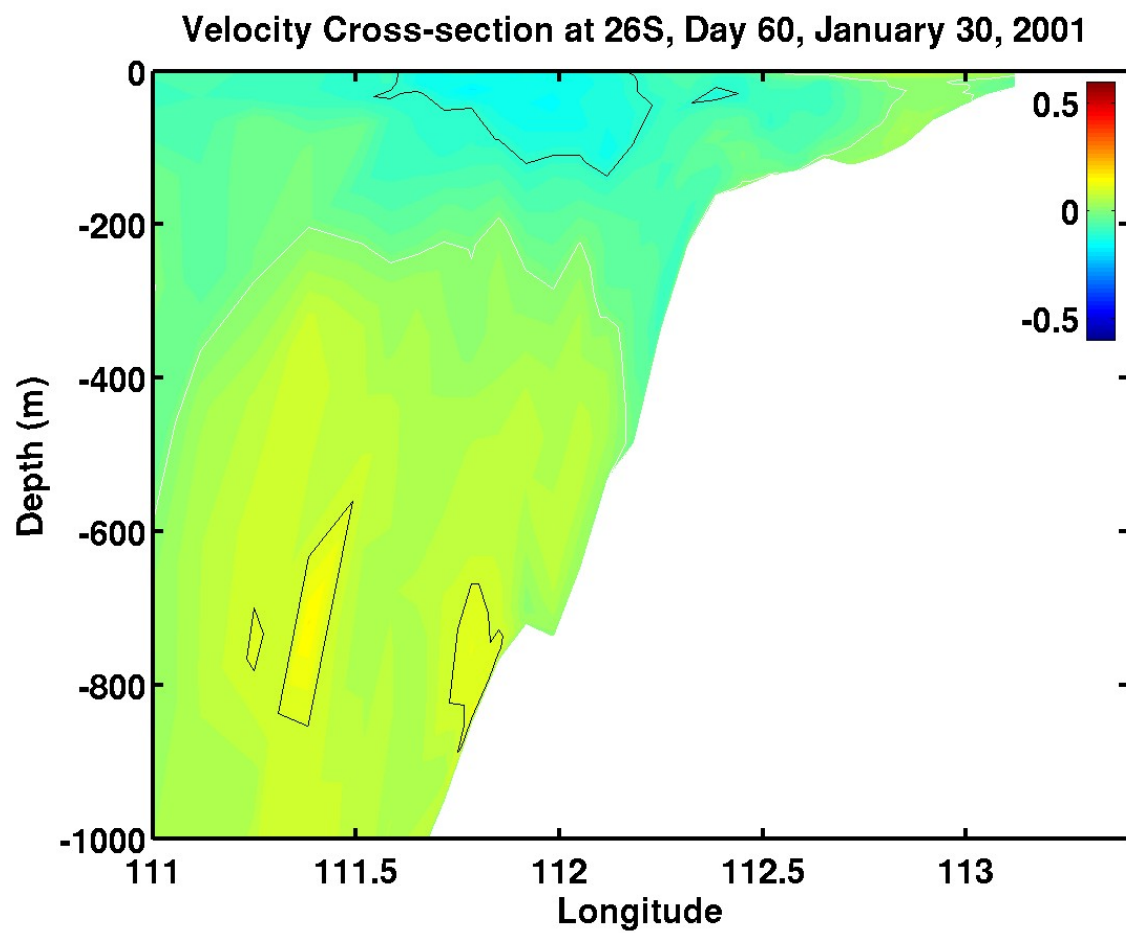


Figure 5.13b. Cross-section of meridional velocity component (m s^{-1}) at 26°S for daily wind Experiment 3 on day 60, January 30, 2001. Red is equatorward (north) and blue is poleward (south). The white contour is zero.

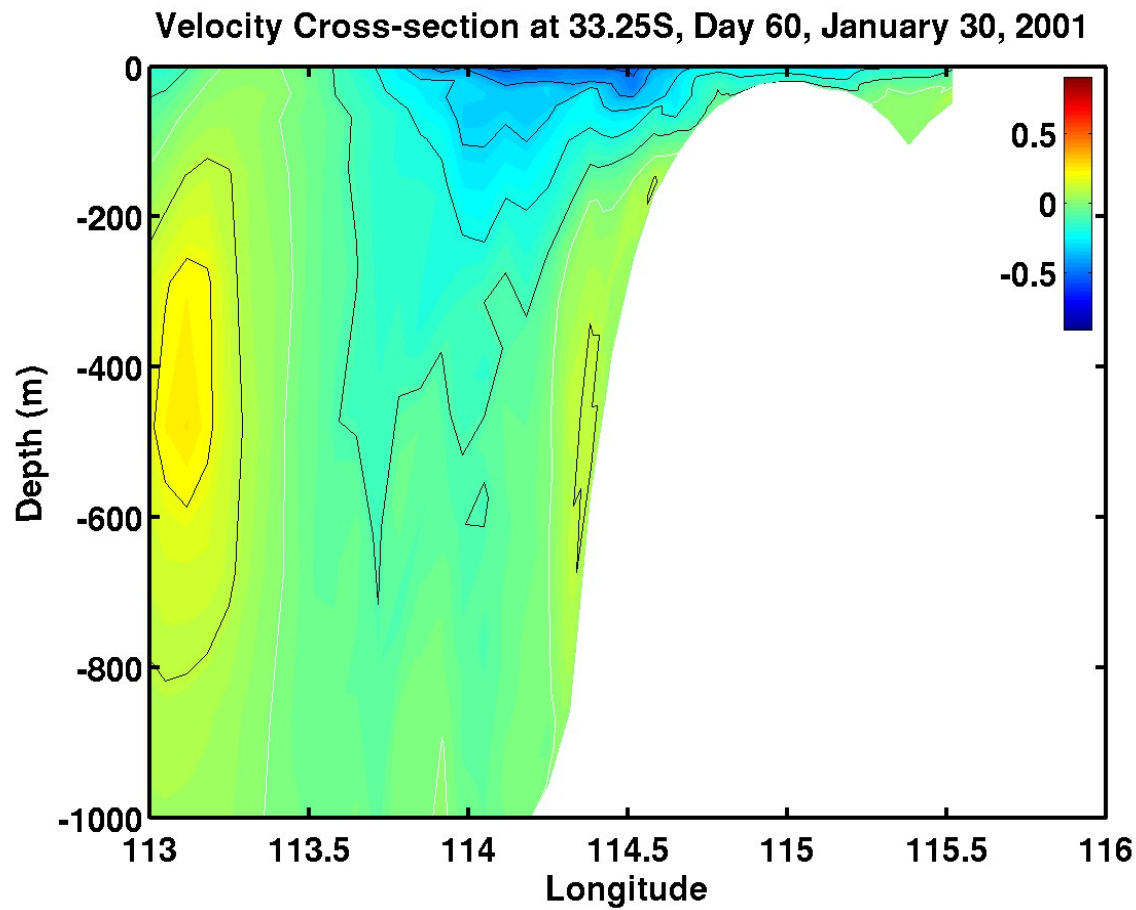


Figure 5.13c. Cross-section of meridional velocity component (m s^{-1}) just north of Cape Leeuwin at 33.25°S for daily wind Experiment 3 on day 60, January 30, 2001. Red is equatorward (north) and blue is poleward (south). The white contour is zero.

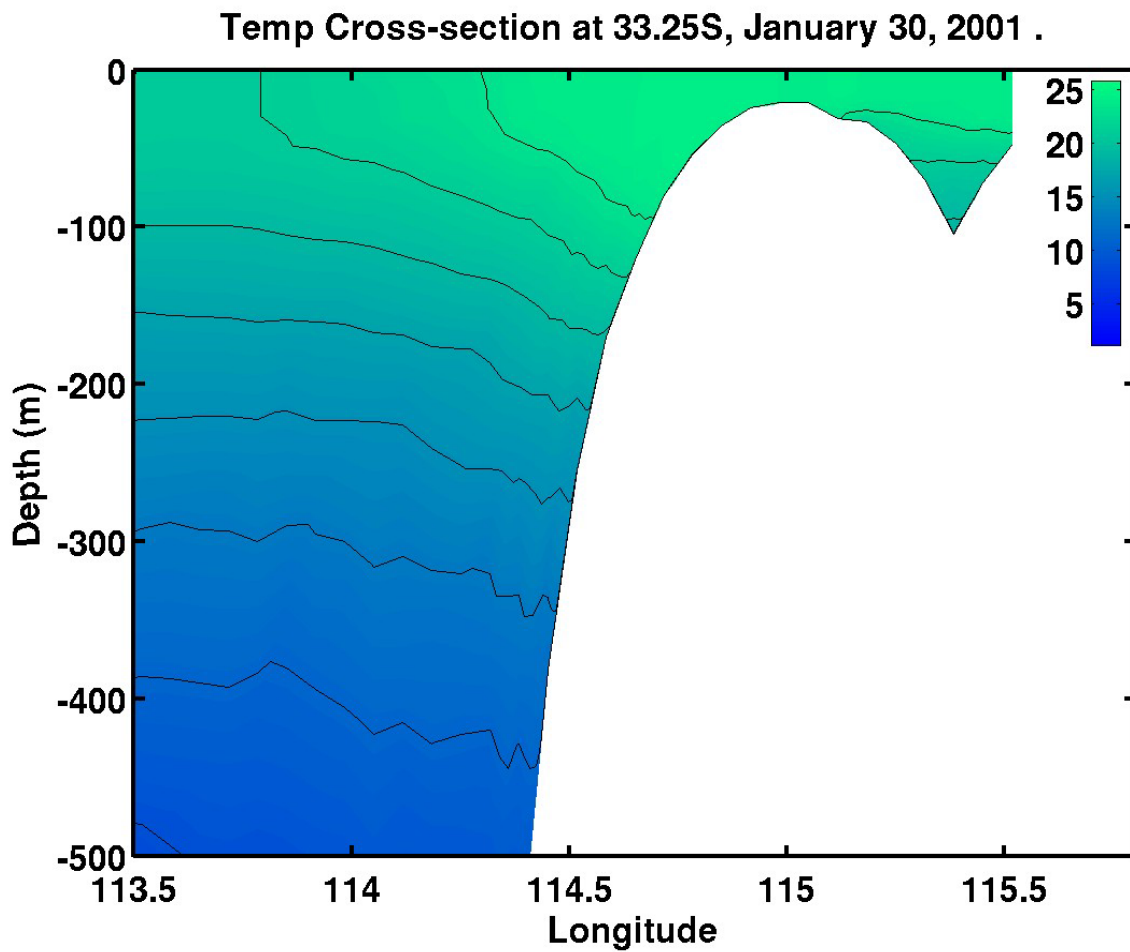


Figure 5.13d. Cross-section of temperature (°C) along an east-west transect just north of Cape Leeuwin at 33.25°S for daily wind Experiment 3 on day 60, January 30, 2001.

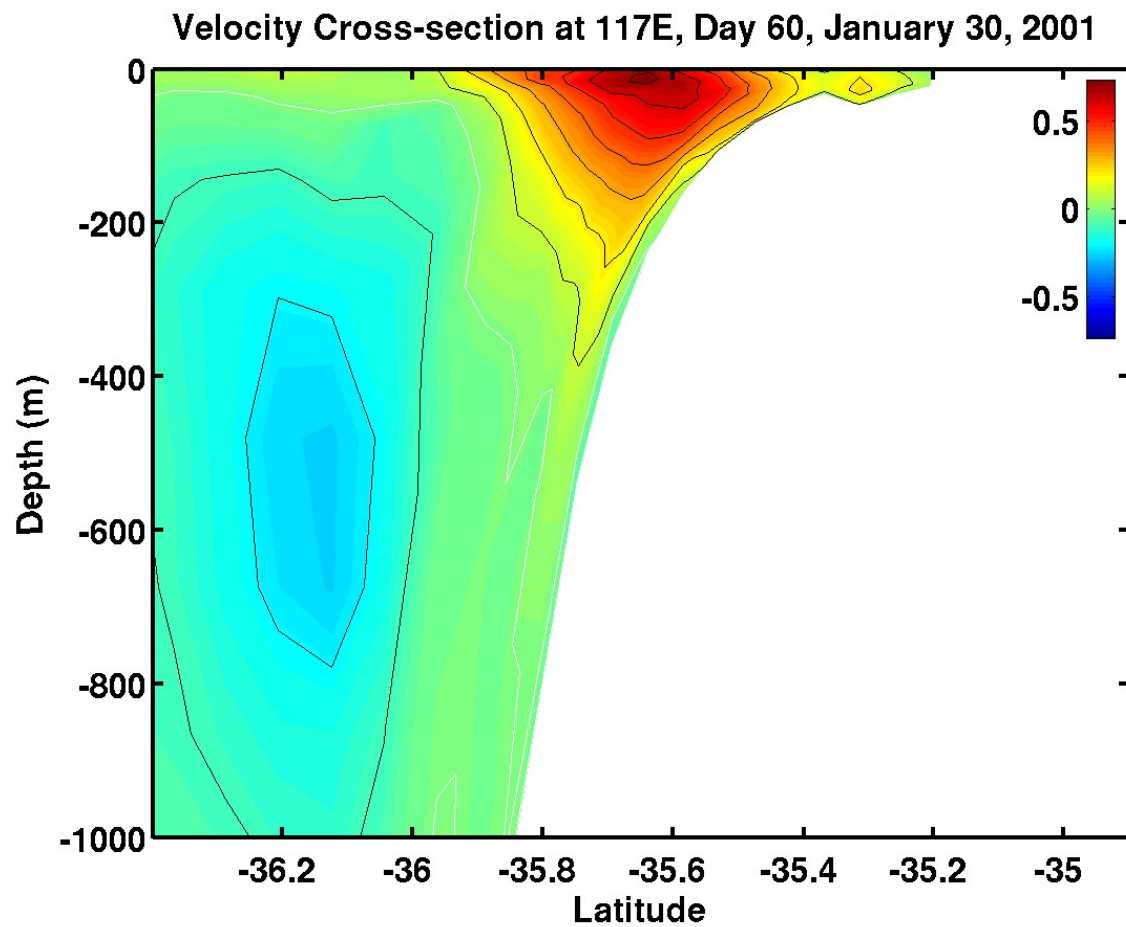


Figure 5.13e. Cross-section of zonal velocity component (m s^{-1}) at 117°E for daily wind Experiment 3 on day 60, January 30, 2001. Red is eastward and blue is westward. The white contour is zero.

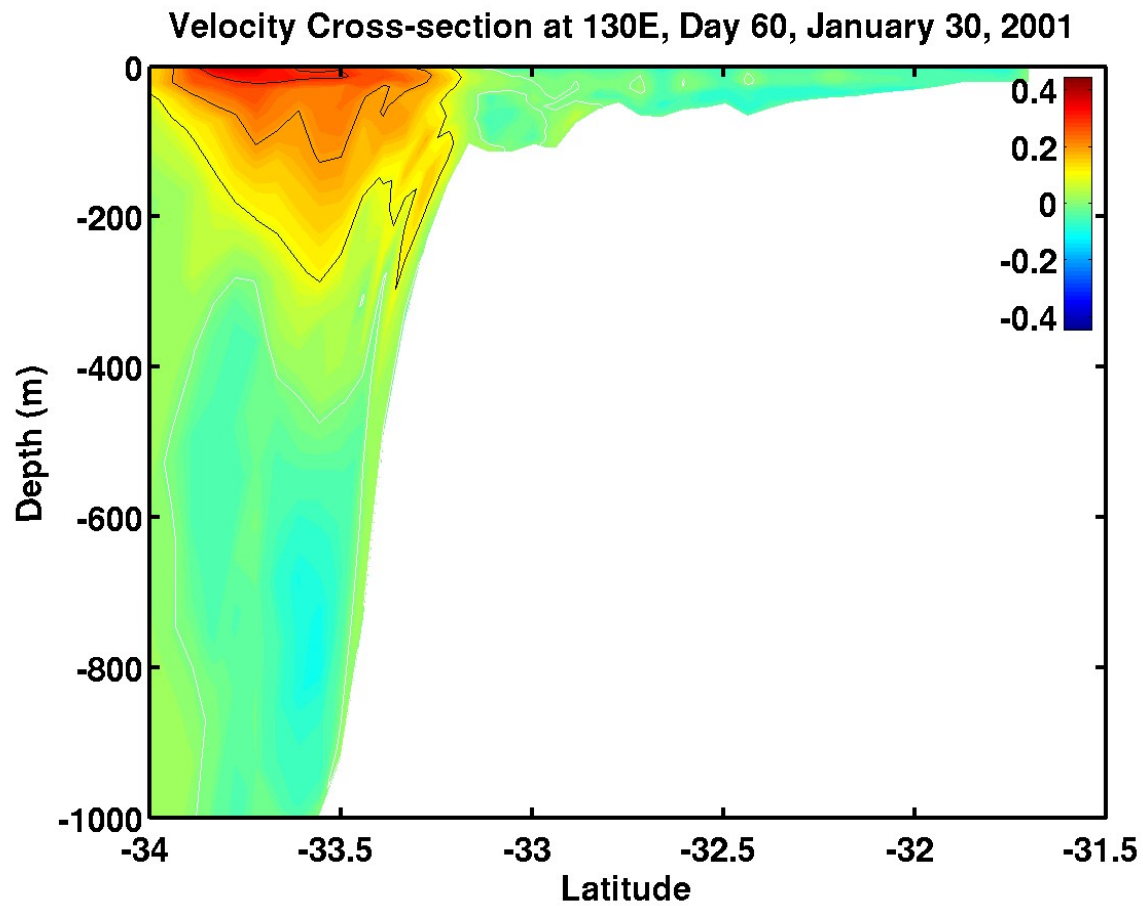


Figure 5.13f. Cross-section of zonal velocity component (m s^{-1}) in the Great Australian Bight (130°E) for daily wind Experiment 3 on day 60, January 30, 2001. Red is eastward and blue is westward. The white contour is zero.

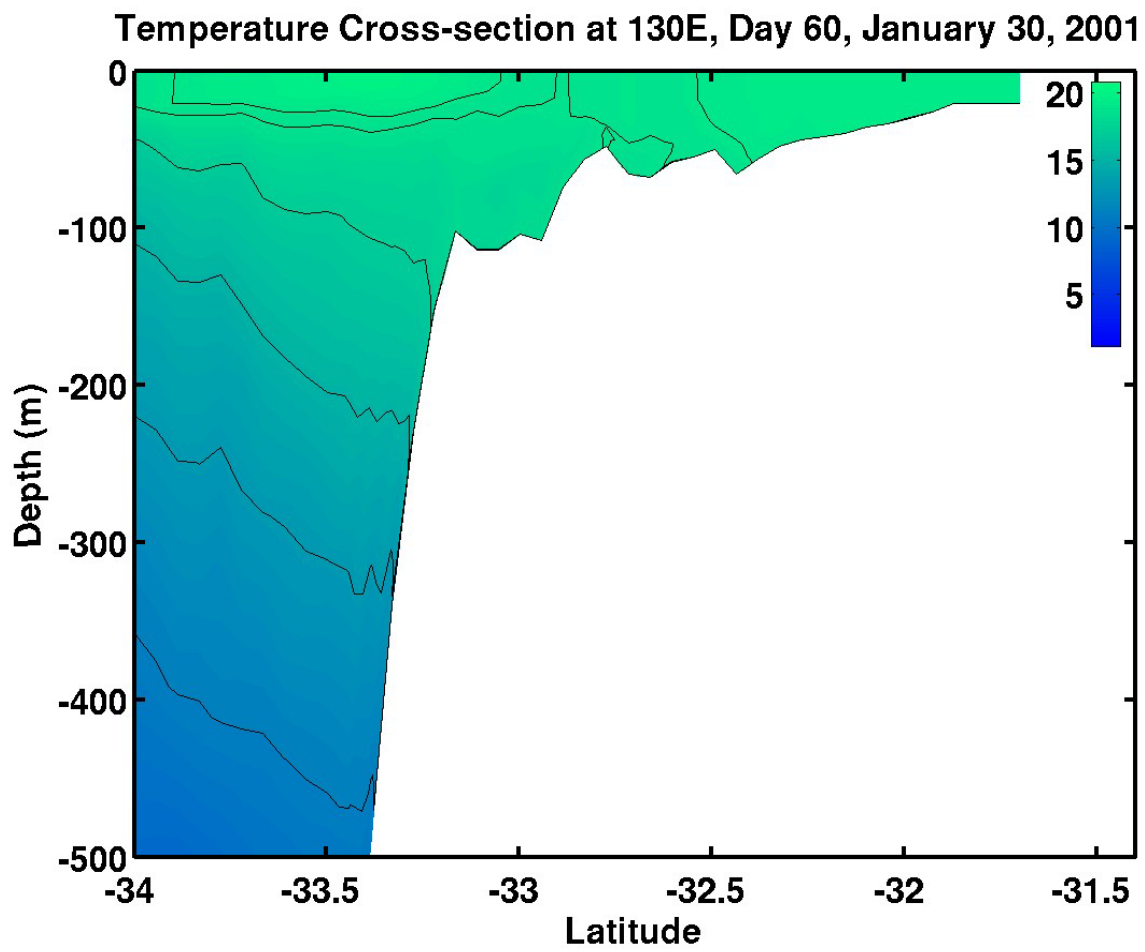


Figure 5.13g. Cross-section of temperature ($^{\circ}\text{C}$) along a north-south transect in the Great Australian Bight (130°E) for daily wind Experiment 3 on day 60, January 30, 2001.

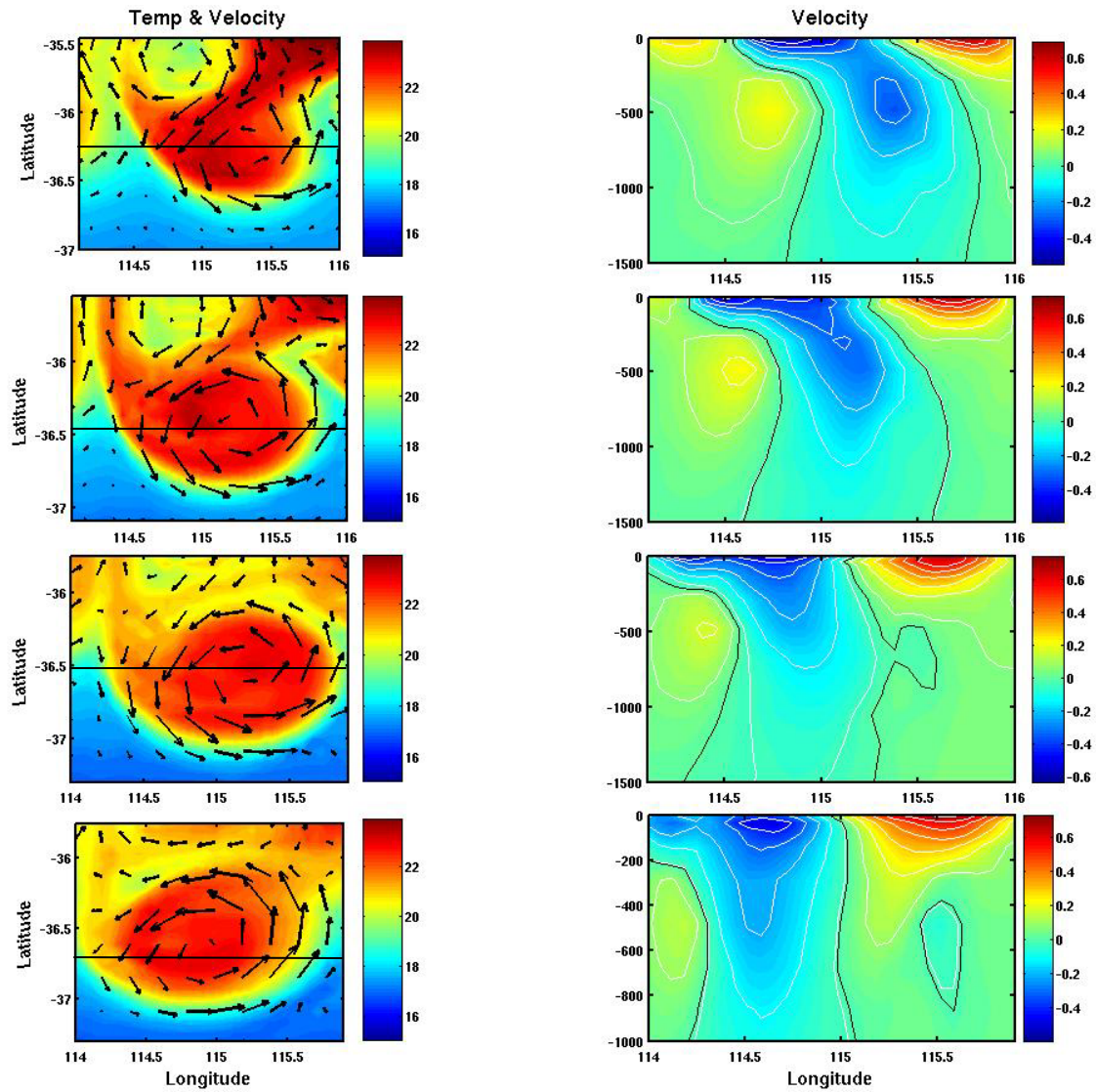


Figure 5.14. Daily wind Experiment 3 close-up views of an eddy southeast of Cape Leeuwin. Black line across surface view indicates location of corresponding cross-section. a. Surface temperature ($^{\circ}\text{C}$) and velocity vectors, day 54 (January 24, 2001). b. Cross-section of meridional velocity component (m s^{-1}) at 36.25°S , day 54. c. Surface temperature ($^{\circ}\text{C}$) and velocity vectors day 57 (January 27, 2001). d. Cross-section of meridional velocity component (m s^{-1}) at 36.47°S , day 57. e. Surface temperature ($^{\circ}\text{C}$) and velocity vectors, day 60 (January 30, 2001). f. Cross-section of meridional velocity component (m s^{-1}) at 36.52°S , day 60. g. Surface temperature ($^{\circ}\text{C}$) and velocity vectors, day 63 (February 2, 2001). h. Cross-section of meridional velocity component (m s^{-1}) at 36.72°S , day 63. Note: On all cross-section figures, red is equatorward (north), blue is poleward (south), and the black contour is zero.

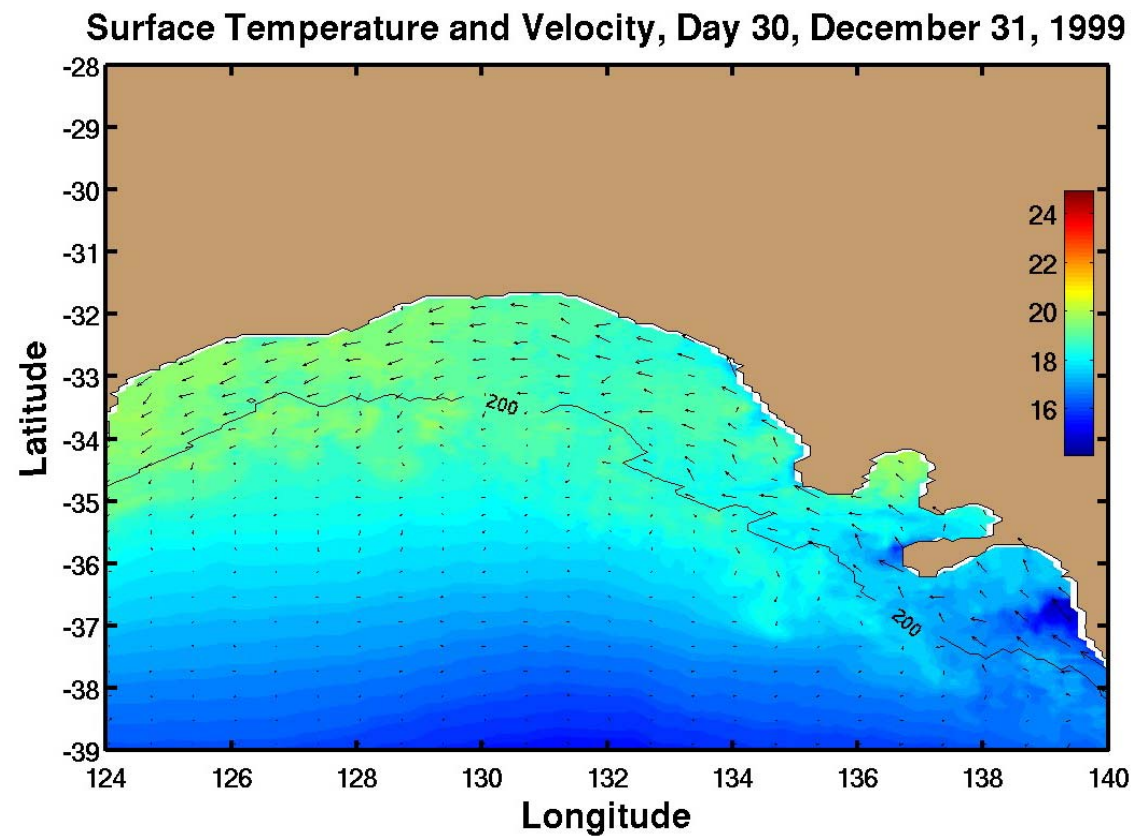


Figure 5.15a. Sea surface temperature ($^{\circ}\text{C}$) and velocity vectors in the Great Australian Bight for daily wind Experiment 3a on day 30, December 31, 1999.

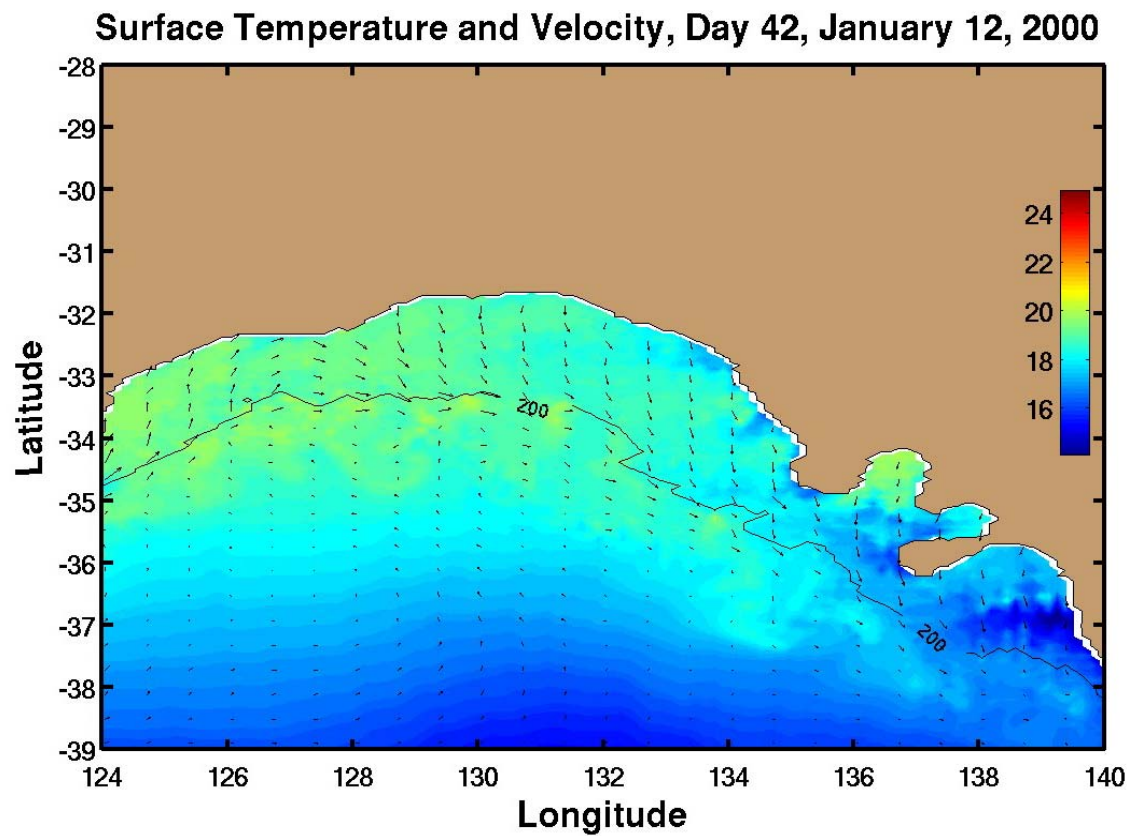


Figure 5.15b. Sea surface temperature ($^{\circ}\text{C}$) and velocity vectors in the Great Australian Bight for daily wind Experiment 3a on day 42, January 12, 2000.

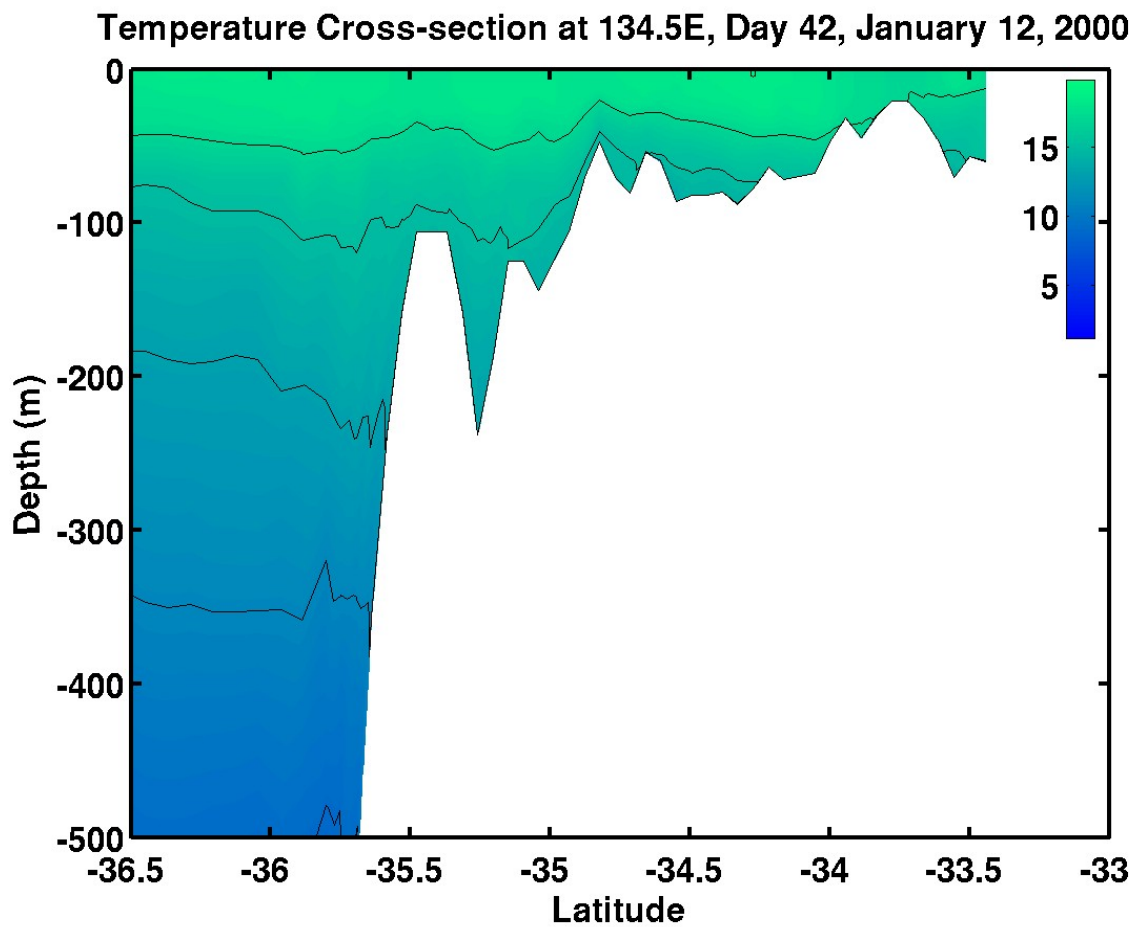


Figure 5.15c. Cross-section of temperature ($^{\circ}\text{C}$) along a north-south transect in the eastern Great Australian Bight (134.5°E) for daily wind Experiment 3a on day 42, January 12, 2000.

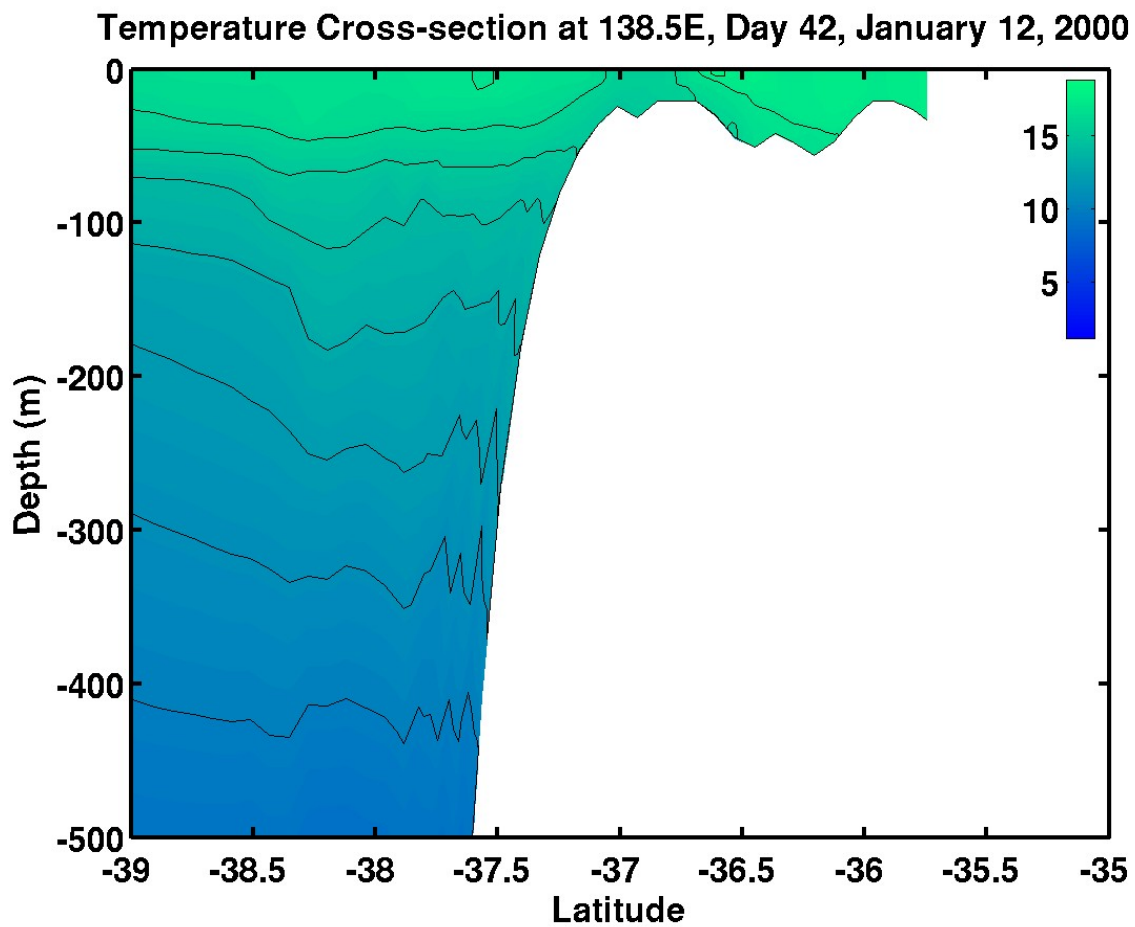


Figure 5.15d. Cross-section of temperature ($^{\circ}\text{C}$) along a north-south transect just east of Kangaroo Island (138.5°E) for daily wind Experiment 3a on day 42, January 12, 2000.

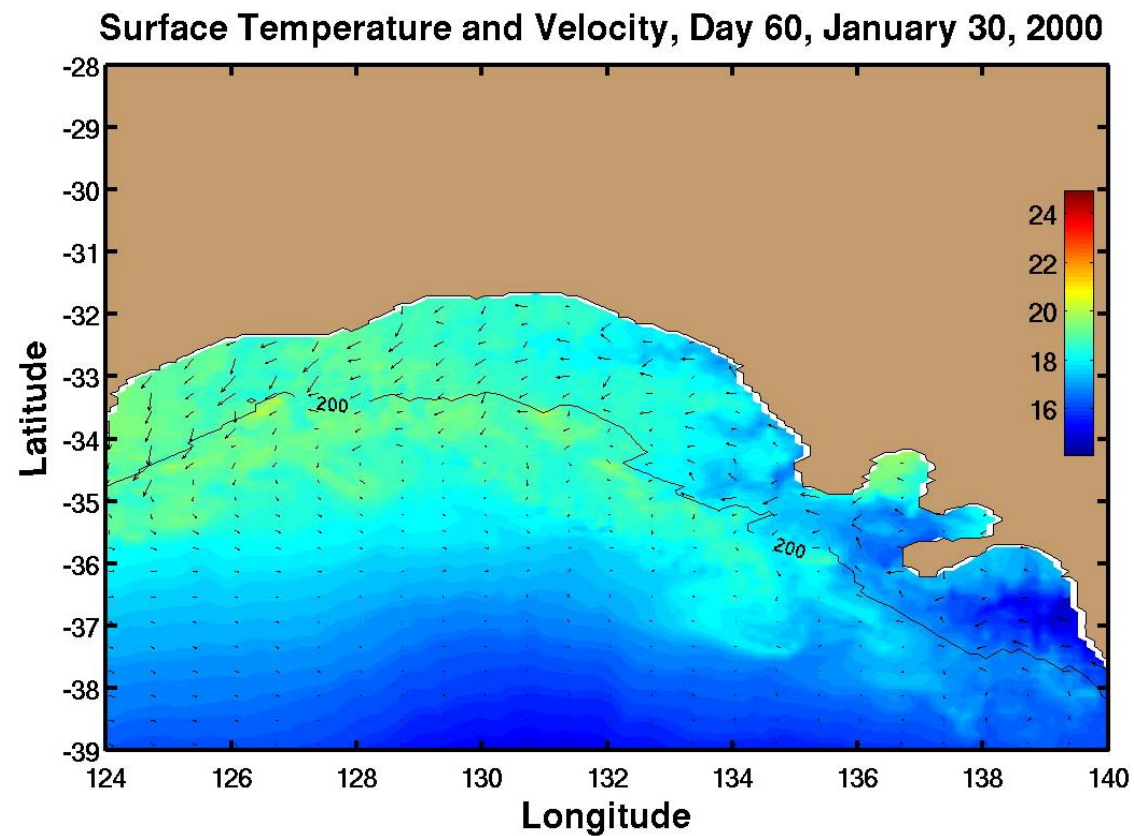


Figure 5.15e. Sea surface temperature ($^{\circ}\text{C}$) and velocity vectors in the Great Australian Bight for daily wind Experiment 3a on day 60, January 30, 2000.

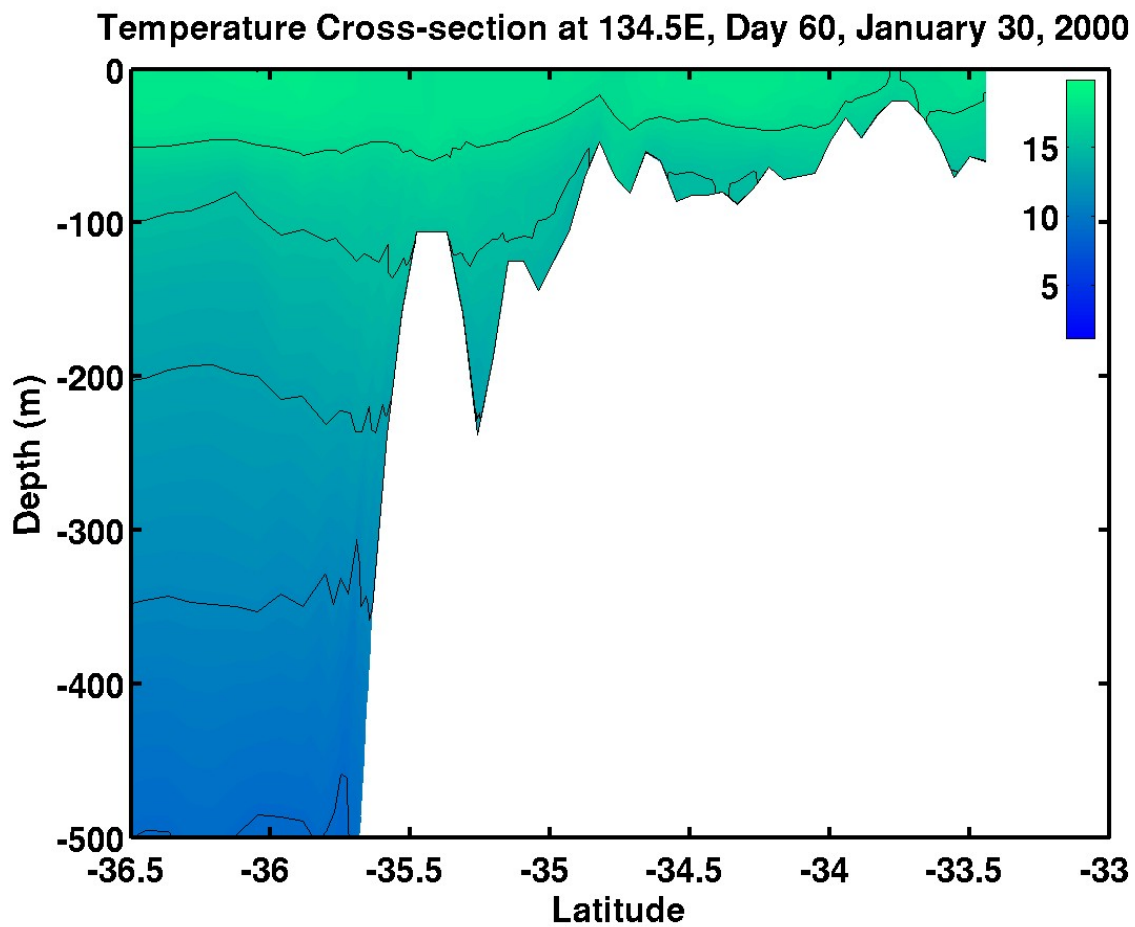


Figure 5.15f. Cross-section of temperature ($^{\circ}\text{C}$) along a north-south transect in the eastern Great Australian Bight (134.5°E) for daily wind Experiment 3a on day 60, January 30, 2000.

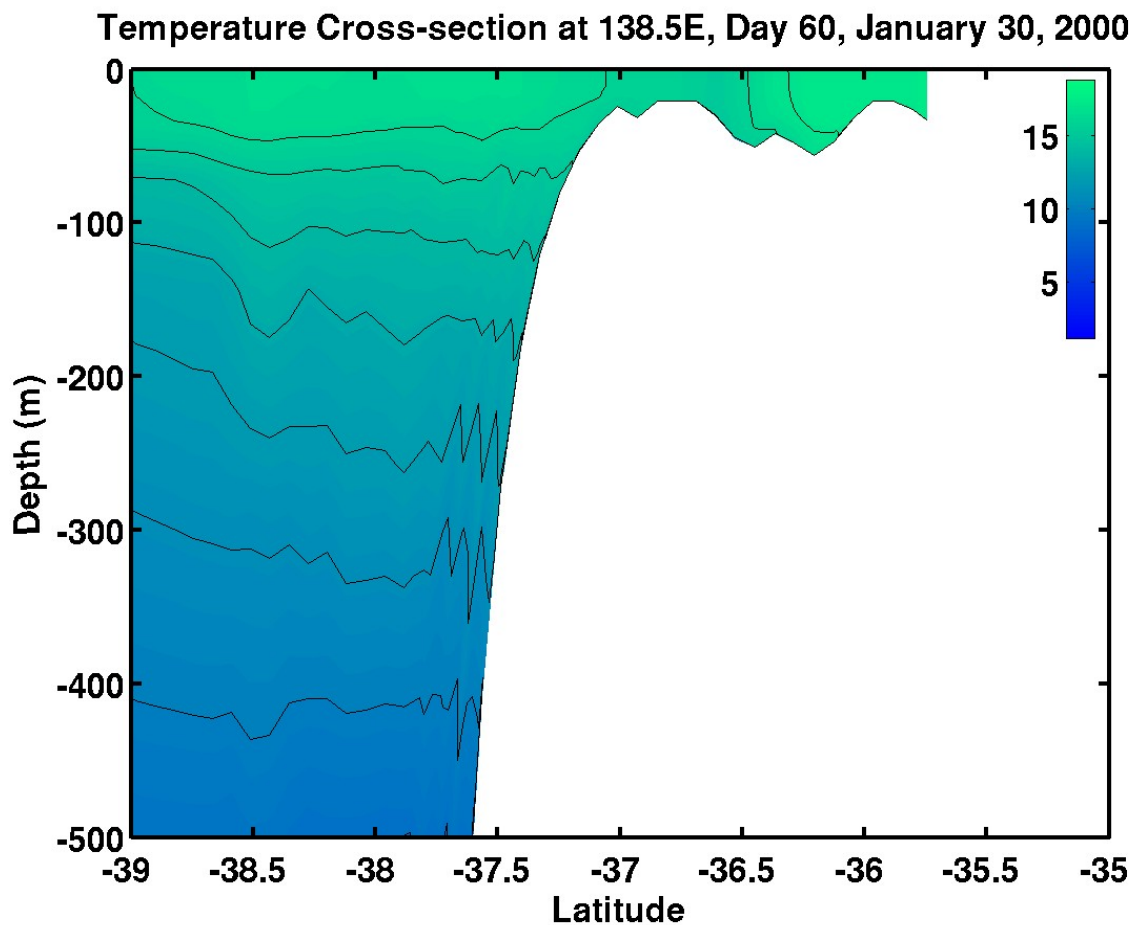


Figure 5.15g. Cross-section of temperature ($^{\circ}\text{C}$) along a north-south transect just east of Kangaroo Island (138.5°E) for daily wind Experiment 3a on day 60, January 30, 2000.

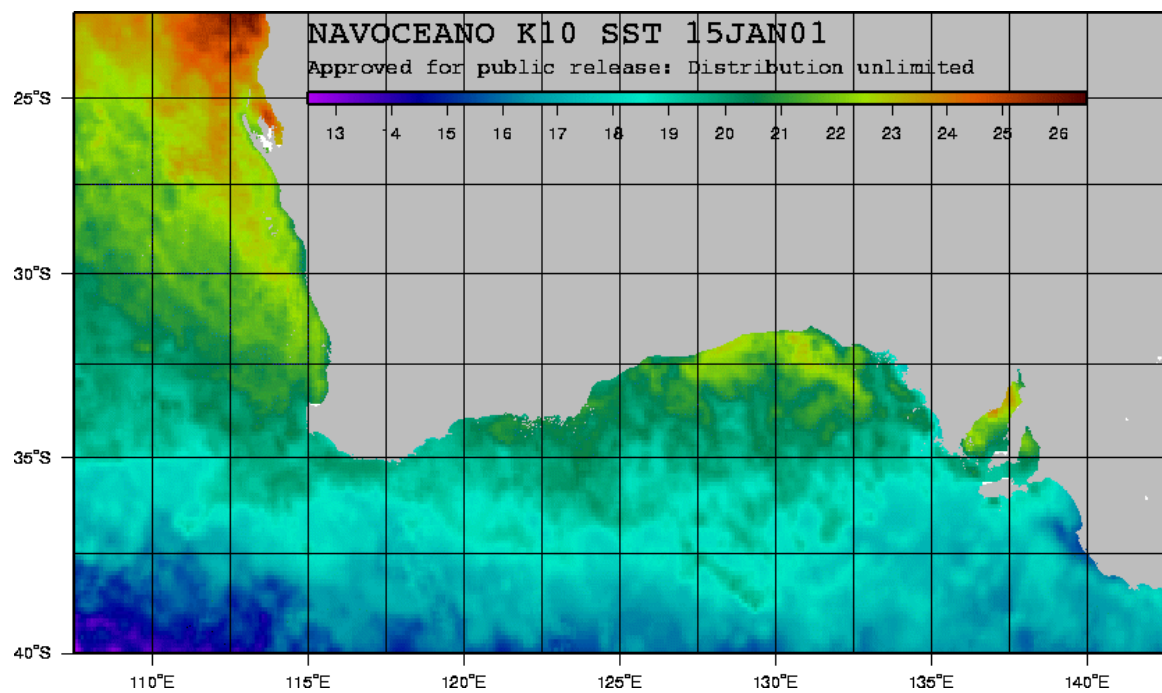


Figure 5.16a. Multi-Channel Sea Surface Temperature (MCSST) satellite imagery for southwestern Australian coastal area for January 15, 2001. Temperatures are in °C.

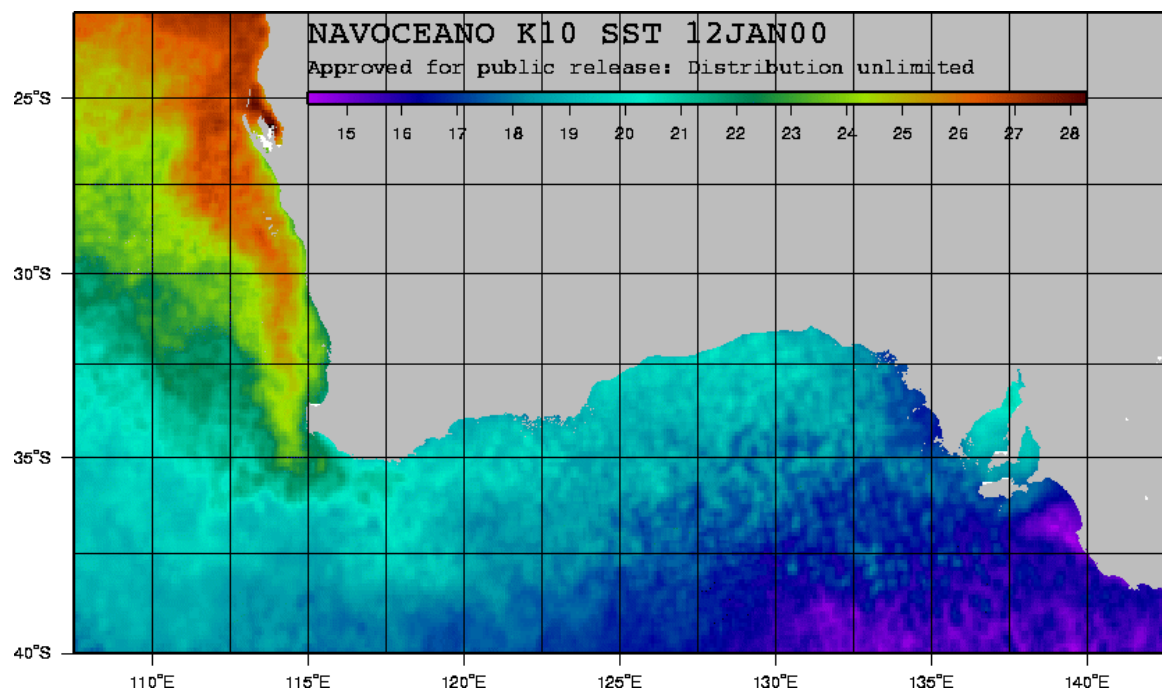


Figure 5.16b. Multi-Channel Sea Surface Temperature (MCSST) satellite imagery for southwestern Australian coastal area for January 12, 2000. Temperatures are in °C.

Surface Temperature and Velocity, Day 20, June 21, 2001

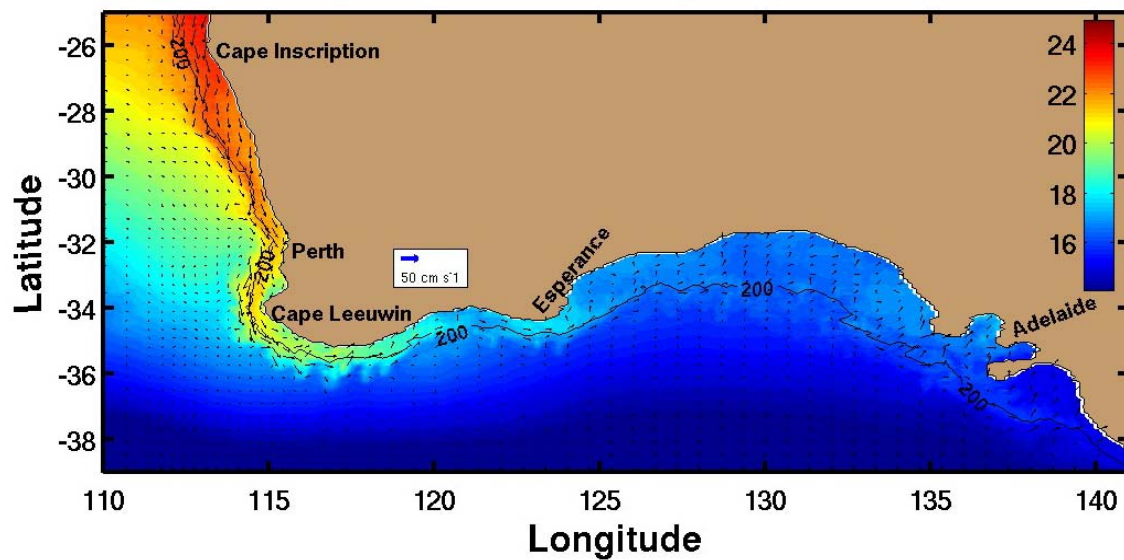


Figure 5.17a. Sea surface temperature ($^{\circ}\text{C}$) and velocity vectors for daily wind Experiment 4 on day 20, June 21, 2001.

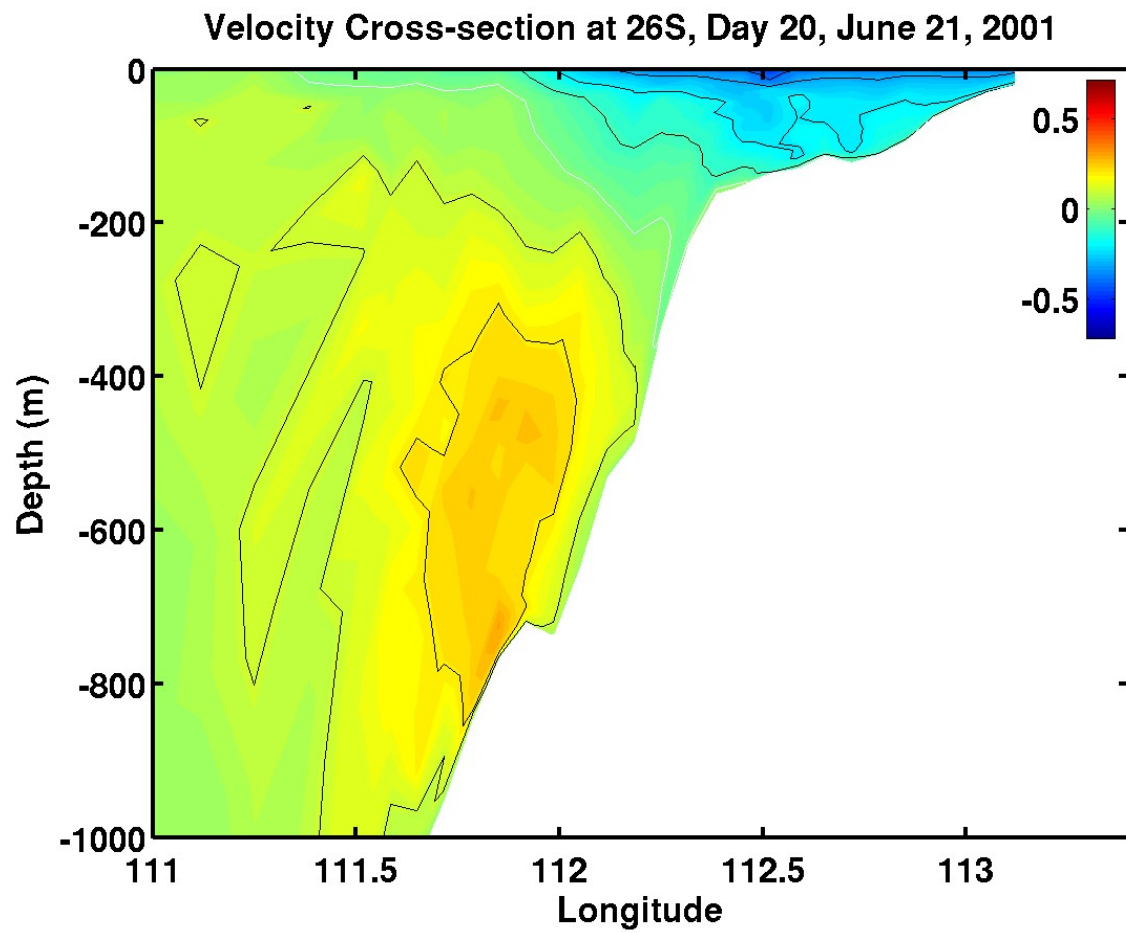


Figure 5.17b. Cross-section of meridional velocity component (m s^{-1}) at 26°S for daily wind Experiment 4 on day 20, June 21, 2001. Red is equatorward (north) and blue is poleward (south). The white contour is zero.

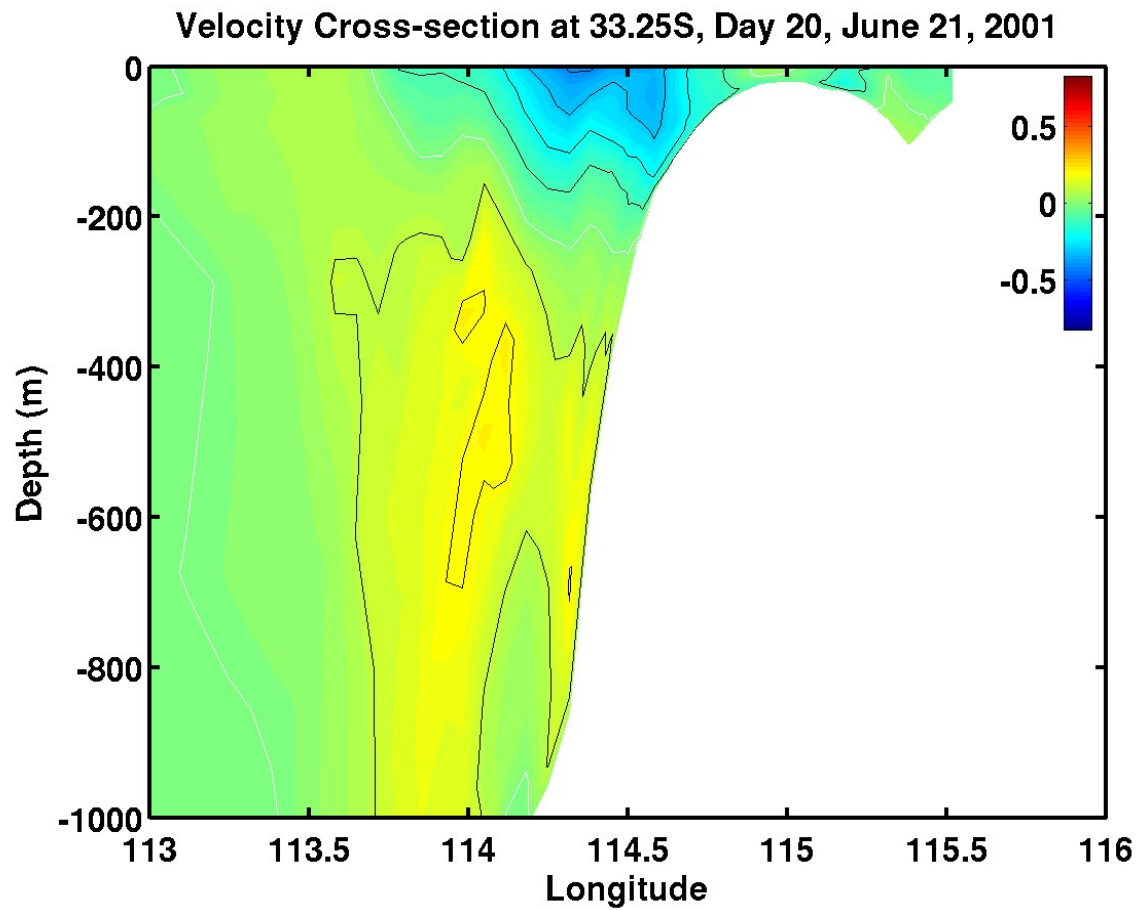


Figure 5.17c. Cross-section of meridional velocity component (m s^{-1}) 33.25°S for daily wind Experiment 4 on day 20, June 21, 2001. Red is equatorward (north) and blue is poleward (south). The white contour is zero.

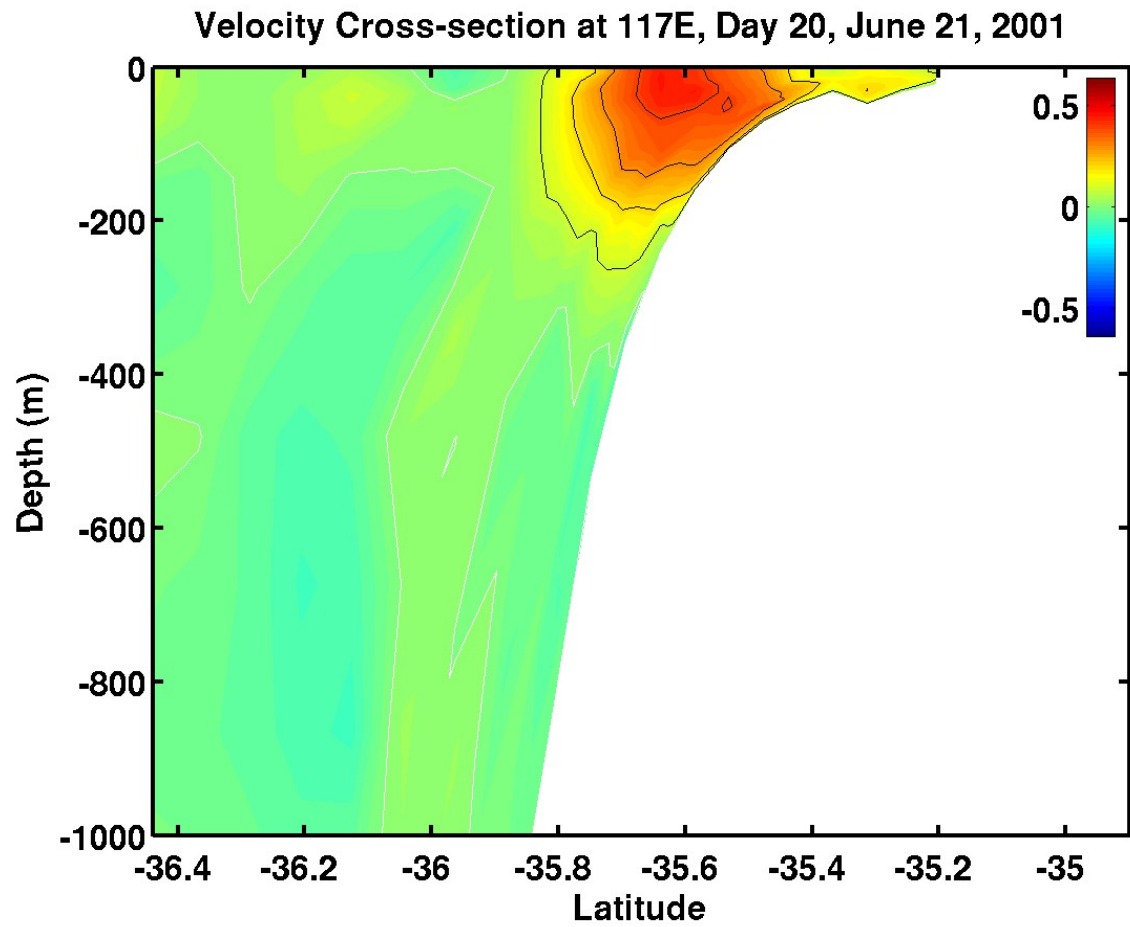


Figure 5.17d. Cross-section of zonal velocity component (m s^{-1}) at 117°E for daily wind Experiment 4 on day 20, June 21, 2001. Red is eastward and blue is westward. The white contour is zero.

Surface Temperature and Velocity, Day 30, July 01, 2001

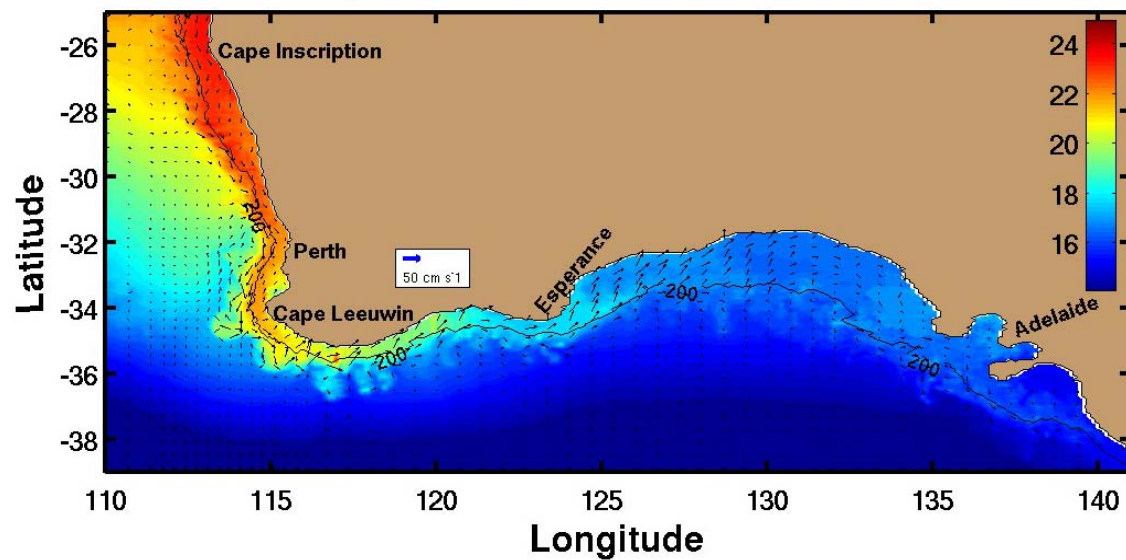


Figure 5.18a. Sea surface temperature ($^{\circ}\text{C}$) and velocity vectors for daily wind Experiment 4 on day 30, July 1, 2001.

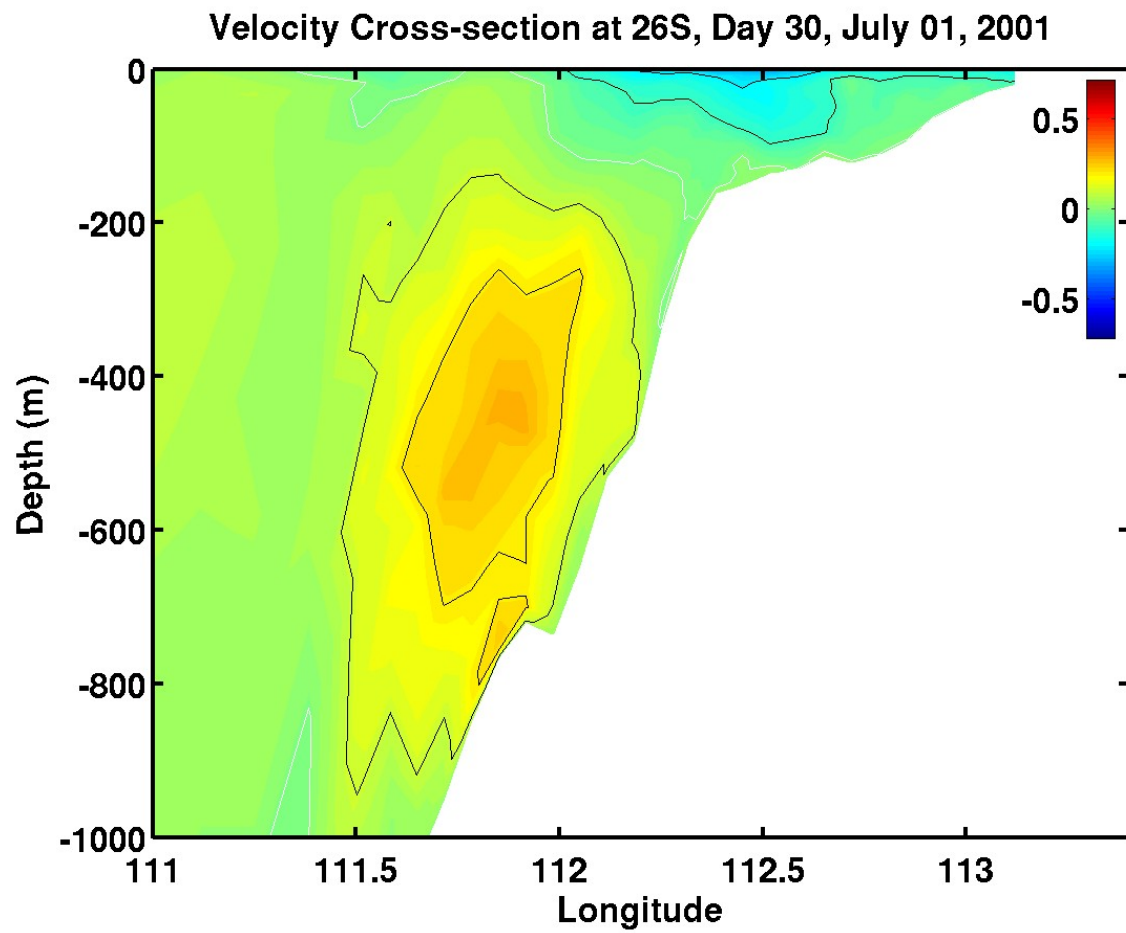


Figure 5.18b. Cross-section of meridional velocity component (m s^{-1}) at 26°S for daily wind Experiment 4 on day 30, July 1, 2001. Red is equatorward (north) and blue is poleward (south). The white contour is zero.

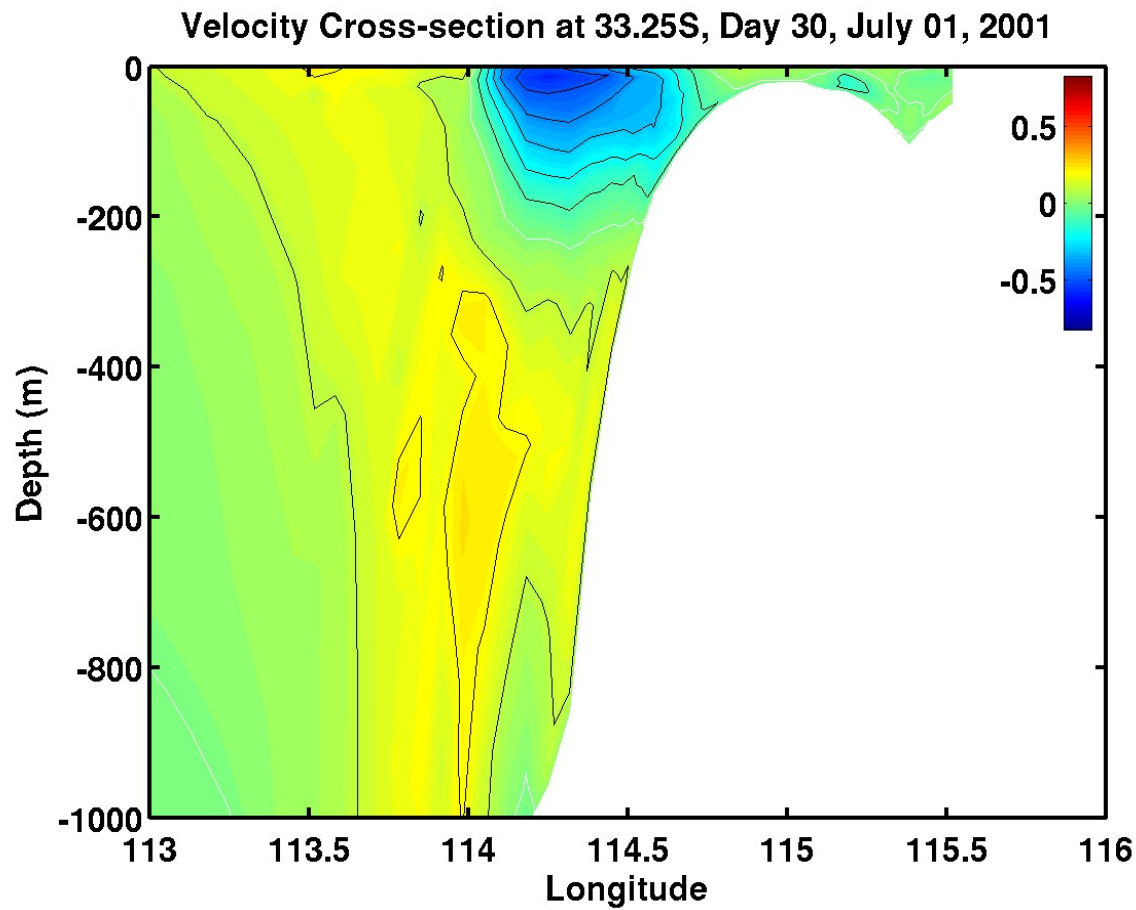


Figure 5.18c. Cross-section of meridional velocity component (m s^{-1}) just north of Cape Leeuwin at 33.25°S for daily wind Experiment 4 on day 30, July 1, 2001. Red is equatorward (north) and blue is poleward (south). The white contour is zero.

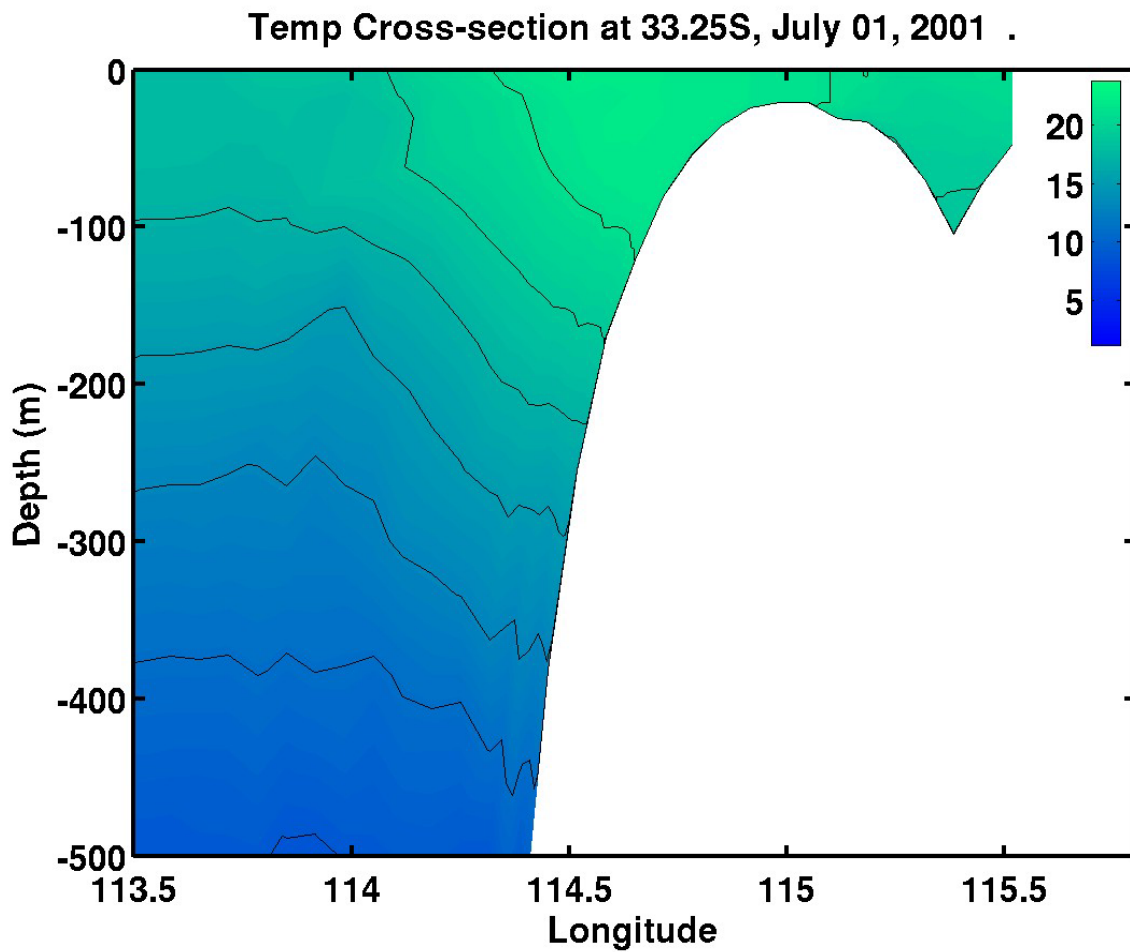


Figure 5.18d. Cross-section of temperature (°C) along an east-west transect just north of Cape Leeuwin at 33.25°S for daily wind Experiment 4 on day 30, July 1, 2001.

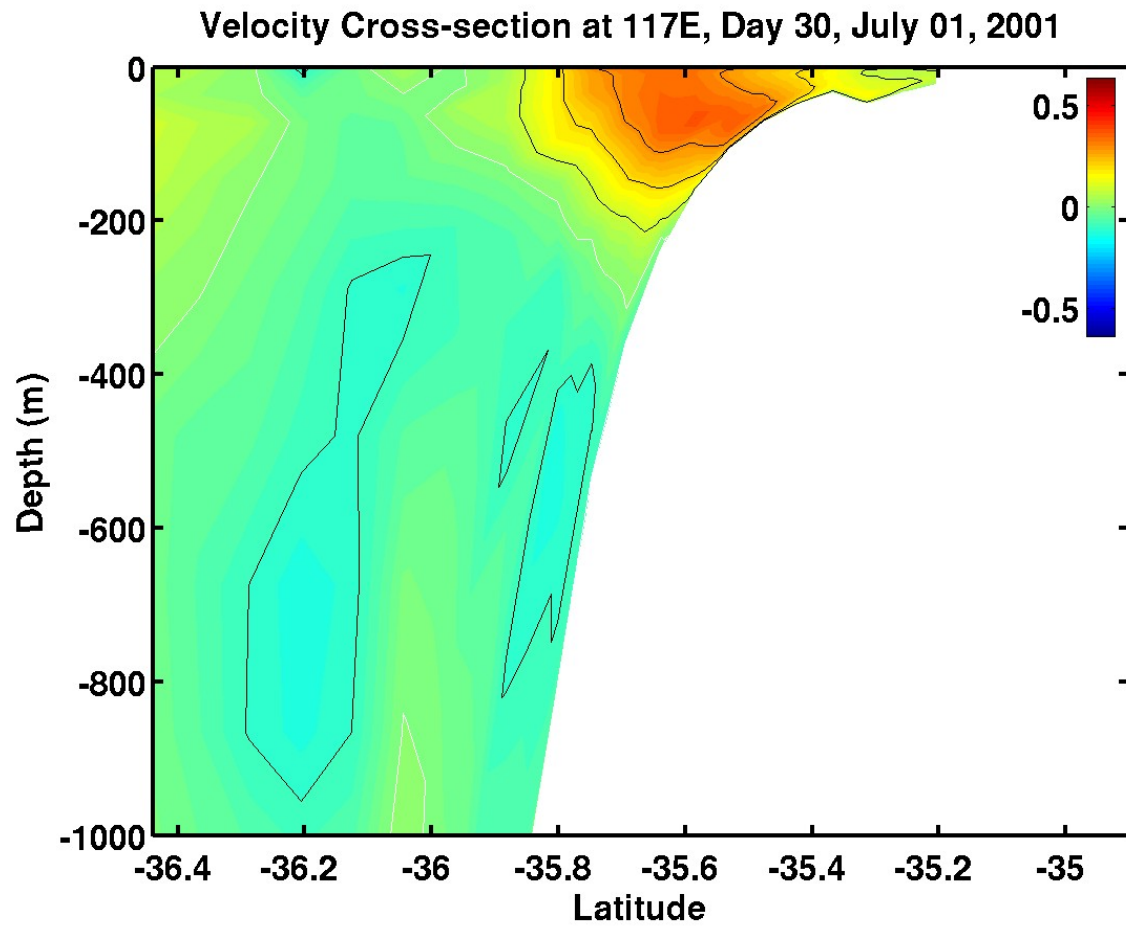


Figure 5.18e. Cross-section of zonal velocity component (m s^{-1}) at 117°E for daily wind Experiment 4 on day 30, July 1, 2001. Red is eastward and blue is westward. The white contour is zero.

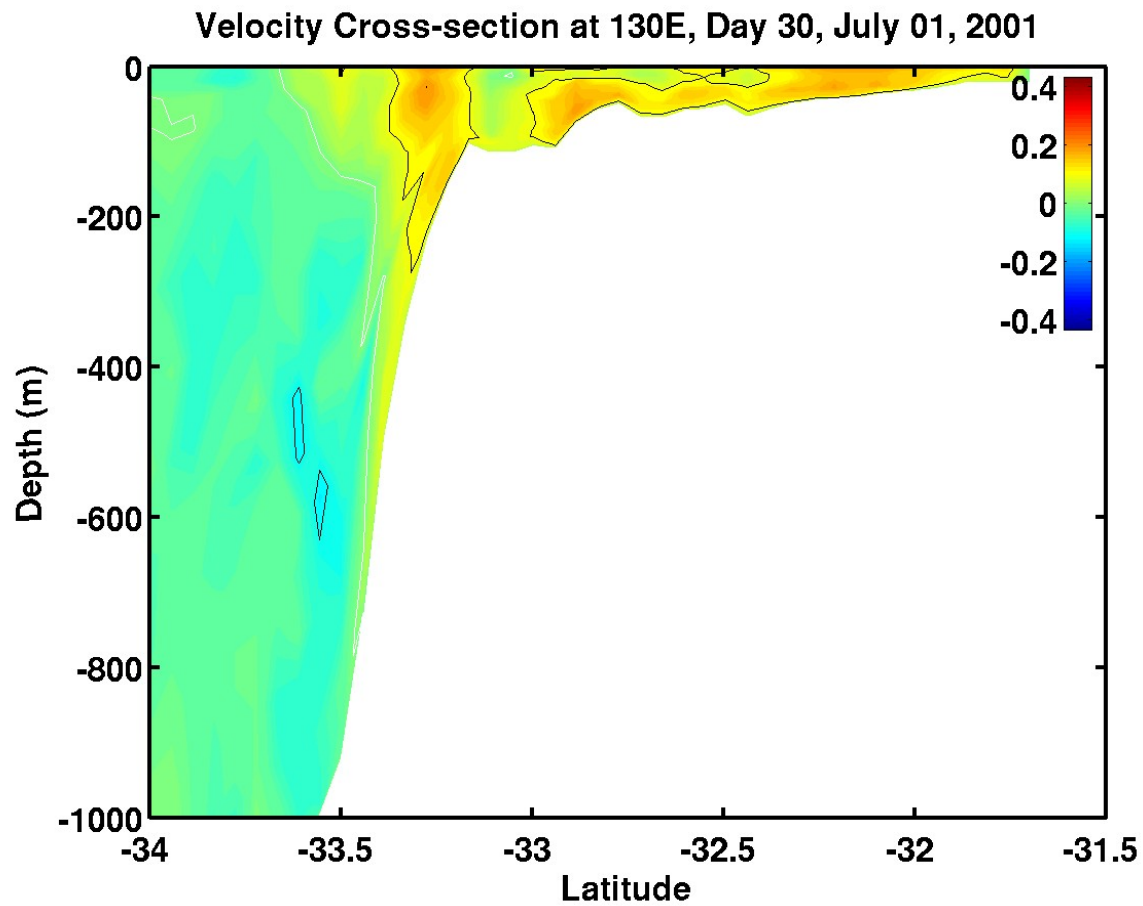


Figure 5.18f. Cross-section of zonal velocity component (m s^{-1}) in the Great Australian Bight (130°E) for daily wind Experiment 4 on day 30, July 1, 2001. Red is eastward and blue is westward. The white contour is zero.

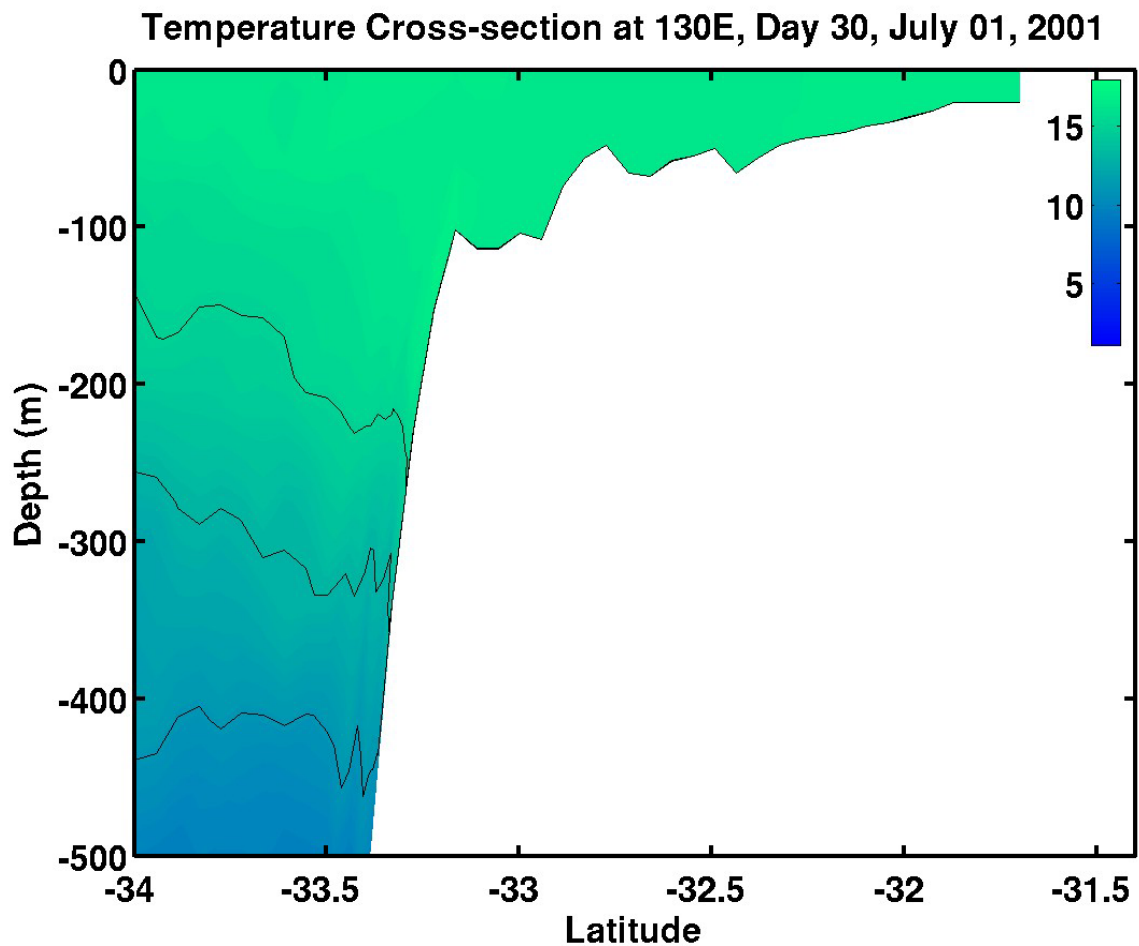


Figure 5.18g. Cross-section of temperature ($^{\circ}\text{C}$) along a north-south transect in the Great Australian Bight (130°E) for daily wind Experiment 4 on day 30, July 1, 2001.

Surface Temperature and Velocity, Day 45, July 16, 2001

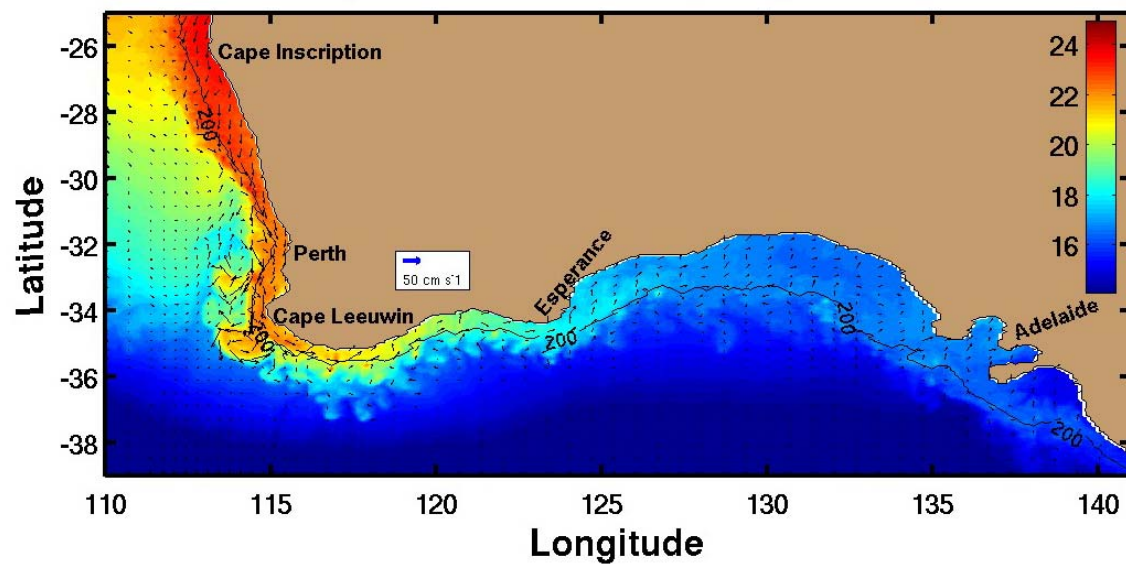


Figure 5.19a. Sea surface temperature ($^{\circ}\text{C}$) and velocity vectors for daily wind Experiment 4 on day 45, July 16, 2001.

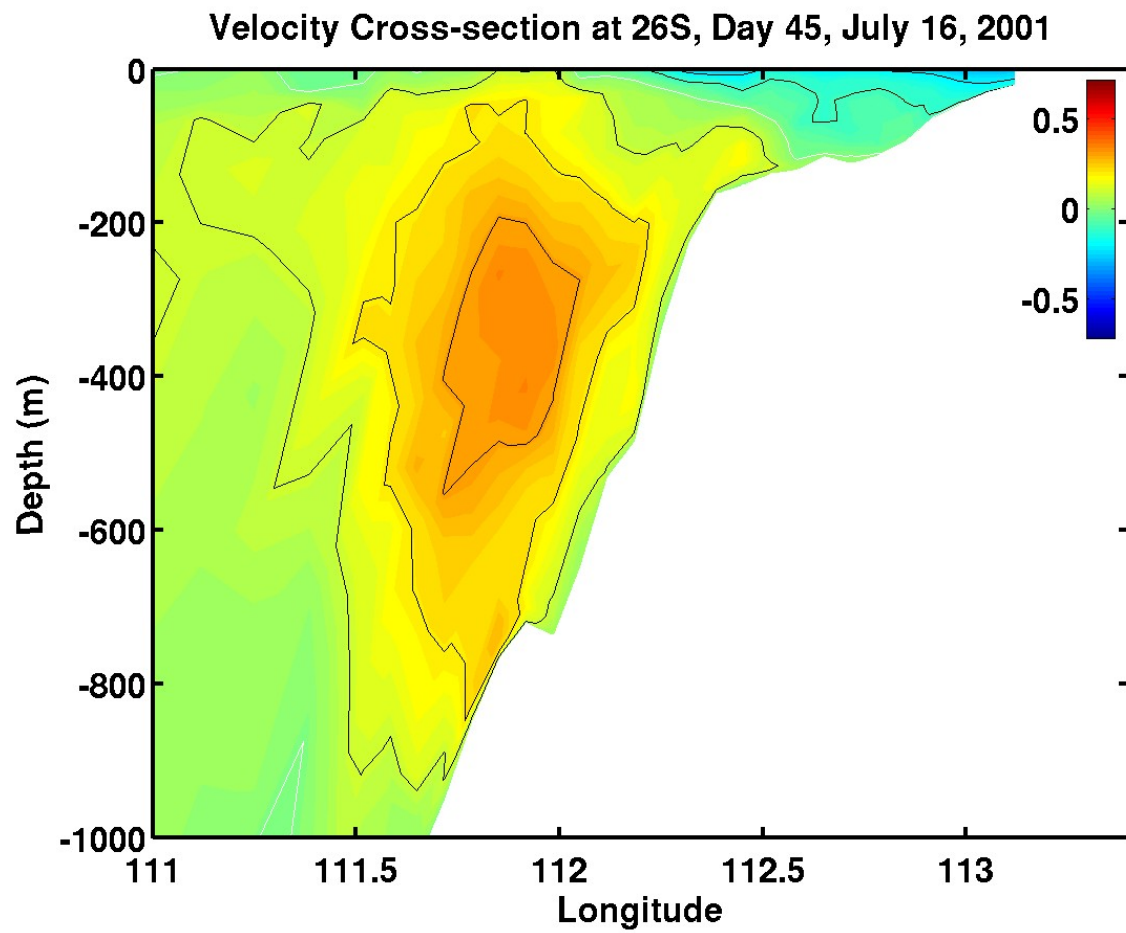


Figure 5.19b. Cross-section of meridional velocity component (m s^{-1}) at 26°S for daily wind Experiment 4 on day 45, July 16, 2001. Red is equatorward (north) and blue is poleward (south). The white contour is zero.

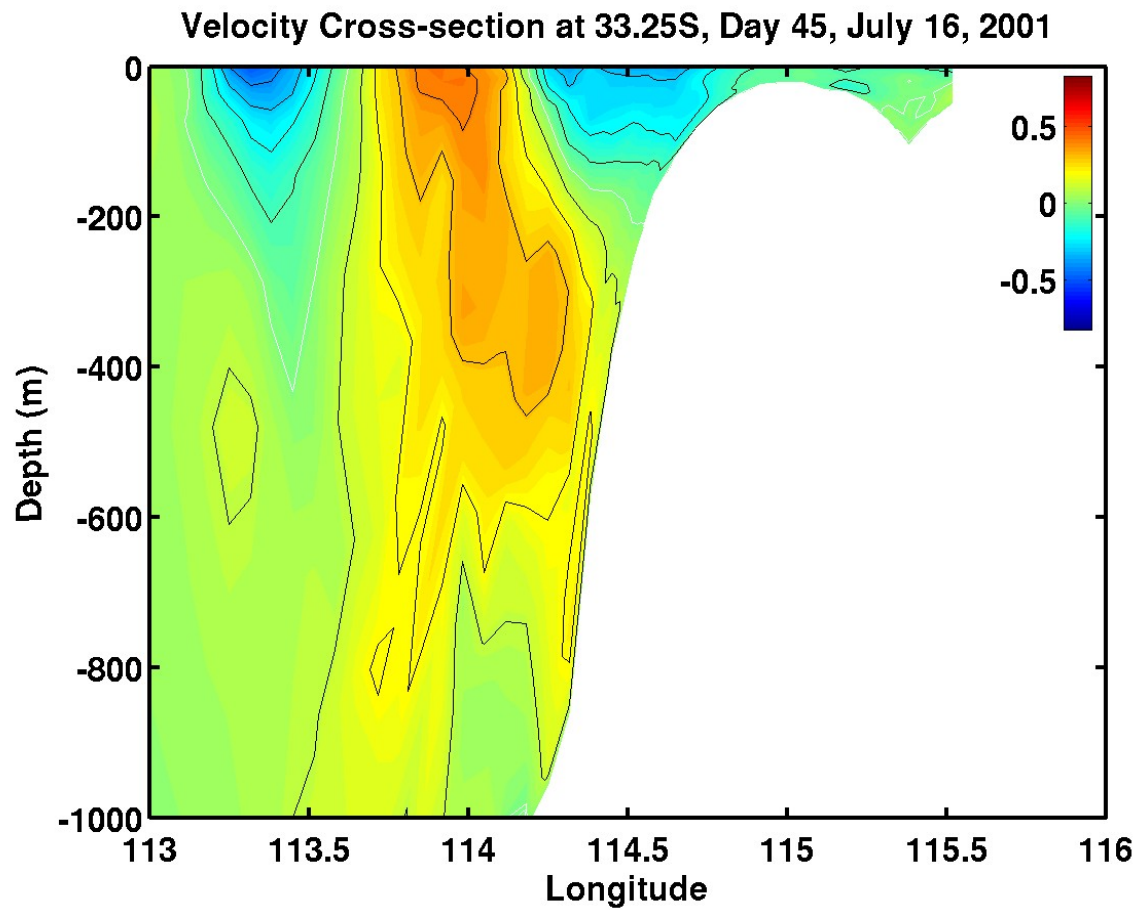


Figure 5.19c. Cross-section of meridional velocity component (m s^{-1}) just north of Cape Leeuwin at 33.25°S for daily wind Experiment 4 on day 45, July 16, 2001. Red is equatorward (north) and blue is poleward (south). The white contour is zero.

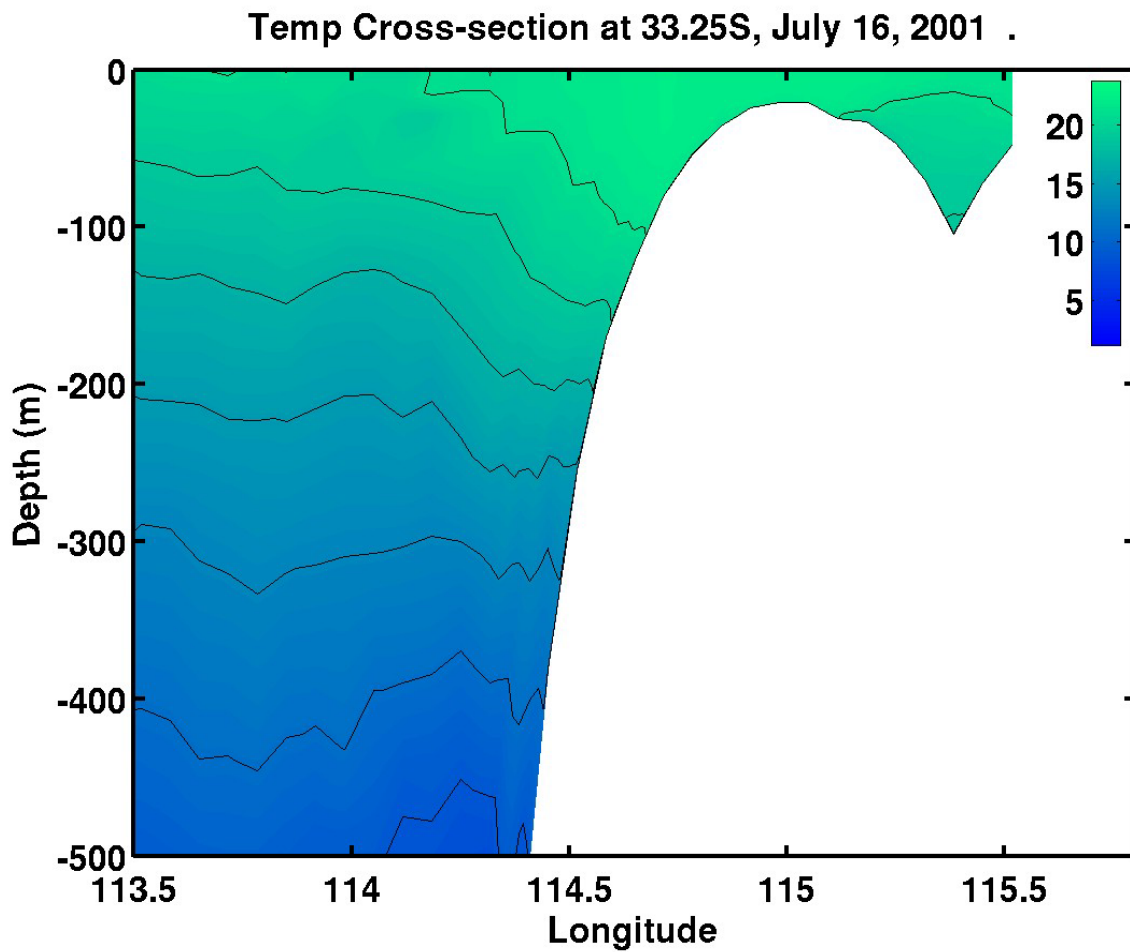


Figure 5.19d. Cross-section of temperature (°C) along an east-west transect just north of Cape Leeuwin at 33.25°S for daily wind Experiment 4 on day 45, July 16, 2001.

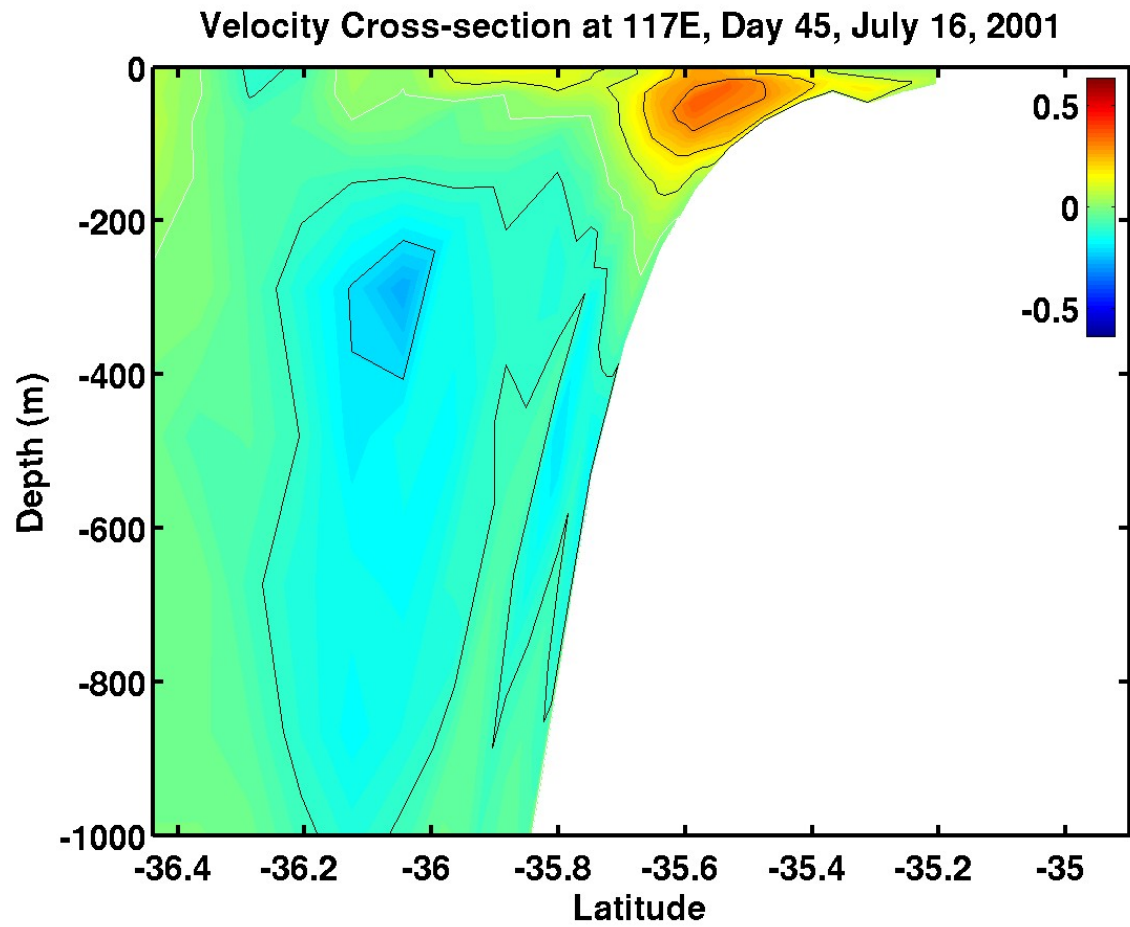


Figure 5.19e. Cross-section of zonal velocity component (m s^{-1}) at 117°E for daily wind Experiment 4 on day 45, July 16, 2001. Red is eastward and blue is westward. The white contour is zero.

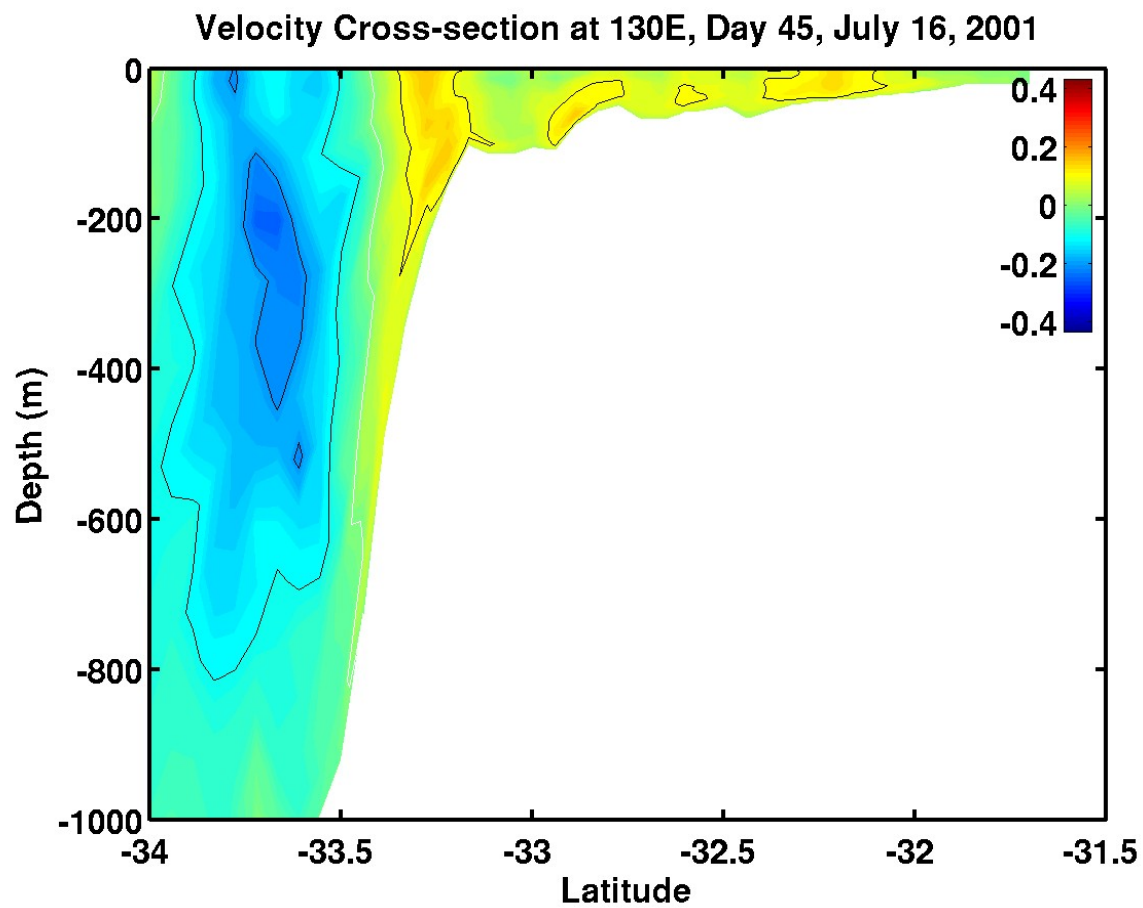


Figure 5.19f. Cross-section of zonal velocity component (m s^{-1}) in the Great Australian Bight (130°E) for daily wind Experiment 4 on day 45, July 16, 2001. Red is eastward and blue is westward. The white contour is zero.

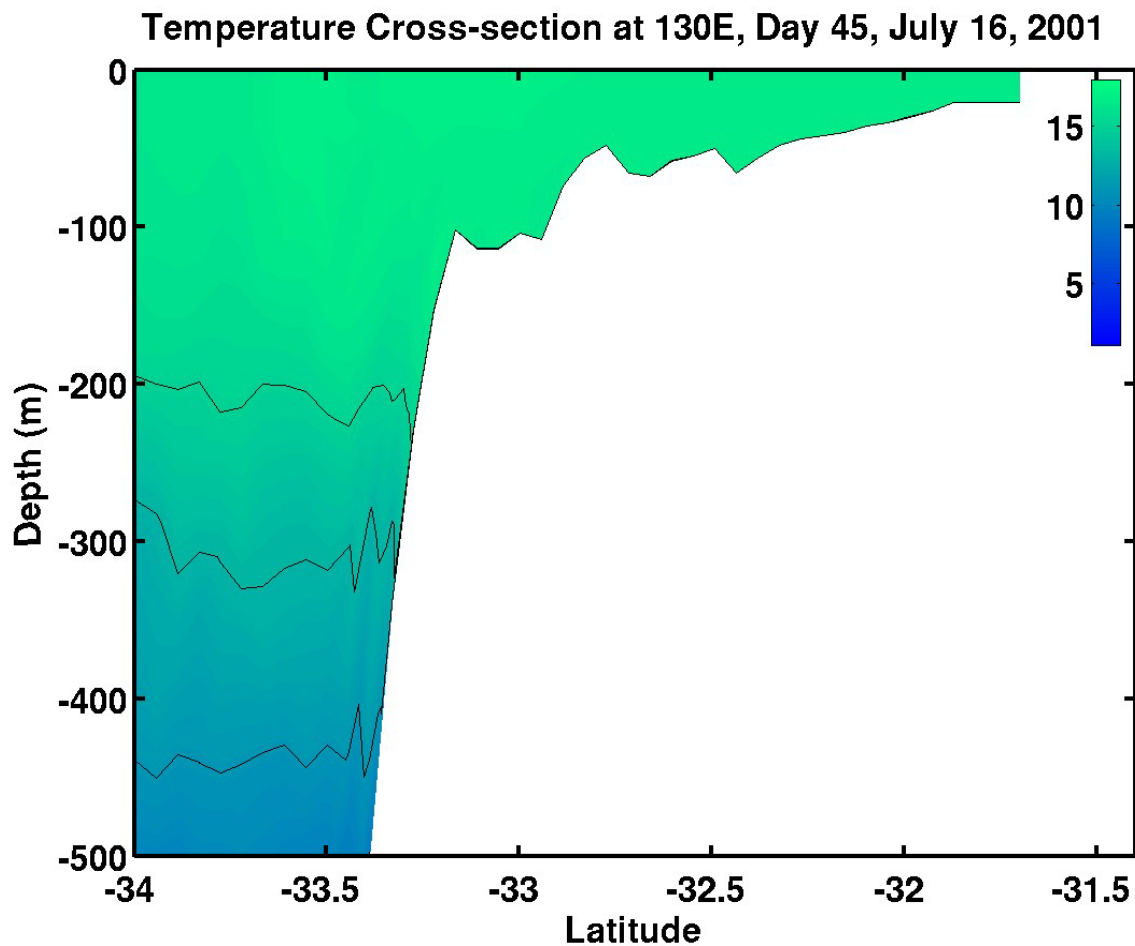


Figure 5.19g. Cross-section of temperature ($^{\circ}\text{C}$) along a north-south transect in the Great Australian Bight (130°E) for daily wind Experiment 4 on day 45, July 16, 2001.

Surface Temperature and Velocity, Day 60, July 31, 2001

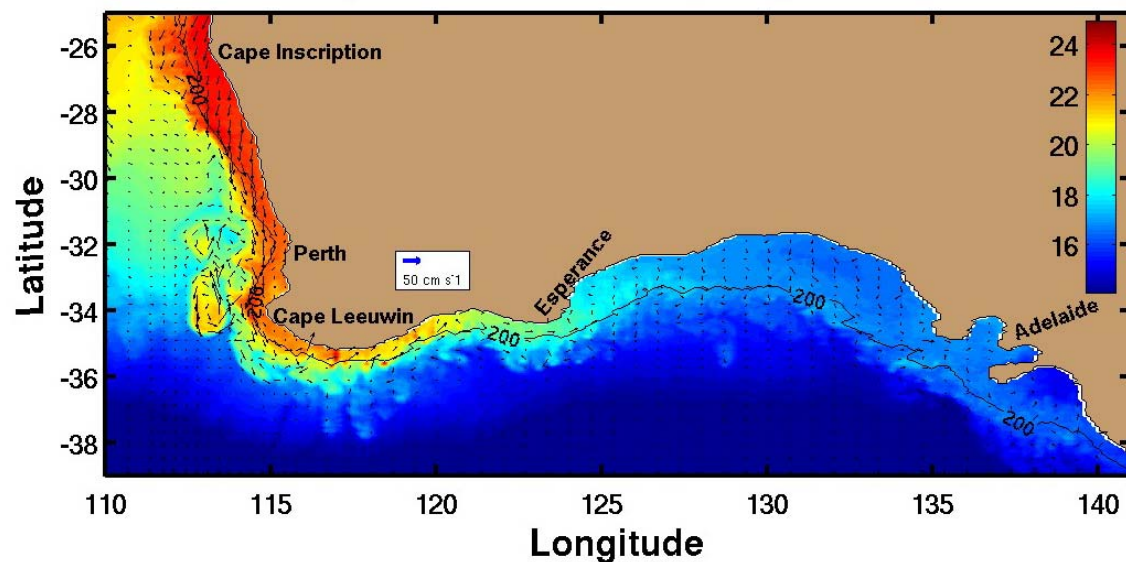


Figure 5.20a. Sea surface temperature ($^{\circ}\text{C}$) and velocity vectors for daily wind Experiment 4 on day 60, July 31, 2001.

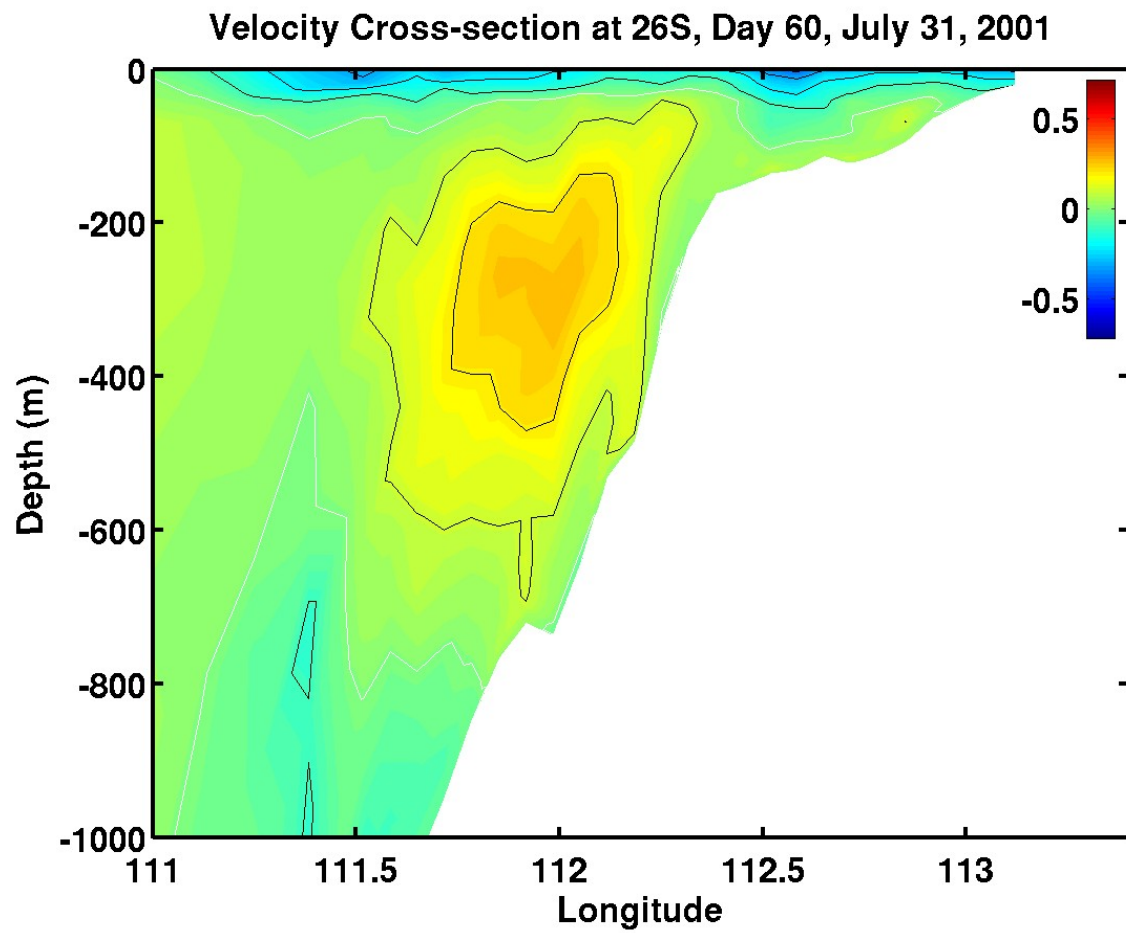


Figure 5.20b. Cross-section of meridional velocity component (m s^{-1}) at 26°S for daily wind Experiment 4 on day 60, July 31, 2001. Red is equatorward (north) and blue is poleward (south). The white contour is zero.

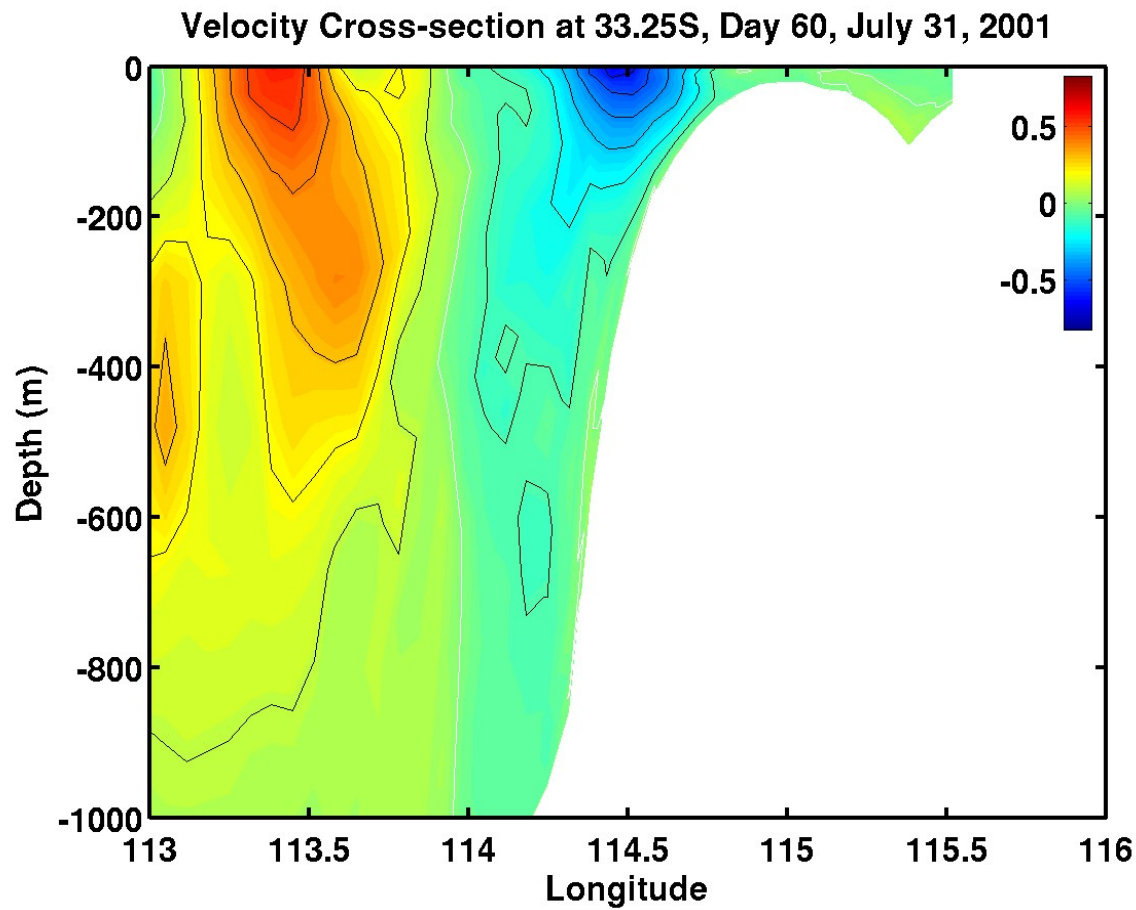


Figure 5.20c. Cross-section of meridional velocity component (m s^{-1}) just north of Cape Leeuwin at 33.25°S for daily wind Experiment 4 on day 60, July 31, 2001. Red is equatorward (north) and blue is poleward (south). The white contour is zero.

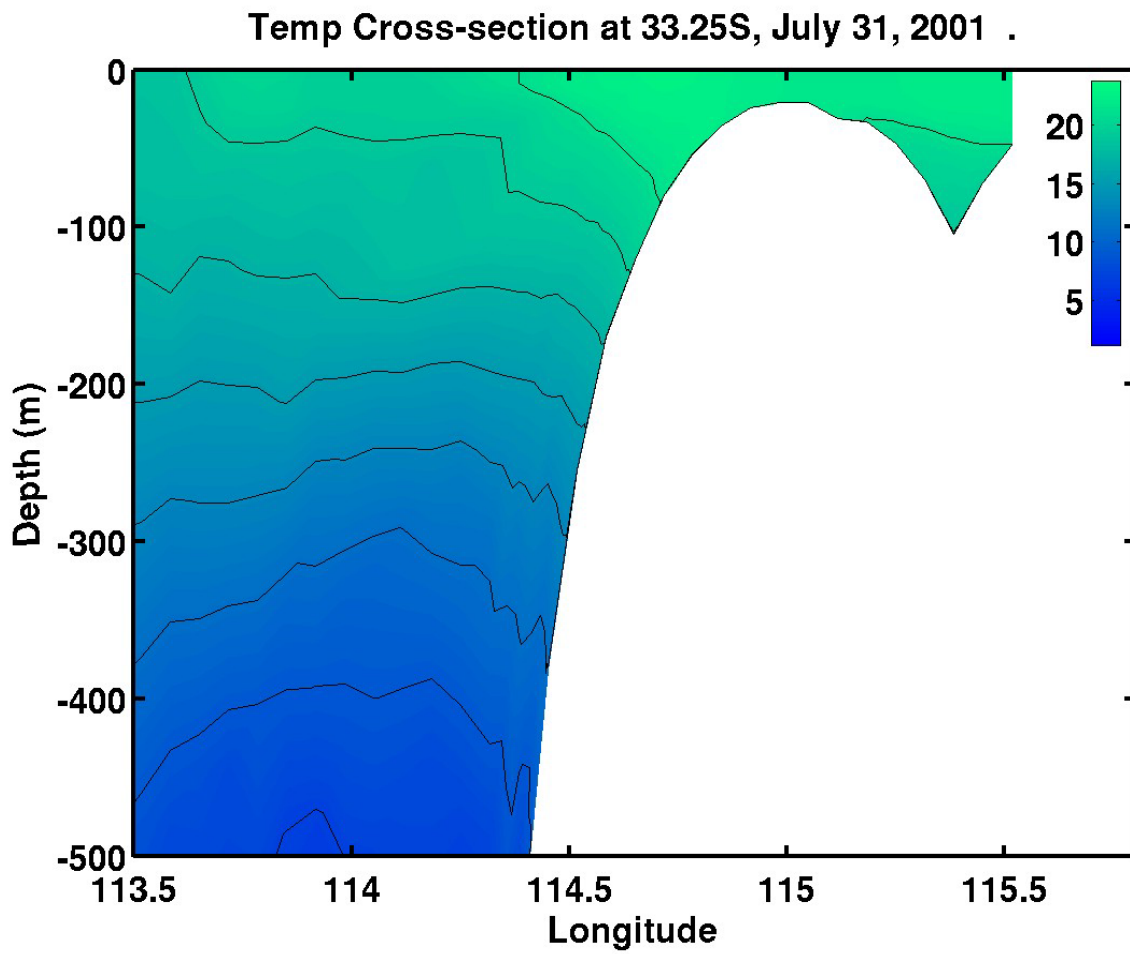


Figure 5.20d. Cross-section of temperature (°C) along an east-west transect just north of Cape Leeuwin at 33.25°S for daily wind Experiment 4 on day 60, July 31, 2001.

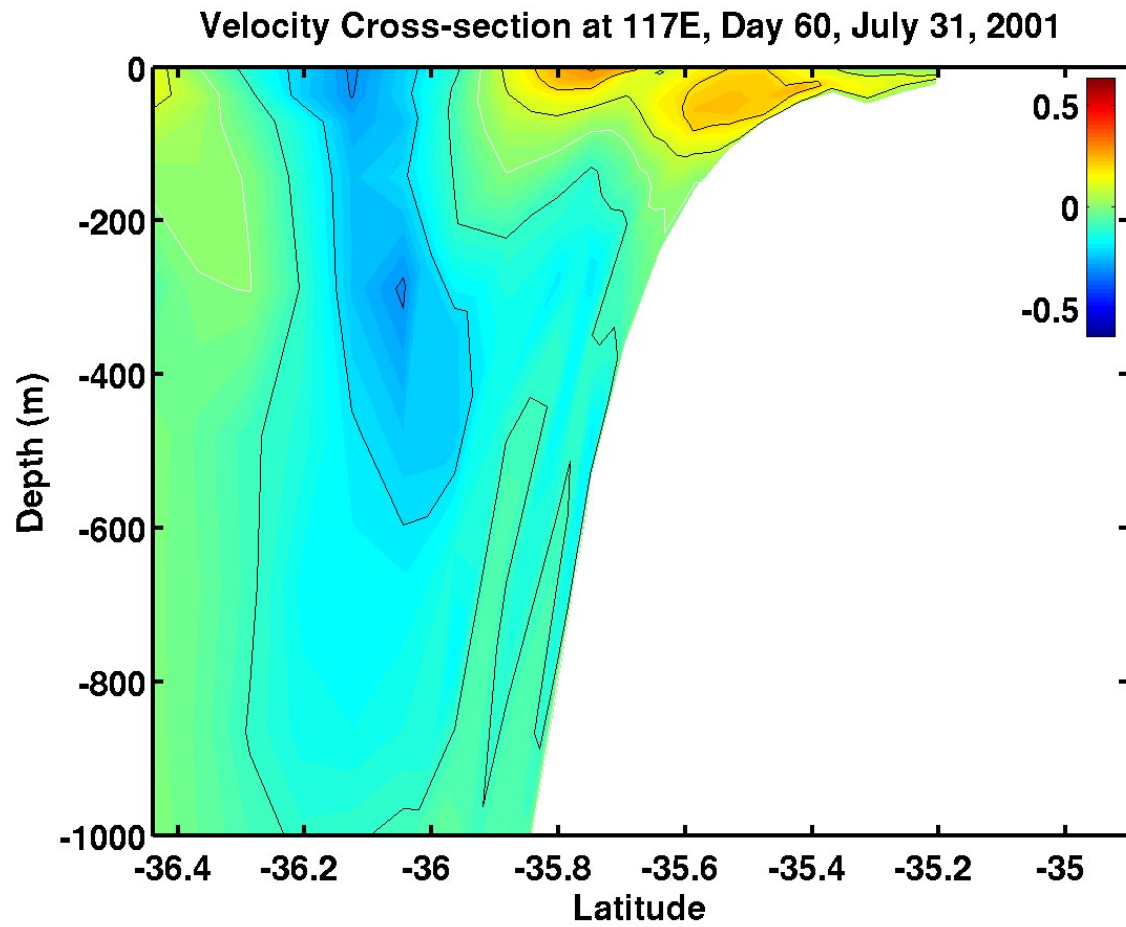


Figure 5.20e. Cross-section of zonal velocity component (m s^{-1}) at 117°E for daily wind Experiment 4 on day 60, July 31, 2001. Red is eastward and blue is westward. The white contour is zero.

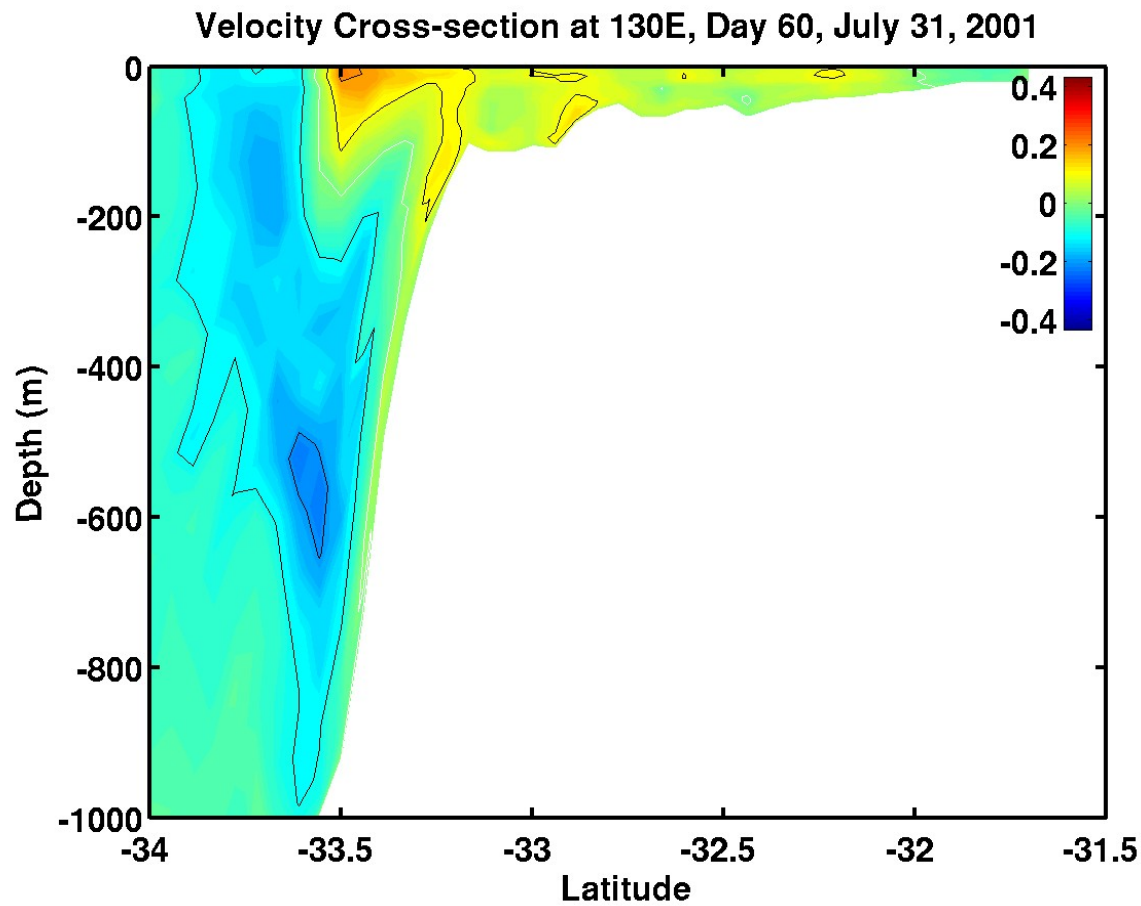


Figure 5.20f. Cross-section of zonal velocity component (m s^{-1}) in the Great Australian Bight (130°E) for daily wind Experiment 4 on day 60, July 31, 2001. Red is eastward and blue is westward. The white contour is zero.

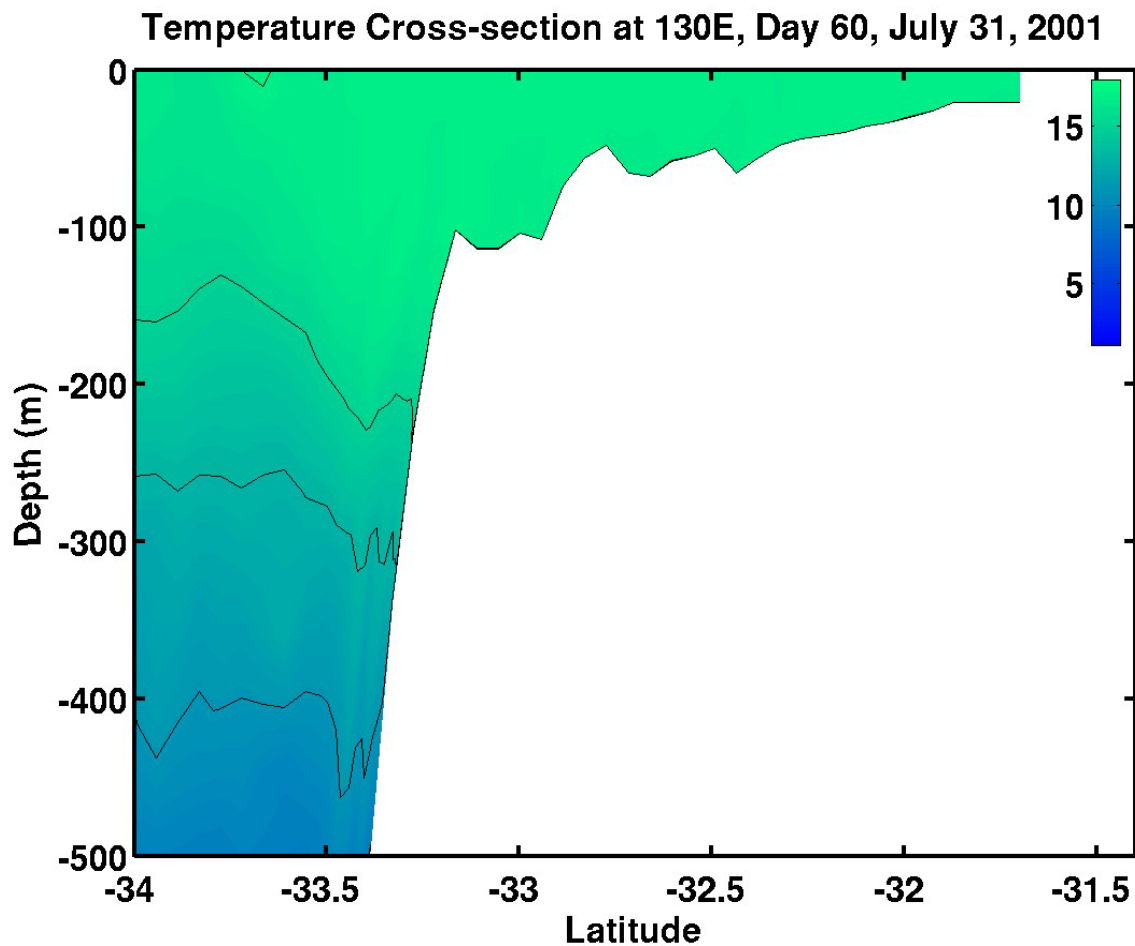


Figure 5.20g. Cross-section of temperature ($^{\circ}\text{C}$) along a north-south transect in the Great Australian Bight (130°E) for daily wind Experiment 4 on day 60, July 31, 2001.

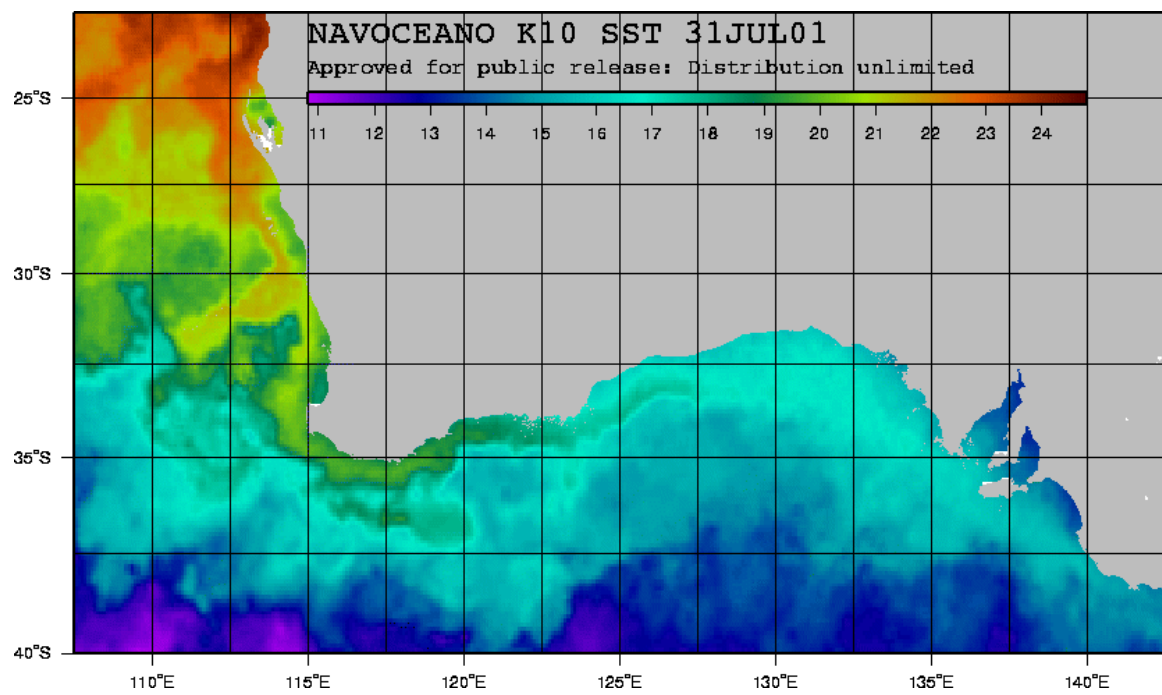


Figure 5.21. Multi-Channel Sea Surface Temperature (MCSST) satellite imagery for southwestern Australian coastal area for July 31, 2001. Temperatures are in °C.

Surface Temperature and Velocity, Day 45, July 16, 2001

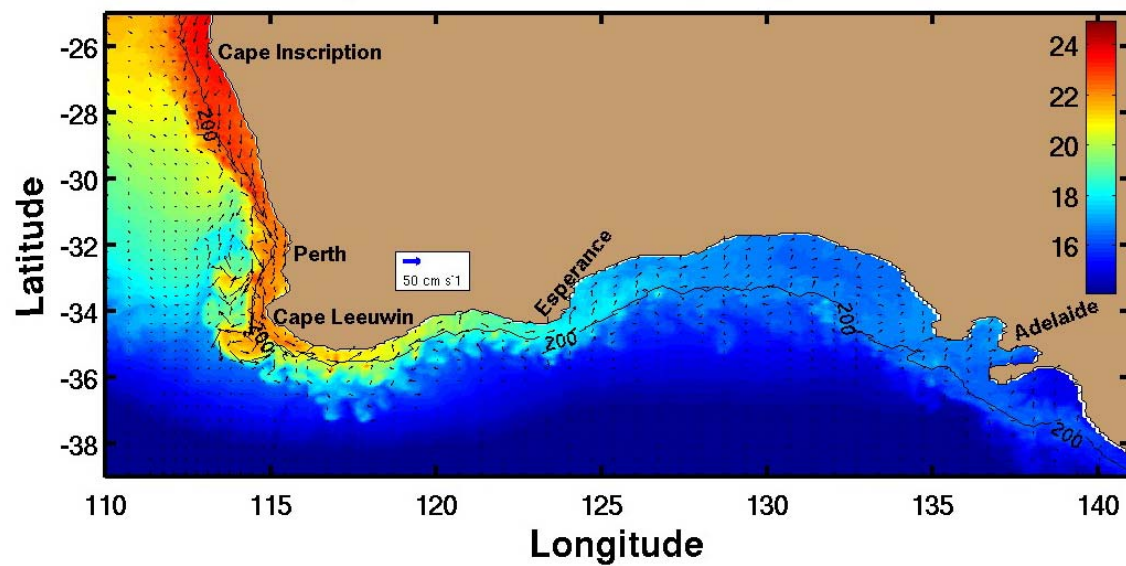


Figure 6.1a. Sea surface temperature ($^{\circ}\text{C}$) and velocity vectors for daily wind Experiment 4 on day 45, July 16, 2001.

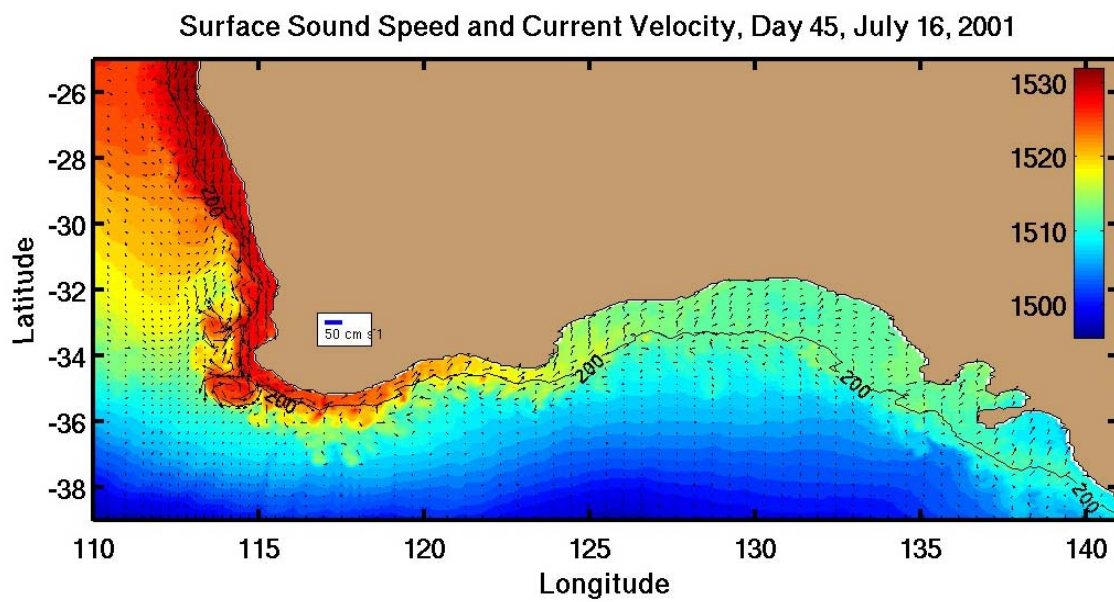


Figure 6.1b. Surface sound speed (m/s) and current velocity vectors for daily wind Experiment 4 on day 45, July 16, 2001.

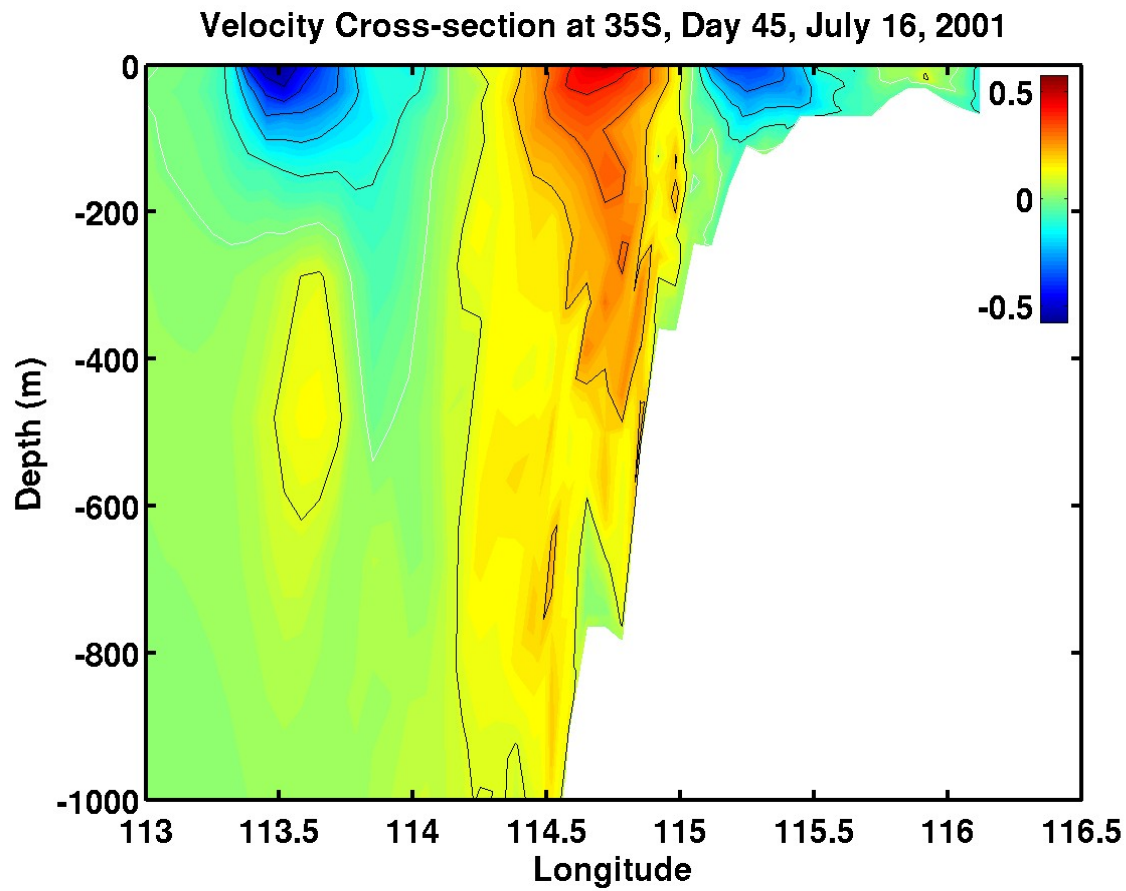


Figure 6.1c. Cross-section of meridional velocity component (m s^{-1}) at 35°S for daily wind Experiment 4 on day 45, July 16, 2001. Red is equatorward (north) and blue is poleward (south). The white contour is zero.

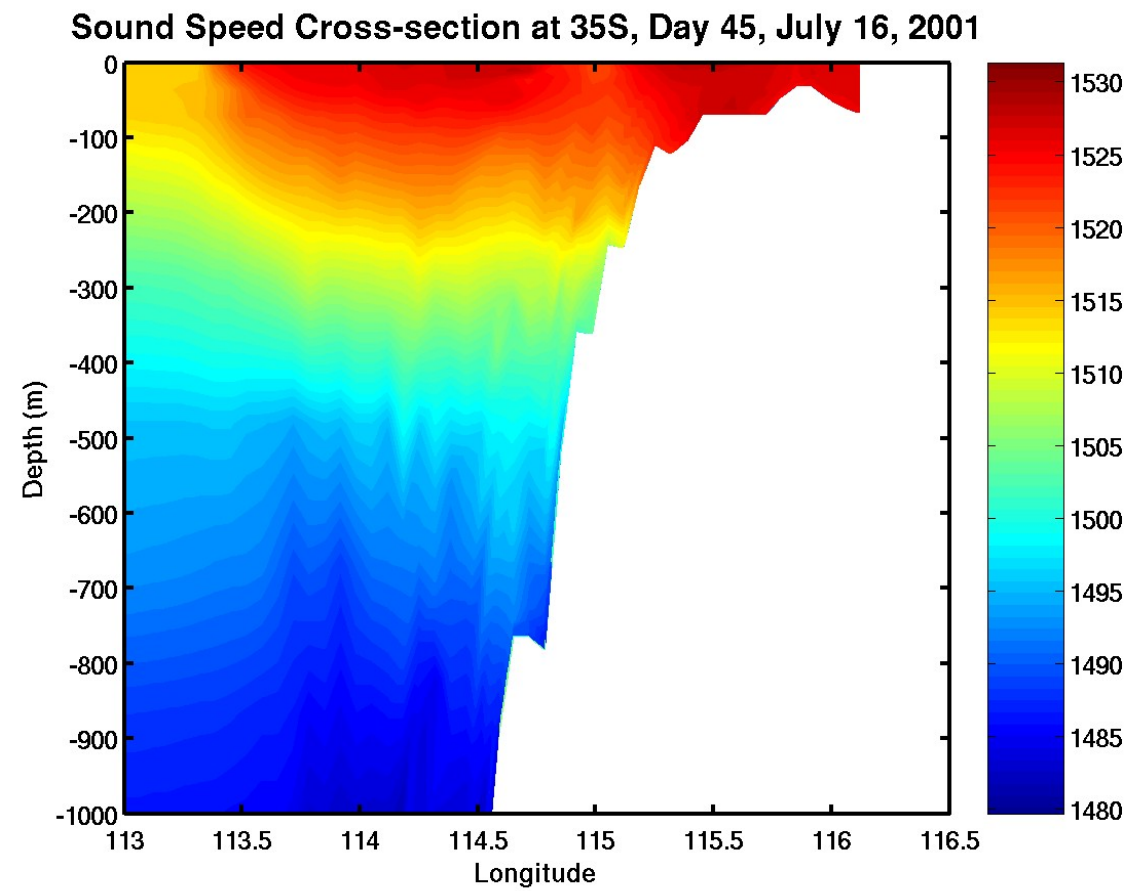


Figure 6.1d. Cross-section of sound speed (m s^{-1}) at 35°S for daily wind Experiment 4 on day 45, July 16, 2001.

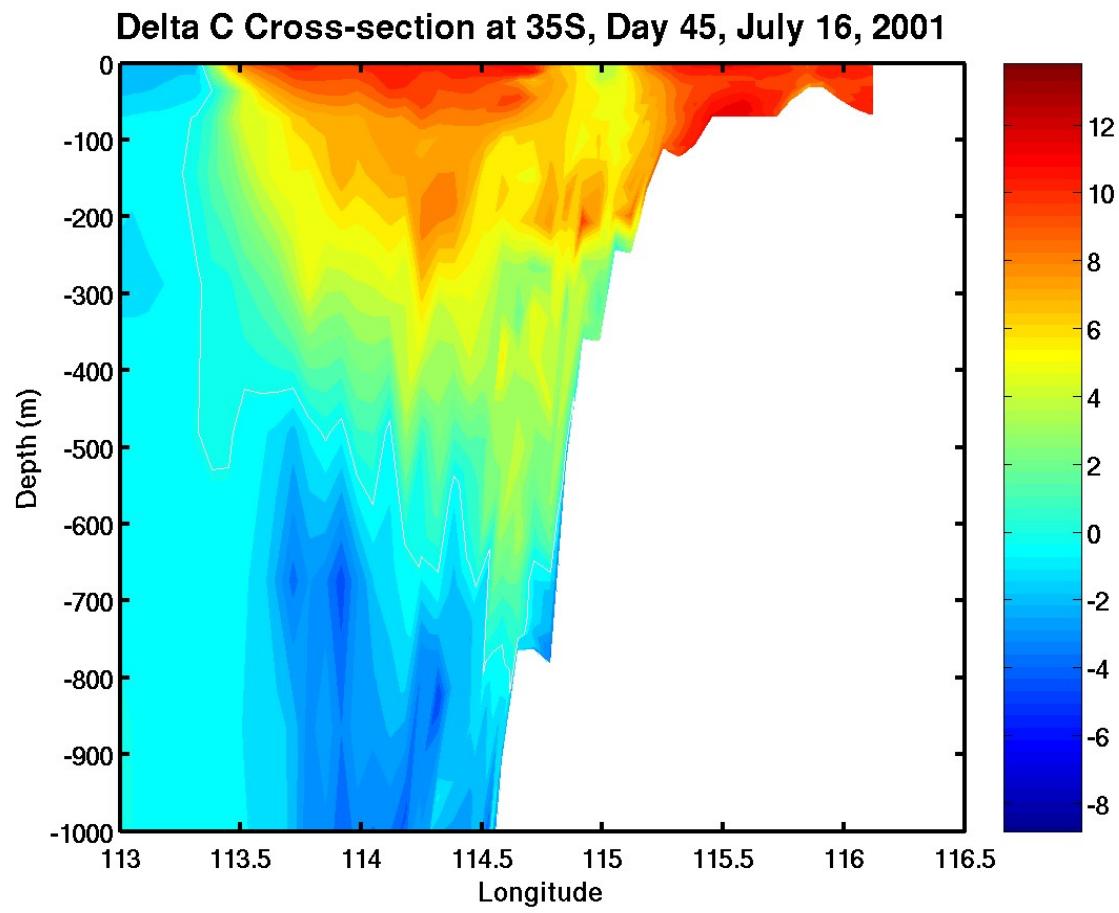


Figure 6.1e. Cross-section of sound speed (m s^{-1}) change at 35°S for daily wind Experiment 4 on day 45, July 16, 2001. Sound speed change is the difference in sound speed between Day 0 and the current day.

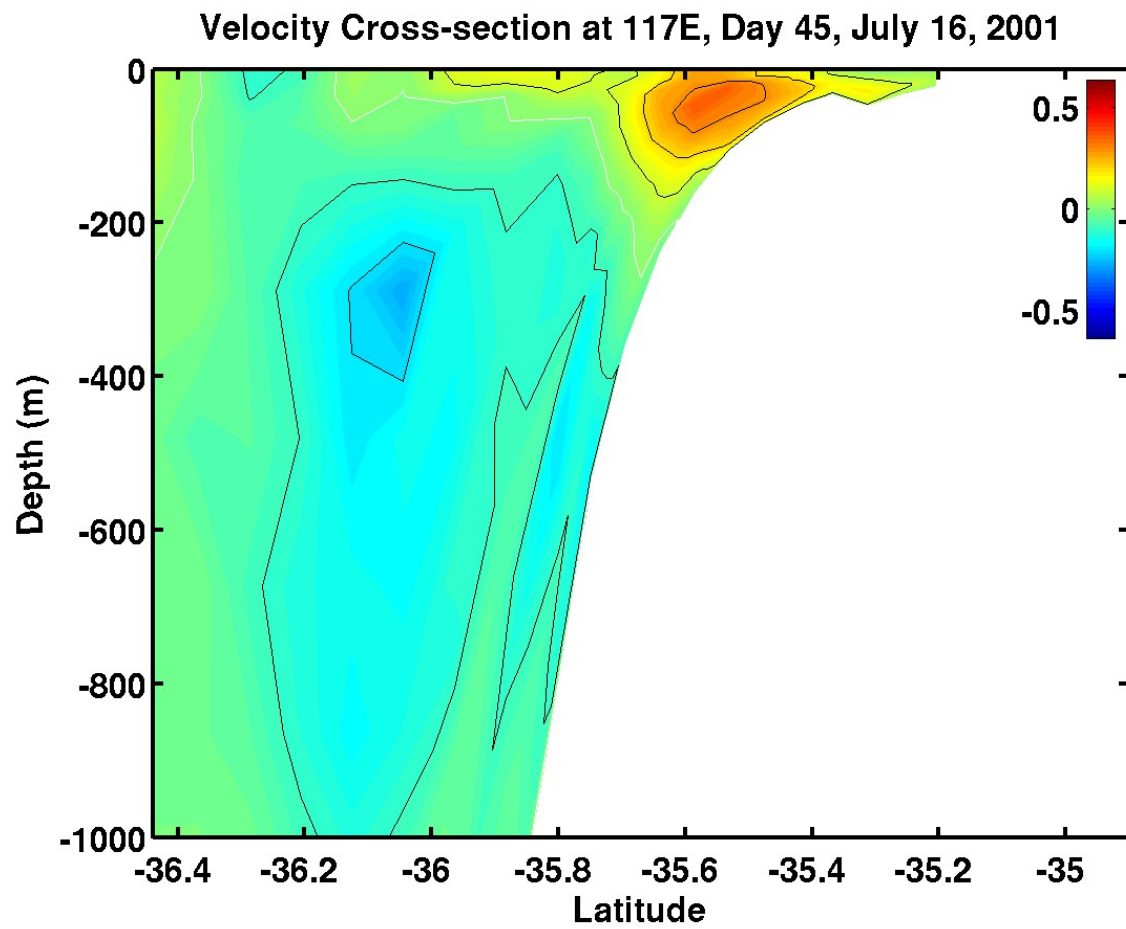


Figure 6.2a. Cross-section of zonal velocity component (m s^{-1}) at 117°E for daily wind Experiment 4 on day 45, July 16, 2001. Red is eastward and blue is westward. The white contour is zero.

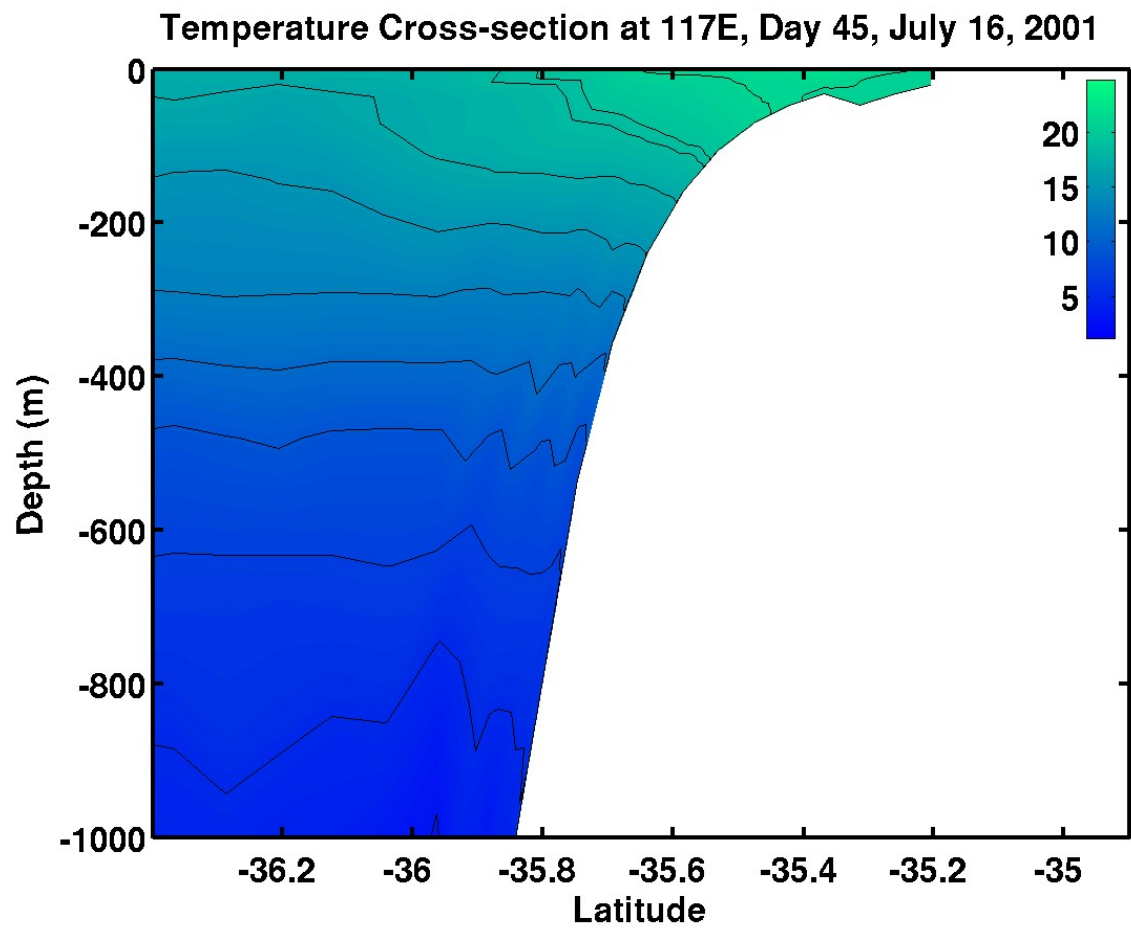


Figure 6.2b. Cross-section of temperature ($^{\circ}\text{C}$) at 117°E for daily wind Experiment 4 on day 45, July 16, 2001.

Sound Speed Cross-section at 117E, Day 45, July 16, 2001

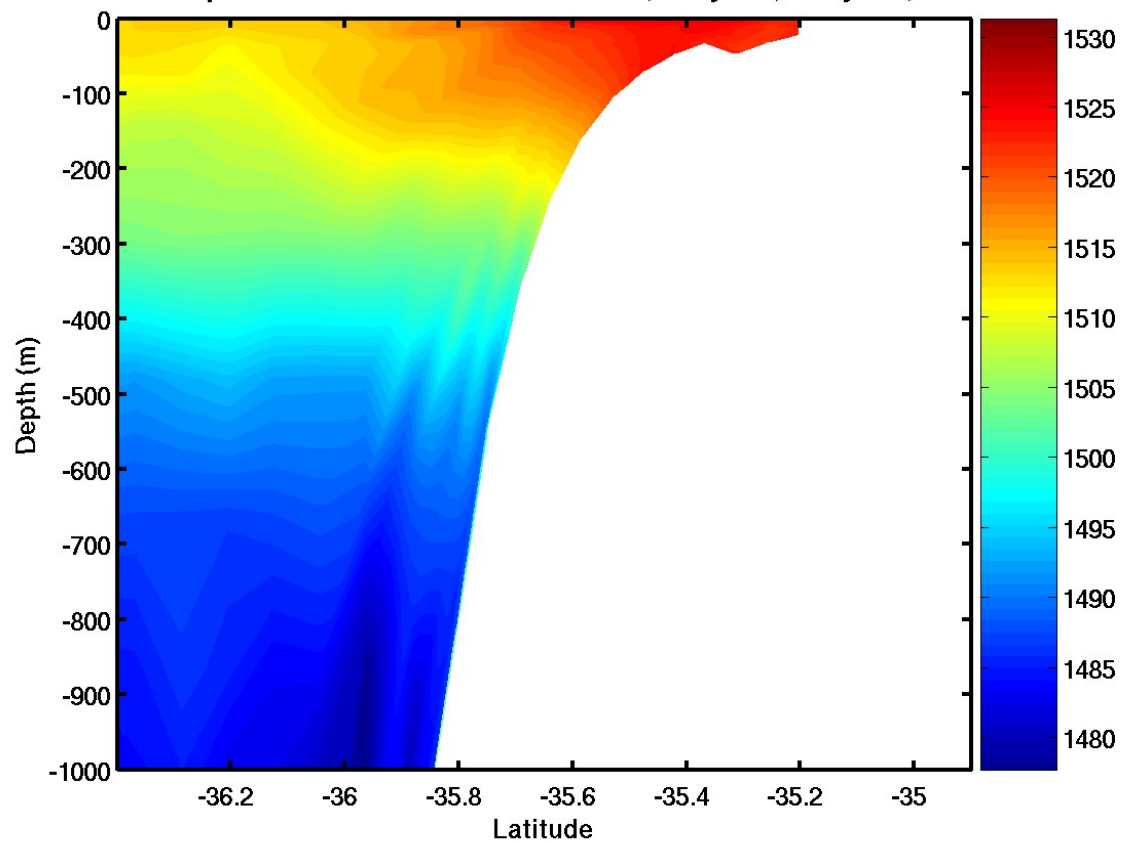


Figure 6.2c. Cross-section of sound speed (m s^{-1}) at 117°E for daily wind Experiment 4 on day 45, July 16, 2001.

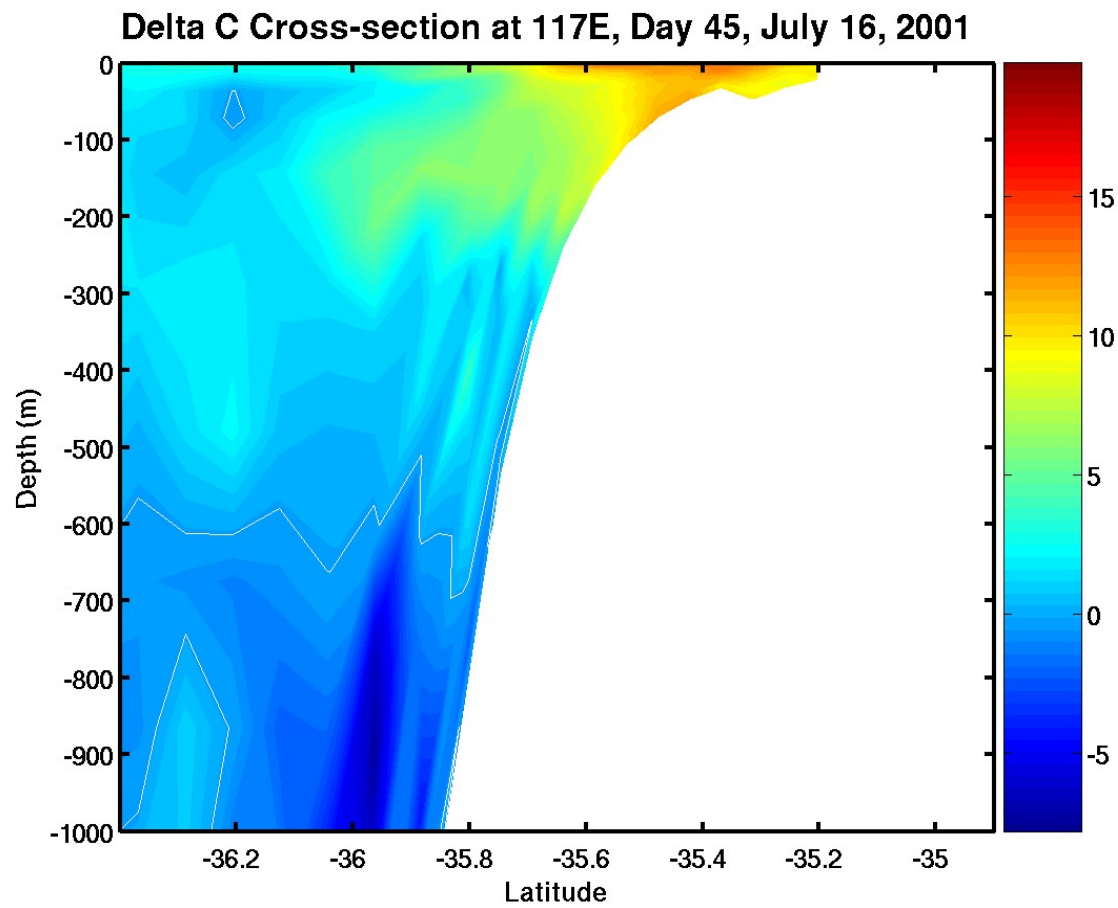


Figure 6.2d. Cross-section of sound speed (m s^{-1}) change at 117°E for daily wind Experiment 4 on day 45, July 16, 2001. Sound speed change is the difference in sound speed between Day 0 and the current day.

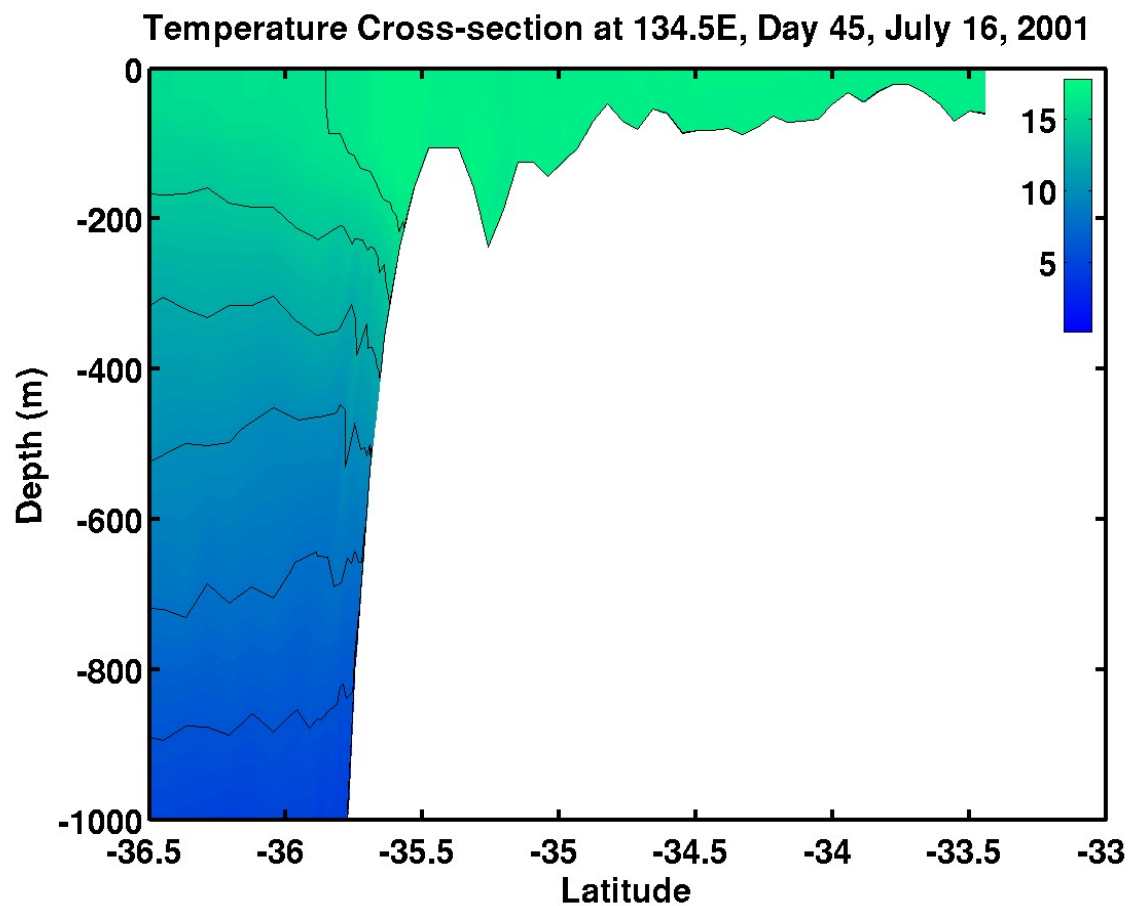


Figure 6.3a. Cross-section of temperature ($^{\circ}\text{C}$) in the eastern Great Australian Bight (134.5°E) for daily wind Experiment 4 on day 45, July 16, 2001.

Sound Speed Cross-section at 134.5E, Day 45, July 16, 2001

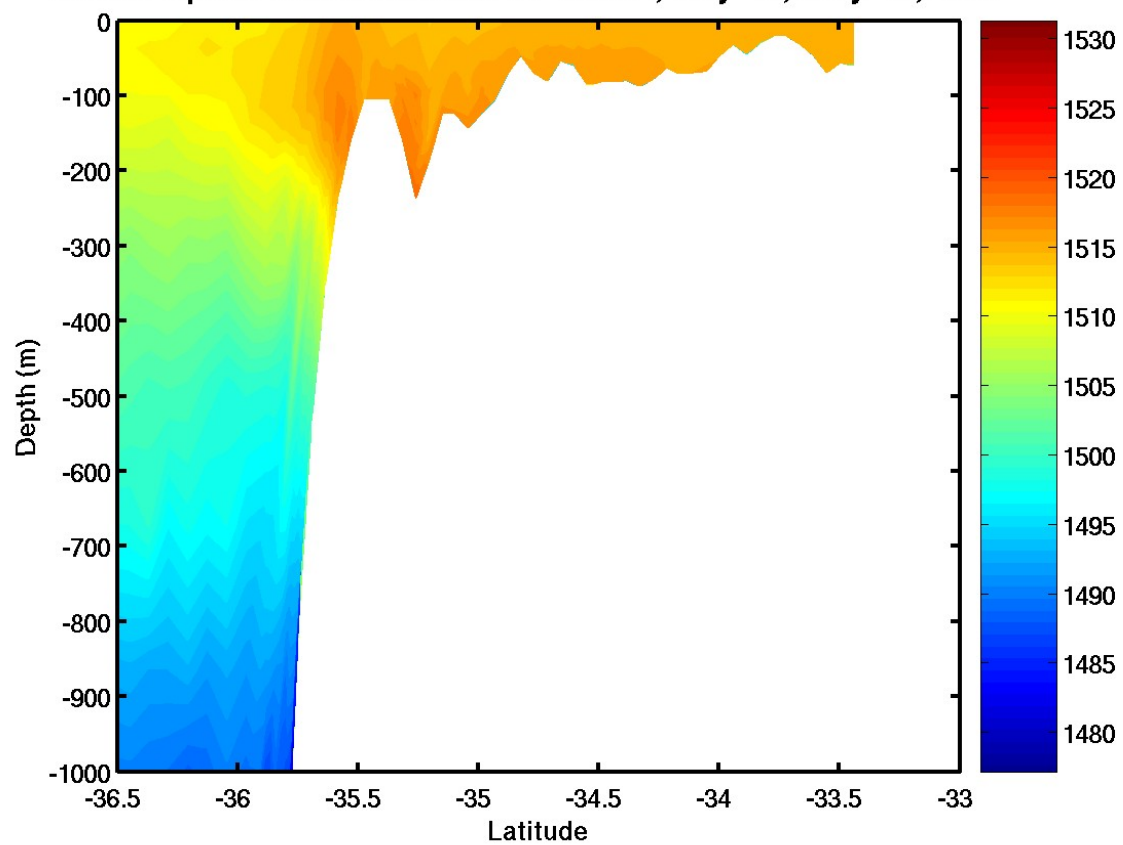


Figure 6.3b. Cross-section of sound speed (m s^{-1}) in the eastern Great Australian Bight (134.5°E) for daily wind Experiment 4 on day 45, July 16, 2001.

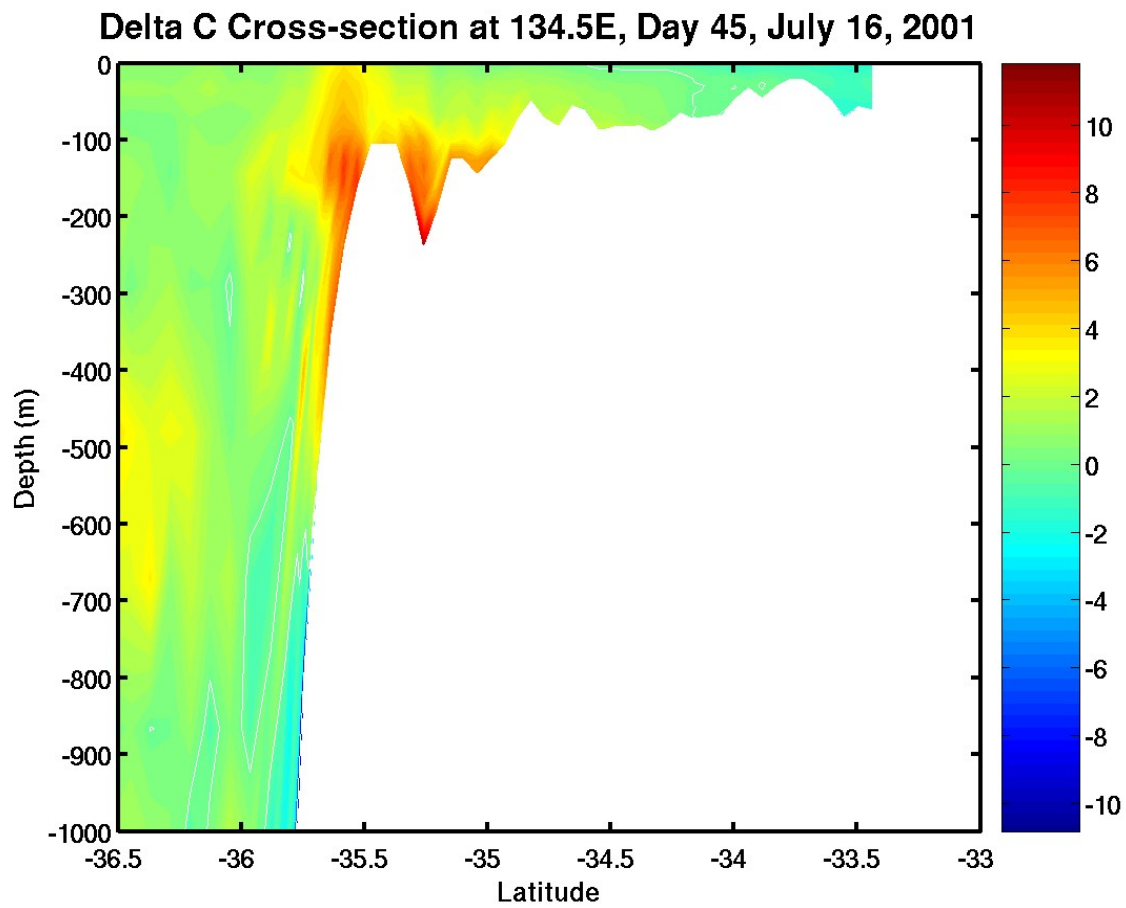


Figure 6.3c. Cross-section of sound speed change (m s^{-1}) in the eastern Great Australian Bight (134.5°E) for daily wind Experiment 4 on day 45, July 16, 2001. Sound speed change is the difference in sound speed between Day 0 and the current day.

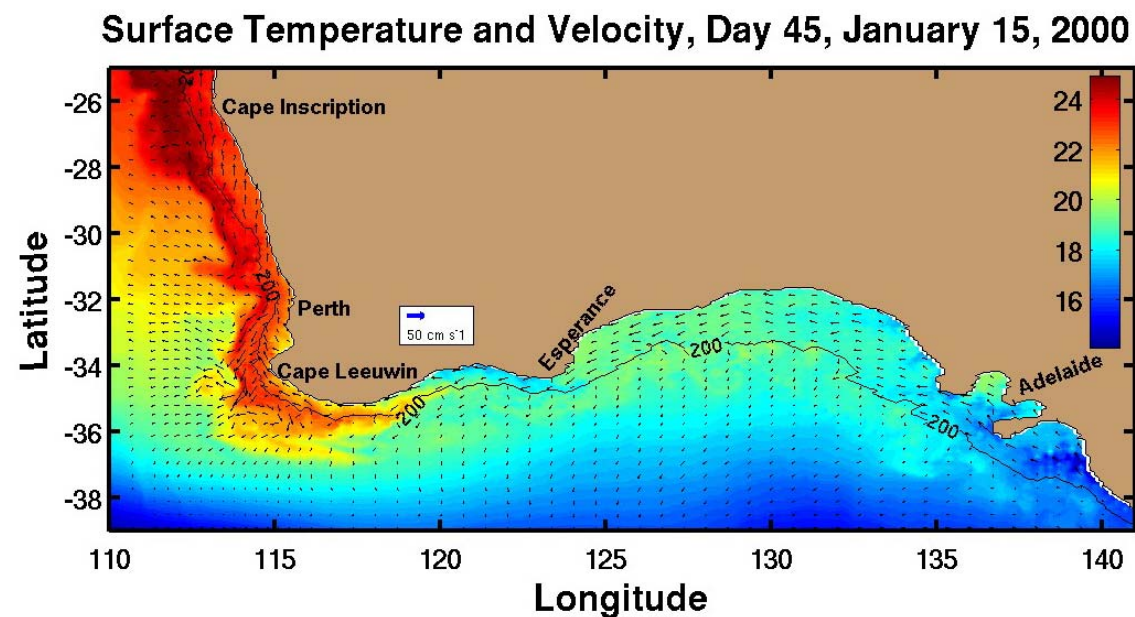


Figure 6.4a. Sea surface temperature ($^{\circ}\text{C}$) and velocity vectors for daily wind Experiment 3 on day 45, January 15, 2000.

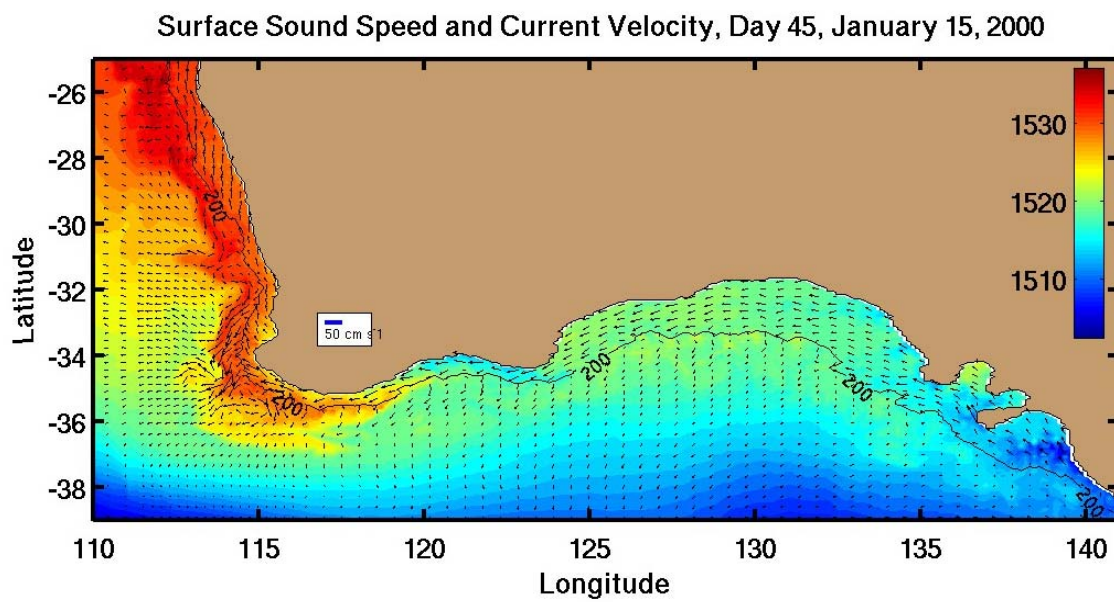


Figure 6.4b. Surface sound speed (m/s) and current velocity vectors for daily wind Experiment 3 on day 45, January 15, 2000.

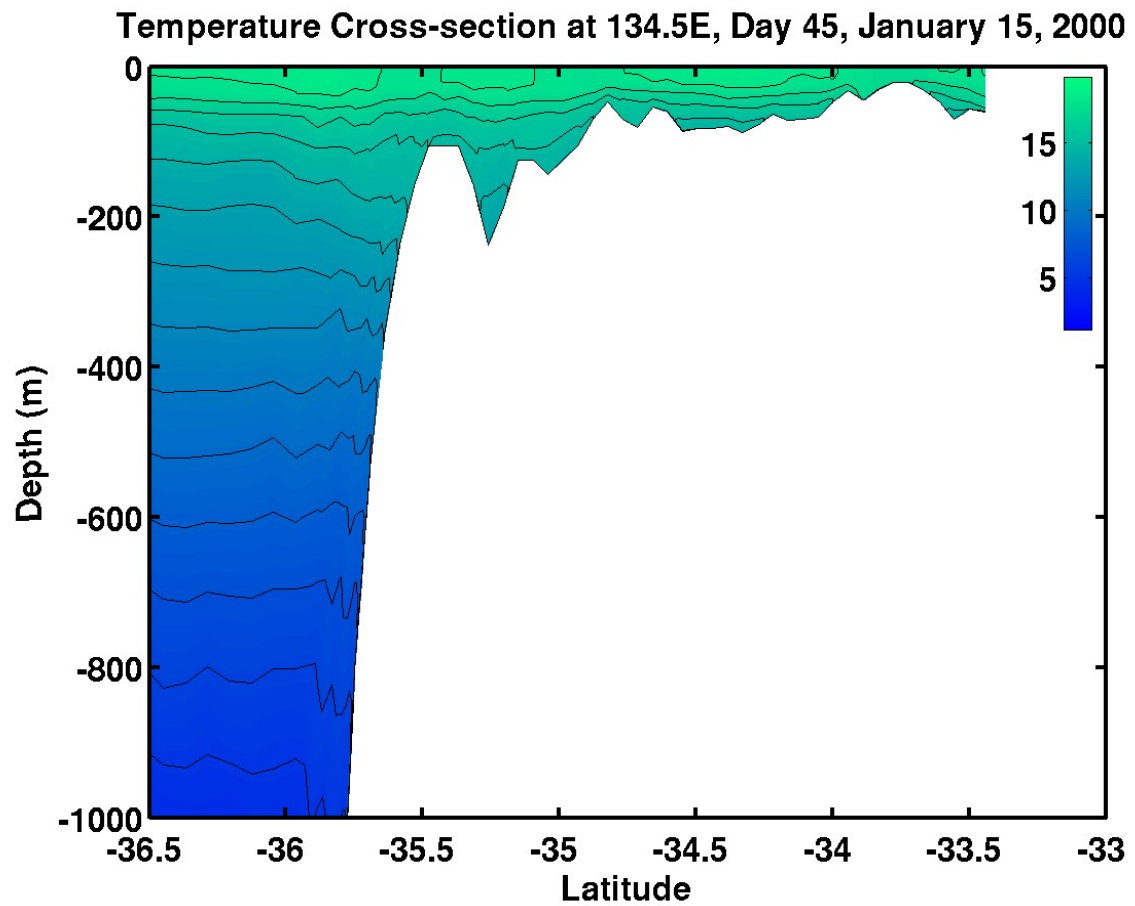


Figure 6.4c. Cross-section of temperature ($^{\circ}\text{C}$) in the eastern Great Australian Bight (134.5 $^{\circ}\text{E}$) for daily wind Experiment 3 on day 45, January 15, 2000.

Sound Speed Cross-section at 134.5E, Day 45, January 15, 2000

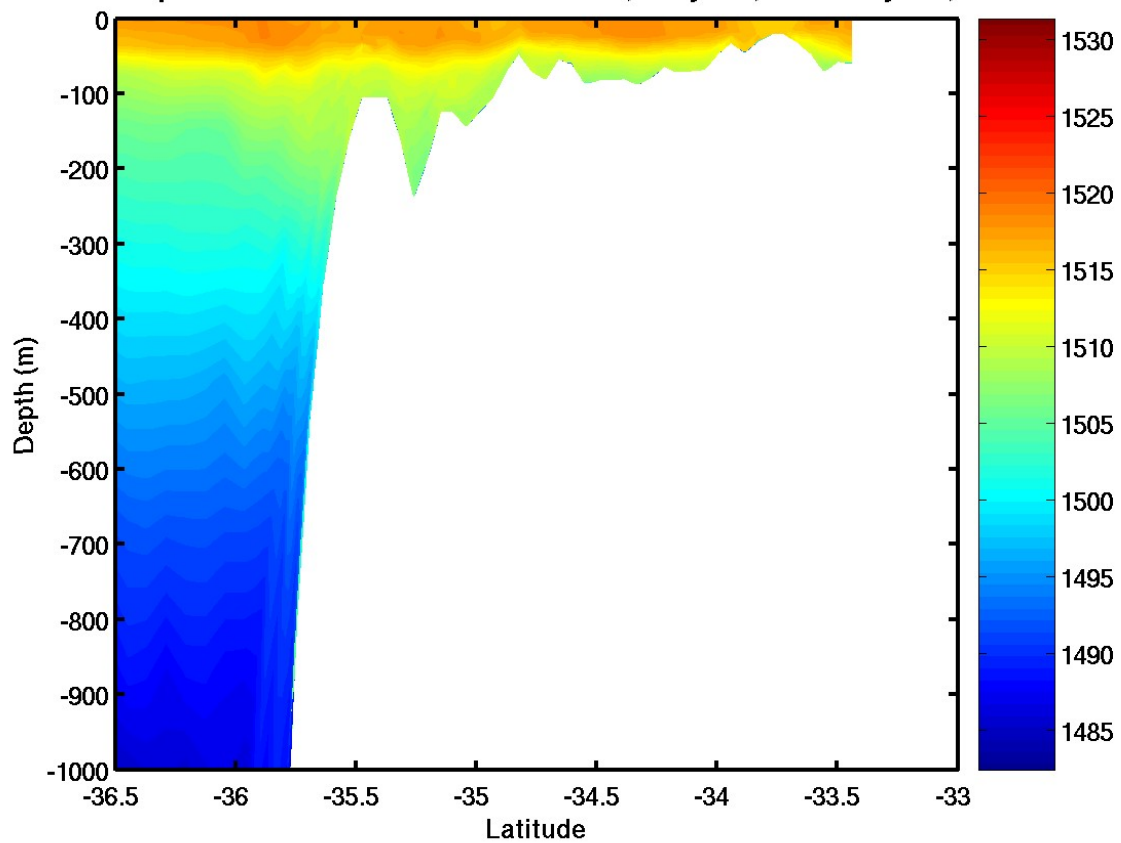


Figure 6.4d. Cross-section of sound speed (m s^{-1}) in the eastern Great Australian Bight (134.5°E) for daily wind Experiment 3 on day 45, January 15, 2000.

Delta C Cross-section at 134.5E, Day 45, January 15, 2000

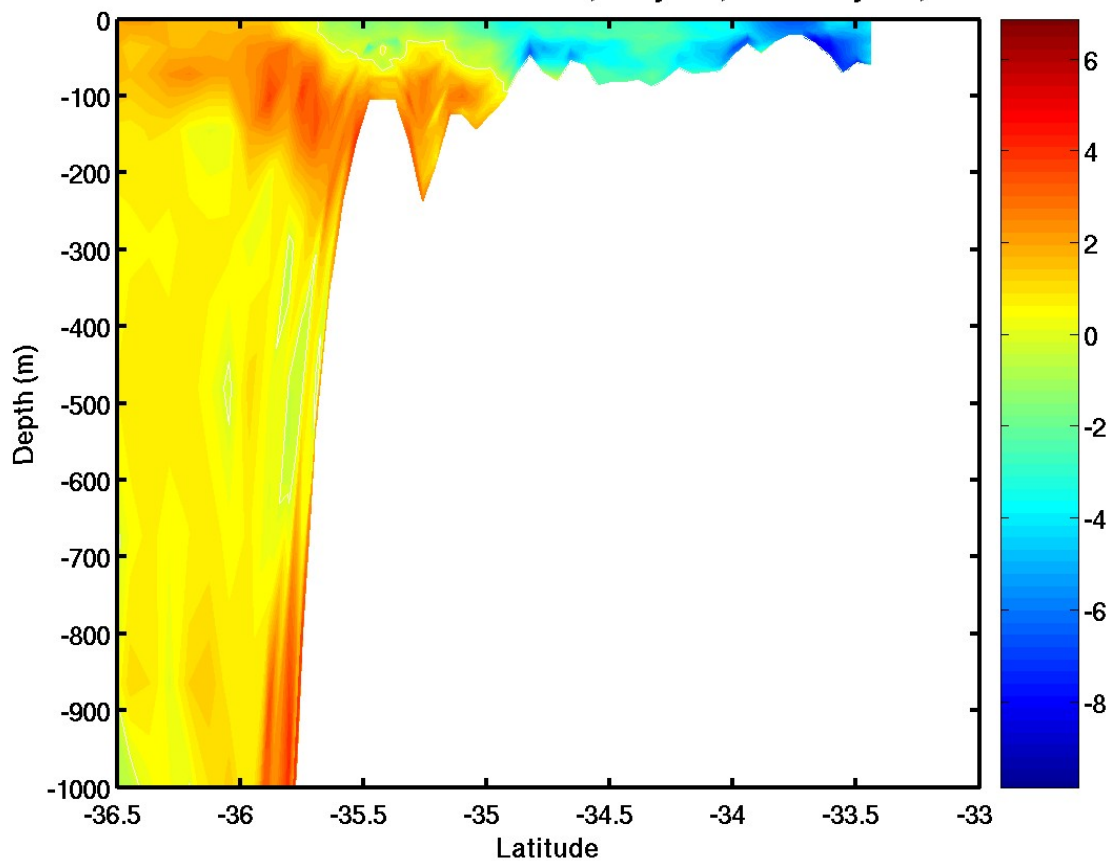


Figure 6.4e. Cross-section of sound speed change (m s^{-1}) in the eastern Great Australian Bight (134.5°E) for daily wind Experiment 3 on day 45, January 15, 2000. Sound speed change is the difference in sound speed between Day 0 and the current day.

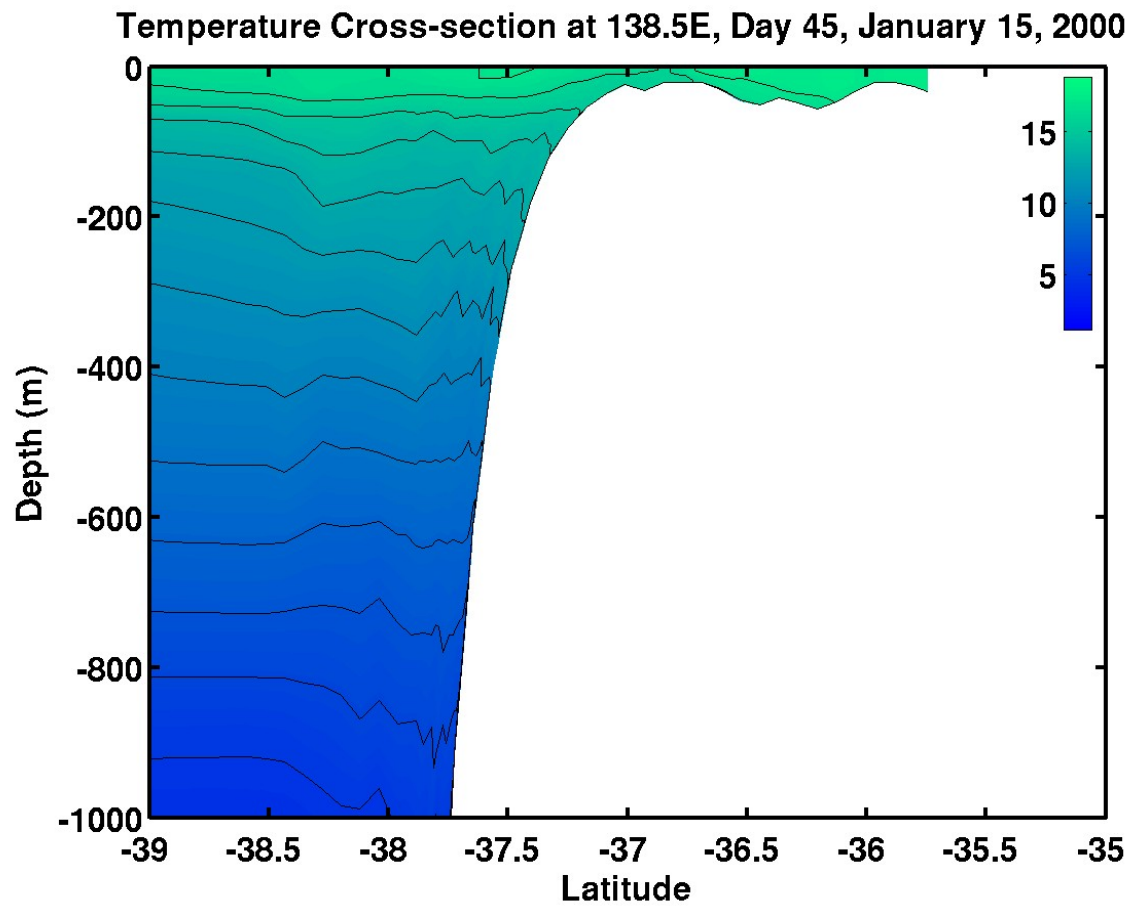


Figure 6.5a. Cross-section of temperature ($^{\circ}\text{C}$) at 138.5°E for daily wind Experiment 3 on day 45, January 15, 2000.

Sound Speed Cross-section at 138.5E, Day 45, January 15, 2000

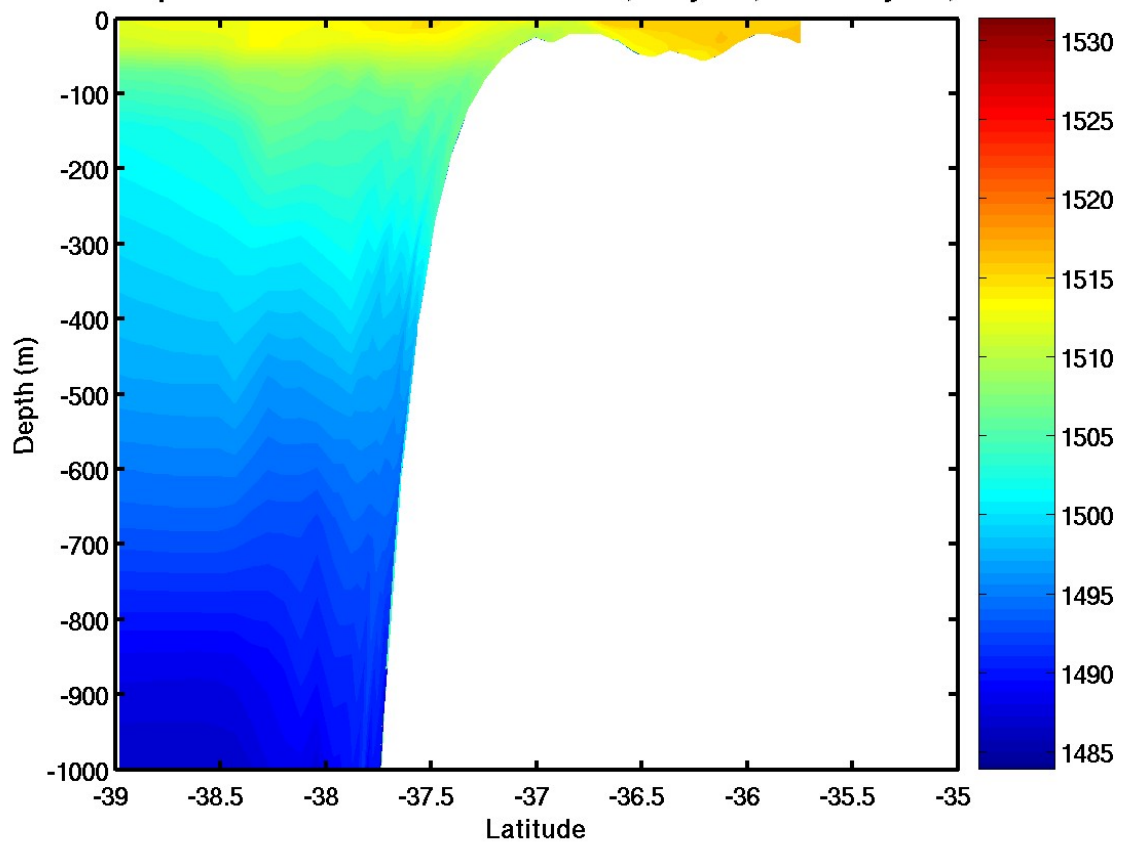


Figure 6.5b. Cross-section of sound speed (m s^{-1}) at 138.5°E for daily wind Experiment 3 on day 45, January 15, 2000.

Delta C Cross-section at 138.5E, Day 45, January 15, 2000

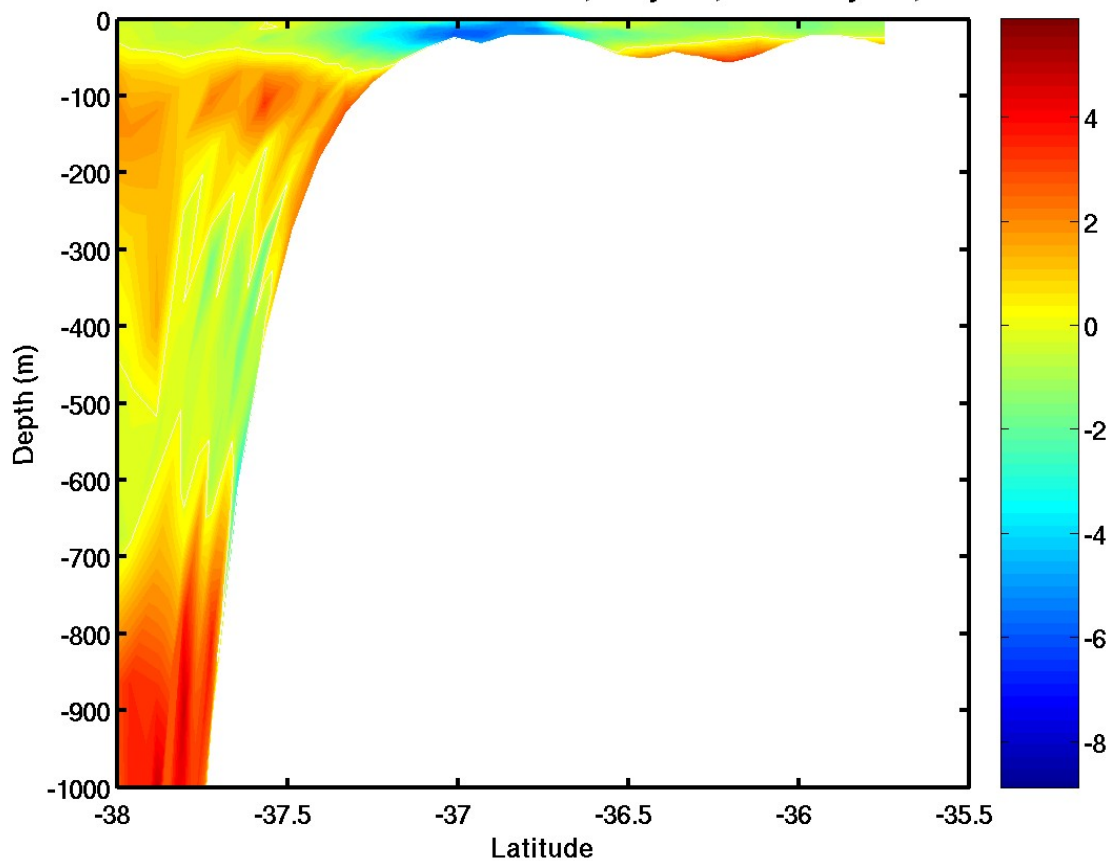


Figure 6.5c. Cross-section of sound speed change (m s^{-1}) at 138.5°E for daily wind Experiment 3 on day 45, January 15, 2000. Sound speed change is the difference in sound speed between Day 0 and the current day.

THIS PAGE INTENTIONALLY LEFT BLANK

INITIAL DISTRIBUTION LIST

1. Defense Technical Information Center
Ft. Belvoir, VA
2. Dudley Knox Library
Naval Postgraduate School
Monterey, CA
3. Professor Mary Batteen
Oceanography Department
Naval Postgraduate School
Monterey, CA
4. Professor Emeritus R. T. Williams
Meteorology Department
Naval Postgraduate School
Monterey, CA
5. Assistant Professor Timour Radko
Oceanography Department
Naval Postgraduate School
Monterey, CA
6. Research Associate Professor Robin Tokmakian
Oceanography Department
Naval Postgraduate School
Monterey, CA
7. CDR Henry Jones
Oceanography Department
United States Naval Academy
Annapolis, MD
8. Arlene Guest
Oceanography Department
Naval Postgraduate School
Monterey, CA
9. Mike Cook
Oceanography Department
Naval Postgraduate School
Monterey, CA

10. Bob Creasey
Meteorology Department
Naval Postgraduate School
Monterey, CA
11. Ed Elizondo
Naval Oceanographic Office
Stennis Space Center, MS
12. Bruce Mackenzie
Naval Oceanographic Office
Stennis Space Center, MS